Technical Report Documentation Page

1. Report No.	2. Government Accession No.	3. Recipient's Catalog No.
TX-99/4925-1		

4. Title and Subtitle	5. Report Date
ANALYSIS OF FIELD MONITORING DATA OF CRC PAVEMENTS CONSTRUCTED WITH GRADE 70 STEEL	March 1999
	6. Performing Organization Code

7. Author(s)	8. Performing Organization Report No.
Dan G. Zollinger, Andrew McKneely, Joshua Murphy, and Tianxi Tang	Report 4925-1

9. Performing Organization Name and Address	10. Work Unit No. (TRAIS)
Texas Transportation Institute Texas A&M University System College Station, Texas 77843-3135	11. Contract or Grant No. Project No. 7-4925

12. Sponsoring Agency Name and Address	13. Type of Report and Period Covered
Texas Department of Transportation Research and Technology Transfer Office P. O. Box 5080 Austin, Texas 78763-5080	Research: January 1998 - August 1998
	14. Sponsoring Agency Code

15. Supplementary Notes

Research performed in cooperation with the Texas Department of Transportation.
Research Project Title: Evaluation of Grade 70 Steel

16. Abstract

This report addresses important factors associated with the design of steel reinforcement in terms of layer configuration, bond characteristic, climatic affect, and others relative to an assessment of the suitability of the CRCP 8 program to represent and predict steel stresses in CRC pavement systems. It was necessary to instrument an actual section of CRC pavement for concrete and steel strains as they fluctuated under climatic and seasonal changes. The steel rebars were instrumented in a manner that would limit disturbance of the bond between the steel and the concrete, yet allow for precise measurements of the steel strain at various distances from the crack face. Other field sections containing Grade 70 steel were also included in this study. Crack spacing and crack width data were collected and reported.

In light of this emphasis, the researchers recognized that a key aspect of the steel design considerations is how important parameters—such as the steel surface area, degree of bond, the grade of steel, and the amount of steel—relate to the maximum opening transverse cracks in the pavement may attain over the design life of the pavement. Inherent in configuring the reinforcement in CRC pavement to perform at a adequate level below its yield limit is the maintenance of the transverse crack widths below specified levels to insure adequate stiffness at the transverse cracks. Crack width data varied as a function of the distance from the pavement surface, and it was noted in the report that the vertical position of the steel within the slab affects this variation and consequently should be a consideration in determining the vertical position of the reinforcing layer in construction.

17. Key Words	18. Distribution Statement
Concrete, Performance, Reinforcing Steel, Mechanistic Design, Crack Spacing, Crack Width	No restrictions. This document is available to the public through NTIS: National Technical Information Service 5285 Port Royal Road Springfield, Virginia 22161

19. Security Classif.(of this report)	20. Security Classif.(of this page)	21. No. of Pages	22. Price
Unclassified	Unclassified	311	

Form DOT F 1700.7 (8-72) **Reproduction of completed page authorized**

ANALYSIS OF FIELD MONITORING DATA OF CRC PAVEMENTS CONSTRUCTED WITH GRADE 70 STEEL

by

Dan G. Zollinger
Associate Research Engineer
Texas Transportation Institute

Andrew McKneely
Texas Transportation Institute

Joshua Murphy
Texas Transportation Institute

and

Tianxi Tang
Assistant Research Engineer
Texas Transportation Institute

Report 4925-1
Project Number 7-4925
Research Project Title: Evaluation of Grade 70 Steel

March 1999

TEXAS TRANSPORTATION INSTITUTE
The Texas A&M University System
College Station, Texas 77843-3135

IMPLEMENTATION RECOMMENDATIONS

The results of this project have resulted in correction factors to be applied to the results of the CRCP 8 design program relative to steel stresses and crack widths. The findings have indicated that use of the CRCP 8 program for design purposes is very promising and that future updates of the program code in terms of improved characterization creep and drying shrinkage models is highly encouraged. Improvements of this nature will advance the overall utility of the program for use in project design and should eliminate the need to apply correction factors to the program results.

DISCLAIMER

The contents of this report reflect the views of the authors who are responsible for the facts and the accuracy of the data presented herein. The contents do not necessarily reflect the official view or policies of the Texas Department of Transportation (TxDOT). The report does not constitute a standard, specification, or regulation, nor is it intended for construction, bidding, or permit purposes. The engineer in charge of this project was Dan G. Zollinger, P.E. #67129.

ACKNOWLEDGMENTS

Research findings presented in this report are a result of a project carried out at the Texas Transportation Institute (TTI), Texas A&M University. The authors would like to thank the staff of the Texas Department of Transportation for their support throughout this study.

TABLE OF CONTENTS

TABLE OF CONTENTS (Continued)

LIST OF FIGURES

LIST OF FIGURES (Continued)

LIST OF FIGURES (Continued)

LIST OF FIGURES (Continued)

LIST OF FIGURES (Continued)

LIST OF FIGURES (Continued)

LIST OF FIGURES (Continued)

LIST OF FIGURES (Continued)

LIST OF FIGURES (Continued)

LIST OF FIGURES (Continued)

LIST OF FIGURES (Continued)

LIST OF FIGURES (Continued)

LIST OF FIGURES (Continued)

LIST OF FIGURES (Continued)

LIST OF FIGURES (Continued)

LIST OF FIGURES (Continued)

LIST OF FIGURES (Continued)

LIST OF TABLES

CHAPTER 1
PROJECT BACKGROUND AND DEVELOPMENT

The purpose of this report is to provide background data, analysis, and information relative to the use and design of Grade 70 reinforcing steel configured in a single mat for the construction of continuously reinforced concrete (CRC) pavement. In order to develop a basis for this report, a CRC pavement test section was established on I-45 in North Central Houston near the FM 1960 interchange to establish a database of field-measured concrete and steel strains and movements in which to analyze relative to the identification and delineation of findings regarding the use of Grade 70 reinforcement. This report includes: 1) a brief theoretical discussion of the cracking behavior of CRC pavement in terms of environmentally and load-induced concrete and steel strains, 2) a description of the available analysis tools applicable to the behavior of CRC pavement systems, 3) an instrumented test site, 4) collected data categories, 5) an analysis derived from the collected data. Verification of the available analytical models is accommodated through a variety of comparisons to the typical responses that characterize the structural behavior of CRC pavement systems.

CRC pavement, widely used in the Houston District, ideally should develop a transverse crack pattern that manifests average crack spacings and crack widths within certain performance limits. Although structural performance limits for CRC pavement with respect to crack spacing have been well established and delineated for several years [1,2] performance limits with respect to the width of the transverse cracks have not, particularly in terms of structural design criteria. The consequence of this negligence is reflected in the lack of attention to crack width limits and their relationship to assured levels of load transfer efficiency as reflected in current versions of the *AASHTO Design Guide* and other design procedures for CRC pavements. Nonetheless, one of the purposes of longitudinal reinforcing steel in CRC Pavement is to hold the widths of the transverse cracks within a certain range. Over the history of the development of the use of CRC pavement in the Houston District, performance limits relative to crack spacing have been emphasized and included in the design criteria and, to some extent, the factors which affect the development of the ultimate crack pattern. The percentage of steel reinforcement, bonding area

between the reinforcing steel and the volume of concrete (q), coarse aggregate type, weather conditions at the time of construction, and the degree of bond between the steel and the concrete have been identified as the key factors that affect the characteristics of the cracking pattern (i.e., the average crack spacing and crack width) and the first two are under the control of the design engineer towards meeting the criteria of the design.

Underlying the design engineer's choices of the controllable cracking factors, is the selection of steel grade. The grade is selected to insure that the stress levels in the reinforcing steel are at an adequate level below the yield limit which is assured, according to design practice in the Houston District, by keeping the calculated stresses less than a limit of 75 percent of the yield strength. Although the basis of the 75 percent limit is not clearly supported, the same limit is used in the *AASHTO Design Guide*. Discussion and definition of this level below the yield limit it provided in Chapter 5. The greatest strains in the reinforcing steel typically occur at the locations of the transverse cracks. It is generally accepted that the performance of CRC pavement would be compromised if the steel stress were allowed to exceed the yield strength at these locations. Yielding of the steel most likely would result in excessive crack widths causing loss of pavement stiffness and load transfer across the transverse cracks which would dramatically affect performance. Unfortunately, this is the extent most CRC pavement design procedures consider the effect of crack width in the design process. Nonetheless, in terms of design and performance, it is important to understand how the steel reinforcement parameters (percent steel, bond area, yield strength, etc.) relate to the development of the crack pattern.

These parameters were of particular interest in this study with respect to the field experience that was gained from the Grade 70 CRC pavement sections placed in I-45 (previously noted) and on SH 249 in Houston. The SH 249 section consisted of pavement sections containing Grade 60 steel (at p = 0.67 percent steel and q = 0.036) and sections containing Grade 70 steel (at p = 0.49 percent steel and q = 0.026). Data collected from these sections since construction comparing the pavement crack patterns are shown in Figure 1.1 (along with average crack spacing and standard deviation data) at various ages after construction. This pavement, located near the Willow Brook Mall on SH 249 near Tomball, Texas, was constructed 13 inches thick during the last week of September 1996 and was actually the first project in the Houston

District to incorporate Grade 70 steel. Grade 70 steel rebars in a single mat were used in place of Grade 60 steel rebars that were in a two-layer configuration. The accumulative crack spacing shown in Figure 1.1 (at various ages) is based upon crack spacings between adjacent consecutive cracks. The crack pattern, as characterized in this figure, is more favorably distributed in the Grade 60 section than in the Grade 70 section because the crack pattern is not as widely spaced. This trend was still evident 15 months after construction. As noted in Figure 1.1, the average crack spacing of the Grade 60 steel section was 5.2 ft, which was within the allowable range of the *AASHTO Guide* - 3.5 ft to 8 ft - but the average crack spacing of the Grade 70 steel section was 9.9 ft, as surveyed in December 1997, was far beyond the upper limit of 8 ft. However in terms of cluster cracking, the Grade 70 section showed better characteristics than the Grade 60 section if consideration is given to the spacing between groups of two adjacent consecutive cracks and groups of five adjacent consecutive cracks. A comparison of this nature, shown in Figure 1.2, serves as a measure of cluster cracking which can be derived from distributions made from these groupings. Cluster cracking is the occurrence of adjacent or consecutive groups of closely and widely spaced transverse cracks and is considered to be an undesirable feature in the crack pattern and is characterized in terms of the cluster ratio (CR) as:

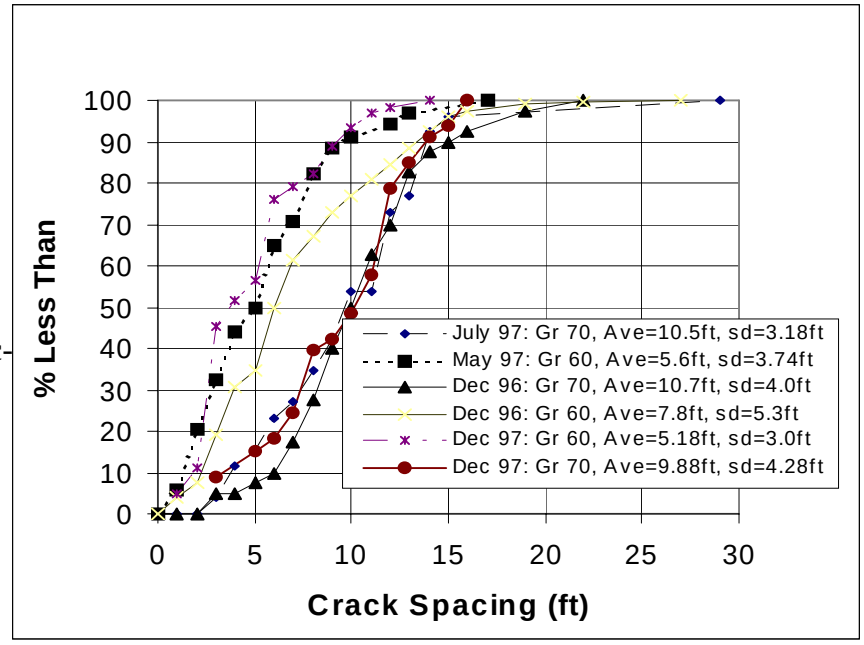

Figure 1.1 CRC Pavement Crack Spacing Distribution - SH 249, Houston District Grade 60 and 70 Sections.

$$CR = \left[1 - (NC - 1) * \frac{X_1}{X_2}\right] * 100$$

where X_1 is the cracking interval at a given % less than and X_2 is the cracking distance over a given number of consecutive cracks at a given % less than and NC is a the number of consecutive cracks considered at a time (which was 5 in this case). A perfect crack pattern would displace 0 percent clustering but 20 percent clustering should be considered acceptable [27]. Although the details associated with the development and application of the cluster cracking concept are explained elsewhere [27], the Grade 60 CRC sections indicated 31 percent clustering while the Grade 70 section showed only 10 percent. It should be pointed out, the lower clustering manifest by the Grade 70 pavement section has less to do with the grade of steel and more to do with the use of one layer of steel reinforcement and the variability of the curing process.

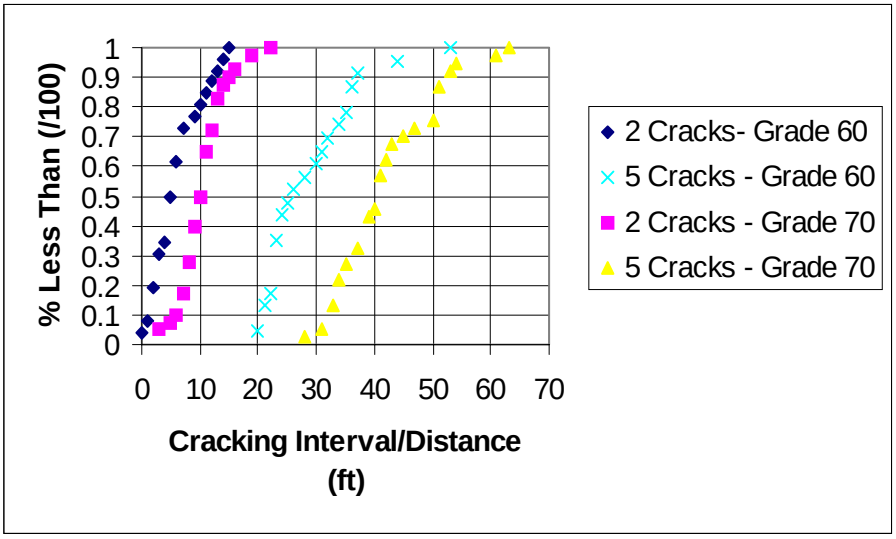

Figure 1.2 Cluster Cracking: Grade 60 and 70, SH 249.

Although all the crack widths on SH 249 sample sections were below the limit established by the AASHTO Guide, the Grade 70 steel section presented larger average crack widths. An average crack width of 19.8 mils in the Grade 70 steel section was observed in January 1997 [26], much larger than the average crack spacing of 6.2 mils in the Grade 60 steel section observed at the same time. Crack width distribution data surveyed in July 97 comparing both Grade 60 and Grade 70 steel sections on 249 (Figures 1.3 and 1.4) indicated nearly similar average crack widths but very different crack width distributions as noted in the figures. The standard deviation of the Grade 70 was calculated at 6.6 mils and the Grade 60 was 3.4 mils. As will be noted in Chapter 5, crack width (and crack width deviation) has an important effect on CRC pavement performance.

The trends in crack width between the Grade 60 and Grade 70 sections continued to be manifest in later surveys (Figure 1.5) with the Grade 70 section cracks developing greater widths. In addition to the wider crack trends, the Grade 70 steel section also manifests noticeably more minor severity spalling at the transverse cracks. This difference may be due to the wider crack widths displayed by the Grade 70 section. Again, the differences manifest in crack spacing, crack widths, and crack spalling between the Grade 60 and the Grade 70 sections on SH 249 have less to do with the grade of the reinforcing steel and more to do with the q factor (or the amount of steel).

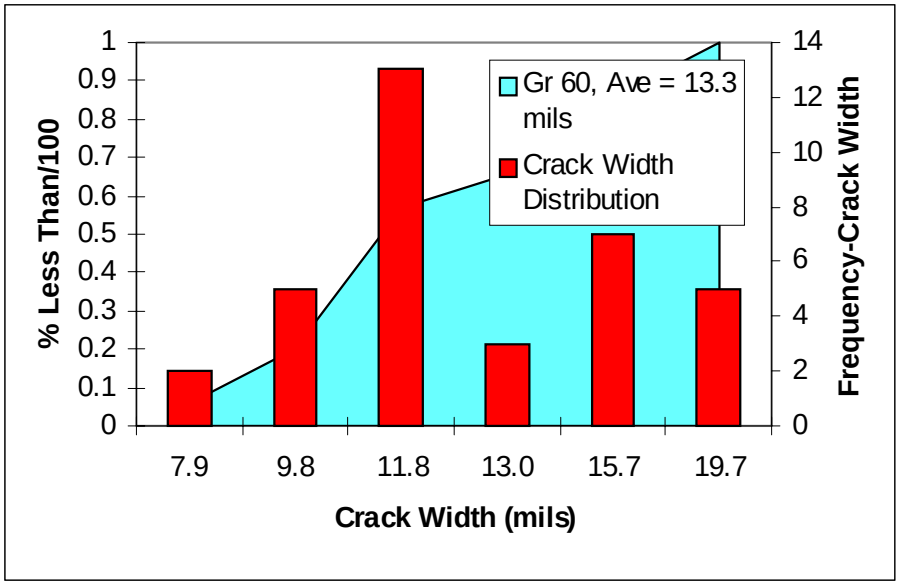

Figure 1.3 Crack Width Distributions for the Grade 60 SH 249 Pavement Section - July 97.

The use of Grade 70 steel appears to have some merit and the intent of this report is to examine the feasibility of using this grade of reinforcing steel in CRC pavement (particularly in

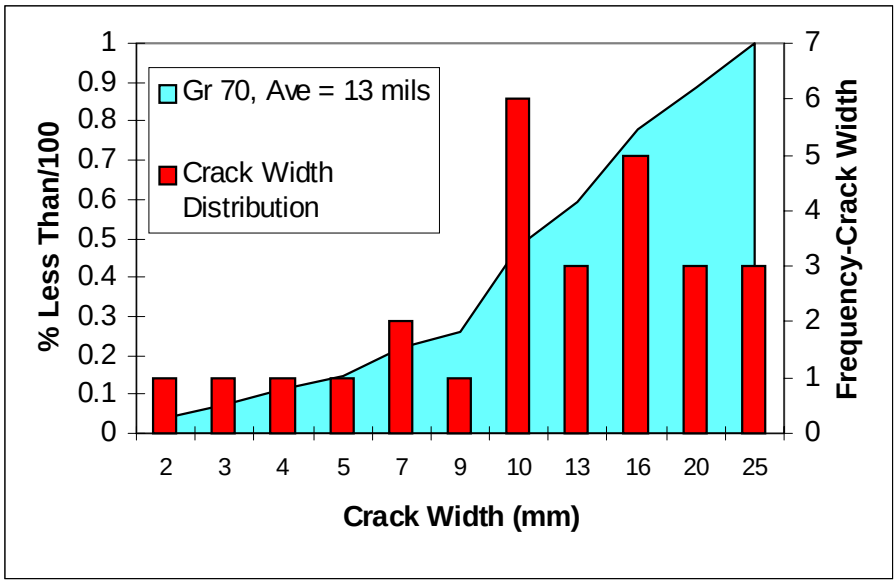

Figure 1.4 Crack Width Distributions for the Grade 70 SH 249 Pavement Section - August 97.

a single layer configuration). It is important to point out that key findings can be derived from the performance observations of the SH 249 Grade 70 section - primarily that q factor and weather conditions at the time of construction must be carefully considered in the design and construction of CRC pavement systems. This point will be further emphasized in later portions of this report. Further analysis delving to greater depths into the behavior noted above is pursued in the subsequent chapters with the aid of available response models applicable to CRC pavement performance. An important aspect to be revealed and elaborated in this analysis will be the sensitivity of the q factor and construction weather conditions to crack width and their combined effect on design requirements relative to the selected grade of reinforcing steel.

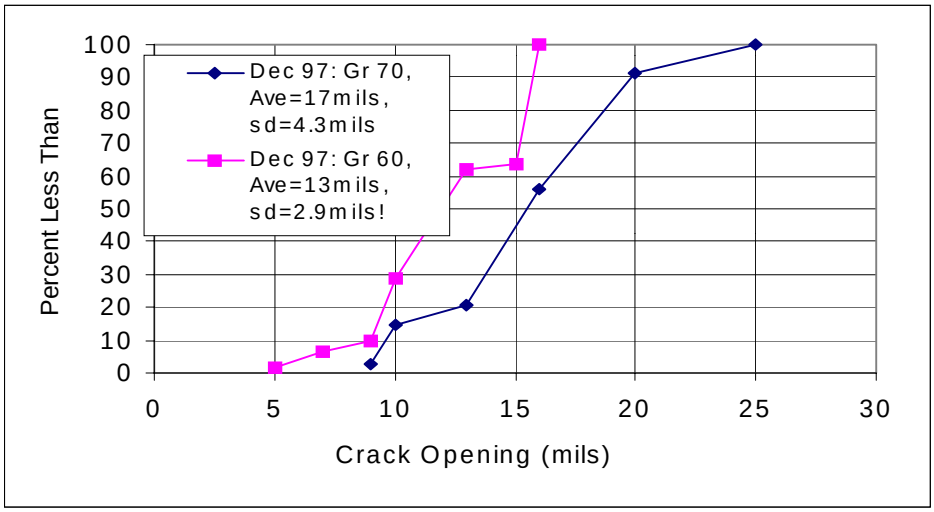

Figure 1.5 CRC Pavement Crack Width Distribution - SH 249, Houston District Grade 60 and 70 Sections.

Project Objectives

The objectives associated with this study are as follows:

1. Instrument Grade 70 longitudinal reinforcing bars, place them in actual CRC pavements, and monitor the strains in the bars during the placement and hardening of the concrete for selected days during the development of the cracking pattern.

2. Conduct an evaluation of the behavior of the instrumented sections based upon analysis of the collected test data using the CRCP 8 computer program. Assess the suitability of the CRCP 8 program to predict steel and other strains related to the structural behavior of CRC pavement systems.

3. Summarize findings from the analysis relative to the use of Grade 70 reinforcing steel in the construction of CRC pavements in the Houston District. The results of this investigation will be the provision of data and information relative to the best use of Grade 70 steel in CRC pavement construction.

Analysis Approach and Report Organization

The approach taken to the analysis of the monitoring data involved several steps. The first step consisted of downloading and reducing of the raw data. Much of the strain data was recorded electronically in milivolts which had to be converted empirically to microstrain. After the data was downloaded, it was stored in categories based on type of strain (whether concrete or steel strain) and the location of the strain gage. Concrete strength, temperature, and moisture data were also stored as separate categories. Weather data was also recorded as a separate data category. The next step was to place data in easily recognizable formats that vary primarily as a function of time. For applicable strains, the average value with time was shown with daily maximum and minimum values shown as upper and lower limits.

The third step involved the selection of available tools or models to represent the structural behavior of CRC pavement in a design process. The CRCP 8 program was originally included for evaluation purposes as stated in the objectives. Nonetheless, principle among the tools for this purpose are the CRCP 8 and the TTICRCP programs which are computerized formats of crack width, steel stress, concrete stress, and crack spacing models. The TTICRCP program was included for comparative purposes and to assist in the evaluation of the CRCP 8 program since it includes a bond slip function that can be easily calibrated from measured bond-slip strain data. Where the CRCP 8 program is more focused on a design emphasis, the TTICRCP program is more focused on an analysis emphasis and is also more suited for calibration to field data. The next step involved developing the input data for each computer model from the prepared field strains and test data. The last step focused on simulation of specific days and site conditions relative to the I-45 test conditions.

This report is organized into five chapters. Chapter 1 focuses on the background information relative to this study. Chapter 2 provides in-depth discussion of the structural

characteristics of CRC pavement and the factors associated with development of the crack pattern. This discussion also provides a description of the models included in the computer programs previously noted. Chapter 3 provides a description of the test site location and instrumentation along with a description of the collected test data which is listed in the appendices of this report. Chapter 4 consists of a discussion of the analysis of the data that includes an evaluation of the CRCP 8 program. Several categories of data considered in this chapter are: steel stress and strain, concrete stress and strain, slab cracking, steel-concrete interaction, concrete strength data, and others. The fifth chapter elaborates on the implications of Chapter 4 in terms of crack width limits for design purposes and steel stress variability on the selection of steel grade for construction purposes.

CHAPTER 2
CRACKING BEHAVIOR OF CRC PAVEMENTS

There are many reasons why the cracking behavior factors associated with CRC pavements affect the nature of the transverse crack pattern that forms initially at early concrete pavement ages and continues for several months thereafter. Many factors have been identified relative to the formation of the crack pattern and are discussed in some detail in this chapter.

Cracking Restraint Factors

The primary factor affecting transverse crack development in CRC pavement systems is resistence or restraint to change of length of the paved concrete segment. The change in length is the result of a temperature change in the concrete material and shrinkage due to the loss of moisture during the concrete hardening and maturing stages. The restraint to cracking can be characterized and itemized in two forms: internal and external.

Internal Restraints [1]:

- Reinforcing Steel: amount (i.e., percent), surface area, deformations, coatings (corrosion protection), connection to transverse steel, yield strength or grade, coefficient of thermal expansion, creep characteristics.
- Concrete: thickness, strength, modulus of elasticity, shrinkage, creep, coefficient of thermal expansion.
- Bond characteristics between the reinforcing steel and the concrete.

External Restraints [1]:

- Bonding or friction between the slab and the subbase and\or interlayer.
- Mechanical tie to adjacent lanes.

Construction factors also have an influence on cracking restraint. This influence affects the degree that either the internal or the external restraints are effective in the cracking process (i.e., the lapping of reinforcement may effect bond-slip relationships). The construction factors work interactively with prevailing environmental conditions at the time of construction.

Consequently, the following should be considered relative to the construction of CRC pavements:

- Time of placement (fall or winter), and
- Temperature at the time of placement.

If the transverse cracks are spaced at adequate and uniform intervals, the potential for widened cracks and punch-out development, which is the primary distress type in CRC pavement, is reduced. Based on the above factors, one would expect that CRC pavements which develop crack patterns with adequate intervals would typically show the best performance. Most of the failures in CRC pavements occur because of either widened transverse cracks or closely spaced transverse cracks. However, there are instances where good performance has been achieved in CRC pavements with average crack intervals of less than 2 ft but excellent support conditions have also accompanied these pavements. Several researchers have suggested that the crack pattern should consist of cracks displaying crack widths small enough to minimize the entrance of surface water and maintain adequate load transfer through aggregate interlock [1,2, 10]. Many naturally occurring CRC pavement crack patterns can frequently display average crack spacings that fall within the preferred range of 3.5 to 8 ft, but the typical variability associated with them can result in a number of cracks spaced less than 3.5 ft [1-6].

Crack development may be thought of in two phases as initial crack development and secondary crack development. Initial cracking occurs rapidly and will be equal to or less than 4.4 ℓ where ℓ is the radius of relative stiffness of the pavement surface layer. Secondary cracking results in a stable crack pattern and is a function of the factors discussed above.

In CRC pavements, the concrete is typically subjected to non-uniform/non-linear (from top to bottom) volumetric changes that result in stress development due to temperature, moisture, and shrinkage effects. The resulting stresses caused by these effects are relieved by the formation of transverse cracks. Figure 2.1(a) shows a typical CRC pavement section between two adjacent transverse cracks [1]. When the pavement experiences a change in temperature or a change in drying shrinkage, the concrete movement in the longitudinal direction is restrained by the longitudinal steel and subbase friction.

The reinforcing steel which is embedded in the concrete behaves stress and strain-wise in a different manner than the concrete. This behavior results in interfacial shear stress (so-called bond stress) at the interface between the steel bar surface and the concrete. The magnitude of the bond stress depends on the concrete strength and mechanical shape of the bearing face of the ribs on the longitudinal bar. These factors have been the subject of recent improvements in the design of reinforcing steel rib patterns [7]. Because of the anchor and lug characteristics of the reinforcing promoting strong bond between the concrete and the embedded steel, a bond stress will develop. Figure 2.1(b) shows a typical bond stress distribution between concrete and steel [1] over a segment of cracked CRC pavement.

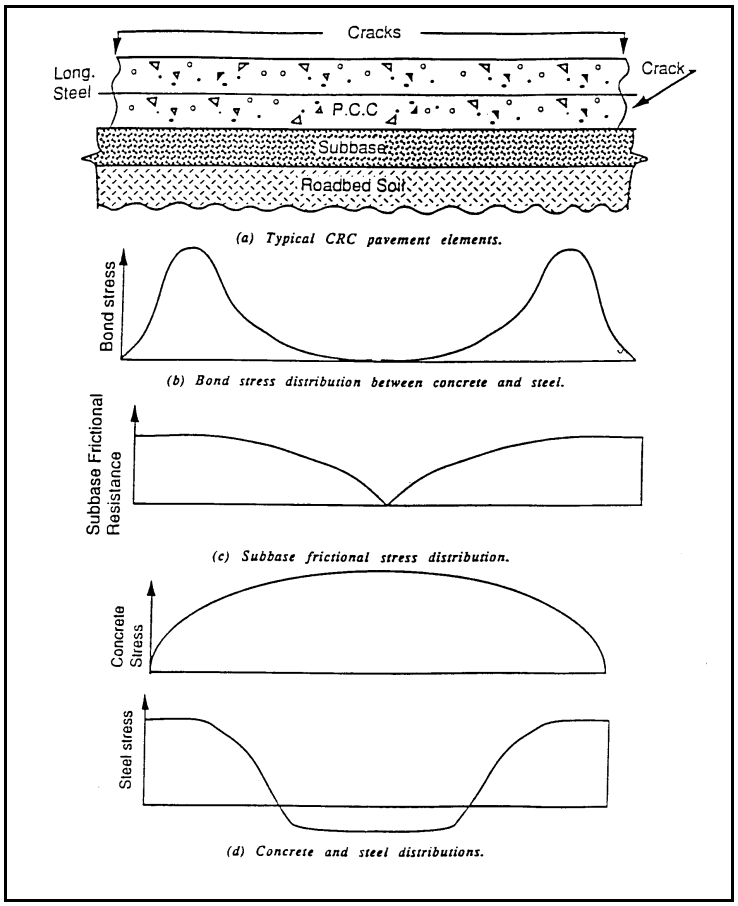

Figure 2.1 CRC Pavement Elements and Distributions of Various Stresses [1].

The direction of frictional resistance provided by the subbase is opposite to that of concrete displacement. Subbase friction depends upon the subbase material type and when the concrete contracts, the subbase friction and the steel resist the concrete displacement, thereby increasing the level of concrete tensile stress which contributes to the resultant crack spacing. Figure 2.1(c) shows a typical distribution of frictional resistance [1]. The resistance to the concrete contraction through bond stress and subbase friction causes the concrete tensile stress to build up and the concrete displacement to be reduced. Figure 2.1(d) illustrates the concrete and steel stress distribution along the CRC pavement slab [1]. If the resultant concrete stress exceeds

the concrete tensile strength, a crack will develop. Past performance data has indicated that dense graded asphaltic concrete interlayer provides the most desirable subbase frictional characteristics.

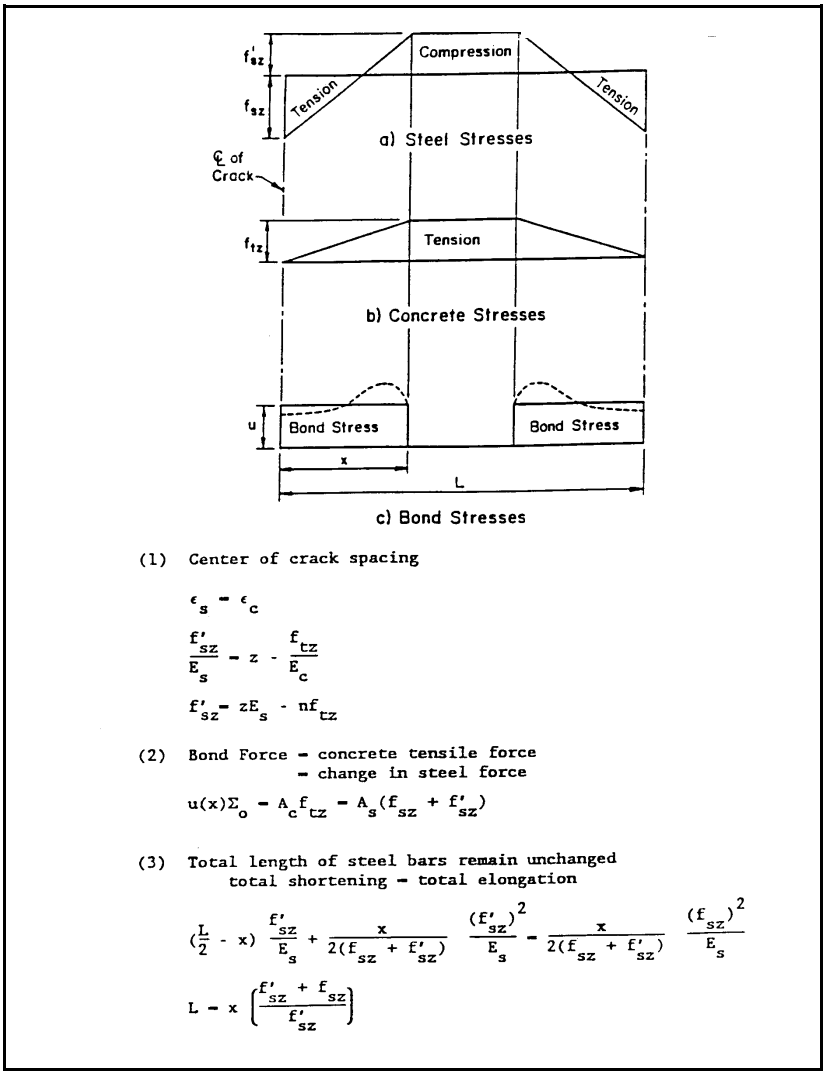

Figure 2.2 Stress Distribution between Cracks of CRC Member Subject to Shrinkage [2,9].

Cracking in CRC Pavements

As noted above, several factors have been identified which affect how cracks form in CRC pavements. Initial cracking in CRC pavements may be due to environmentally induced temperature and moisture gradients related to slab curling and warping. Field observations of initial or primary cracks suggest that these cracks form within the first 3-7 days after placement of the concrete. Secondary cracks form due to the continuity of reinforcement (i.e., internal restraint) which inhibits free movement of the concrete matrix after the formation of primary cracks. Stresses that develop at this stage are referred to as restraint stresses. According to data recently obtained in Texas [8], primary cracks constitute the rapidly evolving crack pattern at intervals greater than approximately 4.4 ℓ (radius of relative stiffness) or

less which form the beginning secondary crack intervals with respect to the development of a stable cracking pattern.

A significant contribution was made by Vetter [9], who developed relationships for crack spacing in reinforced concrete illustrated in stress diagrams for drying shrinkage and temperature drop shown in Figures 2.2 and 2.3 (L is the crack spacing and u is the bond stress). After the formation of the first crack due to restrained shrinkage, a new state of equilibrium and strain compatibility develops. The restrained shrinkage is accommodated by the crack, by the bond slip, and by the uncracked concrete. The following equations for average crack spacing are derived from Vetter's basic equations [9], Vetter assumed that secondary cracks form within this initial crack interval. A formula for the average crack spacing based on shrinkage is as shown below:

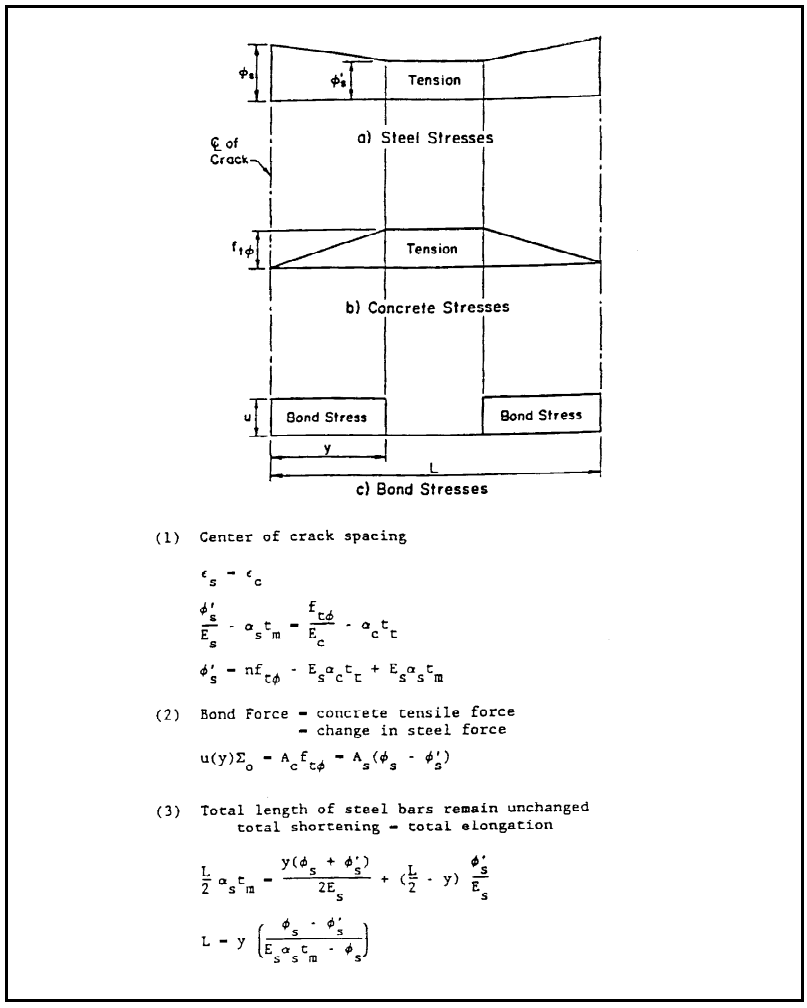

Figure 2.3 Stress Distribution between Cracks of CRC Member Subject to Temperature Drop [2,9].

$$L = f_{tz}^2/\{Q \cdot n \cdot p \cdot u(z \cdot E_c - f_{tz})\} \qquad (2.1)$$

where

L = crack spacing (L)

f_{tz} = concrete tension stress due to shrinkage strain at the center of crack (F/L^2)

Q = ratio of bond area to concrete volume x p = 4*p/db*p = q*p

u = average bond stress (F/L^2)

p = percent reinforcement

d_b = reinforcing bar diameter (L)

n = modular ratio (E_s/E_c)

E_c = elastic modulus of concrete (F/L^2)

z = drying shrinkage

A formula for the average crack spacing formula is also derived for temperature drop in a similar manner:

$$L = f_{t\varphi}^{\ 2}/\{Q \cdot n \cdot p \cdot u(\alpha_s t_m E_c - f_{t\varphi})\} \quad (2.2)$$

where

$f_{t\varphi}$ = concrete tension stress due to temperature drop at the center of the crack spacing (F/L^2)

α_s = coefficient of thermal expansion of steel (per °F)

A formula for the average crack spacing when both shrinkage and temperature drop occur simultaneously is later derived [9] by considering the combined stress diagram for the steel and concrete which is expressed in a simplified form as:

$$L = f_t^2/\{Q \cdot p \cdot u(E_s \alpha_s t_m + z \cdot E_s - n \cdot f_t)\} \quad (2.3)$$

where

f_t = concrete tension stress due to temperature drop at the center of the crack spacing (F/L^2

All the other terms are as defined in equations 2.1 and 2.2. Equation 2.3 indicates a close crack spacing may be obtained by a high bond stress. The same effect can also be obtained through increasing the percentage of reinforcement or using smaller diameter bars. These factors also combine to create small crack openings as well. Major factors that affect the crack pattern in terms of material, climatic, and pavement design factors are subsequently discussed.

Crack width and crack spacing are characteristic indicators of CRC pavement performance and are therefore important to predict. Although Zuk [28] developed a theoretical relationship between these two parameters as a function of steel percentage, concrete shrinkage, and

temperature coefficients, other parameters such as pavement age and depth of steel cover may also be important. Most of these are included in the Zuk expression for crack width:

$$cw = L(z + \alpha_c t_m) + \frac{f_t}{E_c}\left[L - \frac{f_t d_b}{4up}\right] \tag{2.4}$$

An important aspect of crack width characterization is the estimate of the variability which may develop due to the factors such as the concrete tensile strength and drying shrinkage. A form of the variance of crack width (cw) (Var[cw]) is shown below:

$$Var[cw] = \sum_i \left(\frac{\partial cw}{\partial X_i}\right)^2 Var[X_i] + \sum\sum \frac{\partial cw}{\partial X_j}\sigma_{X_j}\frac{\partial cw}{\partial X_k}\sigma_{X_k}$$

Table 2.1 Crack Width Variability Derivatives.

X_i	$\frac{\partial f_s}{\partial X_i}$
L	$z + \alpha_c t_m + f_t/E_c$
z	L
α_c	$L\ t_m$
t_m	$L\ \alpha_c$
f_t	$L/E_c - 2f_t d_b/(E_c 4up)$
E_c	$-f_t/(E_c)^2\{L - f_t d_b/(4up)\}$

where the derivatives of the crack width function (equation 2.4) are shown in Table 2.1. Using the variability in crack width, a crack width for design purposes can be defined relative to a normal deviate multiple of the crack width standard deviation. Assuming a normal distribution, the design crack width (cw_{des}) associated with the crack width variance (Var(cw)) is:

$$cw_{des} = \overline{cw} + Z_r\sqrt{Var(cw)} \tag{2.5}$$

where

Z_r = value of the variate corresponding to a given level of reliability

$\overline{cw}$ = mean crack width

cw_{des} = crack width at a given level of reliability

Vetter also developed an expression for the stress in the steel reinforcement (f_s) of a continuously reinforced structure as:

$$f_s = f_t(\frac{1}{p}+n) + E_s(t(\alpha_s-\alpha_c) - z) \quad (2.6)$$

Although the effect of the subgrade friction is not considered in this expression, it does serve a useful purpose in describing how the relevant factors associated with the design of CRC pavement affect the variance of steel stress. The variability of the steel stress (Var[f_s]) can be formulated much in the same fashion as it was done for crack width:

$$Var[f_s] = \sum_i (\frac{\partial f_s}{\partial X_i})^2 Var[X_i] + \sum \sum \frac{\partial f_s}{\partial X_j} \sigma_{X_j} \frac{\partial f_s}{\partial X_k} \sigma_{X_k}$$

The derivatives can be defined relative to the maximum concrete temperature drop (t), the concrete coefficient of thermal expansion (CTE or α_c), and concrete shrinkage. The definitions of these derivatives are shown in Table 2.2.

Table 2.2 Steel Stress Variability Derivatives

X_i	$\frac{\partial f_s}{\partial X_i}$
z	$-E_s$
α_c	$-E_s\ t_m$

Now that the important design parameters and their relationship to the development of cracking in CRC pavements have been identified, important material and climatic characteristics can be discussed. An expression for the grade of the reinforcing steel could be formulated based on the mean value and the variability of the calculated stress in the steel:

$$SteelGrade \geq \overline{f_s} + Z_r\sqrt{Var(f_s)} \quad (2.7)$$

Concrete Characteristics

The primary constituents of concrete, mortar, and coarse aggregate, have coefficients of thermal expansion (CTE) relative to the makeup and nature of the materials with the CTE for concrete being a combination of the two constituents. Since a major portion of the concrete volume is coarse aggregate, the primary factor influencing the coefficient of thermal expansion of concrete appears to be the coarse aggregate type. However, the CTE of the paste is approximately double the CTE of the coarse aggregate. Of all the factors which may influence the development of the crack pattern, coarse aggregate type may be the most significant (a river gravel coarse aggregate may have a coefficient of thermal expansion of approximately 60 percent higher than that for a crushed limestone coarse aggregate). Figure 2.4 [1], indicates how the CTE of the coarse aggregate affects the CTE of the concrete. Thermal coefficient of expansion of concrete can influence the volumetric change due to a temperature change in the concrete. Thermal strains in concrete usually result from dissipation of the heat of hydration or cyclic changes in the ambient temperature. Figure 2.4 indicates, for practical purposes, that a linear relationship exists between the CTE of the aggregate and the CTE of the concrete. Table 2.3 gives the thermal coefficient values of different coarse aggregate types that were measured during a project conducted at the University of Texas at Austin [1]. This research and other similar studies have clearly indicated that as the siliceous gravel content decreases the thermal coefficient value decreases. It has also been shown that the effect of silica content in the

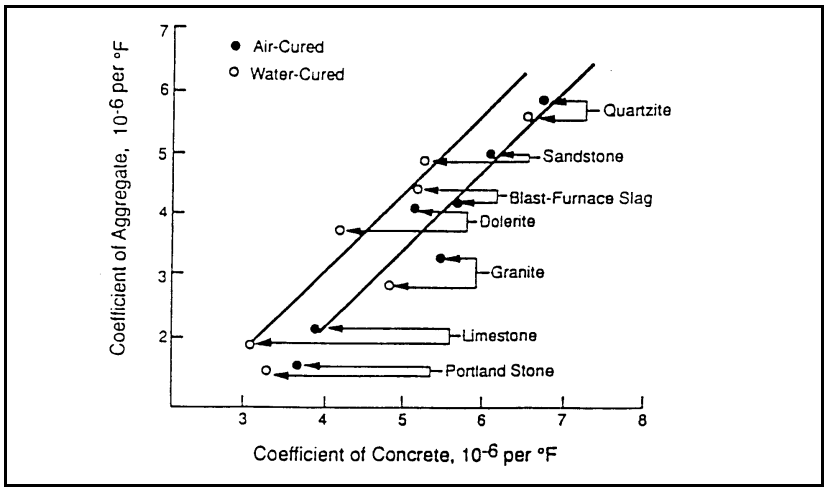

Figure 2.4 Influence of the Linear Coefficient of Thermal Expansion of Aggregate on the Coefficient of Thermal Expansion of Concrete [1].

aggregate on the CTE of the concrete is very significant. The greater the silica content of the aggregate the greater the CTE of the aggregate [1].

Table 2.3 Thermal Coefficient Values [1].

Aggregate Type	Thermal Coefficient (με/°F)
SRG (Siliceous River Gravel)	8.18
SRG-LS	6.15
Dolomite	5.90
Granite	5.74
LS-SRG	5.44
LS/LS-SRG*	4.84

*Blend of 50 % LS (limestone) and 50 % LS-SRG

Loss of moisture is another characteristic of concrete that is related to the environmental conditions at the time of construction. Loss of moisture can affect concrete in terms of strength gain and in terms of induced strain relative to drying shrinkage [8]. Drying shrinkage depends to a great extent upon the water cement ratio used to place the concrete pavement. Other factors are related to the degree of hydration, moisture diffusivity, and the method of curing (discussed later) used during the concrete hardening process. These factors, which are indirectly related to the strength of concrete, are also important to the degree of permeability and durability achieved by the concrete. In design, although the amount of drying shrinkage that concrete will ultimately achieve is difficult to predict, the degree of drying shrinkage has been correlated to the concrete strength [13].

Reinforcing Steel Characteristics

Steel is used in CRC pavement to develop the crack pattern because of high yield and tensile strength characteristics. Since steel exhibits these characteristics, it is used in CRC pavements to maintain crack widths below a certain limit. There are several pavement design variables related to steel bars which have significant effect on the cracking behavior of CRC pavements. They include such factors as percentage of longitudinal steel (p), longitudinal bar diameter (d_b), steel rib pattern characteristics, depth of cover and the number of layers of

longitudinal steel. Pavement engineers in some countries are placing extra steel to stiffen free edges to minimize punch-out development [14-17].

Percent of Longitudinal Steel

The reinforcement in CRC pavement causes a restraining effect to contraction strain which increases as the percentage of steel increases. Figure 2.5, shows a classic example of how decreased crack spacing is associated with increased steel percentages for a section of CRC pavement in Illinois [12]. In terms of crack spacing, steel percentages of 0.55 to 0.70 have provided suitable CRC pavement performance. Relative to practical limits, it has been reported that the average crack interval does not significantly decrease with steel amounts above 1 percent while average cracking intervals may greatly increase with steel amounts below 0.4 percent. As the percentage of longitudinal steel increases, the crack widths decrease, the aggregate interlock increases, the load transfer increases, and stiffness at the transverse cracks improves [1]. Both field observations and design theories confirm that crack width in CRC pavements decreases with an increase in percentage of longitudinal reinforcement [18]. However, this does not mean the same correlation may exist between crack spacing and crack width. Season of placement may override the effect of crack spacing on crack width.

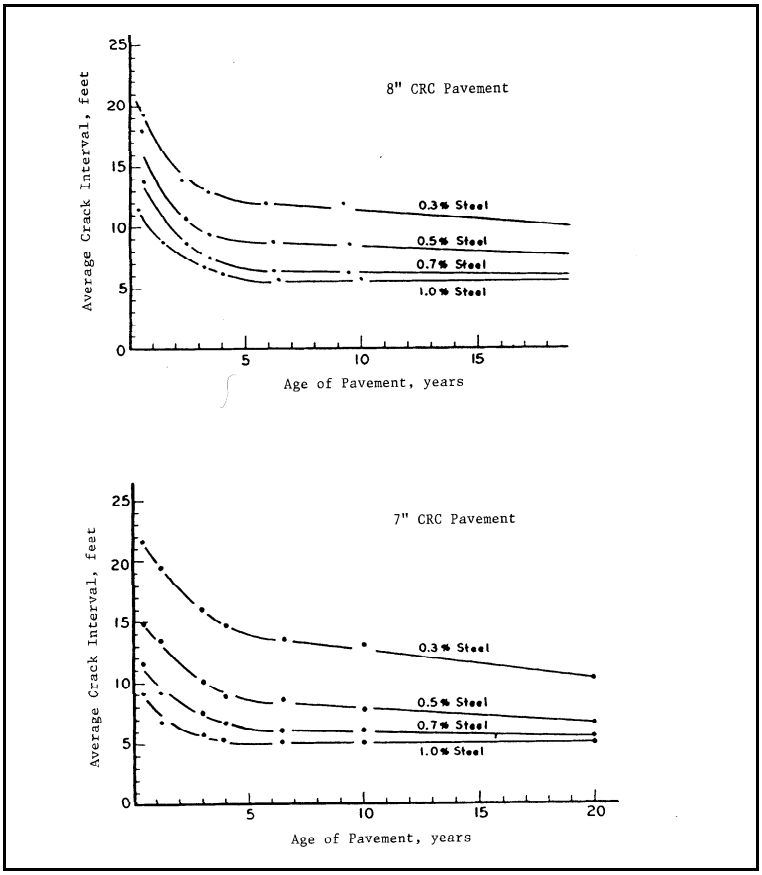

Figure 2.5 Change in Average Crack Interval Over Time for 7 and 8 Inch CRC Pavement [12].

Bar Size and Bond Characteristics

Bar size has an influence on crack development in that the restraint of the longitudinal steel depends on the bond area provided by the reinforcing bar. The development of concrete stress in CRC pavements results from the transfer of stress from steel to the concrete at the vicinity of the transverse crack. The stress transfer from the longitudinal steel to the concrete depends on the reinforcing steel surface area and the surface deformation shape of the longitudinal steel. For the same percent of longitudinal steel, the smaller size bar results in a larger steel surface area, which increases stress transfer from the steel to the concrete and results in a shorter crack spacing [1].

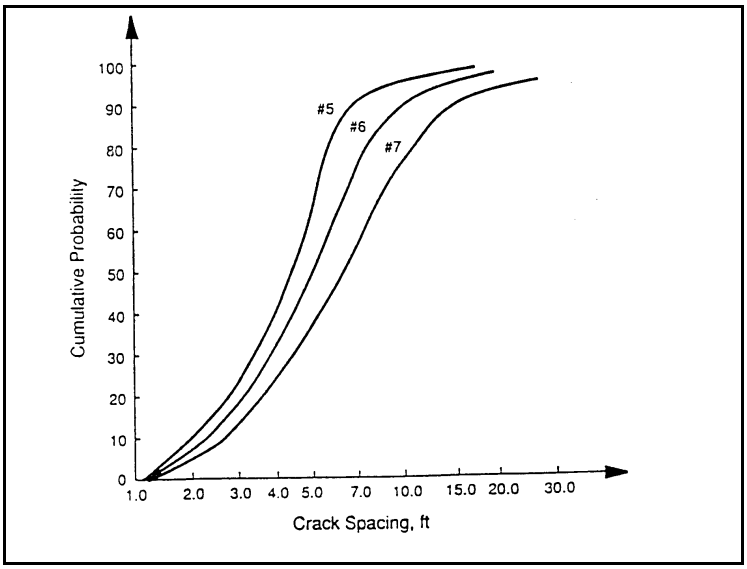

Figure 2.6 Effect of Bar Size on Crack Spacing [1].

Figure 2.6 [19], shows the effect of bar size on the crack spacing. McCullough and Ledbetter [19] noted that the crack spacing was inversely proportional to the ratio of the bond area to concrete volume as shown in Figure 2.7 which is referred to as the q factor. The 1972 AASHTO Interim Guide suggests that the ratio of the bond area to concrete volume

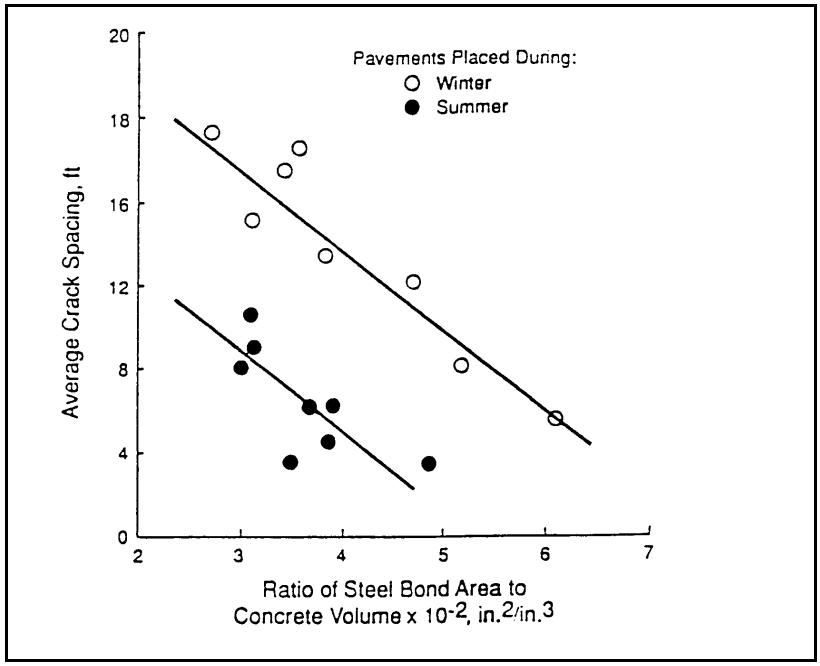

Figure 2.7 Relationship between Steel Bond Area and Crack Spacing [22].

(q) be greater than 0.03 $inch^2/inch^3$ for all the climatic regions but typically ranges from 0.026 to 0.035. The value of q can affect the average crack spacing to some extent but plays a greater role in its effect on crack widths.

Depth of Cover of Longitudinal Steel

The vertical location of longitudinal steel has an effect on the crack pattern. The volumetric strains are greatest at the pavement surface and decrease with depth. If the steel is placed near the surface of the slab, the restraint to the induced movements increases which results in an increase in the number of transverse cracks. Figure 2.8 [20], shows the significance of the effect of the vertical steel location on the crack pattern for Illinois CRC 7 and 8 in pavements with deformed bars and wire fabric reinforcement. Other studies [21] indicate that the reinforcement placed above mid-depth in the pavement will tend to cause an irregular cracking pattern although the average crack spacings are closer, as was manifest in the SH 249 section where the two-layer configuration resulted in a higher level cluster cracking. A survey [1] of CRC pavements in South Dakota shows an average crack spacing of 1.7 ft with the steel 2.5 in below the surface, and an average spacing of 2.9 ft with the steel 3.68 in below the surface. An aspect related to the depth of steel is the use of two layers of longitudinal steel. The position of the top layer of steel has been shown to be significant in past studies and the use of

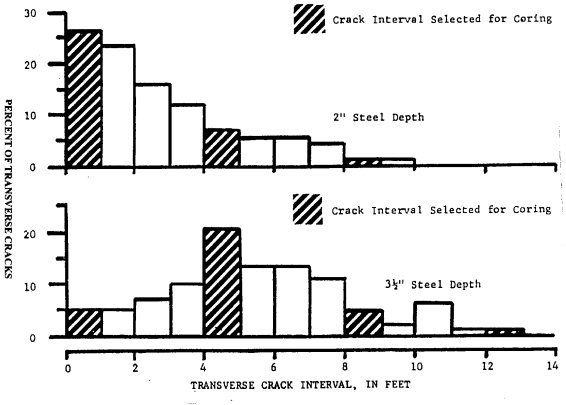

Figure 2.8 Frequency Histograms Showing Crack Interval Distributions [20].

two-layer placements has been adopted in Texas DOT construction standards [1] for pavements thicker than 11 in in order to maintain adequate steel spacing for construction purposes. As pointed out previously, thicker pavements may experience a greater degree of volumetric restraint due to a reduced depth of cover caused by the use of two layers of reinforcing steel. Two layers of reinforcing steel also require two layers of transverse steel which tend to cause a weakened plane of transverse cracking. A high incidence of transverse cracking was noted on projects in Texas [23] which used two layers of reinforcing steel where the transverse bars were vertically aligned.

Climatic and Construction Factors

Ambient temperature conditions will affect the crack pattern in CRC pavements primarily to the extent it influences the thermal gradient and uniform temperature changes within the slab. Naturally, geographic location affects the climate to which concrete pavement may be exposed. Temperature ranges (the concrete set temperature minus lowest annual temperature) can be as large as 150°F, depending on the location. However, normal temperature ranges are generally not this severe. The concrete set temperature and minimum yearly temperatures are used in design because they have correlated well in terms of prediction of crack width of the transverse crack based on the average crack spacing and the amount of linear slab movement.

The cracking process in CRC pavement involves cracking developing at early and at later ages. It is important to point out that some cracks that initiate at an early age may not become evident at the surface for several years. Cracking of this nature in CRC pavements is propagated in part by daily, non-uniform temperature and moisture change within the pavement due to changes in ambient temperature and humidity conditions. Shrinkage and contraction stress that cause cracking to develop at an early age are the result of restrained movement caused by temperature and moisture changes. Even though concrete and steel can have a relatively similar coefficient of thermal contraction (0.000005 in/in/°F) depending on the coarse aggregate type, stresses develop in part because the reinforcing steel has a higher modulus of elasticity than the concrete. Consequently, the stress intensity within the concrete becomes too high and the crack propagates. A similar effect may result from early-aged concrete shrinkage. The stress intensity

in both instances is enhanced due to the resistance between the subbase and the slab. As a result, high temperature drops and moisture loss are conducive to rapid crack development. This can occur under summer weather and windy conditions where the concrete pavement is placed in the morning hours leading to maximum setting temperatures and stresses that can cause cracking as early as the next day or later (2 to 3 days) depending on the type of aggregate used [24]. Delayed early aged cracking can result due to a buildup of drying shrinkage in combination with temperature effects.

In order to achieve adequate cracking patterns, a certain amount of temperature change and drying shrinkage needs to occur to insure a certain level of cracking. If induced stress levels are too low, then crack patterns may be too far apart or contain too many clusters of closely spaced cracks to provide adequate performance or the opposite can be the case if the induced stress levels are too high. In terms of the crack patterns, concrete properties and support conditions, there are a number of combinations that can be optimized to achieve the required pavement performance. Additional research will lead to design products for CRC pavements to indicate material combinations and construction methods to achieve appropriate shrinkage and temperature sensitivity levels to enhance optimal performance of the pavement.

Time and Season of Placement

Concrete strength gain rates due to environmental conditions during fall and winter time periods are the lowest since the prevailing temperatures are typically the lowest. Therefore, concrete placed in this time of year will have lower temperatures and less time to develop sufficient concrete strength before maximum cracking stress occurs than concrete paving placed in the spring or summer. Concrete pavements placed in the fall develop a shorter crack spacing than that placed in the spring due to the relatively lower concrete strengths caused by typically lower ambient temperatures [1]. However, this effect may be somewhat offset because the reference temperature (upon which the concrete stresses are based) is also lower in comparison to construction periods at hotter times of the year. CRC pavements, particularly those placed with river gravel coarse aggregates, constructed under cool weather conditions develop longer crack spacing and but smaller crack widths than those placed in the summer months under warm

weather conditions. Because of the greater drying shrinkage under hot weather conditions, CRC pavement performance may be significantly affected due to the effect the seasonal conditions have on the resulting crack widths [23].

Whether the concrete was placed in the morning or the afternoon can affect CRC pavement cracking behavior, as previously discussed. Concrete placed in the morning typically sets at higher temperature and consequently develops greater stress-related cracking than concrete placed in the afternoon. Concrete placed in the morning tends to have shorter crack spacings than concrete placed in the afternoon [24].

Curing Conditions

The curing temperature at the time of placement of the concrete slab also affects cracking in CRC pavements. The pavements constructed at higher curing temperatures have shorter cracking spacings than the pavements constructed at lower temperatures [24]. A significant amount of cracking occurs early in the pavement life. The cause of this cracking may be related to the way concrete is cured.

It is generally accepted that the more the water loss from the concrete mixture during the hardening process the greater will be the shrinkage and the lower the degree of hydration. Therefore, concrete shrinkage stress will have a greater potential to exceed the concrete strength inducing early-aged cracks in the CRC pavements. Curing of CRC pavements is a crucial step in minimizing early cracking potential of CRC pavements. The most common method for curing concrete pavements is membrane curing. The curing methods are as follows:

- Membrane curing compound,
- Polyethylene film curing, and
- Cotton mat curing.

The research conducted by Tang et al. [23] revealed that both cotton mats and polyethylene film reduced daily temperature variation and reduced moisture loss from the pavement surface. Accordingly, the number of surface cracks in pavements that develop initially with cotton mat or polyethylene curing are much lower than that cured with membrane compounds.

It should also be mentioned that drying shrinkage in the field may not match the drying shrinkage found from laboratory specimens since the drying condition may be very different. Under hot weather paving conditions, early shrinkage and creep may be absorbed by the early-aged cracks which then tend to be wider than the cracks which develop at a later age. Therefore, a different amount of drying shrinkage should be taken into account depending not only on the age of the concrete but also on the method and conditions of curing.

Current CRC Pavement Cracking Models for Numerical Simulation

Since the transverse cracking process in CRC pavement involves an on-going sequence of change in concrete strength and environmental conditions, it is advantageous to computerize certain stress and strain algorithms to model the pavement cracking. To simplify the analysis, certain assumptions are made with regard to material properties and environmental conditions. The computer models are useful for the prediction of structural response parameters related to contraction restraint such as the crack spacing, crack width, and the stresses in the steel and the concrete for a given set of environmental and material conditions. The basic equations and assumptions upon which these models are based have been previously discussed. CRC pavement response under wheel load, considered in Chapter 5 relative to crack width design criteria, is a key factor in the process of punch-out development. Pavement response in terms of bending and shear-related stresses is influenced by the crack width and the load transfer across the transverse cracks.

Overview of Numerical Models for Restraint Cracking

Several pavement models (both closed form and numerical) have been developed in the past 50 to 60 years to aid the designer in the prediction of design-related stresses. In recent years numerical models specific to CRC pavement design have been developed based on the use of high-speed computers in the design and analysis of structural response parameters. Foremost among the tools for design is the CRCP 8 program [1] which has resulted from a long series of revisions and improvements relative to the prediction of in-plane stress in the pavement caused by drying shrinkage and temperature drop. Included in this model is equilibrium analysis of

stress in the concrete, steel reinforcement and resistance due to friction at the pavement subbase interface. The friction on the subbase is a function of the pavement movement which depends upon the concrete strains. The model also accounts for the age-strength relationship of the concrete which allows for analysis of crack formation with time as the internal tensile stress exceeds the tensile strength of the concrete [25].

McCullough et al. [18] developed basic equations from force equilibrium of bond, steel, and subbase friction in the pavement system as a basis for the prediction of structural responses due to contraction restraint in CRC pavement. Many of the assumptions listed for the Vetter derivations apply to the CRCP 8 model. The model assumes a crack forms when the concrete stress calculated from the equilibrium equations is greater than the concrete strength at that location. The stress in the concrete at the crack is zero. The stresses due to volumetric changes are also assumed to be uniformly distributed throughout the slab thickness. Since the model contains an algorithm for the change in concrete strength with time, the criteria for cracking also change with time. Other assumptions associated with the model are as follows:

- Concrete and steel properties are linearly elastic.
- In the fully bonded sections of the concrete slab, there is no relative movement between the steel and the concrete.
- Material properties are independent of space.
- Effects of concrete creep and slab warping are neglected.

The model also assumes fixed-end (fully restrained) conditions at the midslab location and for the reinforcement at the crack centerline. Although not included in the original list of assumptions, fully restrained conditions are used as a basis for the development of the equations since the total length of steel bars is assumed to be constant. The model includes a characterization of the frictional resistance between the concrete slab and the underlying base between existing cracks. The basic equations for McCullough's model are derived by considering a full length of CRC pavement in which a free body diagram is developed in Figure 2.10. By considering overall equilibrium [1]:

$$F_{sc} + \int F_i dx - F_{sx} - F_{cx} = 0 \qquad (2.8)$$

where

F_{sc} = force in steel at the crack face

F_s = subbase friction force per unit length

F_{sx} = force in steel at position x

F_{cx} = force in concrete at position x

Conversion of the equilibrium expression in terms of stresses yields:

$$\sigma_{sx} + \frac{\sigma_{cx}}{p} = \sigma_{sc} + \frac{\int_x^L F_i dx}{ph} \tag{2.9}$$

where

σ_{cx} = concrete stress at position x

σ_{sx} = steel stress at position x

h = slab thickness

A generalized compatibility equation that applies to the partially and fully bonded regions and accounts for the volumetric changes due to environment effects in the steel and the concrete is:

$$\frac{du_{sx}}{dx} = -\alpha_s \Delta t + \frac{\sigma_{sx}}{E_s} \tag{2.10a}$$

$$\frac{du_{cx}}{dx} = -\alpha_c \Delta t - \varepsilon_{sh} + \frac{\sigma_{cx}}{E_c} \tag{2.10b}$$

where

u_{sx} = displacement of the steel at location x

u_{cx} = displacement of the concrete at location x

The distribution of concrete and steel stresses with distance from the crack face (x) is defined relative to the bond stress (τ_b) between the steel and the concrete. The effect of subbase friction (F_s) is also included in equations expressing the change in steel and concrete stress with distance as:

$$\frac{d\sigma_{sx}}{dx} = -\tau_b(x)\frac{q}{p} \tag{2.11a}$$

$$\frac{d\sigma_{cx}}{dx} = -\tau_b(x)q - \frac{F_i}{A_c} \tag{2.11b}$$

The stress in the concrete at the crack is assumed to be zero and it is defined in the fully bonded region as:

$$\sigma_{cx} = \frac{\sigma_{sx}}{n} + E_c\left\{\left[\alpha_c - \alpha_s\right]\Delta t + \varepsilon_{sh}\right\} \tag{2.12}$$

Equation (2.11b) for the slope of the concrete stress (Figure 2.9) shown above is used to define the concrete stress in the bonded and partially bonded regions. The change in either the concrete or the steel stress in the fully bonded region is assumed to be small since the change in bond stress and friction effects is small in that region. In any case, the main influence on the change in stresses is due to the bond stress (τ) since in many instances the friction effects are relatively small. Nominally, the change in steel stresses is a factor of "n" times the change in concrete stress.

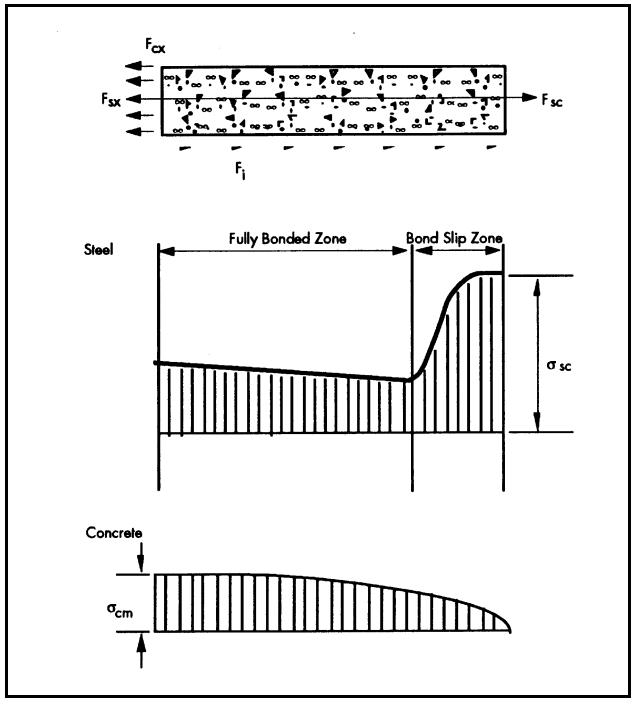

Figure 2.9 CRC Pavement Stress Diagram and Distribution for CRCP 8 Program [1].

The frictional resistance is modeled as a function of the displacement of the concrete. An example of the relationship between frictional resistance and horizontal movement is shown in Figure 2.10. The frictional resistance under the pavement is not constant with movement and the typical maximum coefficient of frictional resistance is 3.5.

In order to relate the stress in the steel at the crack (σ_{sc}) to the stress in the steel at any point (σ_{sx}), equations 2.11 (a and b) are also related to the percent of steel:

$$\frac{d\sigma_{sx}}{dx} = \frac{-F_i}{h\left\{p + \frac{1}{n}\right\}} \qquad (2.13a)$$

$$\frac{d\sigma_{cx}}{dx} = \frac{-F_i}{nh\left\{p + \frac{1}{n}\right\}} \qquad (2.13b)$$

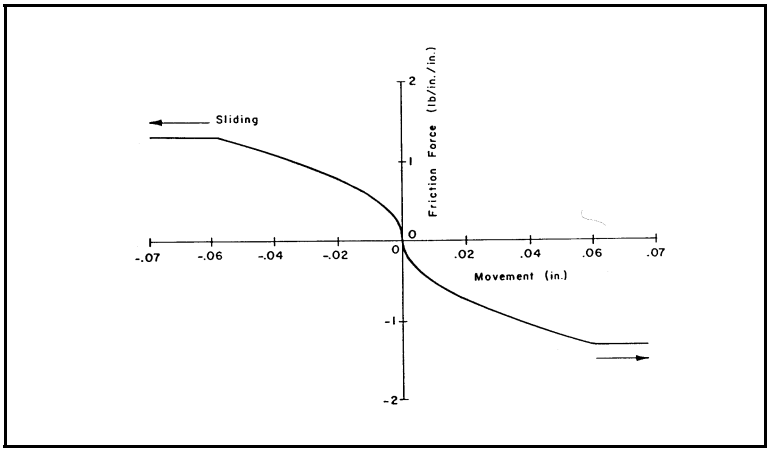

Figure 2.10 Relationship between Frictional Resistance and Horizontal Movement [18].

Equations 2.11 and 2.13 are key components combined to relate σ_{sc} and σ_{sx} as:

$$\sigma_{sc} = \left(1 + \frac{1}{np}\right)\sigma_{sx} + \frac{E_c}{p}\left[(\alpha_c - \alpha_s)\Delta t + \varepsilon_{sh}\right] - \frac{\int_x^L F_i dx}{ph} \qquad (2.14)$$

The steel stress at any point is also related to the bond stress between the steel and the concrete as it should be:

$$\sigma_{sx} = \sigma_{sa} - \frac{q}{p}\int_a^x \tau_b(x)dx$$

where σ_{sa} is the steel stress at the transition point between the fully bonded and partially bonded regions. This expression suggests that a bond function is required to describe the distribution of the bond stress as a function of the distance from the crack face (x). The expression used to accomplish this is:

$$t_b(x) = K w(x) + C x^2 + D + E \frac{\pi x}{2\ell} \quad (2.15)$$

where

K	=	bond stiffness
w(x)	=	bond slip
ℓ	=	bond development length
C, D, E	=	constants determined based on boundary conditions.

Equation 2.15 is also referred to as a bond-slip function that is further defined in reference [1] with respect to the boundary conditions w(x) = w'(x) = w"(x) = 0. The definitions of the constants involved second derivatives of equations 2.10a and 2.10b and an empirical relationship for bond development length (ℓ):

$$\ell = K_p \frac{P_{tran}}{\Sigma_0}$$

where

K_p	=	constant determined from pull-out test results
P_{tran}	=	transfer load = $(\sigma_{sc} - \sigma_{sa}) A_s$
Σ_0	=	steel reinforcing bar perimeter

The bond development expression shown above effects how the bond development length is related to the stress in the reinforcement as shown in Figure 2.11.

A program developed at the Texas Transportation Institute [29], referred to as TTICRCP, takes a similar approach to cracking in CRC pavement as the CRCP 8 program by characterizing the bond stress distribution between the steel reinforcement and the concrete other than assuming it to be

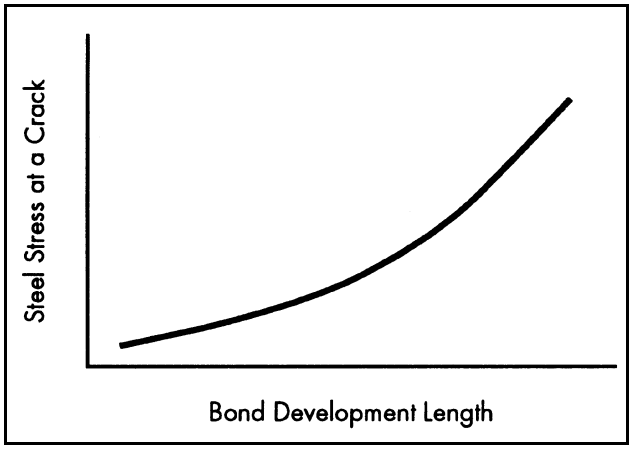

Figure 2.11 Relationship of Steel Stress at a Crack to Bond Development Length Used in CRCP 8 Program [1].

uniformly distributed. This program is particularly useful as an analysis tool since it can be easily calibrated to specific site conditions. No direct relationship is assumed between the bond stress and the crack width. The bond stress distribution, represented in Figure 2.12, is determined by the program as a function of the relative slip between the concrete and the reinforcement. As the slip increases from zero, the bond stress increases at a rate of K_1 to the peak value which occurs at a slip of δ_b. Increasing slip leads to a decrease in the bond stress at a rate of K_2. Zero bond stress occurs at slips equal to or greater than δ_{bl}. The parameters K_1, K_2, and δ_b are assumed to be a function of the concrete strength properties and the style of steel reinforcement ribbing.

The frictional resistance between the subbase and the pavement is also represented in the TTICRCP program. The friction force is determined as a function of the slab displacement where the general shape of the friction force-displacement curve is quite uniform. The friction force is represented as a friction stress which is the friction force divided by the area over which it acts. Figure 2.13 shows the friction stress function used by TTICRCP. The slope value K_4 is taken as negative which means the sliding friction decreases slightly with slab displacements greater than δ_f. It is assumed the accuracy of the model is not compromised with this generalization since it is accepted that the friction stress is constant beyond the threshold displacement. This slope value allows a similarity to exist

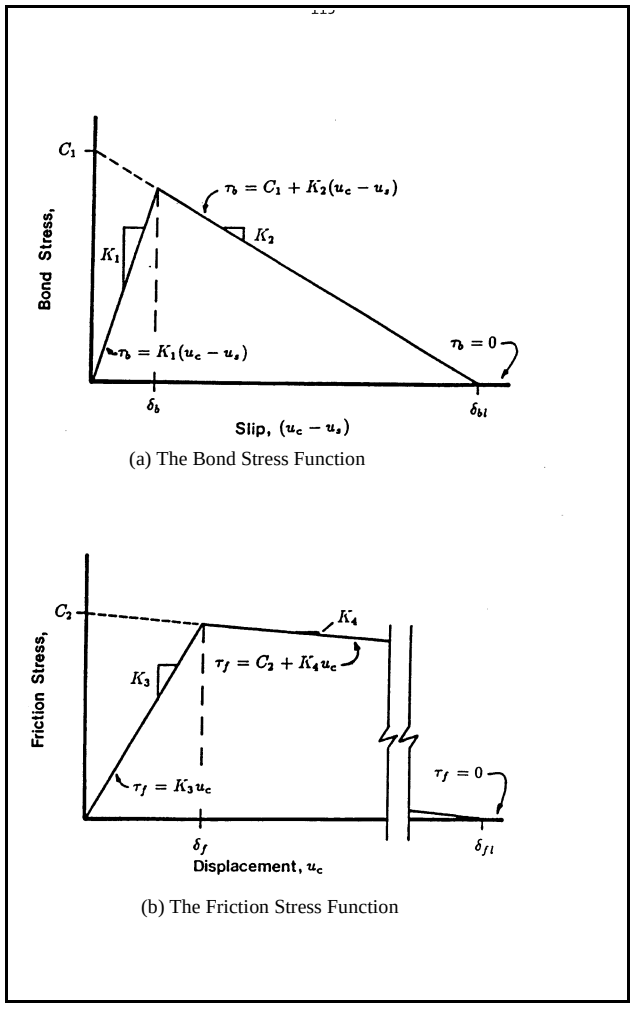

(a) The Bond Stress Function

(b) The Friction Stress Function

Figure 2.12 Bond and Friction Stress Characterization in TTICRCP Program [29].

between the bond stress function and the friction stress function which permits a more convenient mathematical modeling of the functions.

The basic assumptions behind the TTICRCP algorithms are similar to those used in CRCP 8. The effect of curl and creep are ignored and the slab behavior is assumed symmetrical about the slab midpoint. The derivation of the governing equations for the model can be understood by examining a slice of a prism (taken along the length of the pavement) of width $\triangle x$ containing rebar at the center (Figure 2.14a). A change in the concrete and the steel stresses ($\triangle\sigma$) occurs across the slice. A bond stress (τ_b) exists between the steel and the concrete and a friction stress (τ_f) is present between the pavement and the subbase. The forces acting on the corresponding concrete and steel elements are shown in Figure 2.13b and c. The summation of forces based on Figure 2.13 is:

$$\sum F = (\sigma_c + \triangle\sigma_c)A_c - \sigma A_c - \pi d_b \tau_b \triangle x - b_1 \tau_f \triangle x$$

In order to maintain equilibrium the summation of forces must equal zero:

$$(\sigma_c + \triangle\sigma_c)A_c - \sigma_c A_c - \pi d_b \tau_b \triangle x - b_1 \tau_f \triangle x = 0$$

being simplified to:

$$(\triangle\sigma_c/\triangle x) - (\pi d_b/A_c)\tau_b - (b_1/A_c)\tau_f = 0 \qquad (2.16)$$

The same type of development was applied to the reinforcement element by setting the summation of forces equal to zero:

$$(\sigma_s + \triangle\sigma_s)A_s - \sigma_s A_s + \pi d_b \tau_b \triangle x = 0$$

being simplified to:

$$(\triangle\sigma_s/\triangle x) - (\pi d_b/A_s)\tau_b = 0 \qquad (2.17)$$

Equations 2.16 and 2.17 are defined in terms of displacement in the concrete (u_c) and the steel (u_s) by using the definitions for stress ($\sigma = E\varepsilon$) and strain ($\varepsilon = du_i/dx$):

$$\sigma = E(du_i/dx)$$

and upon differentiation:

$$d\sigma/dx = E(d^2u_i/dx^2) \qquad (2.18)$$

By allowing $\triangle\sigma/\triangle x$ in equations 2.16 and 2.17 to become sufficiently small, it can be replaced by $d\sigma/dx$. Making the appropriate substitutions, equation 2.16 can be reduced to:

$$(d^2u_c/dx^2) - (\pi d_b/E_cA_c)\tau_b - (b/E_cA_c)\tau_f = 0 \qquad (2.19)$$

and equation 2.17 to:

$$(d^2u_s/dx^2) + (\pi d_b/E_sA_s)\tau_b = 0 \qquad (2.20)$$

Equations 2.19 and 2.20 are the general differential equations that govern the model structural response. The displacements in the concrete (u_c) and the steel (u_s) are found from the solutions of the differential equations. The slip between the concrete and the steel is determined from the relative displacements ($u_c - u_s$). Closed form solutions of the differential equations are found by making appropriate substitutions for τ_b and τ_f in terms of the linear functions described previously (Figure 2.13). Different linear functions are implemented (nine possible combinations) for the stresses depending on the magnitude of either the slip (u_c-u_s) or the displacement of the concrete (u_c) for the case of interest.

The final stresses and strains in the concrete and the steel are determined on the basis of energy considerations. All the energy that is available to displace the slab through a drop in temperature and drying shrinkage must be accounted for. In the program, energy can be consumed as:

- Potential energy in the concrete and the steel,
- Frictional work energy lost during slab movement, and
- Stress relief energy lost because of slab movement.

Since force equilibrium is satisfied by any solution of the displacement equations, energy equilibrium becomes the deciding criteria for obtaining the displacements, stresses, and strains for a given set of environmental conditions. The total potential energy in the concrete and the steel is found by integrating the stress strain curve for a unit volume (assuming the concrete and steel behave linear elastically where $\varepsilon_{c=}\sigma_c/E_c$ and $\varepsilon_s=\sigma_s/E_s$):

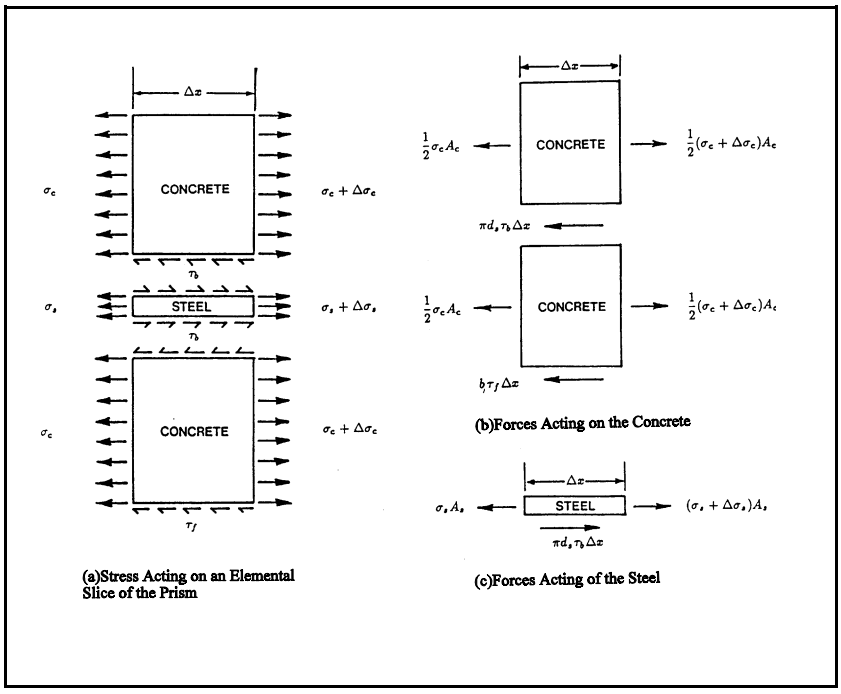

Figure 2.13 (a) Elemental Slice, (b) Concrete Forces, (c) Steel Forces for TTICRCP [29].

$$E_{pot} = A_C \int_0^{L_2} \frac{\sigma_C^2}{2E_C} dx + A_S \int_0^{L_2} \frac{\sigma_S^2}{2E_S} dx$$

The frictional work energy that is expended is found by the model from the area under the bond stress and friction stress functions for a unit contact area (between the steel and concrete or the subbase and the concrete):

$$E_{pot} = \pi d_b \int_0^{L_2} \int_0^{u_c - u_s} \tau_b \, d\tau_b \, dx + b_1 \int_0^{L_2} \int_0^{u_c} \tau_f \, d\tau_f \, dx$$

The stress relief energy is dependent on the displacement of the concrete since movement signifies a release of the stress condition. The stress relief only applies to the concrete since no relief movement occurs in the reinforcement. The relief energy, for a unit volume of concrete, is equal to:

$$E_{rel} = A_c \int_0^{L_2} \int_0^{\varepsilon_c} E_c \varepsilon_c \, d\varepsilon = A_c \int_0^{L_2} \frac{E_c \varepsilon_c^2}{2} dx$$

The total energy available from the thermal and shrinkage effects is equal to:

$$E_{total} = (L_2/2)\{A_c(\alpha_c \triangle T)^2 + A_s(\alpha_s \triangle T)^2 + A_c(\varepsilon_{shr})^2\}$$

The stress and strains are dependent upon the displacements which are obtained when the sum of the potential, frictional work and stress relief energies equals the total available energy. The crack width is equal to twice the slip between the concrete and the steel.

The resulting bond stress distribution, steel stress, and crack width determinations depend upon the final configuration of the four zones and arrangement of ℓ_1, ℓ_2, and ℓ_3 indicated in Figure 2.14. As previously noted, the arrangement of ℓ_1, ℓ_2, and ℓ_3 constitutes the nine possible cases or combinations that can result depending on the outcome of the energy balance. In contrast with CRCP 8 bond/steel stress trends, TTICRCP demonstrates a reverse trend (Figure 2.15) with steel stress at least in terms of the length ℓ_1. It should be pointed out that the distance ℓ_1 is not equivalent to the bond development length, however it may serve as an indicator of bond develop trends as predicted by the TTICRCP program. In any event, this does not diminish the utility of using the TTICRCP program to check the results of the CRCP 8 program since the TTI model is well suited for calibration studies as is described in Chapters 3 and 4.

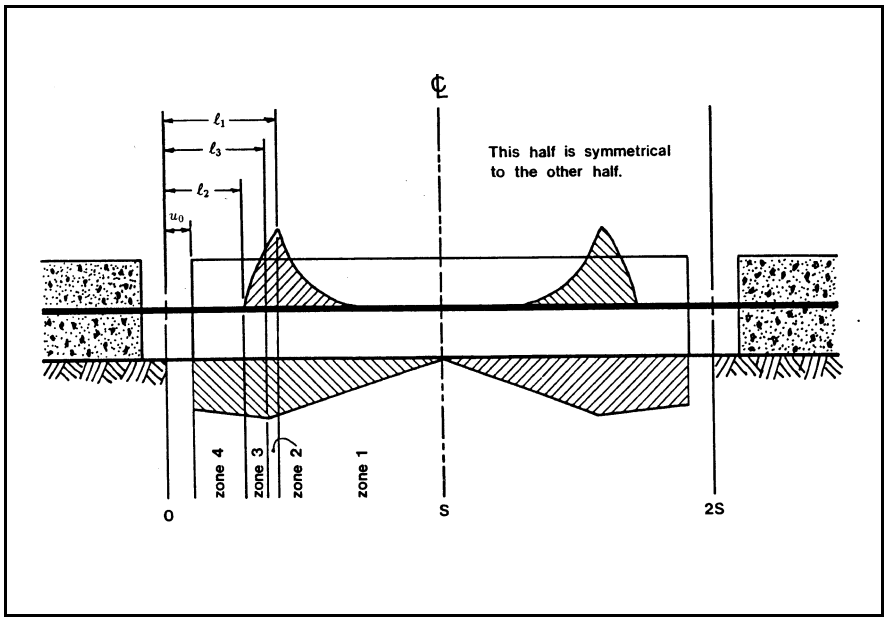

Figure 2.14 The 6th Case in TTICRCP of the Zone and ℓ_1, ℓ_2, and ℓ_3 Configuration [29].

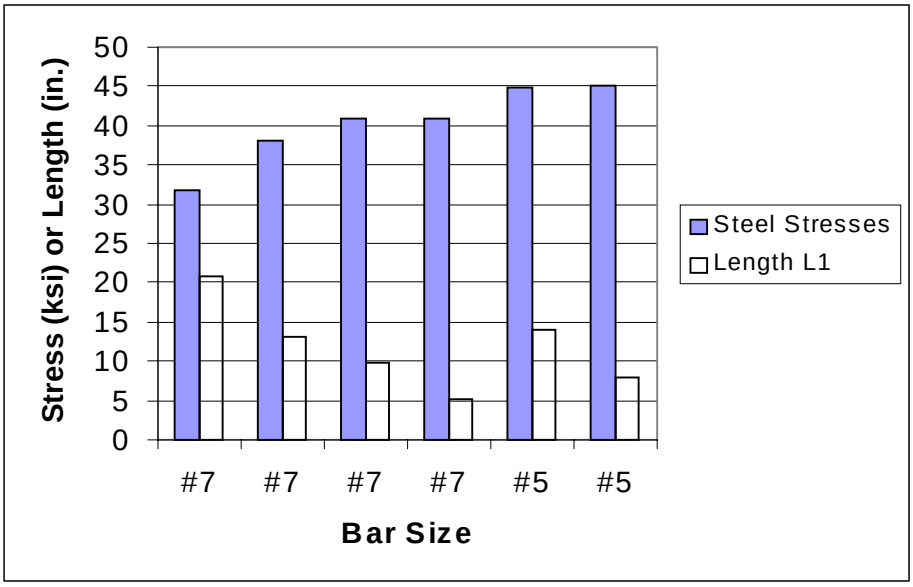

Figure 2.15 Relationship between Steel Stress and Length ℓ_1 as Represented in the TTICRCP Program.

CHAPTER 3

TEST SECTION INSTRUMENTATION AND DATA COLLECTION

Relative to the objectives of this project, a section of CRC pavement constructed on a section of I-45 in North Houston was instrumented in order to monitor the behavior of both the reinforcing steel and the concrete. The resulting data was also used to assess the predictability of current analytical models based on the interaction between the steel reinforcement and the concrete. This chapter contains a description of the pavement instrumentation site and a detailed description of the instrumentation used in the project and the data obtained therefrom.

Instrumentation and Date Collection Site Location

The instrumented pavement segment is located on the southbound lanes of I-45 in Houston, about one-third of a mile south of FM 1960. The instrumented segment was a CRC pavement that was placed on August 22, 1997 as part of a 555 ft long pavement construction section. The paver placed the concrete while moving from the south to the north (Figure 3.1). The pavement was paved 15 in thick, on a 1 in thick asphalt bond breaker. In addition, a 6 in thick stabilized base course and a 6 in thick lime-treated subcourse were placed underneath the asphalt bond breaker. A single layer of grade 70 steel reinforcement (representing 0.49 % steel) was placed near the mid-plane of the pavement slab.

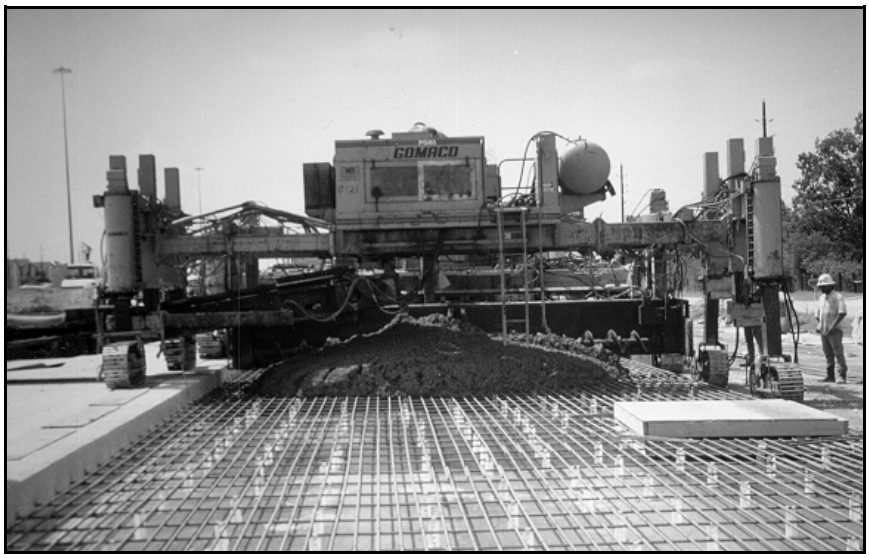

Figure 3.1 Paving Proceeded from South to North, August 22, 1997.

Generally speaking, transverse cracks in CRC pavement are allowed to develop randomly. However, a designated portion of the 555 ft section was set aside for specific crack control study. In the control section, cracks were initiated with swallow transverse sawcut notches at selected locations in order to insure that the crack patterns matched the instrumentation plan. As the concrete reached final set, sawcut notches were placed in the surface of the pavement. In total, thirty-seven 0.75 in deep saw cut notches were placed in the pavement surface throughout the paved section. The first saw cut (saw cut #1) was placed 297 ft from the south end of the pavement section. Different sawcut intervals were used for distinct sections of the pavement in order to provide comparisons on the control of cracking through the use of sawcuts. Sawcuts #1 to #26 were spaced at 6 ft intervals, sawcuts #26 to #29 contained a 10 ft spacing, and sawcuts #29 to #37 were spaced at 12 ft intervals.

Construction Materials

The construction materials used for this 15 in CRC pavement section included use of #6 sized grade 70 steel reinforcement and a crushed limestone concrete mixture. Grade 70 steel reinforcement possesses a minimum yield strength of 72.5 ksi. The #6 reinforcement has a nominal diameter of 0.75 in and a nominal area of 0.44 in^2. The reinforcement was approximately placed at a 6 in spacing interval. The details of the concrete mix proportion used for this project are presented in Table 3.1.

Layout

Figure 3.2 illustrates the layout of the instrumented pavement slab. The sawcut shown in the figure represents sawcut #27. The locations of the concrete gages are designated with the letters CG and the corresponding steel gage locations are designated with the letters SG. Steel strains at the induced crack (#27) were measured with SG-1, SG-3 and SG-5. As shown in Figure 3.2, steel strains at 3, 6, 9, 24, and 36 in from the induced crack were measured by SG-2, SG-4, SG-6, SG-7, and SG-13, respectively. Locations of concrete gages are displayed in the figure as well.

Test Site Instrumentation

In an attempt to obtain an accurate picture of the behavior of the concrete and steel strains and the interaction between the two, a thorough instrumentation plan was developed. Consequently, strain gages were installed in both the concrete and the reinforcing steel. In addition to these gages, LVDTs and manual surveys were used to monitor crack developments and movements. This section will discuss each of these types of instrumentation and the collected data. Also included is a discussion of the historical gain in concrete strength and the weather variations throughout the monitoring period for the pavement section.

Table 3.1 Concrete Mixture Proportions Used for I-45 Site.

CAF	0.68 - Limestone Redland Gr #2 BSG_{ssd} = 2.56 $DRUW_{ssd}$ = 95.84	**%Air**	5.0 Daravair
CF	6.0	**WF**	4.5
% Fly Ash	25 Texas Lehigh	**WRA**	4-8 ozs/100 wt Lubricon - R
FAF	0.825 Cleveland Sand BSG_{ssd} = 2.62 $DRUW_{ssd}$ = 101.03	**UW**	142.7 lbs/cf

Concrete Strain Gages

Roctest gages, which are ideal for shrinkage stain measurements, were used to measure the strains in the concrete. These gages consisted of a thin steel wire held in tension between two anchorages. When the distance between the anchorages changes due to movement in the concrete, the tension in the wire is affected which leads to a change in the natural frequency of the gage. The strain in the concrete is then measured by detecting the change in the natural frequency and using an adjustment factor in order to calculate the corresponding strain measurement. This calculation was carried out using equation 3.1 shown below [36].

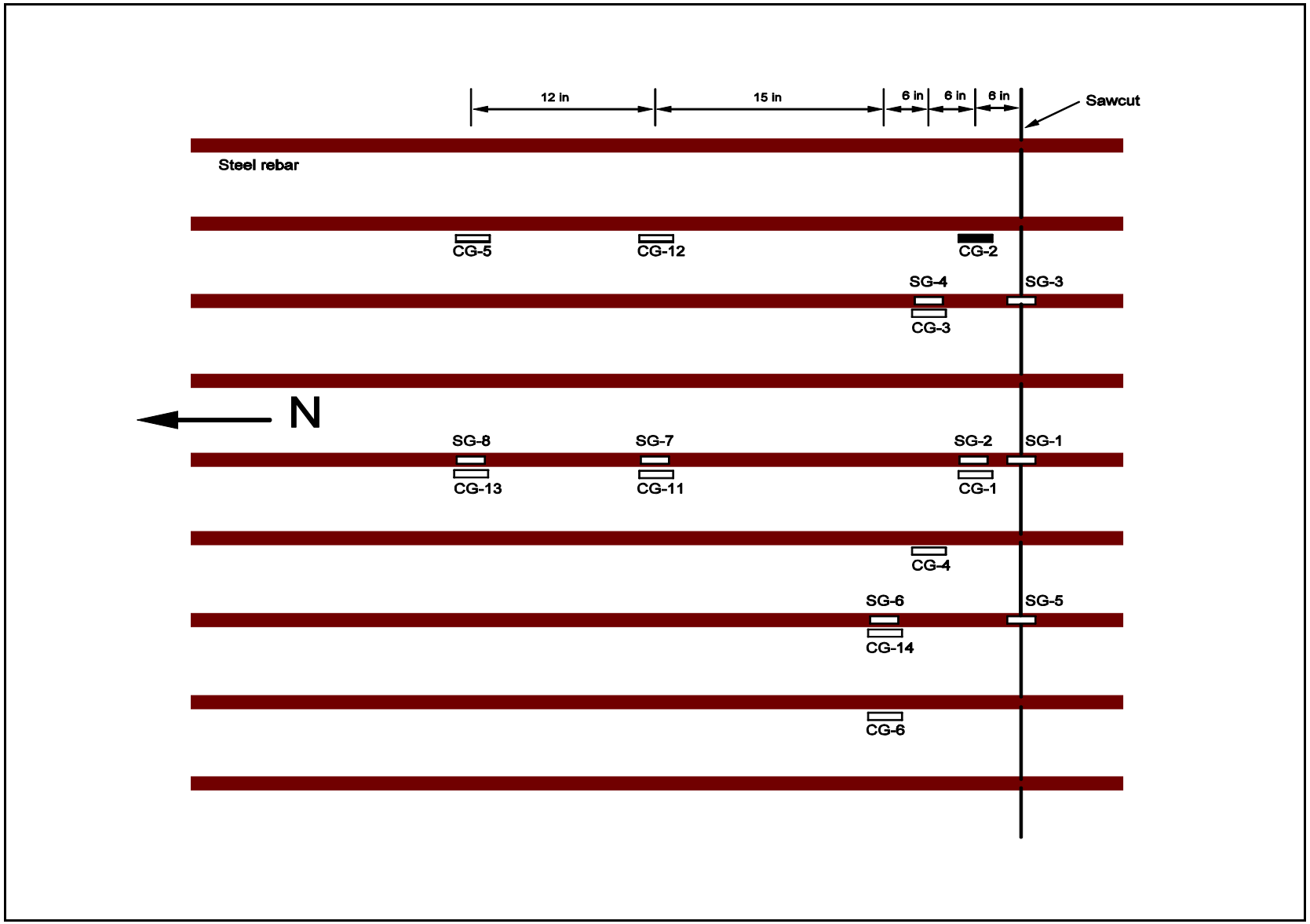

Figure 3.2 Layout of the Instrumented Pavement Slab.

$$\varepsilon = K \times 10^9 \times \left[\frac{1}{N_1^2} - \frac{1}{N_2^2} \right] \tag{3.1}$$

where

K = gage factor

N_1 = initial frequency of the gage

N_2 = current frequency of gage

(K values for the previous equation were obtained from the Roctest Instruction Manual [36] as 4.0624 or 1.1560 depending on whether the gage was 6 in or 3.5 in in length).

Strain gages, for the measurement of strains in the concrete, were installed in the slab between sawcuts #27 and #28, as illustrated in the preceding figure. The section in question possessed a 10 ft crack spacing. The concrete gages (Figure 3.3) were wired to the steel reinforcement in order to assure that they were located at the same depth as the steel mat to facilitate the assessment of bond-slip behavior, subsequently discussed. The installation of all of the concrete gages was completed before paving began. The location of the attached concrete gages was selected to coincide with the steel gage locations as seen in Figure 3.2. This was done in order to allow for the evaluation of bond-slip characteristics based on the measured data. The bond-slip was determined following the procedure presented by Arthur Nilson [37]. The principal equation used for these calculations, discussed further in Chapter 4, is presented below as:

Figure 3.3 Concrete Strain Gages Installed before Paving.

$$S_b = S_a + \int_a^b \varepsilon_s dx - \int_a^b \varepsilon_c dx$$

where

S_a = known slip at point a

S_b = desired slip at point b

ε_s = steel strain

ε_c = concrete strain

In addition to the concrete gages shown in Figure 3.3, a tower composed of six concrete gages (Figures 3.4 and 3.5) was embedded in the pavement. Four of the six gages measured concrete strains in the longitudinal direction and the other two gages measured concrete strains in the transverse direction. Each gage was placed at a different depth below the pavement surface. This was done in order to provide an understanding of the variations in both concrete strain and temperature with respect to the distance from the surface of the concrete pavement.

Figure 3.4. An Assembly of Five Concrete Gages Installed to Measure Concrete Strains in the Longitudinal and Transverse Directions at Different Depths.

Concrete Strain Data

As an example of the recorded concrete strain data, Figure 3.6 shows 72 hours of concrete strain data recorded from various concrete gages beginning at 12:00 p.m., August 26. It is interesting to note that compressive strain in concrete reached the daily maximum value in the afternoon and the daily minimum value in the morning. Most of the concrete gages yielded valid data, however CG-5, CG-12, and CG-14 showed signs of an apparent malfunction. Currently, it appears that 12 of the 16 installed concrete gages are working properly. Daily average strain values from the remaining concrete gages are shown in

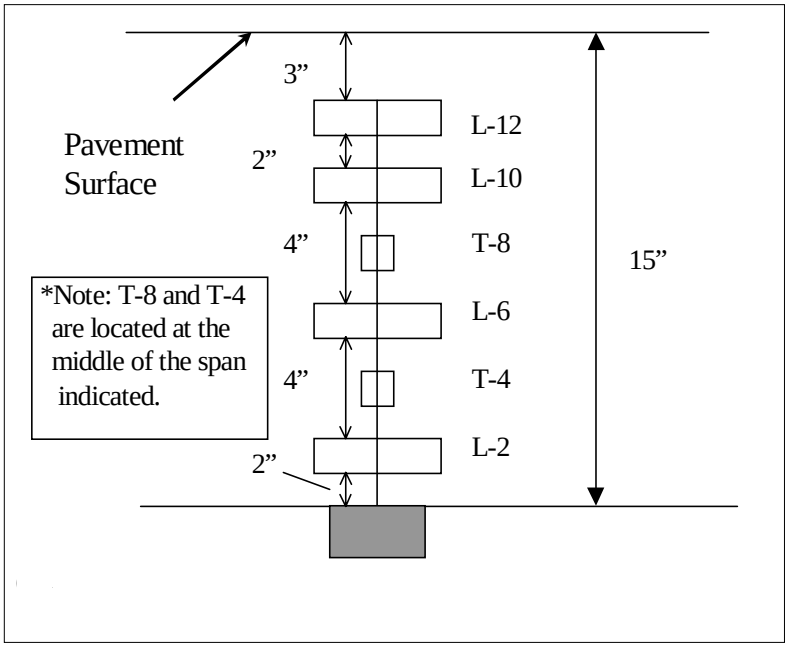

Figure 3.5 Layout of Concrete Strain Gages in Tower Configuration.

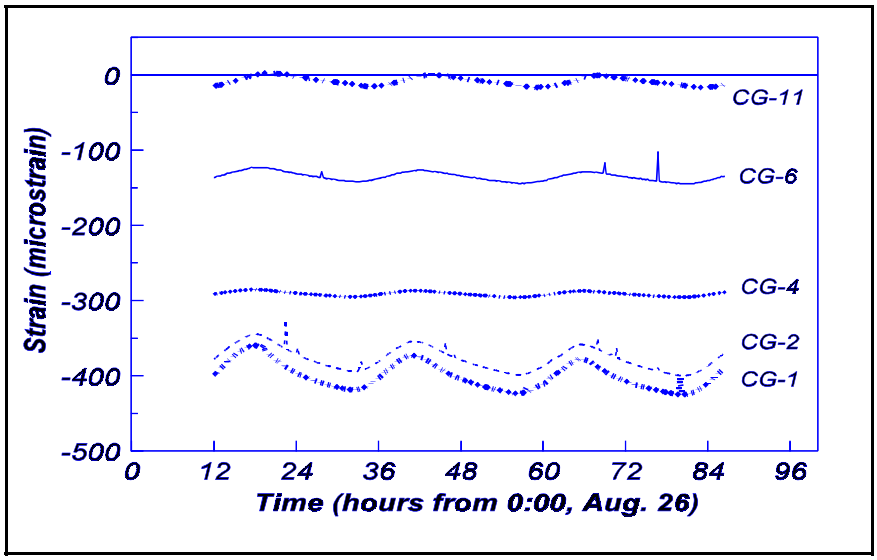

Figure 3.6 Concrete Strains versus Time on August 26-29.

Figure 3.7. Concrete strains oscillated between high and low levels in a similar fashion to the steel strains.

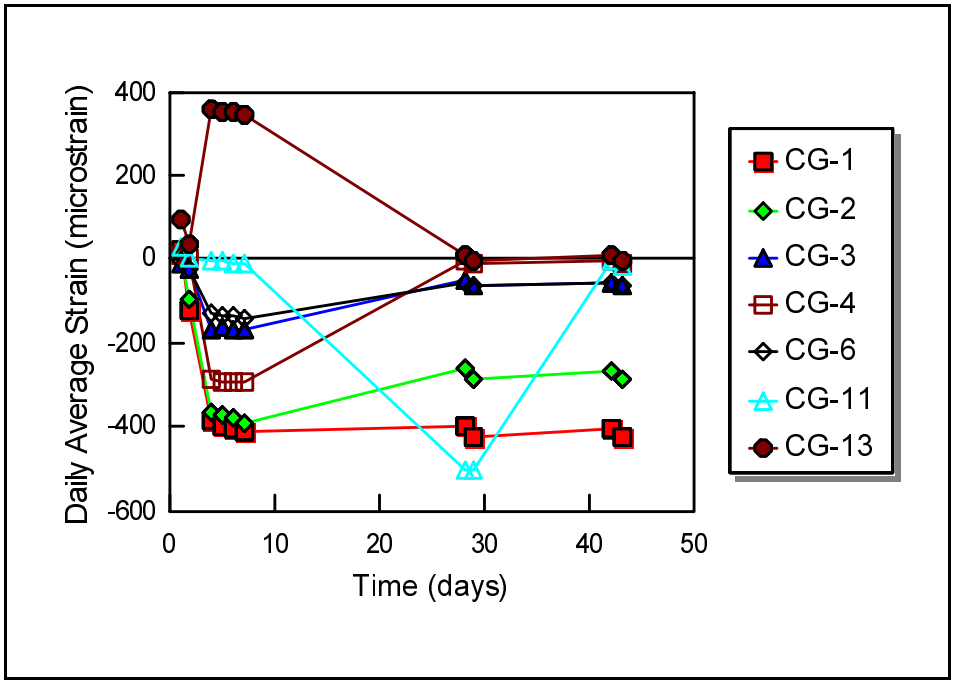

Figure 3.7 Daily Average Concrete Strains versus Time.

The daily temperature cycle causes the concrete and the steel to expand and contract. It appears that the steel rebar expansion occurred to a large extent in the afternoon due to the increase in temperature. The afternoon expansion of the steel led to the compression of the surrounding concrete. A portion of the daily average compressive strain is apparently caused by the shrinkage of the concrete. Thermal expansion of steel reinforcement pushed the concrete causing additional compressive strain in concrete while thermal contraction, which occurred in the morning, pulled the concrete which reduced the compressive strain in the concrete.

There was a total of 16 concrete strain gages placed in the concrete pavement. Six of the gages (CGs 7, 8, 9, 10, 15, and 16) were supported in a vertical configuration as discussed previously. The remaining 10 gages were distributed at different distances from the crack face (3, 6, 9, 24, and 36) parallel to specific longitudinal bars. Two gages were placed at each position on different longitudinal bars. The strain data obtained from these gages is displayed in figures located in Appendix A. These figures display the data over 24-hour time intervals on various days of the pavement life. The day and the position of the particular data can be obtained from the accompanying captions. The day is noted in parentheses and the position of the gage is

given by the distance from the crack face (in inches) and the reinforcing bar number which the gage was placed in reference to. The bar number is merely used to distinguish between two gages located at different distances from the crack face.

In addition to the concrete data displayed at varying distances from the crack, the concrete strain data obtained from the vertical configuration is also available in Appendix B. These figures show the variation in strain over 24-hour intervals. The corresponding variation in ambient temperature at each time is also displayed on the charts. These figures are very useful in demonstrating the variation in concrete strain with respect to depth below the pavement surface. The figures display the data for all six gages on the same chart. Each gage is labeled in the legend with either an "L" (for longitudinal direction) or a "T" (for transverse direction) followed by a number representing the height of the gage in the pavement.

Steel Strain Gages

The installation of strain gages inside of the reinforcing steel required some research. Previous instrumentation efforts consisted of strain gages attached to the outer side of the rebar (after grinding off the pattern lugs) which may have affected the strain measurements. The research team sought to avoid possible errors resulting from this method. For this reason, the research team adopted the following technology in order to minimize the disturbance of the bond between the steel and the concrete. The steel gages were mounted inside the rebar by STRAINSERT at West Conshohocken, Pa. A hole was bored at the center of the cross section of the #6 Grade 70 reinforcement along the longitudinal axis and then resistance strain gages were mounted on the inner wall of the hole. There were four gages mounted inside each piece of steel rebar with two gages in the axial direction and two gages in the circumferential direction. These four gages were connected to form a Wheatstone bridge in order to provide steel strain measurements in the axial direction at each instrumented location. The use of two gages in the axial direction doubled the precision of the measurement, while the use of two gages in the circumferential direction reduced measurement error due to changes in temperature. The hole was then back filled with cement. The instrumented rebar sections were all 3 ft long and were welded in place in the steel mat after it had been laid out in the field prior to paving.

Steel Strain Data

The steel gages as designed output a straight line signal of milivolts per volt which can be recorded by a conventional data-logger. When a load is applied to the reinforcing bar, the induced force acting on the bar corresponds to the output signal read by the gages. The force value (P) was obtained using equation 3.2.

$$P = A \times E \times \varepsilon \qquad (3.2)$$

It was determined from pull tests performed in the laboratory that the strain value used in equation 3.2 is proportional to the mV/V reading output from the gage. In addition, the straight line mV/V reading was adjusted in order to account for the Poisson's ratio effect in the transverse direction for the strain in the axis of the bar. This adjusted reading was also considered as the actual strain value for the reduced cross section. The reduced cross section results from the fact that the gages used did not span the whole cross section of the reinforcing bar. Therefore the strain measured was not representative of the strain in the entire cross section but rather the strain present in the reduced cross section. After determining the strain value for the reduced cross section, a constant of proportionality (C) was calculated to relate the force in the bar at the reduced cross section to the adjusted strain value. The calibration data supplied by the manufacturer was used to determine this constant of proportionality (C). The data used for these calculations is displayed in Figure 3.8. Once the constant (C) was determined for each of the eight gages, these values were averaged resulting in an overall average value of 12 for the constant of proportionality. This value was then used to calculate the force (P) present in the steel bars following equation 3.3.

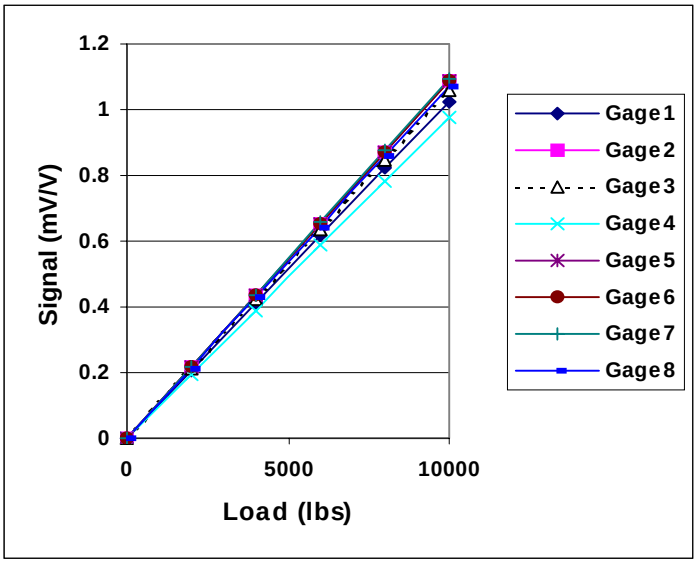

Figure 3.8 Calibration Data Provided by Strainsert.

$$P = C \times \varepsilon \tag{3.3}$$

At this point a calibration check was performed for each of the gages in order to insure that the aforementioned method of determining the force in the bar was accurate. The check was performed using an Instron 4505 test frame. The instron machine was used to load the steel bars in tension to values of 5,000, 10,000, and 15,000 lbs. The force values were then calculated from the straight line voltage reading following the procedure described previously. These calculated force values were then compared with the actual values from the Instron machine. The results of the calculation check are shown in Figure 3.9. As can be seen from this figure, the method described previously provided a satisfactory prediction of the force present in the steel reinforcing bars.

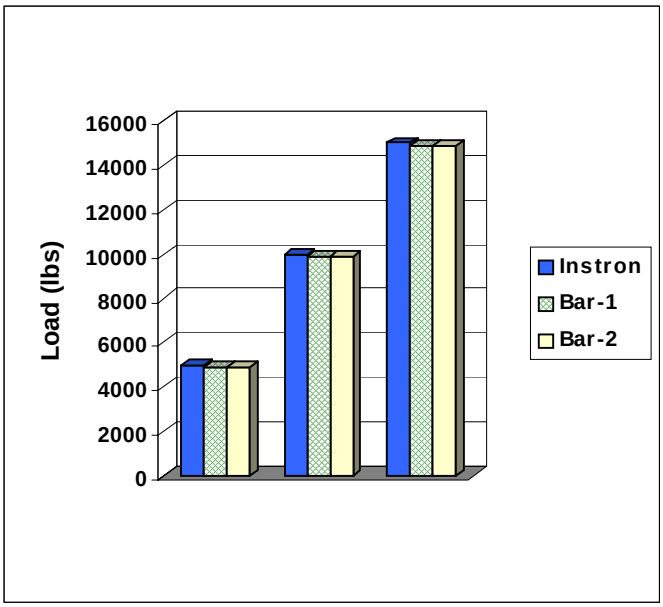

Figure 3.9 Calibration Check for Steel Gages.

Steel Strain

Most of the installed steel gages provided valid data. Gages SG-1 to SG-7 worked well but gage SG-8 apparently malfunctioned. The measured steel strains oscillated within each day, which can be seen in Figure 3.10. The figure presents the strain data from 2:00 p.m. on September 19 to 12:00 p.m. on September 20 for SG-1 to SG-6 and SG-8. (Note: The malfunctioning SG-8 does not show any change in reading with time.) The remaining six gages display an oscillating pattern of strain versus time of day. Temperature variation over a 24-hour period results in both expansion and contraction of the steel reinforcement which leads to varying stress levels in the bar as shown in the figure.

It should also be noted that SG-7, which was located 24 in from the induced crack, recorded compressive strains in the steel. Other functional gage stations, SG-1 to SG-6, were closer to the induced crack than SG-7 and each of them recorded tensile strains.

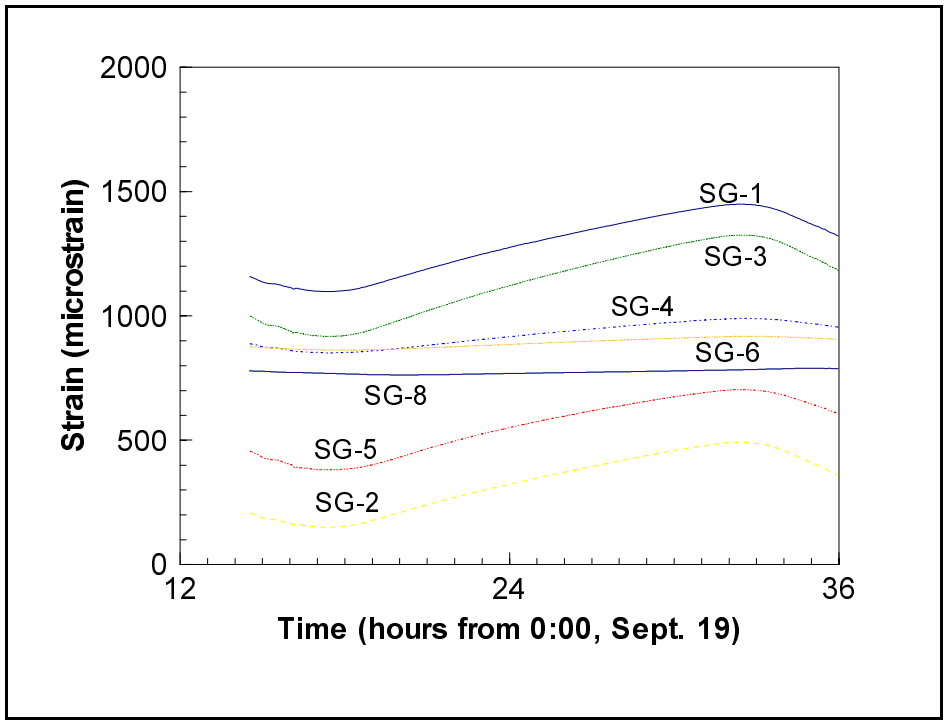

Figure 3.10 Steel Strains versus Time from 2:00 p.m., September 19 to 12:00 p.m., September 20.

The trend in steel gage readings appeared to be reasonable and indicated a dominating affect of drying shrinkage. Even though the thermal contraction of the concrete in the morning hours caused the steel rebar to undergo an additional stretching, resulting in a maximum tensile strain condition this incremental increase in strain is rather insignificant compared to the overall effect of the drying shrinkage on the steel strain. A minimum steel tensile strain condition occurred in the afternoon where the daily average strain is basically caused by concrete shrinkage.

Strain data at the crack face are shown in Figure 3.11. This figure indicates the development of the total strain trend (which was typical of all the steel strain gages) in the concrete with time. Creep strain, noted in this figure, averaged 400 to 500 microstrains for gages near the crack face but as will be elaborated in Chapter 4, diminished with time and displacement from the crack face. As shown in Figure 3.11, concrete creep strain decreased to zero after the concrete reached 5 to 6 days of age.

The steel stress data as calculated from the gage readings is presented in Appendix C. For each steel gauge position, the daily maximum strain, minimum strain, and average strain for steel strain stations SG-1 to SG-7 were calculated and are presented in plots contained in Appendix C. The additional figures in Appendix B display the force readings over 24-hour intervals. The location of each gage is denoted in a similar fashion to the concrete strain plots. The two numbers in the caption represent the distance from the induced crack in inches and the bar number relative to Figure 3.2.

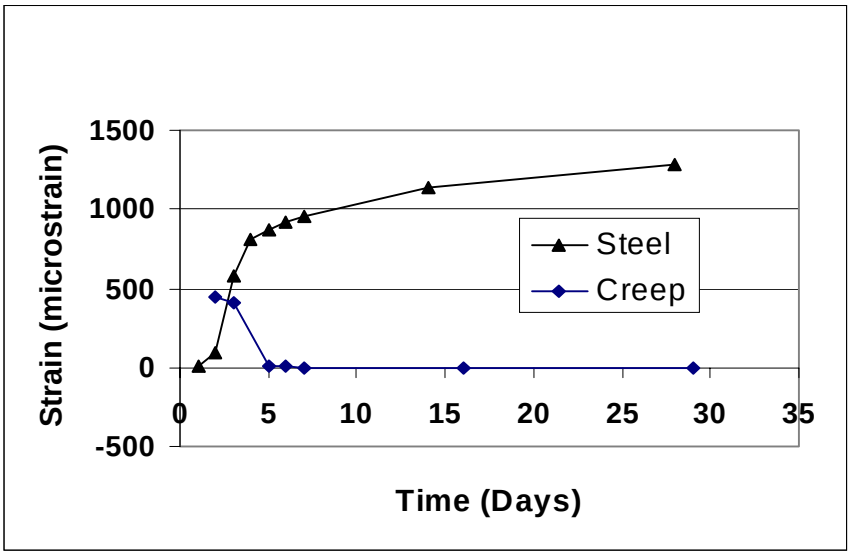

Figure 3.11 Average Steel Strain and Creep Strain Near Crack Face.

Crack Widths

In order to obtain an accurate portrayal of the development of cracks in the pavements a series of four LVDTs were placed across the induced crack at various depths below the surface of the pavement. Difficulties were experienced during the installation of the LVDTs which resulted in unusable data readings. As a result, profile crack width data was obtained via manual measurements on the slab surface and edges. In addition to the manual readings, an additional LVDT was mounted externally on the west side of the pavement (Figure 3.12). This side LVDT was placed at mid height of the pavement and recorded the crack opening width at the induced crack (#27).

Crack Spacing and Crack Width Data

Crack surveys were conducted daily for the first week after placement of the concrete. Initial cracking (particularly at the sawcut location) was observed on August 23 the first day after paving. Crack surveys were also conducted on September 5, 24 days after paving. The average

crack density (the reciprocal of the average crack spacing) of the cracking increased with age, as shown in Figure 3.13. The crack spacing distributions on different days are shown in Figure 3.14. As expected, the average crack spacing in the sawcut regions matched closely to the sawcut spacing. On September 5, the average crack spacing was 4.0 ft for the sawcut spacing of 6 ft, 8.8 ft for the sawcut spacing of 10 ft, and 9.8 ft for the sawcut spacing of 12.0 ft. The crack spacing distributions on September 5 for different sawcut areas are shown in Figure 3.15.

Figure 3.12 An LVDT Installed on the West Edge Side at Sawcut 27 to Measure Crack Opening Width.

The crack width distributions as measured on September 5 for different sawcut areas are shown in Figure 3.16. The collected data showed that the value of the maximum crack width varied directly with the spacing of the sawcuts (Figure 3.17). That is, the larger sawcut spacings led to the development of larger crack widths. In comparison, the maximum crack width

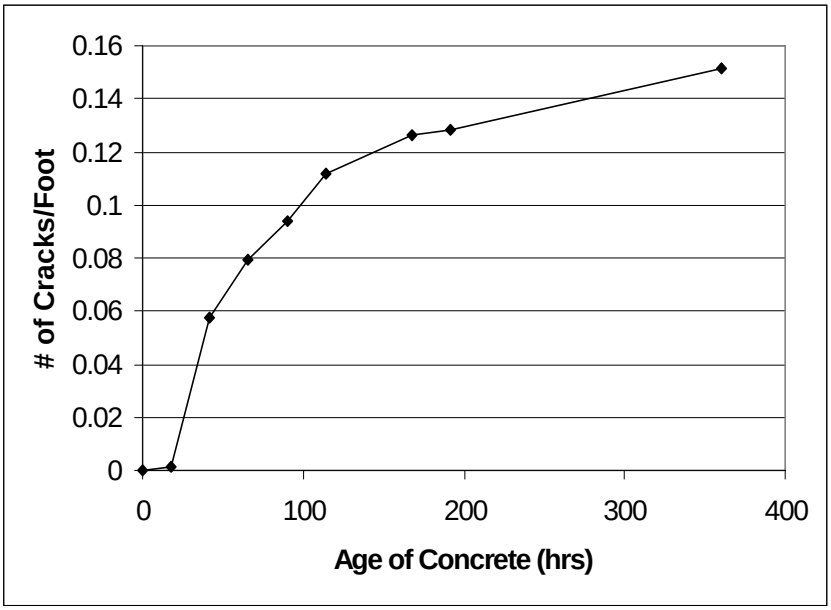

Figure 3.13 The Average Crack Densities of the Entire Paving Segment on September 5.

measured in the portion of the pavement without sawcuts was greater than any of the crack widths located in the sawcut regions. However, all of the measured crack widths were less than 0.5 mm. All of the data displayed in Figure 3.16 was collected on September 5. Crack widths observed between sawcuts #18 and #22 were not included in any of the comparisons made in Figures 3.14 to 3.17. This is because a box-out area formed in the pavement in this area caused severe cracking to the surrounding region. The maximum crack width measured in the area of the box, on September 5, reached 40 mils. This represents the limit of crack width of CRCP specified by the AASHTO Guide for Design of Pavement Structures. The placement of the box-out area and subsequent cracking induced from it points to a need for any cracking in CRC pavement to be uniformly and evenly developed or the result will be isolated, random wide cracks. This may apply particularly in the case of widely spaced early cracks.

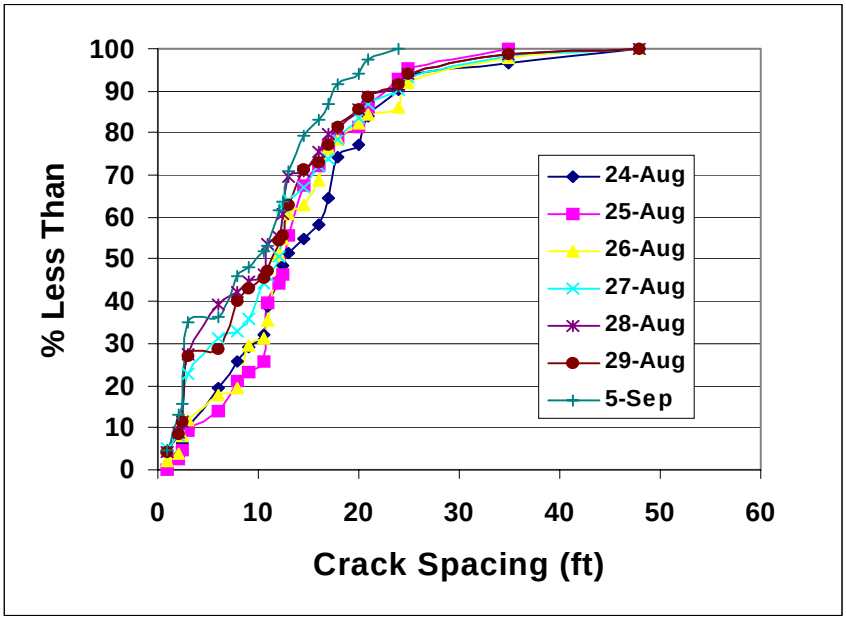

Figure 3.14 Crack Spacing Distributions on Different Days.

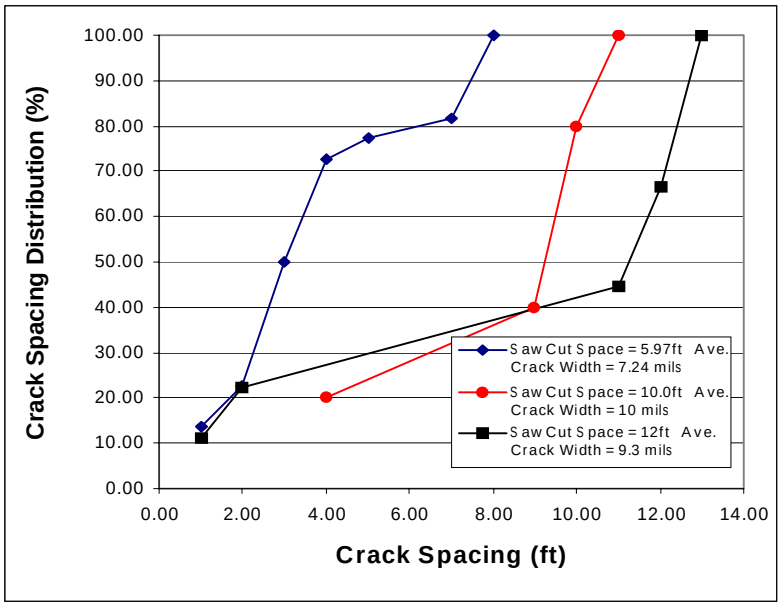

Figure 3.15 Crack Spacing Distributions for Different Sawcut Spacings on September 5.

Additional crack width data is provided in Appendix F. The crack width data displayed in Appendix E represents 24-hour plots of the crack width data obtained from the side LVDT. The plots show the variation of crack width (in mils) with respect to the time of day.

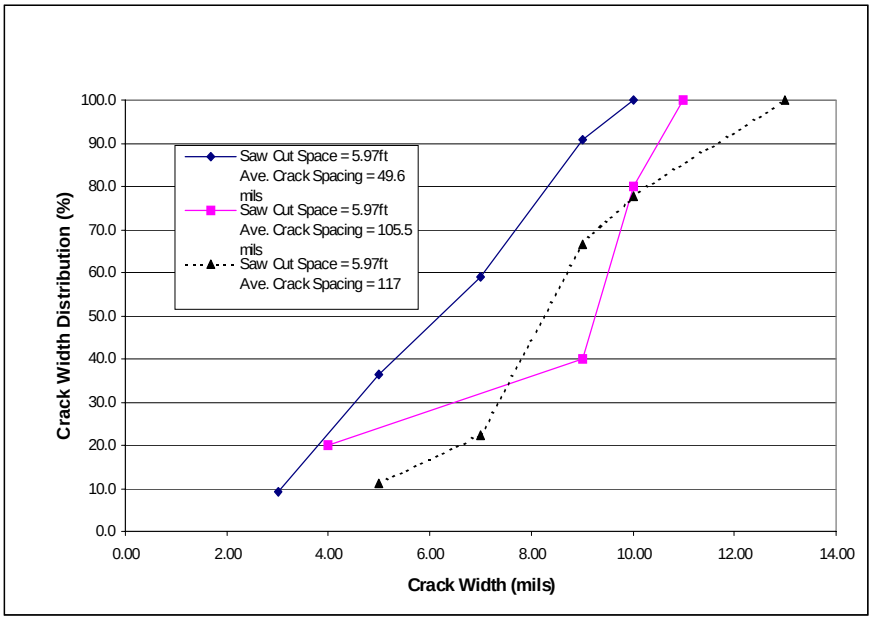

Figure 3.16 Crack Width Distributions for Different Sawcut Spacings on September 5.

Concrete Strength

In order to monitor the strength of the concrete pavement, sixteen 6" x 12" cylindrical specimens of concrete were cast at the paving site on the first day of construction. Half of these specimens were cured on site while the other half of the specimens were transported to a water tank, located in a field lab near the instrumentation site, for curing purposes (normally called "standard cure"). One specimen from each curing set was selected to be tested for compressive strength at 1, 3, 7, and 28 days. The compressive strength tests were performed at a nearby

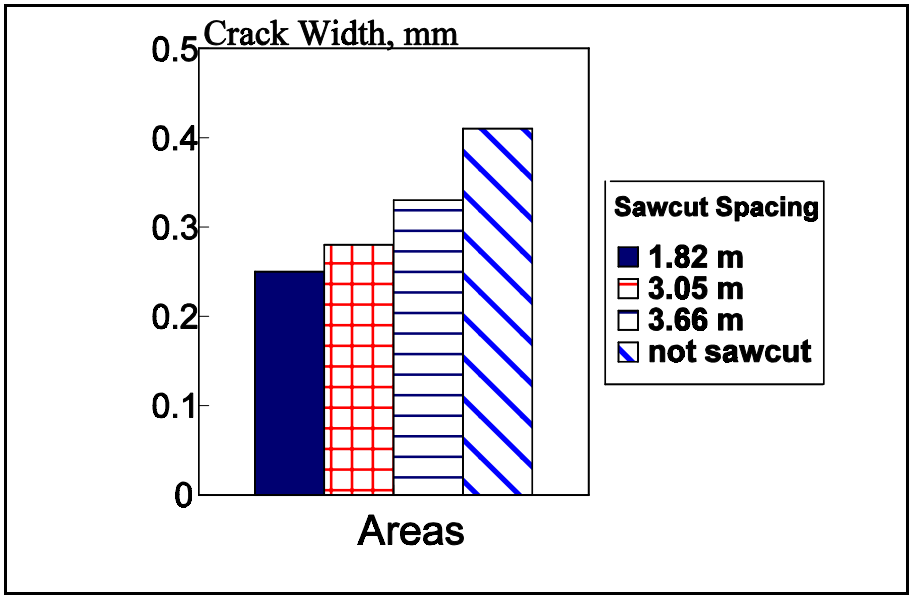

Figure 3.17 The Maximum Crack Widths for Different Areas on September 5.

laboratory following ASTM procedure C469. A second cylinder was tested for split-tensile strength at each day as well. The tensile strength tests were performed according to ASTM procedure C496. The maturity of each curing set was also monitored and recorded at the previously specified ages of the concrete (Figure 3.18).

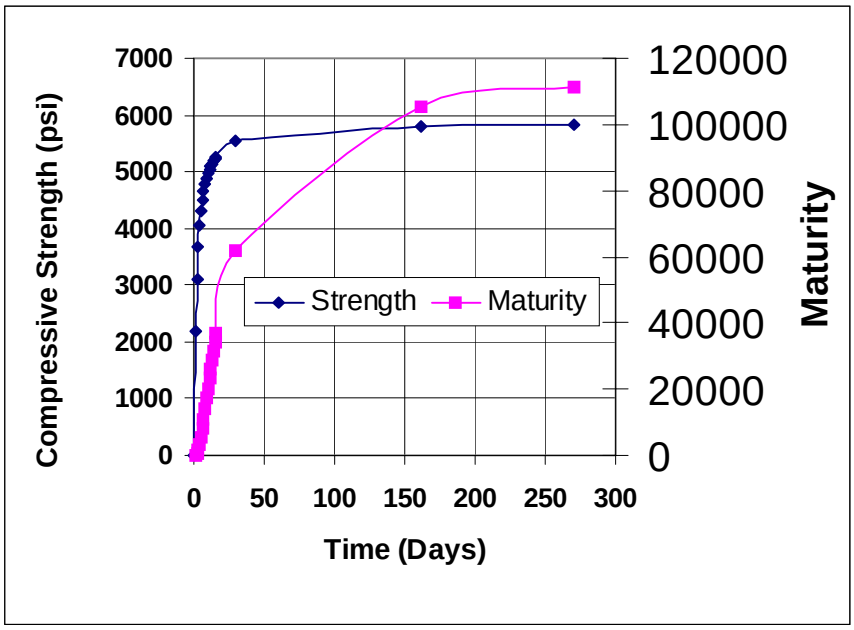

Figure 3.18 Compressive Strength and Maturity Data for Strength Specimens Prepared at the Project Site.

Compressive strength and maturity data for compressive strength specimens are shown in Figure 3.19. Compressive strengths and split tensile strengths of concrete specimens, either cured at the test site or in the lab water tank, increased with age. The increase in compressive strength over time, for both curing conditions, is displayed in Appendix B. The split tensile strength of both sets is also plotted versus time in this appendix.

Figure 3.19 Maturity of Concrete Cylinders Was Monitored at the Test Site.

Moisture and Temperature Measurements

A moisture apparatus containing three moisture meters was installed between sawcuts 26 and 27 in order to measure the temperature and the dew point in the pavement. Figure 3.20 shows the "moisture can" in place before paving. As shown, three brass inserts were placed 1 in, 3 in, and 7 in from the surface of the pavement. The brass inserts protruded outward from the can into the surrounding concrete. Several hours after the placement of the concrete, chilled mirror dew point sensors were inserted into the brass casings from the inside of the moisture can. These gages were used to detect the amount of moisture contained in the concrete.

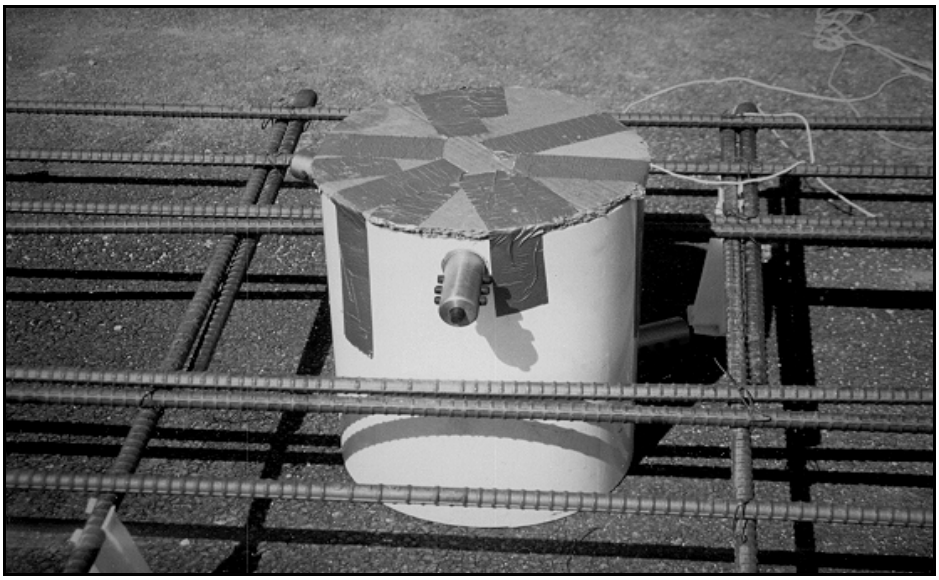

Figure 3.20 The "Moisture Can" in Place Before Paving.

The data collected from this procedure is presented in Appendix E. This appendix contains separate graphs for both the dry bulb temperature and the dew point versus time. The data is separated into 24-hour intervals beginning 5 hours after the concrete was placed. The charts also display the variation in both dry bulb temperature and dew point temperature with respect to depth in the concrete.

Weather

Weather data for the given pavement section was obtained in two distinct ways. During the first week of the pavement life a weather station was left on sight to record the temperature, the relative humidity, the solar radiation, the rainfall, and the wind speed. This data was collected in hourly intervals. After the first week, the weather station had to be removed but

weather data was obtained from the Houston International Airport weather logger for all subsequent days of the project. This data was available in 3-hour intervals. The recorded weather data is displayed in Appendix D of this report. The figures display the maximum, minimum, and average values of each of the weather variables throughout the duration of the pavement analysis. Pavement temperatures are also included in Appendix D.

CHAPTER 4
CHARACTERIZATION OF CRC PAVEMENT STRUCTURAL PARAMETERS

In this project, it was of prime interest to analyze measured steel strain and calculated slip displacements of steel reinforcing bars in CRC pavements based on instrumented measurement of strains of the steel bars and the concrete in the field as part of the effort to develop input data for the CRC pavement analysis models. A model described in Chapter 2 was developed for analysis of concrete/reinforcing steel behavior in CRC pavements at TTI in the late 1980's was used as the theoretical basis for the field tests. This model is selected because of its suitability to be calibrated and to analyze the type of data to be collected in the field and the convenience of making comparisons to the CRCP 8 program. Strain gages were installed in the concrete adjacent to the strain gages in the reinforcement and movements in the steel and concrete were measured directly by these strain gages. These measured strains were used to evaluate the stresses in the reinforcement. Strain measurements of this nature made it possible to determine interaction between the reinforcement and the concrete. From strains in the steel and concrete, slip displacements between the steel and the concrete along the steel bar were calculated. Accordingly, relationships between the bond stress and slip displacement were analyzed through the model aforementioned relative to temperature and moisture effects. Since the TTICRCP model played an important role in certain aspects of the project, further details of it are elaborated, regarding the interpretation of the bond-slip data.

These results were then compared with those obtained from computer simulations performed using the inputs derived from the analyzed data. The following chapter provides a description of the input parameters used in the computer simulations and the methods used to obtain the input values. In addition, a comparison between the results of the computer simulations and the actual field measurements is provided.

The Bond Shear Stress-Slip Relationship

As previously noted, a simplified bond shear stress-slip relation is adopted in the TTI model. This is a three-part linear function with three material constants, k_1, k_2, and δ_b shown in Figure 4.1. Slip or relative displacement between the reinforcement bar and concrete slab is denoted by u, which is the difference between u_s and u_c. Equations for each of the slip zones are given as follows:

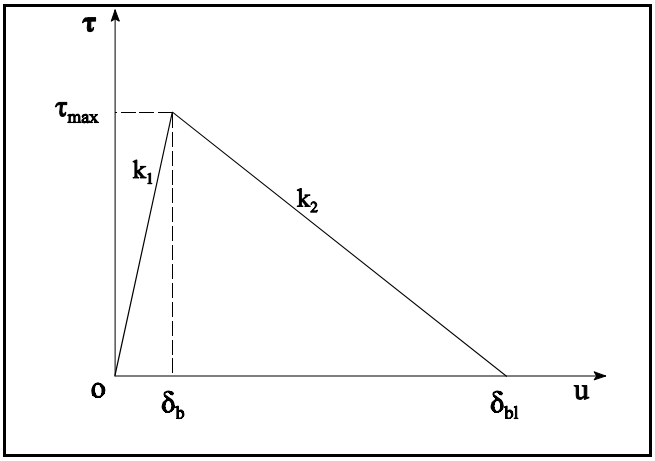

Figure 4.1 The Bond Shear Stress-Slip Model.

Zone 1: $0 < u \le \delta_b$

$$\tau = k_1 u \tag{4.1}$$

Note: at $u = \delta_b$, $\tau = \tau_{max} = k_1 \delta_b$.

Zone 2: $\delta_b < u \le \delta_{bl}$

$$\tau = \tau_{max} - k_2(u - \delta_b) \tag{4.2}$$

or

$$\tau = (k_1 + k_2)\delta_b - k_2 u \tag{4.3}$$

Note: at $u = \delta_{bl}$, $\tau = 0$;

and $\delta_{bl} = \delta_b (1 + k_1/k_2)$.

Zone 3: $u > \delta_{bl}$

Tensile Forces in Steel Reinforcing Bars

When the bond shear stress-slip relation and slip along the steel rebar are all known, the tensile forces in the rebar can be calculated with equation 2.17. The midpoint of the slab length corresponds to the coordinate "o" shown in Figure 4.2. Slip u at point "o" must vanish because both u_s and u_c vanish at this point because of the boundary condition associated with the TTI model. Placement of several strain gages inside the rebars in the concrete pavement (described in Chapter 3) will produce a direct measure of longitudinal strains in the rebar and the concrete to

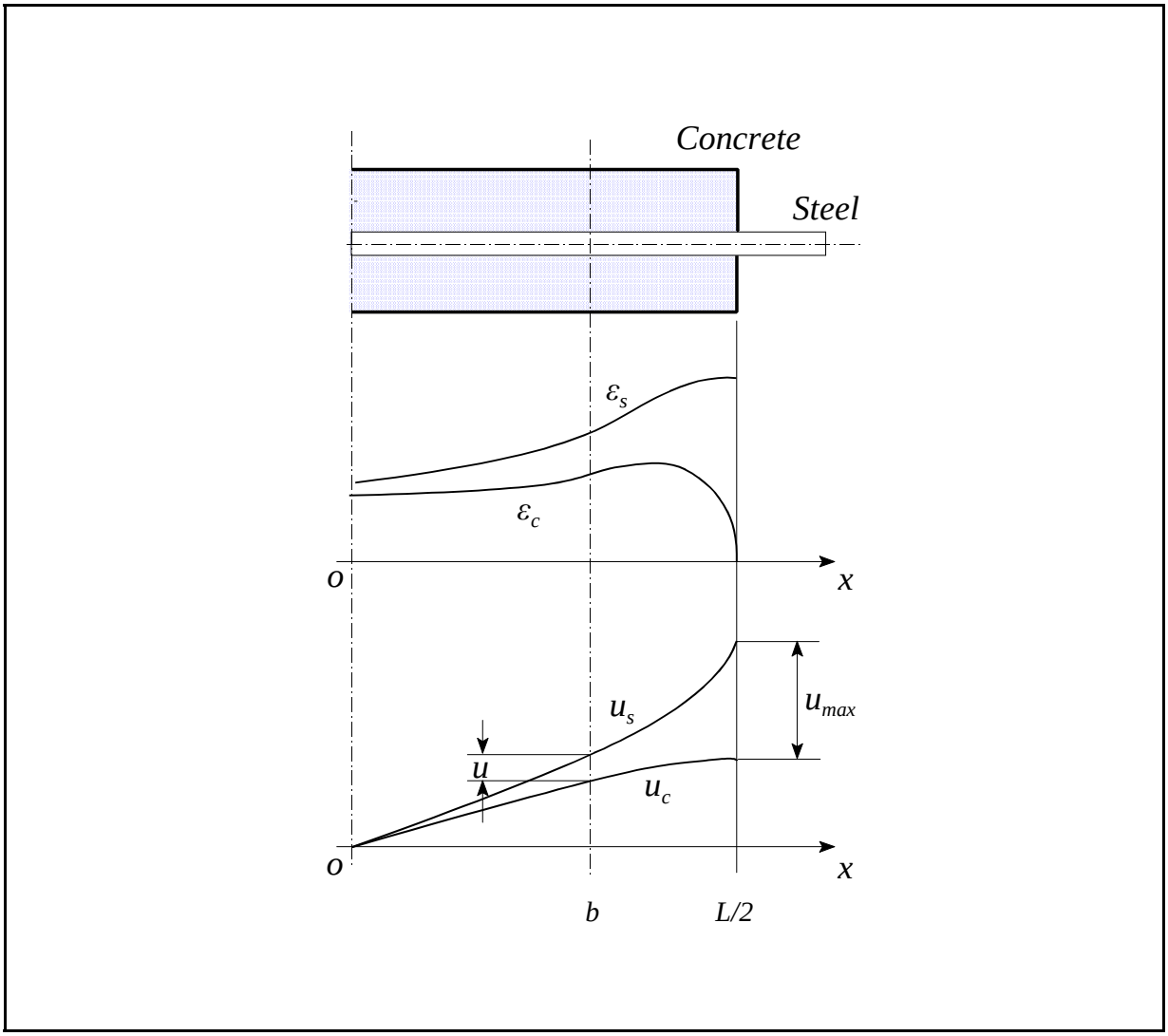

Figure 4.2 Determination of Slip from Strain Measurement [37].

allow the calculation of the slip along the rebar $u = u(x)$ through the following equation modified from that shown previously in Chapter 3:

$$u(x) = u_s(x) - u_c(x) = \int_o^x \varepsilon_s dx - \int_o^x \varepsilon_c da \tag{4.4}$$

The maximum slip u_{max} occurs at the crack surface and contributes to the opening of the crack. Figure 4.2 illustrates the process of the slip calculation.

Substituting $\tau = \tau(u) = \tau[u(x)]$ in equation 2.17, one obtains the tensile force in the rebar:

$$F(x) = A_s\sigma(x) = \pi d_s \int_0^x \tau[u(x)]dx + F_o \tag{4.5}$$

where F_0 is the tensile force in the rebar at $x = 0$, that is, F(0). Since the slip $u(x) = [u_s(x) - u_c(x)]$ is measured, equations 2.19 and 2.20 are decoupled. In other words, investigations on stresses in the steel and in concrete can be independent of each other.

The maximum tensile force and the tensile force at the location of the strain gage can be calculated directly from the measured strain as:

$$F(x) = E_s A_s(x)\varepsilon_s(x) \tag{4.6}$$

F_0 can be calculated based on measured strains with a gage mounted inside the rebar located at the middle point of the instrumented pavement segment. The tension values calculated with equations 4.5 and 4.6 should be identical. Comparison of them can be used to verify the model.

To demonstrate application of equation 4.1, a calculation example is given with an assumption that the measured slip u is a linear function of the location x, $u = kx$.

When $0 < x \le x_1$, where $x_1 = \delta_b/k$,

$$F(x) = \pi d_s \int_o^x k_1 u dx + F_o = \frac{1}{2}\pi d_s k_1 k x^2 + F_o$$

Thus, the tensile force at $x = x_1$ is

$$F_1 = F(x_1) = \frac{1}{2}\pi d_s \frac{k_1}{k}\delta_b^2 + F_o$$

When $x_1 < x \le x_2$, where $x_2 = \delta_{bl}/k$,

$$F(x) = \pi d_s \int_0^x [(k_1 + k_2)\delta_b - k_2 u]dx + F(x_1) = \pi d_s [(k_1 + k_2)k(x - x_1)x_1 - \frac{1}{2}k_2 k(x^2 - x_1^2)] + F_1$$

Thus, the tensile force at $x = x_2$ is

$$F_2 = F(x_2) = \frac{1}{2}\pi d_s \frac{k_1(1 + 2k_1 - k_1 k_2)}{k_2 k}\delta_b^2 + F_0$$

When $x > x_2$, the bond shear stress vanishes, and therefore the tensile force in the rebar remains F_2.

When $u(x)$ is nonlinear, calculations will be more complicated. Figure 4.3 shows an example, where bond shear stress and the tensile force in the steel rebar are derived from the assumed parabolic slip distribution $u(x)$ assuming $F_0 = 0$. It should be noted that F_0 is inherently not zero due to

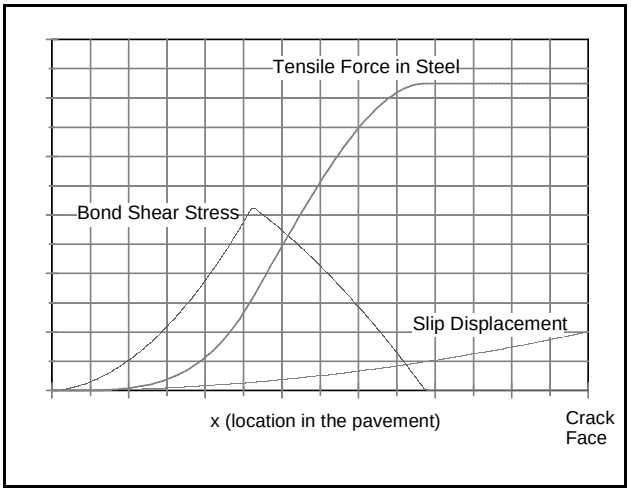

Figure 4.3 Bond Shear Stresses and Tensile Forces in the Rebar Calculated from a Parabolic Slip Distribution along the Rebar.

temperature changes. It is necessary to place a gage located at $x = 0$ to measure F_0, which is the required boundary condition for solution of the governing equation, equation 2.17.

The axial stress in the steel rebar in the CRCP slab may be estimated by a sum of the stress caused by concrete shrinkage and the stress caused by daily temperature fluctuation. Prior to presentation of the data analysis relative to the maximum steel stress observed in the field data, a brief introduction to fundamentals of thermal deformation and governing equations for the behavior of the steel reinforcing bar in CRC pavement is provided.

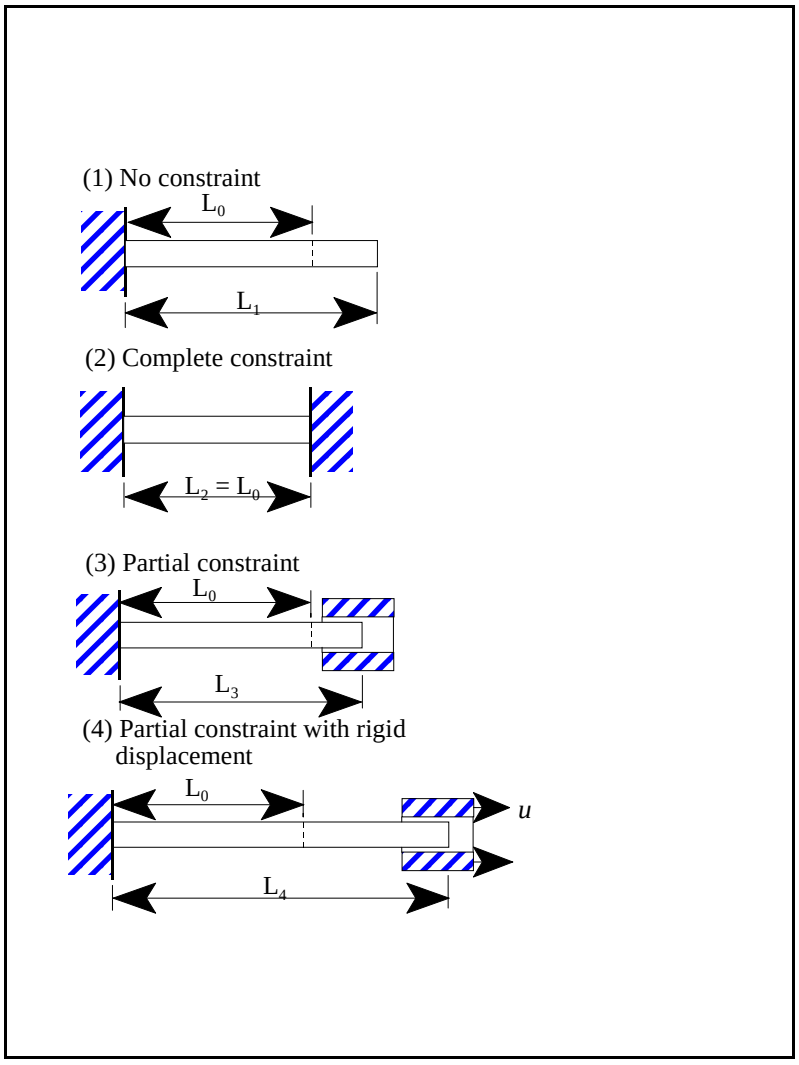

Figure 4.4 Four Cases for Thermal Expansion of a Rebar with and without Constraint.

Thermal and Shrinkage Deformation with Constraint

Rebar under temperature change intends to expand or contract. When constraint (i.e. $\alpha_s > \alpha_c$) exists to restrict the thermal expansion or contraction, compressive or tensile stresses result. Figure 4.4 shows four cases of a rebar when the steel temperature in it increases by ΔT. In case 1, the rebar can expand freely, therefore the axial strain in the rebar is $\varepsilon = (L_1 - L_0)/L_0 = \alpha \Delta T$, where L_1 is the current length of the rod, L_0 is its initial length, and α is the coefficient of thermal expansion of the rebar, but since the restraint is zero there is no axial stress or $\sigma = 0$.

In case 2, the rebar cannot expand because of the complete or rigid constraint ($\alpha_c = 0$). In this case, $\varepsilon = 0$ but $\sigma \neq 0$. To obtain σ, we may imagine two steps. In step 1, the rebar expands freely as in case 1 so that $\varepsilon = (L_1 - L_0)/L_0 = \alpha \Delta T$ and $\sigma = 0$. In step 2, an external compressive force is exerted to the free end of the rebar to push it back to its initial length L_0. As a result, the final length of the rebar is L_0 so that $\varepsilon = 0$ and $\sigma = -E \alpha \Delta T$, where E is the elastic modulus of the rebar and the minus sign denotes compression.

In case 3, constraint is partial. As shown in the figure, the constraint is the friction (or a shear spring) between the rebar and the surrounding concrete. This case can also be decomposed into two steps. Step 1 is free expansion of the rebar. In step 2, the rebar is pushed back by a force, which is supplied by the constraint, from the length of L_1 to L_3. Since the constraint is not complete, L_3 is longer than L_0. Therefore, $\varepsilon = (L_3 - L_0)/L_0 < \alpha \Delta T$ and $\sigma = E(\varepsilon - \alpha \Delta T) < 0$. More clearly, the total strain can be decomposed of two parts: elastic strain ε^e and thermal strain ε^t as $\varepsilon = \varepsilon^e + \varepsilon^t$, where $\varepsilon^t = \alpha \Delta T$ and ε^e is related to σ with Hooke's law $\sigma = E\varepsilon$. If the constraint moves away, the final length of the rebar L_4 is longer than L_3 (which constitutes case 4).

In case 4, σ can be compressive or tensile, depending on how far the constraint displaces. The situation of the steel rebar in CRCP is similar to case 4, where the constraint is the bond between the rebar and concrete and the amount of constraint displacement depends on the amount of creep in the concrete.

Effect of Creep on the Stress in the Steel Rebar

Forces acting on a segment of the steel rebar include the tension (or compression) on the rebar cross section and the shear bond stress around the lateral surface of the rebar segment (Figure 4.5 - as an

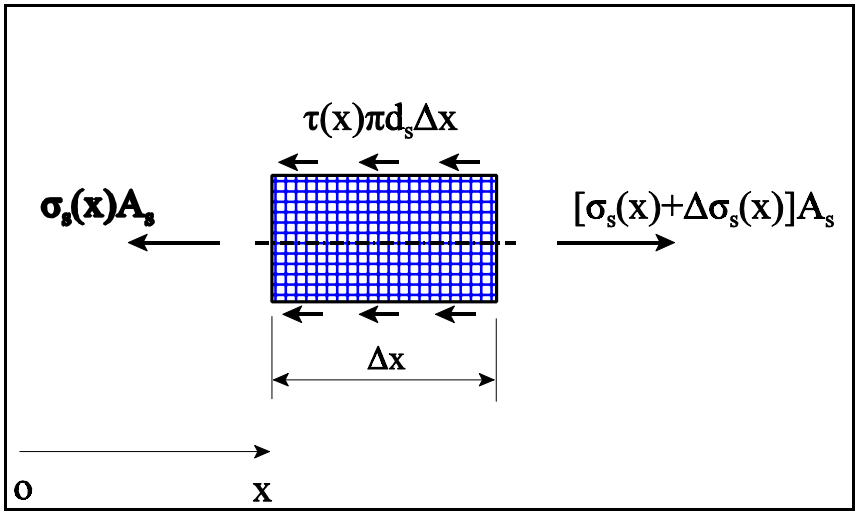

Figure 4.5 Forces Acting on a Small Segment of the Steel Rebar.

expanded view of Figure 2.14). The shear bond stress depends on the slip between the rebar and concrete that provides a partial constraint to the rebar. Equilibrium of the forces at the location x (along the steel bar) in the longitudinal direction leads to equation 2.16 previous noted:

$$[\sigma_s(x) + \Delta\sigma_s(x)] = \sigma_s(x)A_s + \tau(x)\pi d_s \Delta x$$

where A_s is the steel rebar cross-sectional area and d_s is its diameter. As $\Delta x \to 0$, the above equation becomes:

$$A_s \frac{d\sigma_s}{dx} = \pi d_s \tau$$

where the shear bond stress τ depends on the slip between the steel and concrete. The term $(\frac{d\sigma_s}{dx})$ represents the change in the steel stress over the bond development length of the steel bar.

Following a parallel development as Vetter (9), this change in stress can be related to shrinkage, creep, and elastic strain in the concrete as:

$$\tau = \frac{A_s E_s}{d_s \pi}\left[\frac{d(\varepsilon_{sh} + \varepsilon_{crp})}{dx} + \frac{d\varepsilon_s}{dx} - \frac{d\varepsilon_c}{dx}\right] = \frac{A_s E_s}{d_s \pi}\left[\frac{d\varepsilon_s}{dx} - \frac{d(\varepsilon_c - \varepsilon_{crp})}{dx}\right] \qquad (4.7)$$

where ε_{crp} is the creep strain and ε_c is the strain in the concrete. The shrinkage strain (ε_{sh}) component drops out because it is assumed this strain does not vary with distance from the crack face. Figure 4.6 shows experimentally determined relations of the shear bond stress τ versus the slip u. When the slip is less than 40 mils, we may use a proportional function to approximately characterize the τ-u relation relative to equation 4.1. Based on Figure 4.6, k is approximately 7,000 psi/in. The total axial or measured strain of the steel reinforcement bar ε_s consists of two parts, elastic strain ε_s^e and thermal strain ε_s^t, as

$$\varepsilon_s = \varepsilon_s^e + \varepsilon_s^t \qquad (4.8)$$

The thermal strain depends on the temperature change:

$$\varepsilon_s^t = \alpha_s(T - T_0) \tag{4.9}$$

where T is the rebar temperature, T_0 is the initial or reference temperature, α_s is the coefficient of thermal expansion of the steel, and the elastic strain is related to the steel axial stress σ_s:

$$\sigma_s^e = E_s \varepsilon_s^e \tag{4.10}$$

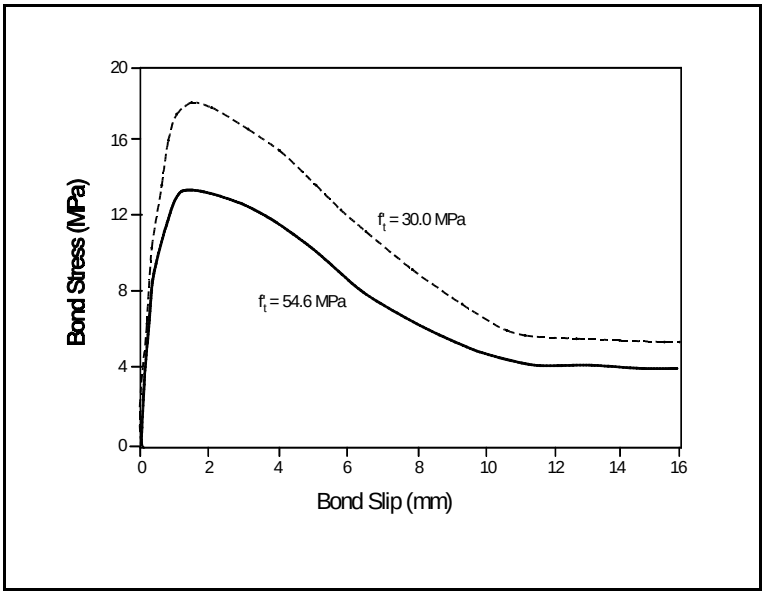

Figure 4.6 Bond Shear Stress versus Bond Slip Relations [25].

where E_s is the elastic modulus of the steel. It is interesting to note that the strain measured with a strain age is the total strain, not the elastic strain. To calculate the axial stress σ_s, we need to combine equations 4.8 to 4.10, which results in:

$$\sigma_s = E_s(\varepsilon_s - \varepsilon_s^e) = E_s[\varepsilon_s - \alpha_s(T - T_0)] \tag{4.11}$$

Substituting equation 2.16 into equation 4.1, we obtain:

$$\frac{d\sigma_s}{dx} = \frac{\pi k d_s}{A_s} u \tag{4.12}$$

or

$$\sigma_s = \frac{\pi k d_s}{A_s} \int_{x_0}^{x} u(x)\,dx \tag{4.13}$$

in which x_0 represents the location where $\sigma_s = 0$. Both equations 4.11 and 4.13 are useful in estimating σ_s. The slip u is the relative displacement between the steel rebar and concrete:

$$u = u_c^{(s)} + u_c^{(t)} - u_s^{(t)} \tag{4.14}$$

where $u_c^{(s)}$ is the displacement of the concrete due to shrinkage, and $u_c^{(t)}$ and $u_s^{(t)}$ are the displacements of concrete and steel, respectively, due to thermal expansion. $u_c^{(s)}$ is positive when concrete shrinks, and $u_c^{(t)}$ and $u_s^{(t)}$ are positive or negative when either the pavement temperature is higher or lower than the reference temperature. These displacements are not fully developed or completely restrained. Basically, $u_c^{(s)}$ changes very slowly where, comparatively, $u_c^{(t)}$ and $u_s^{(t)}$ change more quickly because they change with temperature periodically within a 24-hour period.

Combining equations 4.10, 4.13, and 4.14, we have:

$$\varepsilon_s^e = \frac{\sigma_s}{E_s} = \varepsilon_s - \alpha(T - T_0)$$

$$= \frac{\pi k d_s}{A_s} \int_{x_0}^{x} u_s^{(s)} dx - \frac{\pi k d_s}{A_s} \int_{x_0}^{x} (u_s^{(t)} - u_c^{(t)}) dx$$

To obtain an exact solution of ε_s^e or σ_s , we need to solve all these displacements together with a certain amount of information from lab and field tests. As a simplification, the following method is used to approximately estimate the axial steel rebar stress from existing data.

Since the first term in the right side of the above equation changes slowly and the second part goes up and down once a day, the daily average of the measured steel rebar strain ε_s can approximately be taken as the elastic strain in the steel caused by concrete shrinkage under the existing constraint, corresponding to the strain caused by creep in the concrete (particularly over the first five days). So far as the elastic strain in the steel caused by daily temperature fluctuation

is concerned, the local thermal strains serve as an estimation, that is, - ($\varepsilon_s^t + \varepsilon_c^t$). This assumption may be applicable after creep in the concrete has diminished to a small level since it is presumed a complete constraint replaces the actual partial constraint of the steel-concrete bond. However, any error due to these assumptions may not be significant, because, as previously noted in Chapter 3, stress caused by the thermal effect is relatively small compared to that caused by the concrete shrinkage.

Program Inputs

Each of the computer simulation programs (the CRCP 8 and the TTICRCP programs) require a good deal of input information about the pavement in question. Many of the program inputs do not change over time but some of the inputs are a function of time. However, in this report it is assumed the reader is familiar with the type of inputs required for these programs, and consequently only limited discussion of the program inputs will be given, but some attention will be given to the characterization of key parameters such as strength or the time of setting. A general list of inputs are displayed in Table 4.1 and were obtained from the design plans for the project or through laboratory testing. The concrete set temperature was based on the concrete temperature at the time of final setting as defined by ASTM C 403 (Figure

Table 4.1 Computer Simulation Inputs.

Initial Crack Spacing (in)	120
Steel Diameter (in)	0.75
# of Steel Layers	1
E - Steel (psi)	30600000
Coeff. of Thermal Contraction (Steel)	5.0E-6
Steel Spacing (in)	6
Slab Thickness (in)	15
Ultimate Shrinkage	0.000700
Curing Temperature (°F)	106
Concrete (CTE) x 10^{-6}/°F	6.1*
Wheel Load (lbs)	0
Tire Contact Radius (in)	0
E - Subgrade (psi)	100

*Note: CTE at days 30, 162, and 270 were determined to be 5.5, 14.2, and 13.2 microstrains/°F, respectively.

A.1). However, McCullough and Schindler [44] recommended using 93 percent of the peak temperature as the input set temperature (which in this case is 111°F). The coefficient of thermal expansion (CTE) of the concrete was determined following a procedure outlined in reference 39. The concrete CTE was also evaluated using the concrete strain readings from the gage nearest the induced crack face and temperature data at days 30, 162, and 270. These values are listed at the bottom of Table 4.1. The later two values are approximately double what was expected which may be due to the effect of moisture levels less than saturation in the concrete at that point in time. Neville [43] indicated this affect can insignificantly increase the CTE of concrete. The ultimate shrinkage listed in Table 4.1 was based on laboratory shrinkage data following a procedure similar to that prescribed in ASTM C 157 and is discussed later in the chapter. The general inputs presented here were used in both of the computer simulation programs.

The time-dependent inputs required for each simulation program were distinct. In order to provide a thorough comparison of the computer-simulated predictions with the actual measured values, the research team chose to make comparisons at four different stages of the pavement life. The pavement ages chosen for the comparisons were at 16, 30, 162, and 270 days from the placement of the concrete. All pertinent data dealing with the concrete and steel strain, the crack widths, the pavement temperature, etc. were measured at each of these points in time. Some of the data such as concrete strength had to be estimated for the last two time periods because measurements were made unfeasible due to further construction in the surrounding area.

The remainder of this chapter addresses the development of time-dependent parameters which were used in CRCP 8 and TTICRCP computer simulations for the purpose of comparison to field measurements. Many of the comparisons explained in this chapter are further illustrated in Appendix A. The methods used to obtain these parameters and other necessary inputs are also presented in this section along with appropriate references to the Appendix A figures.

Steel Stress and Strain

It is of interest to develop bond stress and slip data from the field measurements which primary involves the steel strain data. The first step in this process required developing charts

showing the steel strain as a function of distance from the crack face (Figure 4.7). While not used as a program input itself, the change in strains and stresses with distance measured in the reinforcing steel is needed in order to calculate the bond stress and slip. The applied force present in the reinforcing steel was calculated from the data captured by the data logger following the procedure described in Chapter 3 and elaborated in Chapter 4. This data was then used to calculate the strain in the reduced cross-section (or cross-sectional area of the gaged area, which was smaller than the total bar cross sectional area) and the stress in the steel reinforcement. The strain in the cross section was obtained by dividing the force value by the constant of proportionality (C) explained in Chapter 3. The steel stress was obtained by dividing the force calculated for the reinforcing bar by the total cross-sectional area of the bar. Theoretically, these curves should coincide, but due to experimental error, some differences (although small) exist between them. The resulting values are illustrated in Figure 4.7 showing strain and stress as a function of distance from the induced crack. Similar data as shown in Figure 4.7 is provided in Figures A.2 through A.5 and represents the data obtained on selected days. Strains indicated in Figure A.2 were recorded prior to crack development at the sawcut notch. Comparison of the data shown in Figure A.3 to Figure A.2 will indicate the difference in strains at the crack face and along the steel bar before and after crack development and the sawcut notch. However, based on discussions provided in Chapter 3, it appears the data points

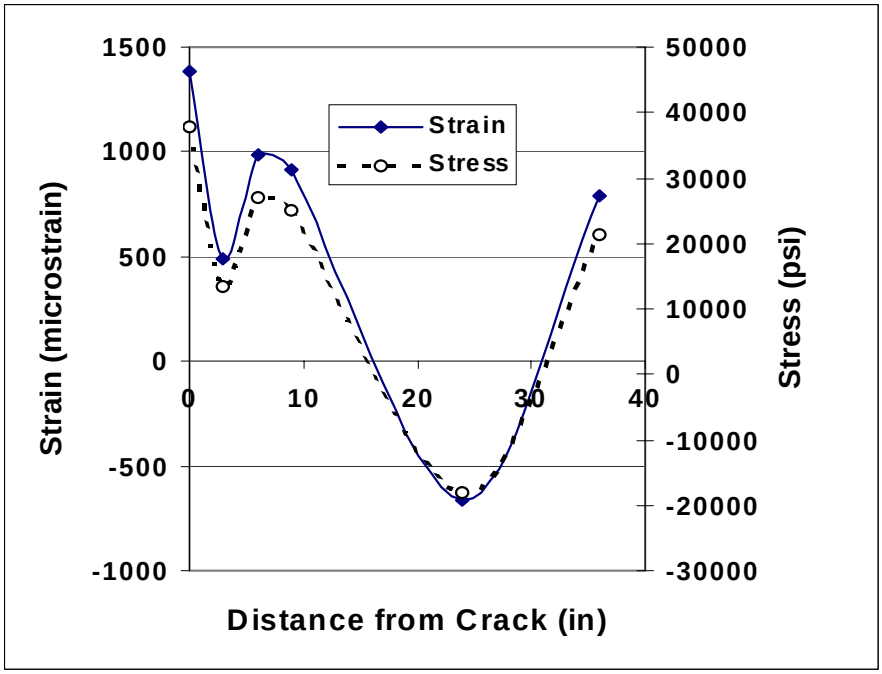

Figure 4.7 Steel Stress/Strain versus Distance from the Induced Crack as Measured on Day 30. (Note: The horizontal axis is vertically centered.)

36 inches from the crack face are in error, as may also be the case with the data 3 inches from the crack face. The maximum stress indicated in Figure 4.7 is 37,700 psi and the maximum stress of 43,600 psi was recorded on day 162 in January 1998.

Concrete Stress and Strains

The concrete data, similar to the steel data, was required in order to obtain values for the bond behavior. Concrete gages, as described in Chapter 3, were used to measure the strain in the concrete surrounding the reinforcing steel. The concrete strain behavior is very different from the steel strain behavior in that the concrete gage reading indicates a degree of relaxation. In other words, the development of stress in the concrete (Figure 4.8) is directly related to the restrained level of strain or the restrained strain which is a component of strain that must be extracted from the reading of the concrete strain gage. The restrained-strain is determined by calculating the difference between the free shrinkage strain (at a certain point in time) and the strain indicated by the concrete gage (less the amount of creep that has occurred at that point in time). The measured characteristics of creep are elaborated further below but a large percentage of creep occurred in the first three days of age while the concrete was stiffening. In order to calculate the restrained strain, it was necessary to estimate the ultimate shrinkage (ε_{ult}) that would occur in the concrete

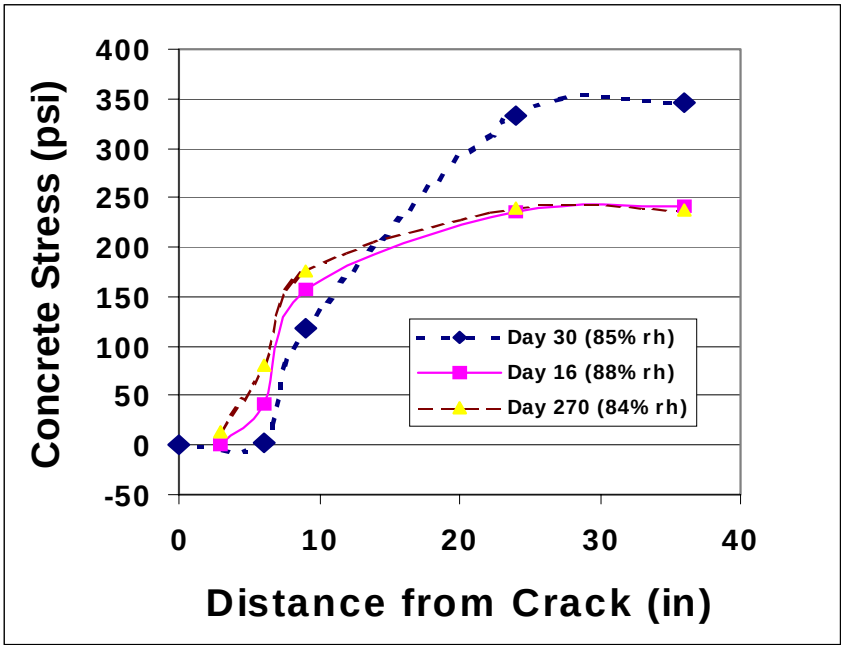

Figure 4.8 Concrete Stress versus Distance from the Induced Crack. (RH values were measured at 1 in below the surface).

placed at the project site. This determination was based on shrinkage measurements made on-site over a 28-day period using the following model [45]:

$$\varepsilon_{shr}(t) = \varepsilon_{ult}\left[\frac{t}{n+t}\right]$$

where t is time of shrinkage and n is the half of the time to achieve the ultimate shrinkage. Fitting this mode to the measured data yielded an ultimate shrinkage of 700 microstrains and a value of n = 25.6 days. The development of the shrinkage strain was projected as shown in Figure 4.9. The relative humidity of the concrete (rh - as indicated in Figure A.6) was used to determine the amount of drying shrinkage at any point in time based on [46]:

$$\varepsilon_{shr}(t) = \varepsilon_{ult}(1 - rh^3)$$

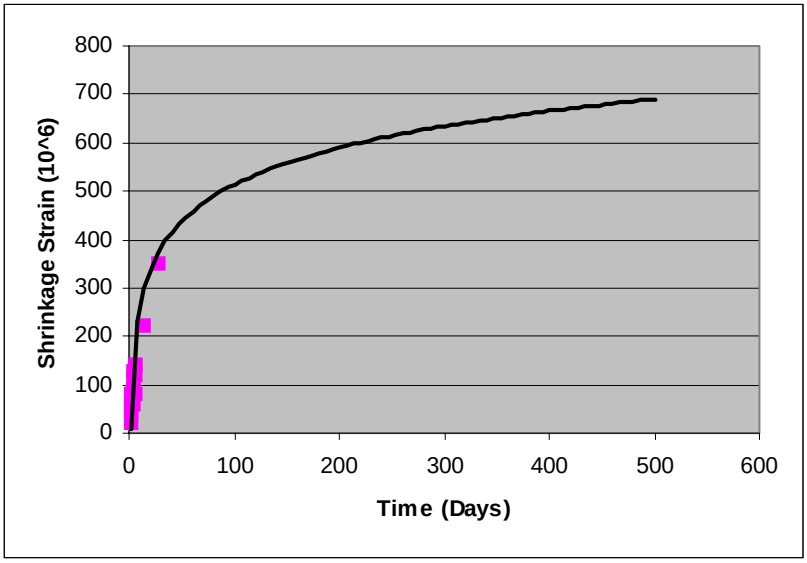

Figure 4.9 Projection of Concrete Shrinkage Based on Field Measured Concrete Shrinkage Strains.

As previously noted, the restrained strain was determined from the difference in the gage reading and drying shrinkage less the amount of creep. This quantity was converted into a stress value by simply multiplying by the modulus of elasticity of the concrete calculated for that particular concrete age. The concrete modulus, for each day of the analysis, were obtained from the compressive strength measurements based on compressive tests on the cylinder specimens cured at the test site. The variation in concrete stress with respect to distance from the induced crack, as measured at days 16, 30, and 270 of the project, is displayed in Figure 4.8. Given the measured relative humidity values of the concrete, as indicated in Appendix A (Figures A.6 and A.7), the corresponding calculated shrinkages, and the noted creep stains subsequently discussed,

stress levels in the concrete matched reasonably well with the concrete stress predictions discussed later in the chapter from the CRCP 8 program. It is interesting to note that the creep strain nearly canceled out any development of restrained strain in the vicinity of the crack face, as noted in Figure 4.8. Even though the degree of drying was greater at day 270, the total state of stress was lower in the concrete since the temperature difference was not as much as it was on days 16 and 30.

Concrete Creep

As noted previously, the majority of creep strain within the concrete occurred during the first five days of the pavement life. The creep was determined by comparing the shift in the reference point of the concrete strain reading from day-to-day at 6:00 am. The strains which were measured on each day are shown in Figure A.8 and summarized in Figure 4.10 as a function of distance from the crack face. This behavior seems to demonstrate a sensitivity of the creep to the state of stress state in the concrete in the vicinity of and along the axis of the reinforcing steel, based on the direction of the shift in the reference point of the gage. Also as noted in Figure 3.10, essentially all of the creep ended after day 5. It is also noteworthy to point out that cracking was observed to initiate at the sawcut notch on the morning of the fourth day after placement of the concrete at the time where the creep strain had nearly diminished to zero (as is indicated in Figure 3.10 for creep development near the crack face). Due to the effects of creep, the steel strain measurements used for the calculation of bond

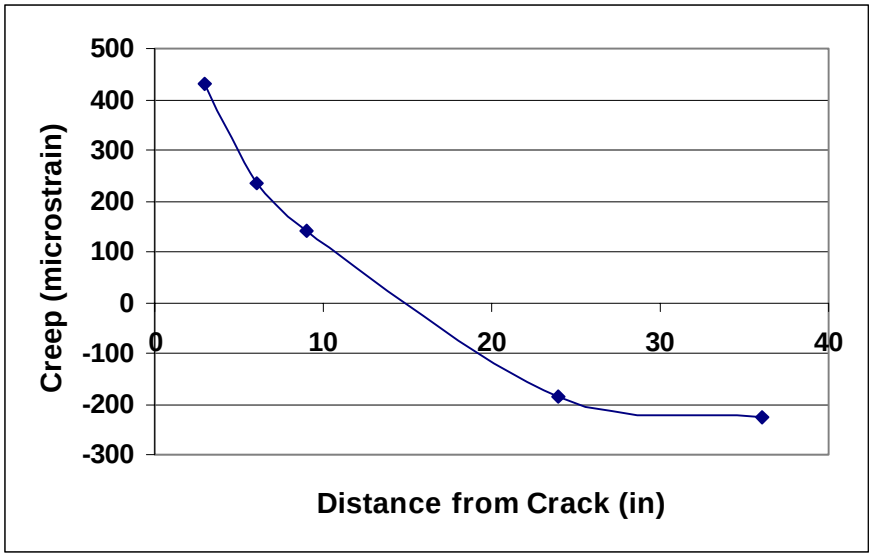

Figure 4.10 Concrete Creep Strain Variation with Distance from the Crack Face.

stress and bond slip were adjusted in order to take creep into account, in accordance with equation 4.7. The creep is mathematically subtracted from the concrete strain, and the resulting value subtracted from the change in steel strain to arrive at bond stress value. Bond stress diagrams derived from the CRCP 8 program are shown in Figures A.9 to A.11 and are discussed further later in this chapter.

Crack Widths

The crack width data was measured during crack surveys which were conducted for the first week after the paving took place. On two of these days, a profile of three distinct crack widths was recorded. The noted crack width measurements were made 2 in below the pavement surface, at mid-depth (7.5 in), and 13 in from the surface of the pavement. Figures 4.11 and 4.12 display the crack width/crack spacing ratio as it varies with depth below the pavement surface. The crack spacing used for these figures was obtained by averaging the crack spacing on each side of the measured cracks.

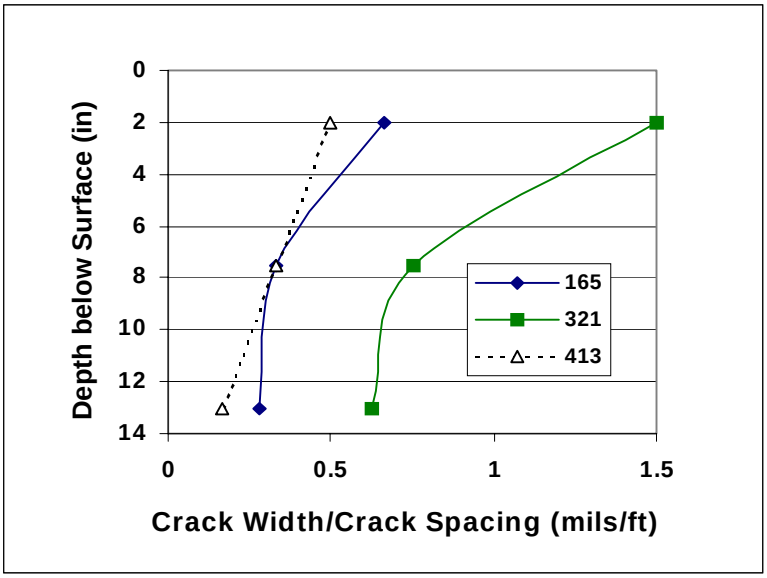

Figure 4.11 Crack Width Profile Data for Day 2.

Additional crack width data was obtained by way of the LVDT installed on the side of the pavement. The maximum, minimum, and average values measured for each day of the pavement life are displayed in Figure 4.13. Comparisons to computer results are presented later in this chapter and Appendix A.

Concrete Pavement Temperature

The computer simulation programs required the input of various pavement temperatures. The pavement temperature was obtained through temperature sensors located on the concrete strain gages. Due to the position of the concrete gages, the recorded temperatures reflect the temperature in the middle of the pavement. Table 4.2 lists the minimum pavement temperatures recorded for each day beginning with the concrete set temperature. The set temperature was determined based on the maximum concrete temperature developing within the 24 hours of placement and to the setting characteristics of the concrete as defined by ASTM C 403 (Figure A.1) as previously noted. Concrete pavement temperatures for the first seven days after placement are shown in Figure 4.14.

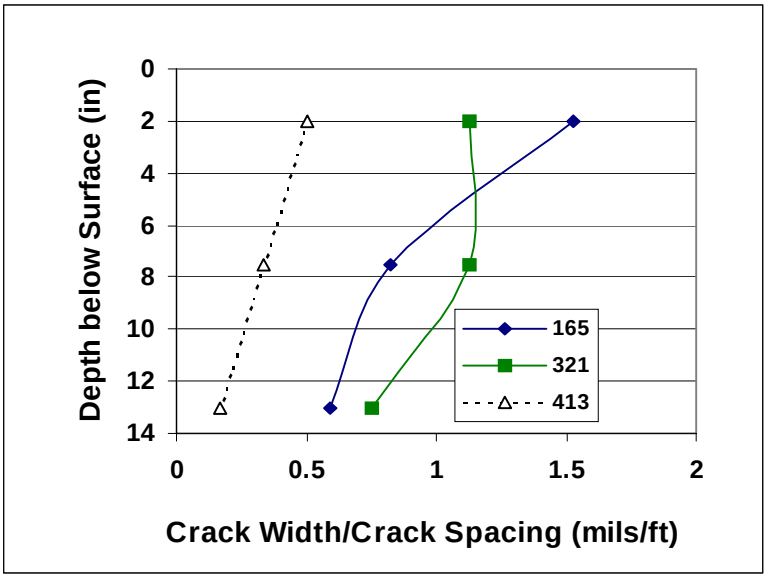

Figure 4.12 Crack Width Profile Data for Day 3 at Various Station Locations.

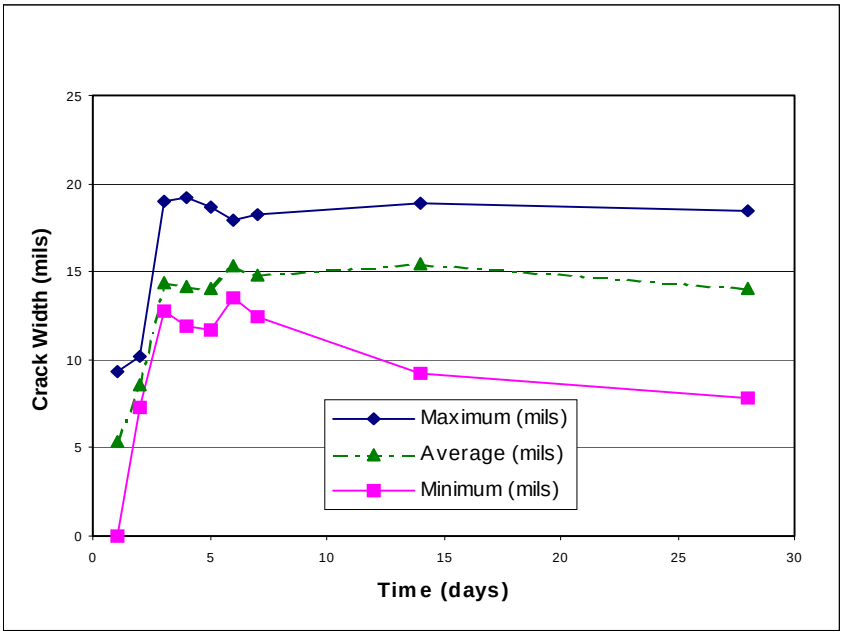

Figure 4.13 Crack Width Measurements versus Time.

Steel-Concrete Interaction

The interaction between the steel and the concrete was analyzed using a series of equations presented by Nilson [37] referred to in Chapter 3 and discussed earlier in this chapter. As it was pointed out, the bond stress (stress present in the bond between the steel and the concrete) can be related in terms of the steel strain by way of equation 4.6.

Table 4.2 Daily Minimum Pavement Temperature Values.

Set Temperature	106 °F
Day 1	105 °F
Day 2	102 °F
Day 4	90.5 °F
Day 5	89.9 °F
Day 6	88.9 °F
Day 7	88.8 °F
Day 16	75 °F
Day 30	79 °F
Day 161	61 °F
Day 270	75 °F

The bond stress values were determined for each location using the slope of the steel strain diagram at that location. Figure 4.15 displays a plot of the bond stress data, for day 30, as it varies with the distance from the induced crack. The bond stresses calculated for other days in which analysis was conducted are found in Appendix A (Figures A.9 to A.11). These figures display expected trends for the bond stress. The bond stress increases with distance over the first interval due to the fact that less and less slip takes place further away from the crack face. With less and less slip, the strain in the concrete and steel approach each other to a greater extent leading to the increase in bond stress. Theoretically speaking, as

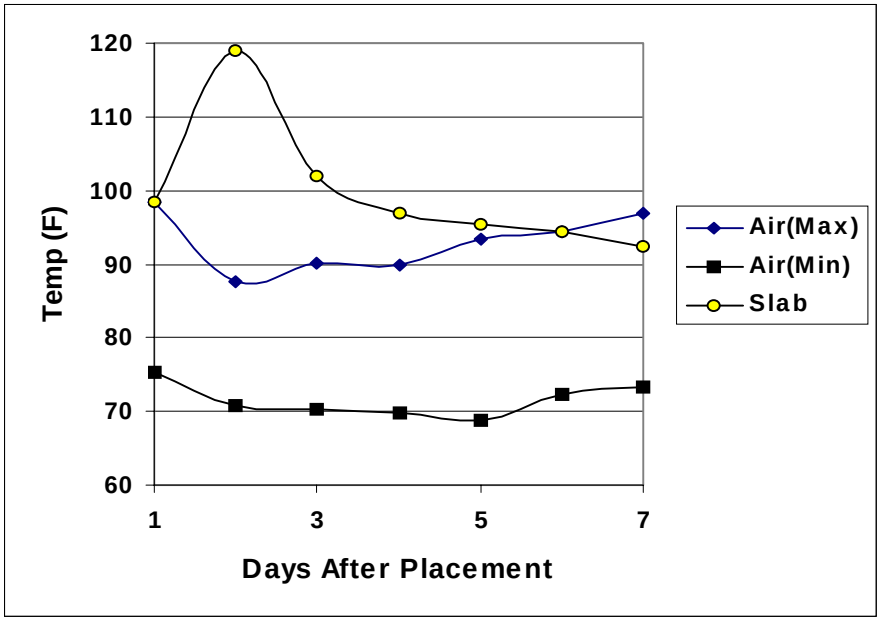

Figure 4.14 Ambient and Slab Temperature the First Seven Days after Construction.

the bond stress exceeds the tensile strength of the concrete, cracking occurs. Then after a point the bond stress begins to decrease due to the greater amount of slip that occurs near the crack face.

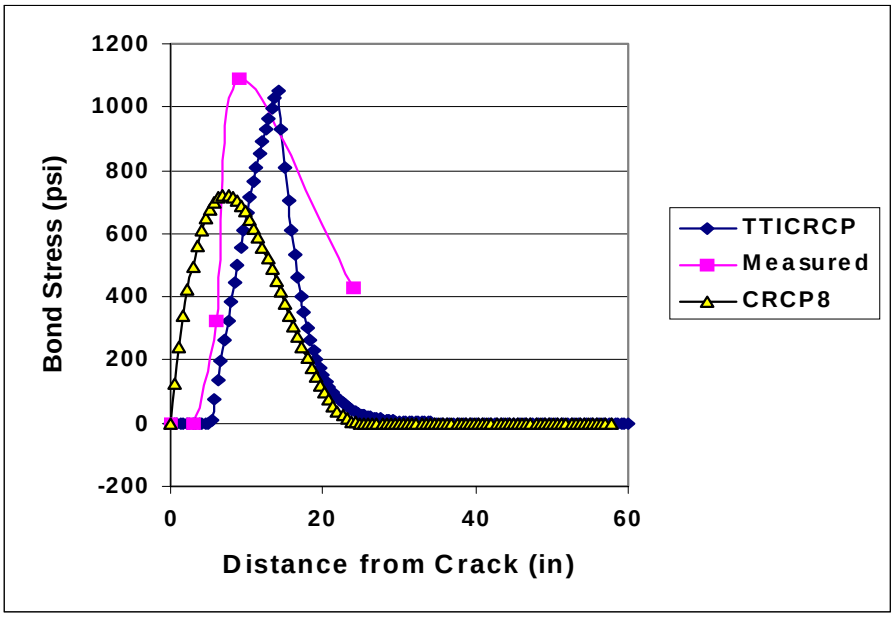

Figure 4.15 Comparison of Bond Stress Distributions as Predicted by CRCP 8 and TTICRCP Programs to Field Data at Day 30.

In addition to the bond stress analysis, further analysis was done to quantify the amount of slip occurring between the steel and the concrete, also known as bond slip. The slip was calculated following the method described by Nilson [37], which was discussed earlier in this chapter. The primary focus of the bond-slip analysis was to obtain a graphical relationship between the bond stress and the bond slip. Figure 4.16 illustrates the results of analysis of the slip between the concrete and the steel. The relationship between bond stress and bond slip was established in order to obtain values for K_1 and K_2, two input

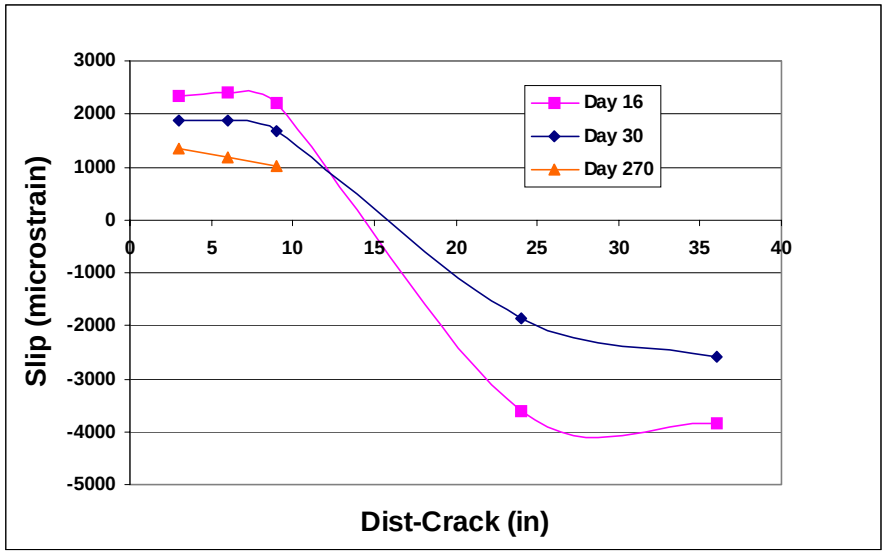

Figure 4.16 Bond Slip between the Steel and Concrete with Distance from the Crack Face.

variables needed for the TTICRCP analysis. K_1 represents the positive slope of the bond stress, bond-slip curve while K_2 is the negative slope of the same curve as previously indicated. The variation in K_1 and K_2 is shown graphically in Appendix A (Figures A.12 to A.14). Figure 4.17 illustrates calculated concrete-steel slip from the steel and concrete strains as a function of the distance from the crack face.

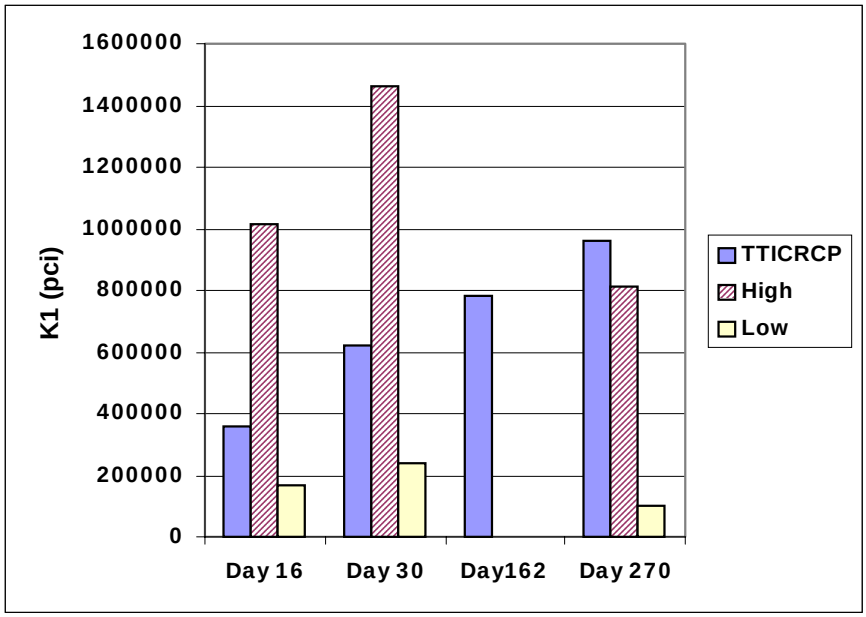

Figure 4.17 Range in Bond Stress - Slip Characteristics Based on Analysis of Steel Slip Data.

Subgrade Friction

The computer simulation programs also required an input of the pavement subgrade interaction. This is necessary because friction between the pavement and subgrade occurs as the concrete shrinks. This friction force applied by the subgrade bond leads to increased stresses in both the steel and the concrete. In order to obtain the necessary data on the pavement subgrade interaction, a 4 ft by 4 ft slab of concrete (push-off slab) was bonded to the subgrade in the same fashion as the pavement section itself. An incremental load was then applied to one end of the push-off slab with a hydraulic jack similar. The side of the slab opposite the load was instrumented with dial gages. These gages measured the movement of the slab (in mils) corresponding to incremental increases in the applied load from the jack. The data obtained from this test was used to establish a curve representing the relationship between the resulting concrete displacement and the friction stress. The curve obtained from this analysis was compared with a series of friction curves for concretes with different textures which were presented by Wimsatt, McCullough, and Burns [38]. Each of these curves is presented in Figure 4.18.

Simulation Comparisons

Computer simulations of the conditions on days 16, 30 , 162, and 270 were conducted with the CRCP 8 program and were compared to the measured field results on the basis of matching the average crack spacing predicted by the CRCP 8 program to the crack spacing of the instrumented section which was 10 ft. On this basis, it was necessary to adjust the input slab temperature distribution over the first 28 days of pavement age from those indicated in Table 4.2 in order to obtain a 10-ft average crack spacing from the CRCP 8 program at each of the pavement ages noted above. The slab temperature distributions used in each case are noted in Table 4.3 which can be compared to those listed in Table 4.2. The simulation results for day 162 are shown in Figure 4.19 and the simulation results for days 16, 30, and 270 are shown in Appendix A (Figures A.15 to A.17). Relative to the prediction of the average crack spacing, it appears the CRCP 8 program manifests a lack of sensitivity to early-aged

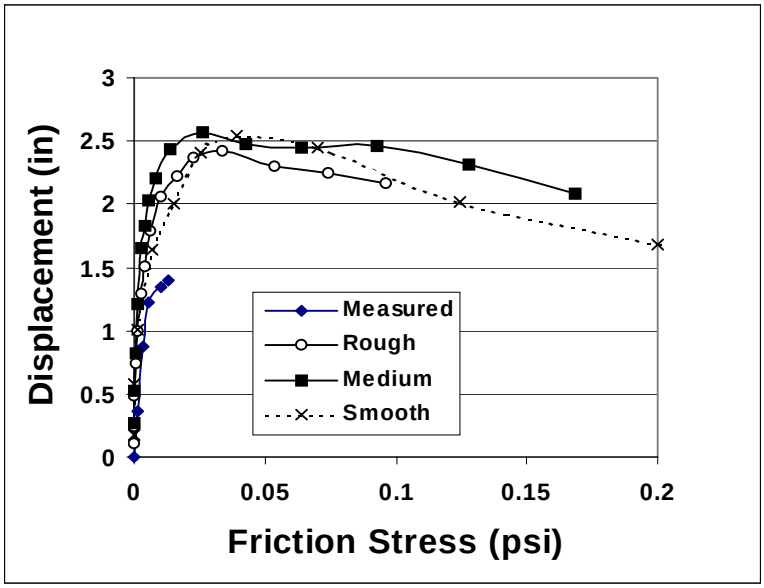

Figure 4.18 Pavement-Subgrade Friction Curve Comparison [38].

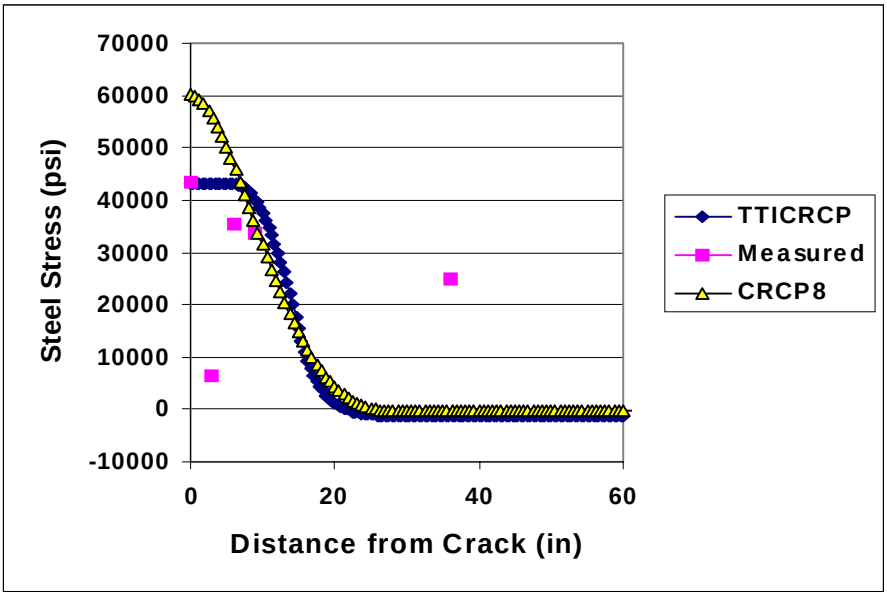

Figure 4.19 Comparison of Steel Stress Distribution between Measured and Predicted Stresses at Day 162.

drying shrinkage since the drops in temperature at early pavement ages needed by the program to match the instrumentation site 10-foot controlled spacing exceeded those recorded at the instrumented site. Given the temperature distributions in Table 4.3, the CRCP 8 tended to overestimate the steel strain at the instrumented crack face but appears to represent them well at distances away from the crack face. Also noted in Figure 4.19 are TTICRCP results which were calibrated to the steel strain at the crack face by adjustment of the parameter K_1. The adjusted K_1 values are shown in Figure 4.17 and fall within the possible range determined from the analysis of the bond-slip data. Critical input data used for the TTICRCP analysis is tabularized in Appendix A in Table A.1.

Table 4.3 Adjusted CRCP 8 Daily Minimum Pavement Temperature Values to Achieve a 10 Foot Cracking Spacing.

Concrete Age (Days)	**Day 16** (°F)	**Day 30** (°F)	**Day 162** (°F)	**Day 270** (°F)
Set	106	106	106	111
1	88	82	79	80
2	81	75	72	72
3	71	66	66	66
4	64	60	60	60
5	58	60	60	60
6	58	60	60	60
7	58	60	60	60
16*	58	60	60	60
30*(28)		52	60	60
161*			40	60
270*				50

Concrete strains were also compared in a similar manner as indicated in charts shown in Appendix A (Figures A.18 to A.20). The CRCP 8 results appeared to compare reasonably well with the field results. However, it should be noted, the field strains shown in these charts were determined based on the gage reading, the amount of shrinkage adjusted according to the measured relative humidities 1 in below the pavement surface (see Figures 4.8 and A.6), and the

amount of creep determined on day 5. Although, neither the CRCP 8 or the TTICRCP programs take into account creep effect directly, it appears feasible that the amount of creep may be indirectly assessed by matching the predicted stress distributions with the field distributions indicating that the effect of creep can be accounted for through adjusted values of the concrete modulus of elasticity. In this manner, the early-aged development of creep and shrinkage and their effects upon the predicted stress pattern needs further consideration in future updates of the CRCP 8 program.

Comparisons relative to crack width measured in the field to those predicted by the CRCP 8 program were also made (Figure 4.20). The crack width measurements were made in the field at mid-depth and appear to be overpredicted relative to the pavement age by the numerical models but no clear trend is evident. Due to moisture and temperature gradients which act in the pavement from the top to the bottom, crack widths tend to be wider at the top than at the mid-depth as indicated in Figures 4.11 and 4.12.

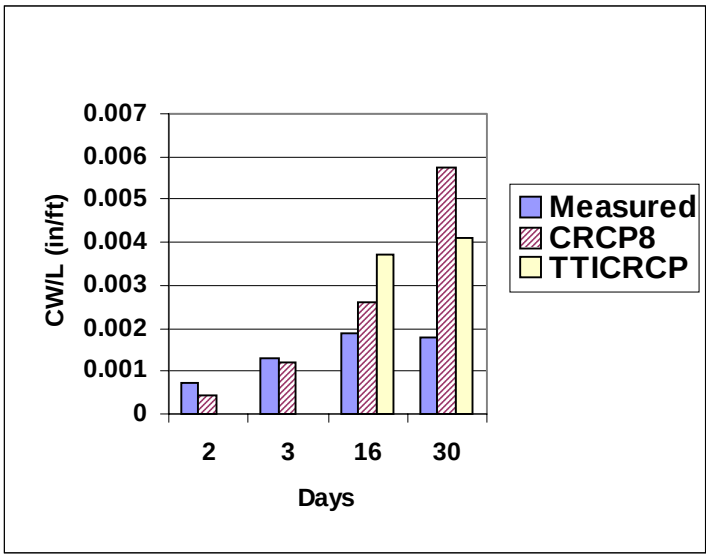

Figure 4.20 Comparison of Measured to Predicted Crack Widths.

Additional consideration was also given to the strain behavior of the concrete slab in profile from top to bottom using the finite element method. Further evidence of the variation from top to bottom is provided in the measured concrete strains near the pavement surface and the level of the steel reinforcement noted in Figure 4.21 comparing strains prior to cracking to those after cracking. It is clear that these strains are not only in opposite directions of each other but that the movement of the pavement surface is much greater than the movement near the steel reinforcement. Prior to cracking at the control joint, the gage reading indicated tensile movements while after cracking compressive movements were indicated. These strain conditions tend to validate the crack width behavior in profile illustrated in Figures 4.11 and 4.12

in that variations in crack width from the top of the slab to the level of the steel should be expected and perhaps considered to a greater extent in design. Relative to these movements, efforts were undertaken to model the change in temperature and moisture as it may have occurred on day 16 and day 30 in the concrete slab. This work was accomplished based on the use of a two-dimensional finite element model developed at TTI for the purpose of modeling climatic conditions in concrete pavements during and after the hardening period. This model is an advanced version of a similar one developed by TTI that was used in the HIPERPAV [40] program. It includes the capability to represent drying in the concrete as a function of the quality of the curing membrane in addition to temperature due to the heat of hydration. The results of the modeling are shown in Figure 4.22 and are compared to measurements taken

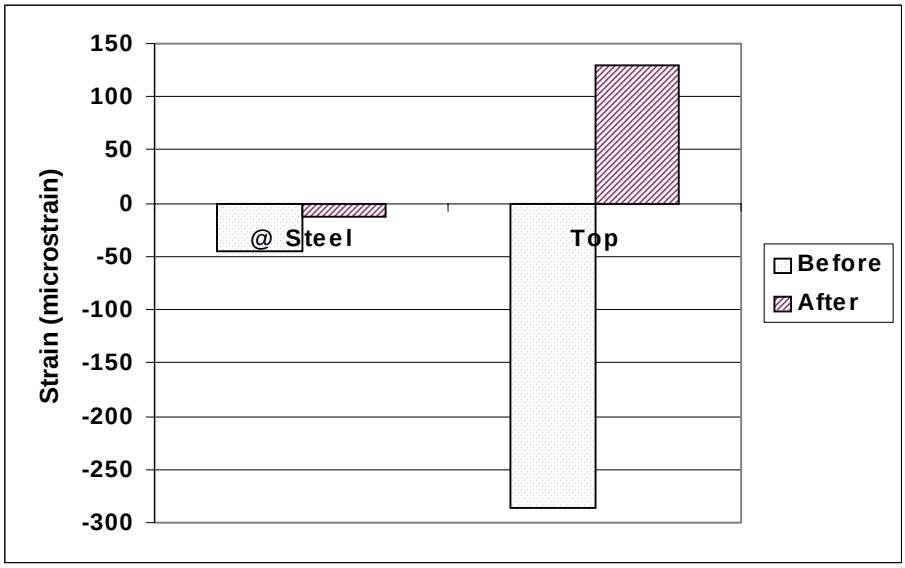

Figure 4.21 Recorded Gage Strains in the Concrete at the Pavement Surface and at the Level of the Steel.

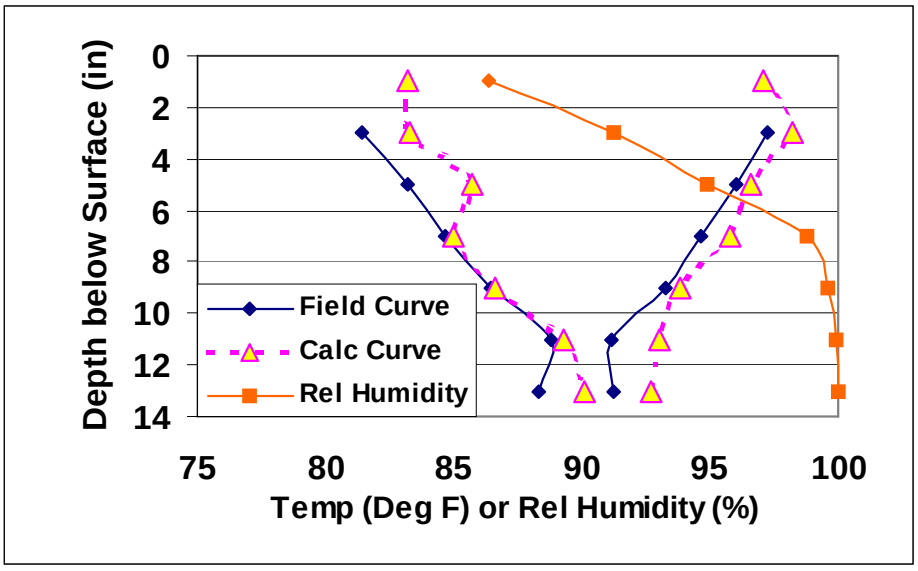

Figure 4.22 Calculated and Measured Pavement Moisture and Temperature Profiles for Day 30.

from the concrete slab in terms of the moisture and temperature range in the profile that occurred over a 24-hour period. The range in the calculated moisture profile was less than 1 percent but is not shown in this figure. Comparison can be made to some extent to the relative humidities measured at 1 in below the pavement surface noted in Appendix A (Figure A.21).

Analysis of this nature suggests a format for future developments to the CRCP 8 program. This format has been introduced in an approach to the analysis of CRC pavement systems described by Kadiyala et al. [41] and later by Kim et al. [42] using a two-dimensional finite element model. Each of these models have the capability of determining the stress and the strain in the concrete slab as a function of depth below the surface of the concrete. Further results and descriptions of these models are provided in the noted references but results relevant to this study based on the Kim model using the moisture and temperature profile data previously discussed are shown in Figure 4.23. A summary of the inputs used for this model is listed in Table A.2. Tools of this nature show great promise in developing algorithms for design purposes that take into account such factors as creep, differential temperature and moisture effects, and bond slip between the concrete and the steel relative to assessing the effects the position of the reinforcing steel may have upon the resulting crack width profile and crack spacing distribution.

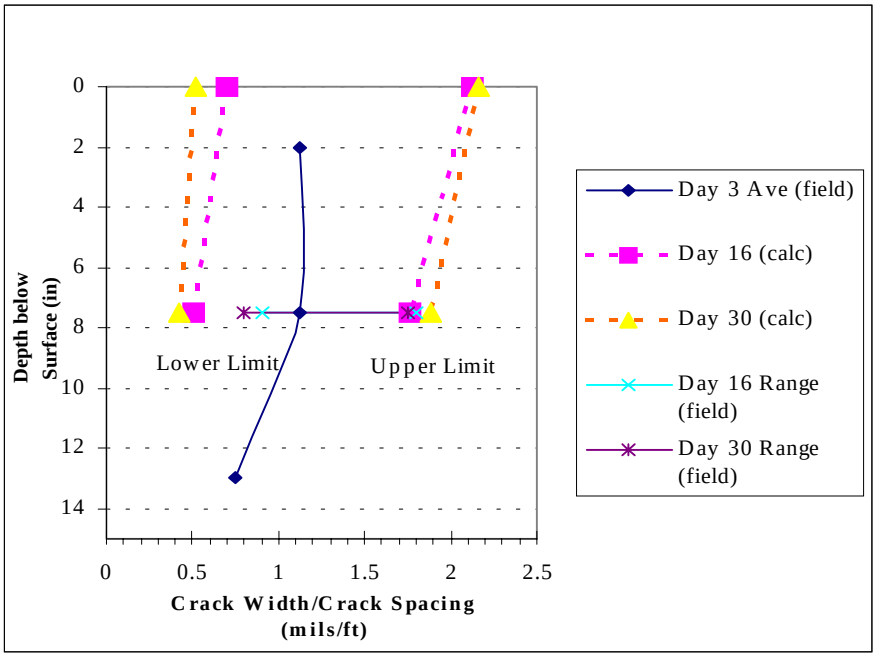

Figure 4.23 Crack Width Analysis Using a Two-Dimensional Finite Element Model.

Analysis of General Design Conditions

Analysis was also conducted using the material characteristics of the instrumented test site to develop a sense of the range of steel stresses and crack widths that may be encountered in design. These ranges were developed by considering typical ranges in bar diameter, percent steel reinforcement, maximum temperature drop, and drying shrinkage which are noted in Table 4.4. As noted in the table, eight combinations were derived from the variety of ranges for each parameter. The CRCP 8 and the TTICRCP steel stress and crack width results for each combination are listed in the table along with relevant material property data. For each run, the results of the programs can be compared and used to develop correction factors for the CRCP 8 results, based on the calibrated TTICRCP results. The actual correction factors are discussed further in Chapter 5 but it appears that in comparison to the TTICRCP results, the CRCP 8 program overestimates the steel stresses and underestimates the crack widths.

Table 4.4 Analysis of General Design Conditions.

Factorial	Bar Diameter	Percent Steel	Max Temp Drop (°F)	Drying Shrinkage Strain	CRCP 8 Results			TTICRCP Results	
					Crack Spacing (Ft)	Steel Stress (ksi)	Crack Width (mils)	Steel Stress (ksi)	Crack Width (mils)
1	#7	0.7	100	500	4.31	43.76	30.8	33.4	39.2
2	#5	0.7	100	500	3.13	43.98	22.3	45.1	22.8
3	#7	0.45	100	200	7.14	57.15	49.8	37.1	53.7
4	#5	0.45	100	200	5.68	59.70	39.4	44.9	42.2
5	#7	0.7	50	200	4.63	31.56	15.2	37.1	18.2
6	#5	0.7	50	200	3.57	33.14	11.6	41.0	13.9
7	#7	0.45	50	500	8.06	43.37	28.6	31.7	53.7
8	#5	0.45	50	500	6.25	45.35	21.8	39.3	41.2

Note: $E_c = 3.704 \times 10^6$ psi, $\alpha_{conc} = 6.29 \times 10^{-6}/°F$, Split Tensile Strength = 668 psi

CHAPTER 5
IMPLICATIONS RELATIVE TO CRACK WIDTH, STEEL STRESS, AND RELATIVE VARIABILITY CONSIDERATIONS IN STRUCTURAL DESIGN CRITERIA FOR CRC PAVEMENT

Since present design procedures for CRC pavement are derived in part from the structural behaviorial characteristic of jointed concrete pavement systems, there is some merit in pointing to the fact that earlier thickness design methodology was based on the premise that CRC thicknesses did not need to be as great as jointed concrete pavement thicknesses due to a certain equivalence in structural capacity. Both past and present thickness design procedures consider several factors associated with the prediction of the average crack spacing due to contraction restraint but recognition of any structural equivalence between these vastly different pavement systems has steadily evaporated due to a lack of consideration of how the transverse crack width affects the CRC pavement design process. Crack pattern prediction methods, as discussed in Chapter 2, relevant to the design of CRC pavement are based on resultant environmental stresses and material thermal properties of the concrete and steel. The design crack spacing is limited to certain criteria to minimize the potential of punch-out distress, which currently is only indirectly related to the final design thickness. Given the nature of punch-out development and its relationship to the opening and closing of the transverse cracks, it is apparent that CRC pavement thickness design procedures need to more completely consider how the width of the crack affects the load transfer characteristics of the transverse crack. The direct impact of such a consideration will be thinner CRC pavement thickness designs than what existing procedures currently yield. In terms of the punch-out process, the prevention of excessive steel stresses, as a design objective, is well encompassed within structural provisions of limiting crack width and load transfer criteria relative to the performance of the pavement in the vicinity of the transverse cracks.

In light of this emphasis, evaluation of the CRCP 8 program is further discussed in latter portions of this chapter. The capability of CRCP 8 to predict crack spacing distribution has been

well documented in previous research reports on the program development and application. Consequently, this particular aspect is given no further consideration in either this chapter or Chapter 4. Emphasis however is given to comparative analysis of the predicted steel stresses and crack widths and implications associated with these comparison.

Present CRC Design Considerations

Past CRC pavement design practices used to yield CRC pavement thickness designs that were approximately 80 percent of jointed concrete pavement design thickness, which was only remotely related to limiting design criteria for selected structural response parameters (i.e., crack width, steel stress, and cracking spacing). The design process then and today still needs to focus on the prediction of crack spacing, crack width, and steel stress as a function of thermal material properties and environmentally induced contraction stress and strain. The design crack width and steel stress are dependent upon the design crack spacing, which is primarily a function of the factor associated with the steel reinforcement. Although very important to the performance of CRC pavement, present CRC design methodology still ignores crack width requirements as far as they pertain to the degree of load transfer afforded by a transverse crack in CRC pavement systems.

Previous field studies [2] have identified definite trends between average crack spacing and percent reinforcement. The average decrease in crack spacing due to an increase in reinforcement may result in a decrease in the rate of punch-out distress. In spite of this, the effects caused by changes in the reinforcement are apparently not as predominant as other factors which also influence the distribution of crack spacing. These other factors are largely dependent on weather conditions at the time of paving and their pertinence to drying shrinkage and moisture loss characteristics of the concrete used for paving. Greater attention should perhaps be afforded concrete mix design and the methods of curing and the effects this may have on the initial and ultimate drying shrinkage. The effects of wheel load stress may also tend to propagate cracking in CRC pavements but this is most likely limited to those cracks initiated during the early life of the pavement. Apparently, few load applications are required to cause this additional cracking to show on the pavement surface since, historically speaking, the cracking pattern in adjacent, less

traveled paving lanes subjected to different traffic levels is similar. The probability of cracking due to Westergaard interior and edge load conditions may be very remote because of the low level of stress in the longitudinal direction due to the nature of the crack pattern. If the focus of the design is based on the pavement stresses associated with short crack intervals, then wheel load stresses in the longitudinal direction are not and should not be a major concern; transverse stresses are more important and are a function of the degree of load transfer provided by the transverse cracks. Another aspect of the inclusion of a punch-out mechanism in the thickness design methodology should be the focus on transverse crack width and how it effects transverse slab stresses, which if great enough (coupled with poor load transfer conditions), will cause longitudinal cracking in CRC pavements.

As previously indicated, existing design procedures (AASHTO [11], CRSI [13], etc.) do not directly consider specific limiting crack width criteria in terms of ranges of load transfer for optimal pavement/punch-out performance. Therefore, a design tool that is needed and would prove to be very useful is one providing a relationship between load transfer, crack width, and the percent reinforcement for a given crack spacing. Control of crack width is the key to good performance of CRC pavement as facilitated through uniformly configured and optimally spaced transverse cracks.

According to AASHTO design methodology [11], correlations between CRC pavement thickness and jointed pavement thickness were derived from a database of serviceability index ratings for jointed concrete pavement. The thickness design of jointed pavements was derived from the performance equations developed from the AASHTO road test predicting the future serviceability as a function of 80 kn (18 kip) single wheel load applications [2]. These methods usually resulted in thicknesses less than that for jointed concrete pavements. The performance equations are based on traffic level, concrete strength, modulus of support, load transfer, terminal serviceability, and design reliability. Although the verification of applicability of these equations to CRC pavement design has been limited, the notion that CRC pavement structures should maintain a greater structural integrity than jointed pavement structures is still valid.

Several early failures in CRC pavements have been attributed to excessive deflections under heavy loads suggesting that greater thickness will improve performance. Moving towards

greater design thicknesses for CRC pavements is likely to be beneficial for performance, but it appears that the resulting increases in thickness design is void of any direct structural relationship to crack width criteria in the most recent version of the AASHTO design guide [11]. Since punch-outs are the primary type of distress in CRC pavements, the need to achieve a greater understanding of punch-out distress, pavement support, crack width and steel stress effects, and load transfer mechanisms and how they relate to design thickness and pavement performance is obvious to establish a basis for improved CRC pavement design practice.

CRC Pavement Crack Widths Related Performance Factors

As previously noted, earlier thickness designs for CRC pavements were formulated on the premise that CRC pavement thickness design could be less than jointed concrete pavements thickness design in light of undefined equivalencies in structural capacity. This reduction in pavement thickness may have also been justified from a first cost basis to allow CRC pavements to be more competitive with jointed concrete pavement systems. These design procedures were limited to the factors which affected the development of the crack pattern due to contraction restraint. However, these methods did not (and still do not) directly address the effect of shear and load transfer across the transverse crack. Since it is clear that the punch-out process, as associated with load transfer mechanisms on transverse cracks in CRC pavements, should be the focus of CRC pavement design, the analysis of the failure modes [30] associated with CRC pavement are closely related to the level of wear-out of load transfer, the width of the crack, and the effective slab bending stiffness across the transverse crack. The loss of load transfer across the transverse crack results from aggregate wear-out and loss of pavement support near the transverse cracks.

Transverse Crack Shear and Load Transfer Mechanism

A reduction in pavement stiffness may result either from bearing failure around the reinforcing steel, spalling, or from aggregate wear-out. All of which have been observed in field studies [2]. With respect to the loss of load transfer due to aggregate wear-out, Colley and Humphrey [31] of the Portland Cement Association (PCA) investigated the effect of the

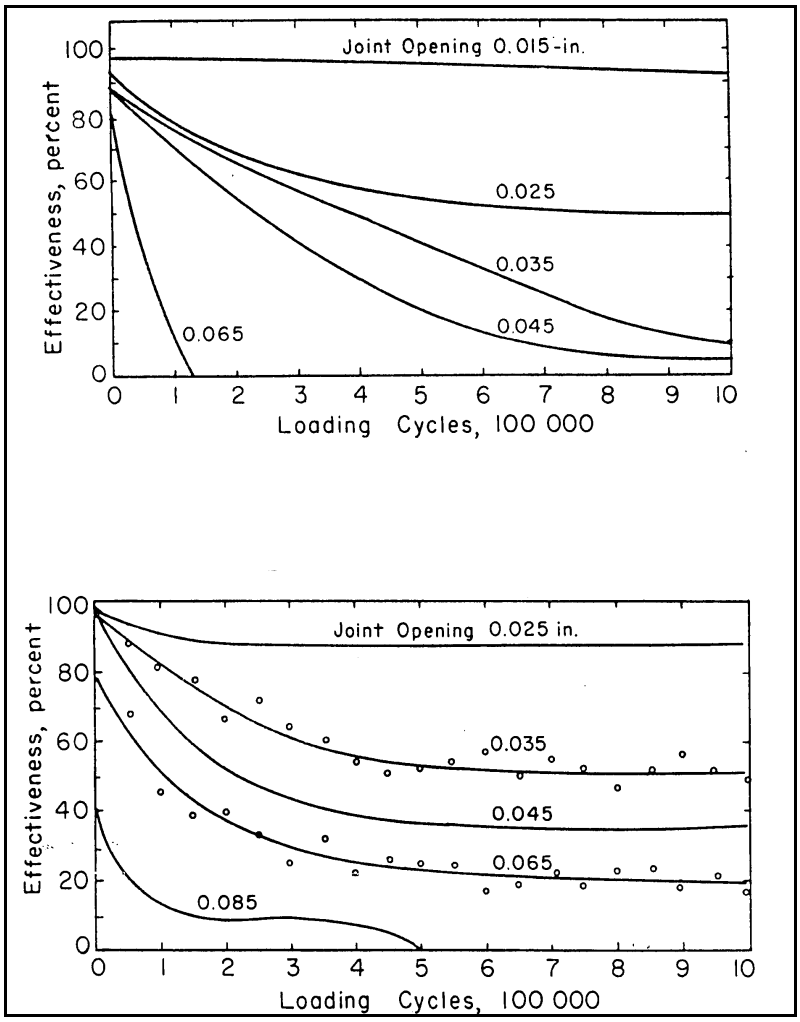

Figure 5.1 PCA Joint Load Transfer Tests [31].

aggregate interlock on load transfer characteristics in concrete pavements (Figure 5.1). This study was conducted using an instrumented test slab containing a transverse joint subjected to a repetitive 9 kip load. The joint in the test slab was an induced crack from a metal strip 1 in in height placed at the pavement bottom and the top. During the repetitive loading, measurements of joint opening and slab deflections on the loaded and unloaded slab were made at regular intervals. The loading sequence across the joint was similar to a continuous application of truck loads traveling approximately 30 mph. Test results in the form of joint effectiveness (EJ - which is different from load transfer efficiency - the load transfer efficiency (LTE) is the unloaded deflection divided by the loaded deflection, in percent), joint opening, and loading cycles for a 7 and a 9 in slab thickness using a 6 in gravel subbase were obtained.

The results indicate the joint effectiveness tends to level off after about 700,000 to 800,000 load applications (Figure 5.1). The levels of joint effectiveness at various levels of applications provide a useful basis relating joint or crack width to joint effectiveness for design purposes. Figure 5.1 provides an indication of the relationship between joint effectiveness and the joint opening for the 7 and 9 in thicknesses.

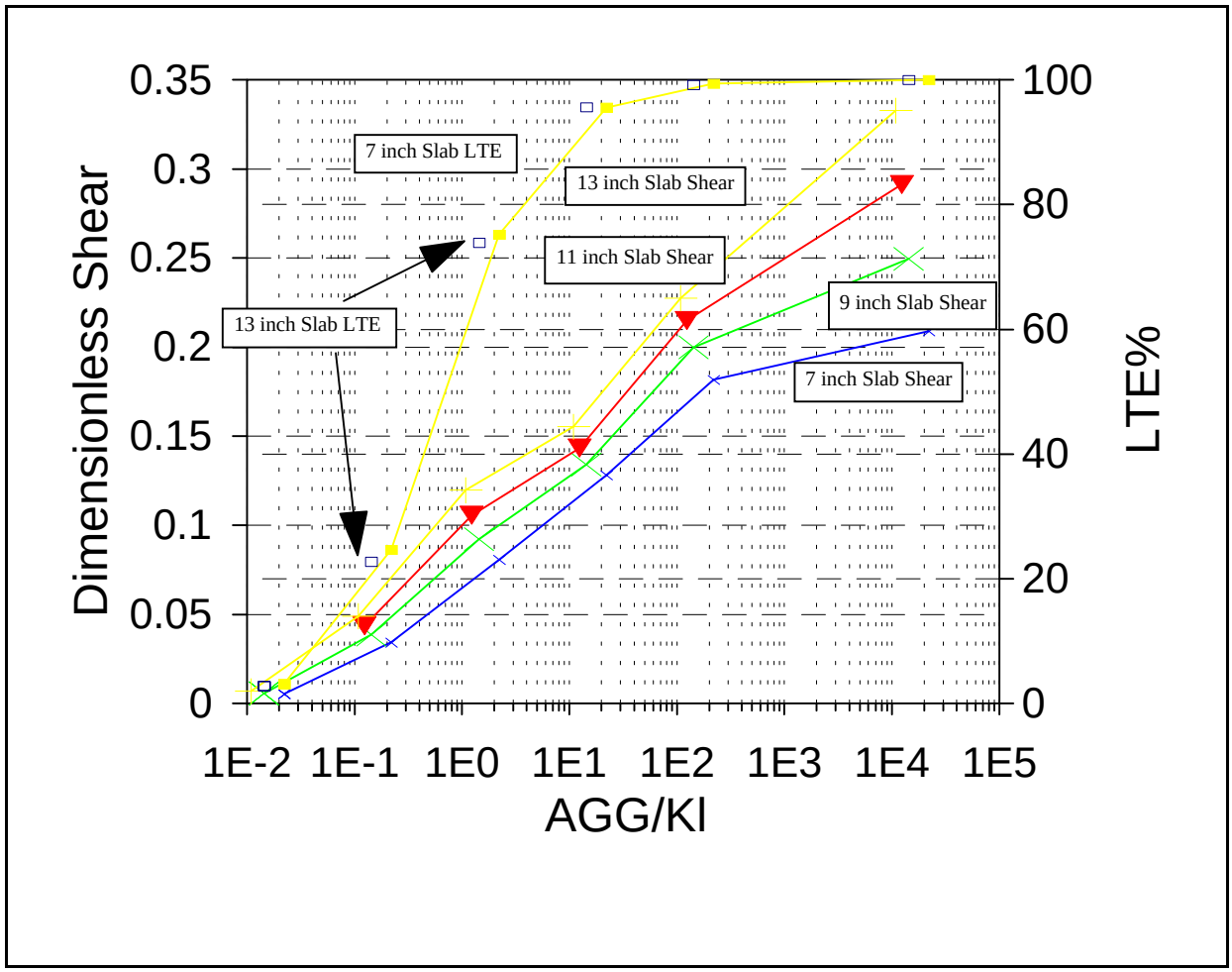

Figure 5.2 PCA Test Slab Results Relative to Dimensionless Shear and Joint Stiffness [30].

The PCA test data provides the basis in which to develop a universal relationship between the shear capacity (τ) generated through aggregate interlock on the transverse crack interface relative to the deflection load transfer efficiency (LTE) of the joint in the test slab. This relationship is key with respect to characterizing the correlation for a CRC pavement configuration and support condition to the degree of shear capacity at a transverse crack interface and the load transfer across a transverse crack. To this end, it is necessary to characterize shear capacity in terms of a dimensionless shear parameter ($\tau h^2/P = s$, where h is the pavement thickness and P is the wheel load) [32]. This dimensionless parameter can be correlated to a dimensionless joint or crack stiffness parameter (AGG/kℓ, where AGG is the aggregate interlock factor, k is the k value of the foundation support, and ℓ is the radius of relative stiffness). The

deflection (LTE) is related to the dimensionless parameter AGG/kℓ which is in turn related to the dimensionless shear as illustrated in Figure 5.2.

Relative to actual CRC slab loading configurations (Figure 5.3), comparison of an edge loading condition (i.e., a CRC pavement with a bituminous shoulder) to an interior loading condition (i.e., a CRC pavement with a two foot extended driving lane) indicates that greater shear stresses (and a greater rate of loss of load transfer) occur in CRC pavements with bituminous shoulders. The edge loading of a bituminous shoulder with poor support conditions represents the most severe loading conditions in terms of shear stresses on the crack interface. The loading condition for a 2 ft extended driving lane condition is not as severe as the loading conditions relative to the PCA test slab. Little difference in shear stress is noted between the interior load position (inner wheel path) and the edge load position in a CRC pavement with an extended driving lane. Similar results were found for a CRC pavement with a tied concrete shoulder that was integrally paved with the main lanes.

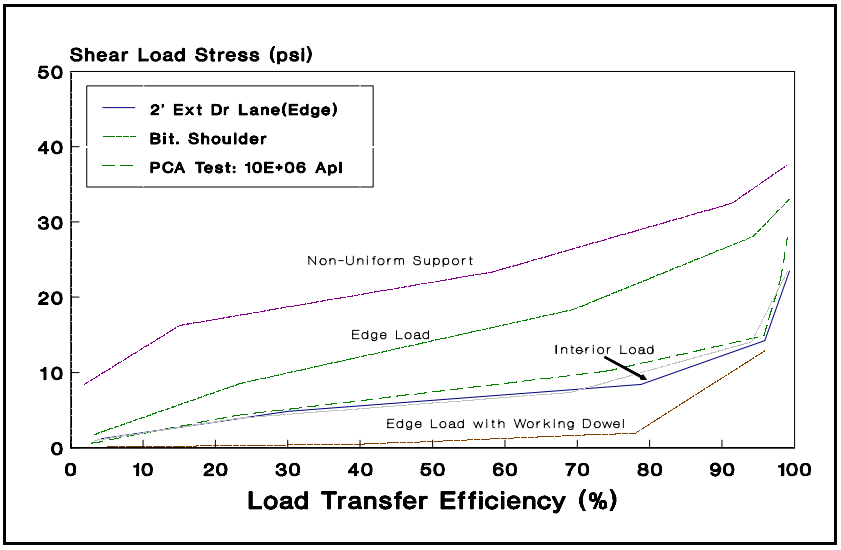

Figure 5.3 Shear Load Stress for Various Load Conditions of a 9 Inch CRC Slab [2].

Shear loading can be represented in terms of dimensionless shear stress ($\tau h^2/P$) and joint stiffness (AGG/kℓ) as a function of pavement thickness (h) and the pavement shoulder configuration [33]. This relationship, illustrated in Figure 5.2, is key to determining how load transfer is lost as shear capacity is reduced due to crack widening or load repetition. The loss of load transfer in a CRC pavement system results in an increase in cracking stress. Since crack width significantly effects load transfer and slab shear capacity, shear capacity-crack width relationships were extracted from the PCA test data. The PCA test and Long Term Pavement

Performance (LTPP) performance data have indicated that there are certain threshold crack widths that must be exceeded before loss of shear capacity will occur. A load transfer wear-out function generated from this data could be a component of a design process for CRC pavements. A function such as this should relate crack width (cw), load cycles (N), and shear stress to the loss in shear stress capacity ($\tau h^2/P$). The PCA and other laboratory test results referred to above have universal applicability to concrete pavement systems through the dimensionless shear parameter where it is unique to each pavement type.

Crack Width - Slab Thickness Considerations

Improved thickness design methods will need to emphasize the maintenance of a high level of load transfer efficiency to limit fatigue cracking and the development of premature punch-out distress. Bending stresses associated with fatigue cracking are closely tied to load transfer efficiency and the degree of support at each transverse crack. As previously pointed out, load transfer efficiency is a function of the crack width and shear capacity of the transverse cracks. The crack width depends upon the crack spacing, the thermal coefficient of expansion of the concrete, and the design steel percentage. This means that the spacing between individual transverse cracks is of vital interest to the pavement design engineer since maintaining a high level of load transfer will be largely dependent upon the width of individual transverse cracks.

In the design of CRC pavements, since the crack spacing pattern occurs randomly over a given range of cracking intervals, a certain amount of variability can be assigned to the crack width and the load transfer across the transverse cracks. As previously developed in Chapter 2, the crack width variability is a function of the variability of the crack spacing, concrete strength, and maximum temperature drop from the concrete set temperature at the time of construction.

As a means to minimize the randomness of the cracking pattern, the crack pattern can be positively controlled through the use of early-aged sawcutting to preselected intervals. However, if it is allowed to occur randomly as is the current practice in CRC pavement construction technology a greater degree of variability must be expected and accounted for in the design process. In either case, the mean crack spacing may be used to estimate the mean crack width. It

should be pointed out that a reduction in crack width and crack spacing variability should result in a reduction of variability in pavement performance.

Transverse Bending Stresses

The basic design process can focus on the prediction of longitudinal cracking prerequisite to the formation of punchout distress. Crack spacing has been shown to significantly effect the magnitude of the lateral stresses illustrated in Figure 5.4 and as shown, the longitudinal stresses also decrease with decreasing crack spacing. However, a more important parameter is the load transfer across the crack. Transverse bending stresses (stress A (σ_a) illustrated in Figure 5.5) are low at high load transverse efficiencies (LTE) and are high at low LTEs. Obviously, the location of the maximum transverse bending stress is between the axle load positions (approximately 30 in from the pavement edge) for a CRC pavement with a bituminous shoulder type. These stresses are significant below a LTE of 80 percent. In comparison, the longitudinal bending stresses (σ_b) are relatively low but may contribute to some extent to further transverse cracking as part of the overall cracking pattern. Interestingly enough, analysis tends to indicate that the effect of loss of support by itself on σ_a and σ_b stresses is surprisingly small. However, if LTE is diminished because of excessive shear stresses (induced by poor or support) then these stresses are significantly affected. The loss of support acts as a catalysis precipitating the loss of LTE particularly since punch-outs observed in field studies were always accompanied with severe erosion and loss of support. Consequently, loss of load transfer is really the dominant effect on

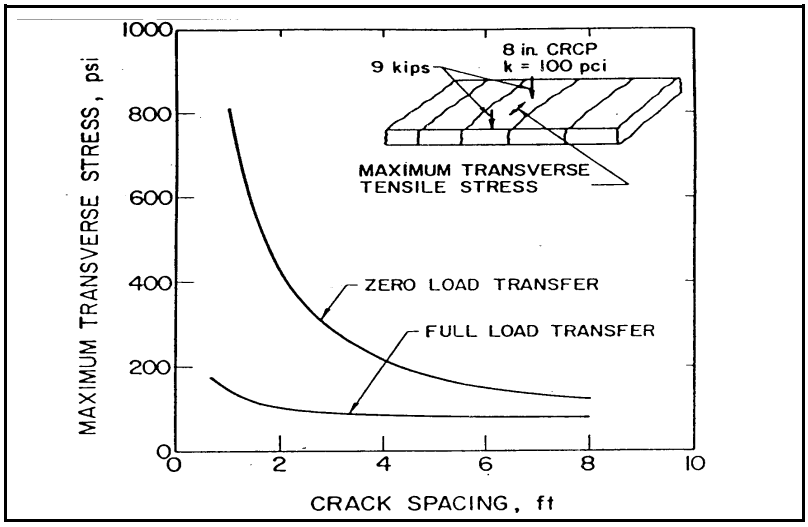

Figure 5.4 Effect of Load Transfer Efficiency across Transverse Cracks on Maximum Transverse Stress in CRC Pavement [34].

excessively high bending stresses which is accelerated due to loss of support and relatively unaffected by environmentally induced slab curling and warping. Coupled with loss of load transfer, curling and warping effects will contribute significantly to longitudinal cracking stresses. However, loss of load transfer is the most significant factor which re-emphasizes the importance of considering aggregate wear-out in design.

Figure 5.5 illustrates a comparison between σ_a and σ_b that provides some basis for selection of optimal design crack spacing. The σ_b stress decreases with decreasing crack spacing as long as the load transfer remains high. For a bituminous shoulder and a given level of aggregate wear-out and loss of load transfer, a crack spacing between 3 to 4 ft may be the most optimal crack spacing for design purposes. The reason being, within this cracking interval if the LTE remains high, σ_b will always be greater than σ_a (notwithstanding the fact that neither of the stresses are excessive). However, if the LTE is lost then these stresses will be approximately equal to each other and, interestingly enough, still lower than the level of σ_b at the high load transfer condition. Crack spacing outside of this range will cause higher stresses for any level of LTE leading to a less optimum fatigue life. The crack spacing range of 3 to 4 ft provides a balance between the maximum stresses σ_a and σ_b causing the stresses to be somewhat independent of the load transfer. Loss of LTE can have a significant influence on the performance of CRC pavement segments on erodible bases dominated by 2 ft crack spacings but would have less of an impact for a 4 ft crack spacing. A CRC pavement with a 2 ft extended driving lane or a 10 ft tied shoulder causes the optimum

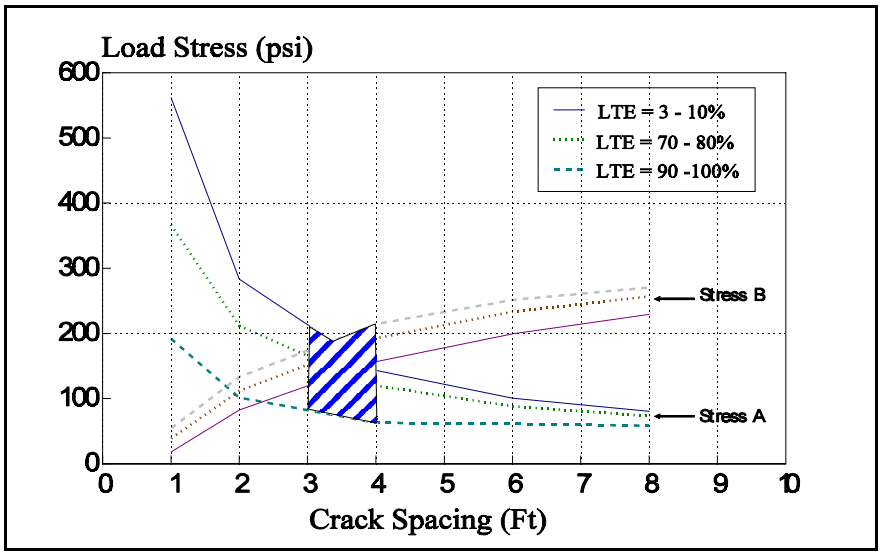

Figure 5.5 Comparison of σ_a and σ_b with Crack Spacing for a 10 Inch Pavement Thickness [2].

crack spacing range (for a balance between stresses σ_a and σ_b) to increase to 5 to 6 ft. The stresses in the 3 to 4 ft range for the 2 ft extended shoulder case are approximately 5 to 6 percent less than the stresses for the bituminous shoulder case in the same range. The load behavior for a 10 ft tied shoulder is similar to a 2 ft extended driving lane except the maximum stresses with a tied shoulder are 20 to 30 psi less.

Previous studies [2] have indicated that non-uniform supported conditions in CRC pavements seem to have a greater affect on transverse shear stresses than on transverse bending stresses. A greater shear stress condition will increase the rate of load transfer loss which will result in increased bending stresses and greater potential for punch-out distress. The shear stresses are reduced with either a 2 ft extended or a 10 ft tied shoulder if sufficient load transfer on the longitudinal shoulder is provided.

The contribution of bending stresses to fatigue damage are negligible prior to wear-out of the aggregate interlock and concomitant loss of load transfer. The level of load transfer may also affect the maximum stress location in a CRC pavement system consisting of a bituminous shoulder and to a lesser degree with other shoulder types. Transverse wheel-load stresses in a CRC pavement system are therefore, at a minimum, a function of crack spacing and shoulder configuration.

The relationship between dimensionless shear stress (s) of the transverse crack and the stiffness of the transverse crack as a function of the degree of load transfer offered by a tied concrete shoulder is illustrated in Figure 5.6. As the degree of load transfer across the concrete shoulder joint increases, the dimensionless shear stress on the transverse crack decreases as noted in the figure.

It should also be noted that shear capacity of the transverse crack is a function of the width of the transverse crack and characterized in the following form [32]:

$$s_{capacity} = \tau h^2/P = a\, e^{-0.039\ cw} \qquad (5.1)$$

where cw = crack width. The value of 'a' ranges from .45 to 1.6 as a function of thickness as shown in Figure 5.7. This figure, which was derived from equation 5.1, demonstrates crack

width requirements relative to slab thickness and load transfer requirements. It should be noted that the limits shown in Figure 5.7 fall between those recommended by PIARC (0.5mm) [35] and those recommended by AASHTO (1mm) [11]. Figure 5.7 suggests that the PIARC requirements are too conservative for typical CRC pavement thicknesses.

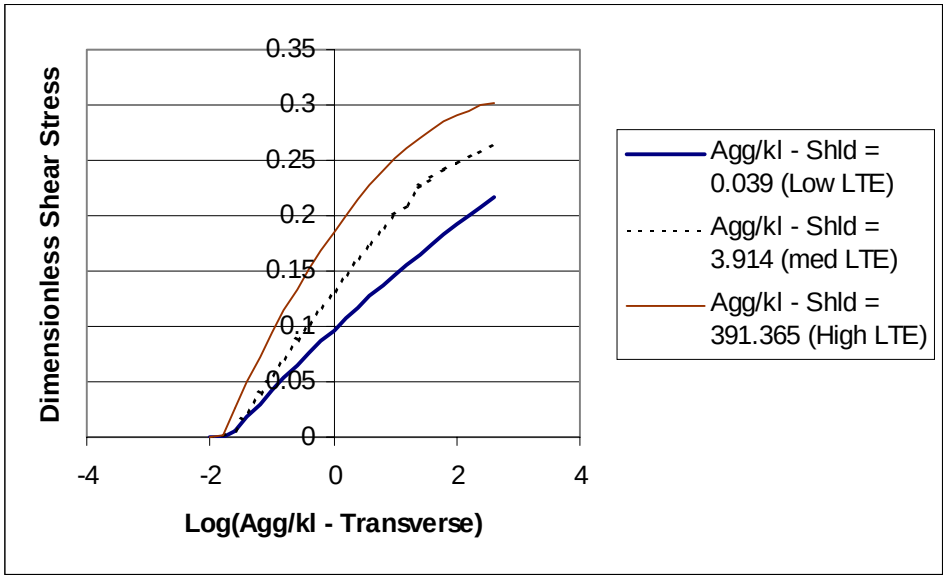

Figure 5.6 Shear Stress as a Function of Load Transfer Efficiency Provided by a Concrete Shoulder [30].

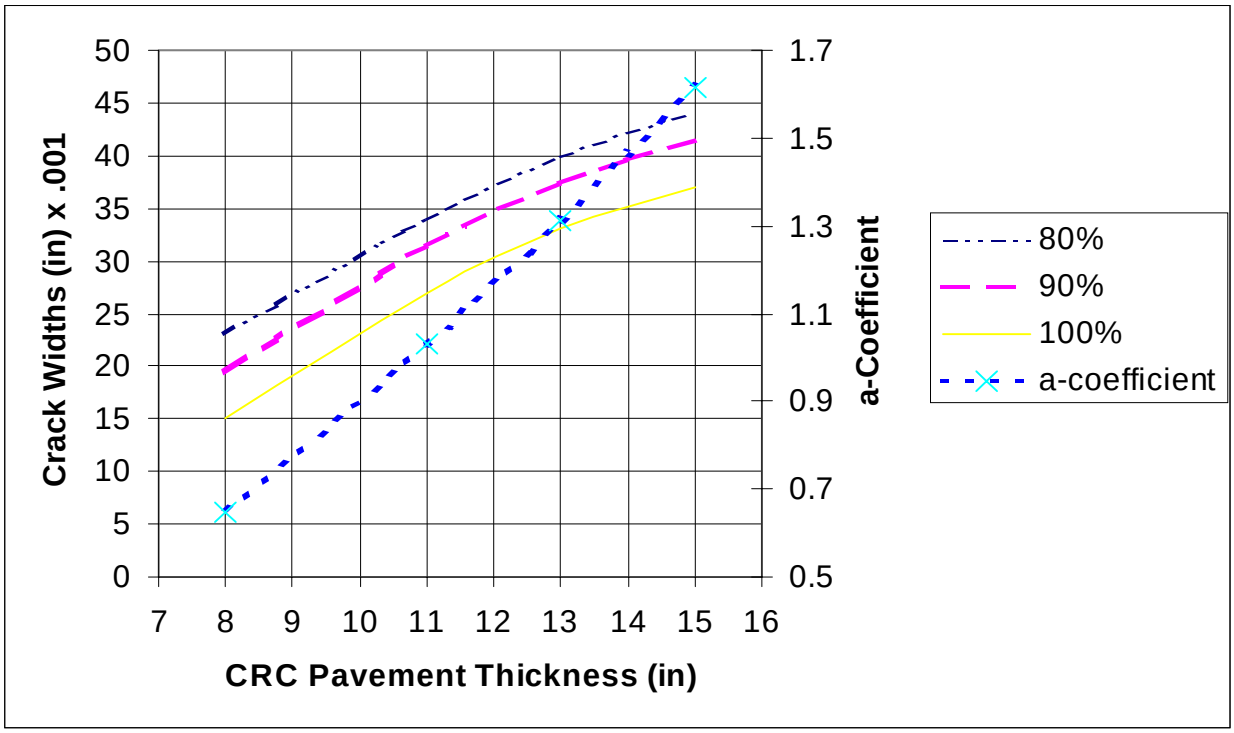

Figure 5.7 Limiting Crack Width Structural Design Criteria [30].

The loss of shear capacity (△s) due to a widening transverse crack is reflected in equation 5.1 but the loss of shear capacity due to wheel load applications is also characterized in terms of the width of the transverse crack as determined by analysis of the PCA test data [30]. Such a relationship (shown below) is important with respect to accounting for the effect of aggregate wear-out in the prediction of performance of CRC pavement systems:

$$\Delta s = \sum_i \sum_j \left[0.069 - 0.418 e^{-cw_j/h}\right] \bullet \frac{N_i}{10^6} \bullet \frac{\tau_{stress}}{\tau_{ref}} \qquad (5.2)$$

where N is the accumulated traffic, τ_{stress} is the shear stress on the transverse crack, and τ_{ref} is a reference shear stress derived from the PCA test results. Figure 5.3 indicates that poor support conditions can result in an increase in shear stress by a factor of two— which contributes to accelerated aggregate wear-out. Equation 5.2 can be used to predict how shear capacity can diminish over time. This expression constitutes the wear-out function that allows for the deterioration of the aggregate interlock to be considered in the performance estimate of CRC pavement systems. The coefficients of this function may vary for different aggregate types but preliminary test results indicate little differences in the shear wear-out behavior of mixes made with different coarse aggregate types [32]. Further research should be conducted to verify this finding. In any event, all the expressions introduced above combine together to characterize how the load transfer efficiency (as a function of crack width) should be factored into the design of a CRC pavement system.

Crack Width - Steel Stress Considerations

Detailed analysis was presented in Chapter 4 indicating the accuracy of the CRCP 8 program to predict stress in the reinforcing steel and the opening of the transverse cracks. Based on the comparisons to the recorded field strains and the tabulated results derived from the calibrated TTICRCP bond-slip model, correction factors should be applied to the results of the CRCP 8 model to adjust the over prediction of the steel stress and the under prediction of the crack width. These correction factors are conveniently illustrated in Figure 5.8. The correction is not constant across the range of the parameter depicted along the x axis which is a

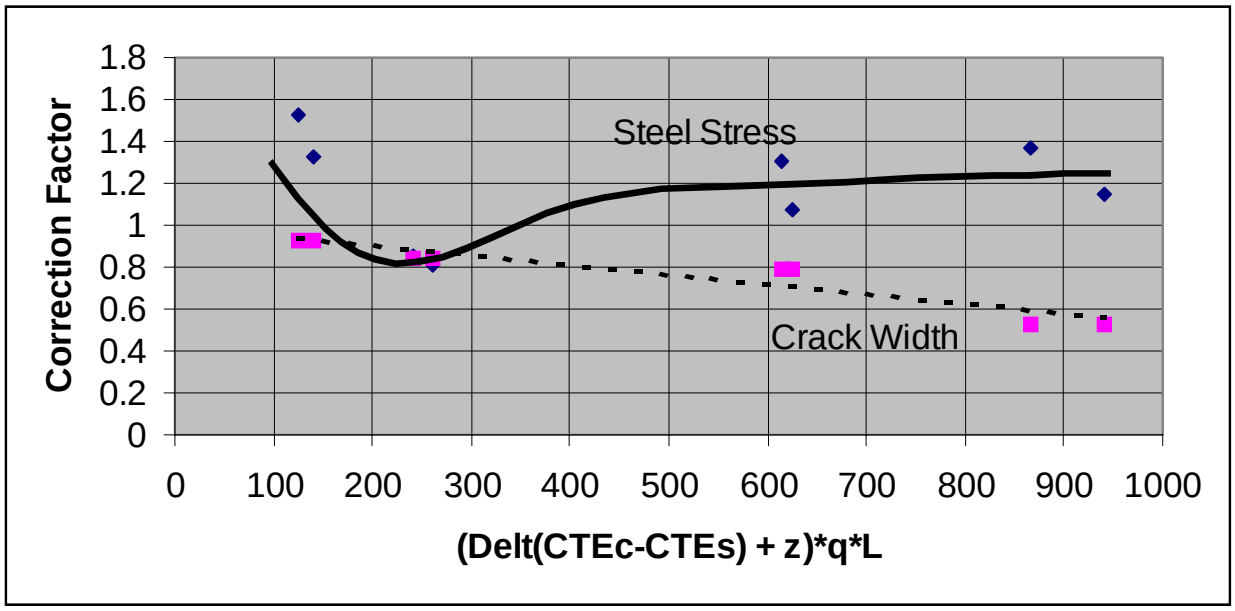

Figure 5.8 CRCP 8 Steel Stress and Crack Width Correction Factors.

dimensionless combination of concrete and steel CTE, drying shrinkage (z in micro strains (με)), design temperature drop (Delt), q factor, and crack spacing (L). The correction factor for both the steel stress and the crack width are determined for the same value of the x axis and divided into the result obtained from the CRCP 8 program.

Crack Width Variability Considerations

Crack width variability expressions were developed from a closed-form expression for crack width by Zuk [28] noted in equation 2.4 with partial derivatives shown in Table 2.1. CRC pavement performance has suggested that load-induced aggregate wear-out on the transverse crack does not proceed above a LTE of 90 percent. On this basis, the 90 percent LTE limit noted in Figure 5.7 can serve as the maximum allowable crack width for a given combination of q factor and expected minimum concrete temperature. The design crack width, as noted in equation 2.5, should be less than or equal to the limiting crack width values noted in Figure 5.7. Using the correction factors determined in Chapter 4 for the CRCP program and noted in Figure 5.8, Figure 5.9 represents crack width relationships as a function of the same dimensionless strain parameter that Figure 5.8 is represented in along the x axis. The significant components of

the strain parameter are noted in Table 2.1 and provide the basis from which different reliability levels can be defined. The effect of variability of the factors which affect the opening of the cracks is also shown in this figure at a reliability level of 95 percent (multiplying factor of 1.645) which could represent the design crack width. The variability of crack spacing, concrete shrinkage, concrete CTE, maximum temperature drop, concrete tensile strength, and elastic modulus of elasticity were assessed at a coefficient of the variability (COV) of 60, 10, 5, 10, 15 and 15 percent, respectively. Obviously, the lower the COV of the significant factors, the smaller will be the design crack width. In this respect, it is interesting to note that reduction of the variability associated with the randomness of the crack spacing, by use of early-aged transverse sawcuts to control the cracking interval, can reduce the crack width variability by nearly 50 percent in the typical ranges of concrete drying shrinkage.

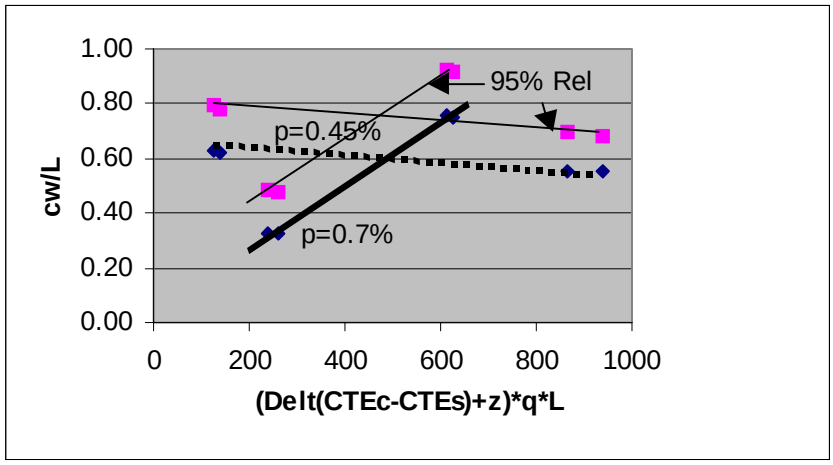

Figure 5.9 Crack Width Determinations Based on Corrected CRCP 8 Results.

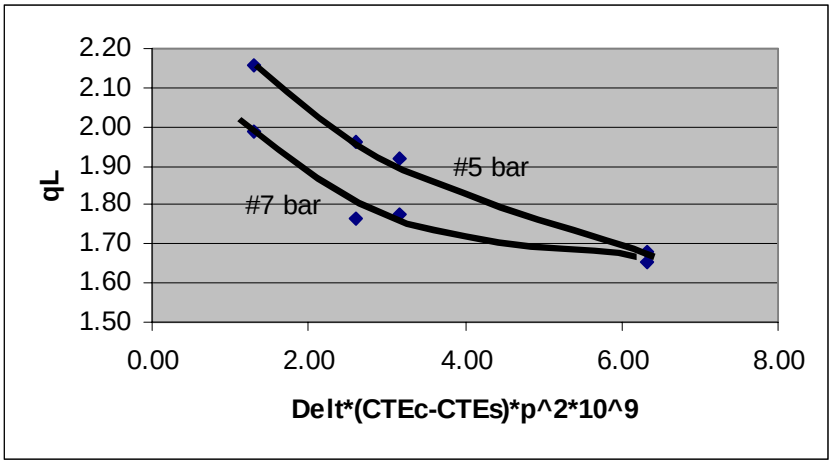

Figure 5.10 Crack Spacing Determinations Based on CRCP 8.

In order to make use of Figure 5.9, one must have an estimate of the design crack spacing. This is easy to achieve using early-aged crack control techniques, but if the crack pattern is allowed to develop randomly, then a graph, as represented in Figure 5.10, developed from

CRCP 8 results could be used to predict the average crack spacing. This figure is based on many of the same factors (on the x axis) as Figure 5.9 within the context of a dimensionless format. However, due to the lack of sensitivity of the CRCP 8 program to concrete drying shrinkage, the data shown in Figure 5.10 is limited to typical drying shrinkages which occur in TxDOT paving mixtures placed under summer, daytime paving conditions. As an example of how Figure 5.9 and 5.8 could be used to predict a design crack width, assume for instance:

- A maximum temperature drop of 70°F,
- A river gravel coarse aggregate (CTE_c = 7 με/°F; note that CTE_s = 5 με/°F),
- A drying shrinkage of 400 με, and
- A percent of steel of 0.55 using #5 bars (q = 0.035).

This yields a qL = 1.80 (corresponding to a value of 4.23 on the x axis of Figure 5.10), which produces an average crack spacing of 51 in or 4.3 ft. The process can be repeated for #6 sized bars but would require interpolation on the graph between the #5 bar and the #7 bar lines. For a given crack spacing of 51 in, Figure 5.9 yields an average cw/L ratio of approximately 0.61 and a design cw/L ratio of 0.79. The design crack width for this example is 40 mils which requires a minimum thickness of 14 in but by increasing the percent of steel to 0.61, the minimum thickness requirement can be lowered by 2 in (corresponding to a crack width of 36 mils). The charts provided can be used in preliminary design decisions in determining if steel configurations are compatible with crack width requirements to assure satisfactory performance over the life of the pavement.

Steel Reinforcement Stress Variability Considerations

As with the variability of the crack openings, steel stress variability can be assessed from a closed-form expression for steel stress by Vetter [9] noted by equation 2.6 with partial derivatives shown in Table 2.2. The variability of the steel stress was assessed relative to the listed factors of concrete drying shrinkage, concrete CTE, and maximum temperature drop at COVs of 10, 5, and 10 percent, respectively. Figure 5.11 represents the deviations in steel stress from the mean value at a reliability level of 95 percent. The x axis dimensionless strain parameter in Figure 5.11 is identical to the x axis parameter in Figure 5.10. According to the

example case noted above for the determination of the crack opening, a steel stress of approximately 16 ksi would be added to the mean steel stress to determine a design steel stress level as is indicated by expression 2.7. The mean steel stress is determined by dividing the average steel stress result from the CRCP 8 program by the correction factor indicated in Figure 5.8. Figure 5.12 is provided as an example of how a combination of CRCP 8 steel stress results and the correction chart given in Figure 5.8 may be configured. The design steel stress is indicated at a reliability level of 95 percent and the parameter on the x axis is presented as a dimensionless representation of an induced temperature strain in the concrete. The difference between the x axis parameter in Figure 5.12 and the previous charts is that crack width (in mils) is substituted in place of crack spacing. Following on with the previous example, the value of the crack width-strain parameter

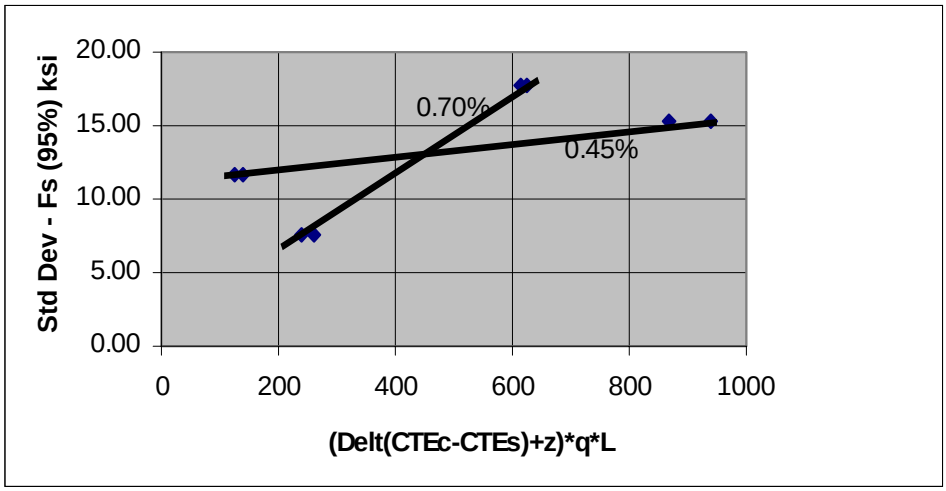

Figure 5.11 Steel Stress Deviations at a Level of 95 % Reliability.

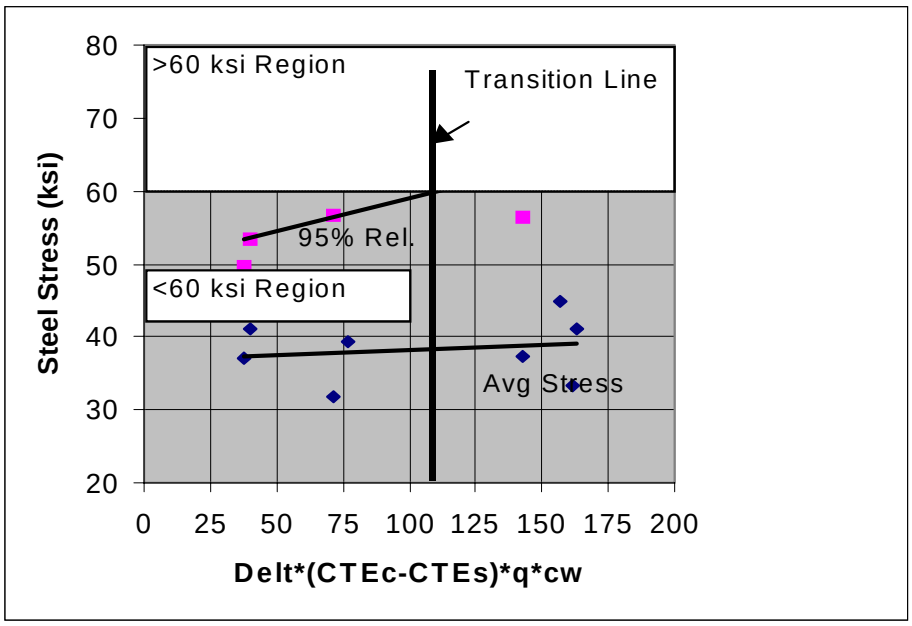

Figure 5.12 Steel Stress Performance Regions Based on Corrected CRCP 8 Stress Results.

in Figure 5.12 at a cw = 40 mils is 197. This corresponds to a design steel stress of approximately 68 ksi. Placement of the concrete under other conditions where the Delt parameter can be reduced may result in lower crack width-strain values but may be offset by larger crack widths due to greater crack spacing. For the example given, switching to a lower CTE concrete should also yield lower design steel stresses. It should be noted that a transition line at a value of Delt*(CTE_c - CTE_s)*q*cw = 107 is provided to indicate where the design steel stresses exceed a level of 60 ksi.

Project Findings

As a part of meeting the objectives of this project, the following findings are provided:

1. The methods used to instrument the reinforcing steel in the I-45 CRC pavement test site proved to be a beneficial and resourceful technique to minimize disturbance of the bond-slip of the reinforcing bar and to obtain steel strains at various distances along the bar from the crack face. The effect of creep on calculated concrete stresses was significant and demonstration of the sensitivity of creep to the state of stress at various distances from the face of the crack signals a need to pay greater attention to this phenomena in future updates of the CRCP 8 program. Creep stains, under applied loads, have traditionally been treated on a long-term basis, although shrinkage-induced creep initially is very large and diminishes within a few days, early-aged creep within this time period completely relaxes any stress development in the concrete. It is during this point in time that cracks begin to appear in the concrete.

2. The performance surveys of the SH 249 grade 70 steel sections, placed at a q factor of 0.026 and under cool weather conditions, indicated undesirably wide (in comparison to the grade 60), average crack spacings. However, it is pointed out the grade 70 sections, which consisted of a single layer of steel, demonstrated the desirable feature of lower clustering within the resulting crack pattern. It is also pointed out that a similar design, placed at the I-45 instrumented section under hot weather conditions, yielded a desirable crack pattern. As many previous studies have noted, the weather conditions at the time of construction are a major factor in the early performance behavior of CRC pavement systems that can eventually impact its later performance— for better or for worse.

3. The numerical algorithm used in the present version of the CRCP 8 program is suitable as a design tool for the prediction of crack spacing, crack width, and steel stress and should be used as a base in which to make future improvements. The numerical algorithm of the TTICRCP program is most suitable as a calibration tool to represent the bond-slip of reinforcement in CRC pavement.

4. The evaluation of the CRCP 8 program indicated that it can be used as a design tool for the prediction of the CRC pavement structural responses but corrections should be applied to the predicted average steel stresses and crack widths. Improvements to the program are encouraged and warranted on the basis of its sensitivity to the concrete temperature assigned to the first day after construction which tended to dominate the effect of temperature inputs for other days of the analysis. In this same vein, the program also seems to offset a lack of sensitivity to drying shrinkage which appears to be presently compensated for by a larger than expected first day, temperature-drop. As a consequence, the 10-foot controlled crack spacing at the instrumentation site was not well predicted when actual concrete pavement temperatures over the first 28 days of age were input into CRCP 8. When the 28-day temperature profile was appropriately adjusted such that the average predicted crack spacing matched the instrumented 10-ft crack spacing, the program tended to overpredict the steel stress and underpredict the crack width. A correction chart was developed to provide factors to adjust the CRCP 8 results for use in design.

However, as previously noted in the introduction of this chapter, these statements are not made in any reference to the programs capability to predict trends in the crack pattern. But it does appear that current versions of CRCP 8 are perhaps better suited to represent later cracking behavior rather than early cracking behavior of CRC pavement systems. In this respect, the field data clearly indicated a high degree of relaxation in the first 3 to 4 days after construction of the pavement which effectively eliminated the build up of early-age shrinkage stress in the concrete, based upon the time that initiation of the observed cracking took place. It is apparent that concrete setting temperature models for CRCP 8 may take the effect of the early creep into account to some extent by the selection of a reference temperature 7% below the concrete peak

temperature. This aspect appears to be an area that further research could yield improved models to advance the capability of CRCP 8 to represent early-aged cracking behavior.

5. The design of CRC pavement systems must include consideration for crack width and its affect upon the load transfer and stiffness of the transverse cracks over the design life of the pavement system. This parameter should be given a greater precedence in the design process even more than the design level of steel stress. Nonetheless, the average steel stress is an important design consideration relative to the selection of the proper grade of steel.

6. Vertical positioning of the steel layer appears to affect the development of cluster cracking. Relative to statement 2) above, data collected at the SH 249 test site indicated a distinct difference in clustering between pavements constructed with one layer versus pavements constructed with two layers of reinforcement. It is clear that the vertical position of the steel layer also influences the degree of restraint in the concrete near the pavement surface and characteristics of the cracking pattern, particularly relative to the development of clustering. Given the fact that restraint by the reinforcement is constant at any vertical position of the steel in the slab, a plausible explanation for cluster cracking is non-uniformity in the depth of curing from point to point along the pavement. Apparently, if the depth of drying varies from point to point, then the induced cracking stress will vary accordingly relative to the vertical position of the reinforcing steel. The deeper the steel layer, the less effect the variation in the depth of drying will have on cracking stress. More uniform curing should help to minimize cluster cracking and allow shallower placements of the steel layer and narrower crack widths at the pavement surface. This is further supported based on information in the literature suggesting the vertical position of the reinforcing steel influences the variation in crack width with distance below the pavement surface. It is pointed out that finite element models can represent this type of behavior as it may be affected by the position of the reinforcement in the presence of temperature and moisture gradients. The advancement of the design and analysis of CRC pavement systems will depend upon the reflection of the finite element results in design models to better account for differential slab behavior.

Recommendations

The CRCP 8 program is a well-founded, computerized approach to the prediction of crack spacing, steel stress, and crack width and is consequently well suited for future improvements to the process it uses to represent the behavior of CRC pavement systems. Improvements should be made to material models used in the program to represent both temperature and moisture changes in profile as they vary with time during the early ages of the concrete and the translation of the profile changes into strain and stress. The roles of drying shrinkage and creep also need further definition in the crack development process. Tools that have the capability to take into account the heat of hydration and the quality of curing during the hardening process have recently been developed to accomplish such a task. Effort to develop such products and additions to the CRCP 8 program should be immediately undertaken to improve how the CRCP 8 program characterizes the effect of moisture and temperature change over the first 28 days of analysis. The consideration of crack width as a function of distance from the surface of the slab will allow for more accurate assessment of the crack opening at the level of the steel based on surface measurements. Changes are also needed and suggested to the bond-slip algorithm to improve its capability to be calibrated and to represent the partial bond region similar to the process used in the TTICRCP program but modified with other bond stress distributions that may accelerate the calculation time while improving the representation of bond stress between the steel and the concrete. The improvements recommended should be complemented with suitable laboratory tests and studies to verify the accuracy of the program models under controlled conditions and followed up with additional field sections to validate their application to design.

REFERENCES

1. Won, Mooncheol, Kenneth Hankins, and B. Frank McCullough, “Mechanistic Analysis of Continuously Reinforced Concrete Pavements Considering Material Characteristics, Variability, and Fatigue,” Report No. 1169-2, Center for Transportation Research, University of Texas at Austin, April 1990.

2. Zollinger, D. G., and E. J. Barenberg, “Continuously Reinforced Pavements: Punchouts and Other Distresses and Implications for Design,” Project IHR - 518, Illinois Cooperative Highway Research Program, University of Illinois, Urbana, Illinois, March, 1990.

3. Verhoeven, K., “Cracking and Corrosion in CRCP,” Belgium Cement Industry Collective Research Centro, Proceedings Vol. 1, 5th International Conference on Concrete Pavement Design and Rehabilitation, Purdue University, April 20-22, 1993, pp. 201-209.

4. Verhoeven, K., “Behavior of Continuously Reinforced Concrete,” RR CRIC 53-f-1992, ISSN 0770-0725, 1992, 65 pp.

5. Verhoeven, K., and P. Van Audenjove, “Cracking and Corrosion in CRCP,” Session 5, 7th International Symposium on Concrete Roads, Vienna, Austria, October 1994, pp. 155-161.

6. Joffre, C., “Spanish Practice and Experience with Concrete Pavements,” Report on the 1992 U.S. Tour of European Concrete Highways, Publication No. FHWA-SA-93-012, FHWA, U.S. DOT, Washington, D.C.

7. “New Rebars Ready for Use,” Transportation Research Board Research Digest, Fall 1994.

8. Kadiyala, Subrahmaya M. and Dan G. Zollinger, "Analysis of CRC Pavement Under Moisture, Temperature, and Creep Effects," Proceedings, 5th International Conference on Concrete Pavement Design and Rehabilitation, Purdue University, April 20-22, 1993, Vol. 2, pp. 211-236.

9. Vetter, C. P., "Stresses in Reinforced Concrete Due to Volume Changes," ASCE proceedings, Paper No. 1848, February 1932.

10. McCullough, B. F., J. C. M. Ma, and C. S. Noble, "Limiting Criteria for the Design of CRCP," Research Report 177-17, The Center for Transportation Research, University of Texas at Austin, August 1979.

11. American Association of State Highway and Transportation Officials. AASHTO Interim Guide for the Design of Pavement Structures. AASHTO Committee on Design, AASHTO, Washington D.C., 1986.

12. Burke, John S., and Jagot S. Dhamrait, "A Twenty-Year Report on the Illinois Continuously Reinforced Pavement," Highway Research Record No. 239, Highway Research Board, 1968.

13. Design of Continuously Reinforced Concrete for Highways, ARBP-CRSI, Chicago, Illinois, 1981.

14. Iwana, S., "Experimental Studies on the Structural Design of Concrete Pavement," Public Works Research Institute, Ministry of Construction, Japan, May 1964 (English Translation).

15. Appendix 6, "Structural Design Method for Rigid Pavement," Manual for Asphalt Pavement, Japan Road Association, 1989, pp. 219-233.

16. Iwana, S., and Y. Anzaki, "Concrete Pavement Technology in Japan Today," Transportation Research Record 1182, TRB, National Research Council, Washington, D.C., 1988.

17. Nakamura, T., and T. Iijama, "Evaluation of Performance and Structural Design Methods of Cement Concrete Pavements in Japan," Session 1 papers, 7th International Symposium on Concrete Roads, Vienna, Austria, October 3-5, 1994, pp. 109-114.

18. McCullough, B. Frank, A. A. Ayyash, W. R. Hudson, and J. P. Randall, "Design of Continuously Reinforced Concrete Pavements for Highways," NCHRP 1-15, Center for Highway Research, The University of Texas at Austin, August 1975.

19. McCullough, B. F., and W. B. Ledbetter, "LTS Design of Continuously Reinforced Concrete Pavement," Proceedings, ASCE, Vol. 86, HW4, December 1960, pp. 1-24.

20. Dhamrait, J. S., F. K. Jacobsen, and D. R. Schwartz, "Condition of Longitudinal Steel in Illinois Continuously Reinforced Concrete Pavements," Physical Research Report No. 89 (IHR-36), Illinois DOT, 1973.

21. Van Breemen, W., "Ten-Year Report on Experimental Continuously-Reinforced Concrete Pavements in New Jersey," HRB, Bulletin 214, 1959.

22. Abou-Ayyash, Adnan, "Mechanistic Behavior of Continuously Concrete Pavement," Ph.D. Thesis, University of Texas at Austin, May 1974.

23. Tang, Tianxi, Dan G. Zollinger, and B. Frank McCullough, “Field Tests and Analyses of Concrete Pavement in Texarkana and La Porte, Texas,” Research Report 1244-7, Texas Transportation Institute, College Station, Texas, October 1996.

24. Nelson, Rick, Terry Dossey, Dan G. Zollinger, B. Frank McCullough, and Jorge Soares, “Evaluation of the Performance of Pavements Made with Different Coarse Aggregates,” Research Report 3925-1F, Center for Transportation Research, The University of Texas at Austin, November 1997 (draft).

25. Soroushian, P., K. Choi, G. Park, and F. Aslani, "Bond of Deformed Bars to Concrete: Effects of Confinement and Strength of Concrete," ACI Material Jounal, Vol 88, No. 3, May-June 1991.

26. Rasmussen, R. O. and D. K. Rozycki, "Evaluation of High Strength Steel in Pavements," Tech Memo No. 296006-7, Transtec, Austin, Texas, January 16, 1997.

27. Tayabji, Shiraz D., Dan G. Zollinger, Jaganmohan R. Vederey, and Jeffrey S. Gagnan, “Performance of Continuously Reinforced Concrete Pavements Volume III: Analysis and Evaluation of Field Test Data,” FHWA-RD-94-180, PCS/Law Engineering, Beltsville, Maryland, October 1998.

28. Zuk, W., "Analysis of Special Problems in Continuously Reinforced Concrete Pavements," Highway Research Board, Bulletin 214, 1959.

29. Palmer, R. P., M. Olsen, and R. L. Lytton, “TTICRCP-A Mechanistic Model for the Prediction of Stress, Strains, and Displacements in Continuously Reinforced Concrete Pavements,” Research Report 371-2F, Texas Transportation Institute, Texas A&M University, August 1987, 275 pp.

30. Zollinger, Dan G., Neeraj Buch, Dapeng Xin, and Jorge Soares, “Performance of Continuously Reinforced Concrete Pavements Volume VI: CRC Pavement Design, Construction, and Performance,” FHWA-RD-94-180, Texas Transportation Institute, College Station, Texas, December 1998.

31. Colley, B. E. and H. A. Humphrey, "Aggregate Interlock at Joints in Concrete Pavements," Highway Research Record, No. 189, Highway Research Board, Washington, D.C., 1967.

32. Buch, N. J., "Development of Empirical-Mechanical Based Faulting Models in the Design of Plain Jointed Concrete Pavements," Ph.D. Dissertation, Texas A&M University, August 1995.

33. Ioannides, A. M,. and G. T. Korovesis, "Aggregate Interlock: A Pure Shear Load Transfer Mechanism," Transportation Research Record 1286, TRB, National Research Council, Washington, D.C., 1990.

34. La Coursiere, S. A., M. I. Darter, and S. A. Smiley, "Performance of Continuously Reinforced Concrete Pavement in Illinois," *Civil Engineering Studies*, Transportation Engineering, Series No. 10, University of Illinois, Urbana, Illinois, 1978.

35. PIARC, "Continuously Reinforced Concrete Pavements," Technical Committee in Concrete Roads, Permanent International Association of Roads Congresses, Paris, France, 1994.

36. "Vibrating Wire Embedment Strain Gage," Instruction Manual, Rocktest, 1995.

37. Nilson, Arthur H., "Bond Stress-Slip Relations in Reinforced Concrete," Research Report No. 345, Department of Structural Engineering, Cornell University, December 1971, 40 pp.

38. Wimsatt, Andrew W., B. Frank McCullough, and Ned H. Burns, "Methods of Analyzing and Factors Influencing Frictional Effects of Subbases," Research Report 459-2F, Center for Transportation Research, The University of Texas at Austin, November 1987.

39. Zollinger, Dan G., Tianxi Tang, David Fowler, Ligang Wang, and Anca Neagu, "Development of a Test Apparatus to Measure Thermal Expansion of Concrete Aggregates," Research Report 2992-1, Texas Transportation Institute, College Station, Texas, June 1998 (draft).

40. McCullough, B. Frank, Robert Otto Rasmussen, and Dan G. Zollinger, "Fast Track Paving: Concrete Temperature Control and Traffic Opening Criteria for Bonded Concrete Overlays," Federal Highway Administration, Transtec, Inc., Austin, Texas, November 1996.

41. Kadiyala, Subrahmaya M., and Dan G. Zollinger, "Analysis of CRC Pavement Under Moisture, Temperature, and Creep Effects," Proceedings, 5th International Conference on Concrete Pavement Design and Rehabilitation, Purdue University, April 20-22, 1993, Vol. 2, pp. 211-236.

42. Kim, Seong-Min, Moon C. Won, and B. Frank McCullough, "Numerical Modeling of Continuously Reinforced Concrete Pavement Subjected to Environmental Loads," Paper Presented at the 77th Annual Meeting of TRB, Washington, D.C., January 11-15, 1998.

43. Neville, A. M., "Properties of Concrete." 4th Edition, John Wiley & Sons, Inc., 1997.

44. McCullough, B. Frank, and Anton Schindler, “Validation of CRCP-8 to Predict Long Term Transverse Crack Spacing Distributions in Continuously Reinforced Concrete Pavements,” Paper Prepared for Presentation at the 78th Annual Meeting of the TRB, Washington, D.C., January 1999. (Draft)

45. Avram, Constantin, Ioan Făcăoaru, Ion Filimon, Ovidiu Mîrsu, and Igor Tertea, “Concrete Strength and Strains,” Elsevier Scientific Publishing Co., New York, 1981.

46. Bažant, Z. P., and Najjar, L. J., “Nonlinear Water Diffusion in Nonsaturated Concrete,” Materials and Structures (RILEM), Vol. 5, No. 25, 1972.

APPENDIX A

ANALYSIS OF MEASURED STRESSES AND STRAINS COLLECTED FROM THE INSTRUMENTATION SITE

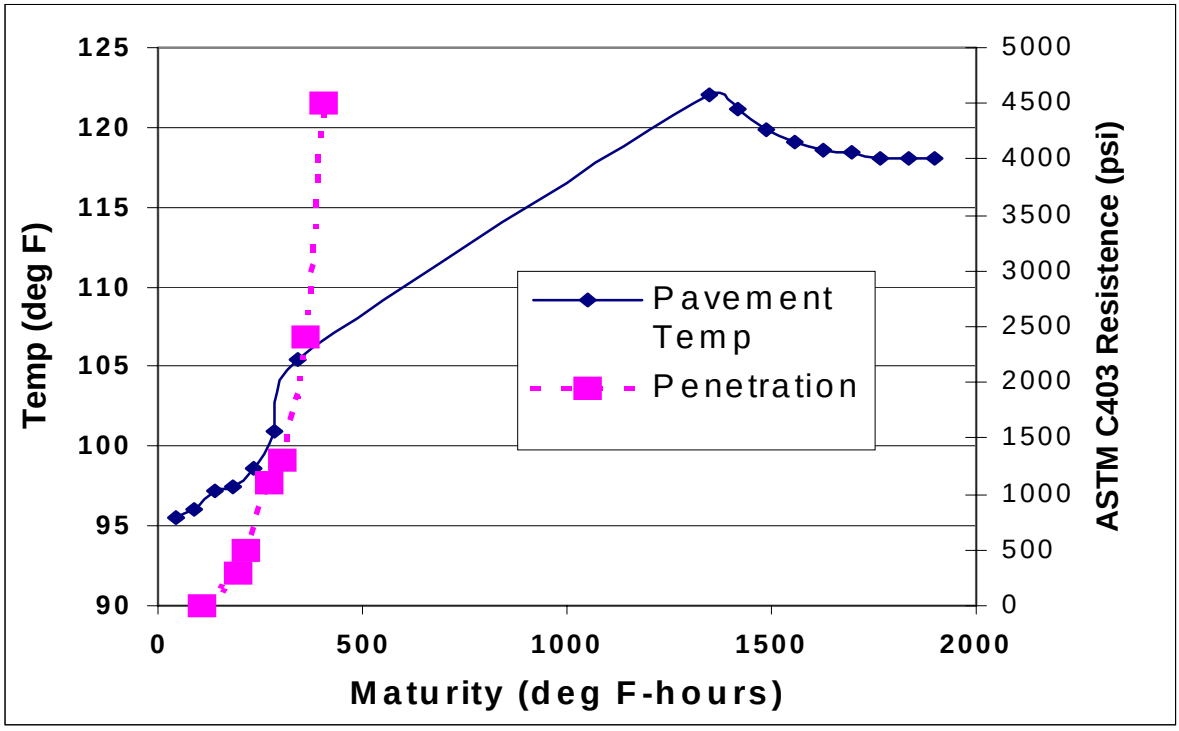

Figure A.1 Concrete Temperature/Setting Characteristics during Hardening.

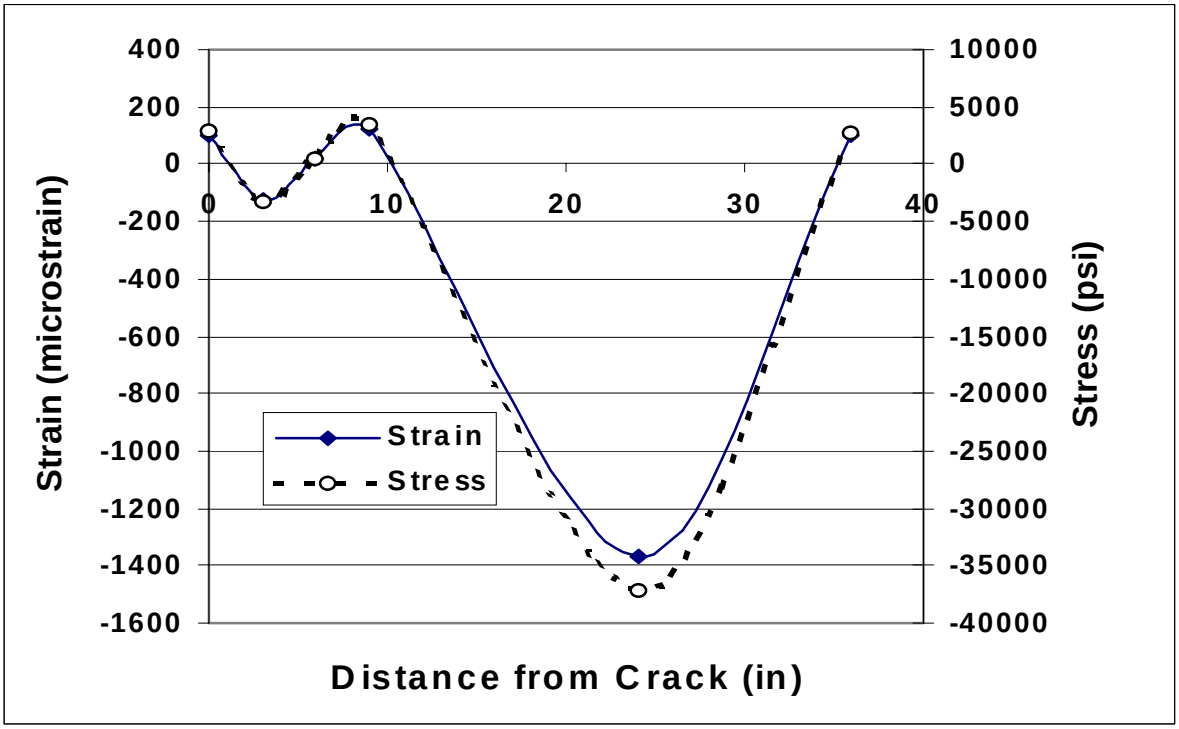

Figure A.2 Steel Stress/Strain versus Distance from Crack (Day 2).

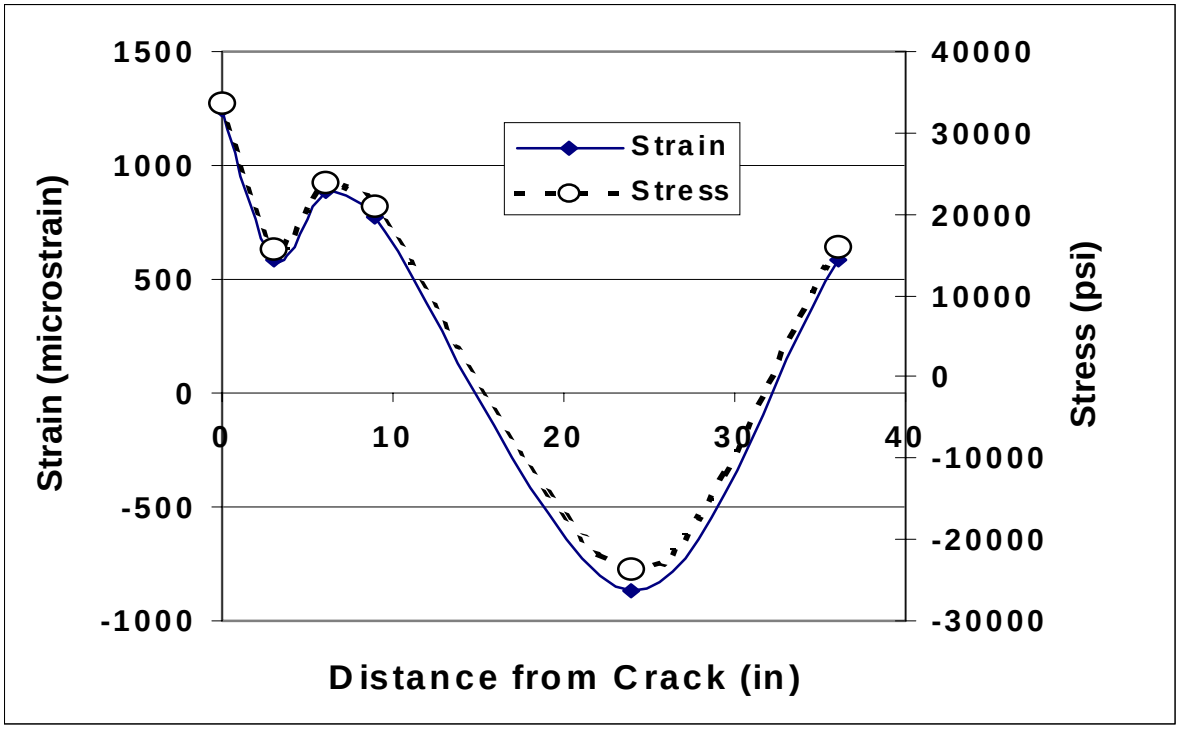

Figure A.3 Steel Stress/Strain versus Distance from Crack (Day 16).

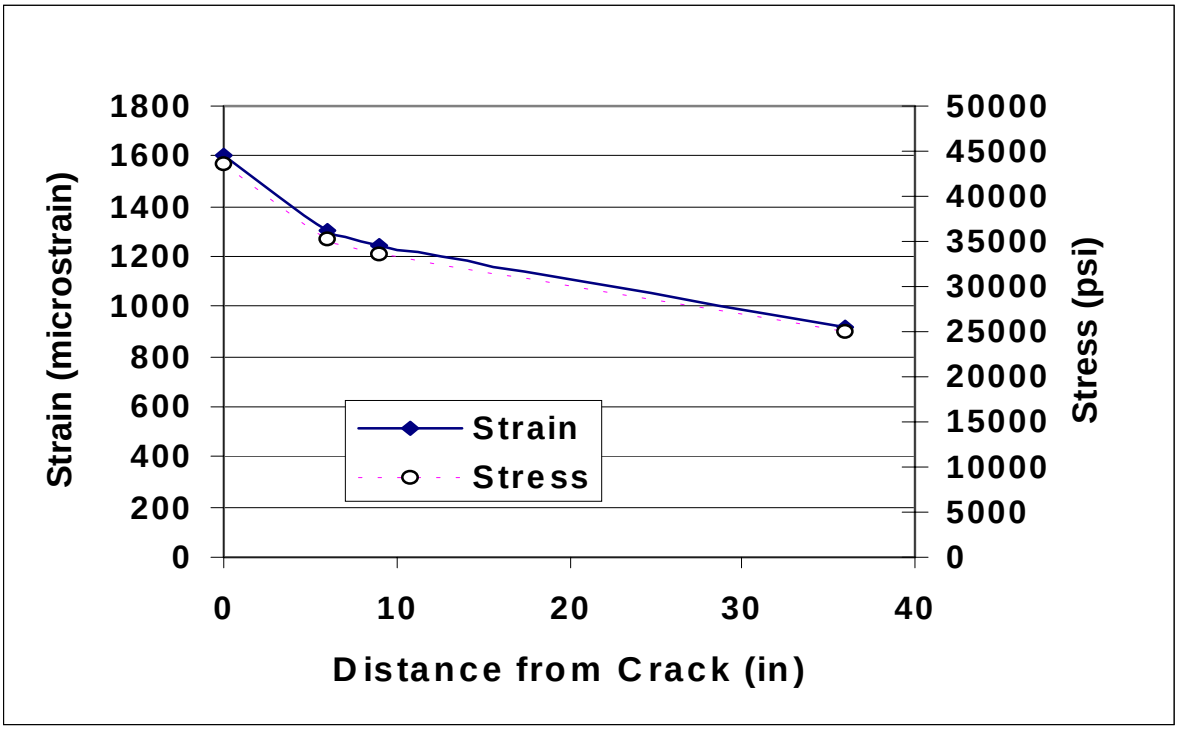

Figure A.4 Steel Stress/Strain versus Distance from Crack (Day 162).

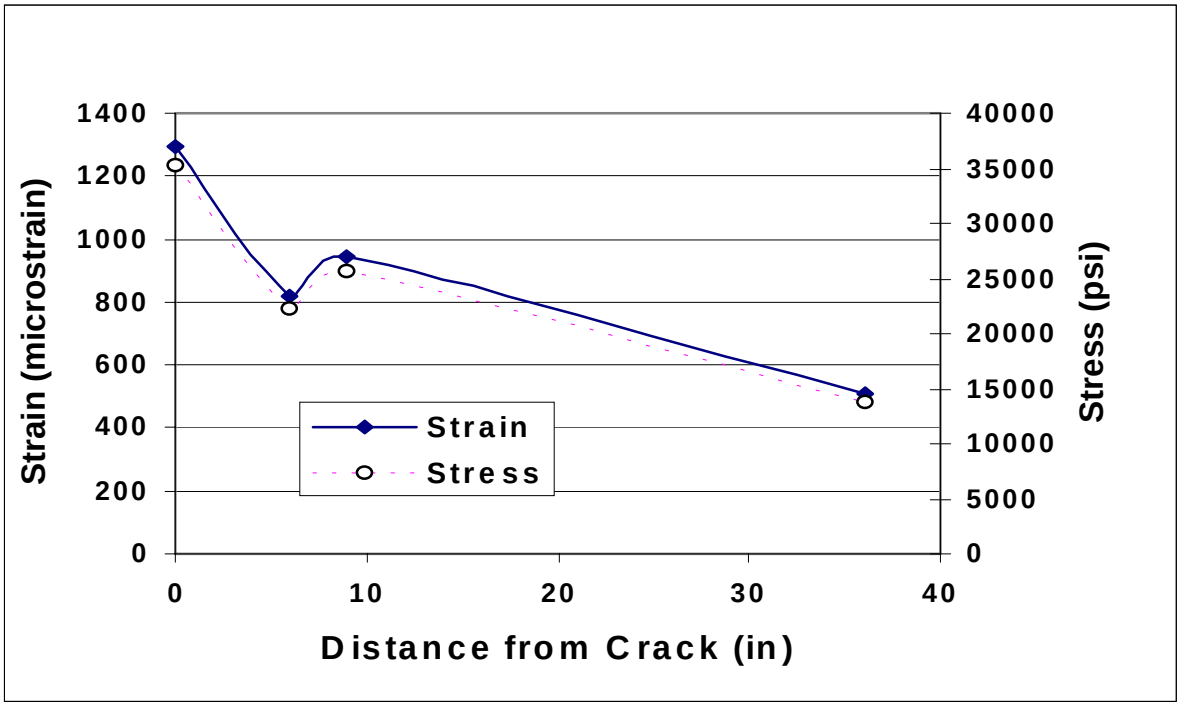

Figure A.5 Steel Stress/Strain versus Distance from Crack (Day 270).

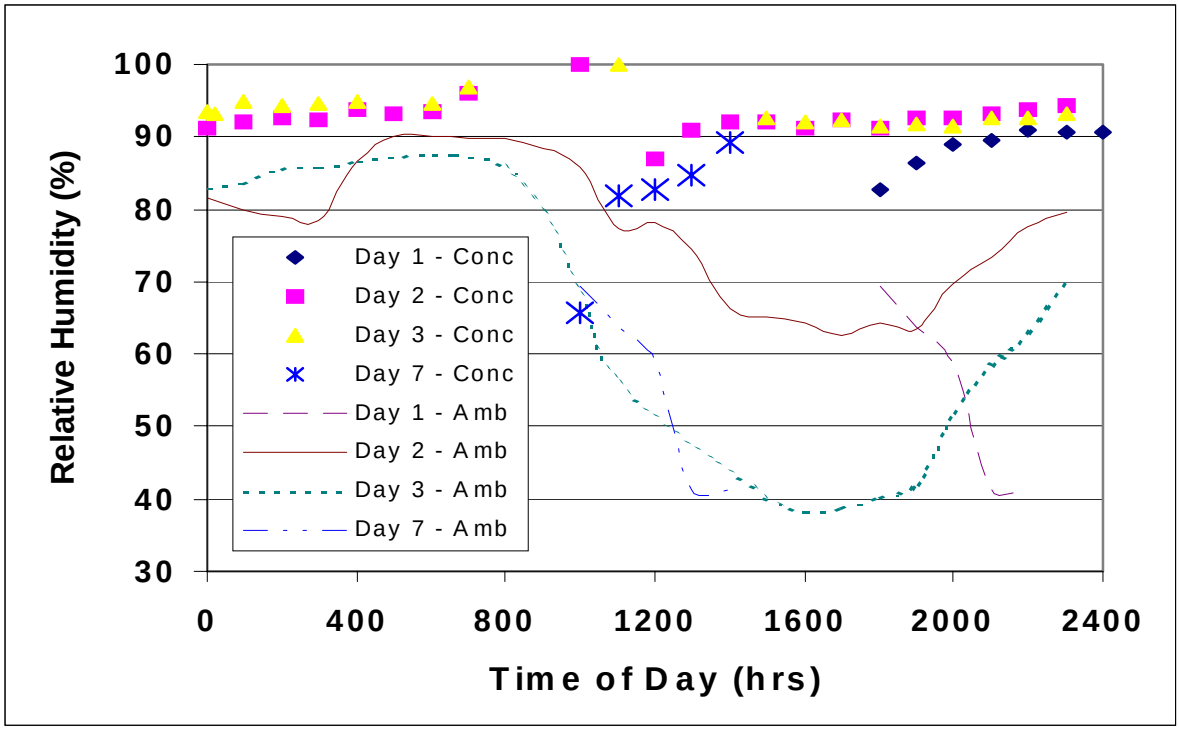

Figure A.6 Ambient and Pavement (1" below the Surface) Relative Humidity at Selected Days after Placement.

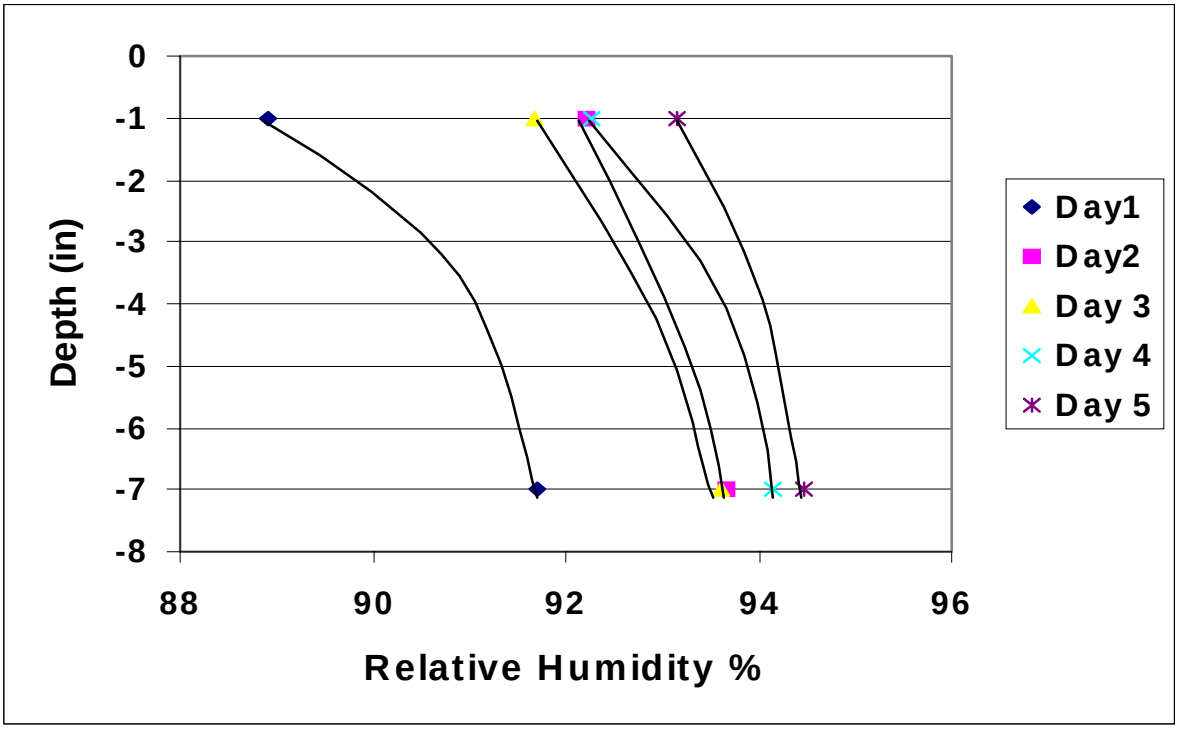

Figure A.7 Concrete Moisture Gradients during Hardening.

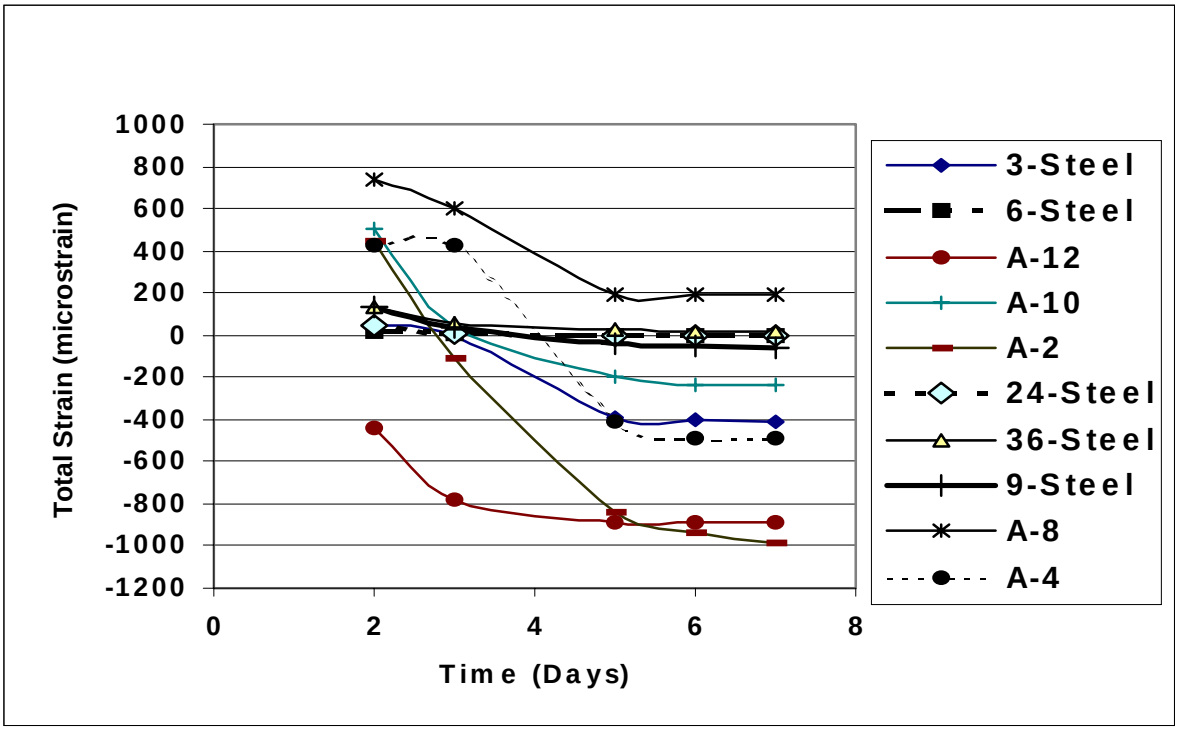

Figure A.8 Initial Concrete Strain Readings for First Week of Pavement Age as a Basis for Creep Determinations.

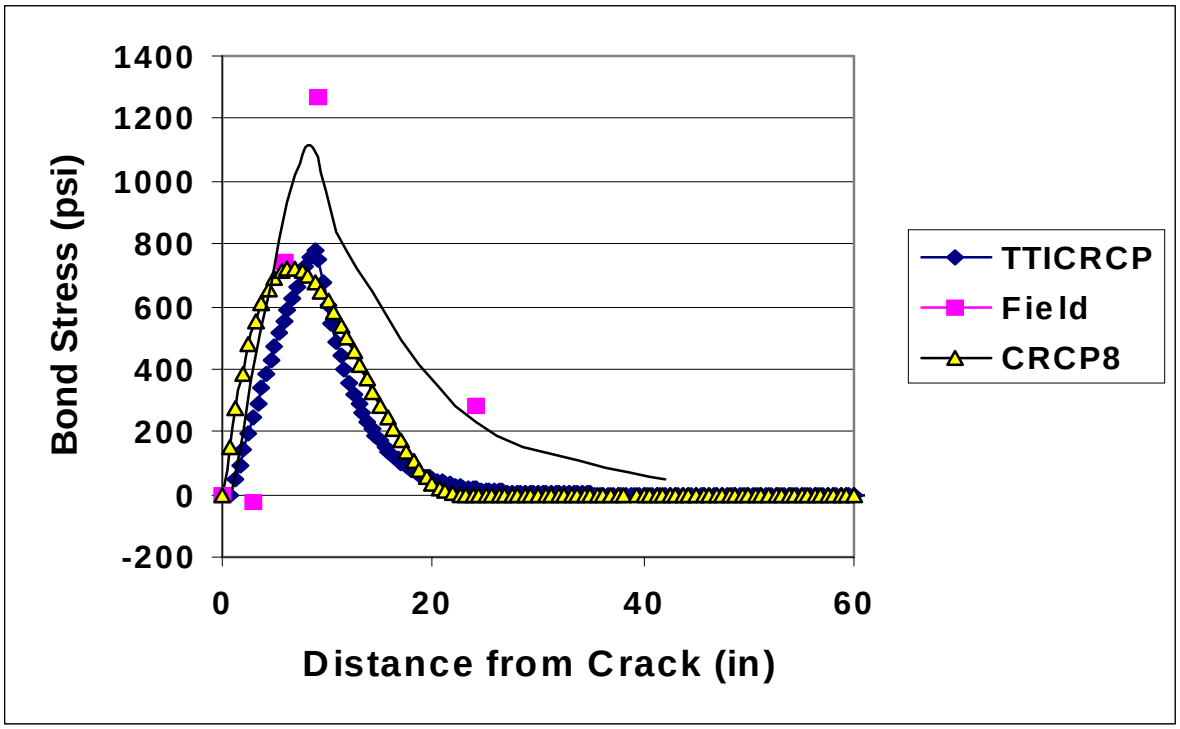

Figure A.9 Comparison of Bond Stress Distributions as Predicted by CRCP 8 and TTICRCP Programs to Field Data at Day 16.

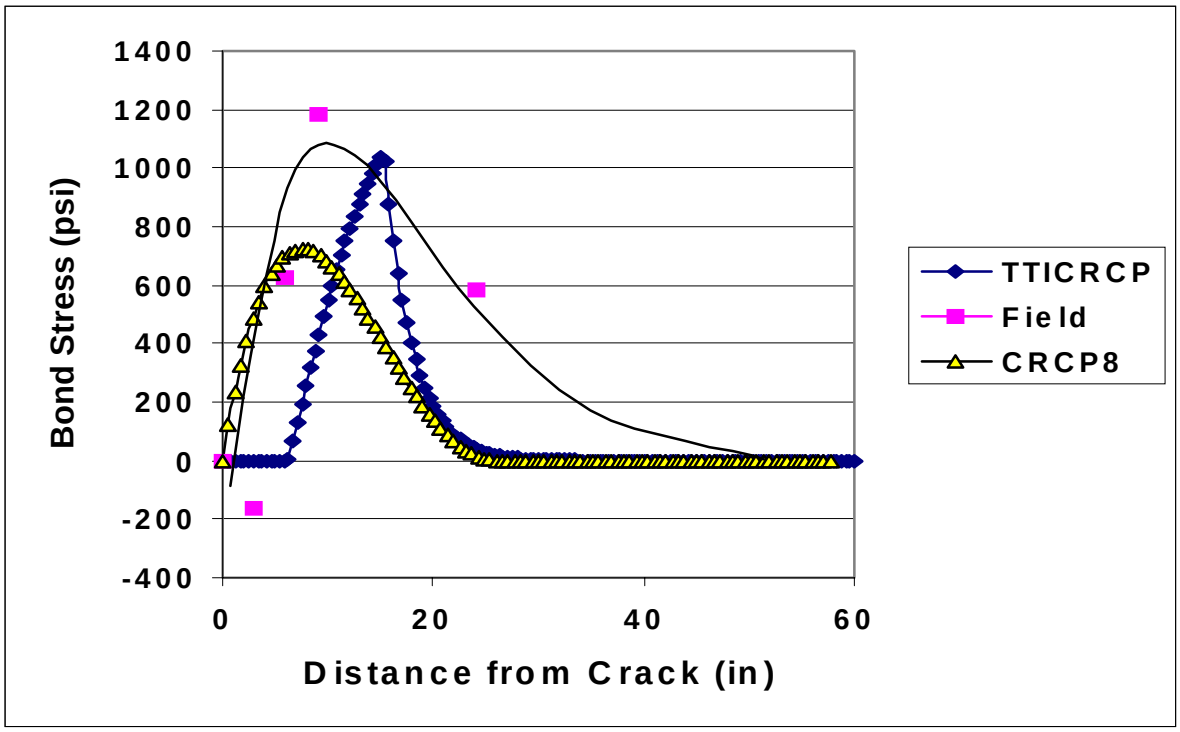

Figure A.10 Comparison of Bond Stress Distributions as Predicted by CRCP 8 and TTICRCP Programs to Field Data at Day 162.

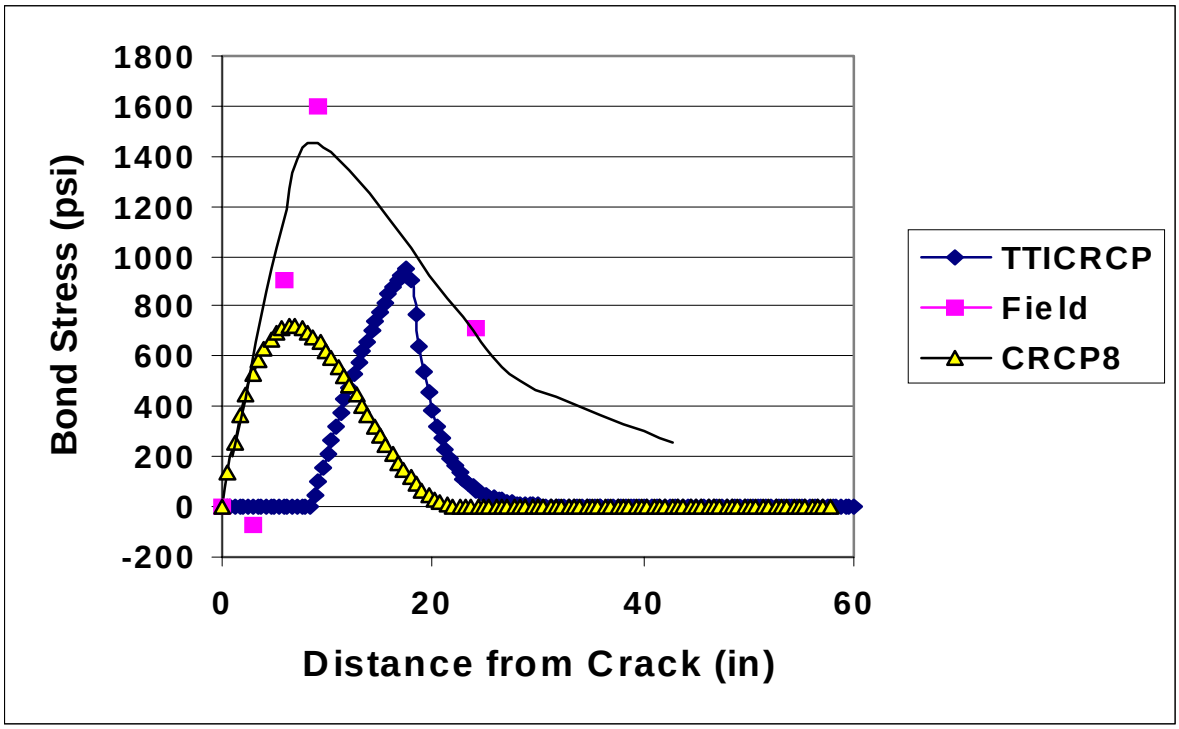

Figure A.11 Comparison of Bond Stress Distributions as Predicted by CRCP 8 and TTICRCP Programs to Field Data at Day 270.

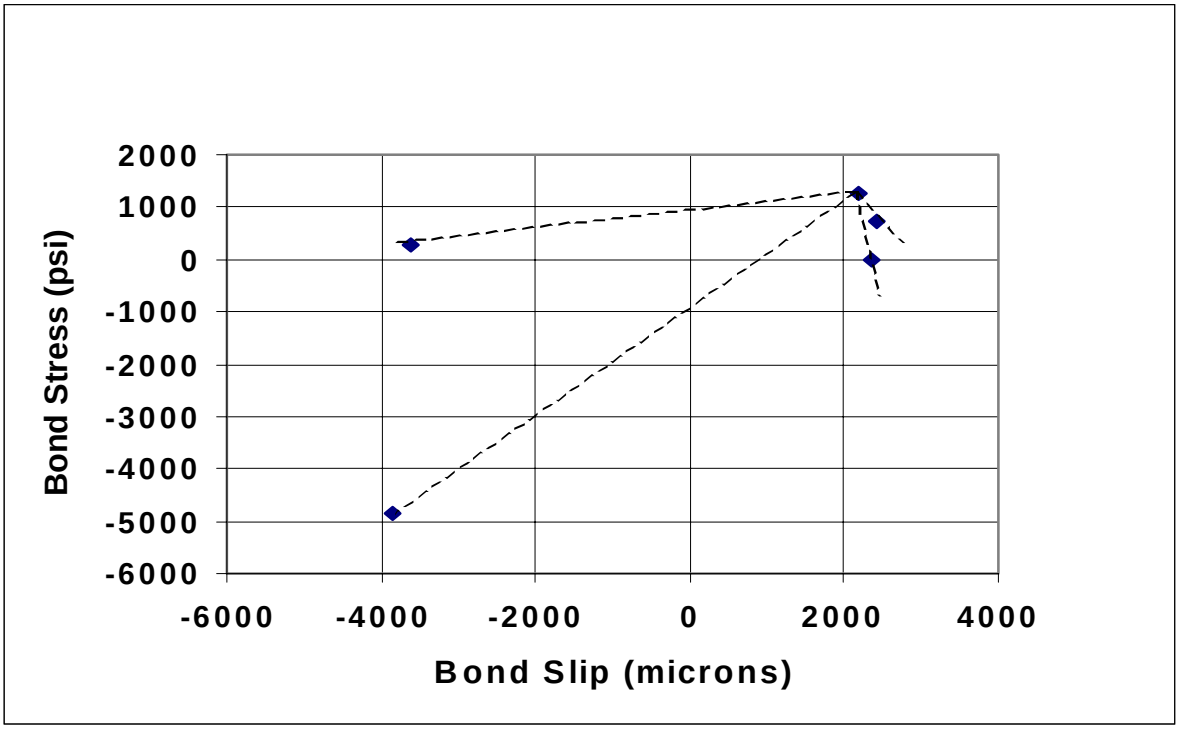

Figure A.12 Bond Stress versus Bond Slip as Calculated for Day 16.

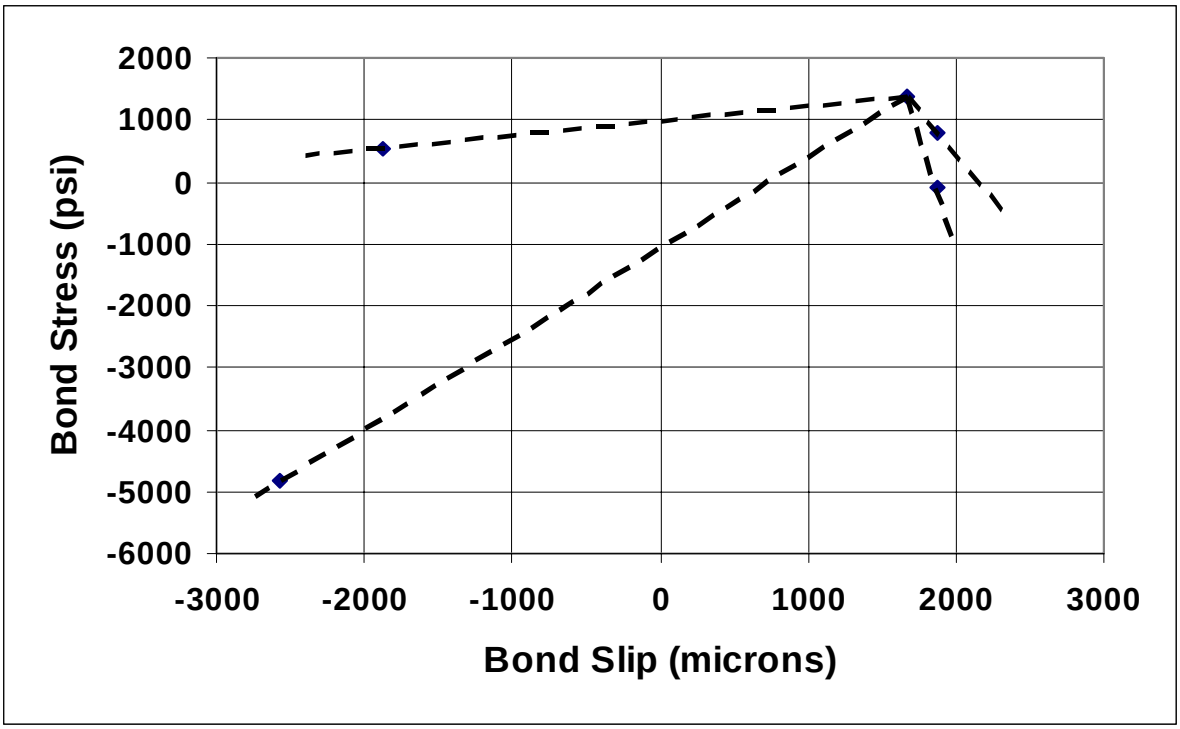

Figure A.13 Bond Stress versus Bond Slip as Calculated for Day 30.

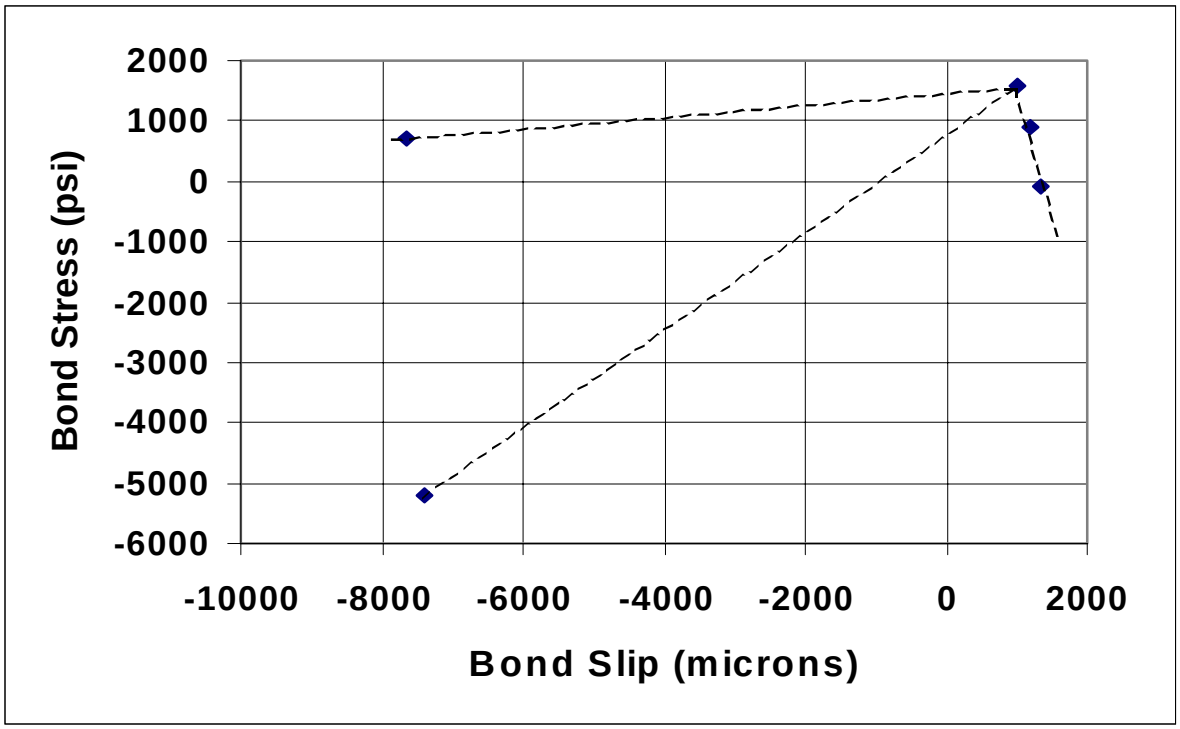

Figure A.14 Bond Stress versus Bond Slip as Calculated for Day 270.

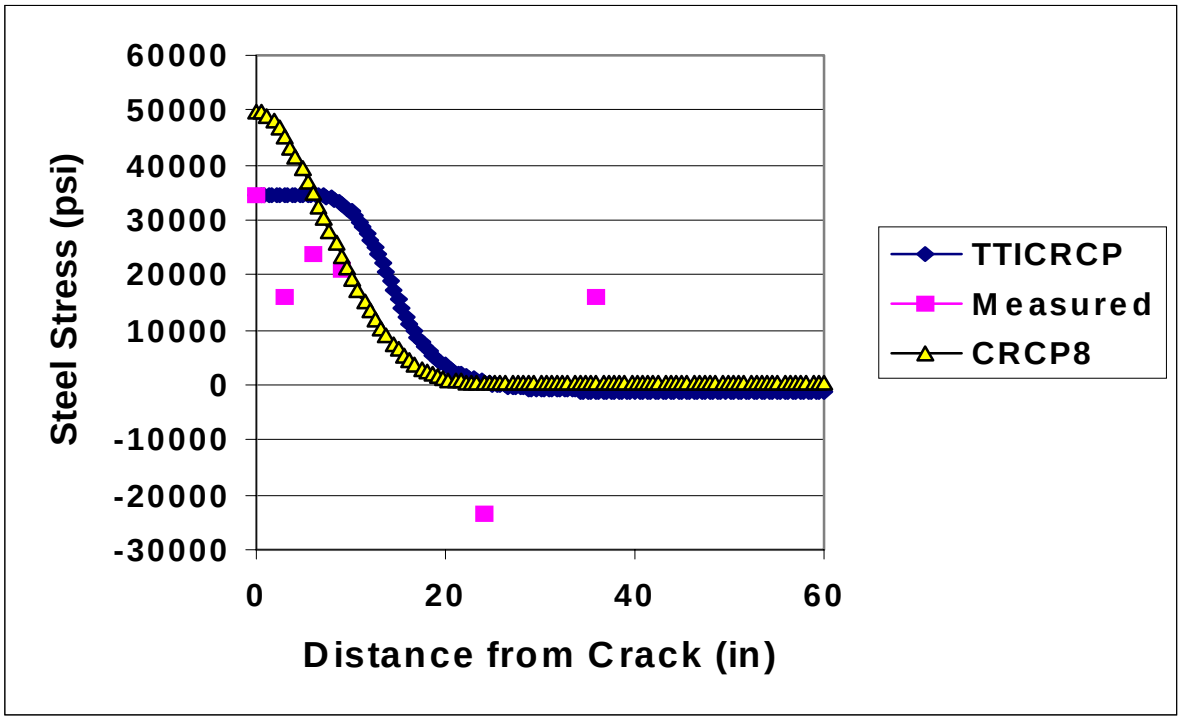

Figure A.15 Comparison of Steel Stress Distribution between Measured and Predicted Stresses at Day 16.

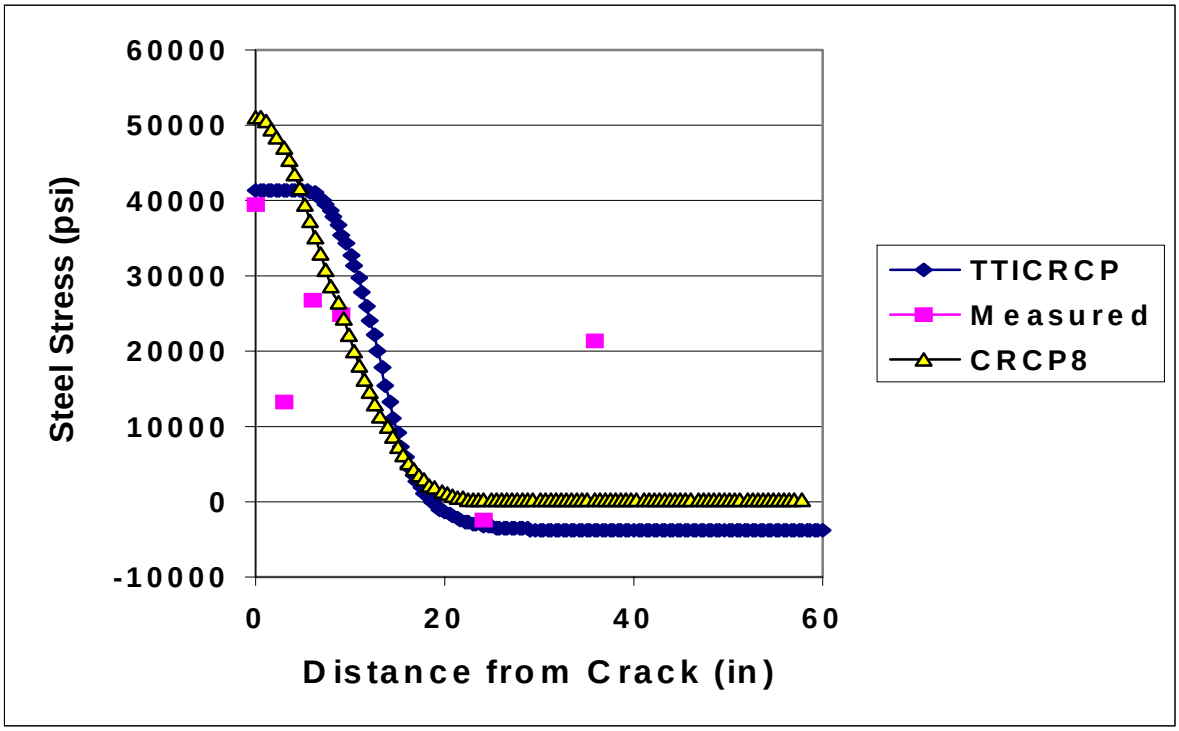

Figure A.16 Comparison of Steel Stress Distribution between Measured and Predicted Stresses at Day 30.

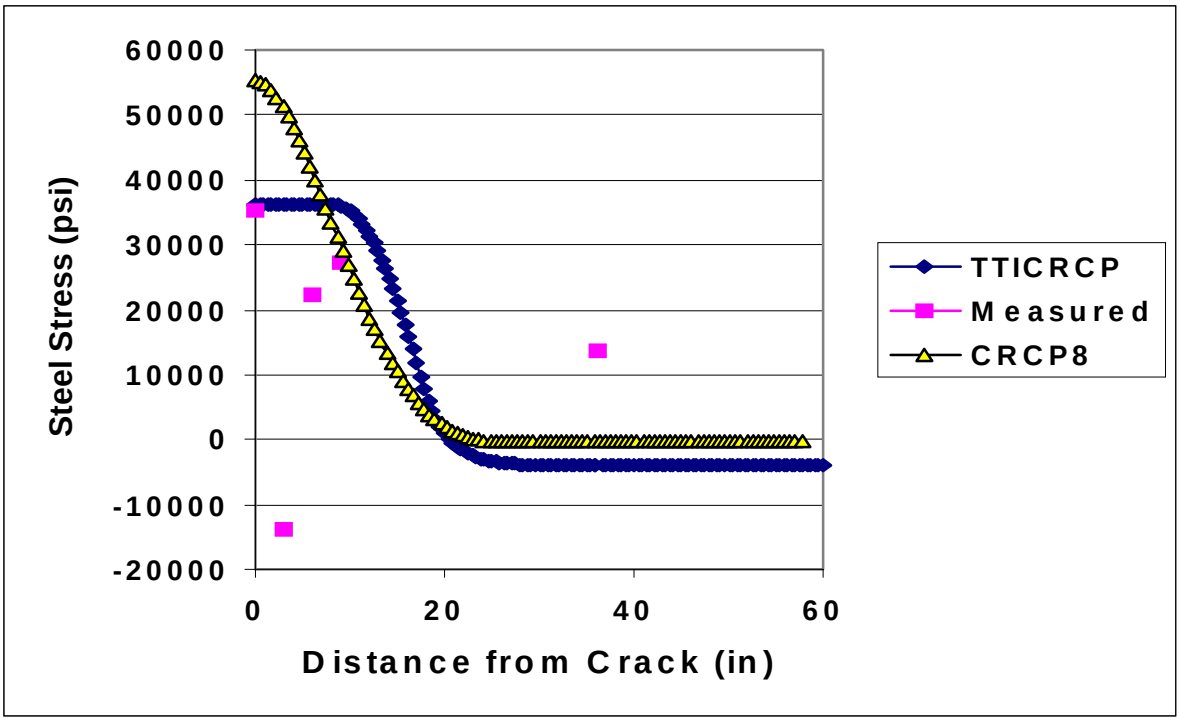

Figure A.17 Comparison of Steel Stress Distribution between Measured and Predicted Stresses at Day 270.

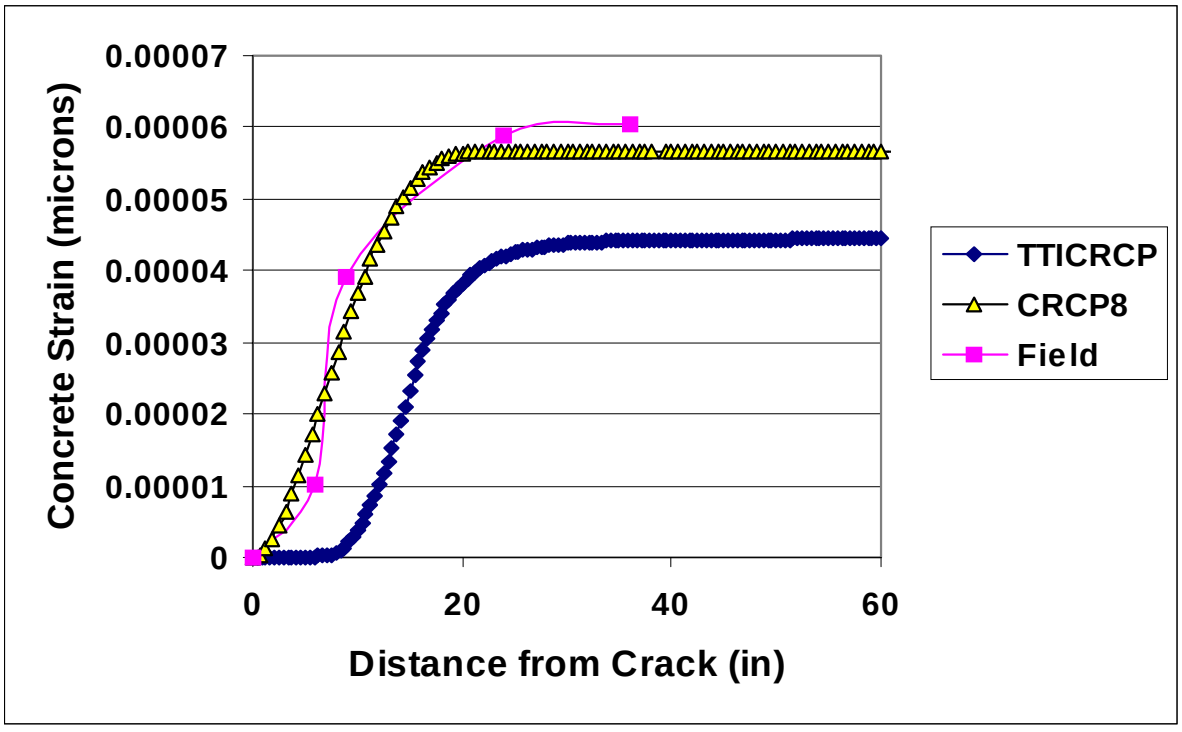

Figure A.18 Comparison of Concrete Stress Distribution between Measured and Predicted Stresses at Day 16.

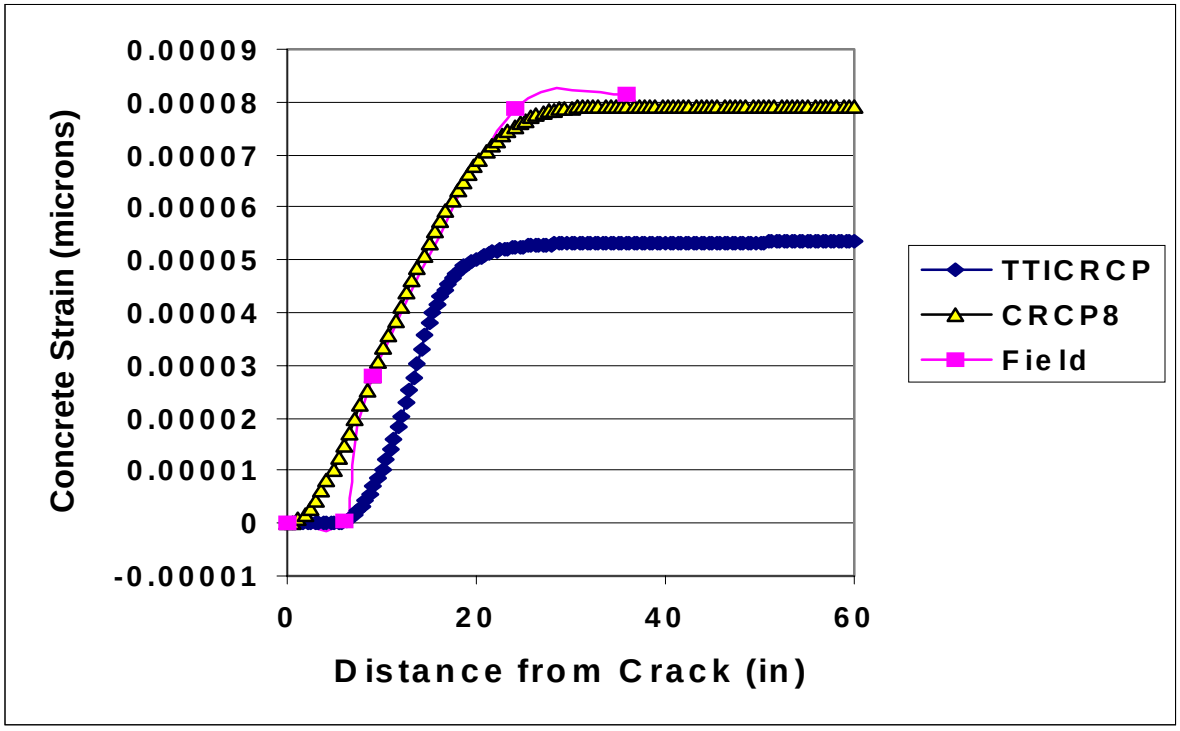

Figure A.19 Comparison of Concrete Stress Distribution between Measured and Predicted Stresses at Day 30.

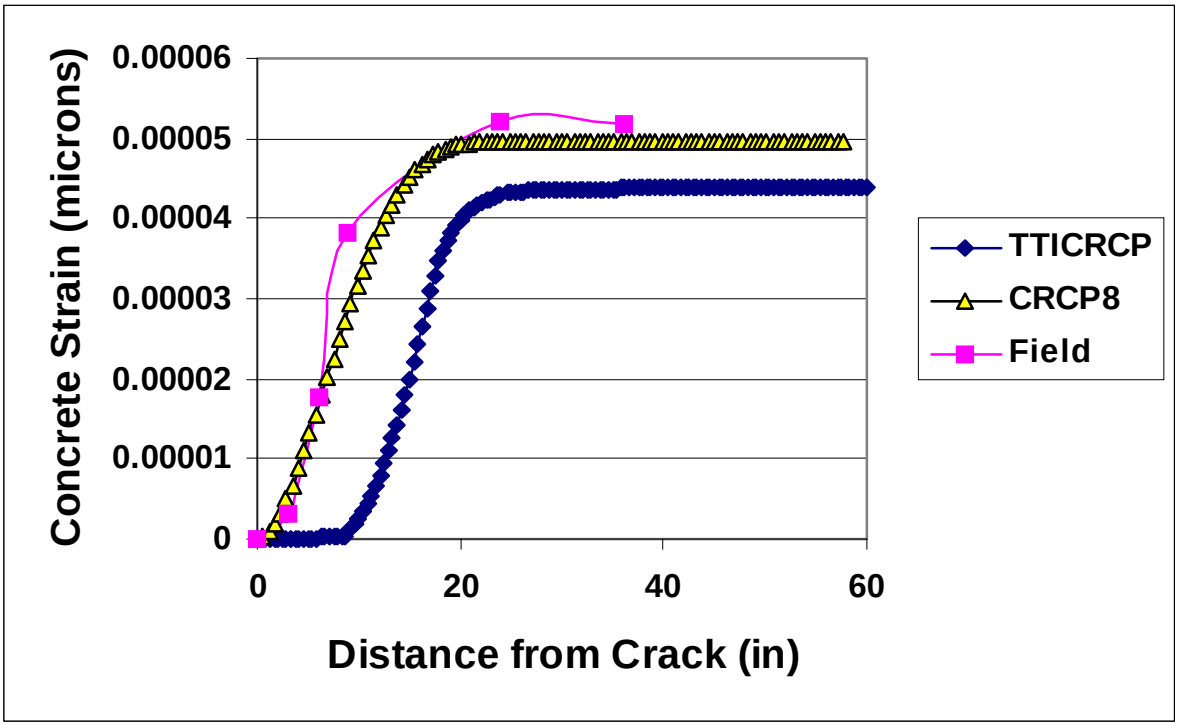

Figure A.20 Comparison of Concrete Stress Distribution between Field Derived and Predicted Stresses at Day 270.

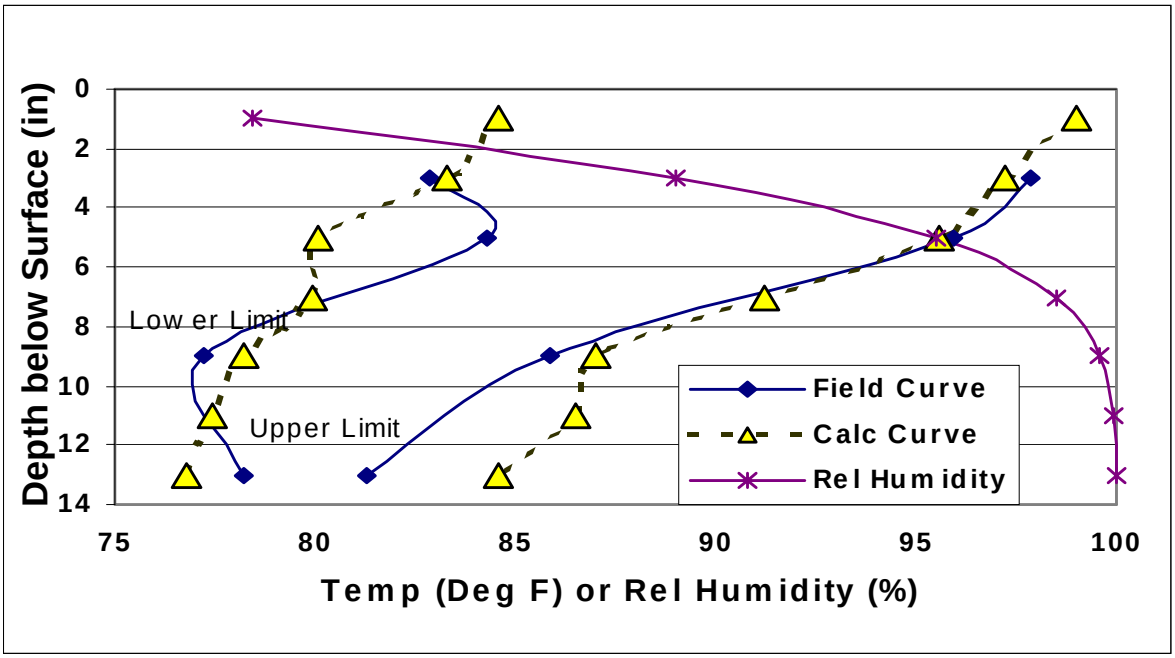

Figure A.21 Calculated and Measured Pavement Moisture and Temperature Profiles for Day 16.

Table A.1 Inputs Values Used for TTICRCP Program.

	Day 16	**Day 30**	**Day 162**	**Day 270**
Compressive Strength (psi)	4964	5510	6281	6502
Tensile Strength (psi)	436	468	533	552
Conc E_c (psi)	4015973	4231074	4517551	4596123
K_1 (pci)	360000	620000	780000	960000
K_2 (pci)	-100000	-100000	-100000	-100000
K_3 (pci)	89.3	89.3	89.3	89.3
K_4 (pci)	-4.17	-4.17	-4.17	-4.17
δ_B (in)	0.002197	0.001671	0.001339	0.001007
δ_F (in)	0.0258	0.0258	0.0258	0.0258
ε_{shr} (x 10^{-6})	269.23	377.7	604.48	639.38

*Note:1) $E_c = 57000(f'_c)^{½}$ 2) Strength data also used for CRCP 8 analysis.

Table A.2 Geometry and Material Properties of the CRCP FE Analysis Model.

Cracking spacing	10 ft	Drying shrinkage strain	0.00008 at surface 0.00000 at bottom
Distance between longitudinal steels	6 in	Vertical stiffness of underlying layers	400 psi/in
Depth of concrete layer	15 in	Bond-slip stiffness between concrete & steel	700000 psi/in
Steel location from surface	7.5 in	Second bond-slip stiffness	70000 psi/in
Young's modulus of concrete	4000000 psi (day 16) 4300000 psi (day 30)	Yield slip between concrete and steel	0.001 in
Poisson's ratio	0.15	Ultimate slip between concrete and steel	0.004 in
Diameter of steel	0.75 in	Bond-slip stiffness between concrete & base	150 psi/in
Coefficient of thermal expansion of concrete	0.000008/°F	Yield slip between concrete and base	0.02 in
Coefficient of thermal expansion of steel	0.000005/°F	Maximum creep ratio	2.0
Surface temperature	85°F - 99°F (day 16) 83°F - 97°F (day 30)	Load duration	12 hr
Bottom temperature	77°F - 85°F (day 16) 90°F - 93°F (day 30)	ϕ_x	0.99
Reference temperature	67°F - 93°F (day 16) 72°F - 89°F (day 30)	t_x	30 days

Note: The bond slip model used Type d described in reference 42.

APPENDIX B

CONCRETE STRAIN DATA

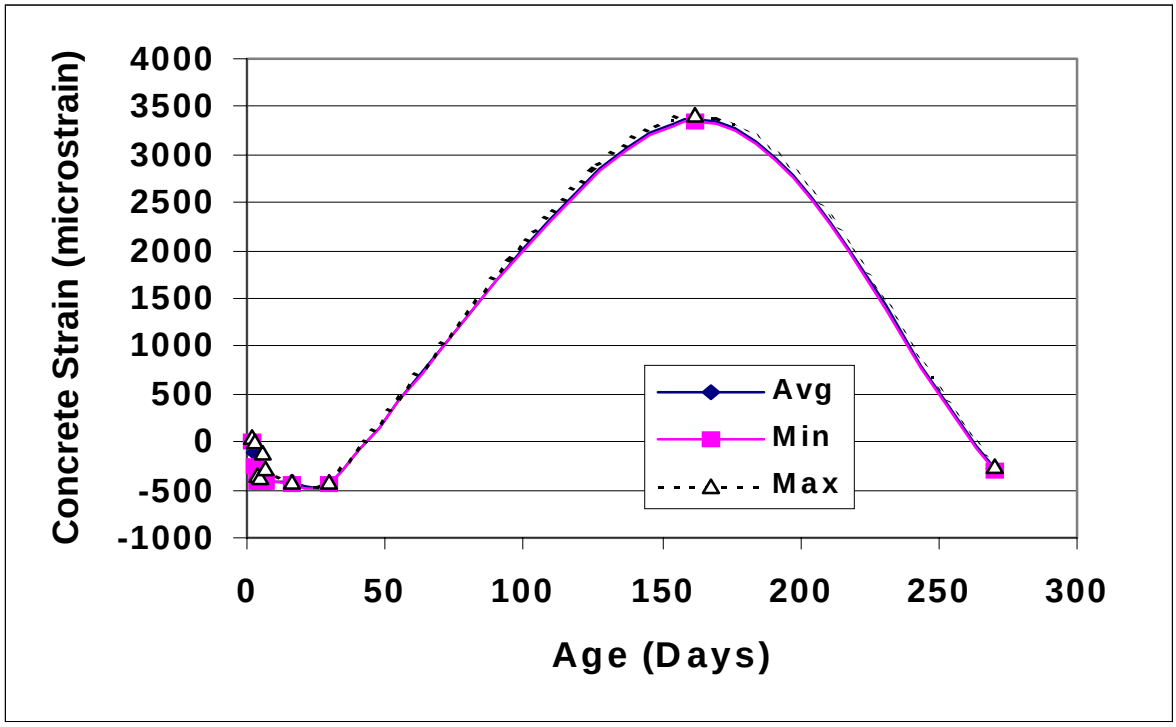

Figure B.1 Concrete Strain versus Age of Pavement Gage CG1.

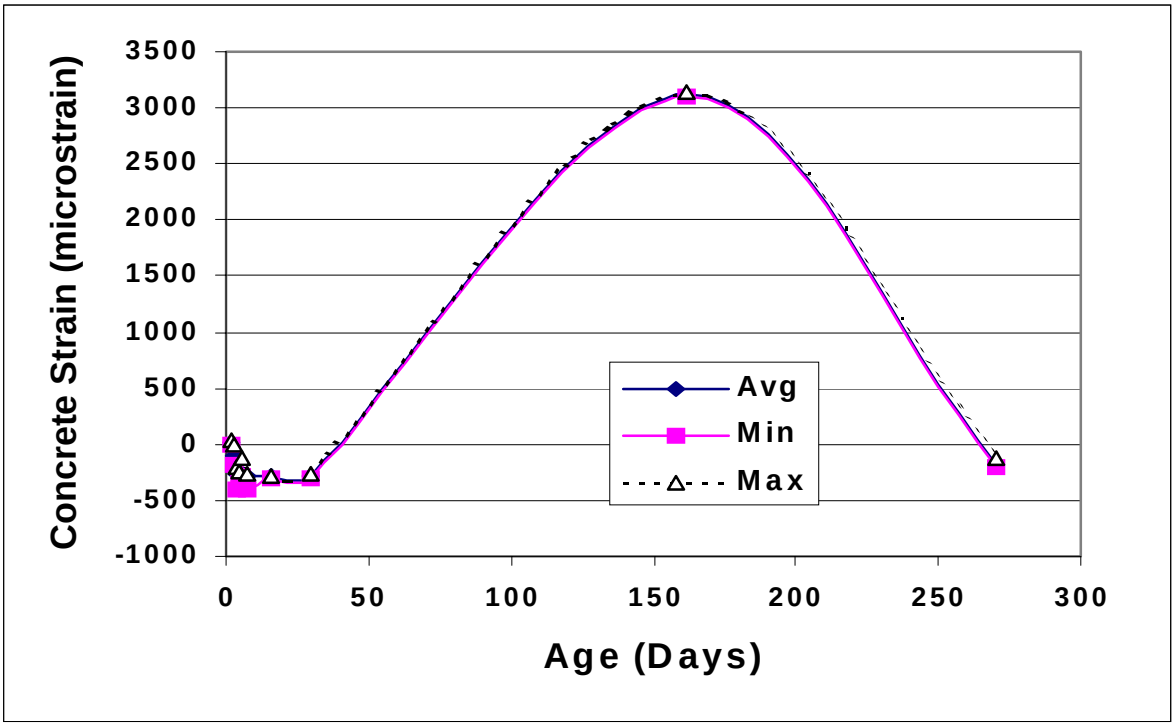

Figure B.2 Concrete Strain versus Age of Pavement Gage CG2.

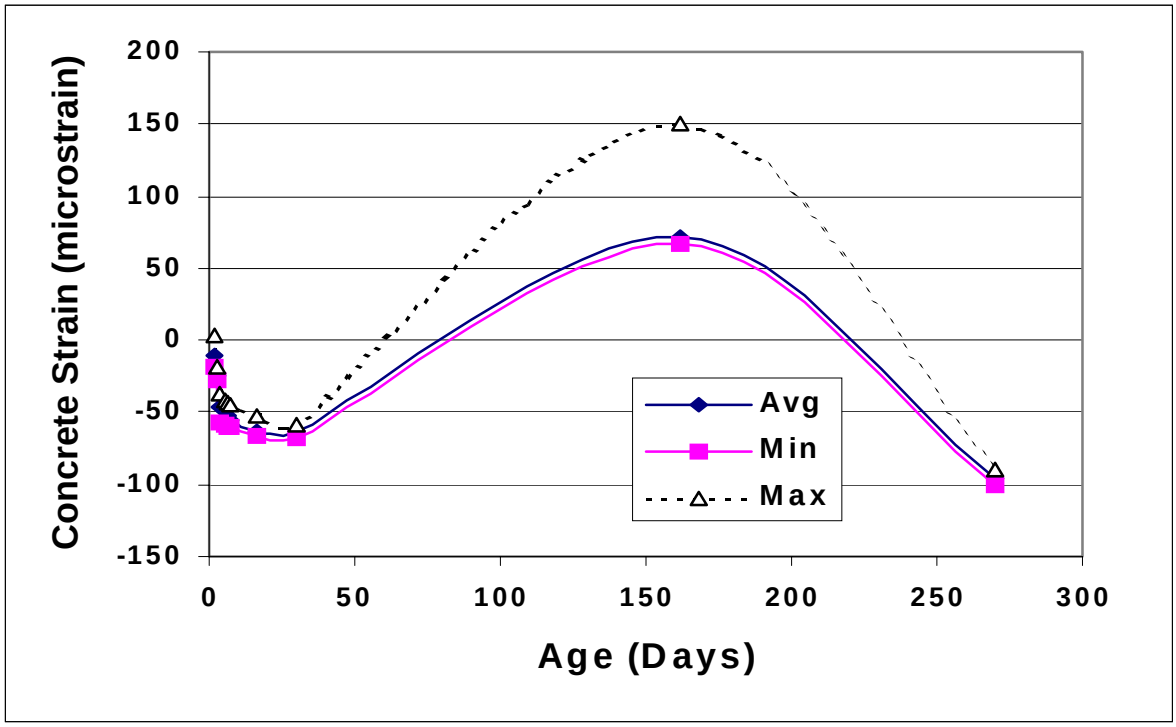

Figure B.3 Concrete Strain versus Age of Pavement Gage CG3.

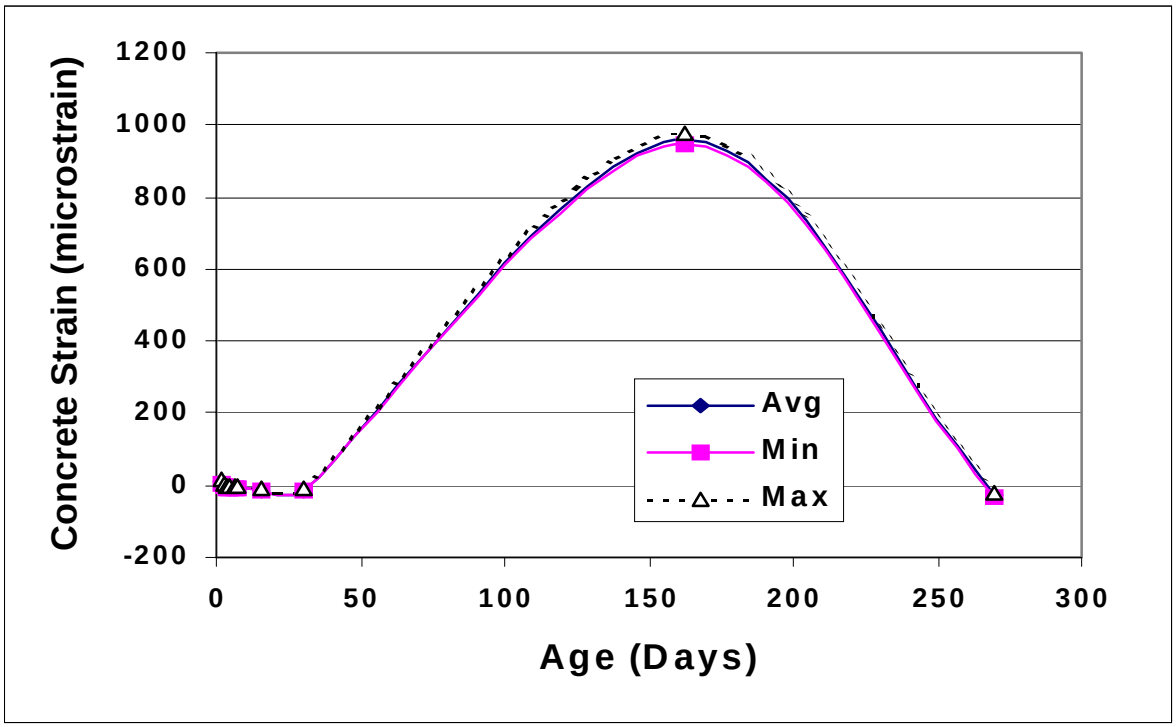

Figure B.4 Concrete Strain versus Age of Pavement Gage CG4.

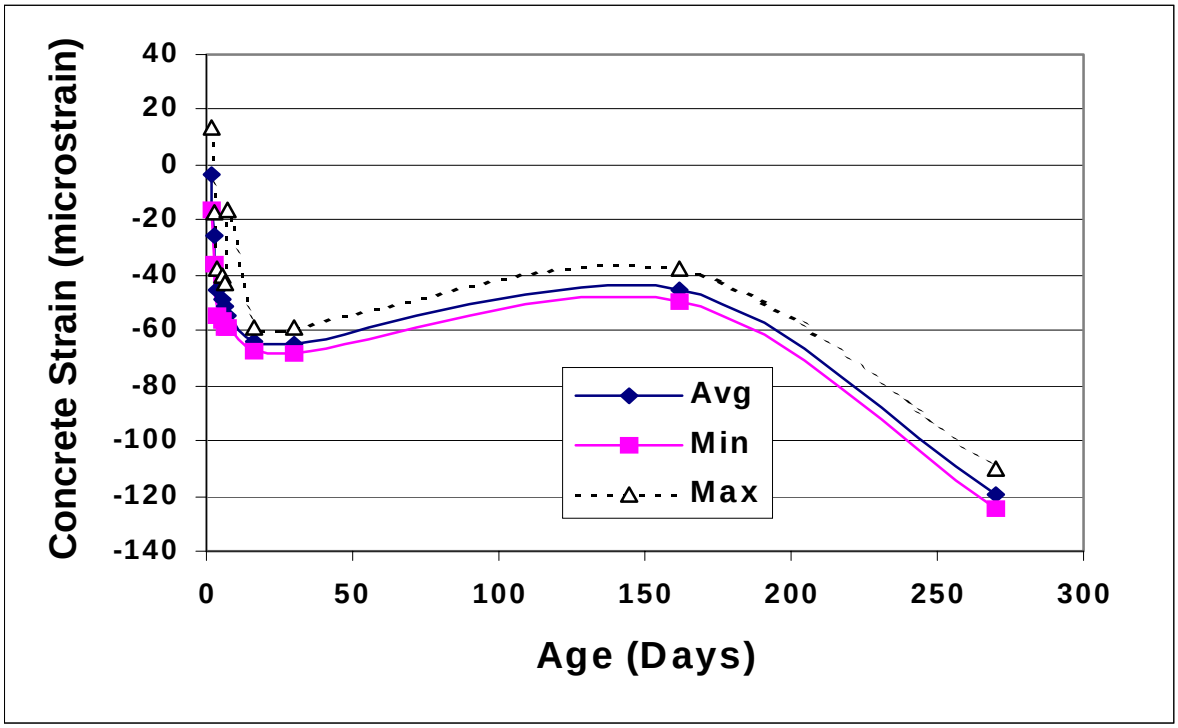

Figure B.5 Concrete Strain versus Age of Pavement Gage CG6.

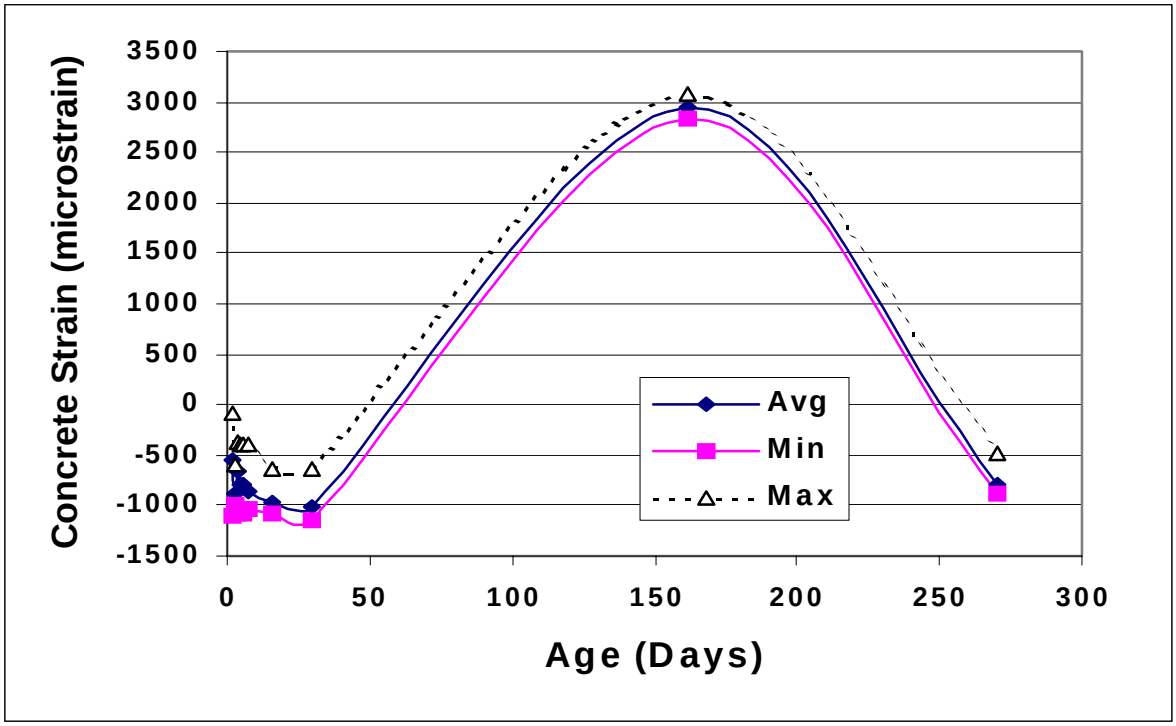

Figure B.6 Concrete Strain versus Age of Pavement Gage CG7.

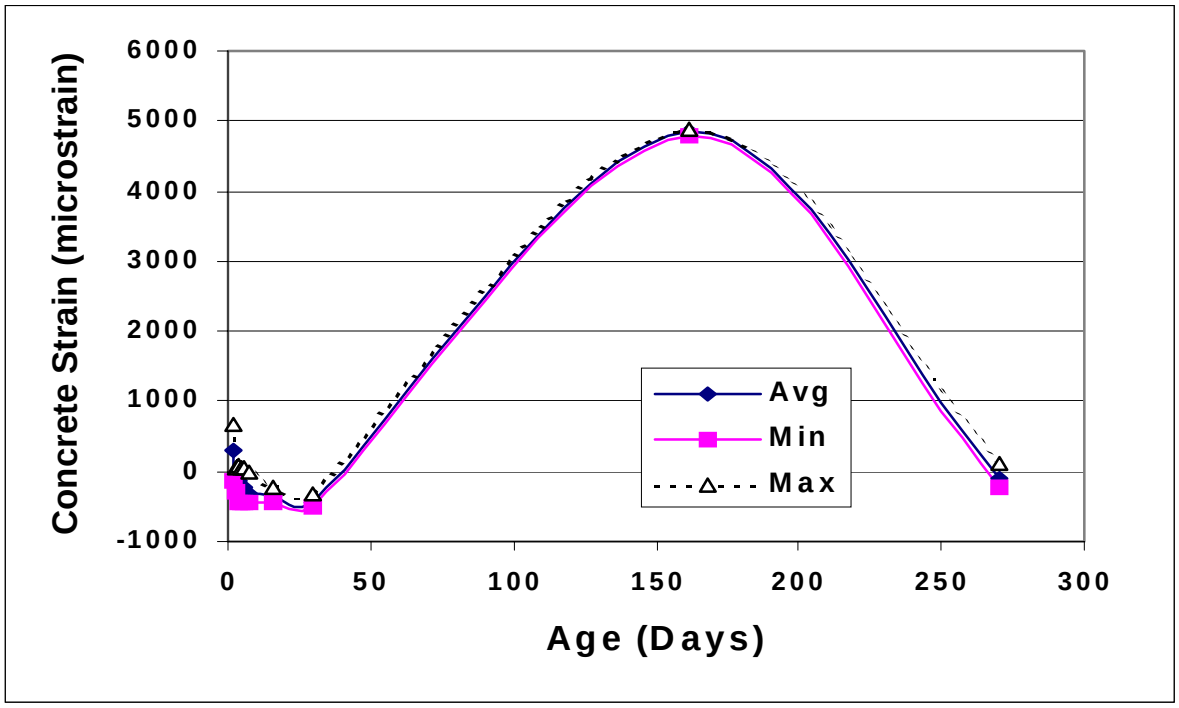

Figure B.7 Concrete Strain versus Age of Pavement Gage CG8.

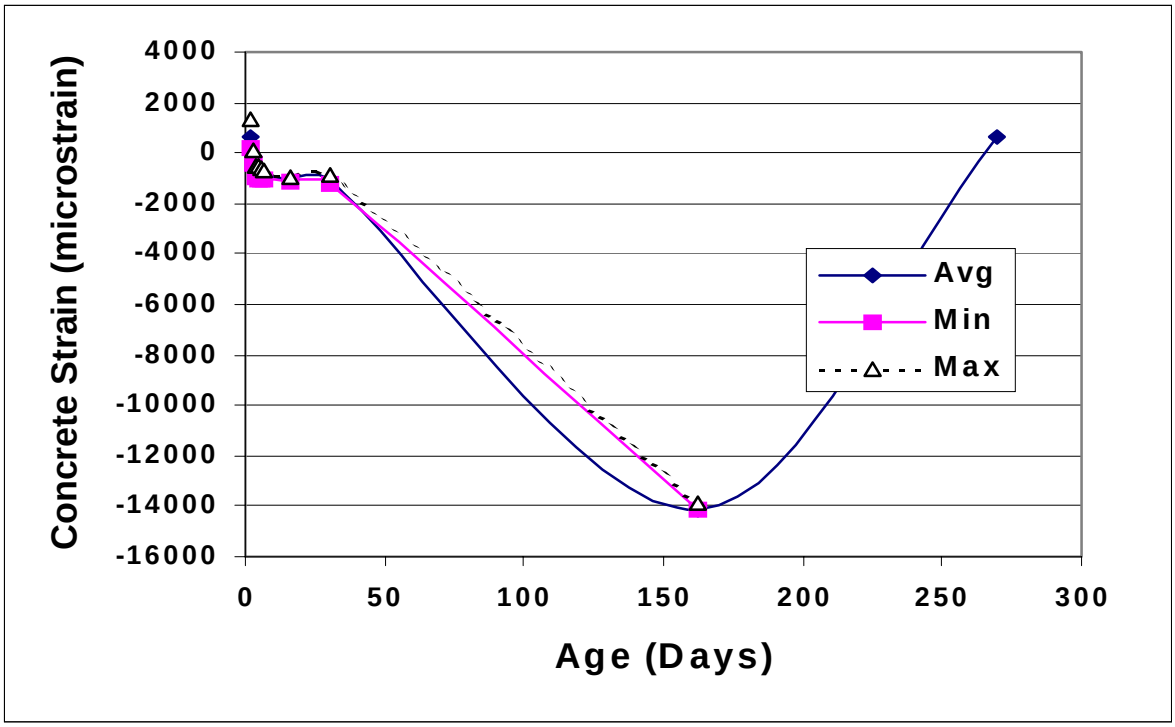

Figure B.8 Concrete Strain versus Age of Pavement Gage CG9.

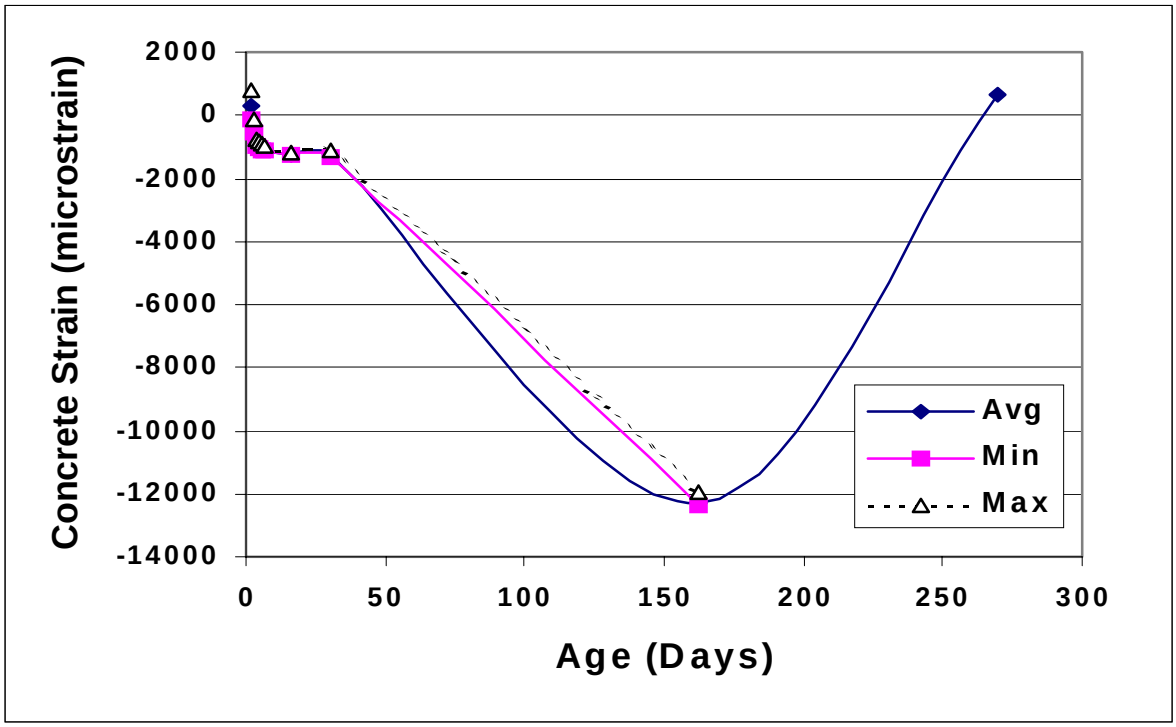

Figure B.9 Concrete Strain versus Age of Pavement Gage CG10.

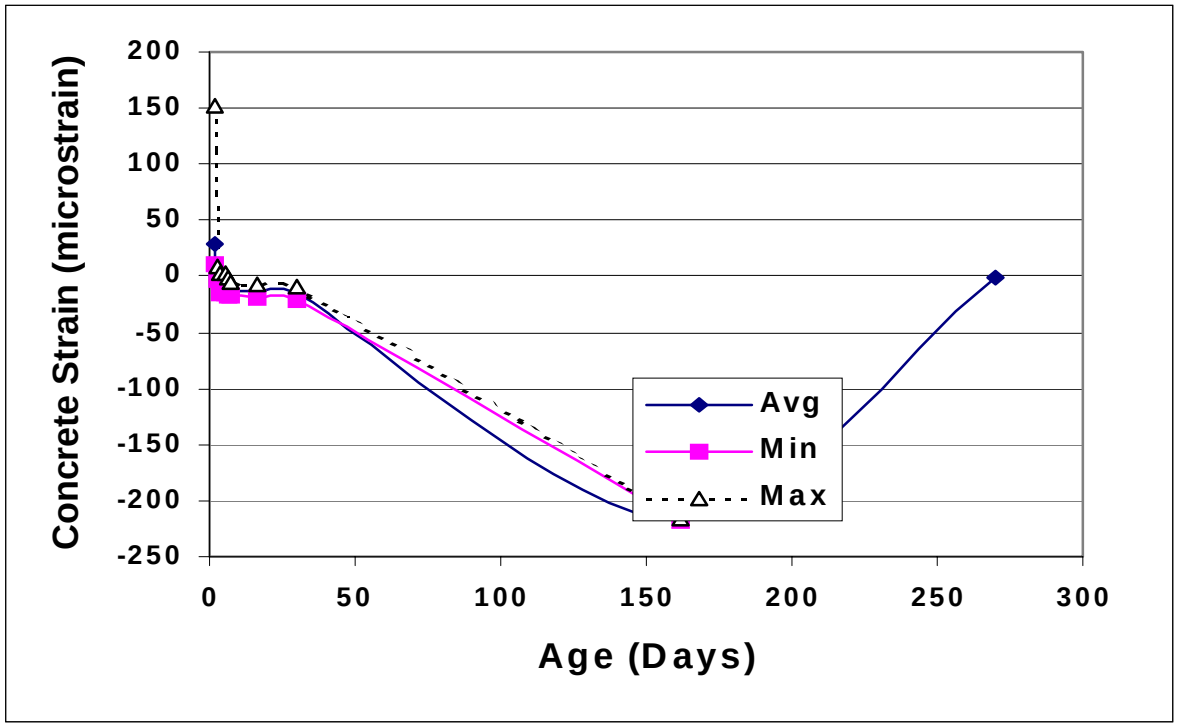

Figure B.10 Concrete Strain versus Age of Pavement Gage CG11.

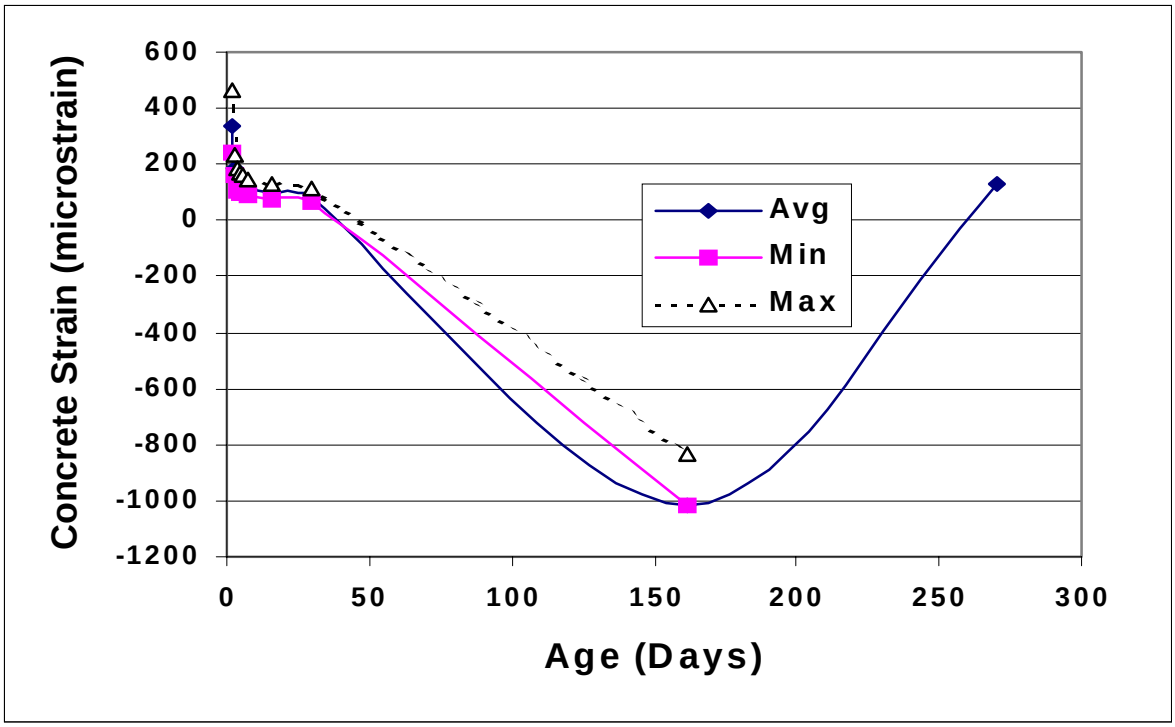

Figure B.11 Concrete Strain versus Age of Pavement Gage CG12.

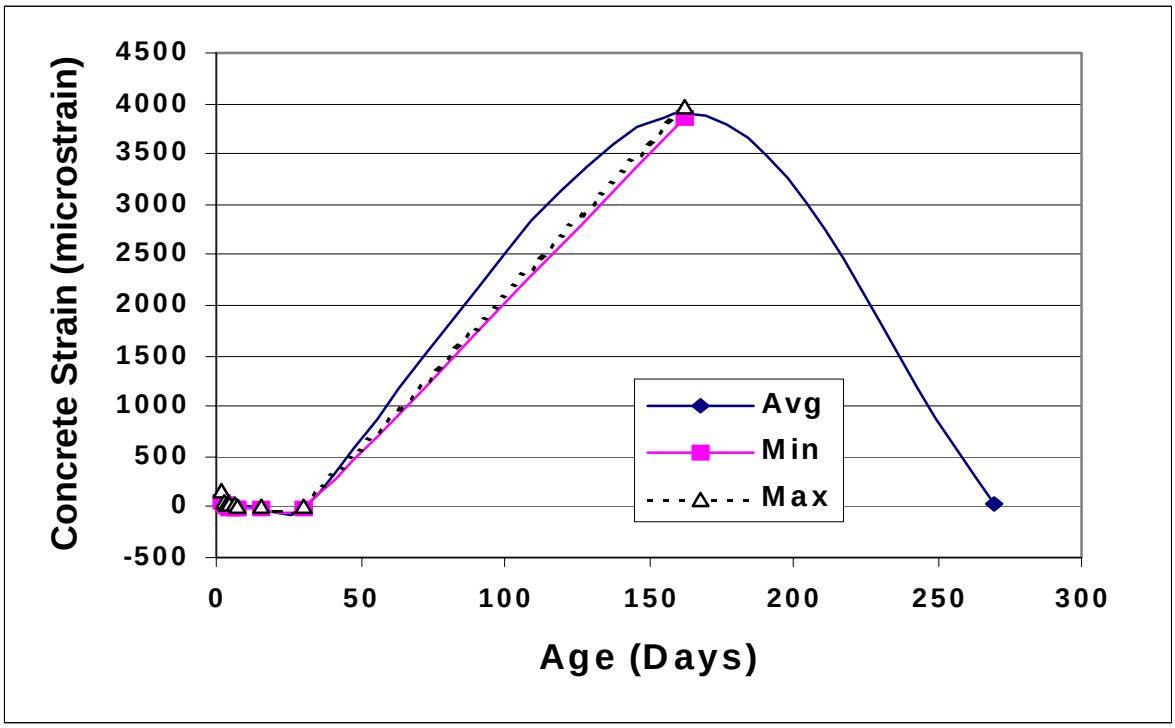

Figure B.12 Concrete Strain versus Age of Pavement Gage CG13.

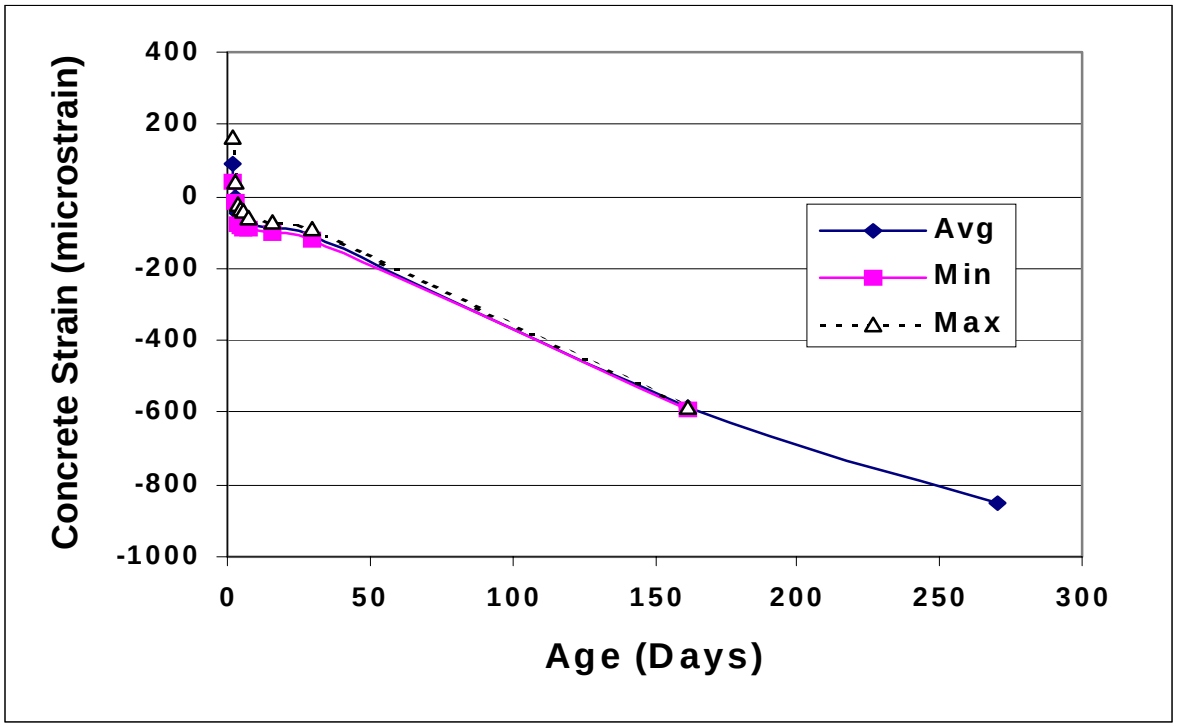

Figure B.13 Concrete Strain versus Age of Pavement Gage CG14.

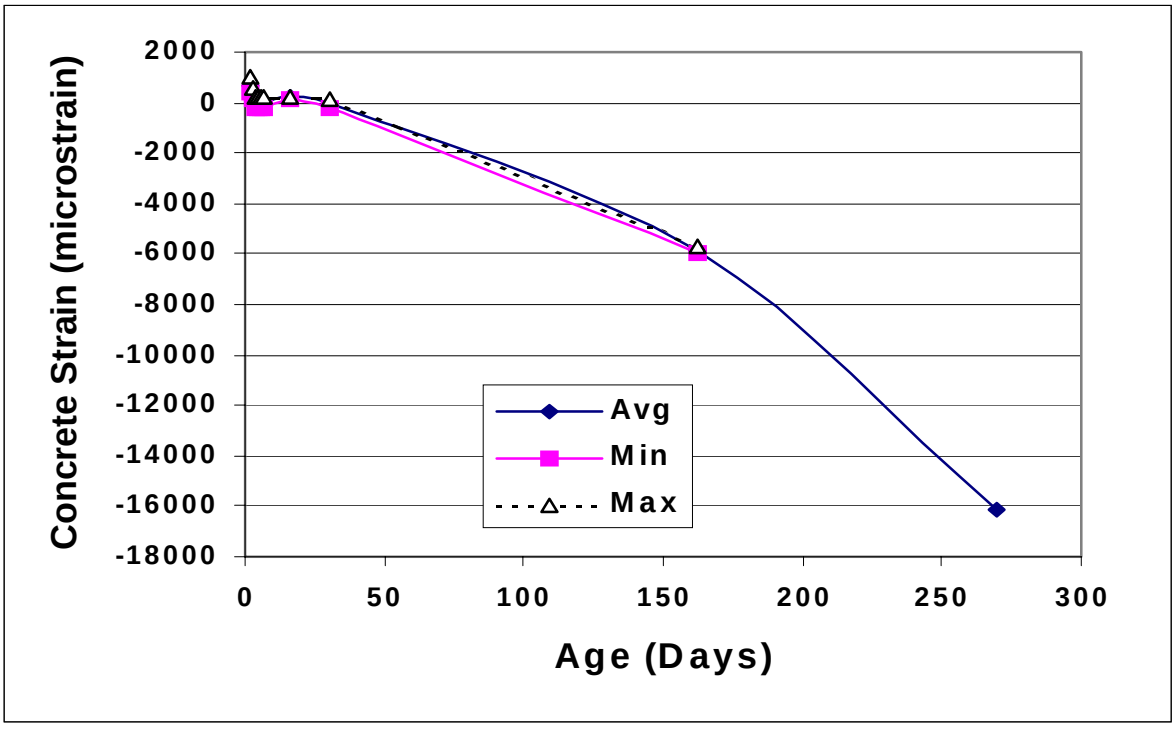

Figure B.14 Concrete Strain versus Age of Pavement Gage CG15.

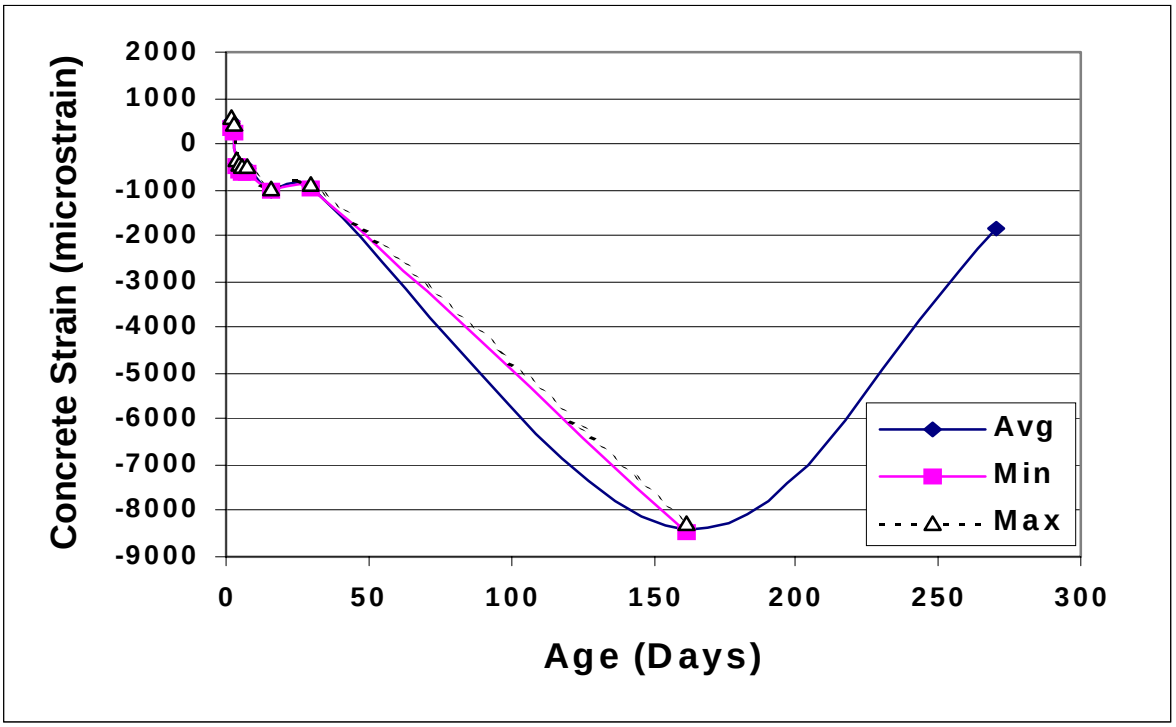

Figure B.15 Concrete Strain versus Age of Pavement Gage CG16.

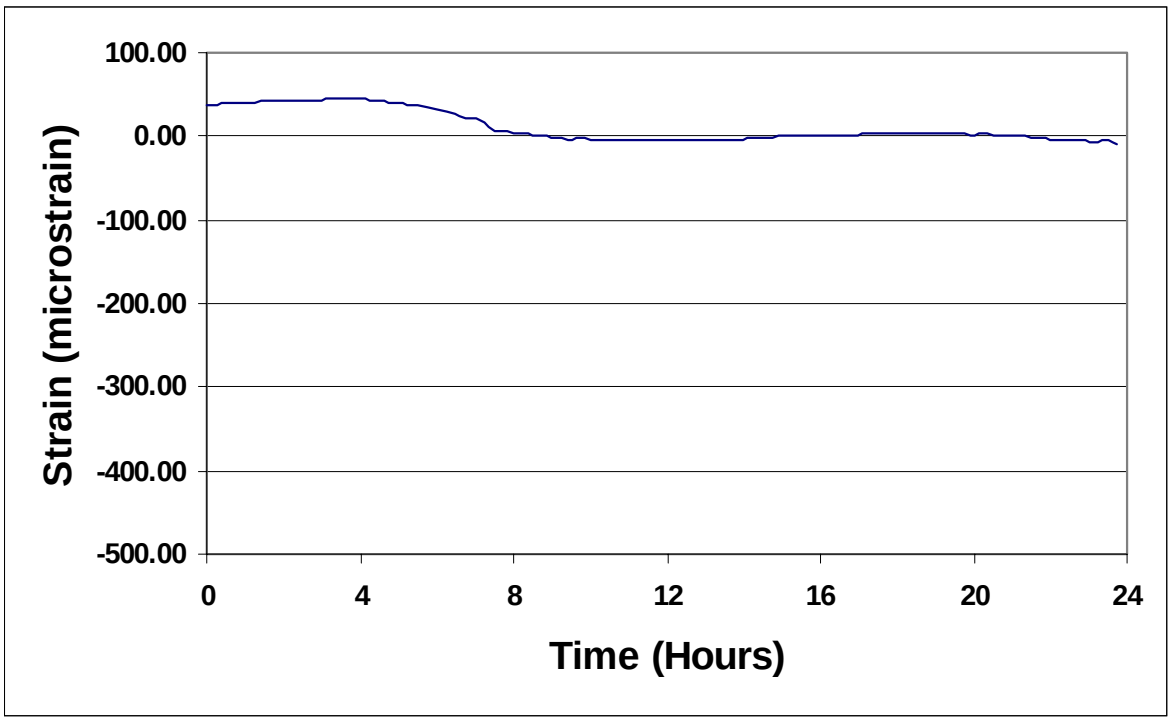

Figure B.16 Concrete Strain versus Time at Gage CG2 (Day 2).

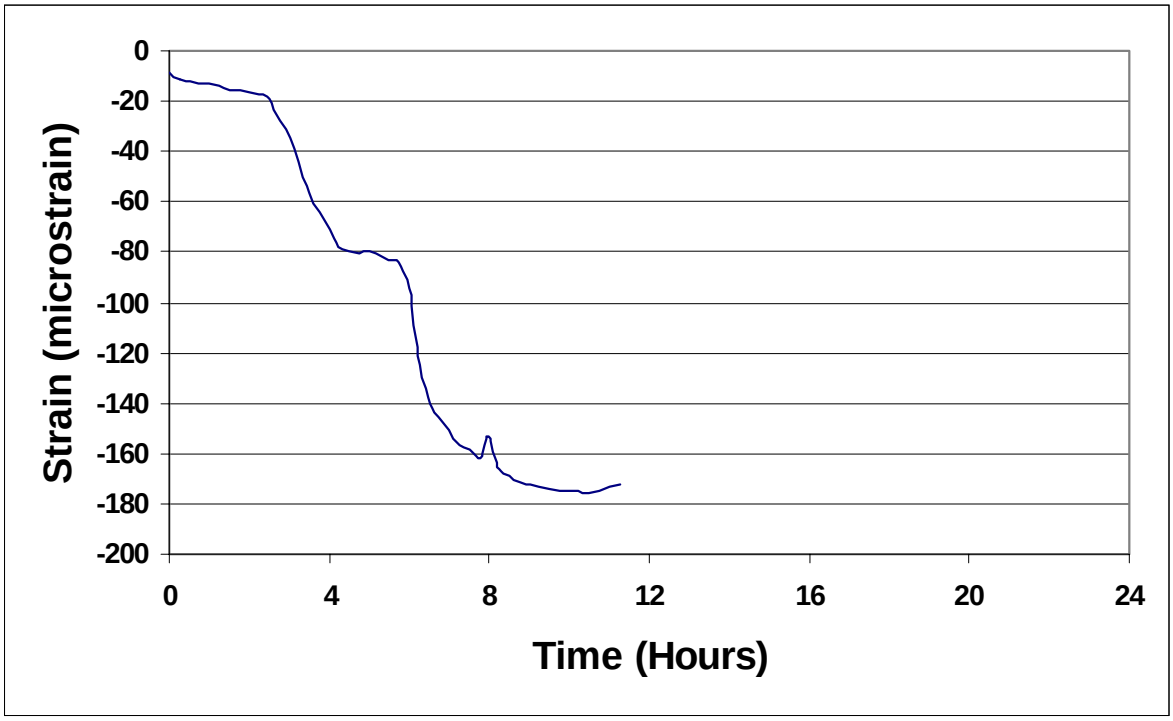

Figure B.17 Concrete Strain versus Time at Gage CG2 (Day 3).

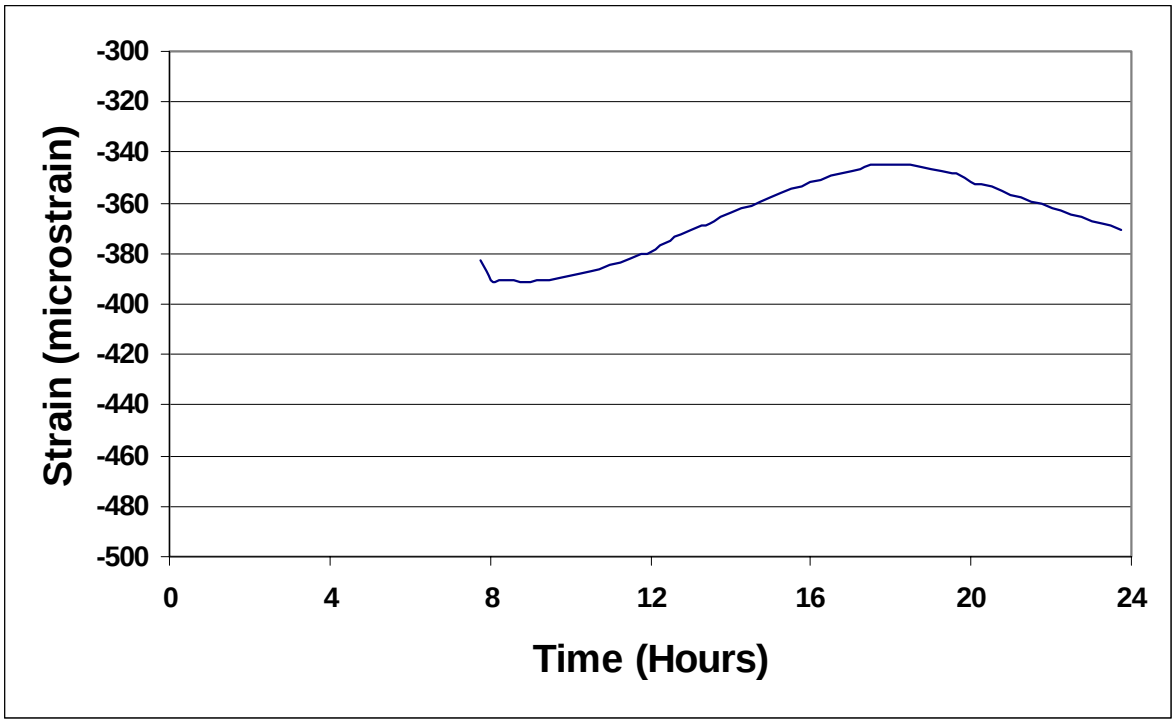

Figure B.18 Concrete Strain versus Time at Gage CG2 (Day 4).

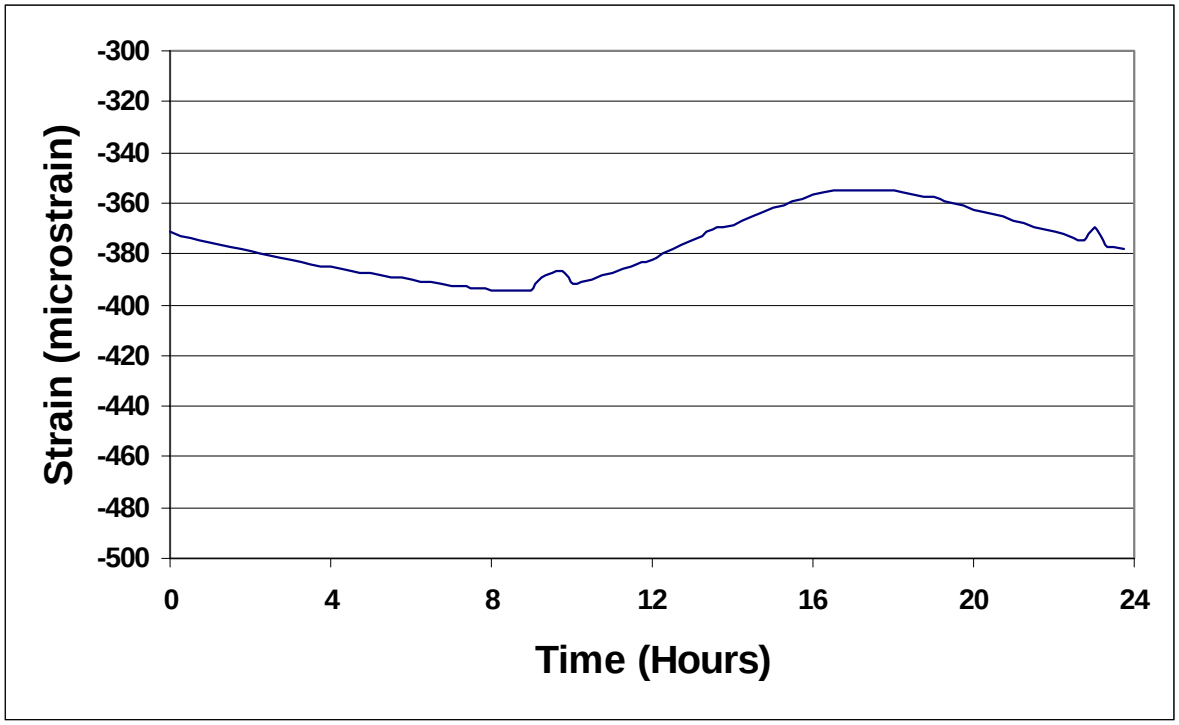

Figure B.19 Concrete Strain versus Time at Gage CG2 (Day 5).

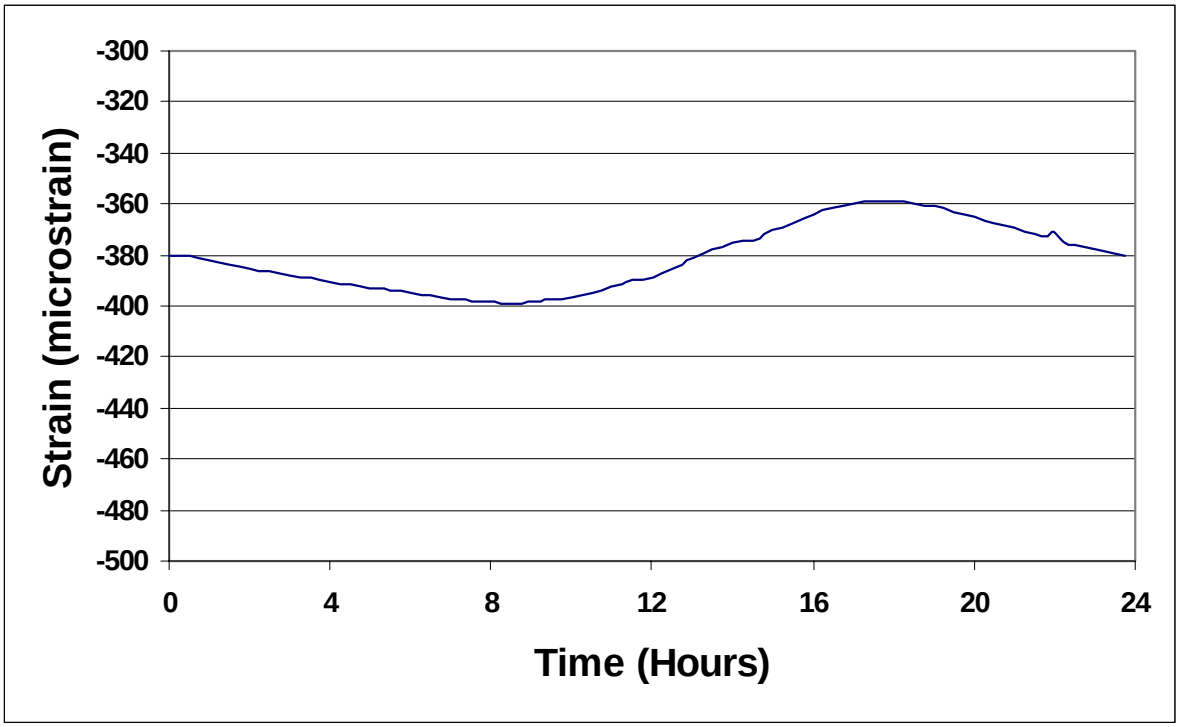

Figure B.20 Concrete Strain versus Time at Gage CG2 (Day 6).

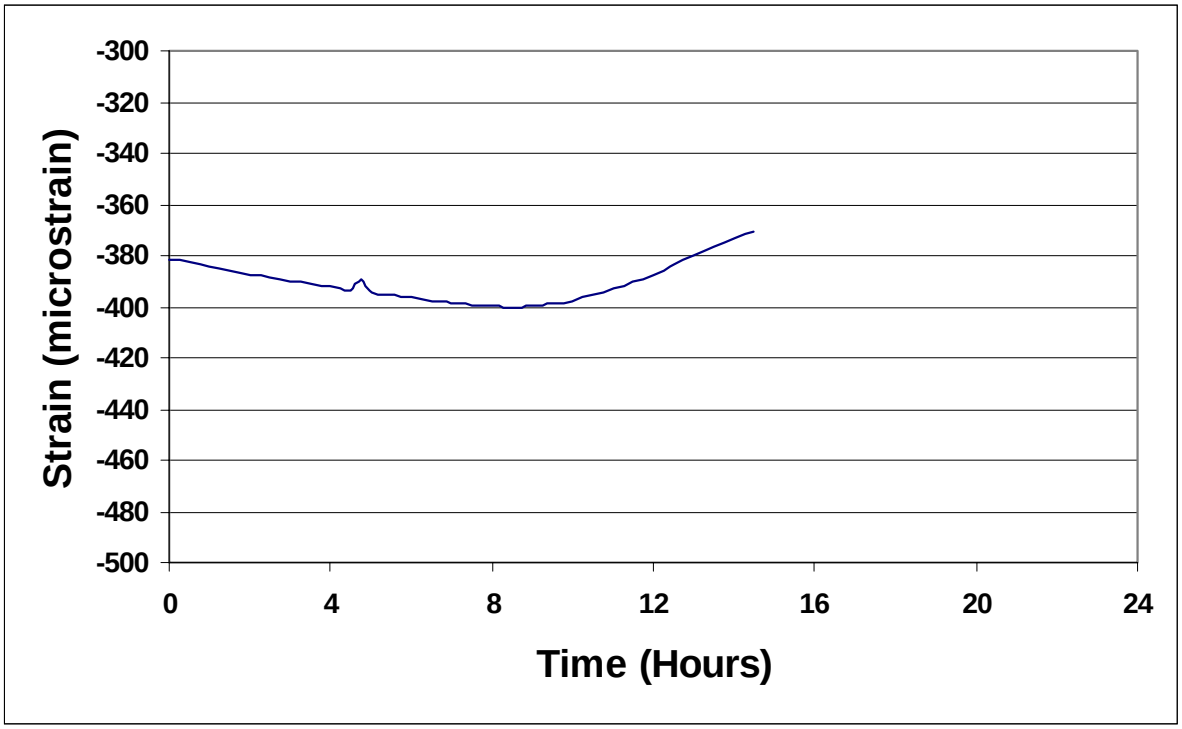

Figure B.21 Concrete Strain versus Time at Gage CG2 (Day 7).

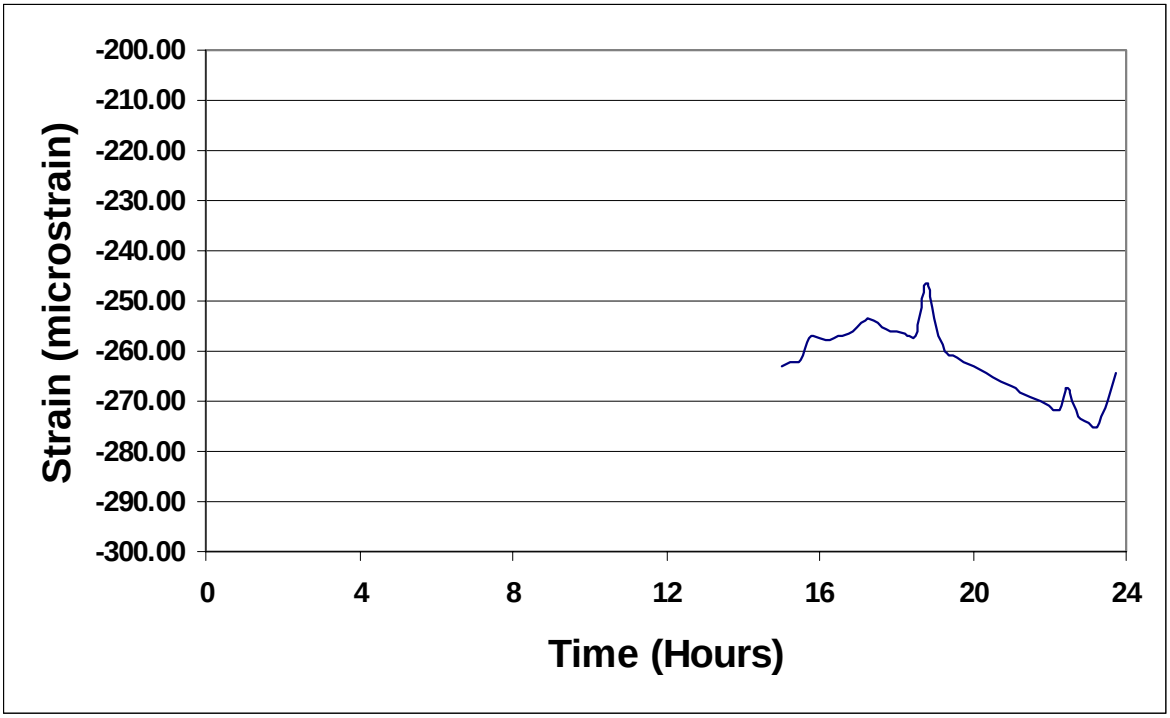

Figure B.22 Concrete Strain versus Time at Gage CG2 (Day 15).

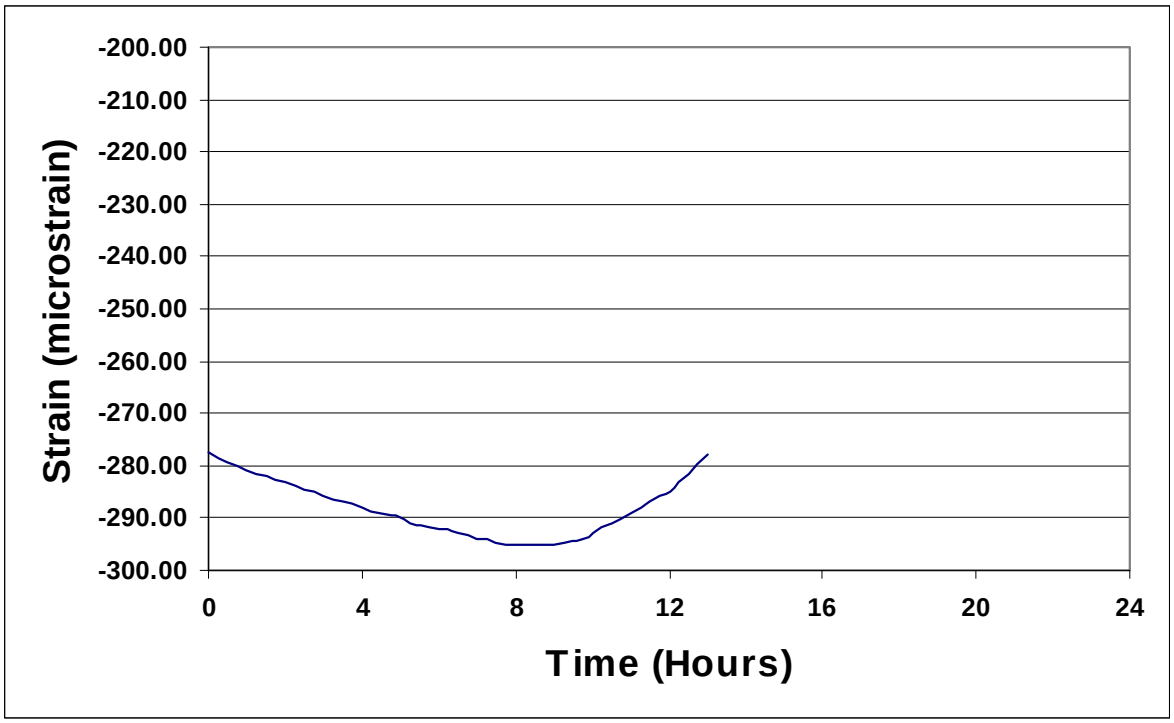

Figure B.23 Concrete Strain versus Time at Gage CG2 (Day 16).

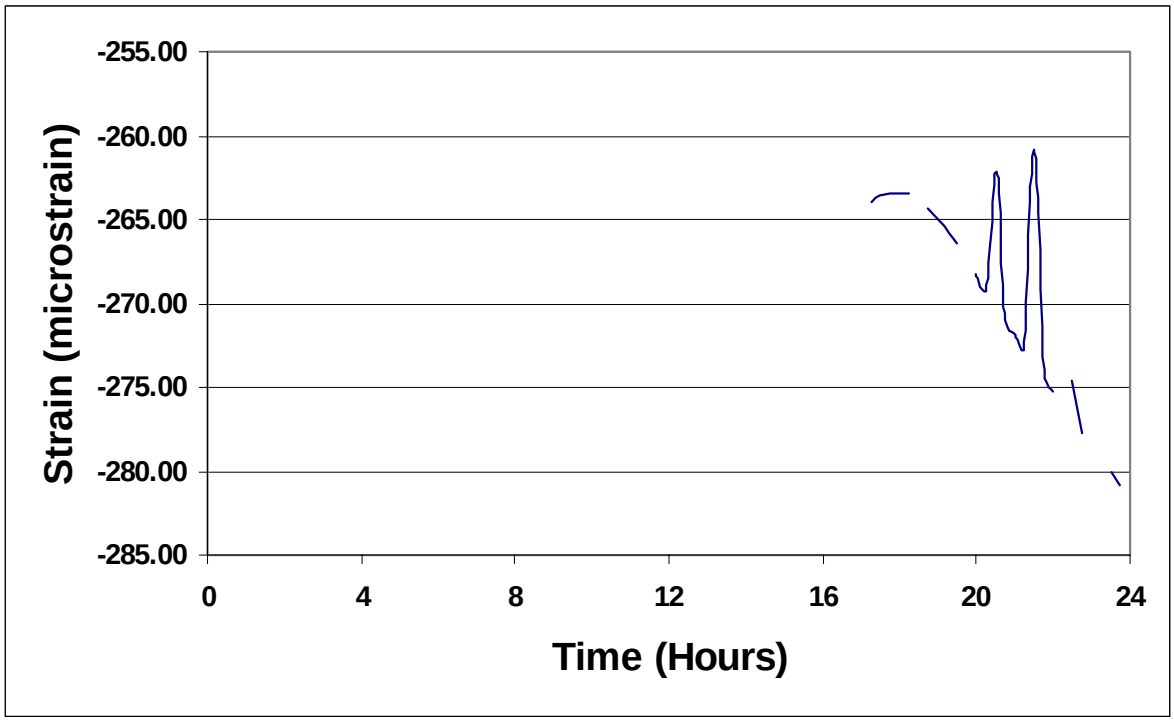

Figure B.24 Concrete Strain versus Time at Gage CG2 (Day 29).

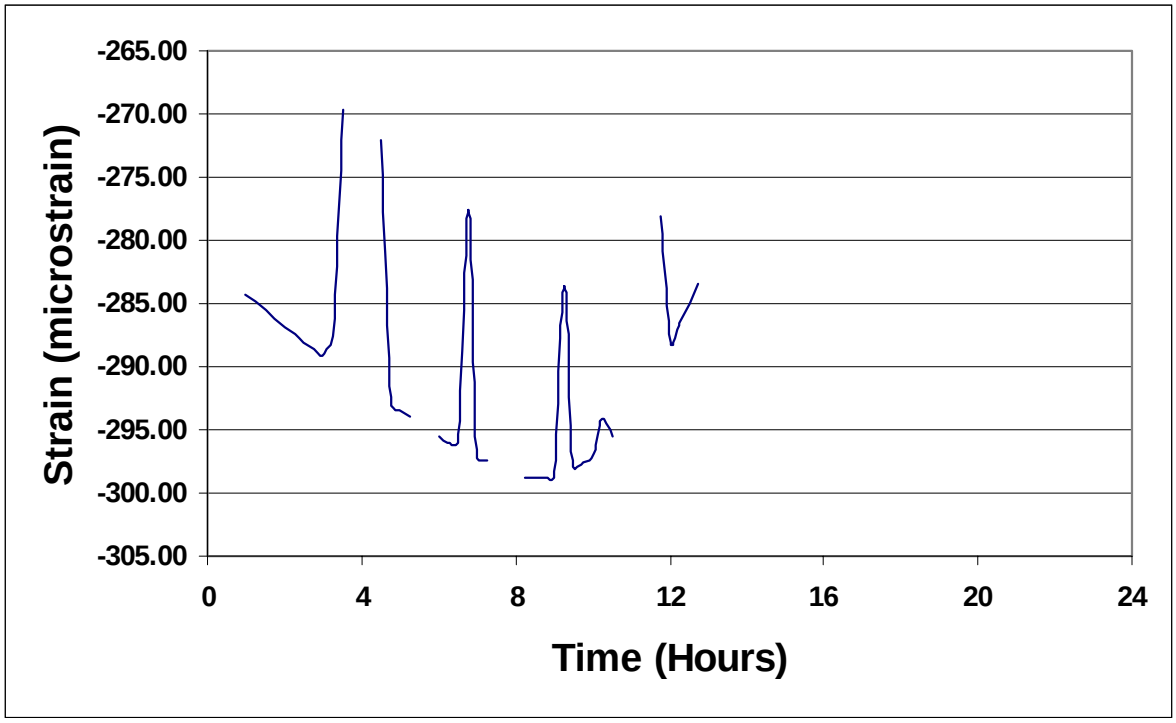

Figure B.25 Concrete Strain versus Time at Gage CG2 (Day 30) .

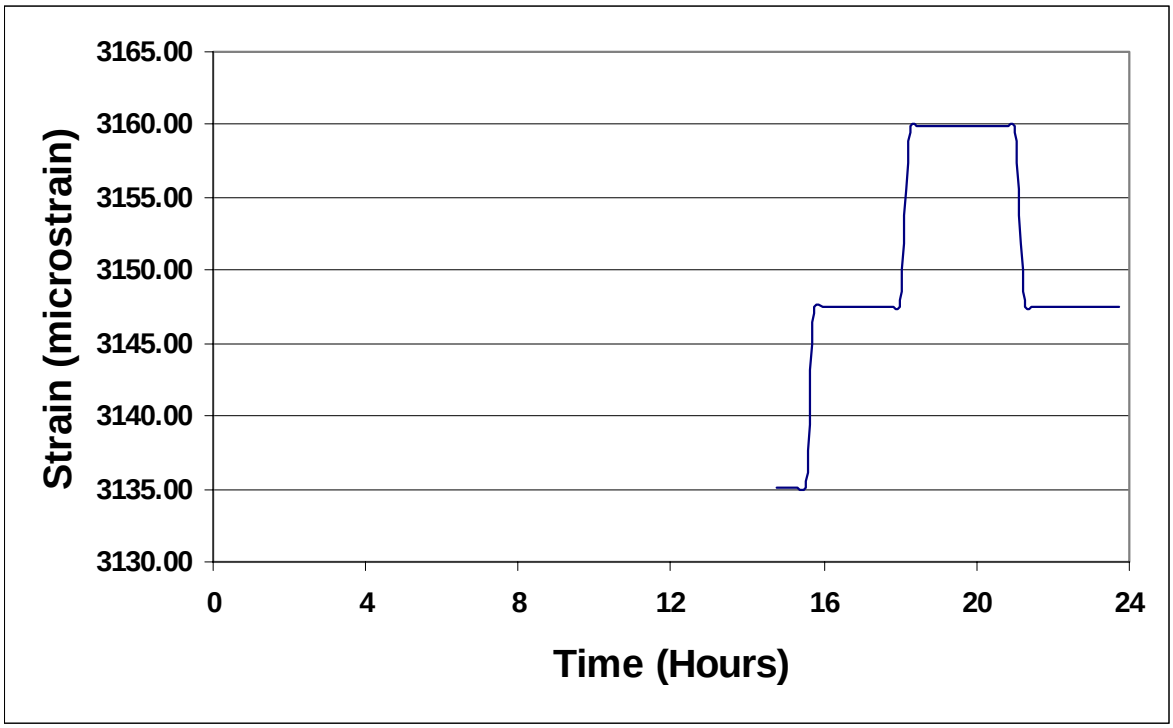

Figure B.26 Concrete Strain versus Time at Gage CG2 (Day 161).

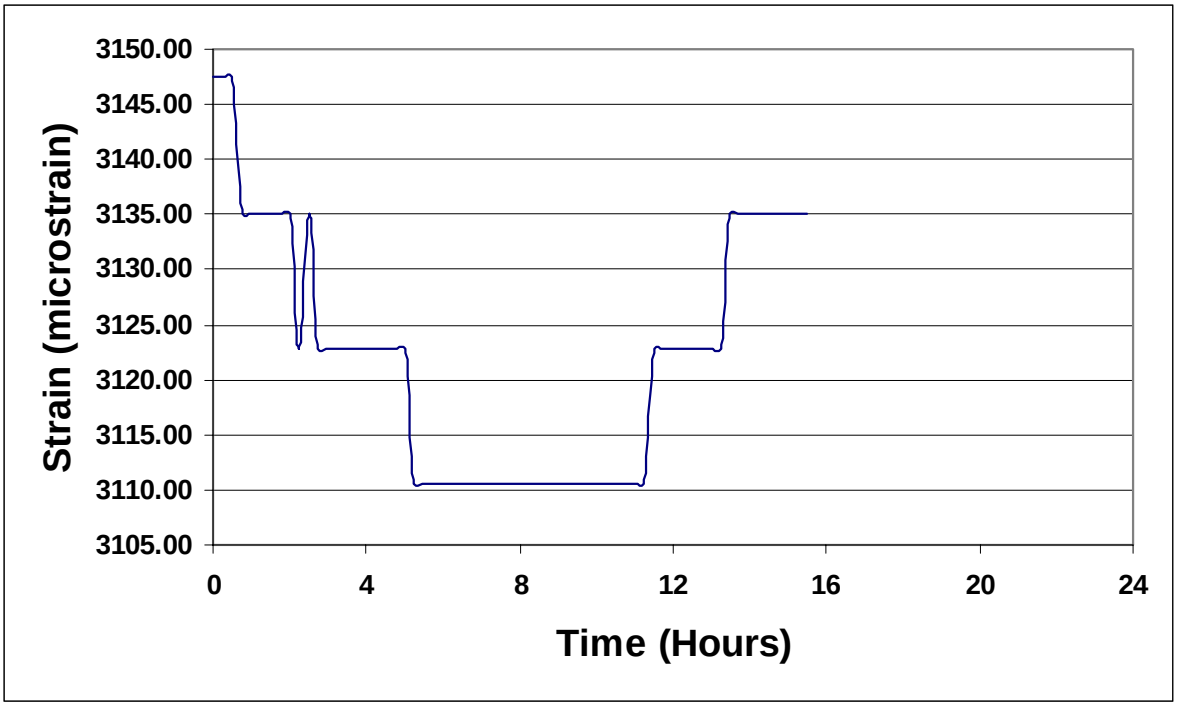

Figure B.27 Concrete Strain versus Time at Gage CG2 (Day 162).

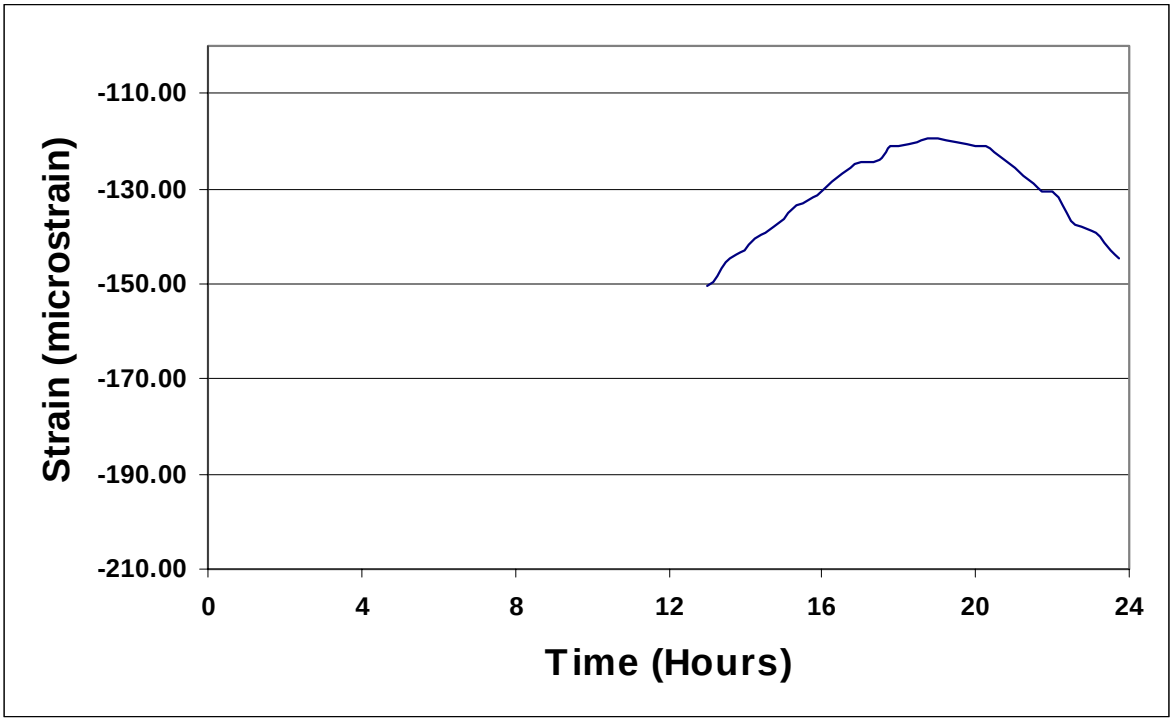

Figure B.28 Concrete Strain versus Time at Gage CG2 (Day 269).

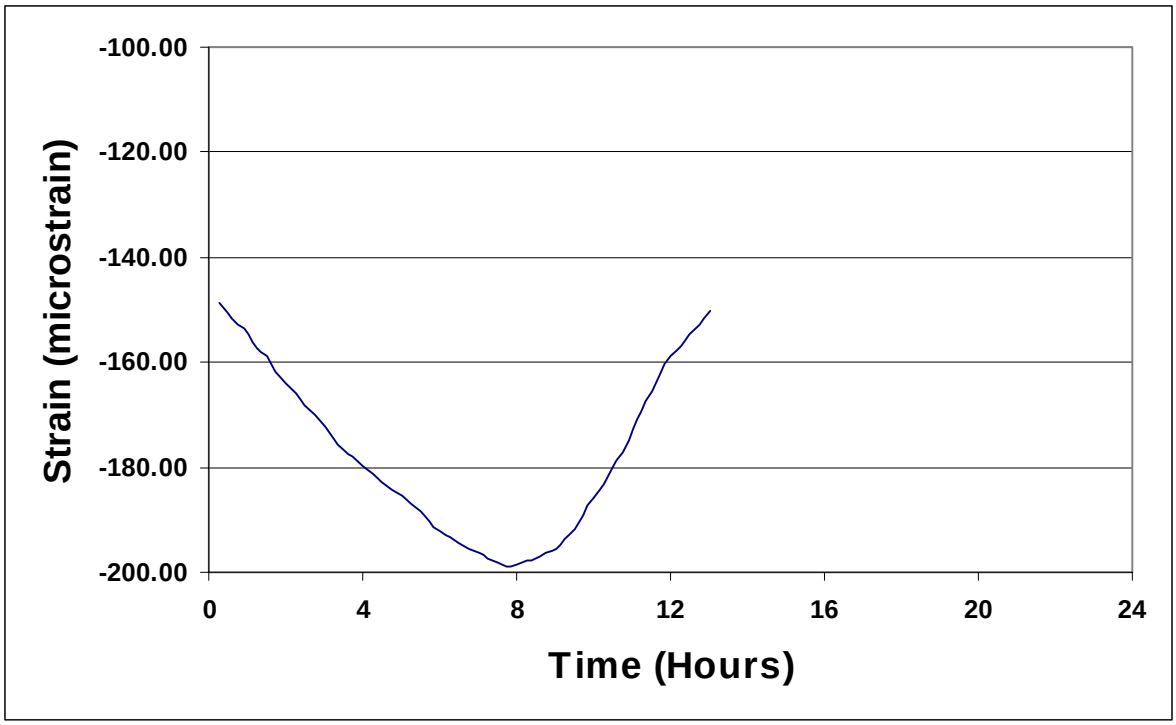

Figure B.29 Concrete Strain versus Time at Gage CG2 (Day 270).

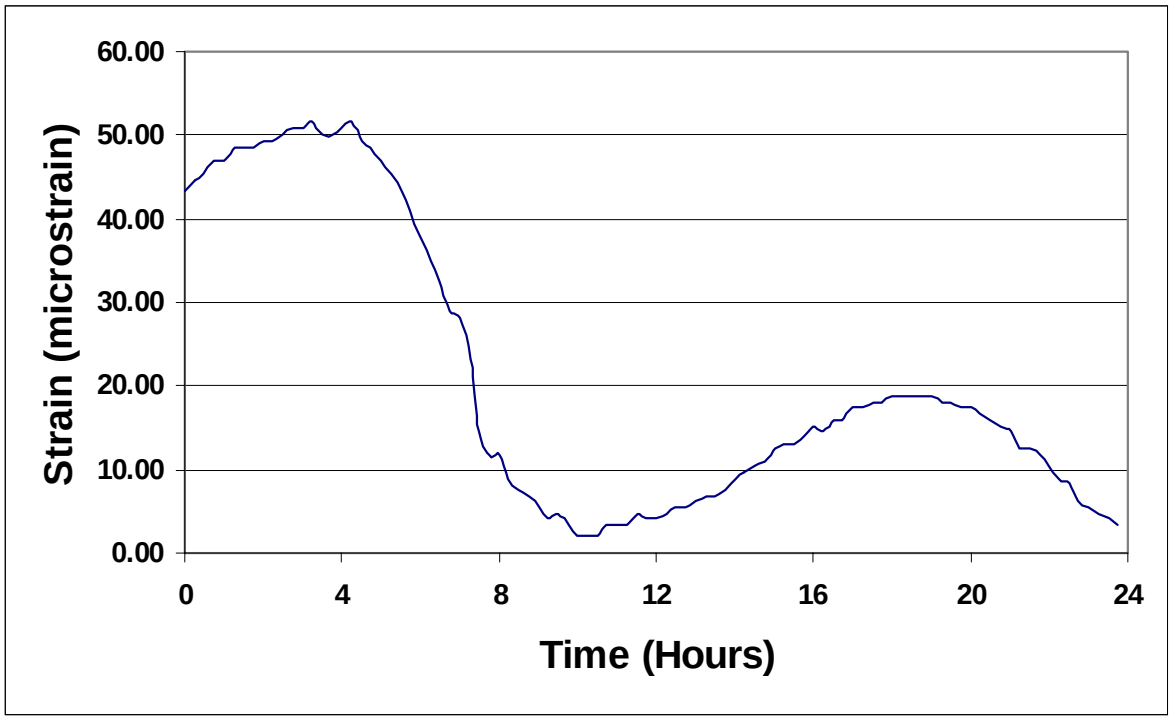

Figure B.30 Concrete Strain versus Time at Gage CG1 (Day 2)**.**

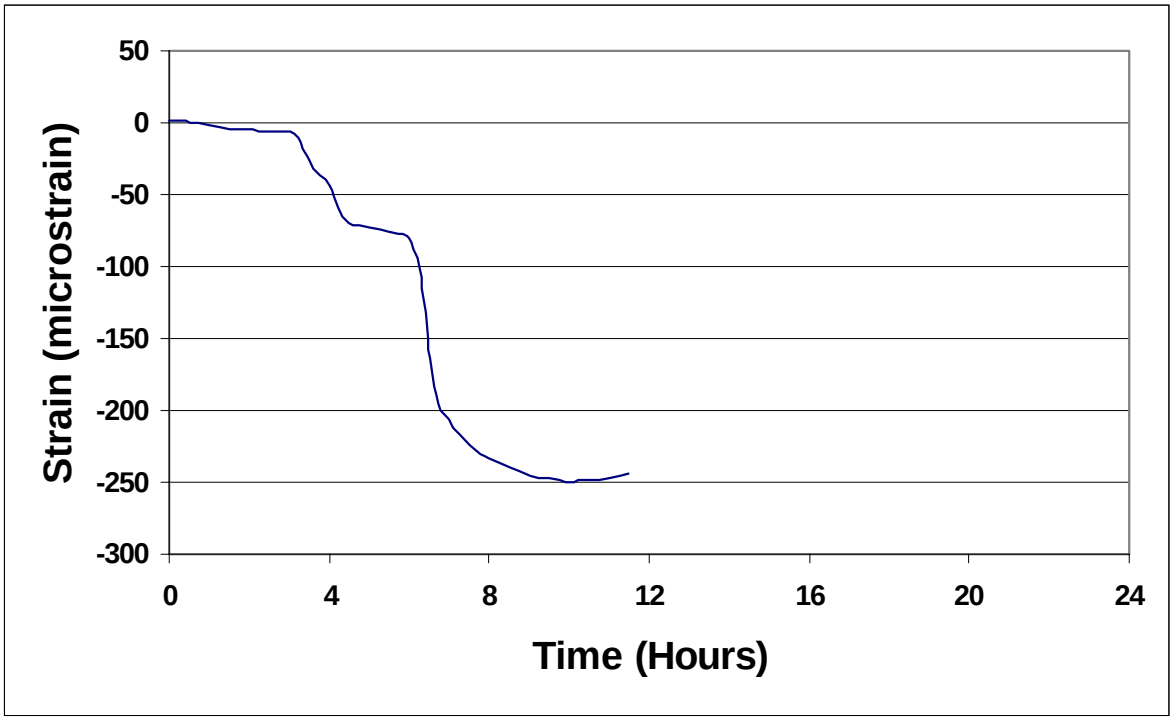

Figure B.31 Concrete Strain versus Time at Gage CG1 (Day 3).

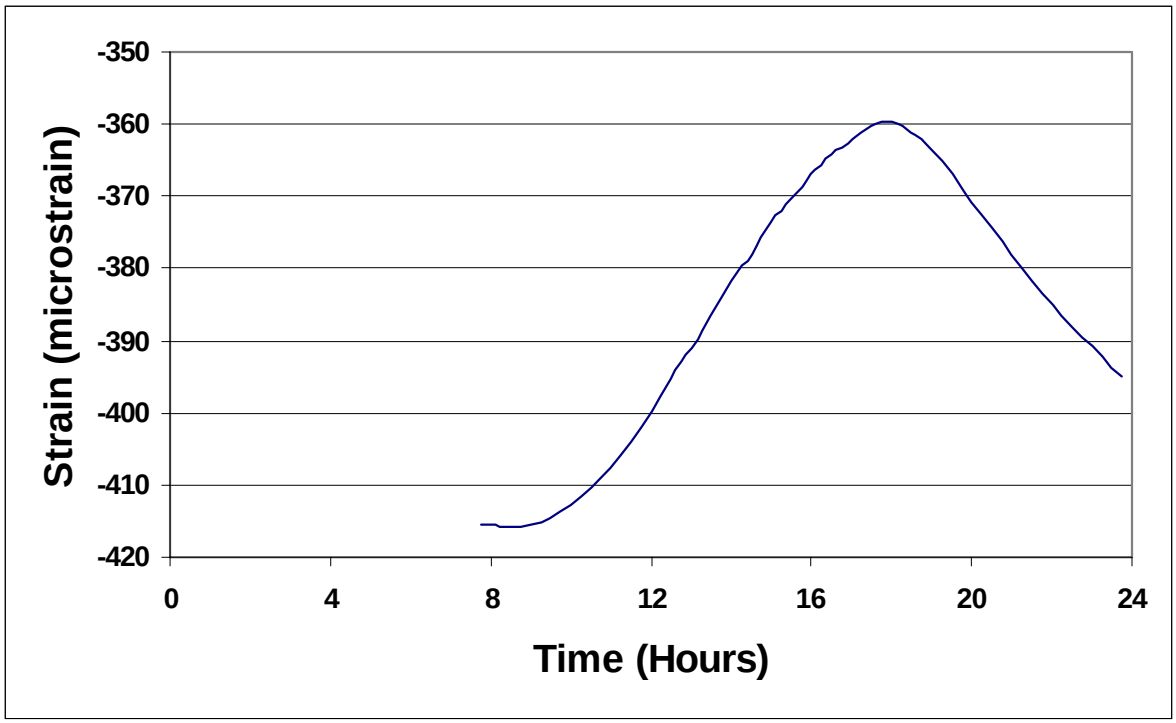

Figure B.32 Concrete Strain versus Time at Gage CG1 (Day 4).

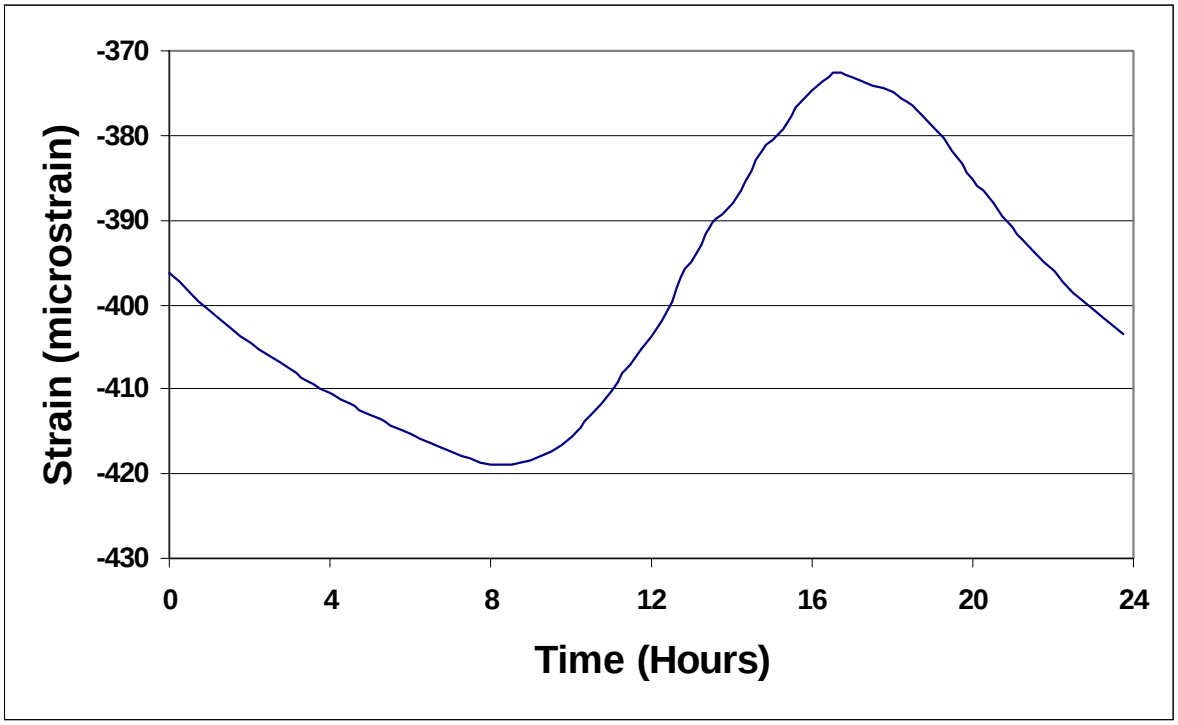

Figure B.33 Concrete Strain versus Time at Gage CG1 (Day 5).

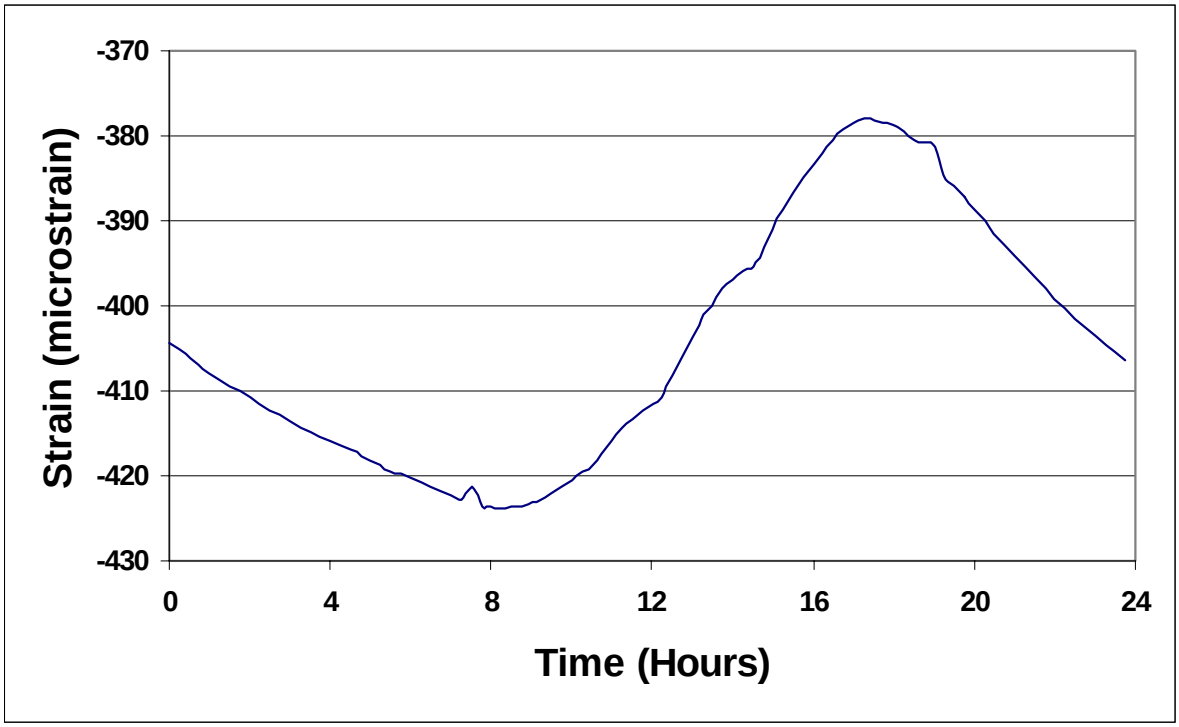

Figure B.34 Concrete Strain versus Time at Gage CG1 (Day 6).

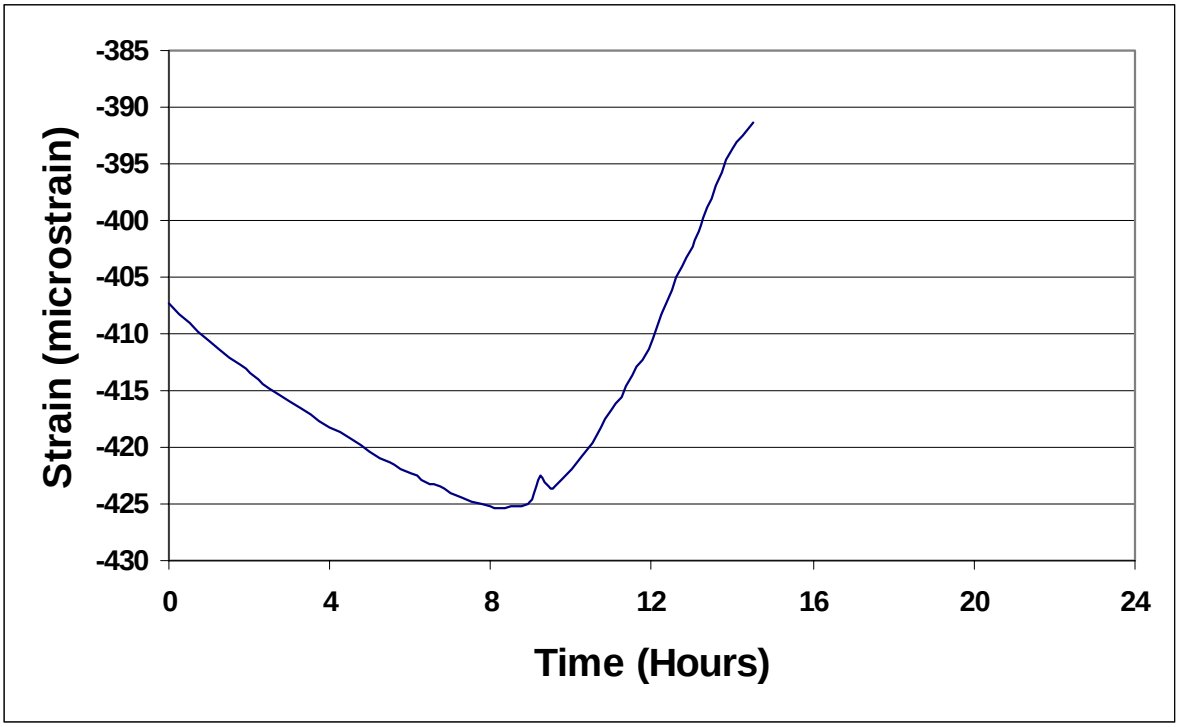

Figure B.35 Concrete Strain versus Time at Gage CG1 (Day 7).

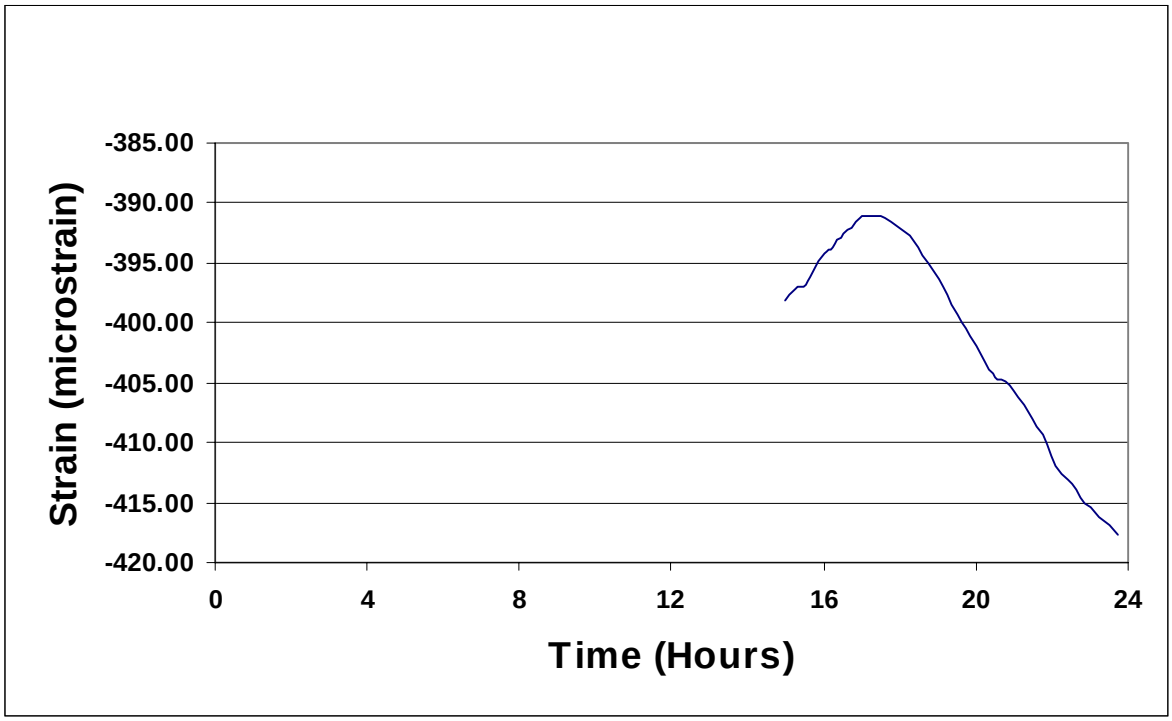

Figure B.36 Concrete Strain versus Time at Gage CG1 (Day 15).

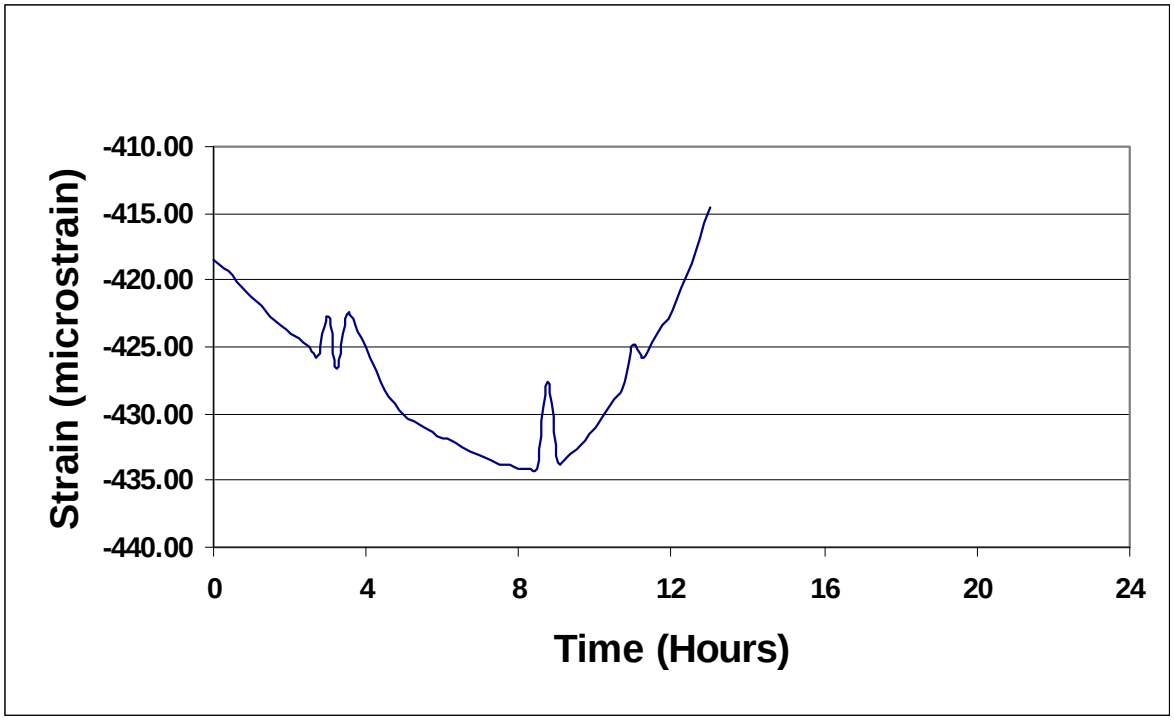

Figure B.37 Concrete Strain versus Time at Gage CG1 (Day 16).

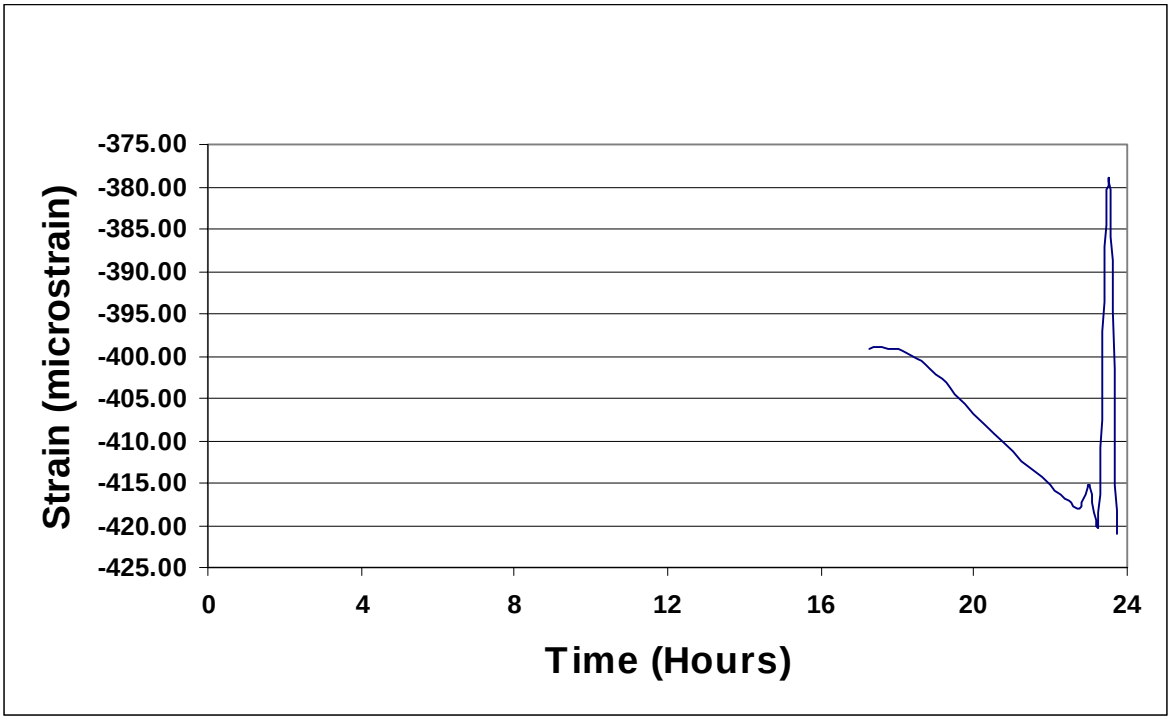

Figure B.38 Concrete Strain versus Time at Gage CG1 (Day 29).

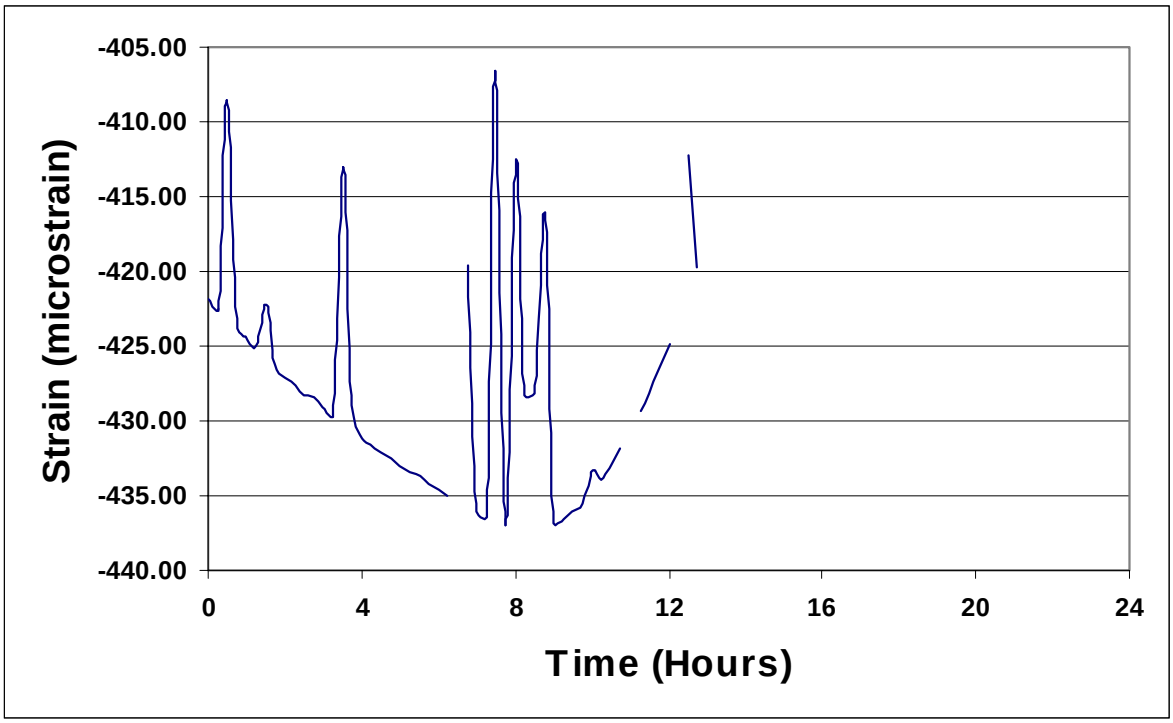

Figure B.39 Concrete Strain versus Time at Gage CG1 (Day 30).

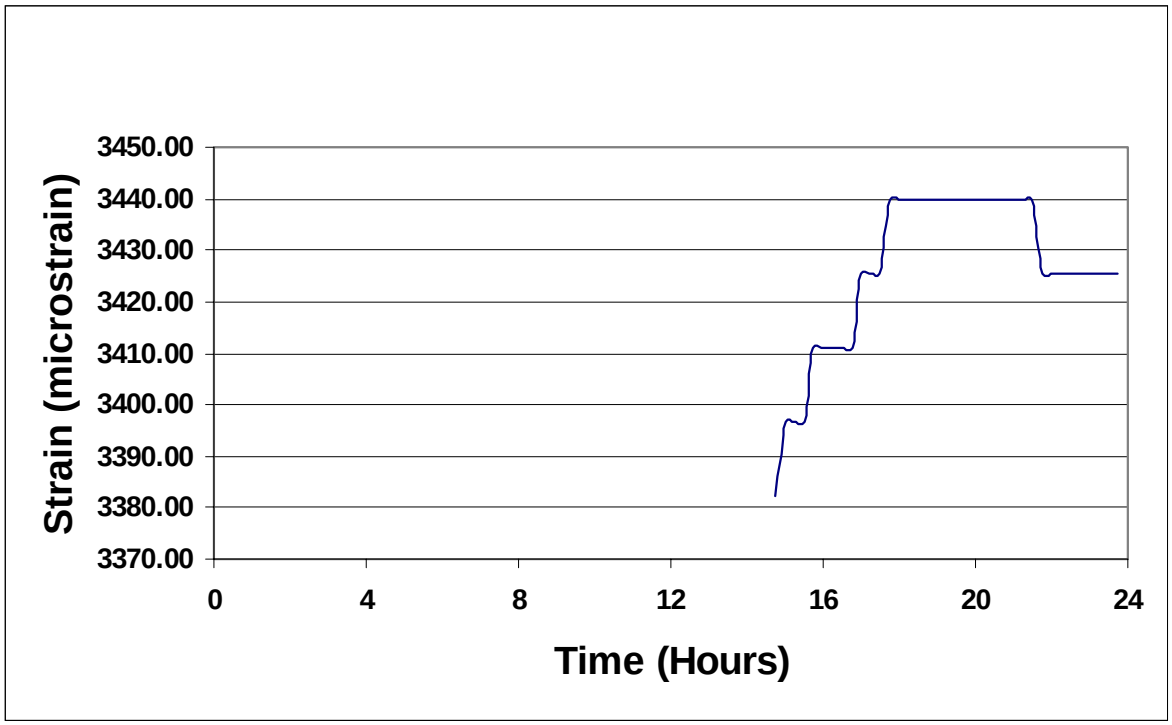

Figure B.40 Concrete Strain versus Time at Gage CG1 (Day 161).

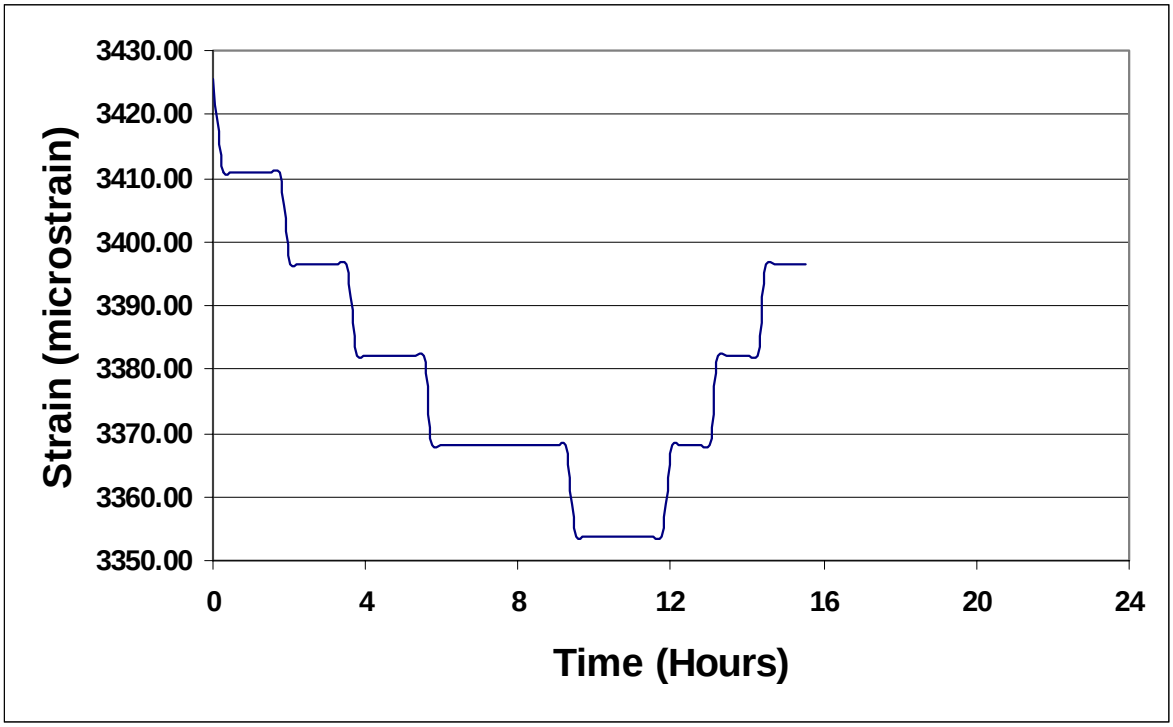

Figure B.41 Concrete Strain versus Time at Gage CG1 (Day 162).

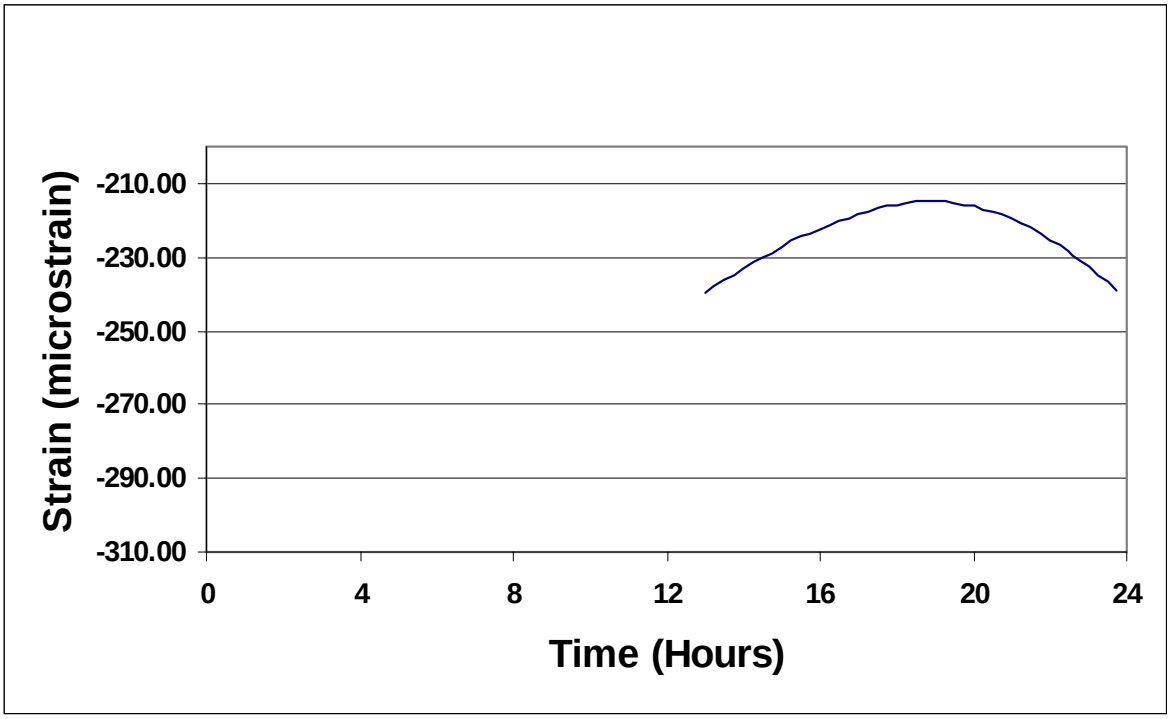

Figure B.42 Concrete Strain versus Time at Gage CG1 (Day 269).

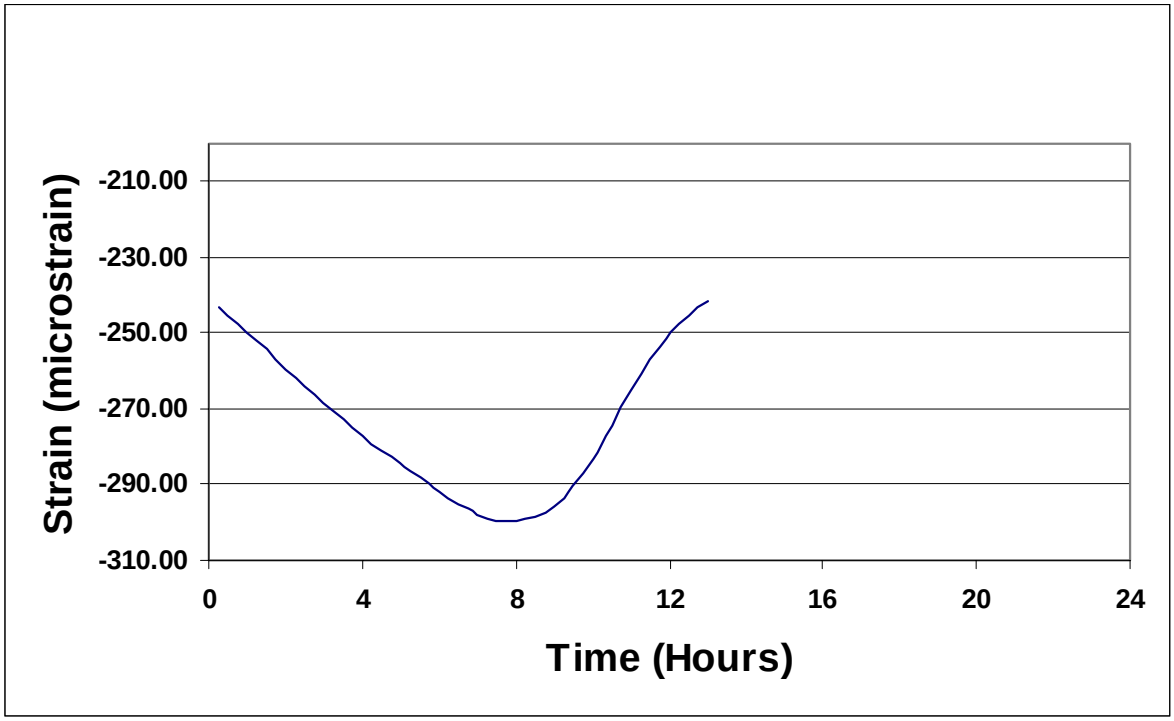

Figure B.43 Concrete Strain versus Time at Gage CG1 (Day 270).

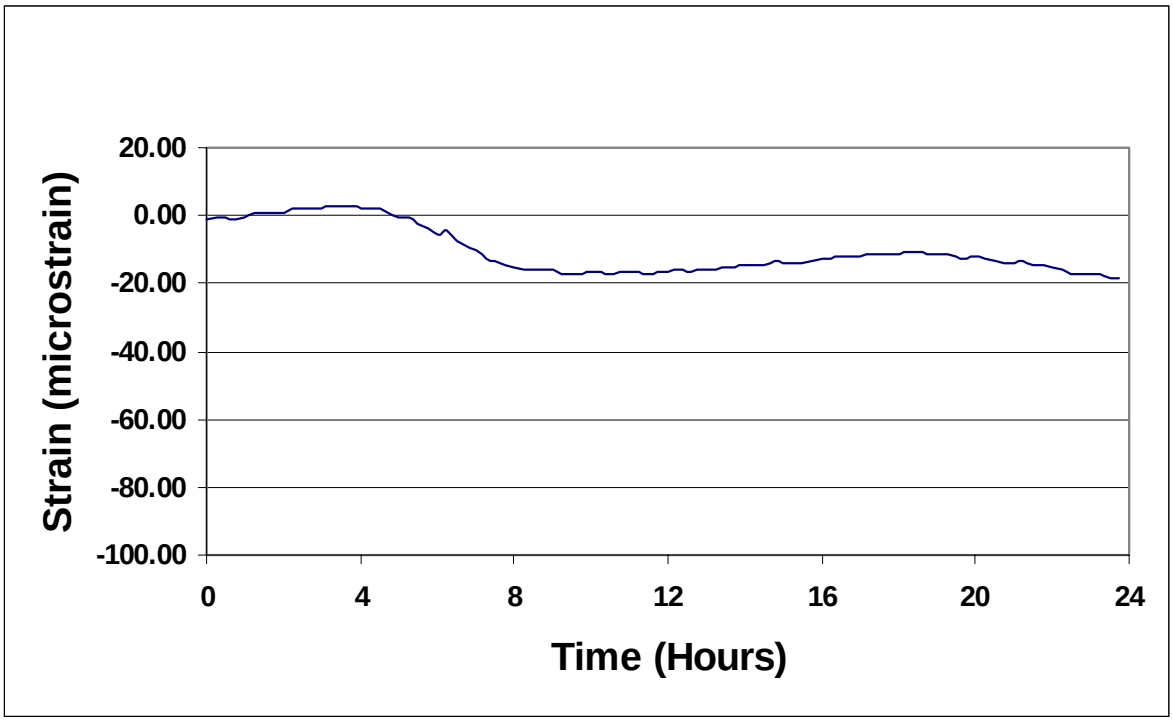

Figure B.44 Concrete Strain versus Time at CG3 (Day 2).

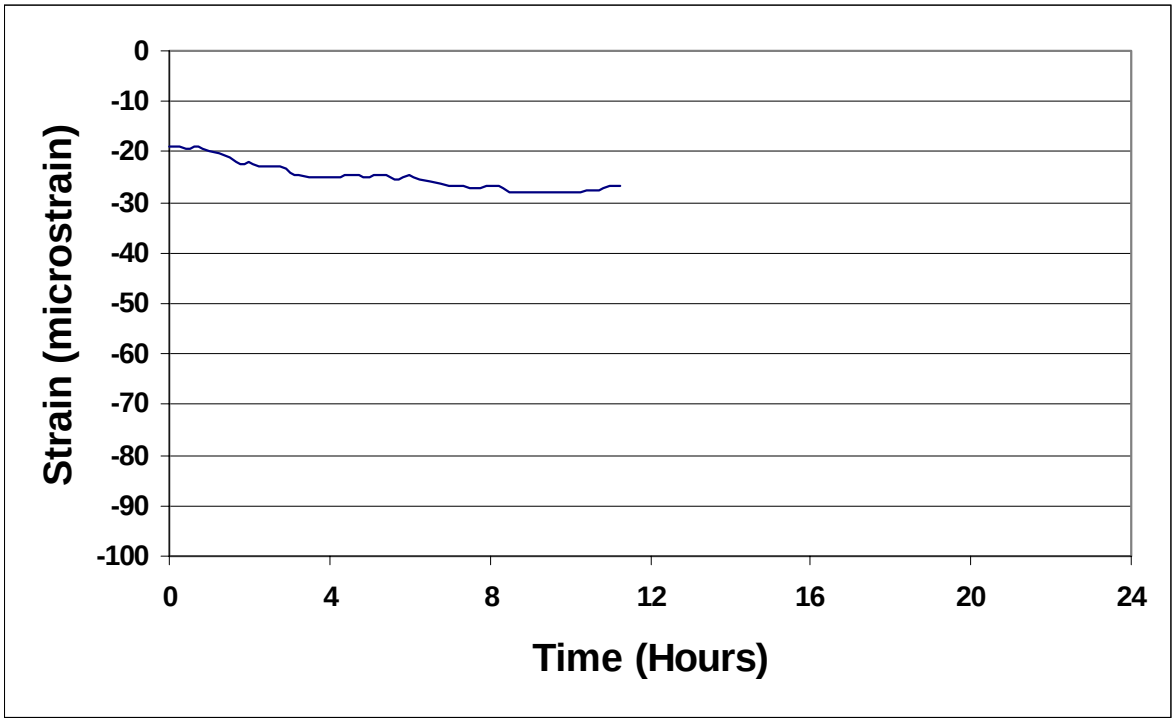

Figure B.45 Concrete Strain versus Time at Gage CG3 (Day 3).

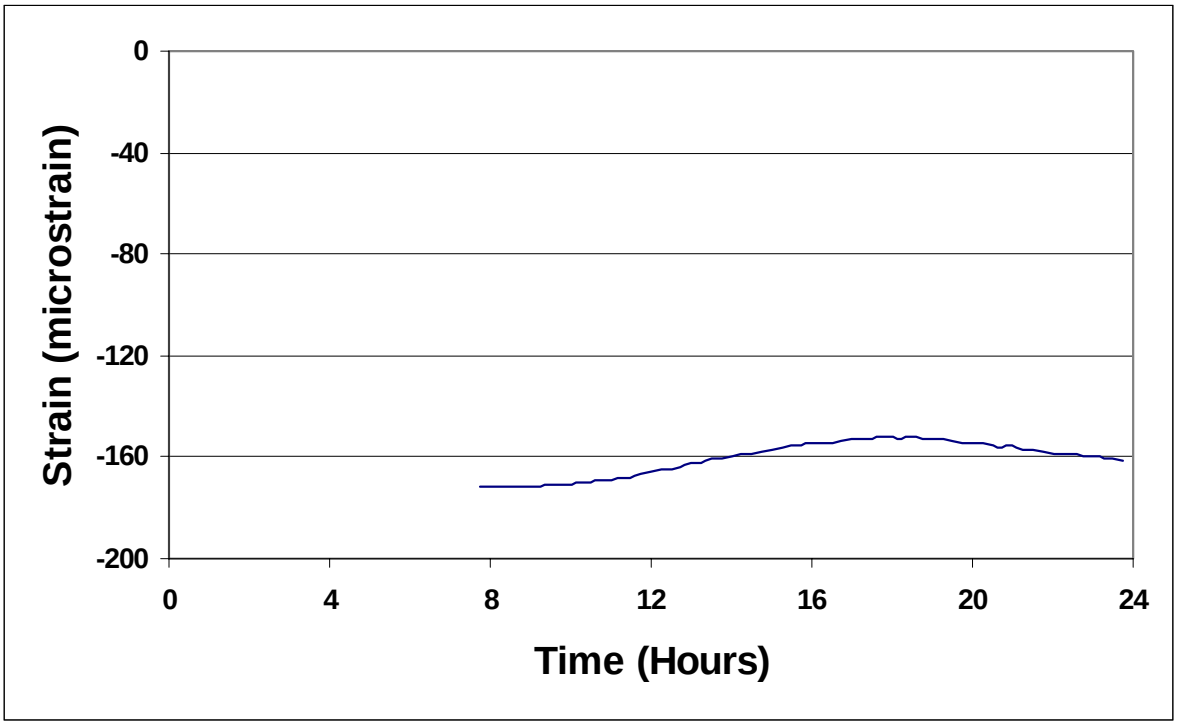

Figure B.46 Concrete Strain versus Time at Gage CG3 (Day 4).

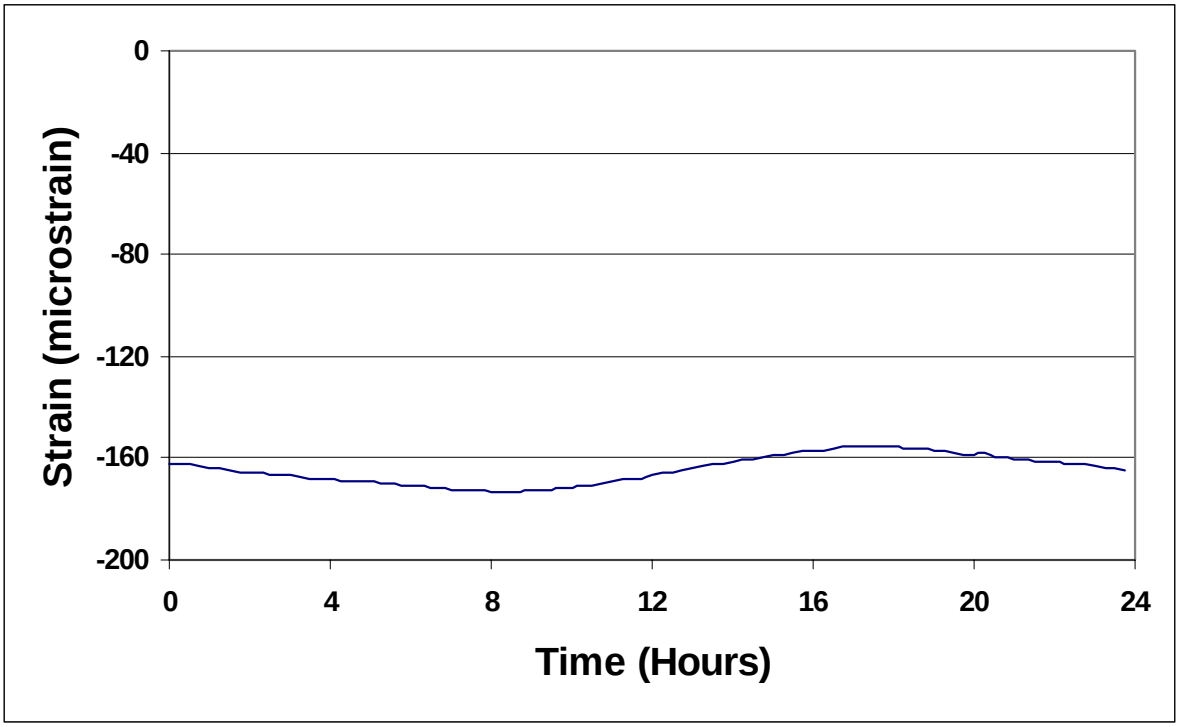

Figure B.47 Concrete Strain versus Time at Gage CG3 (Day 5).

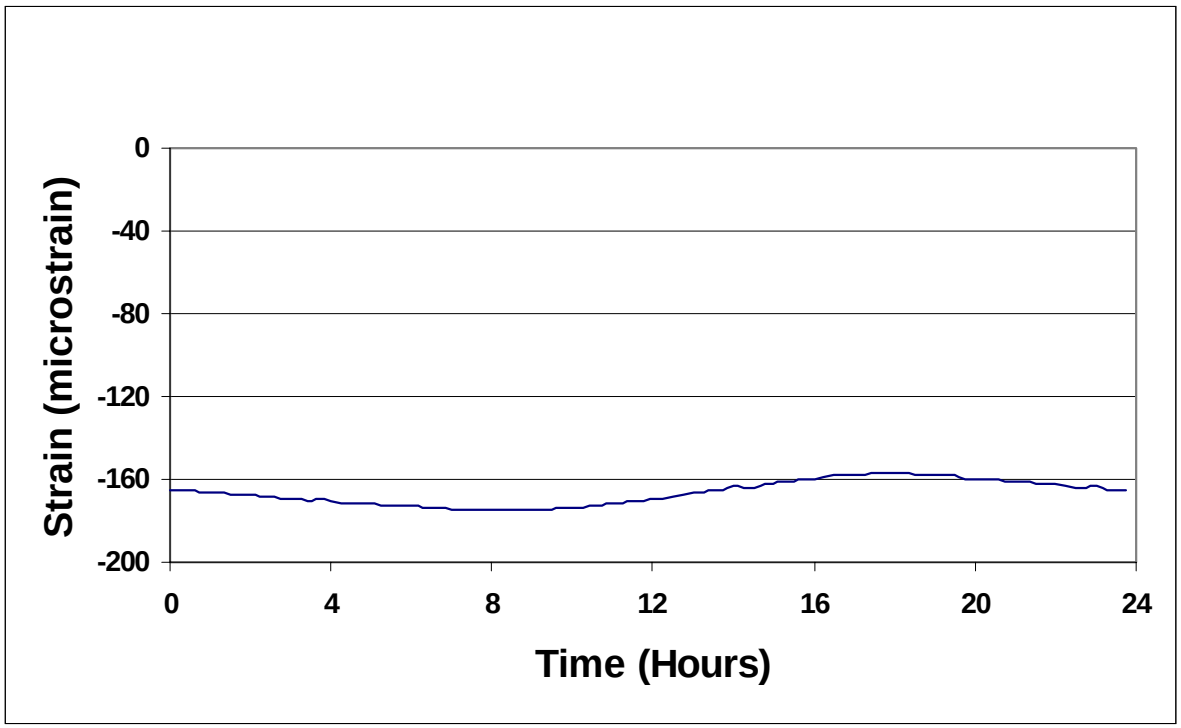

Figure B.48 Concrete Strain versus Time at Gage CG3 (Day 6).

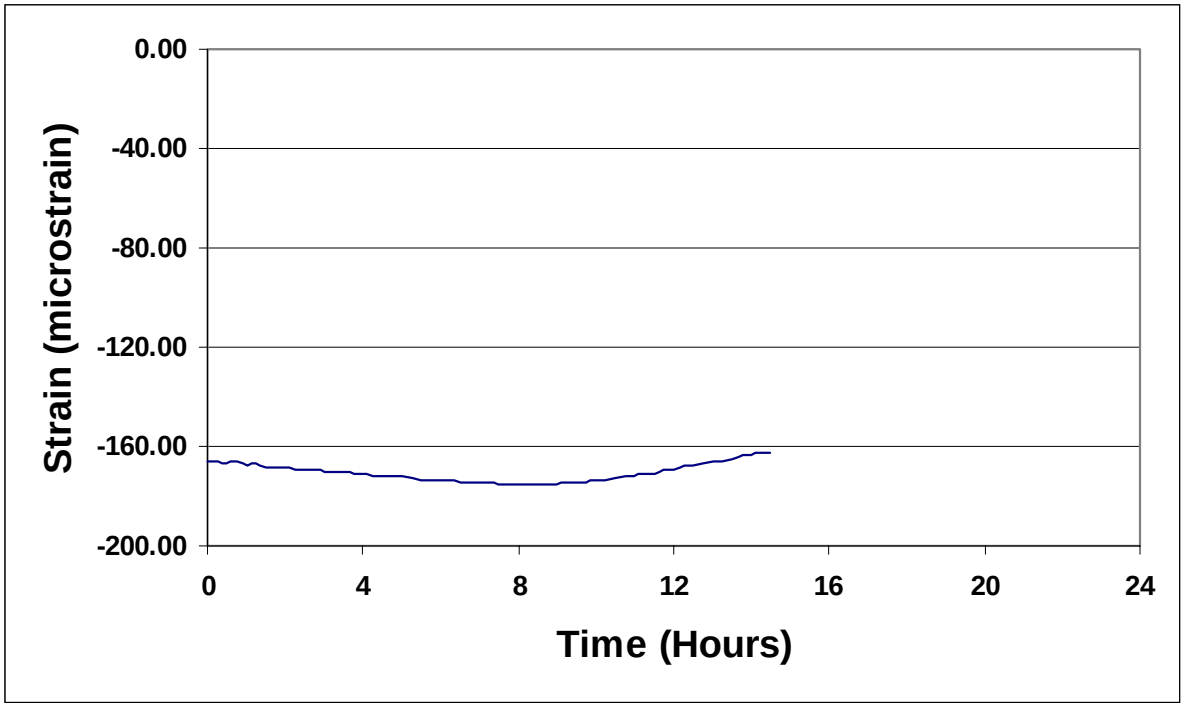

Figure B.49 Concrete Strain versus Time at Gage CG3 (Day 7).

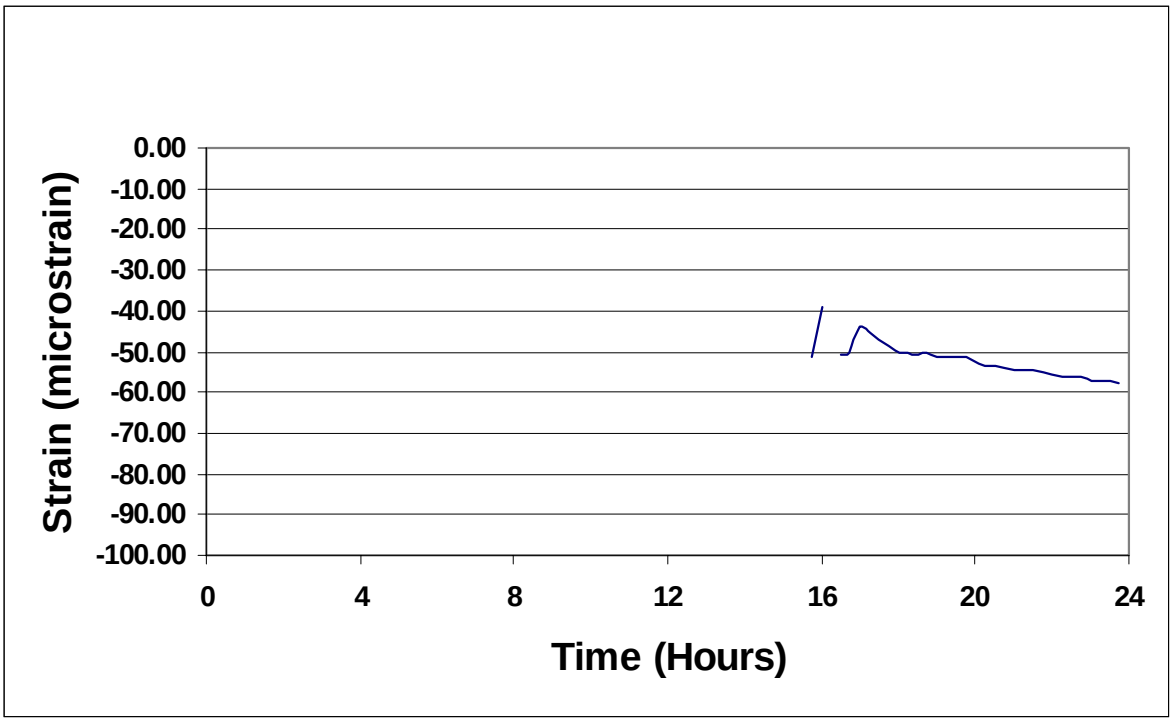

Figure B.50 Concrete Strain versus Time at Gage CG3 (Day 15).

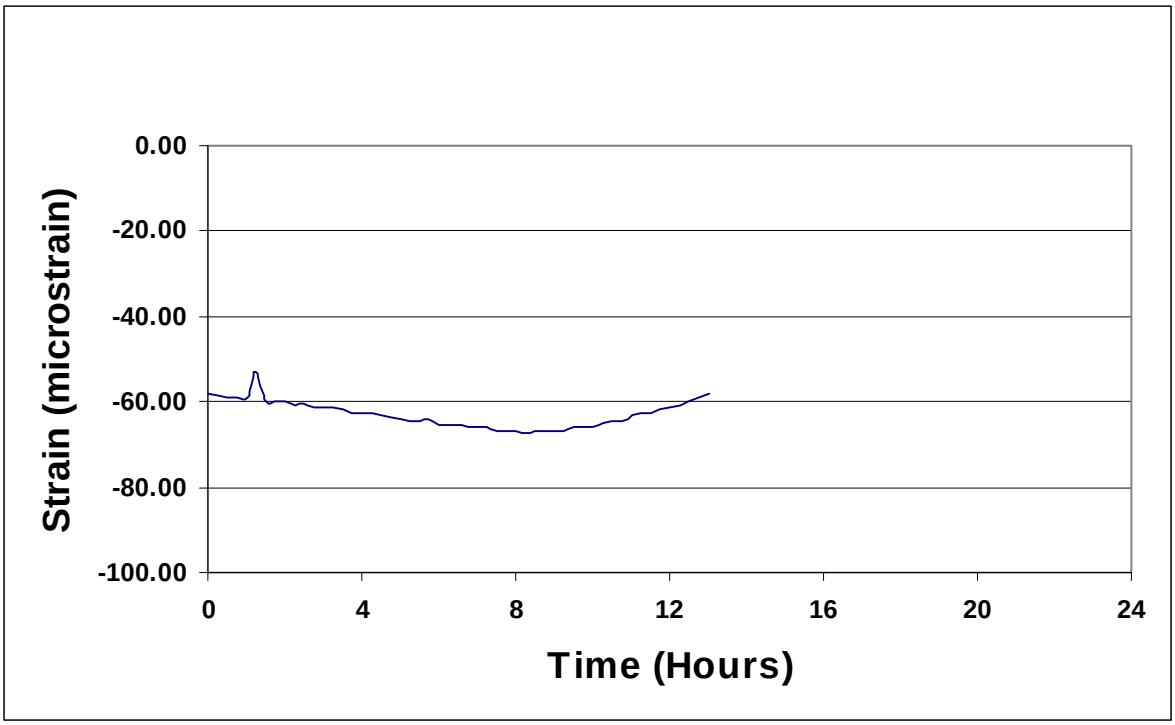

Figure B.51 Concrete Strain versus Time at Gage CG3 (Day 16).

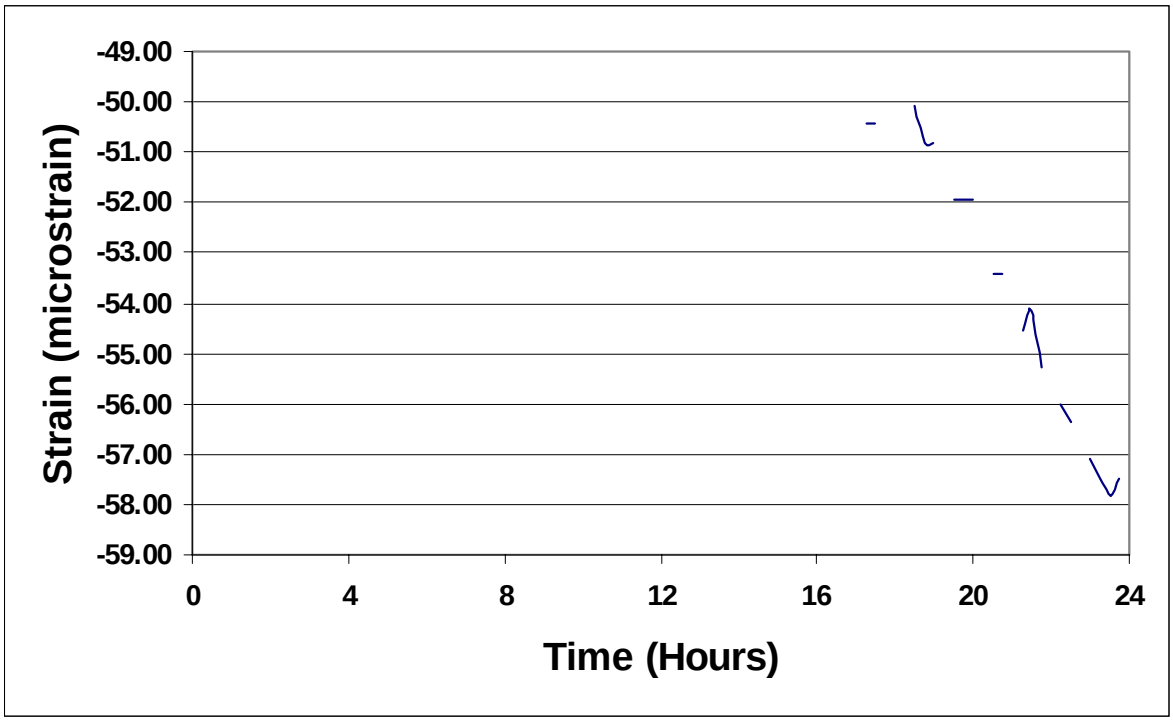

Figure B.52 Concrete Strain versus Time at Gage CG3 (Day 29).

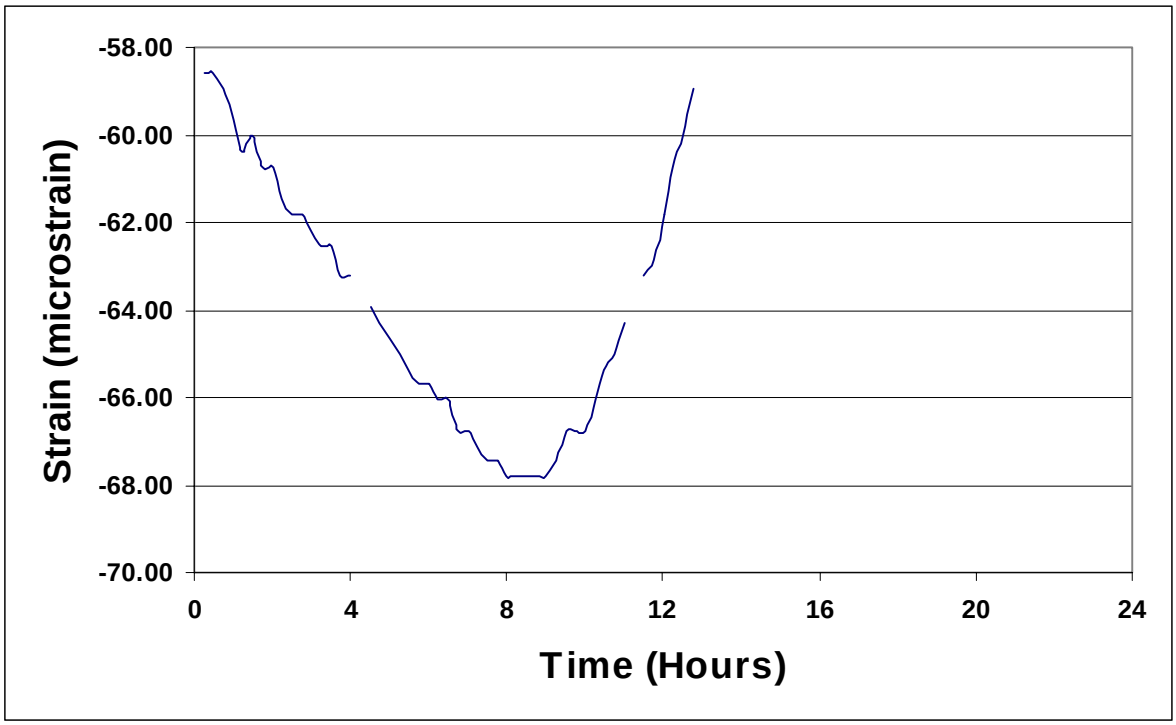

Figure B.53 Concrete Strain versus Time at Gage CG3 (Day 30).

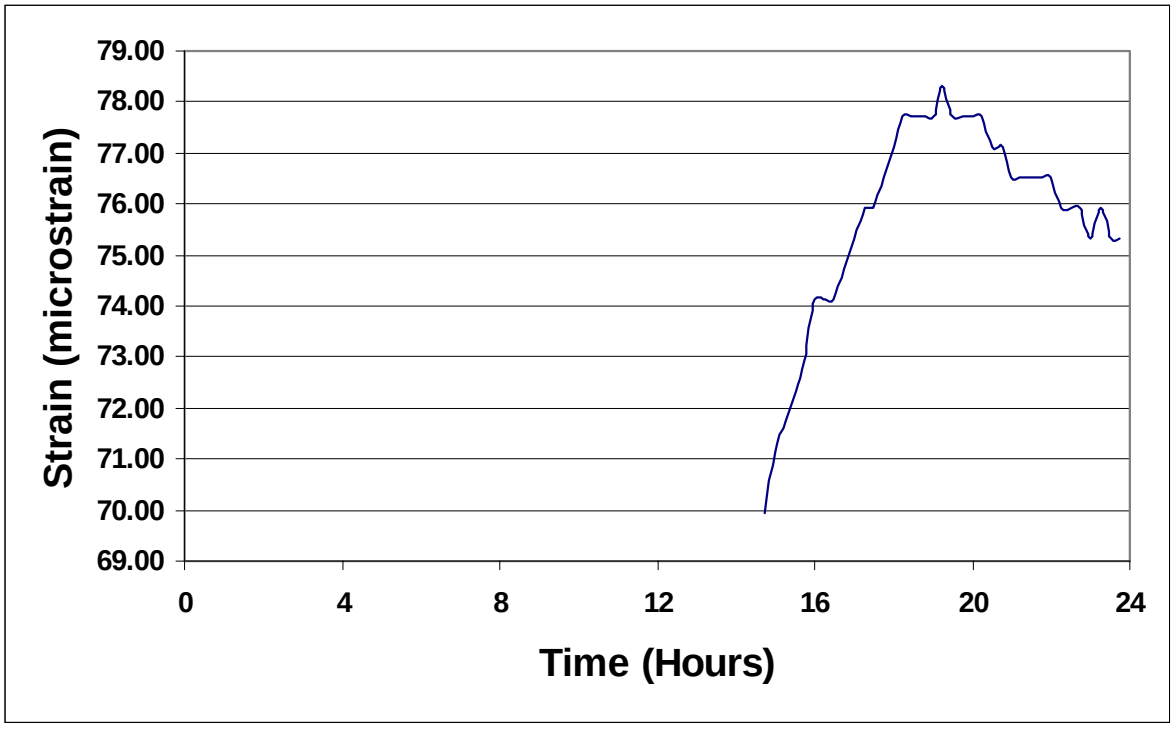

Figure B.54 Concrete Strain versus Time at Gage CG3 (Day 161).

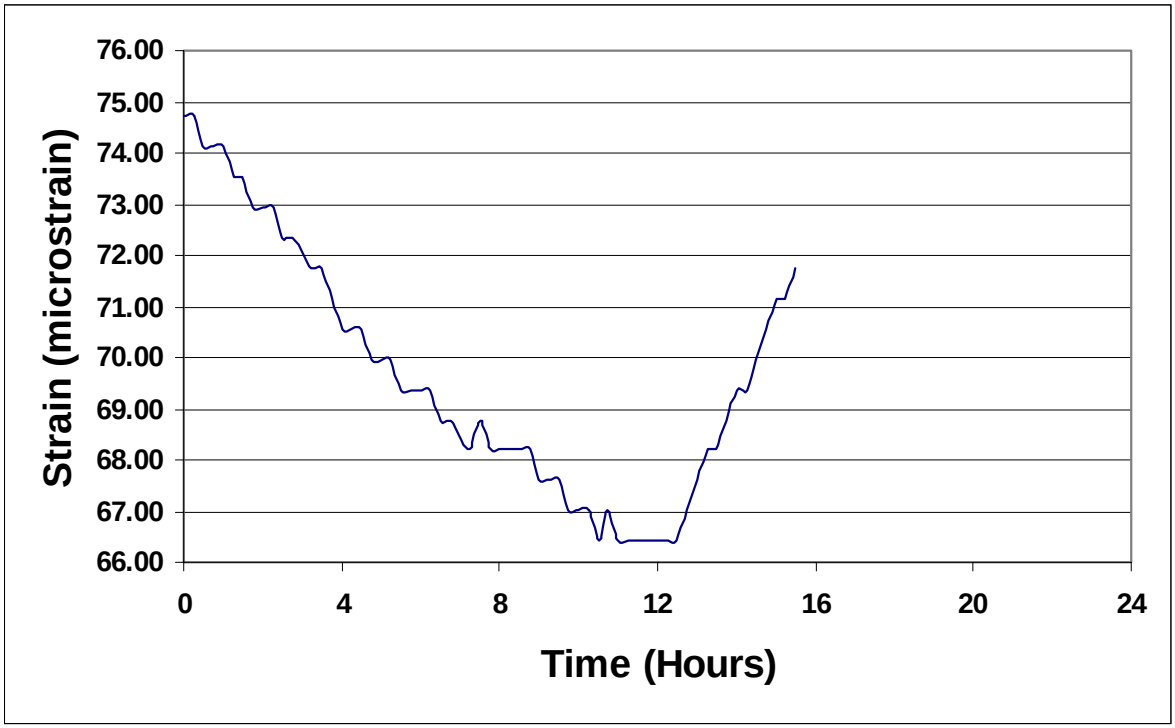

Figure B.55 Concrete Strain versus Time at Gage CG3 (Day 162).

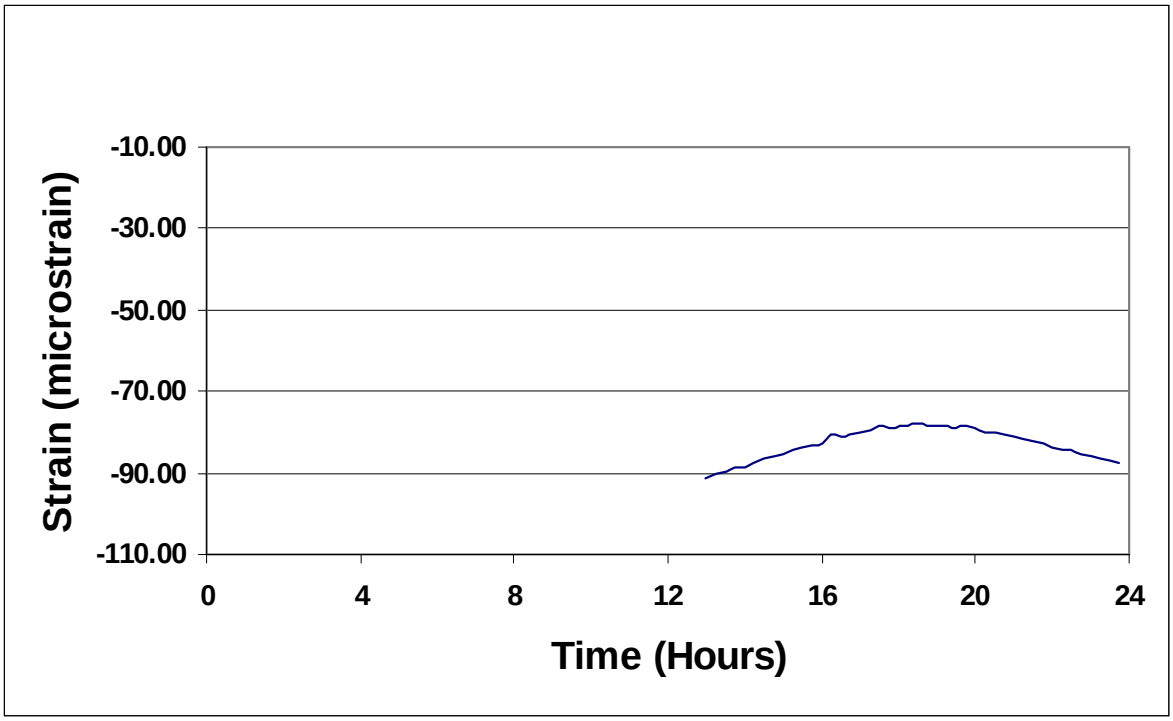

Figure B.56 Concrete Strain versus Time at Gage CG3 (Day 269).

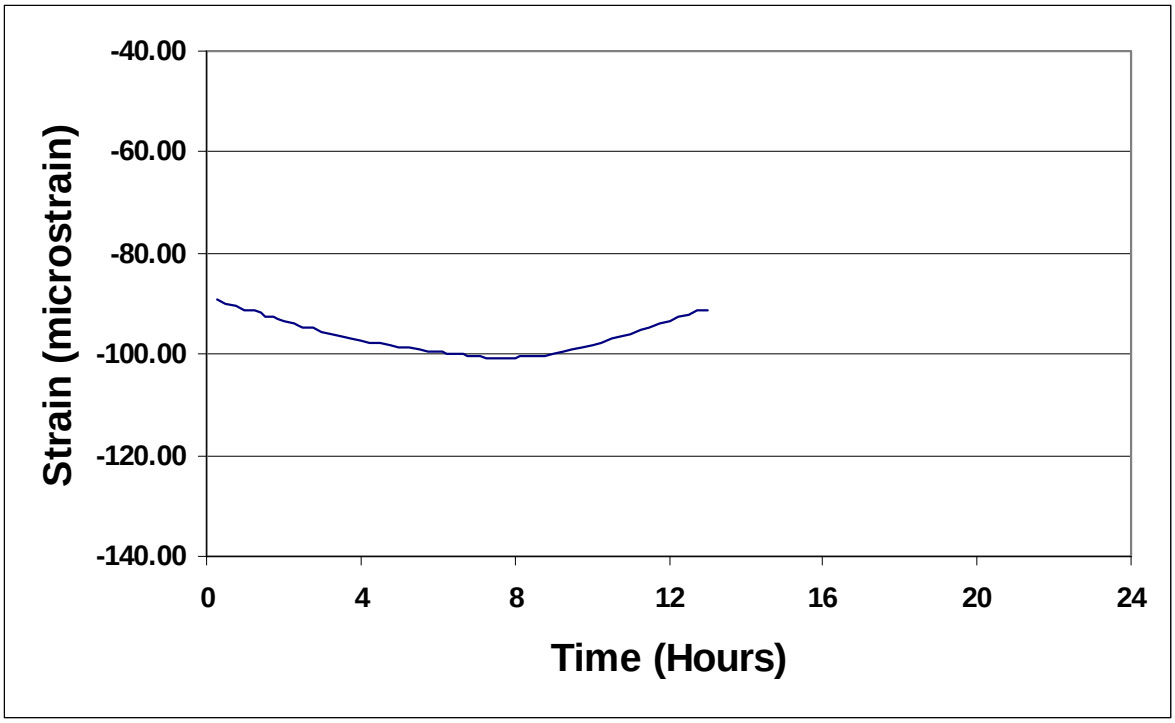

Figure B.57 Concrete Strain versus Time at Gage CG3 (Day 270).

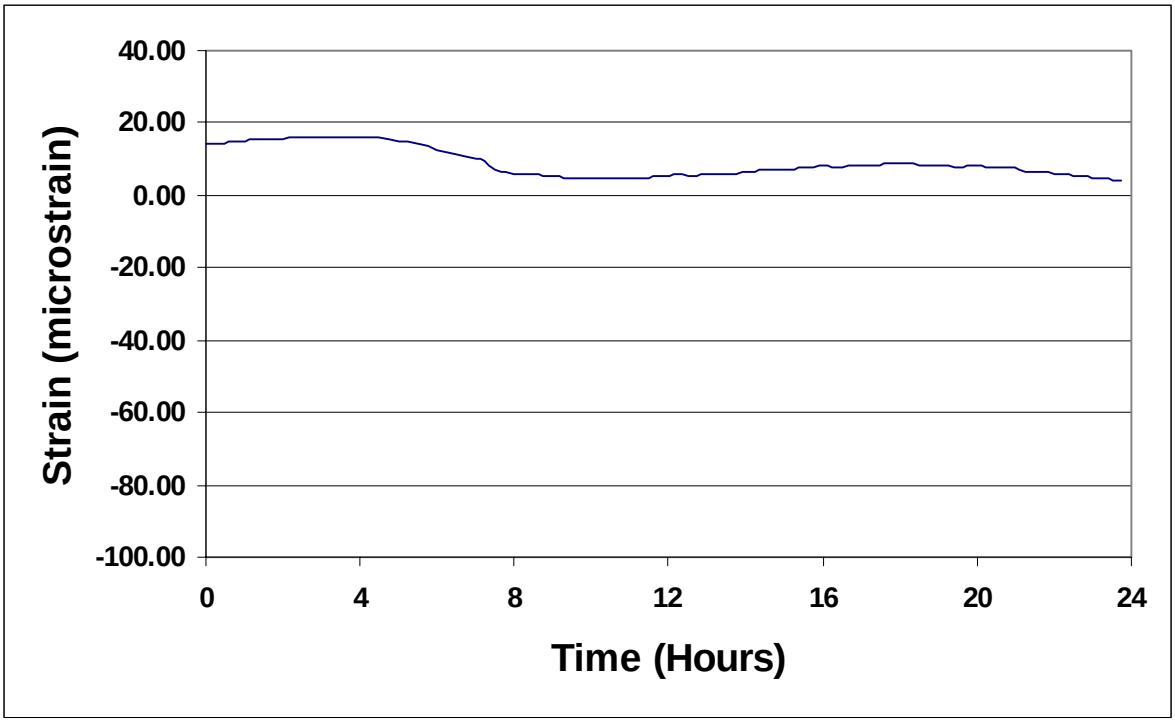

Figure B.58 Concrete Strain versus Time at Gage CG4 (Day 2).

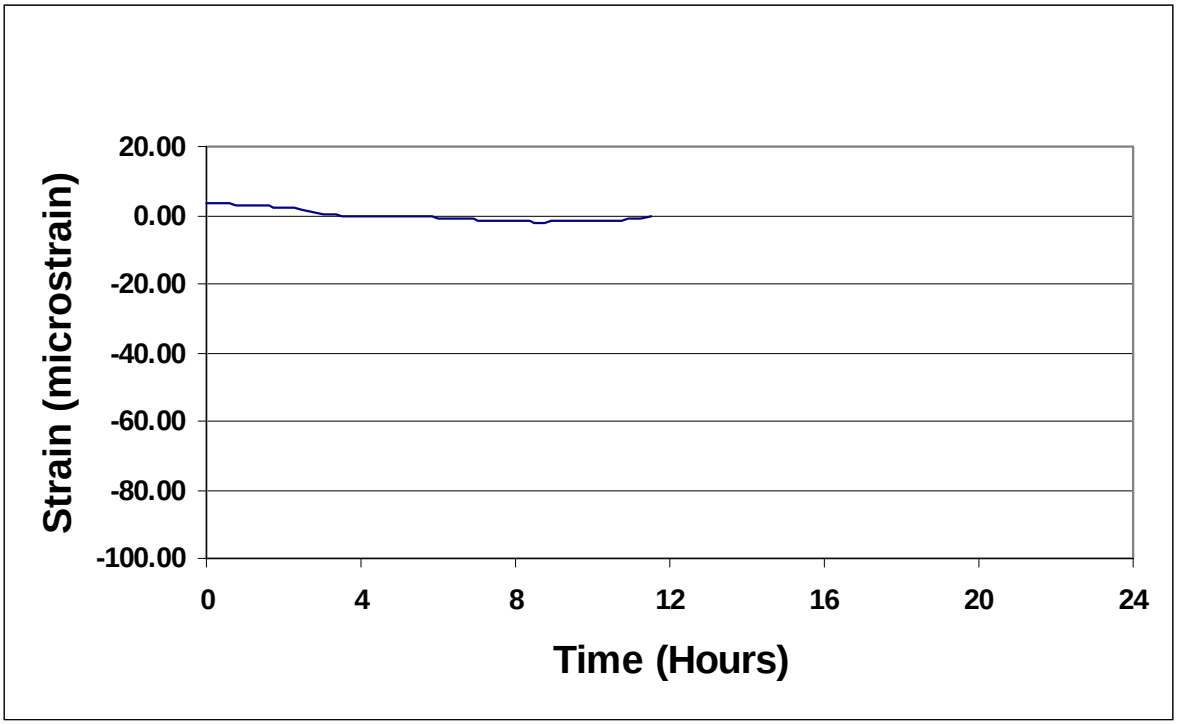

Figure B.59 Concrete Strain versus Time at Gage CG4 (Day 3).

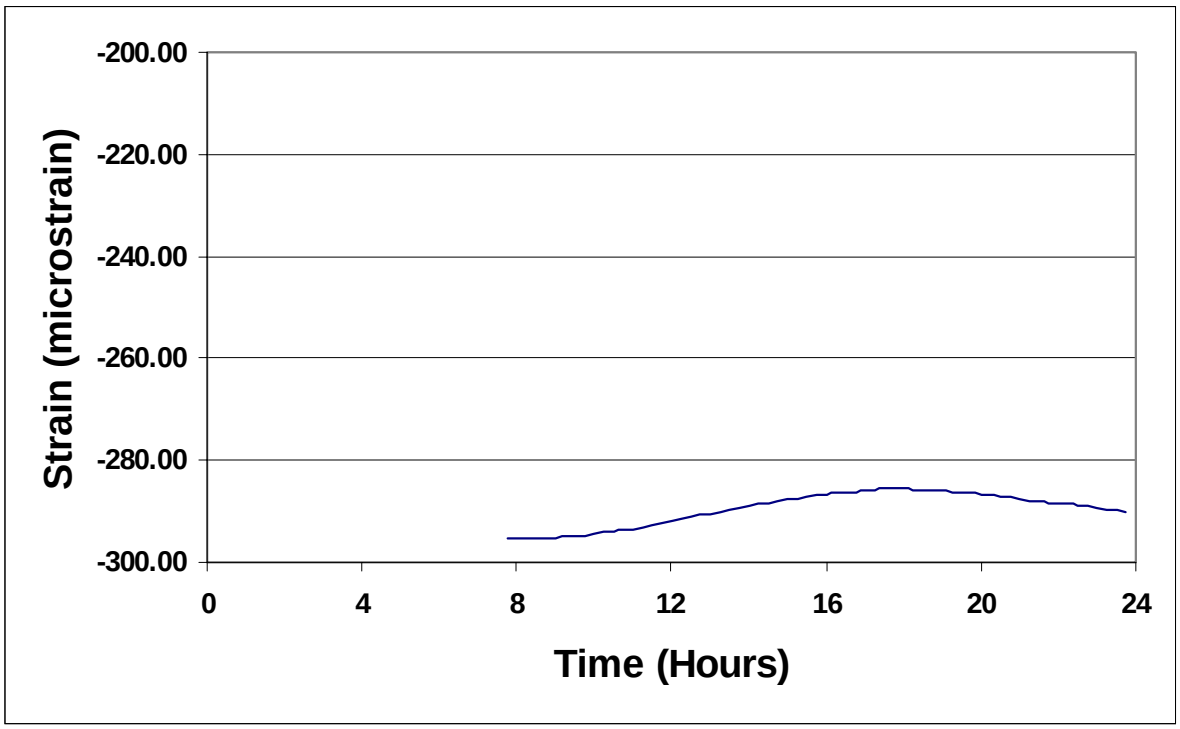

Figure B.60 Concrete Strain versus Time at Gage CG4 (Day 4).

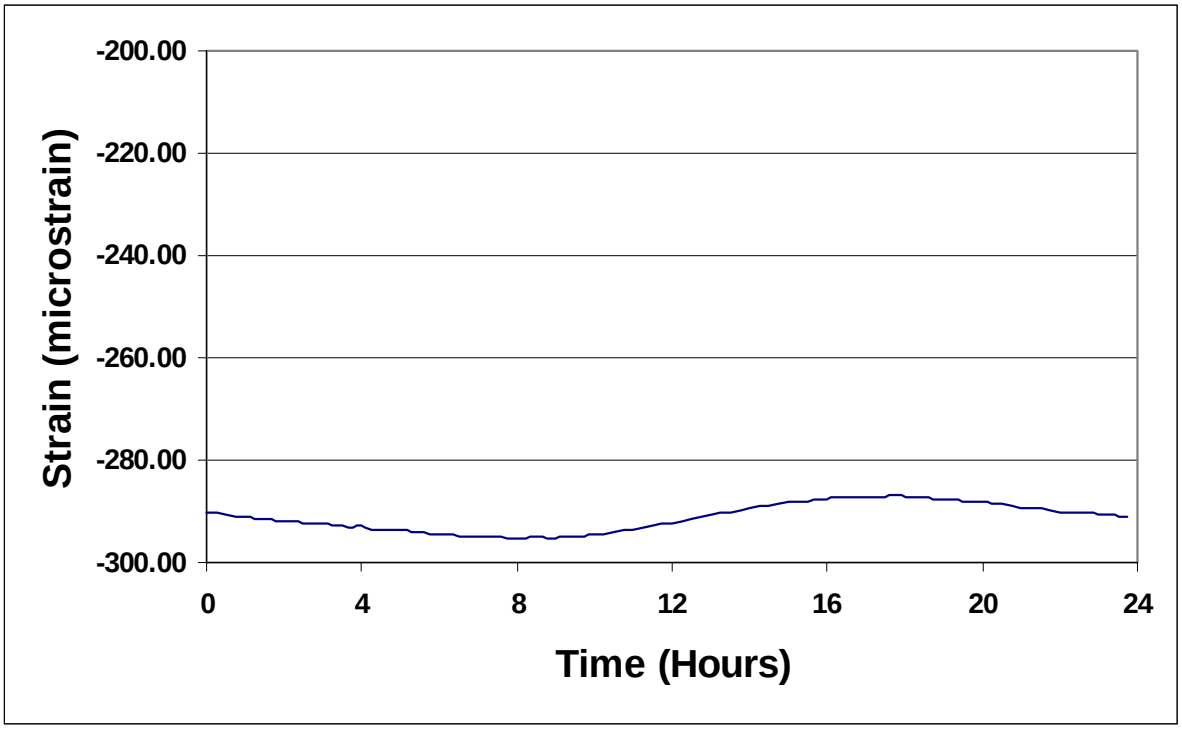

Figure B.61 Concrete Strain versus Time at Gage CG4 (Day 5).

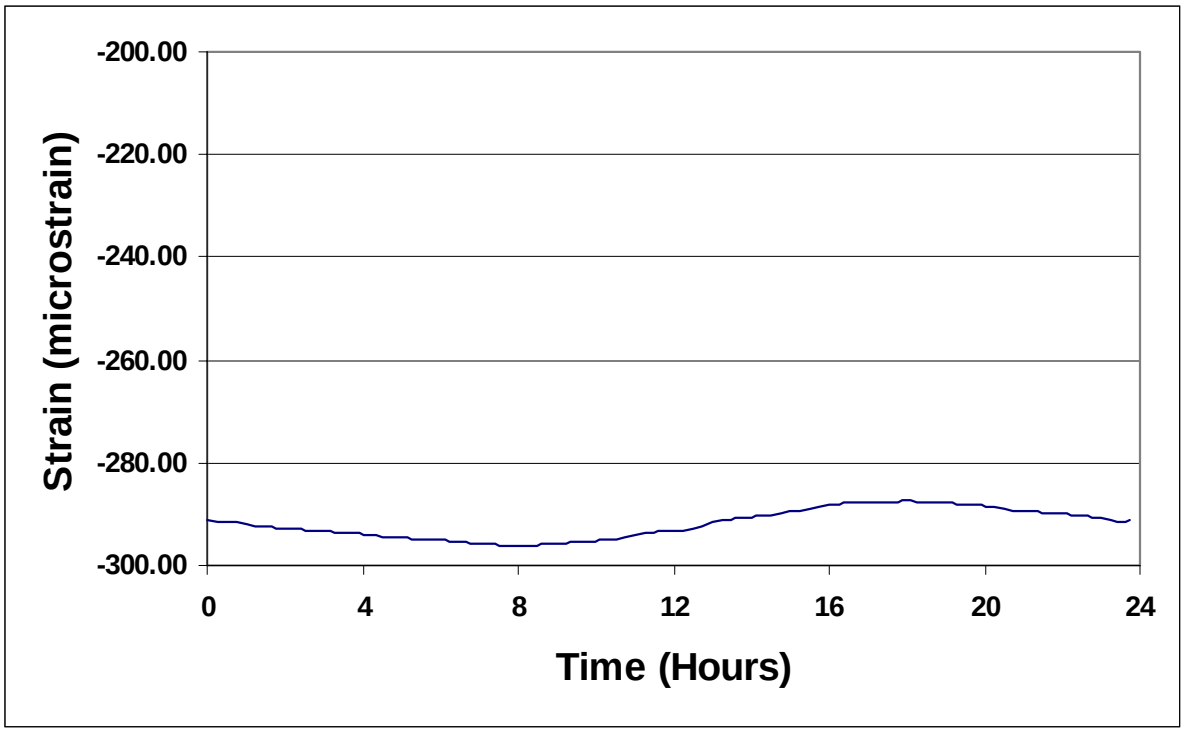

Figure B.62 Concrete Strain versus Time at Gage CG4 (Day 6).

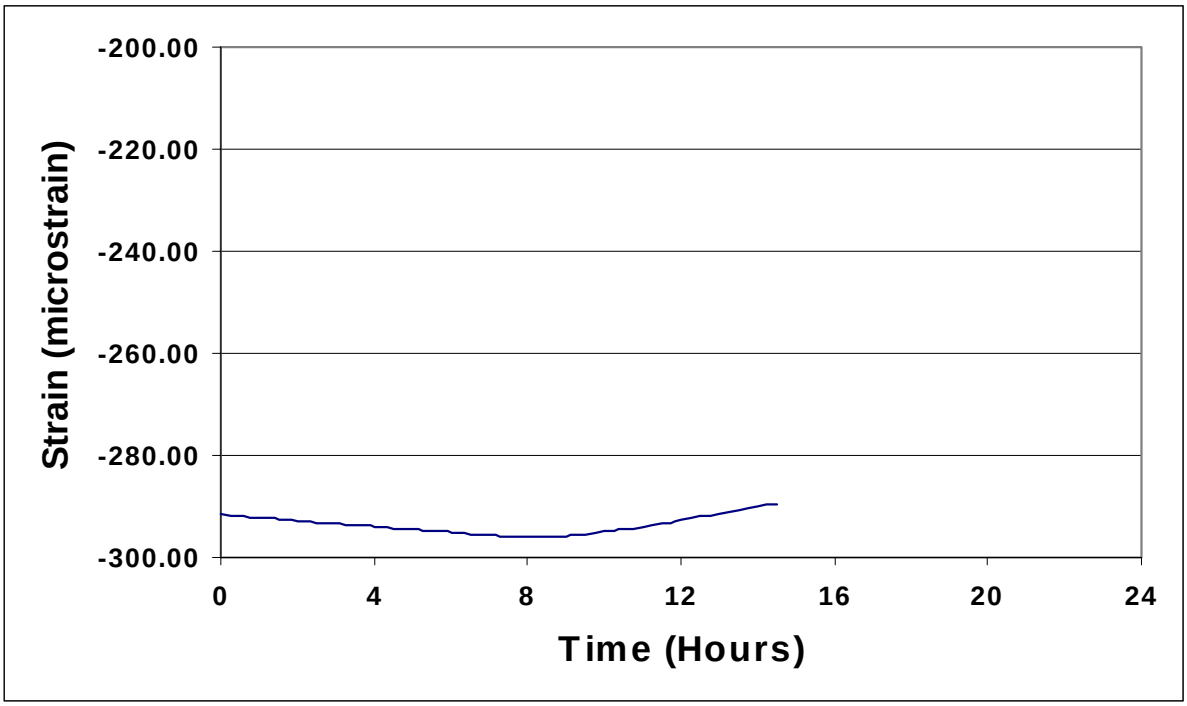

Figure B.63 Concrete Strain versus Time at Gage CG4 (Day 7).

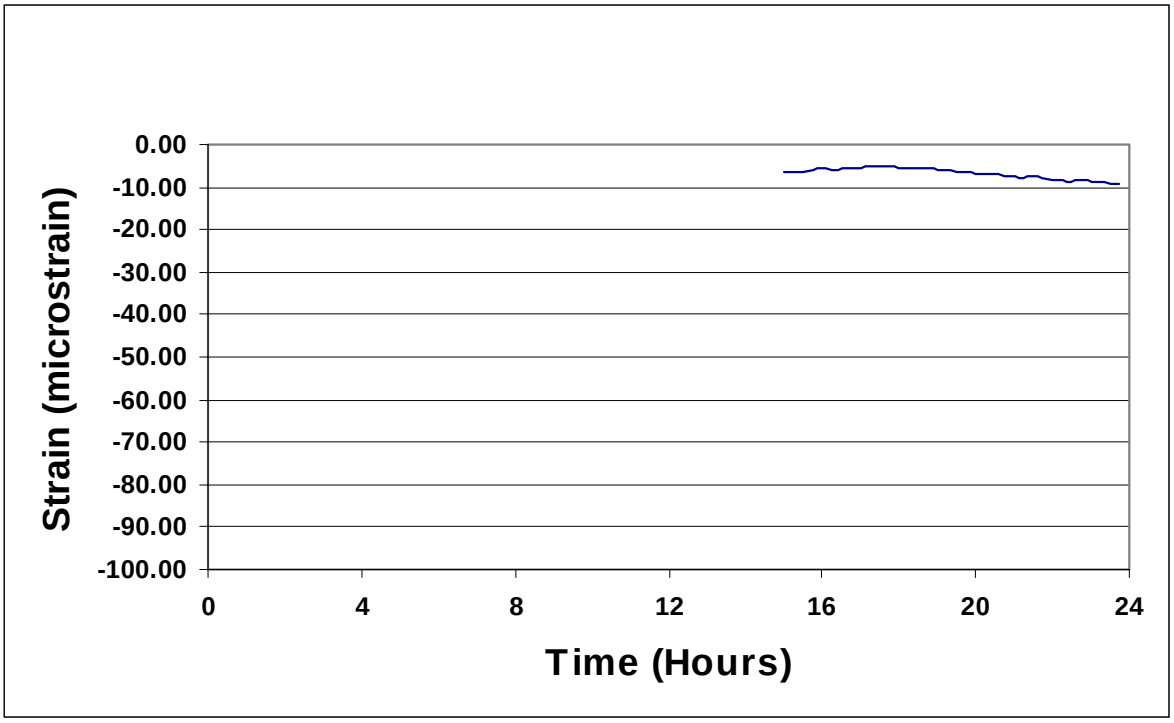

Figure B.64 Concrete Strain versus Time at Gage CG4 (Day 15).

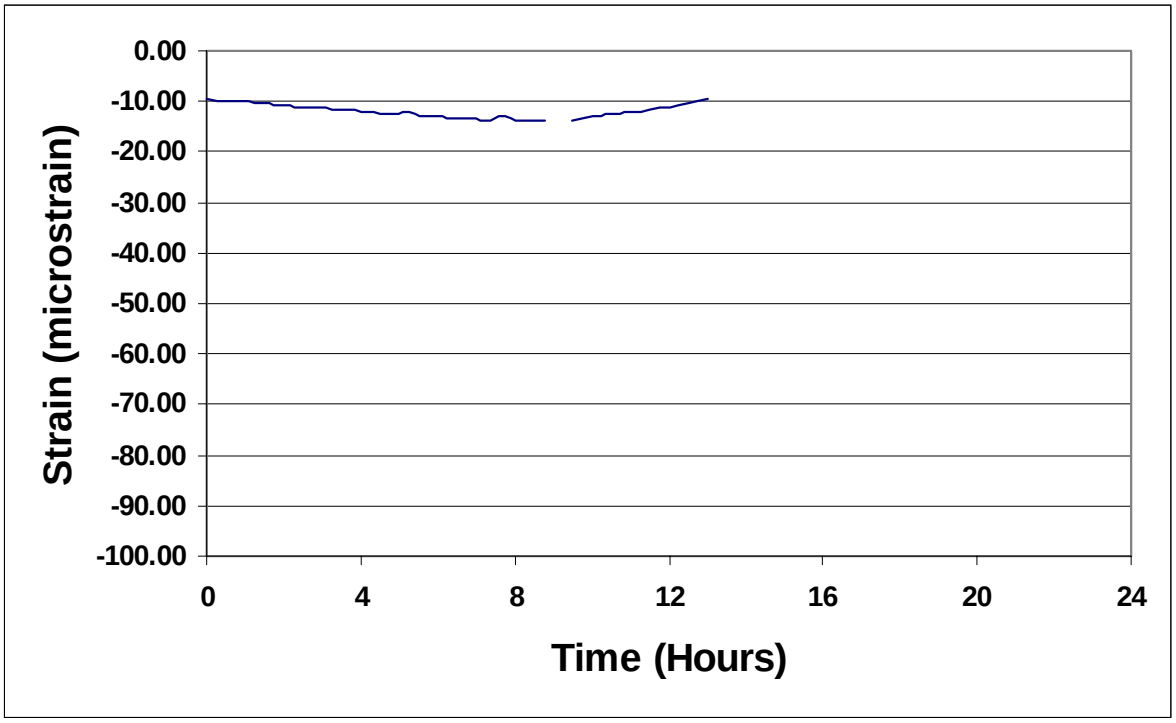

Figure B.65 Concrete Strain versus Time at Gage CG4 (Day 16).

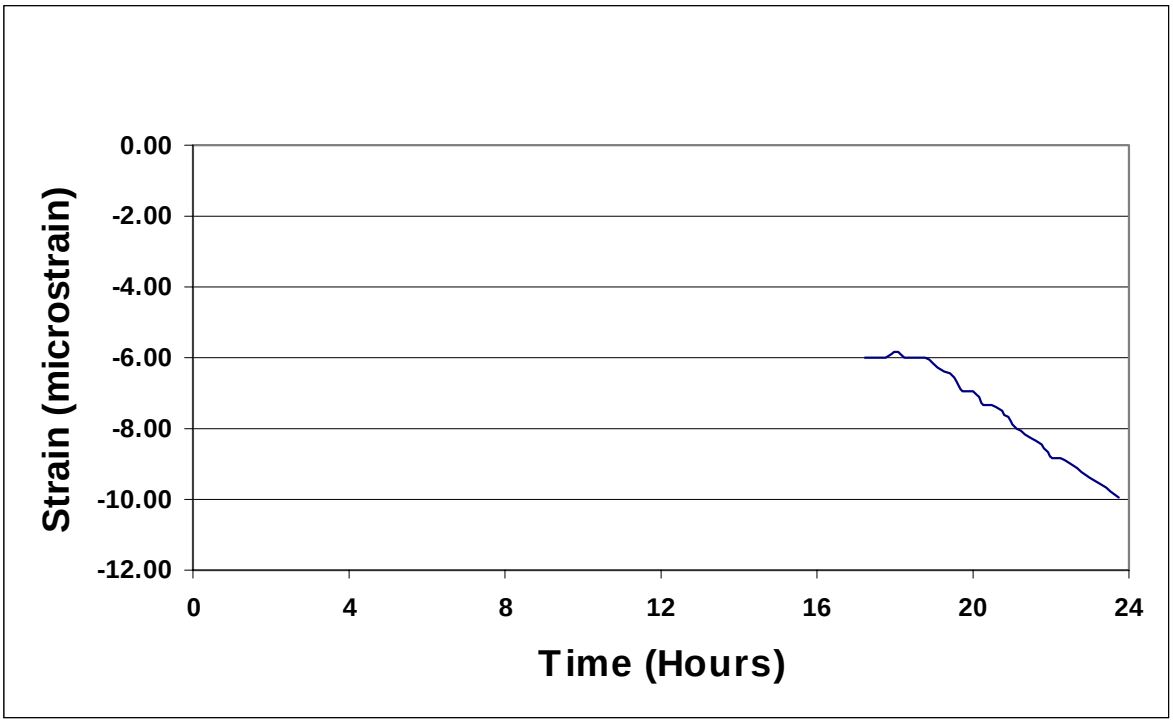

Figure B.66 Concrete Strain versus Time at Gage CG4 (Day 29).

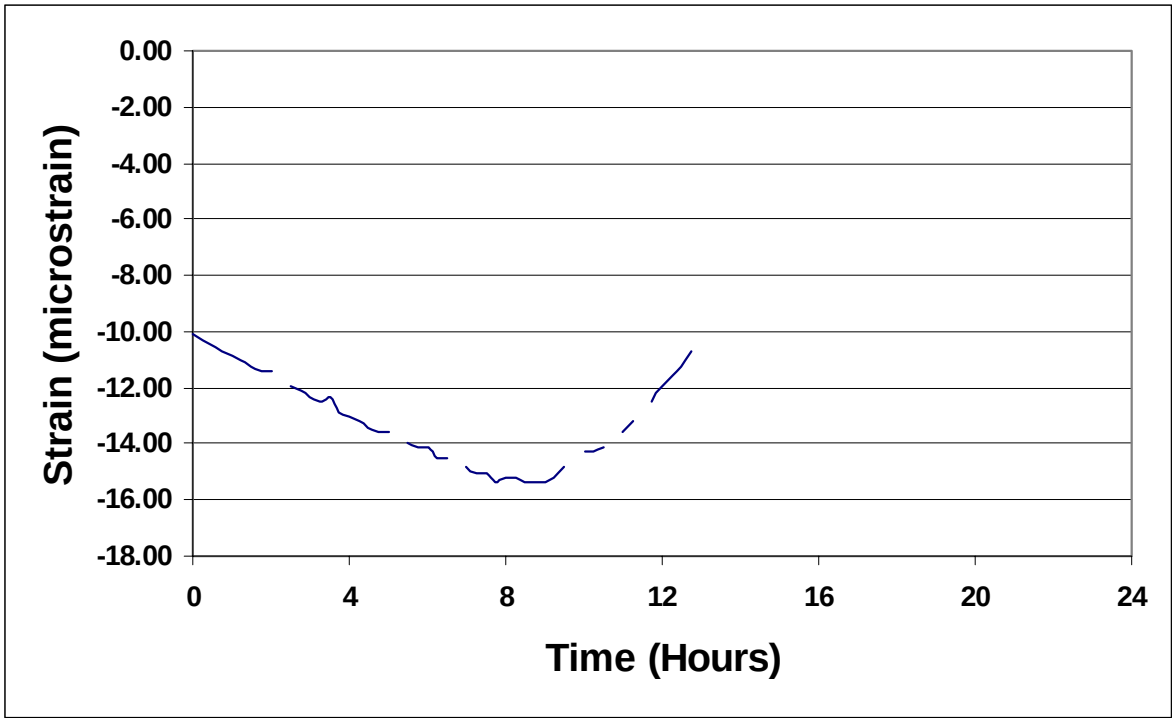

Figure B.67 Concrete Strain versus Time at Gage CG4 (Day 30).

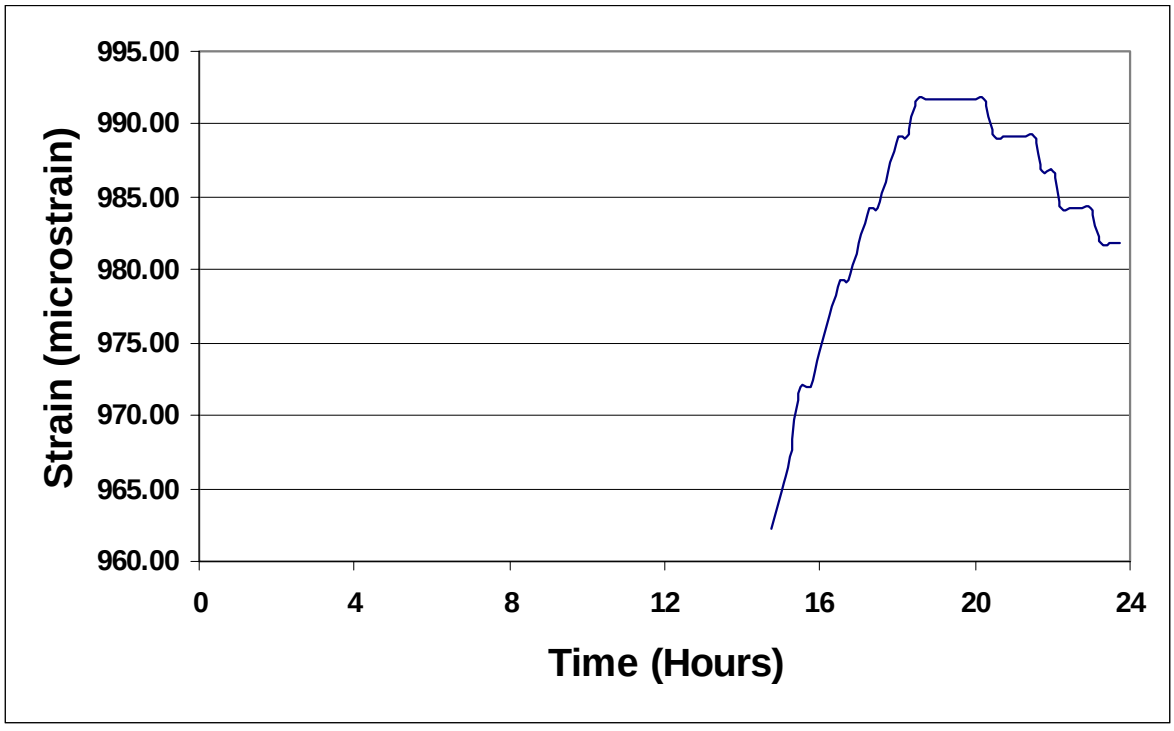

Figure B.68 Concrete Strain versus Time at Gage CG4 (Day 161).

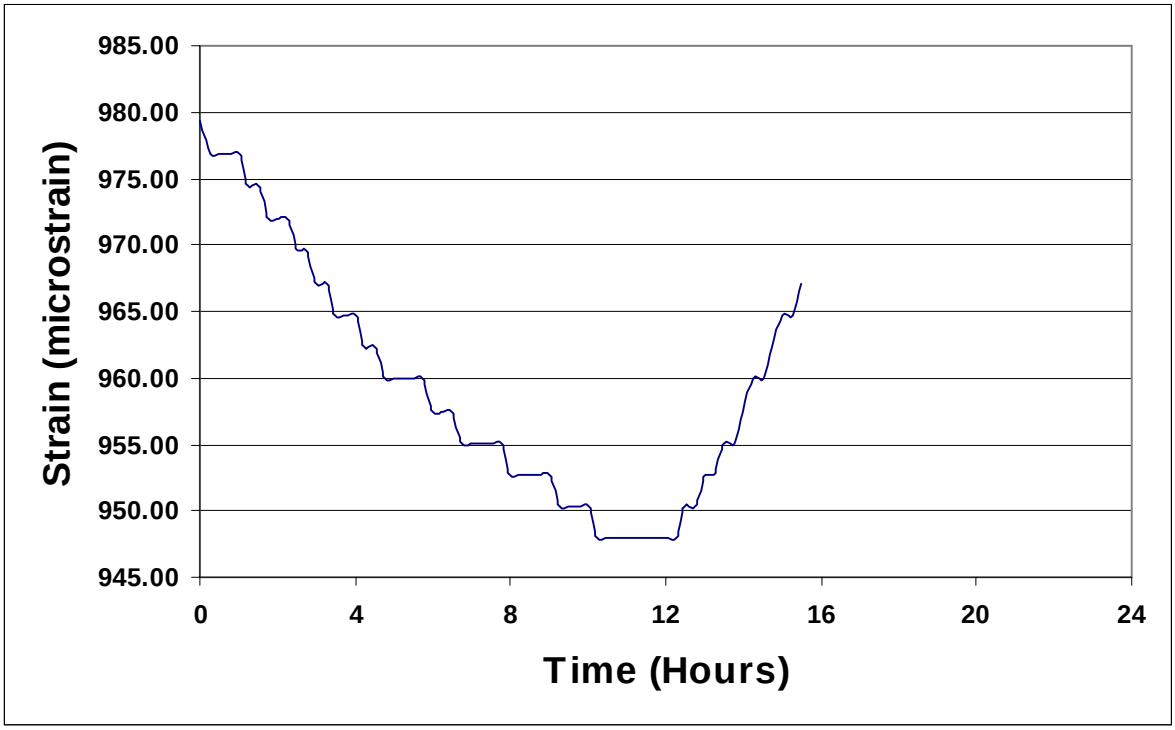

Figure B.69 Concrete Strain versus Time at Gage CG4 (Day 162).

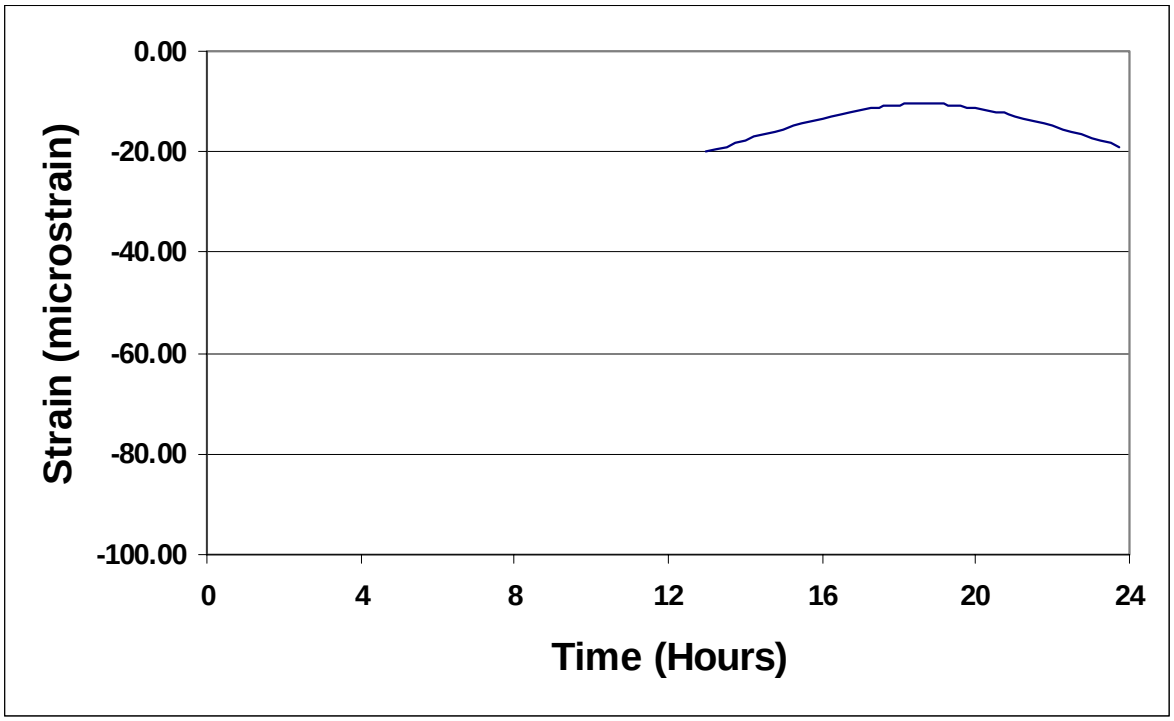

Figure B.70 Concrete Strain versus Time at Gage CG4 (Day 269).

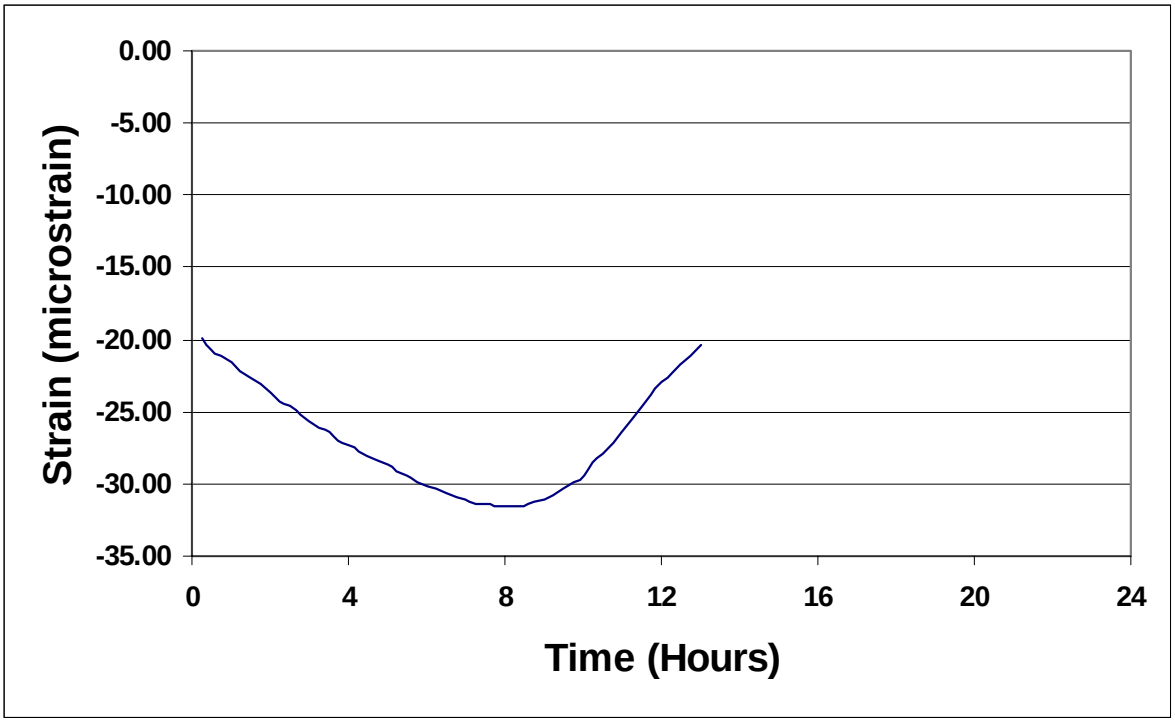

Figure B.71 Concrete Strain versus Time at Gage CG4 (Day 270).

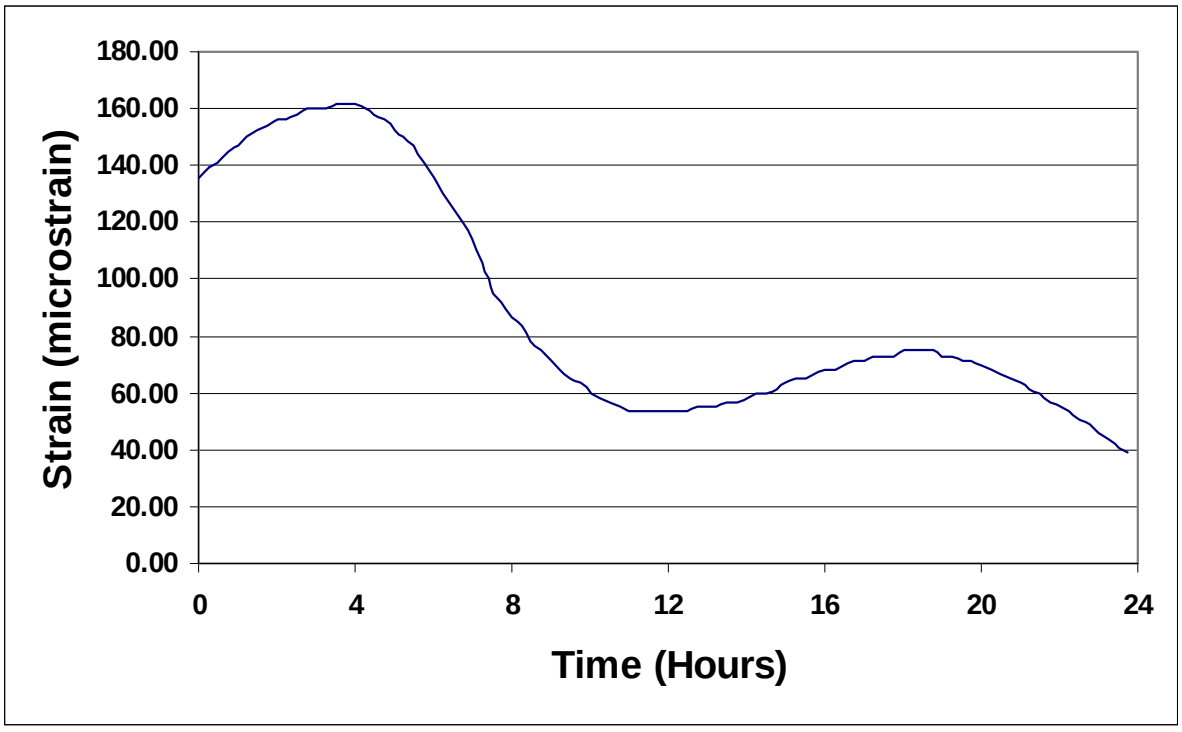

Figure B.72 Concrete Strain versus Time at Gage CG14 (Day 2).

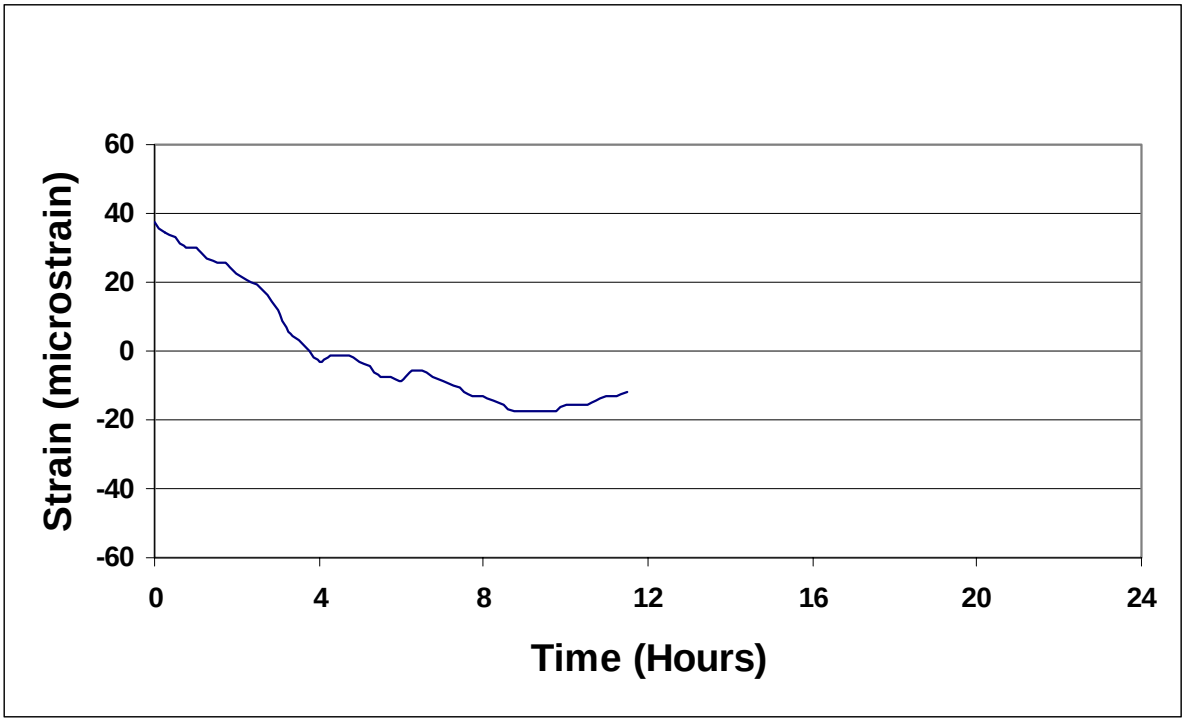

Figure B.73 Concrete Strain versus Time at Gage CG14 (Day 3).

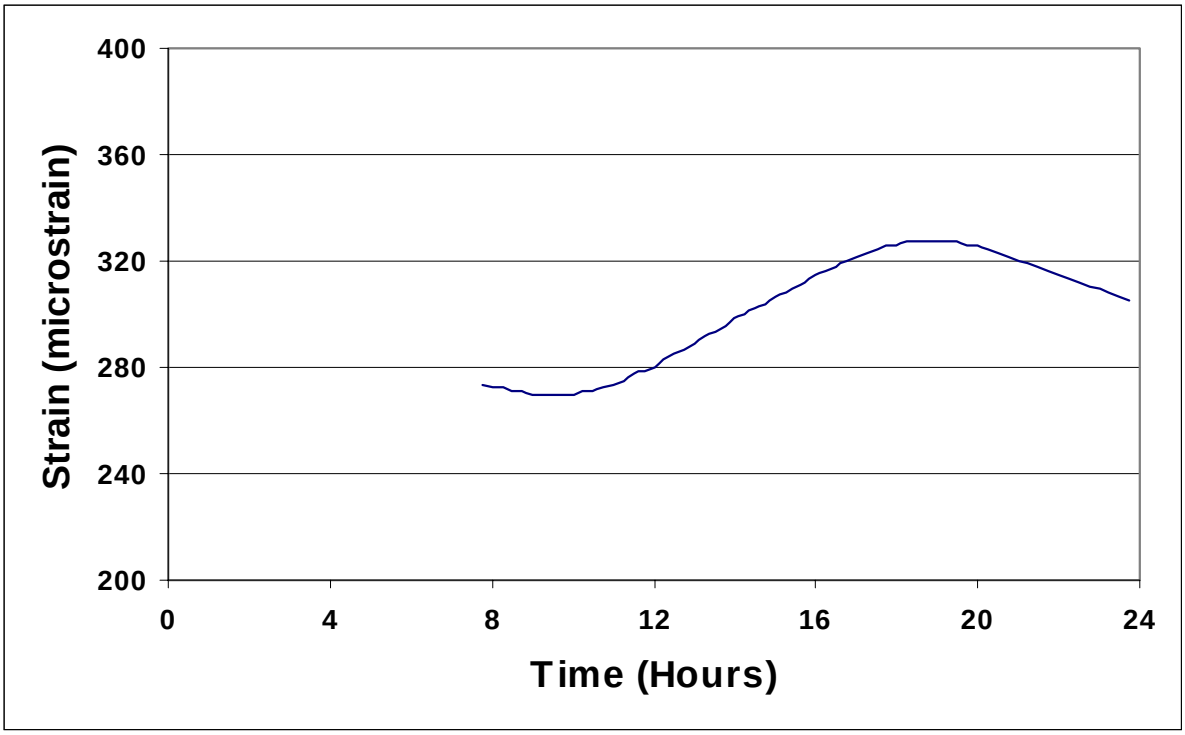

Figure B.74 Concrete Strain versus Time at Gage CG14 (Day 4).

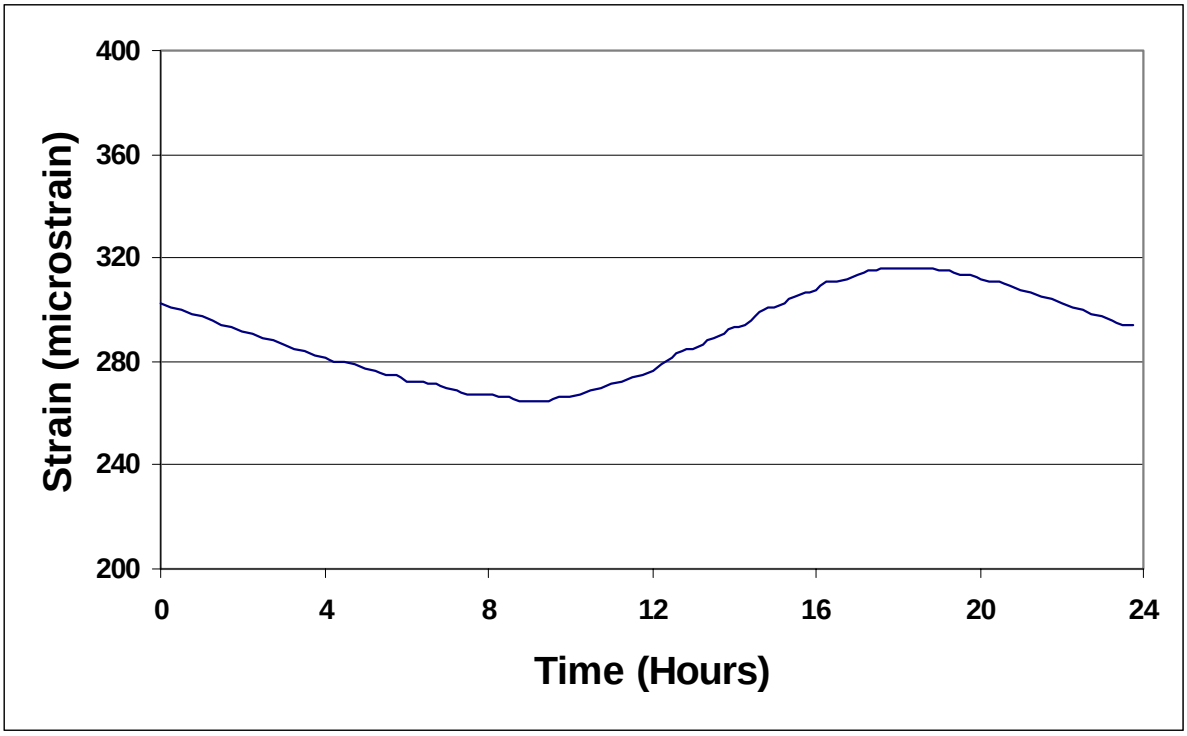

Figure B.75 Concrete Strain versus Time at Gage CG14 (Day 5).

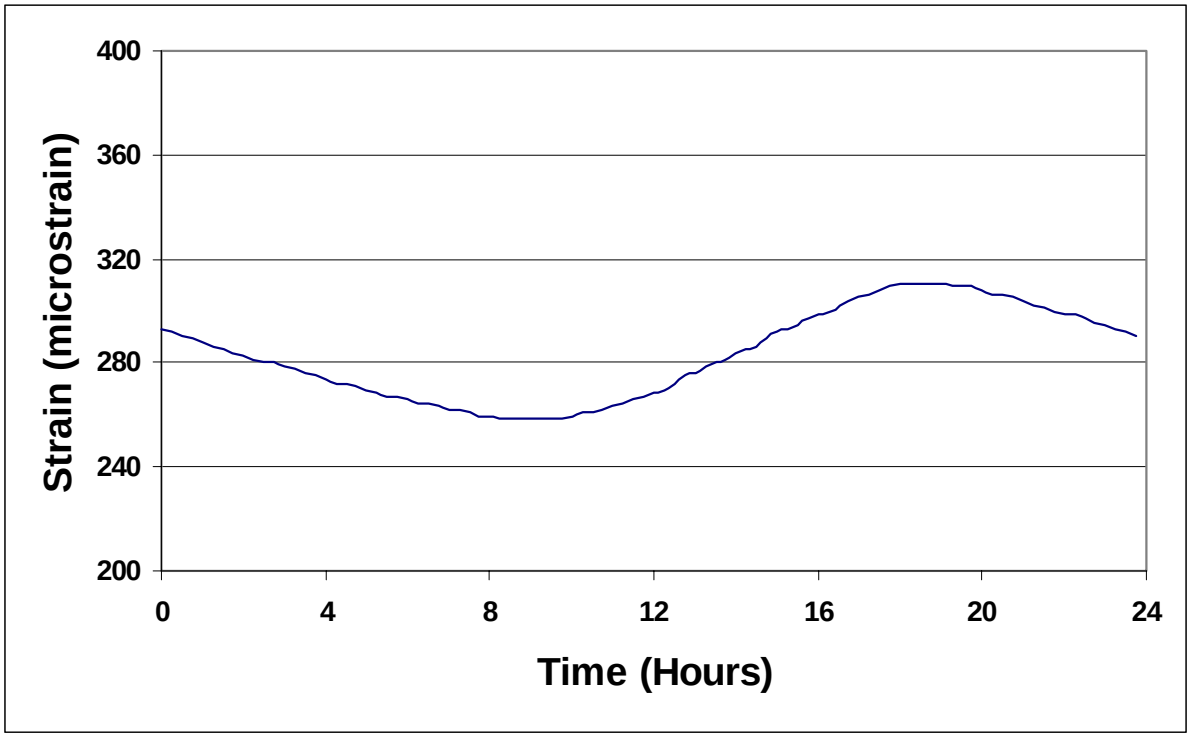

Figure B.76 Concrete Strain versus Time at Gage CG14 (Day 6).

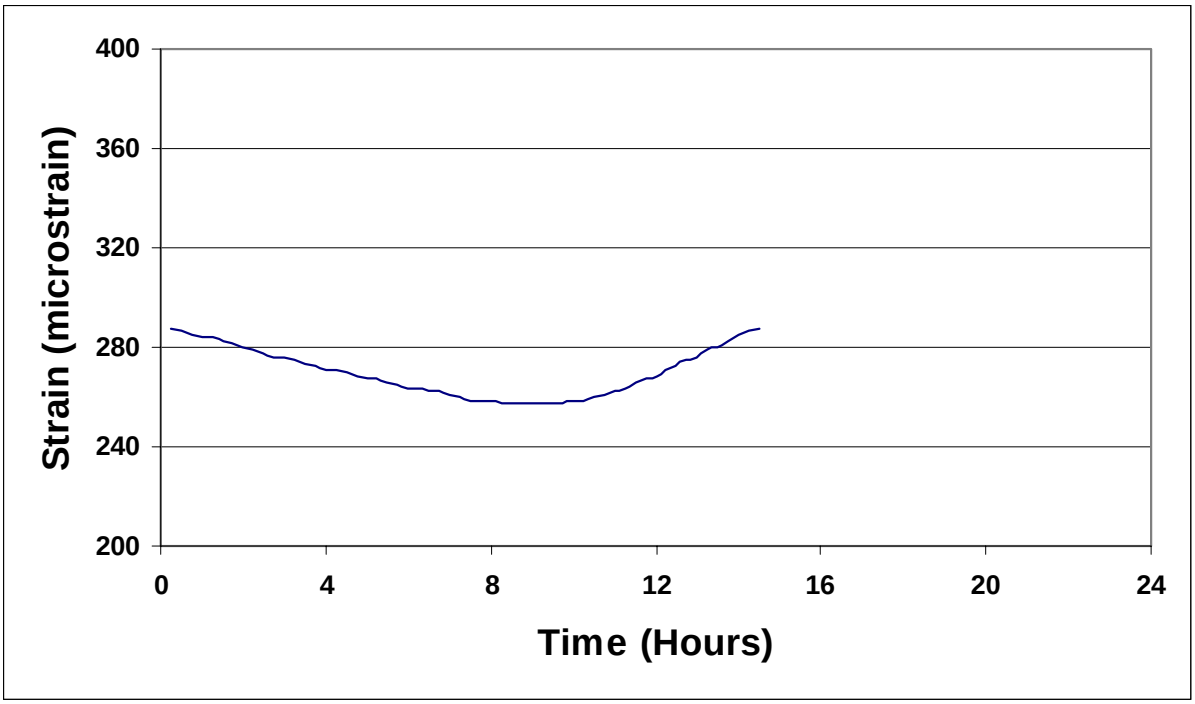

Figure B.77 Concrete Strain versus Time at Gage CG14 (Day 7).

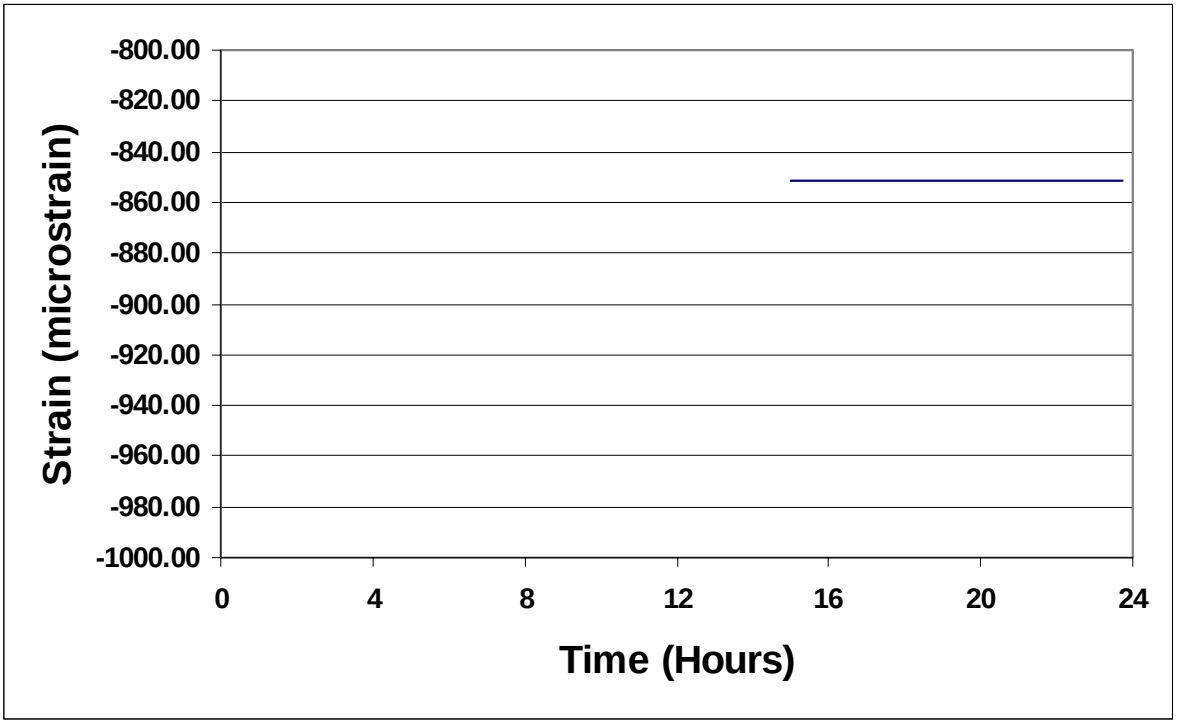

Figure B.78 Concrete Strain versus Time at Gage CG14 (Day 15).

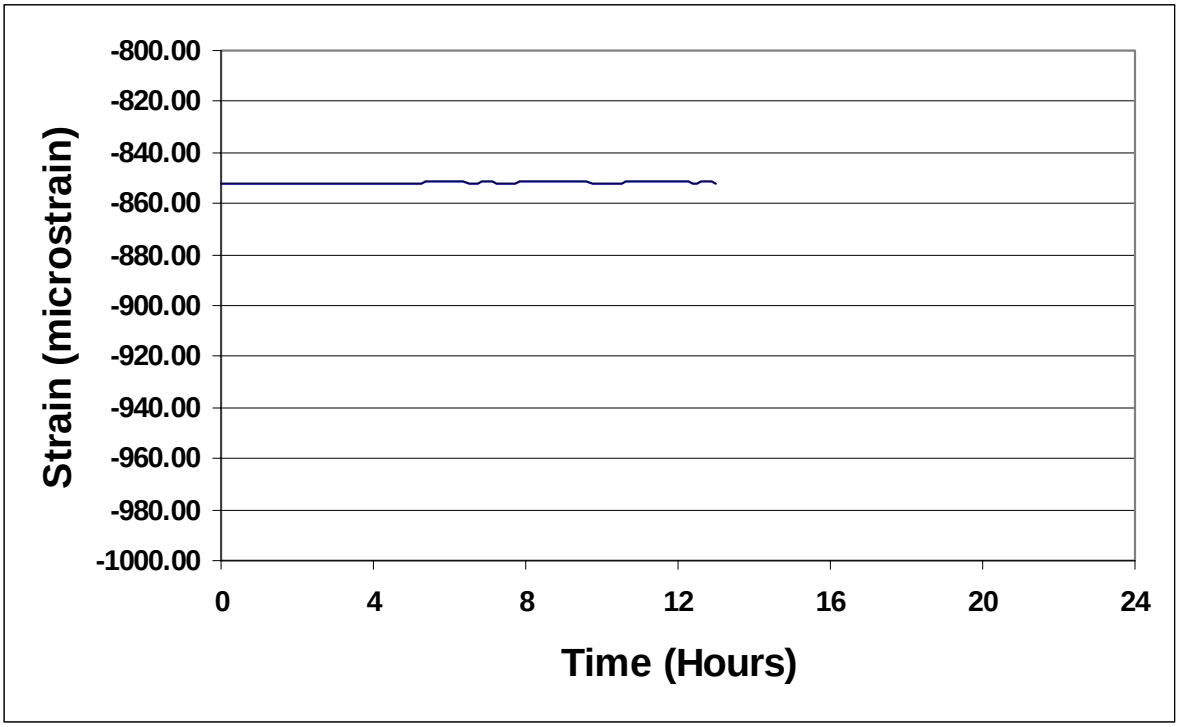

Figure B.79 Concrete Strain versus Time at Gage CG14 (Day 16).

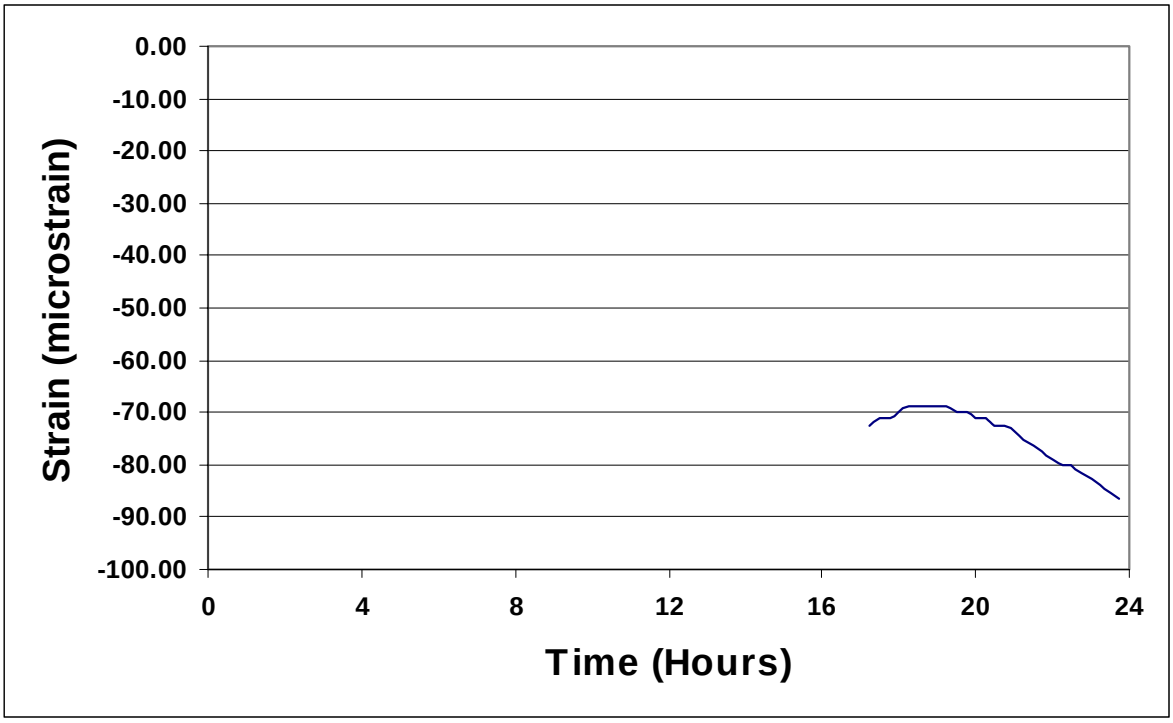

Figure B.80 Concrete Strain versus Time at Gage CG14 (Day 29).

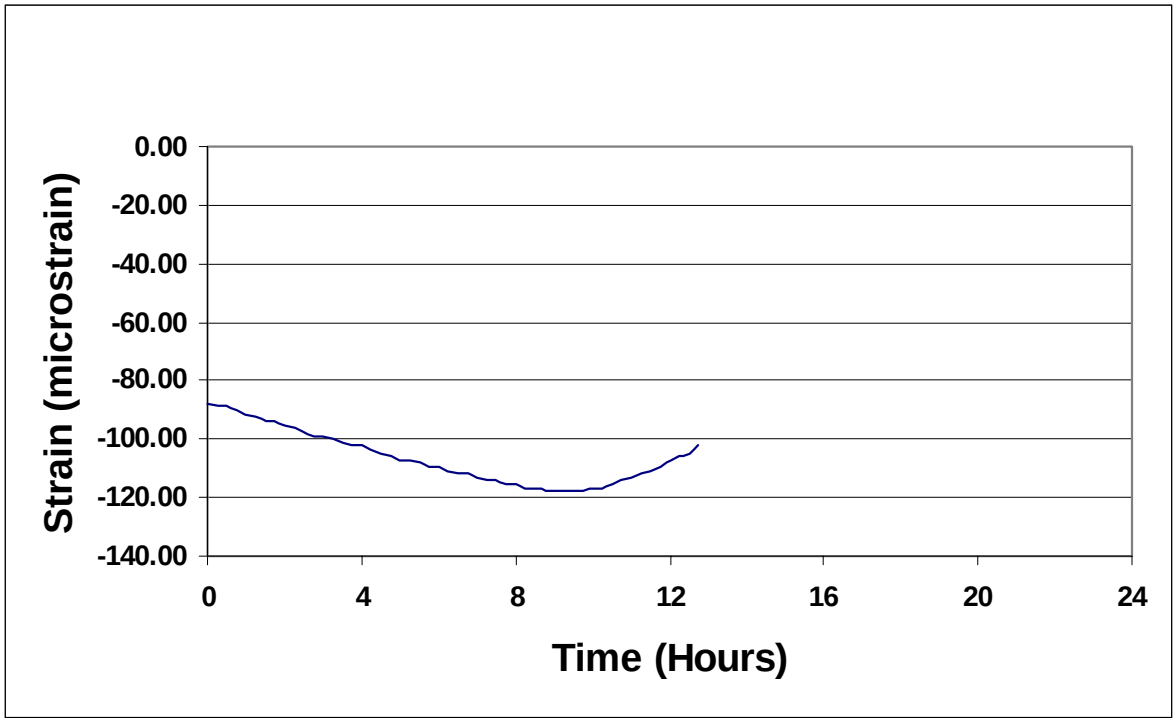

Figure B.81 Concrete Strain versus Time at Gage CG14 (Day 30).

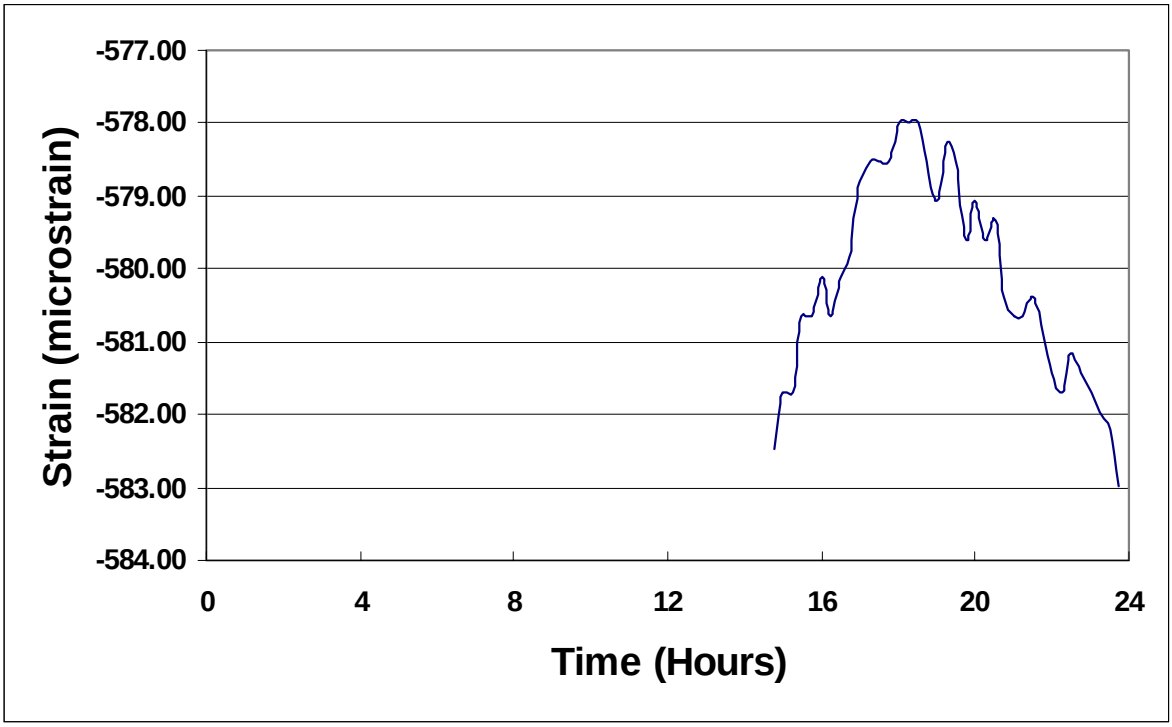

Figure B.82 Concrete Strain versus Time at Gage CG14 (Day 161).

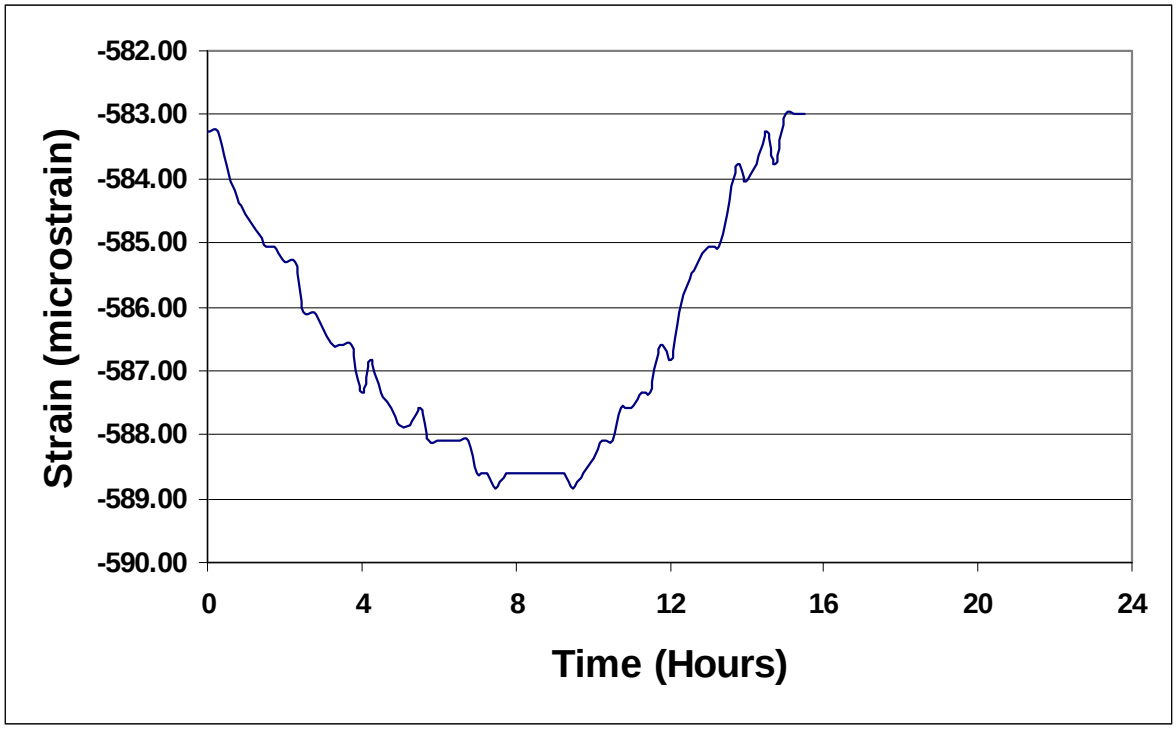

Figure B.83 Concrete Strain versus Time at Gage CG14 (Day 162).

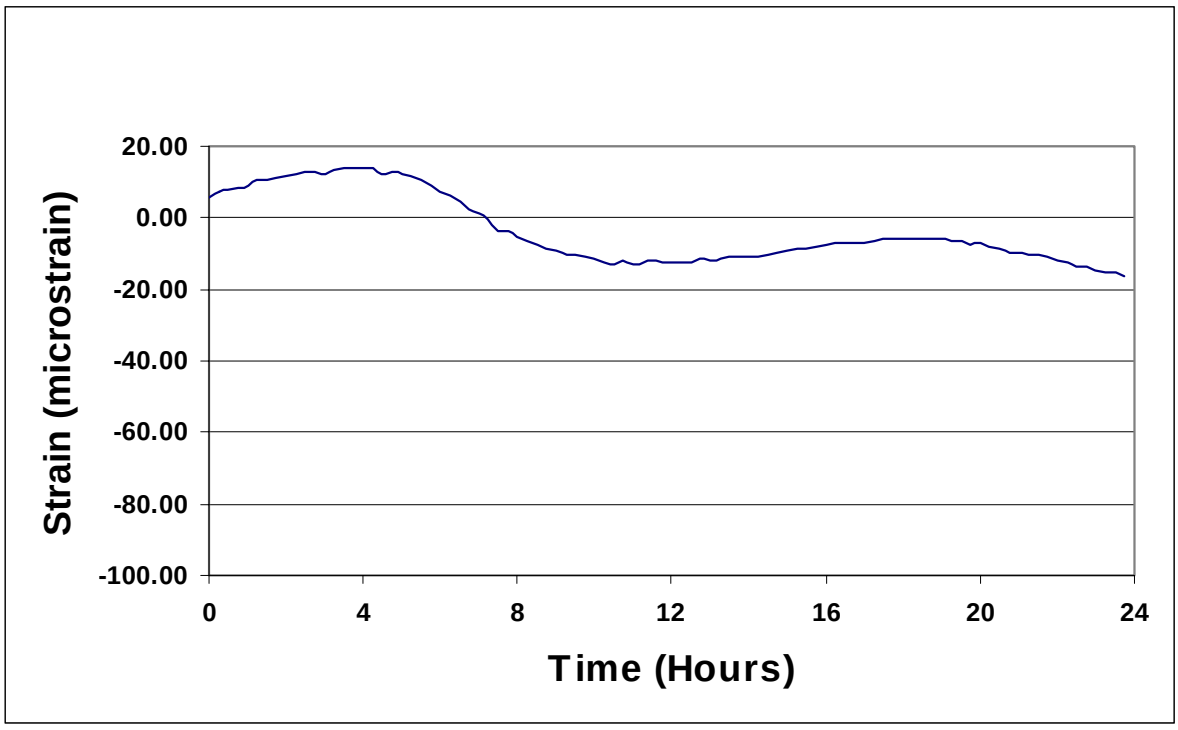

Figure B.84 Concrete Strain versus Time at Gage CG6 (Day 2).

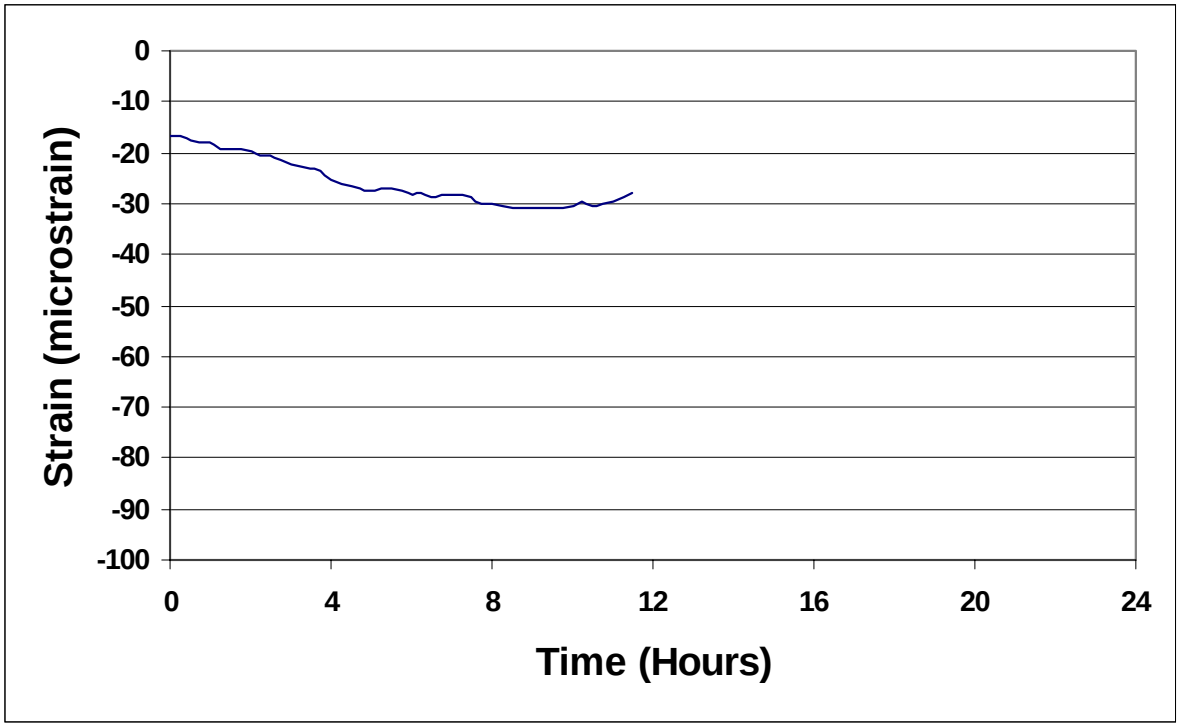

Figure B.85 Concrete Strain versus Time at Gage CG6 (Day 3).

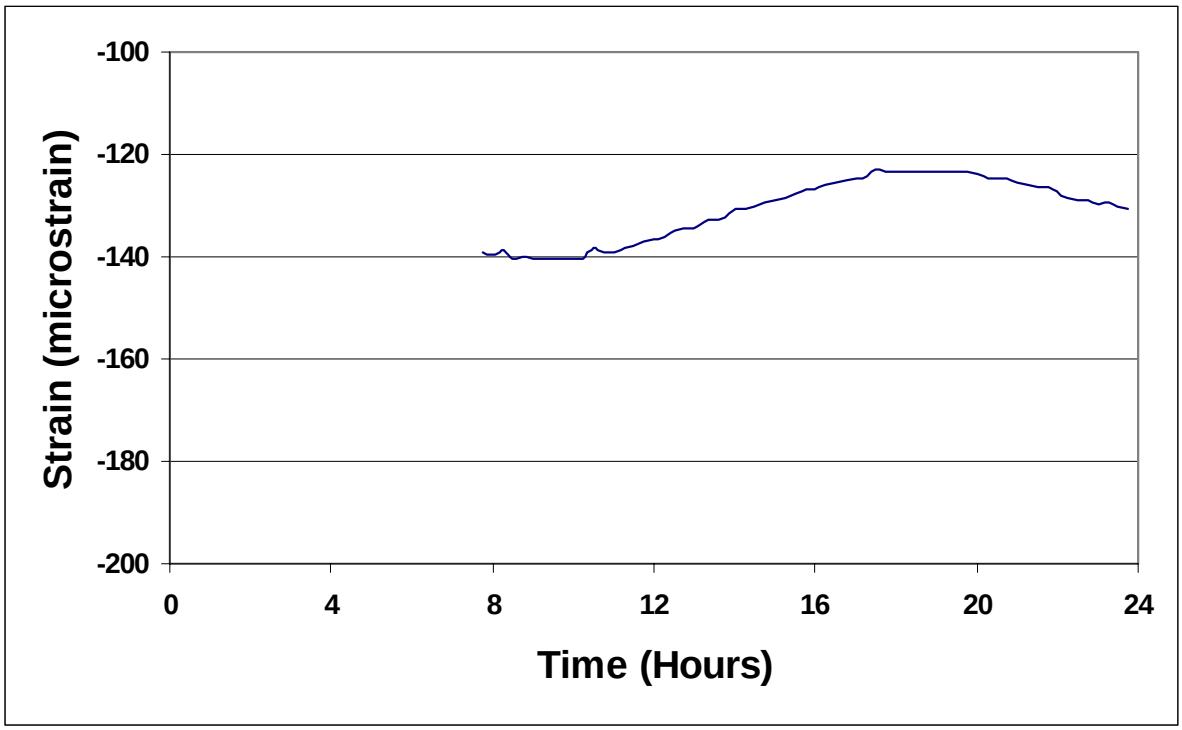

Figure B.86 Concrete Strain versus Time at Gage CG6 (Day 4).

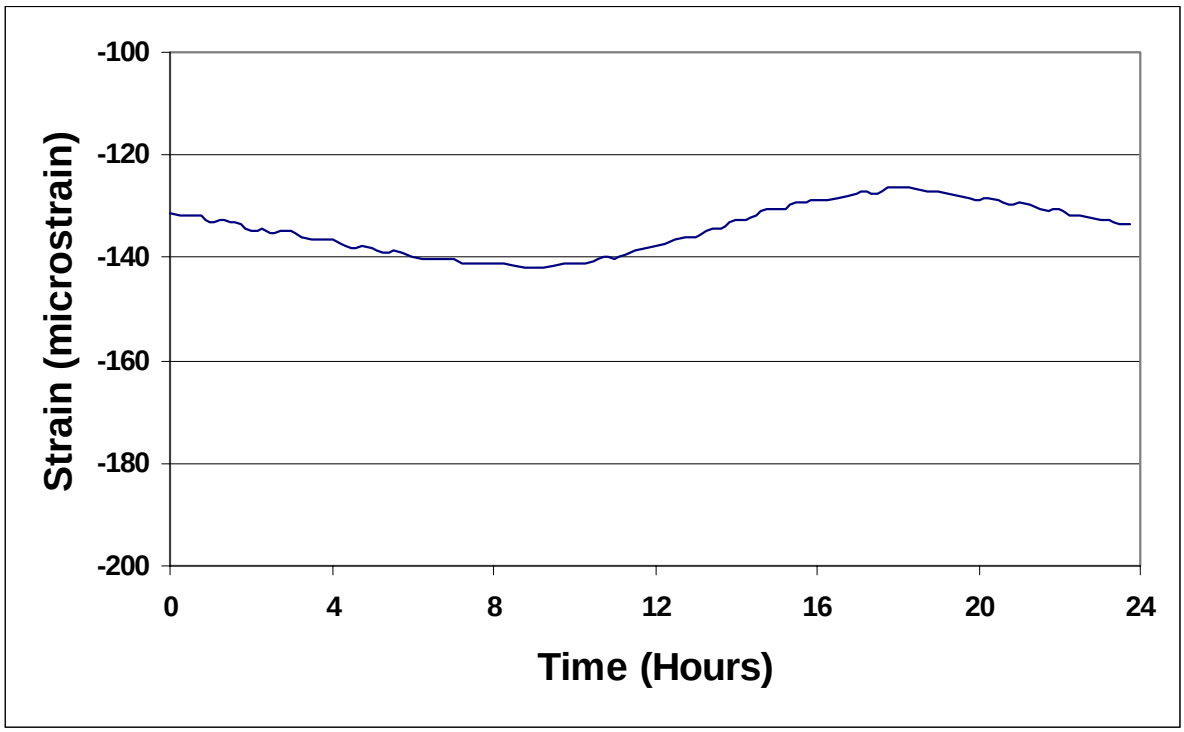

Figure B.87 Concrete Strain versus Time at Gage CG6 (Day 5).

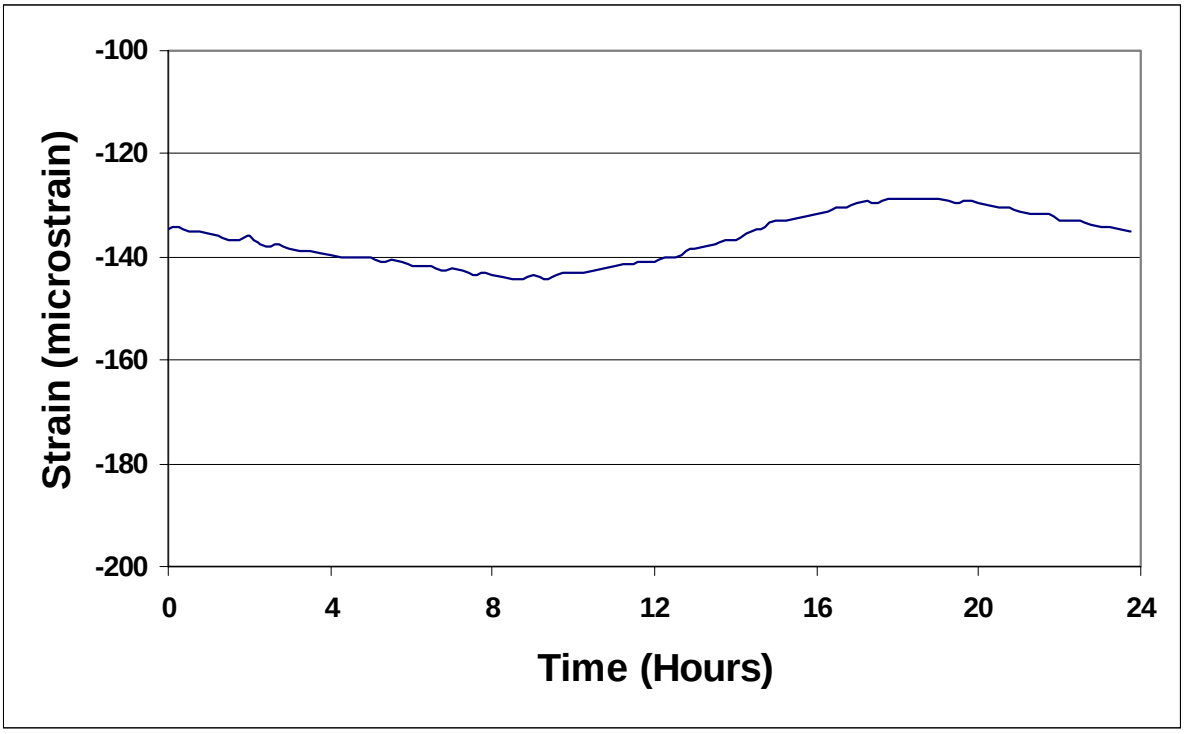

Figure B.88 Concrete Strain versus Time at Gage CG6 (Day 6).

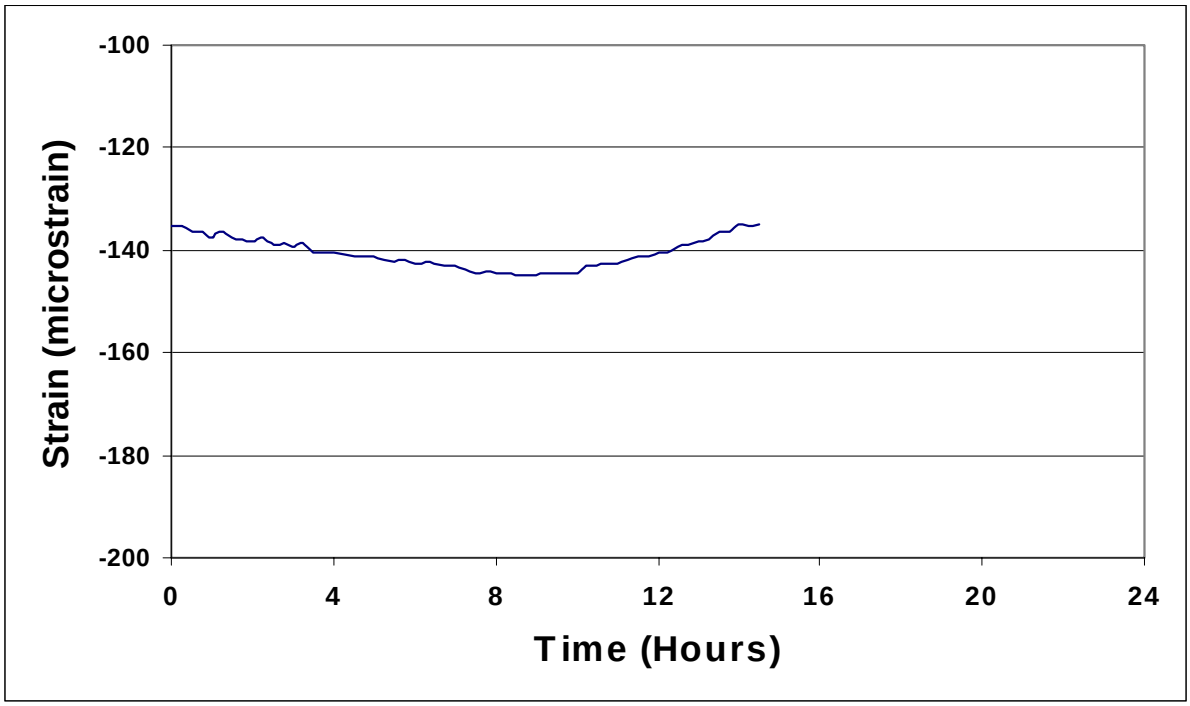

Figure B.89 Concrete Strain versus Time at Gage CG6 (Day 7).

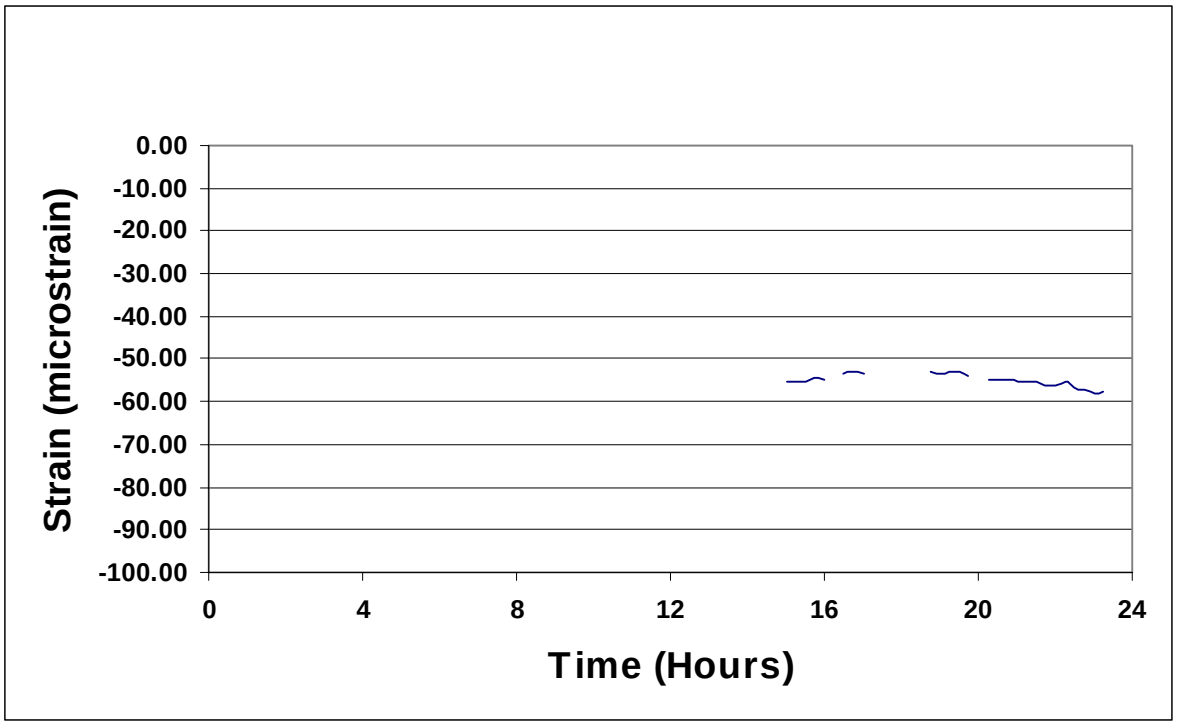

Figure B.90 Concrete Strain versus Time at Gage CG6 (Day 15).

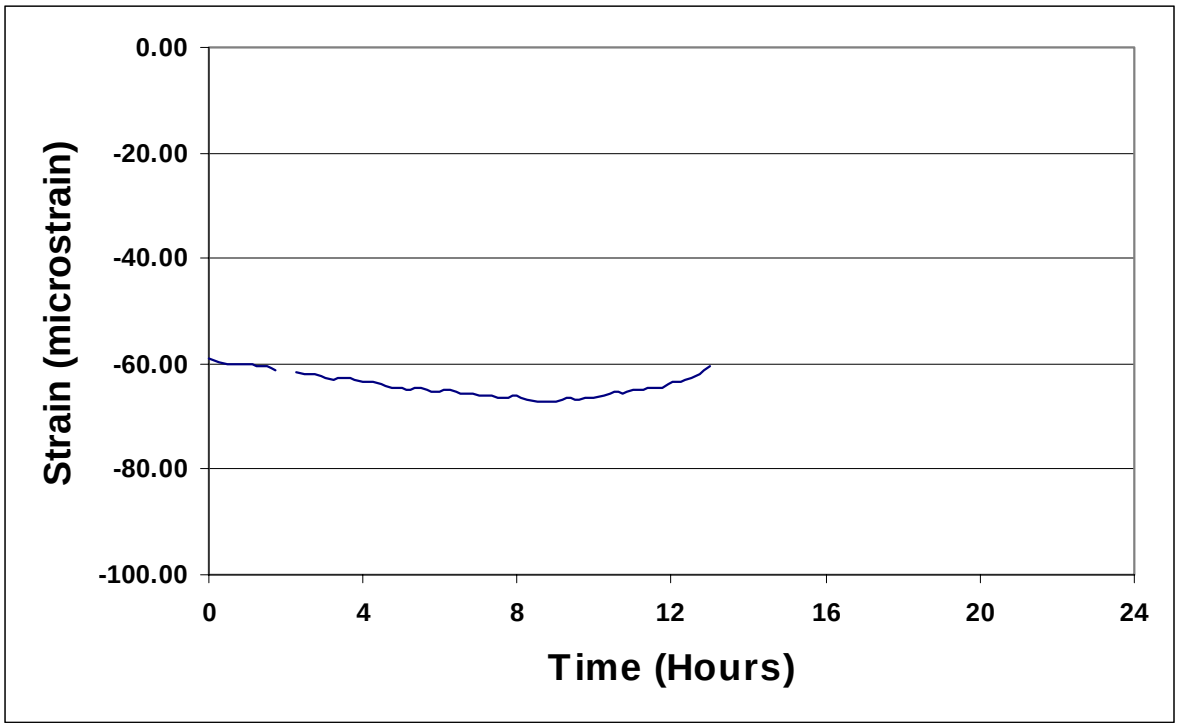

Figure B.91 Concrete Strain versus Time at Gage CG6 (Day 16).

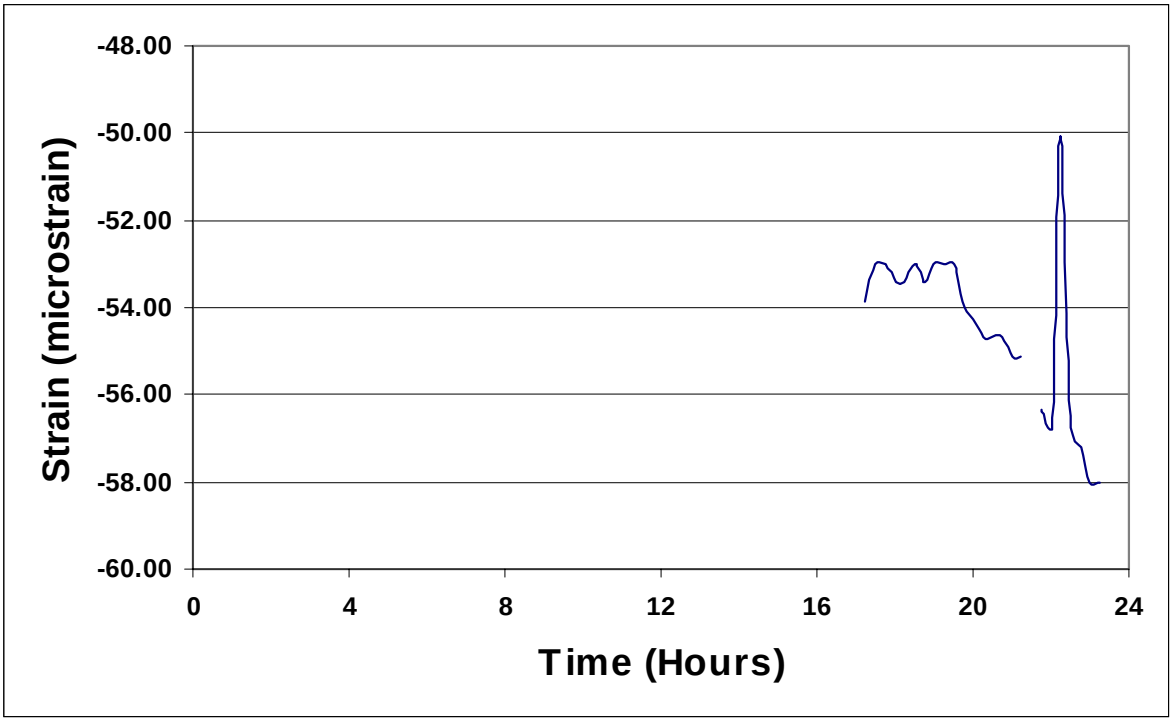

Figure B.92 Concrete Strain versus Time at Gage CG6 (Day 29).

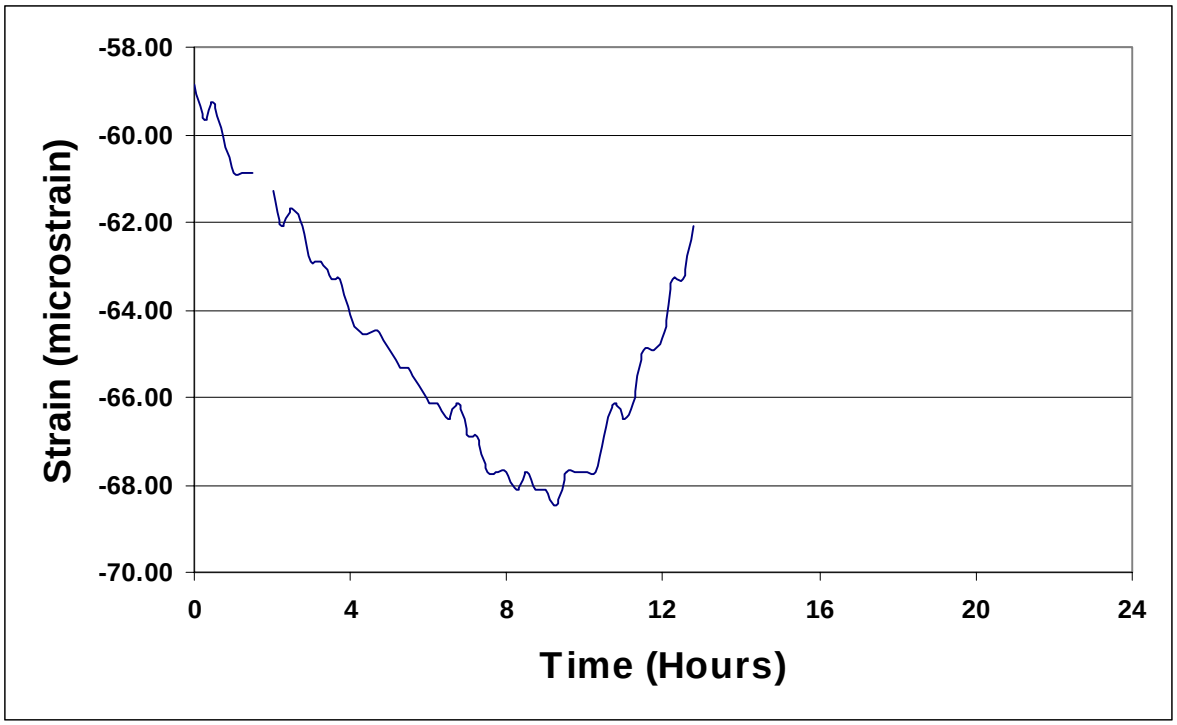

Figure B.93 Concrete Strain versus Time at Gage CG6 (Day 30).

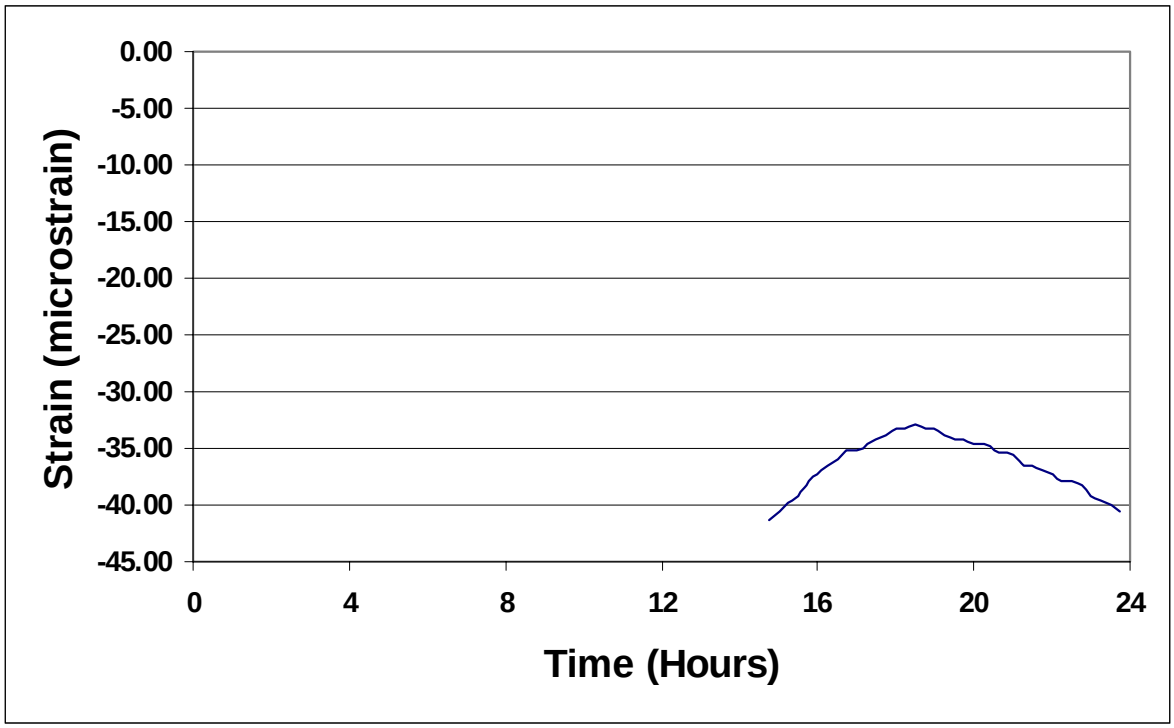

Figure B.94 Concrete Strain versus Time at Gage CG6 (Day 161).

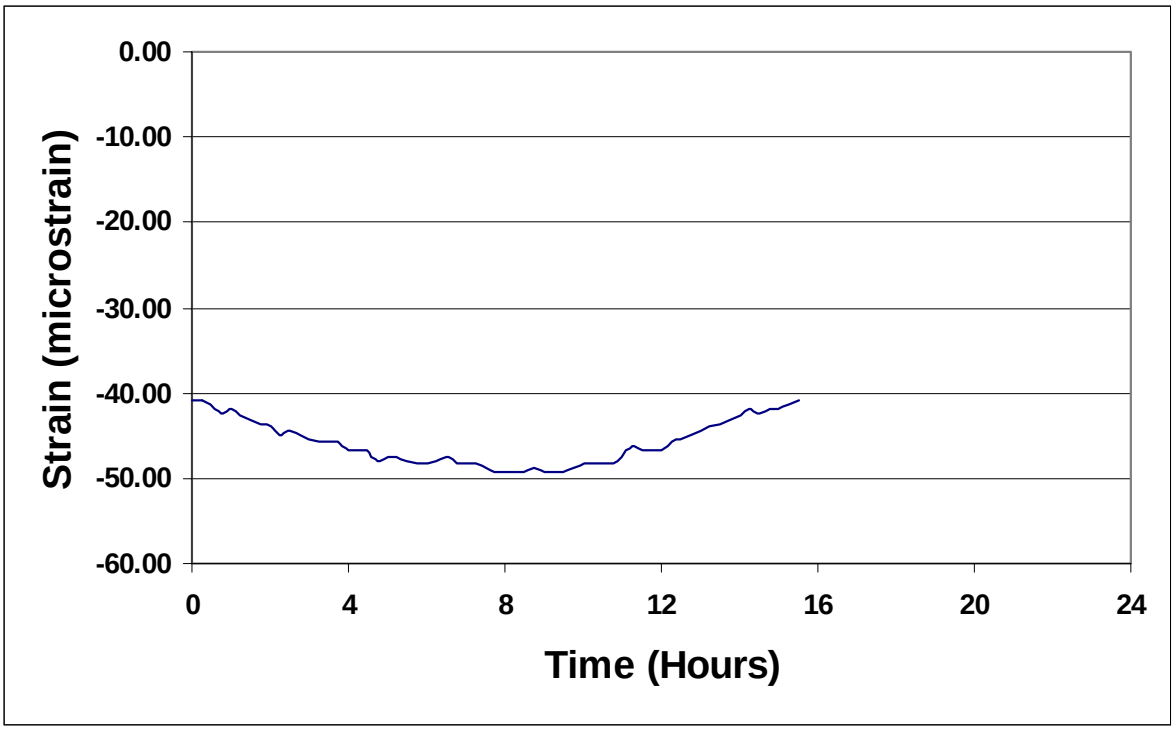

Figure B.95 Concrete Strain versus Time at Gage CG6 (Day 162).

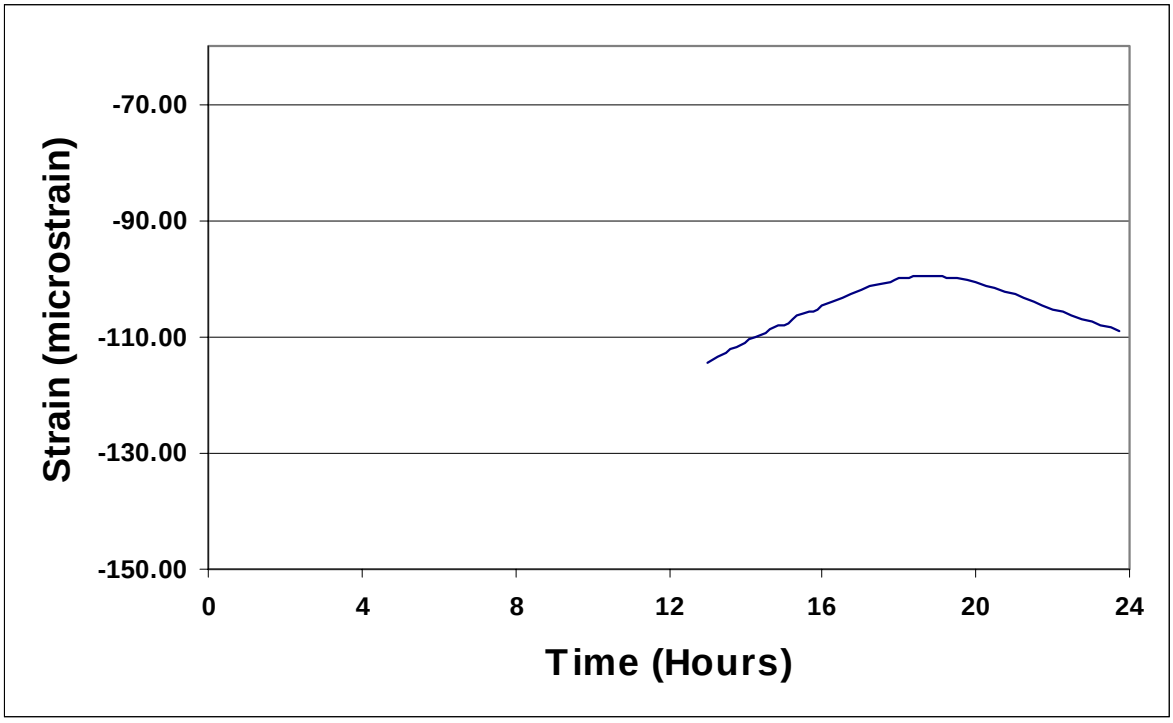

Figure B.96 Concrete Strain versus Time at Gage CG6 (Day 269).

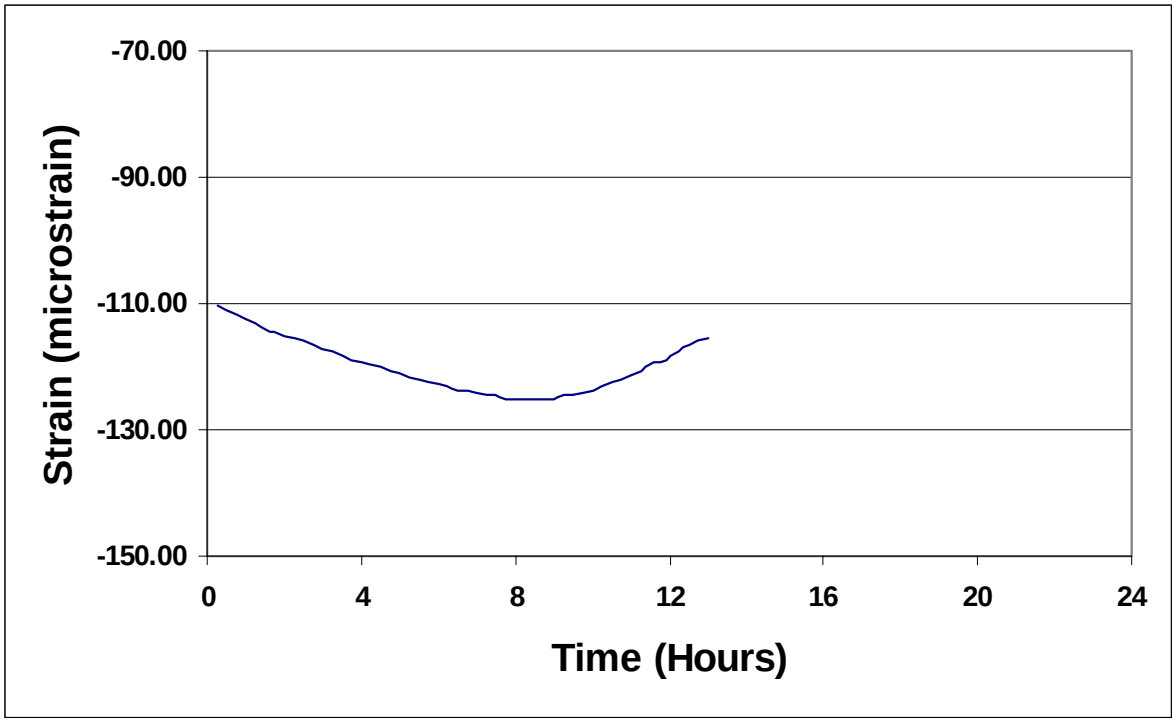

Figure B.97 Concrete Strain versus Time at Gage CG6 (Day 270).

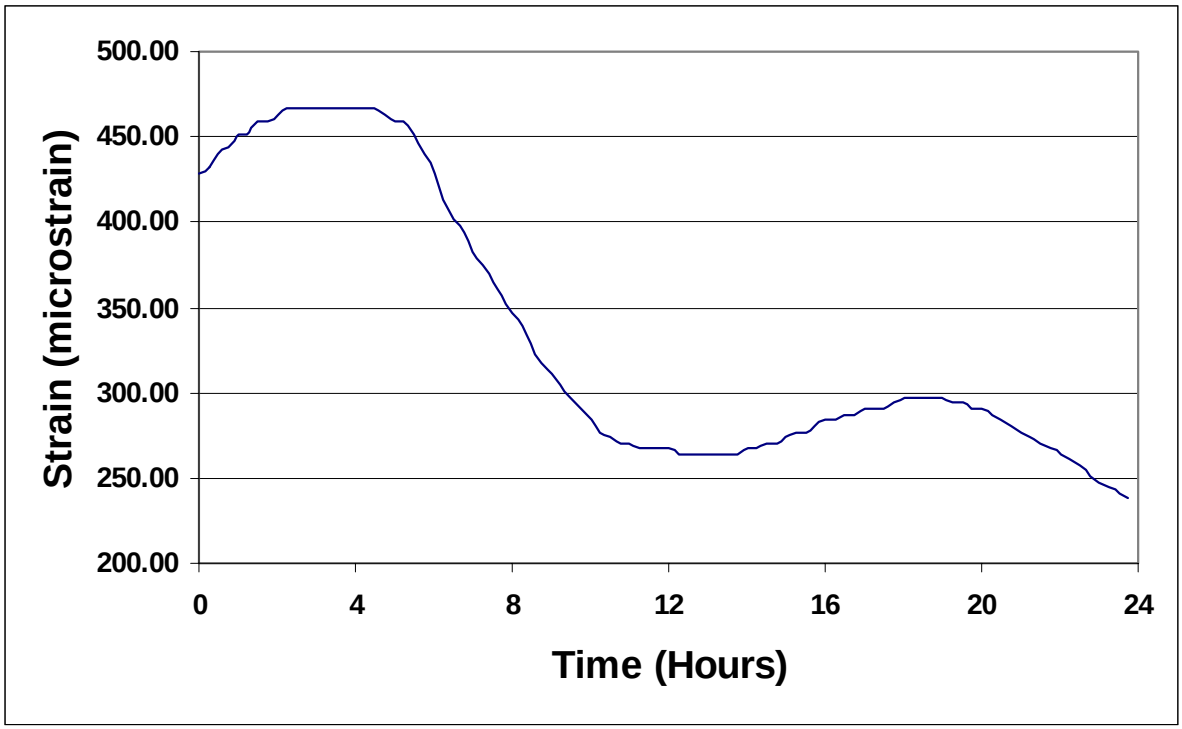

Figure B.98 Concrete Strain versus Time at Gage CG12 (Day 2).

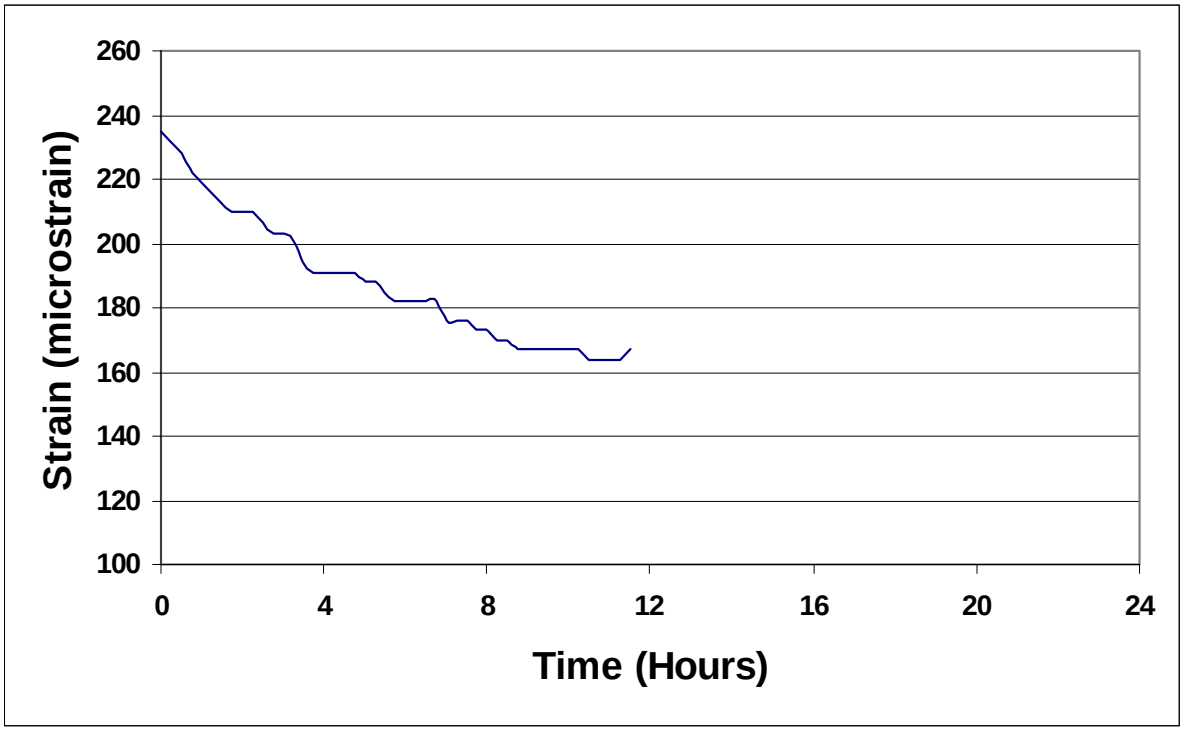

Figure B.99 Concrete Strain versus Time at Gage CG12 (Day 3).

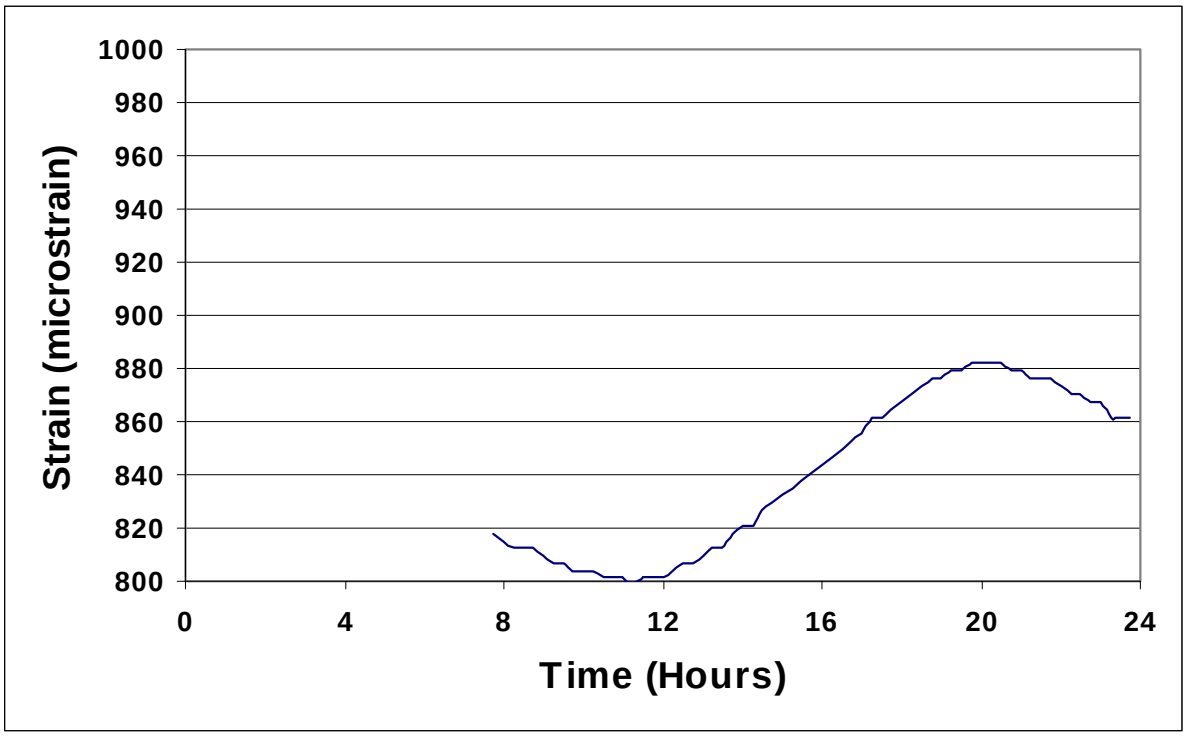

Figure B.100 Concrete Strain versus Time at Gage CG12 (Day 4).

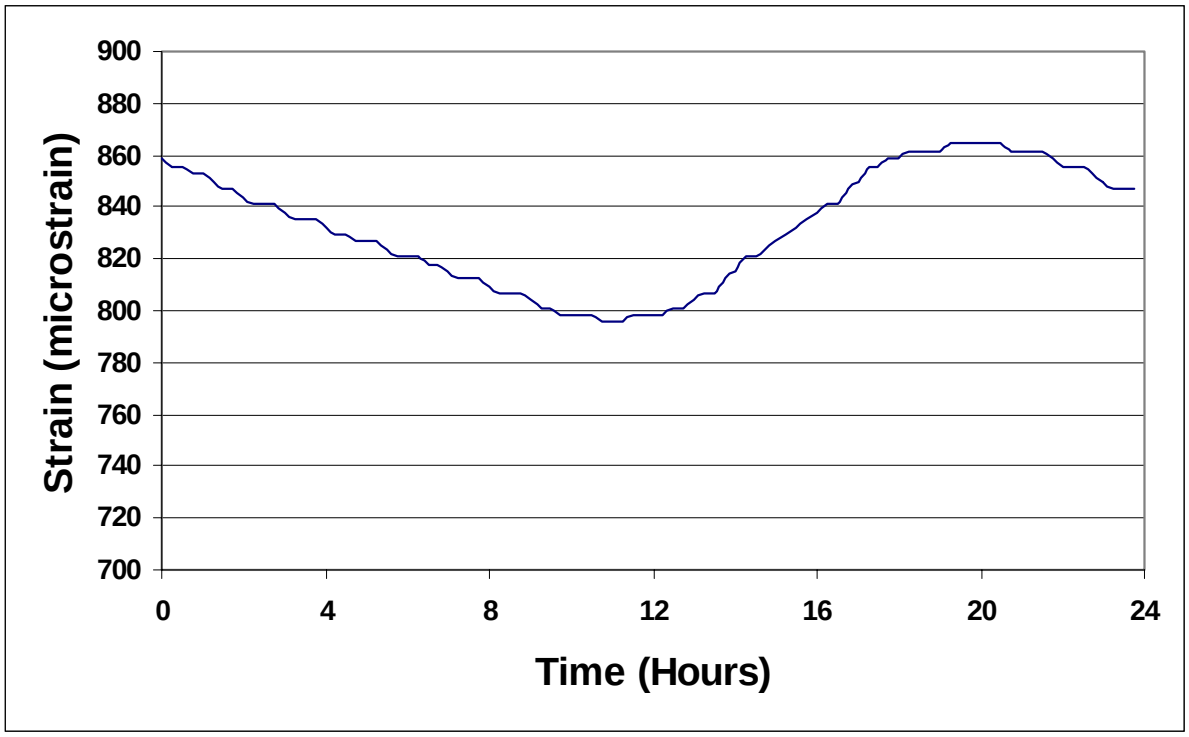

Figure B.101 Concrete Strain versus Time at Gage CG12 (Day 5).

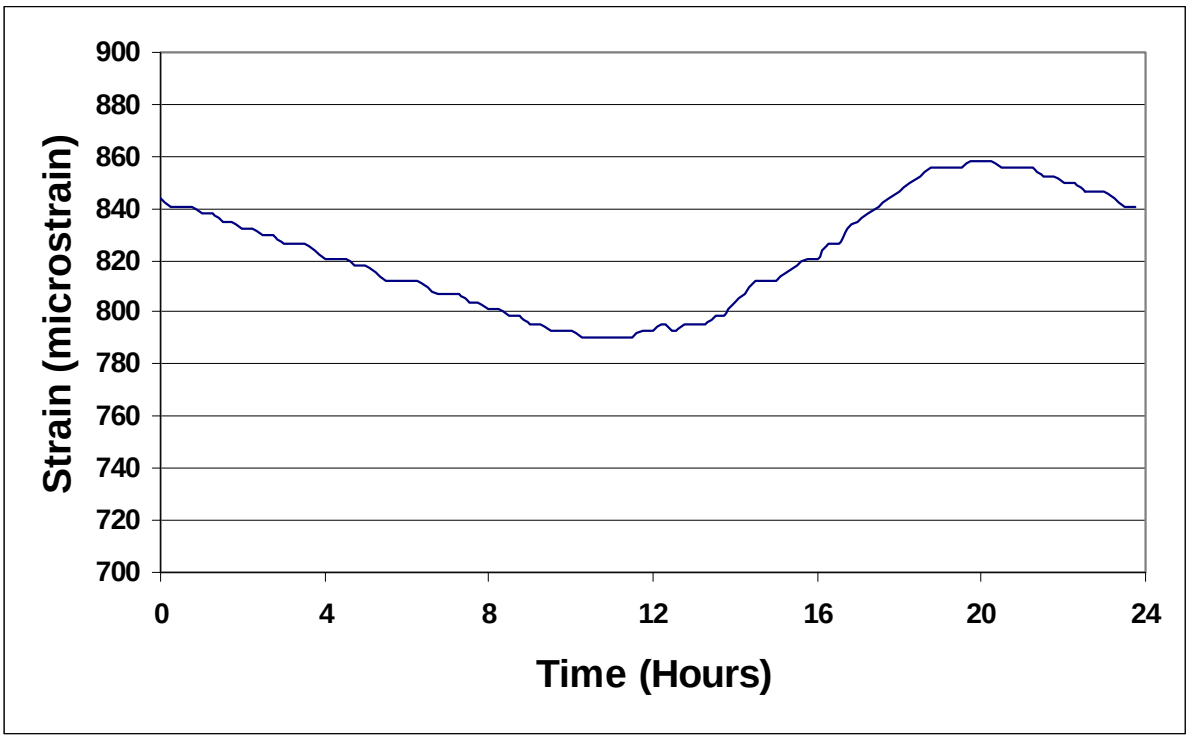

Figure B.102 Concrete Strain versus Time at Gage CG12 (Day 6).

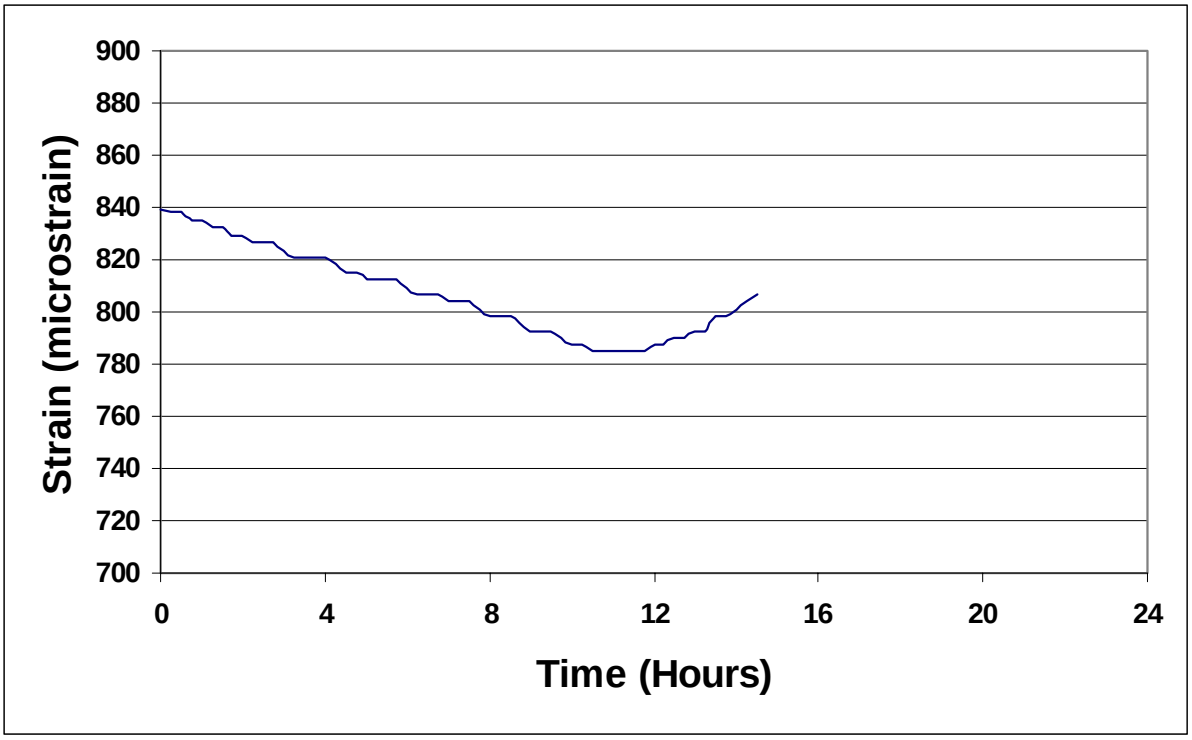

Figure B.103 Concrete Strain versus Time at CG12 (Day 7).

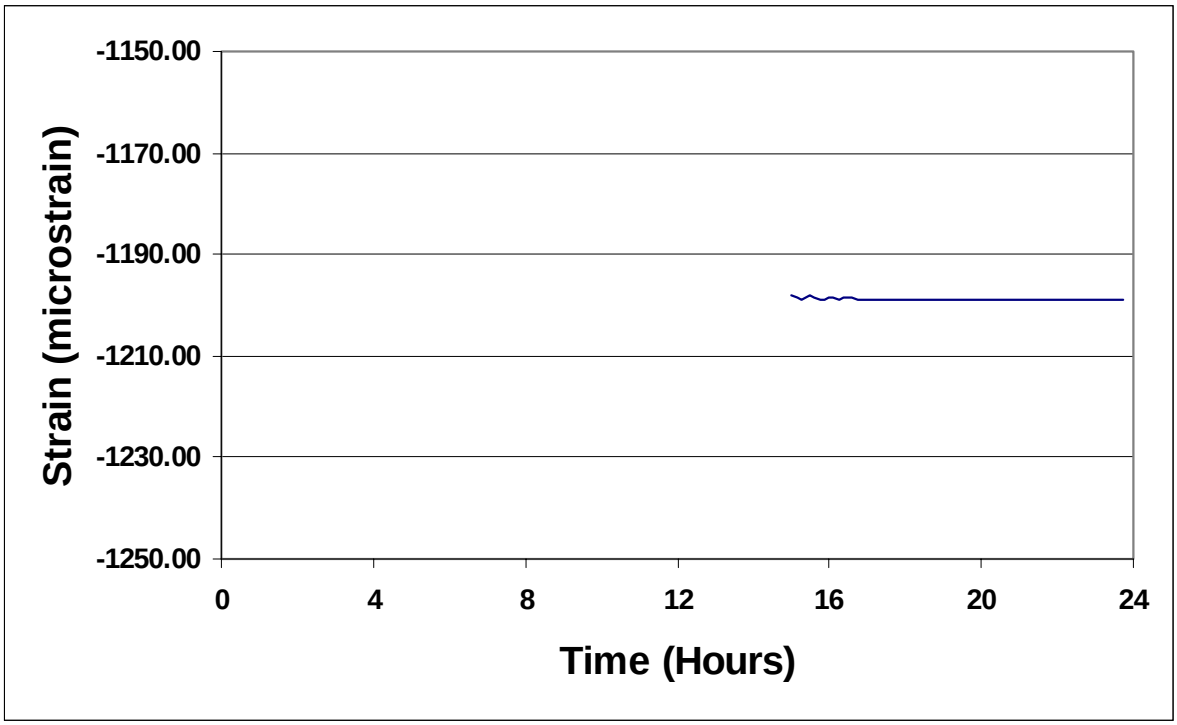

Figure B.104 Concrete Strain versus Time at CG12 (Day 15).

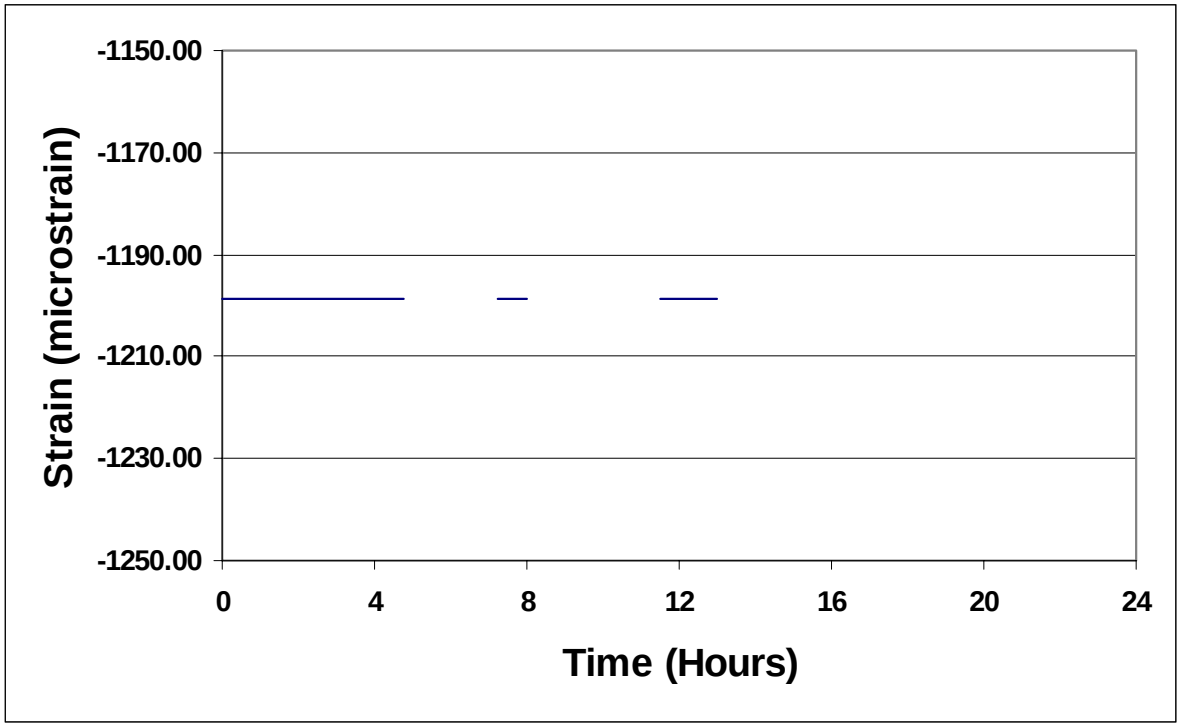

Figure B.105 Concrete Strain versus Time at Gage CG12 (Day 16).

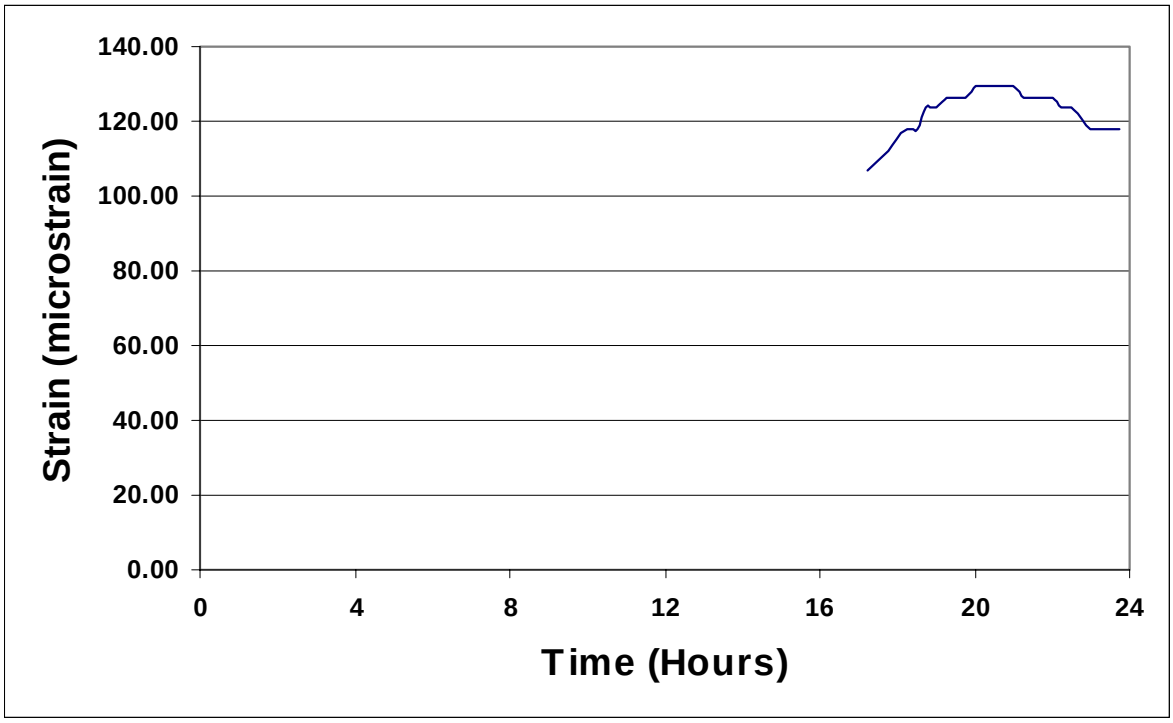

Figure B.106 Concrete Strain versus Time at Gage CG12 (Day 29).

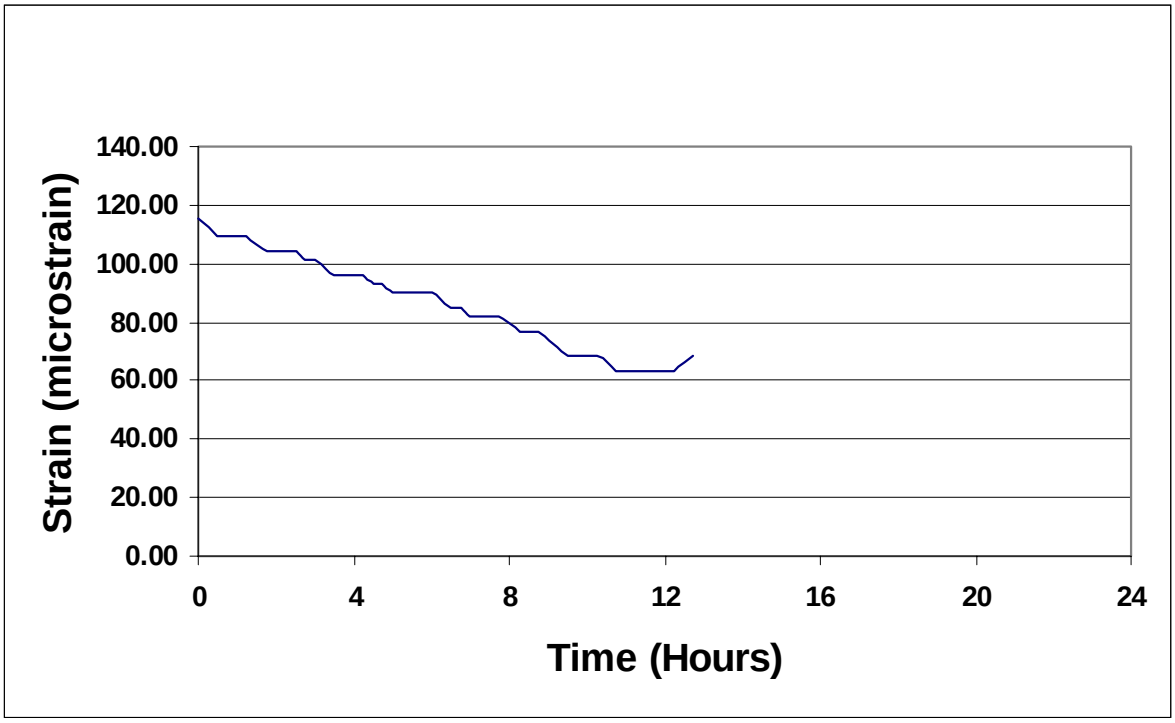

Figure B.107 Concrete Strain versus Time at Gage CG12 (Day 30).

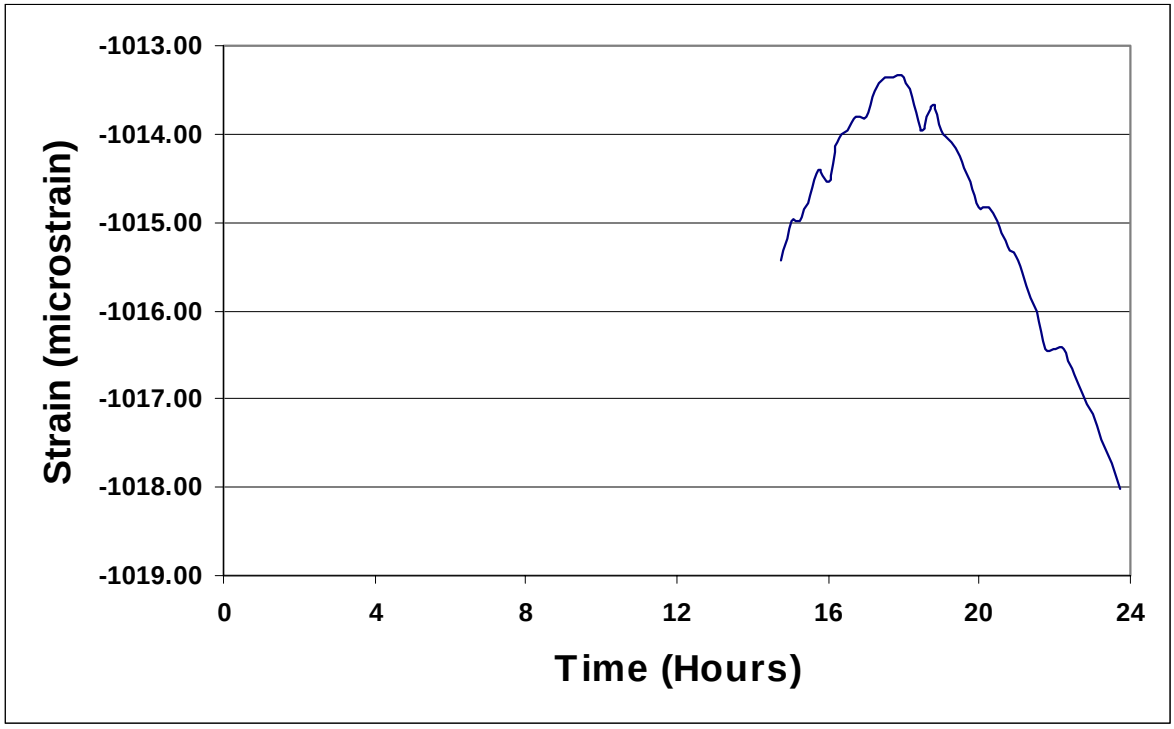

Figure B.108 Concrete Strain versus Time at Gage CG12 (Day 161).

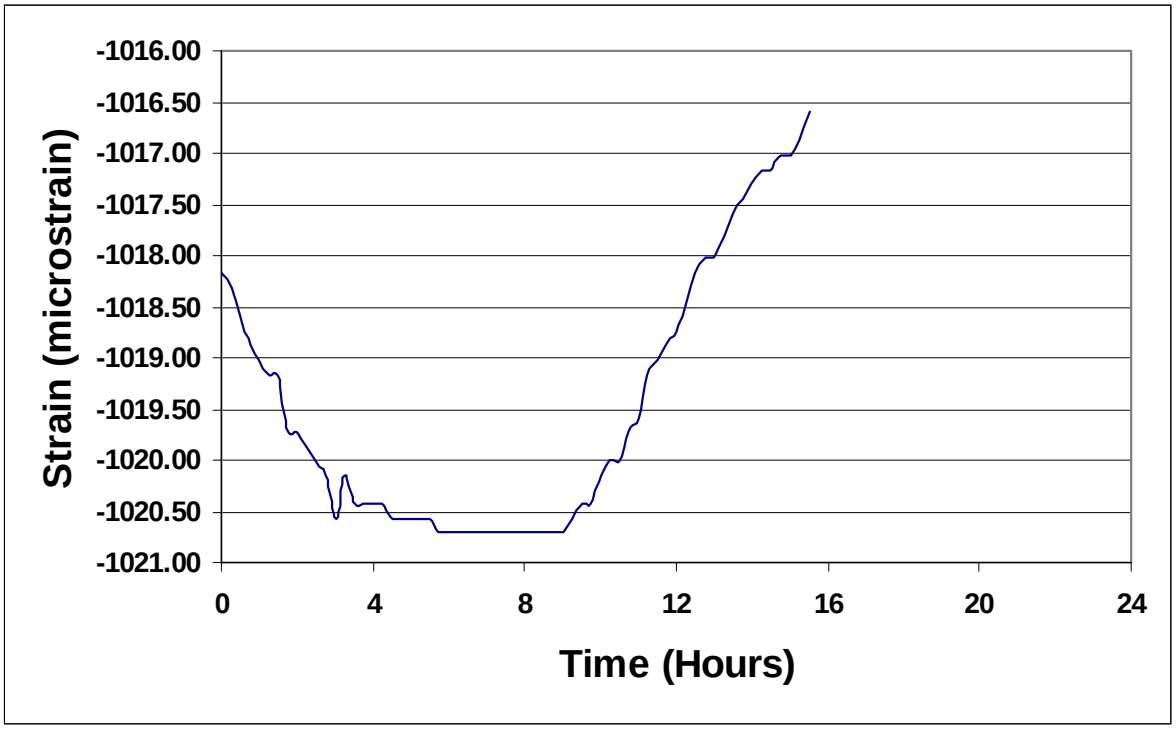

Figure B.109 Concrete Strain versus Time at Gage CG12 (Day 162).

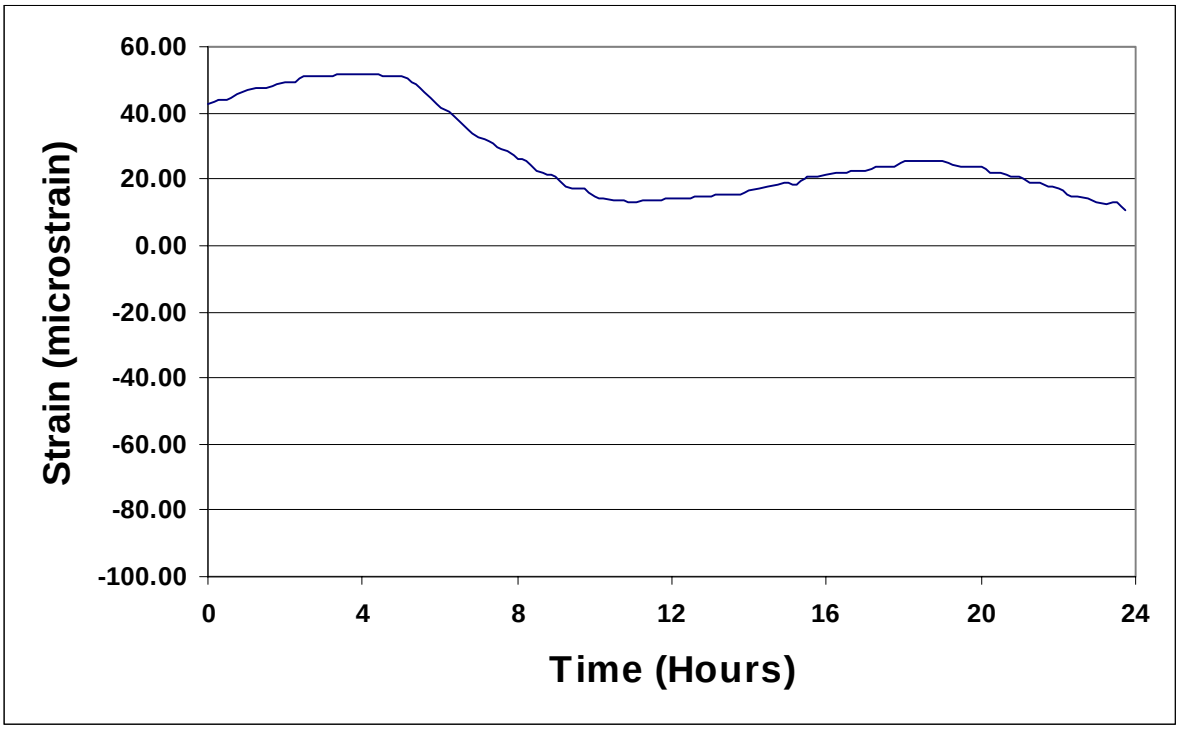

Figure B.110 Concrete Strain versus Time at Gage CG11 (Day 2).

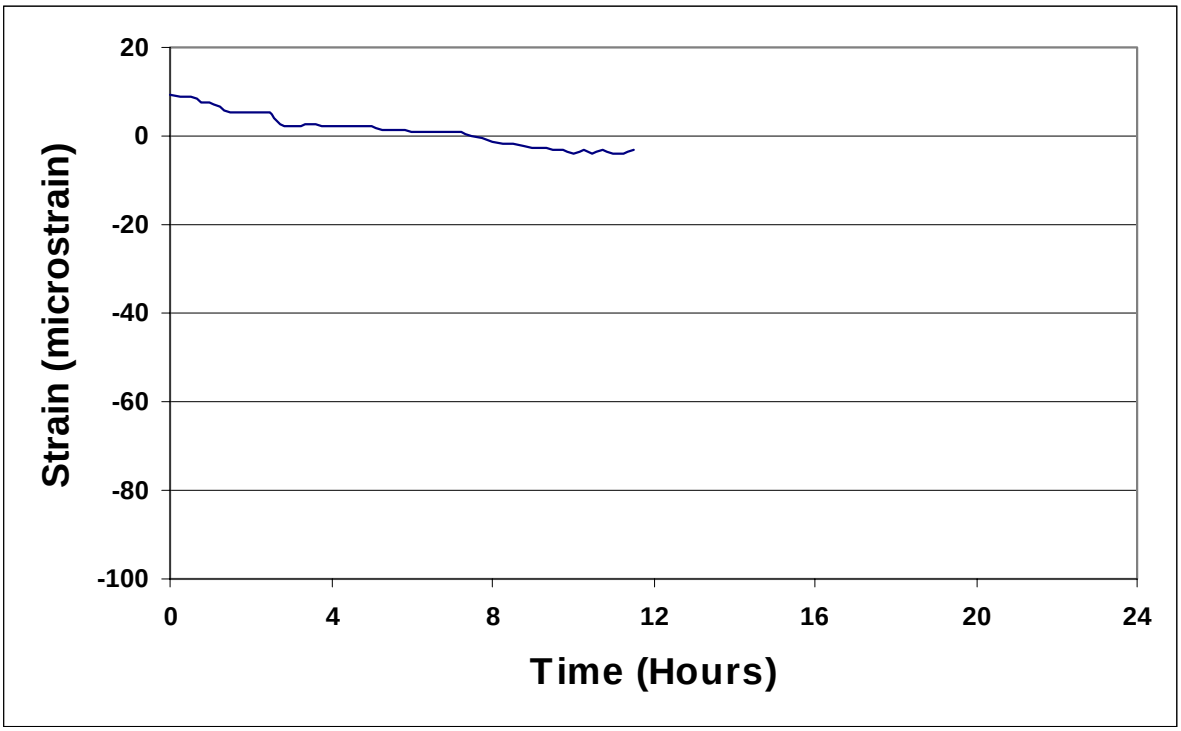

Figure B.111 Concrete Strain versus Time at Gage CG11 (Day 3).

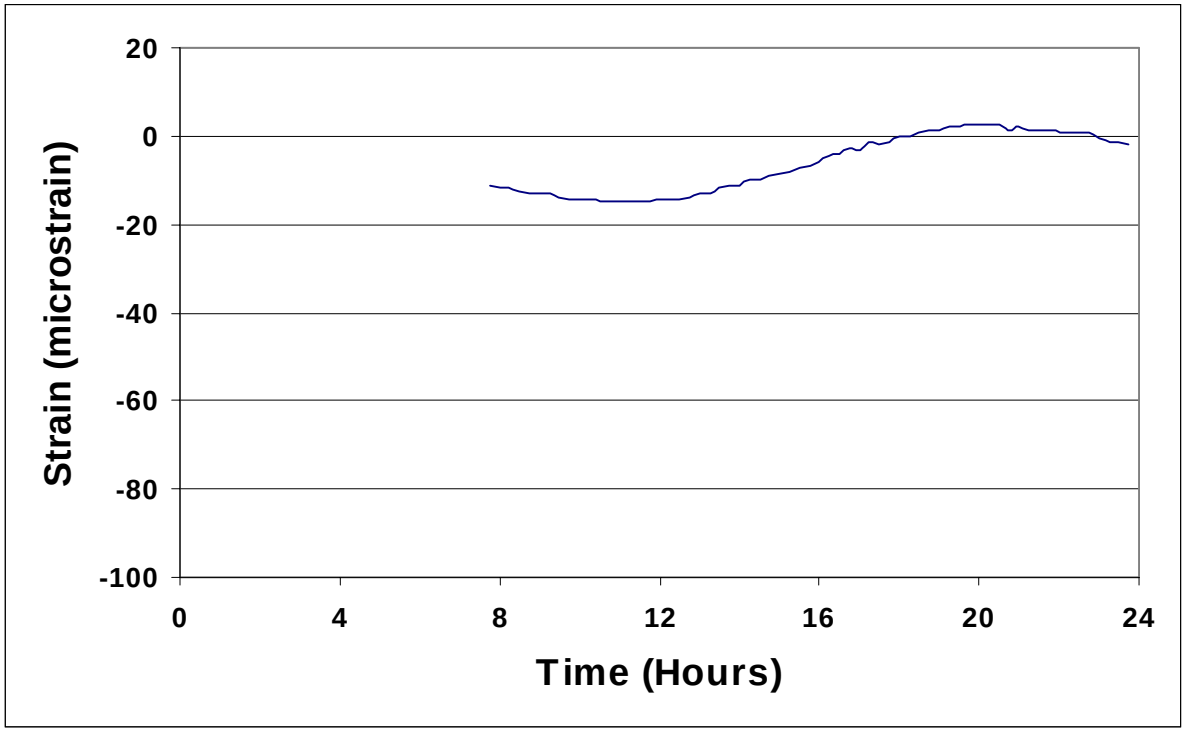

Figure B.112 Concrete Strain versus Time at Gage CG11 (Day 4)**.**

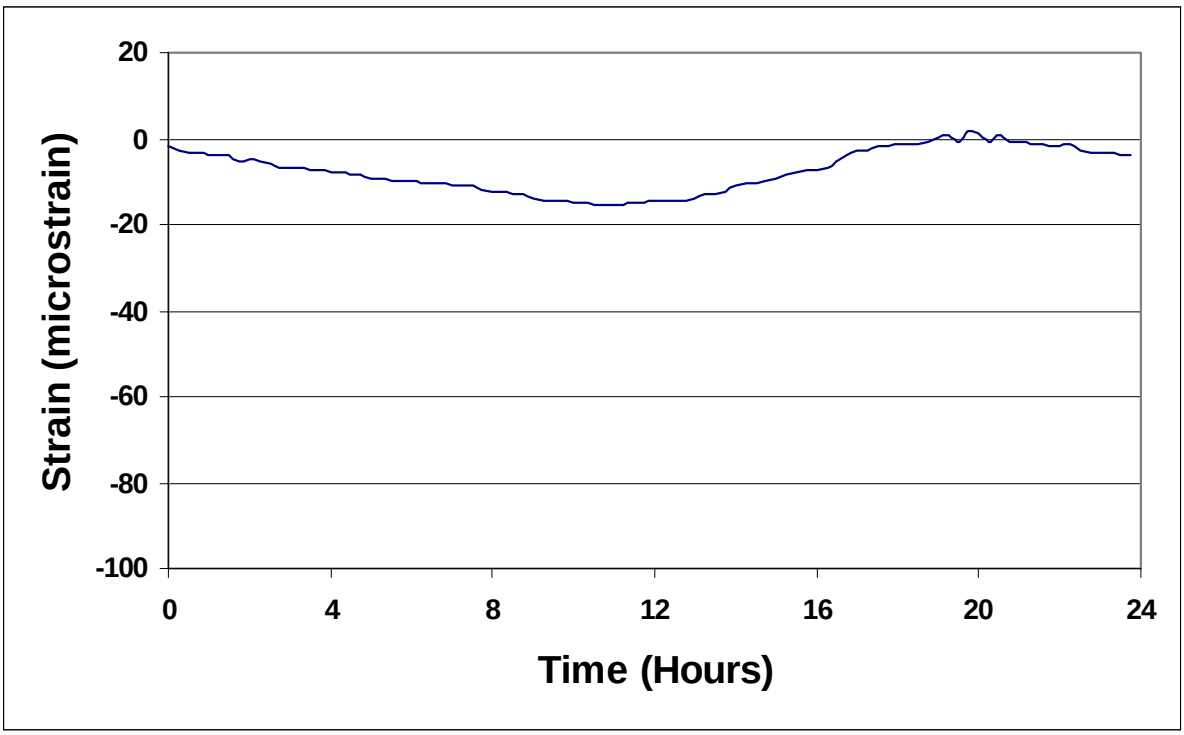

Figure B.113 Concrete Strain versus Time at Gage CG11 (Day 5).

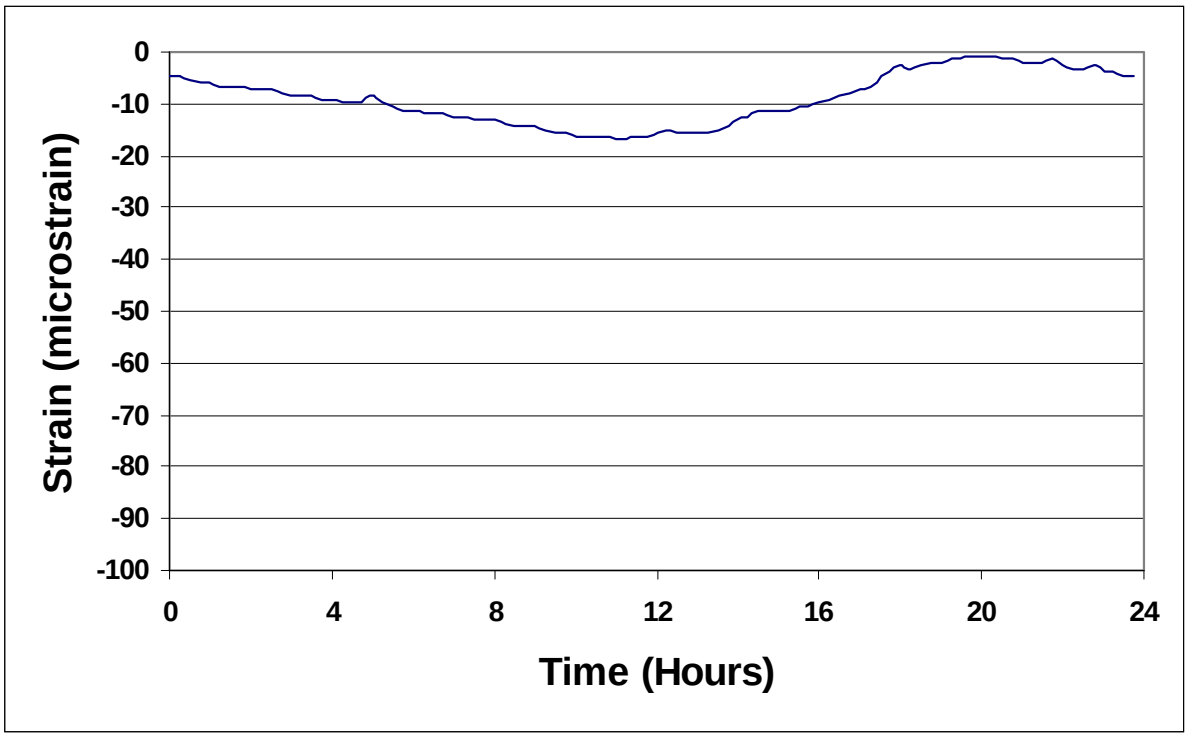

Figure B.114 Concrete Strain versus Time at Gage CG11 (Day 6).

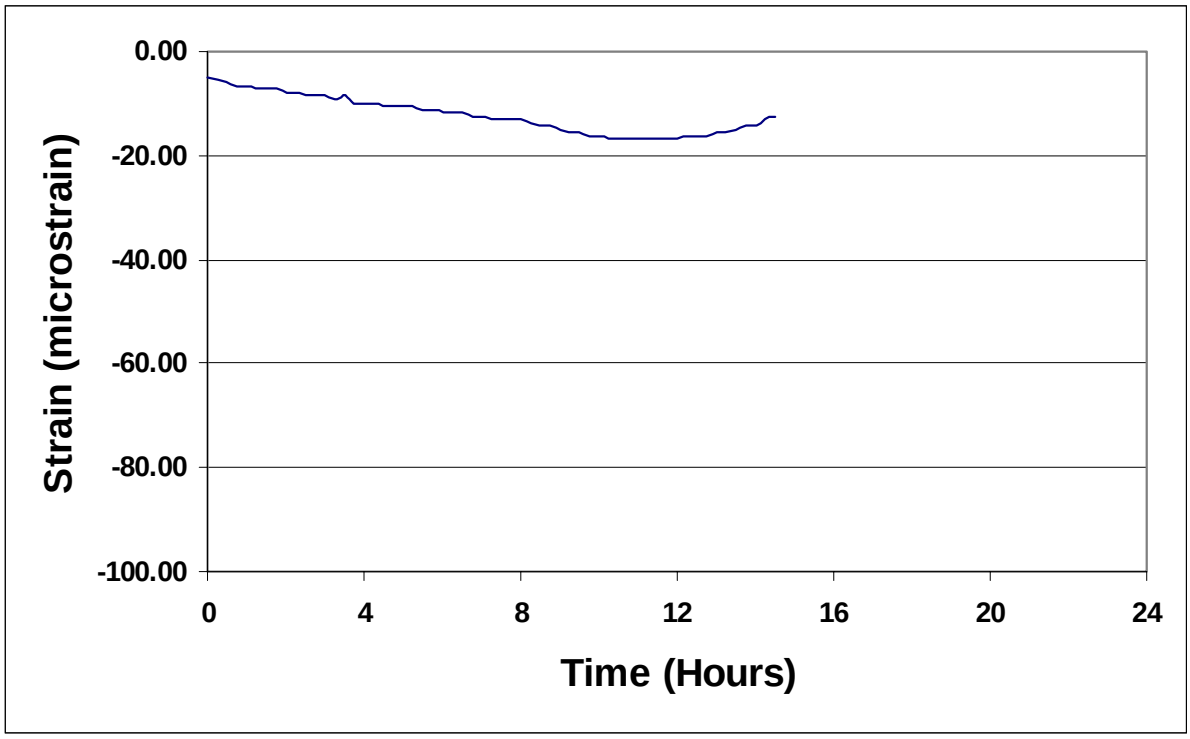

Figure B.115 Concrete Strain versus Time at Gage CG11 (Day 7).

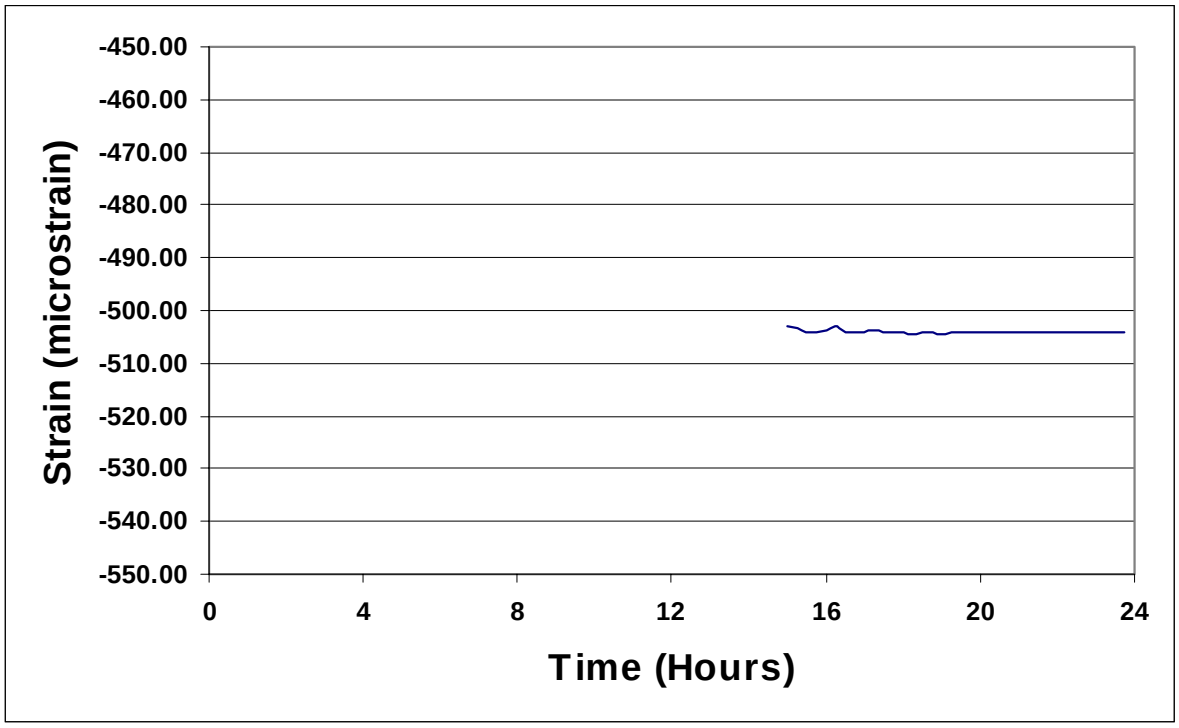

Figure B.116 Concrete Strain versus Time at Gage CG11 (Day 15).

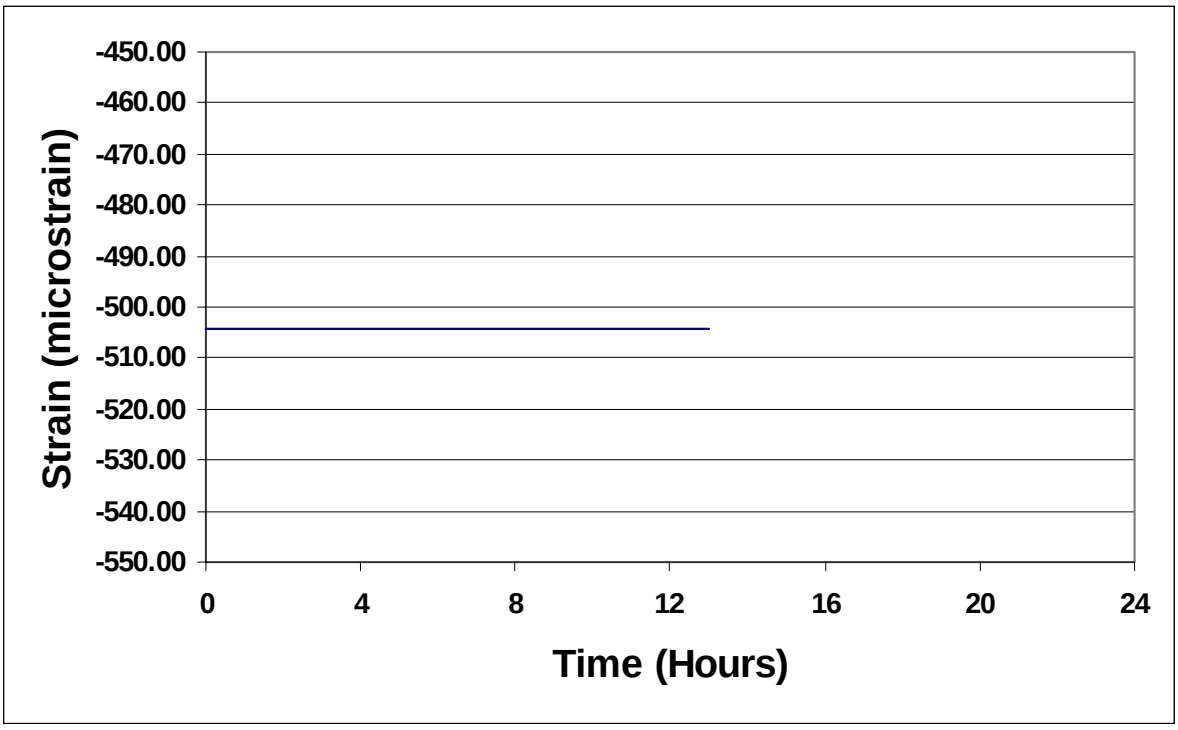

Figure B.117 Concrete Strain versus Time at Gage CG11 (Day 16).

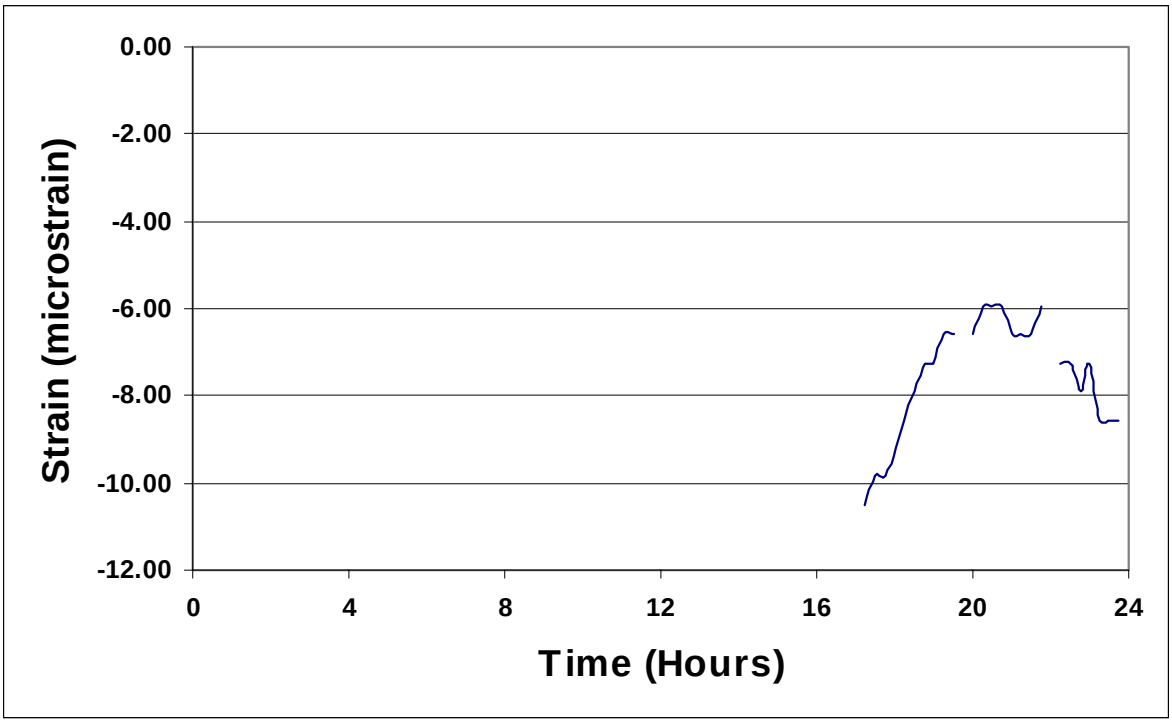

Figure B.118 Concrete Strain versus Time at Gage CG11 (Day 29).

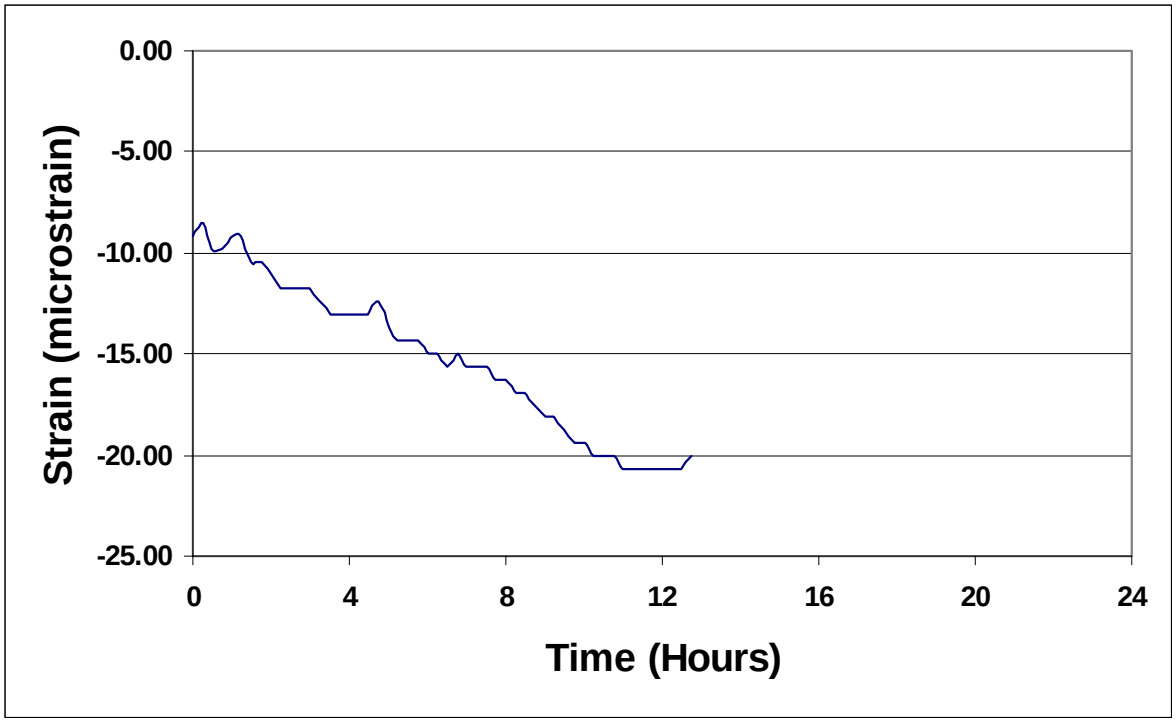

Figure B.119 Concrete Strain versus Time at Gage CG11 (Day 30).

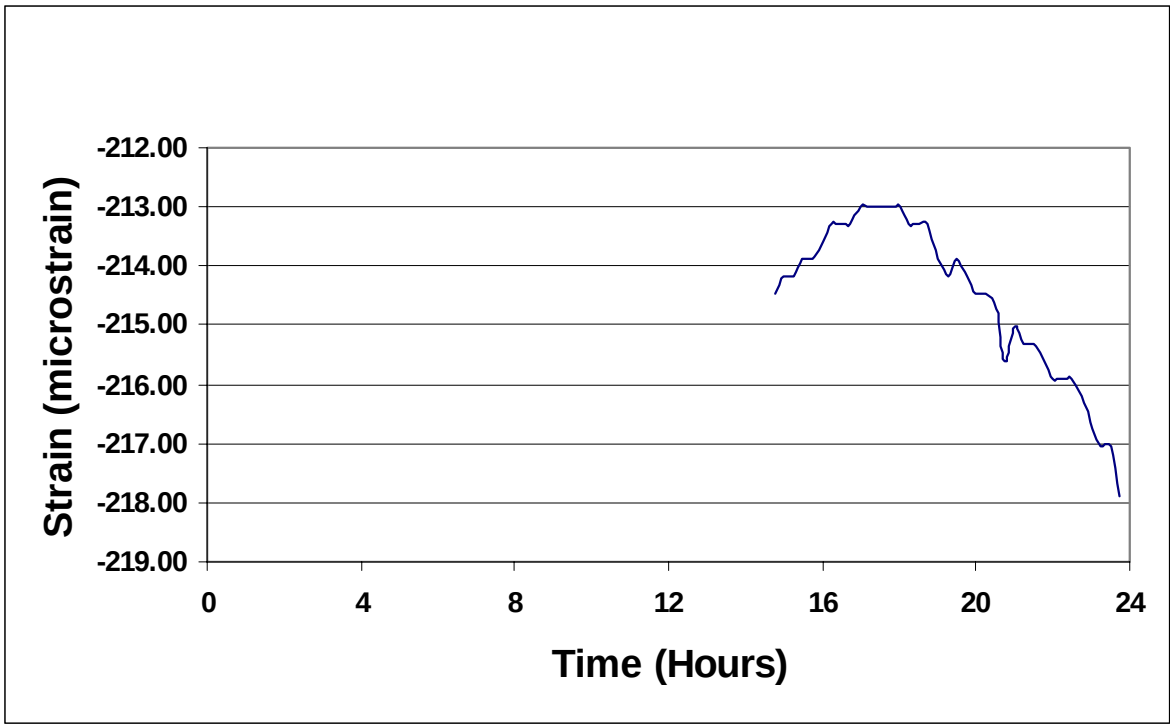

Figure B.120 Concrete Strain versus Time at Gage CG11 (Day 161).

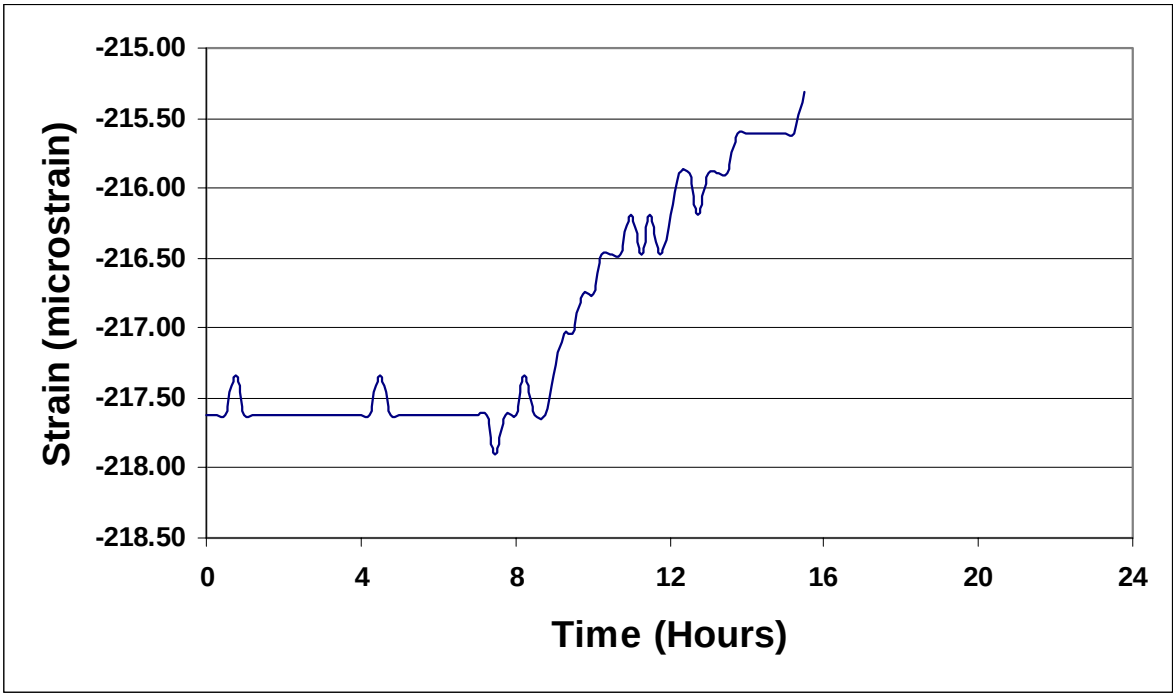

Figure B.121 Concrete Strain versus Time at Gage CG11 (Day 162).

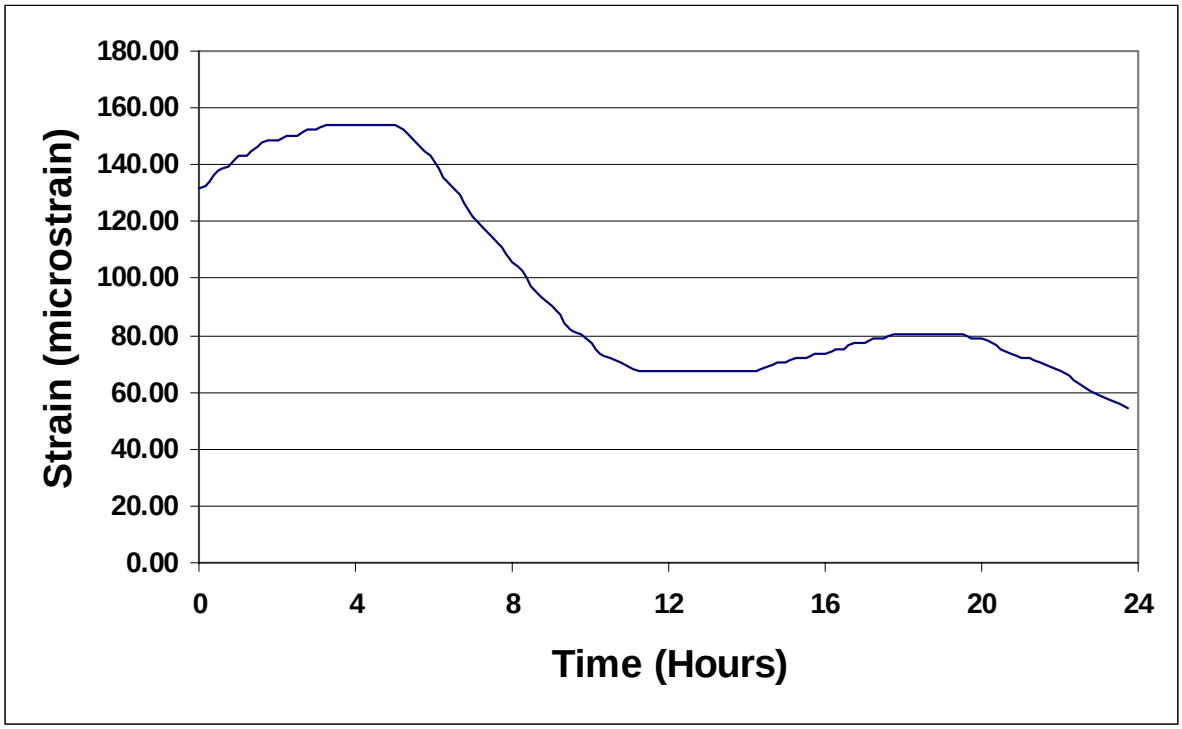

Figure B.122 Concrete Strain versus Time at Gage CG13 (Day 2).

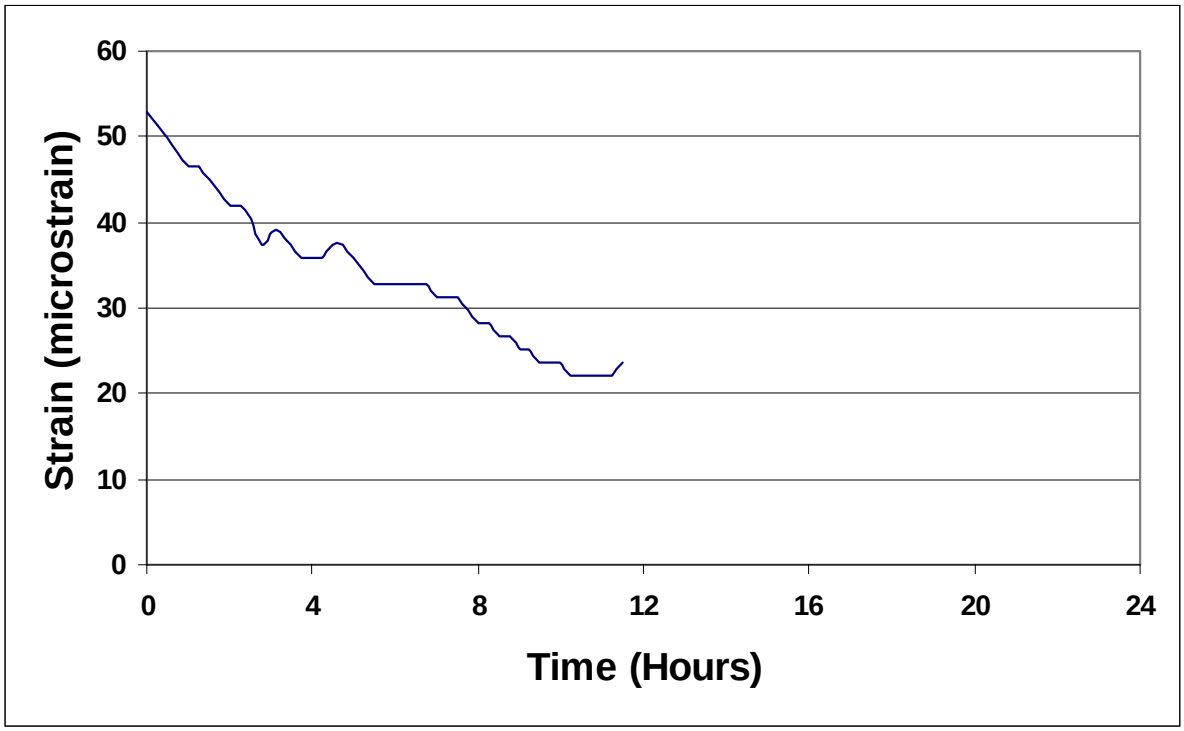

Figure B.123 Concrete Strain versus Time at Gage CG13 (Day 3).

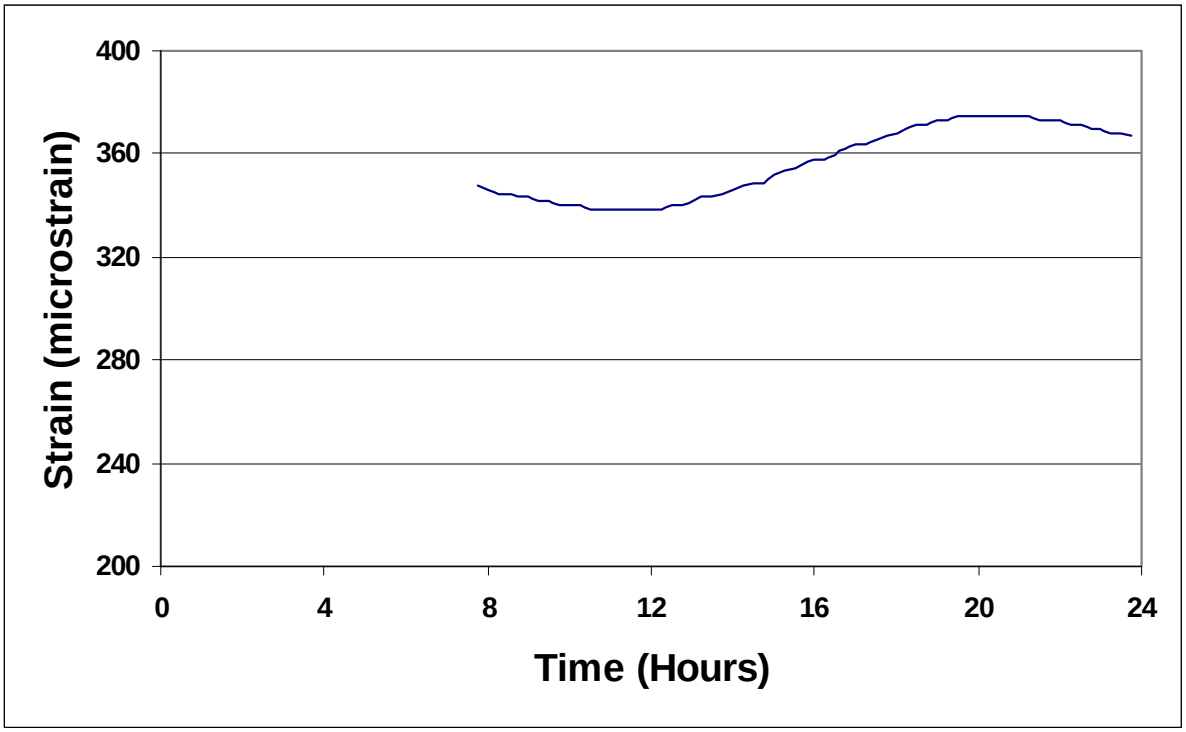

Figure B.124 Concrete Strain versus Time at Gage CG13 (Day 4).

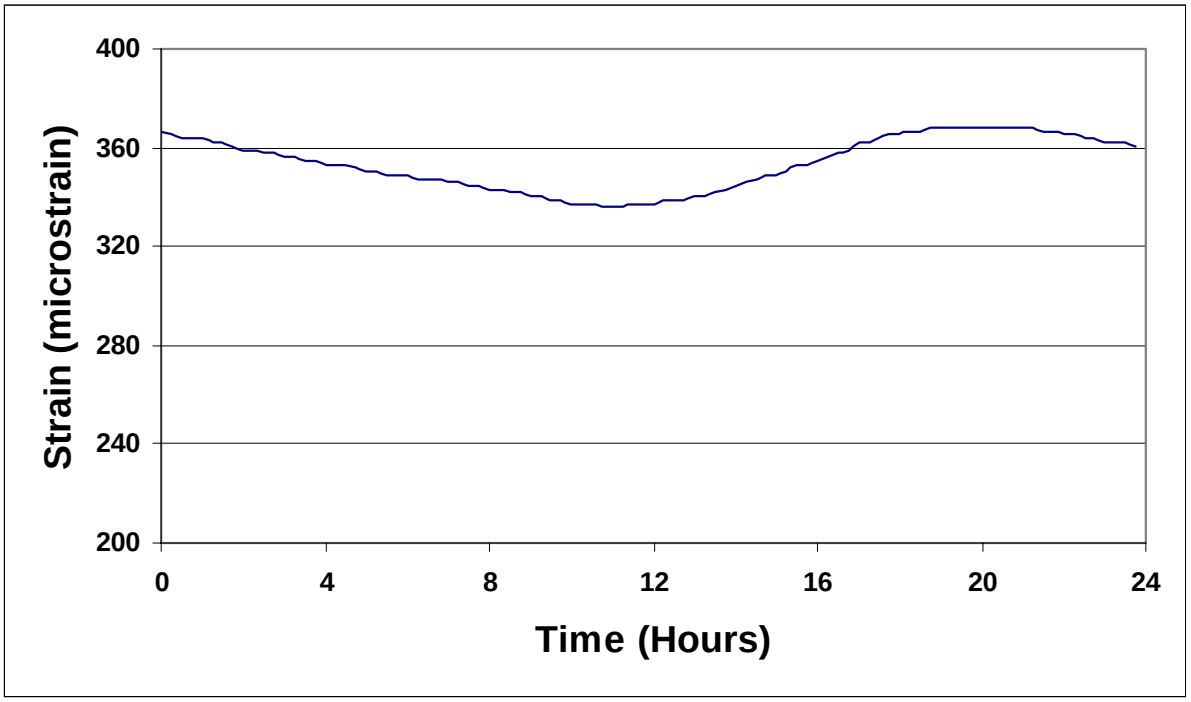

Figure B.125 Concrete Strain versus Time at Gage CG13 (Day 5).

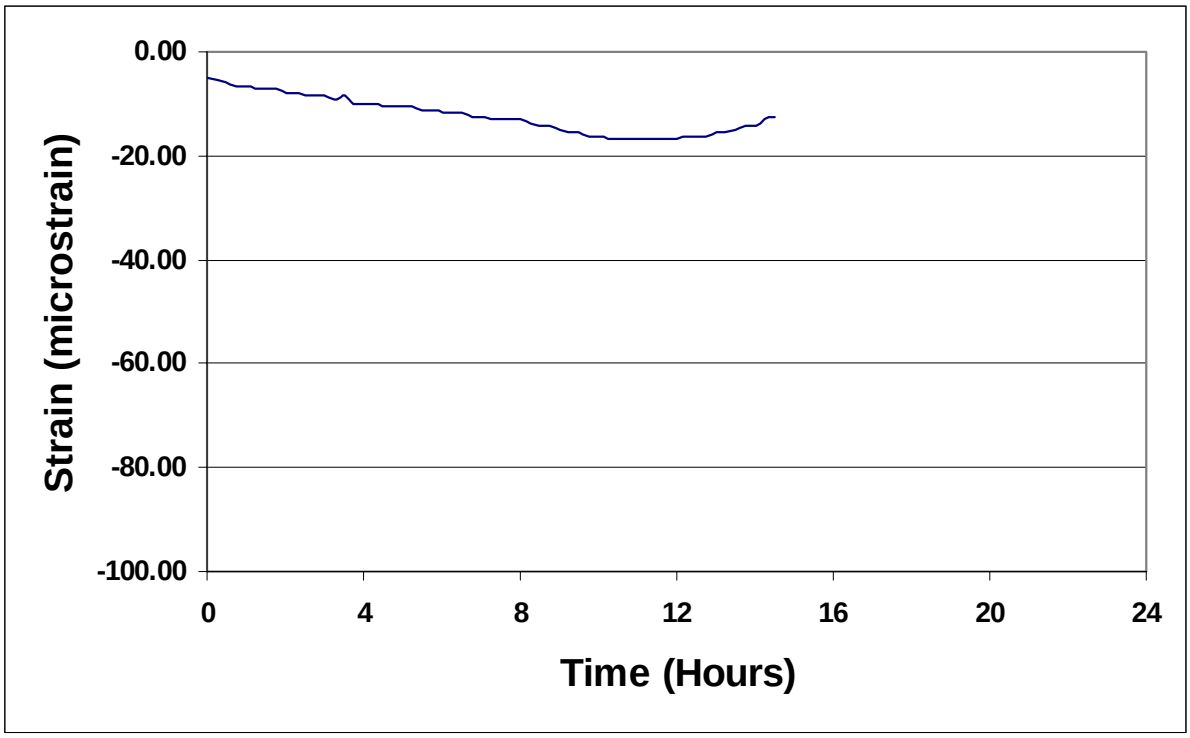

Figure B.126 Concrete Strain versus Time at Gage CG13 (Day 6).

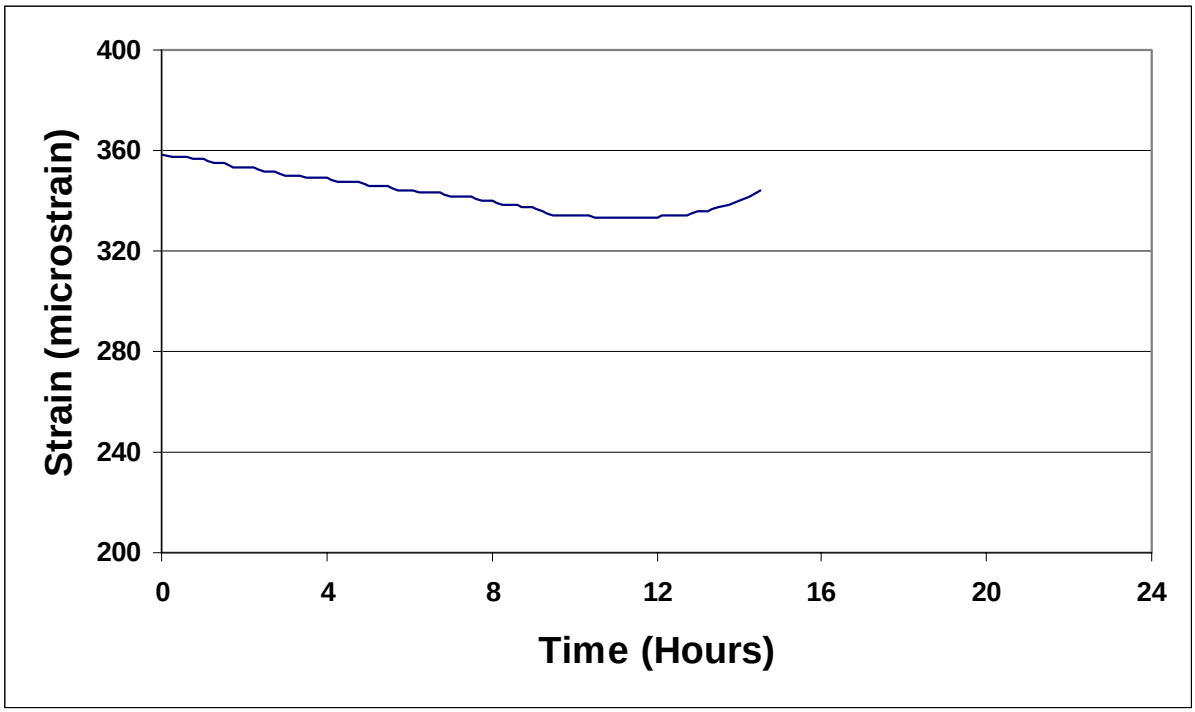

Figure B.127 Concrete Strain versus Time at Gage CG13 (Day 7).

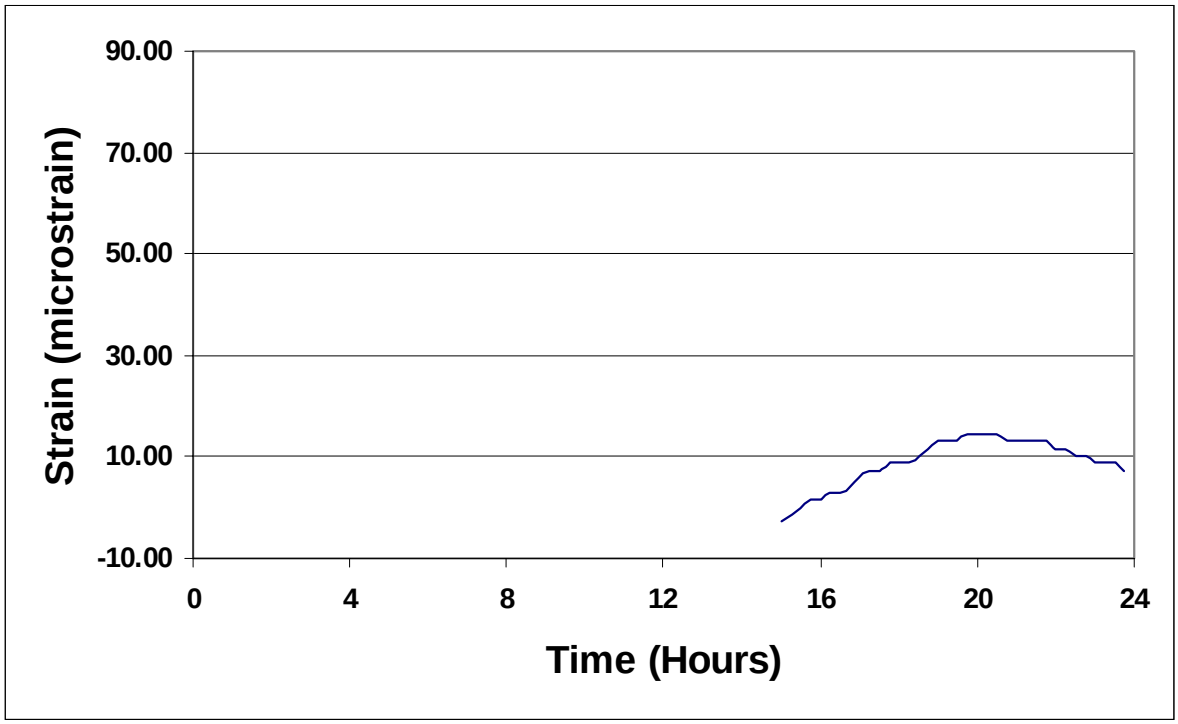

Figure B.128 Concrete Strain versus Time at Gage CG13 (Day 15).

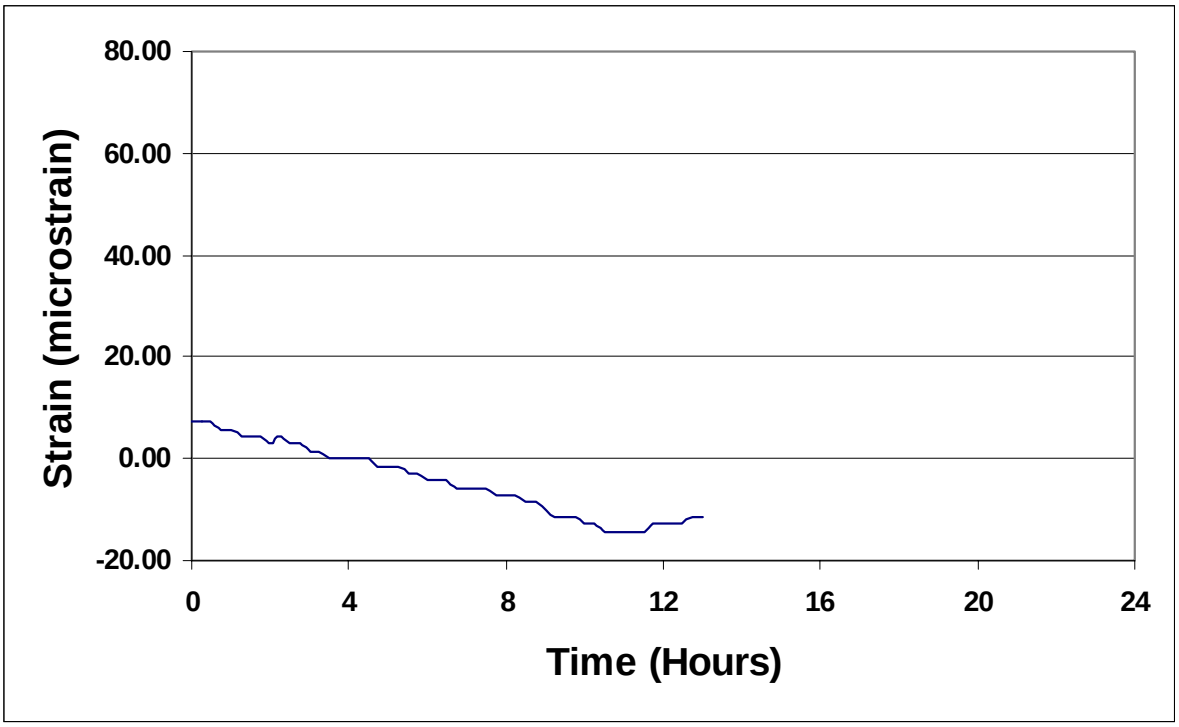

Figure B.129 Concrete Strain versus Time at Gage CG13 (Day 16).

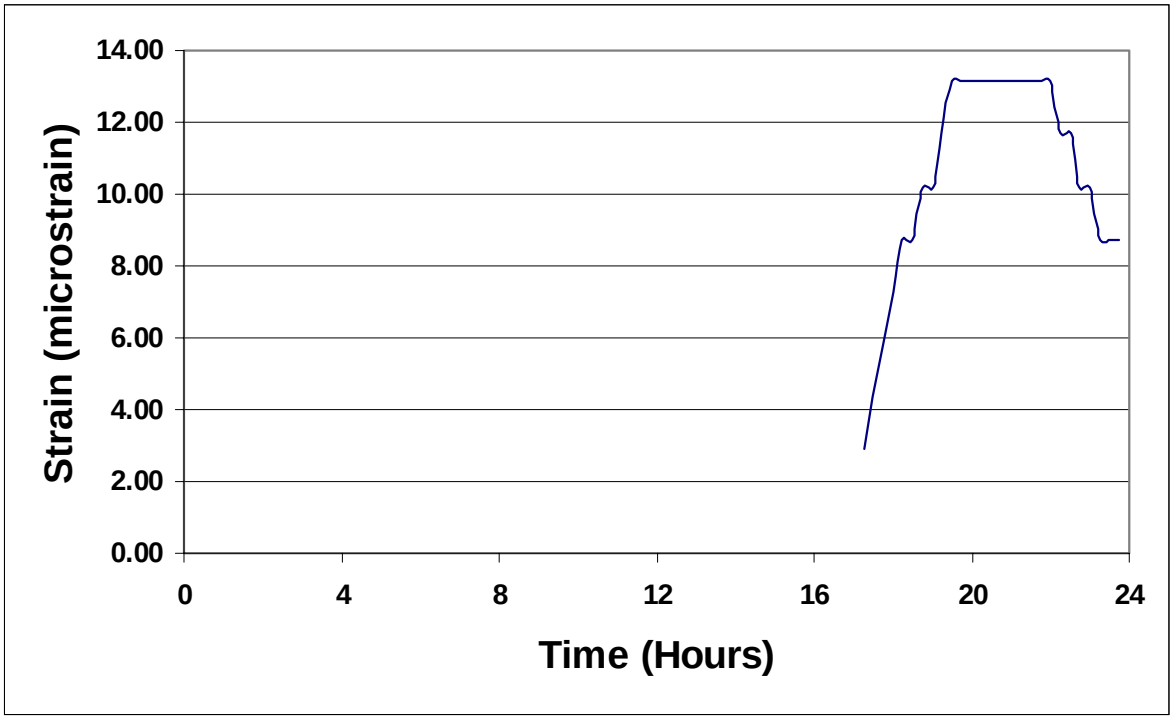

Figure B.130 Concrete Strain versus Time at Gage CG13 (Day 29).

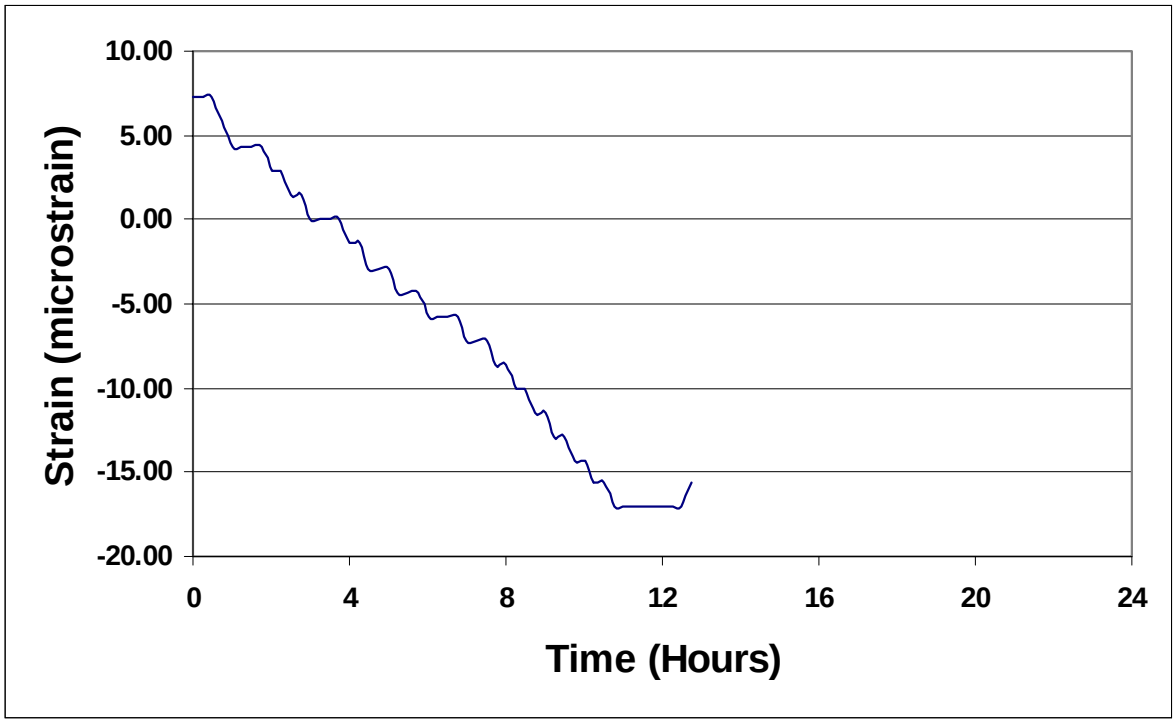

Figure B.131 Concrete Strain versus Time at Gage CG13 (Day 30).

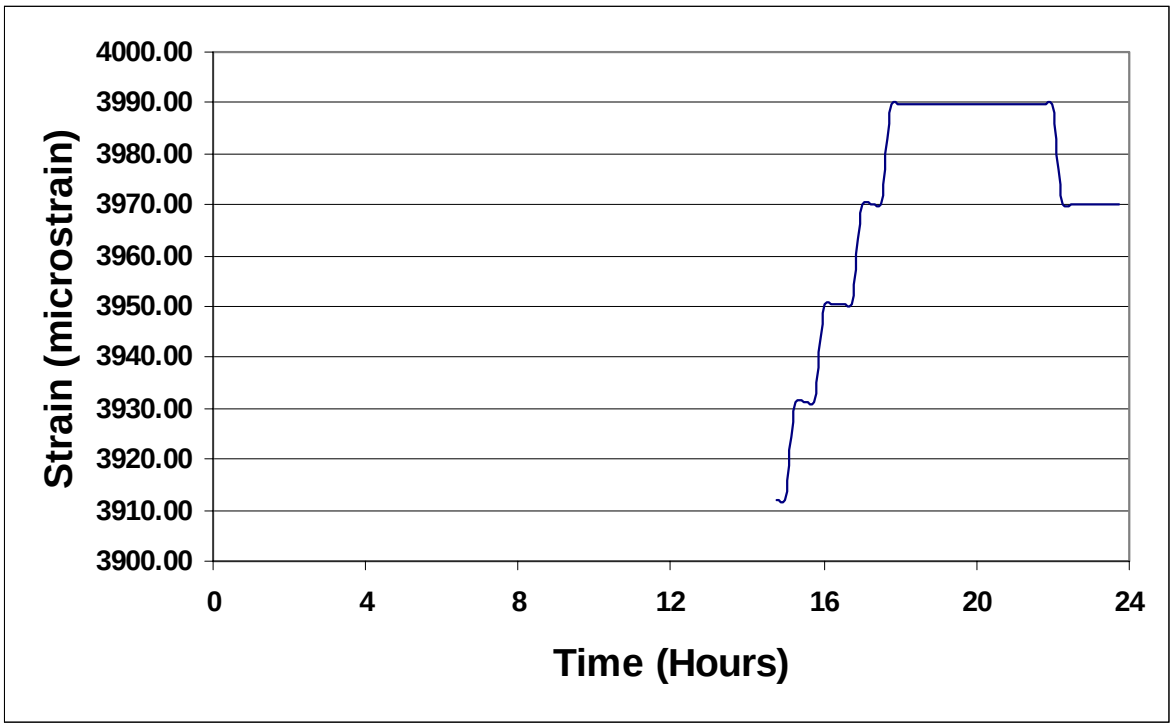

Figure B.132 Concrete Strain versus Time at Gage CG13 (Day 161).

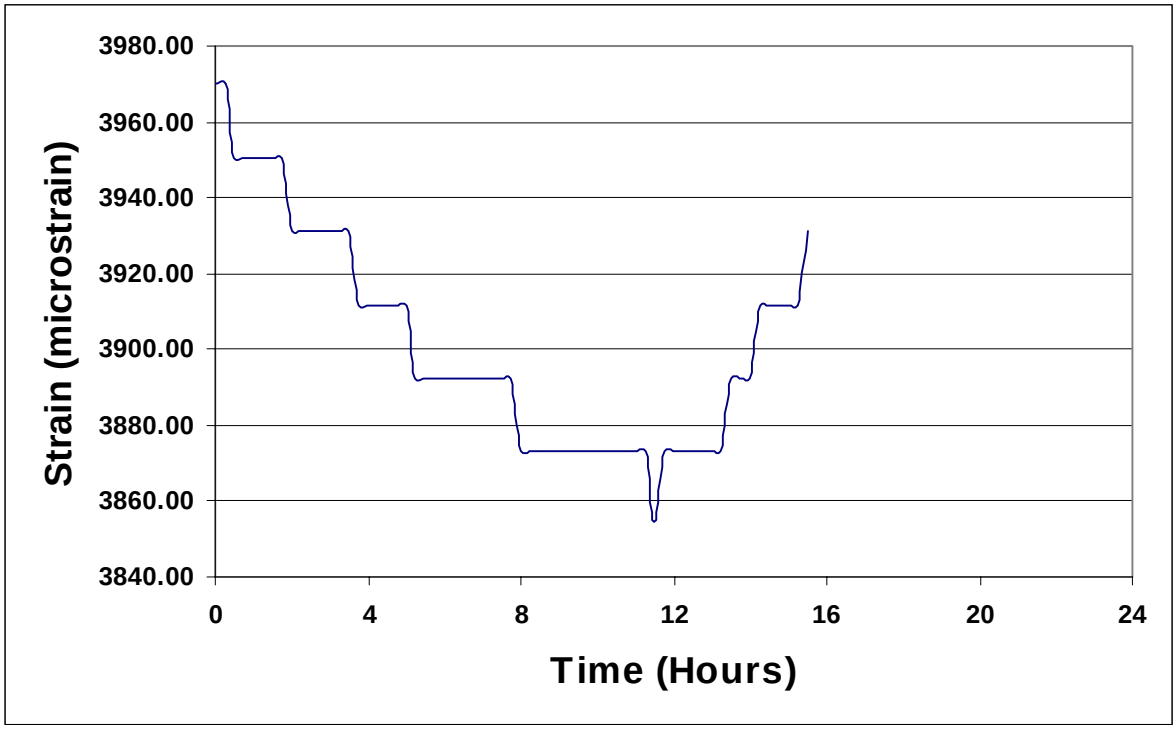

Figure B.133 Concrete Strain versus Time at Gage CG13 (Day 162).

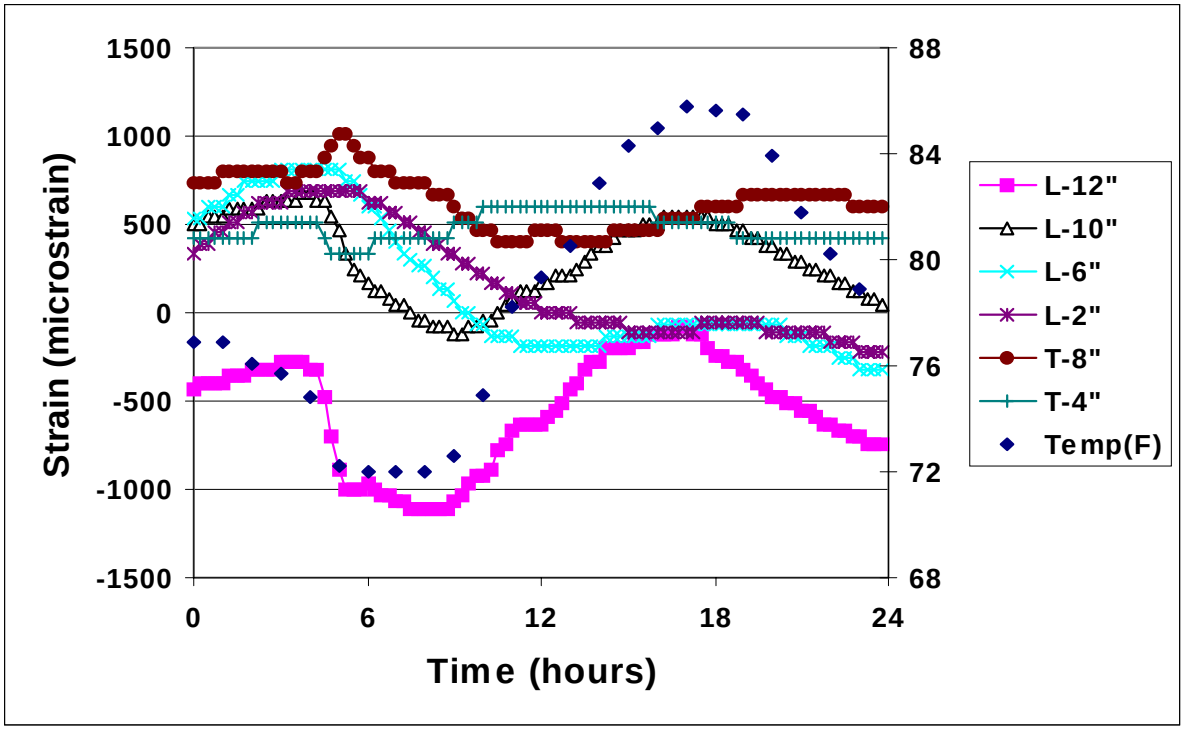

Figure B.134 Concrete Strain at Varying Depths versus Time (Day 2).

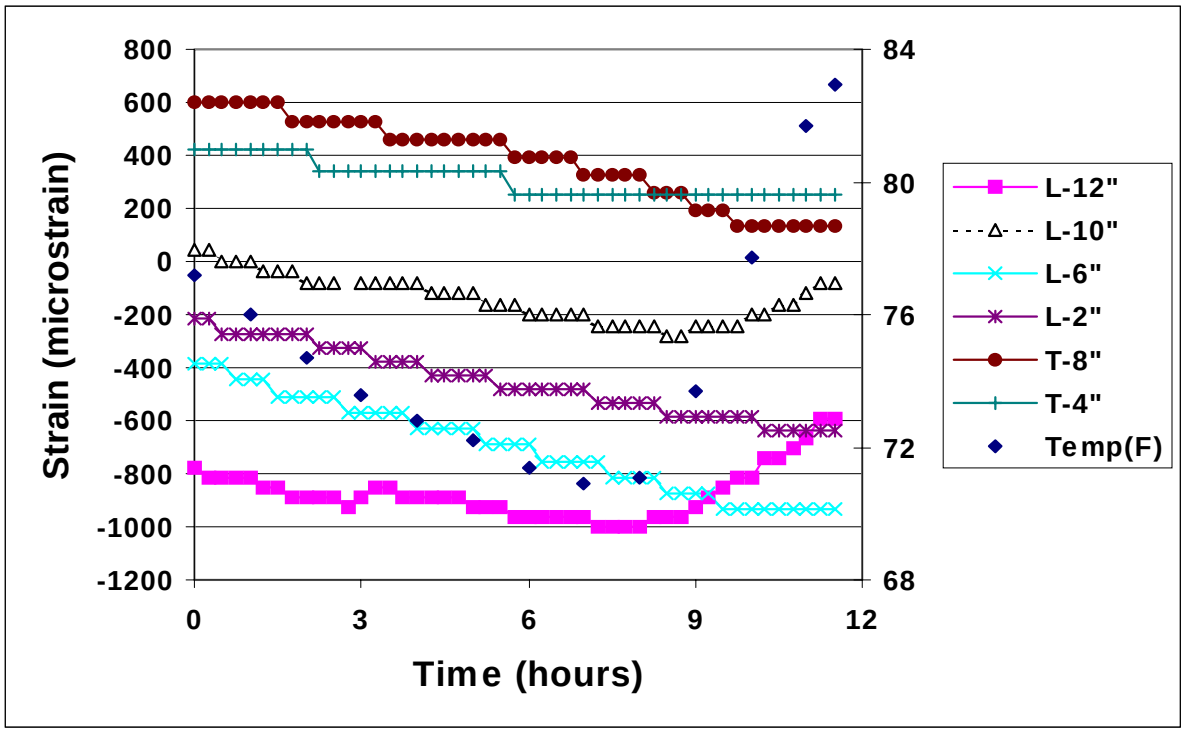

Figure B.135 Concrete Strain at Varying Depths versus Time (Day 3).

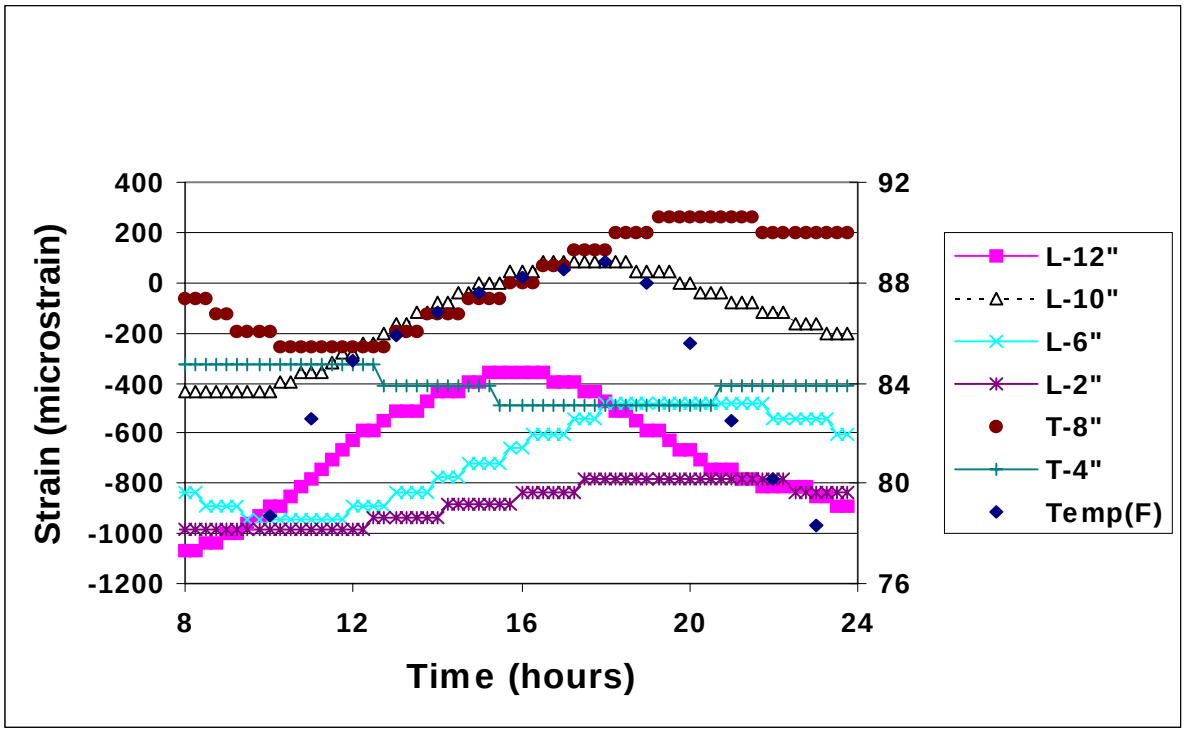

Figure B.136 Concrete Strain at Varying Depths versus Time (Day 4).

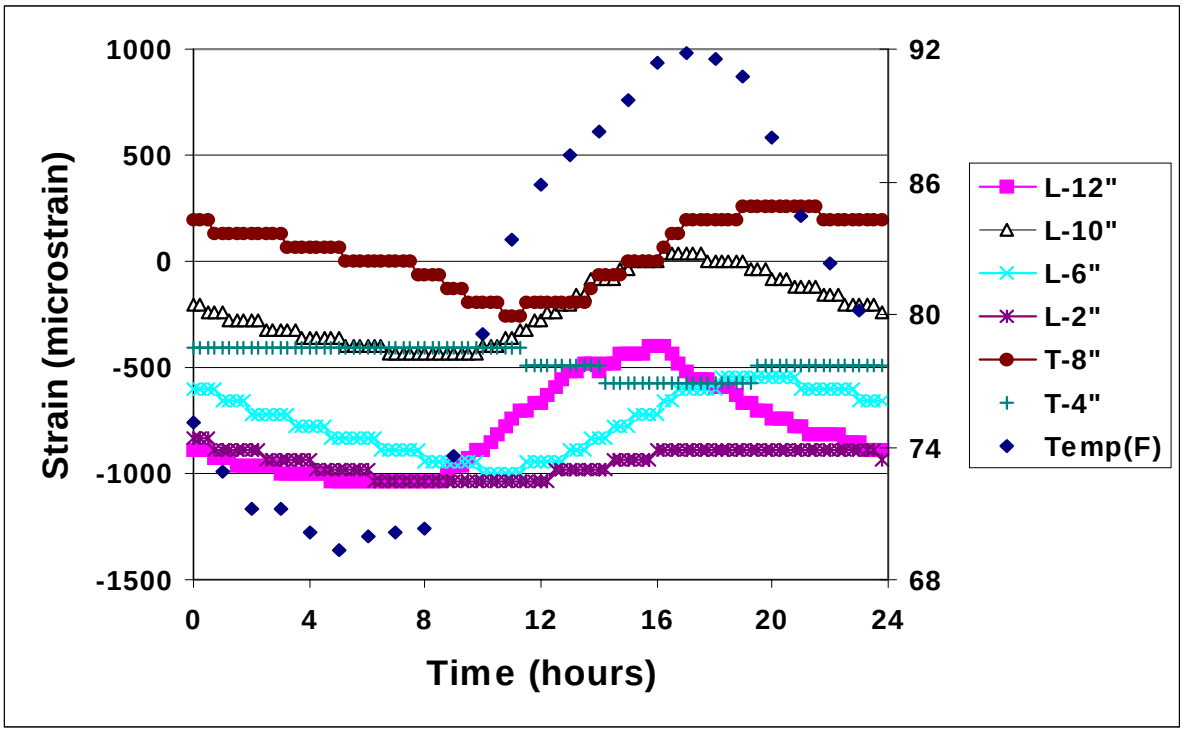

Figure B.137 Concrete Strain at Varying Depths versus Time (Day 5).

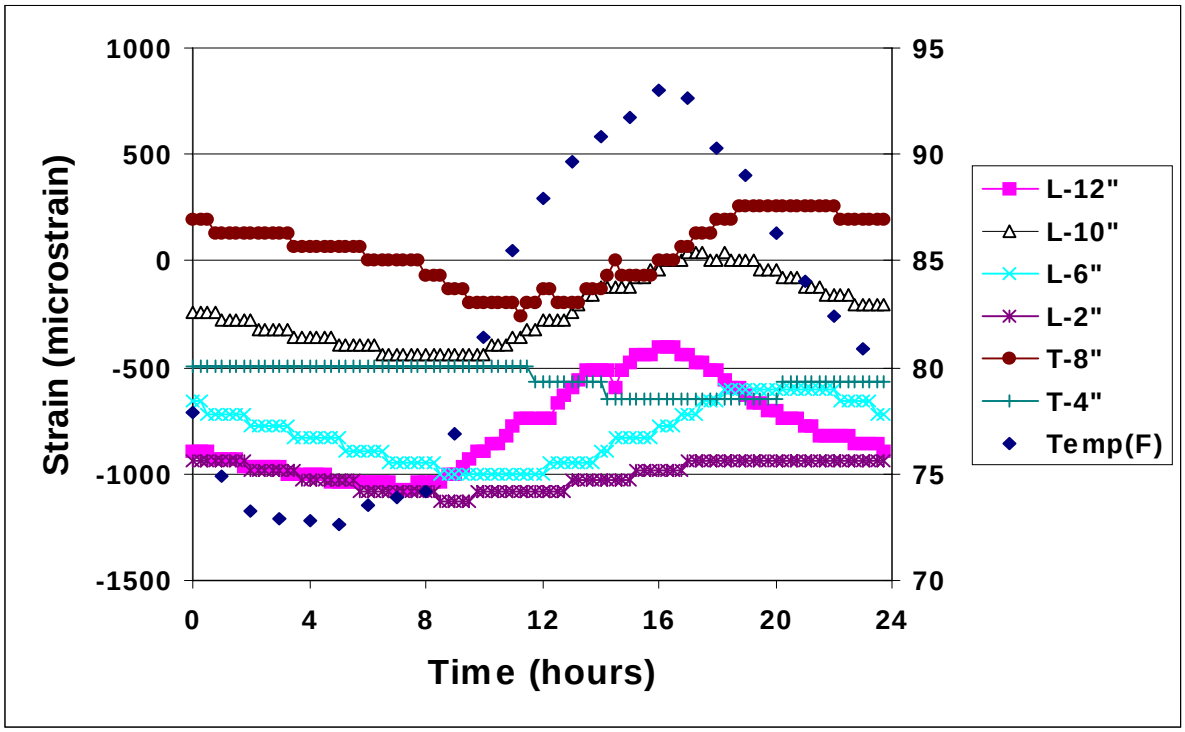

Figure B.138 Concrete Strain at Varying Depths versus Time (Day 6).

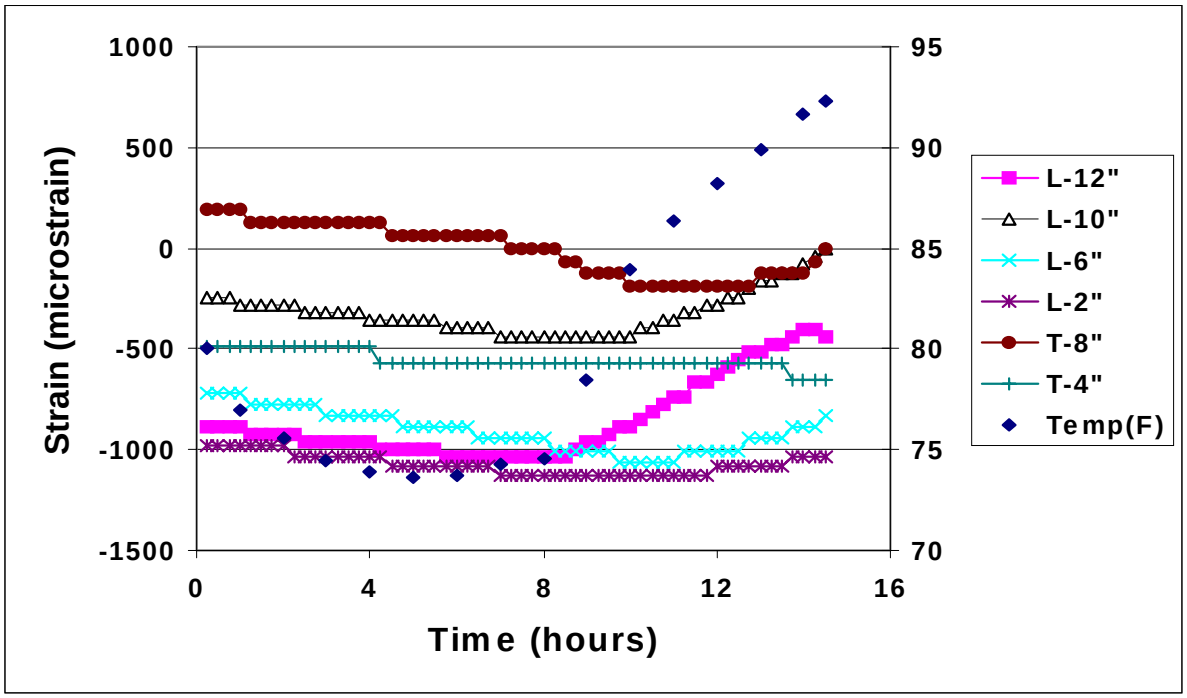

Figure B.139 Concrete Strain at Varying Depths versus Time (Day 7).

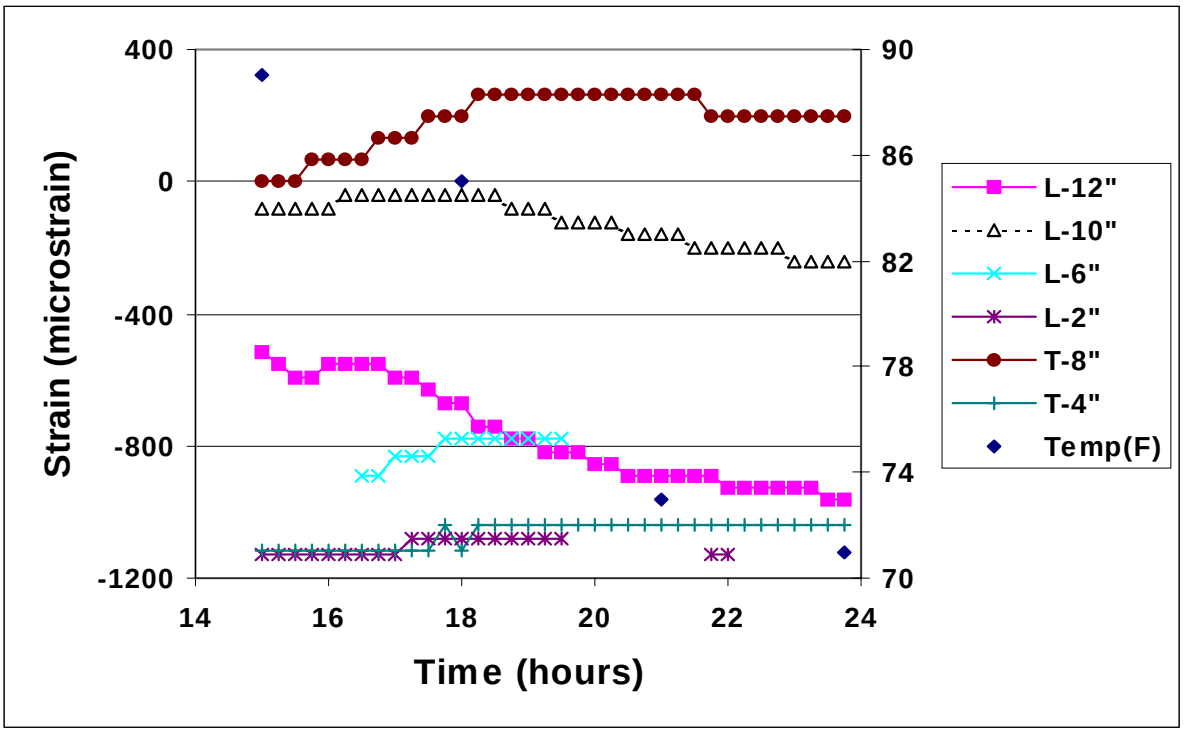

Figure B.140 Concrete Strain at Varying Depths versus Time (Day 15).

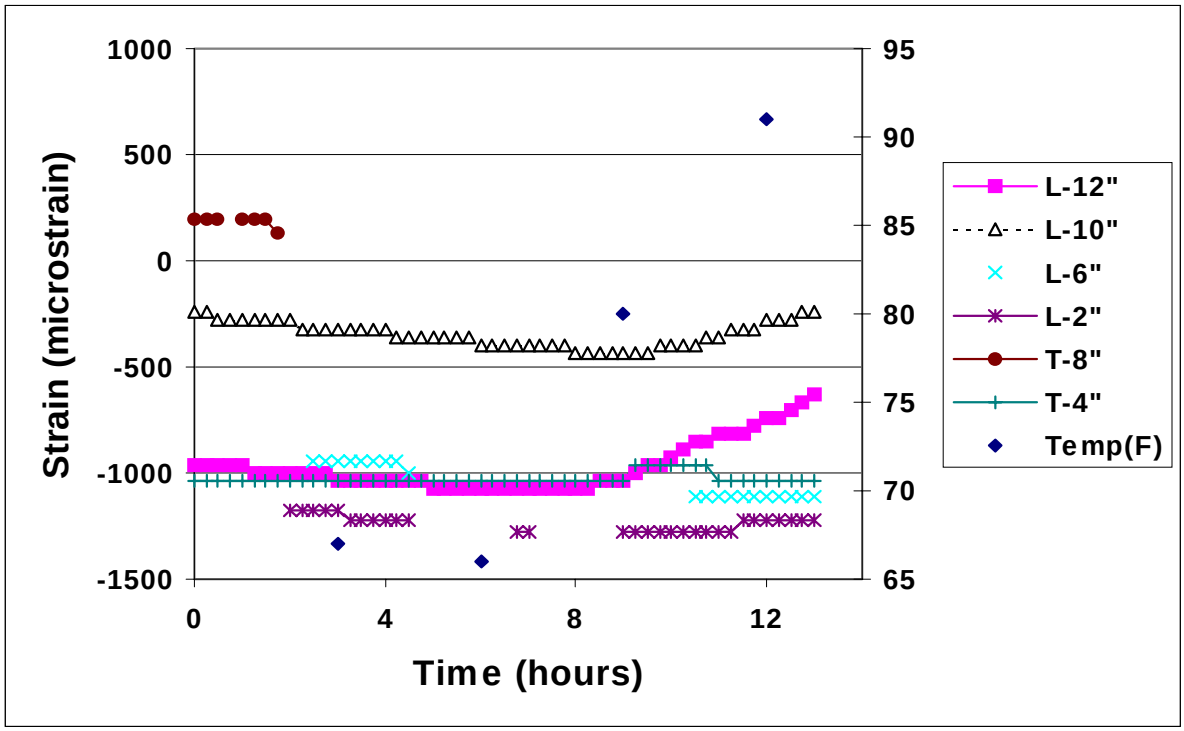

Figure B.141 Concrete Strain at Varying Depths versus Time (Day 16).

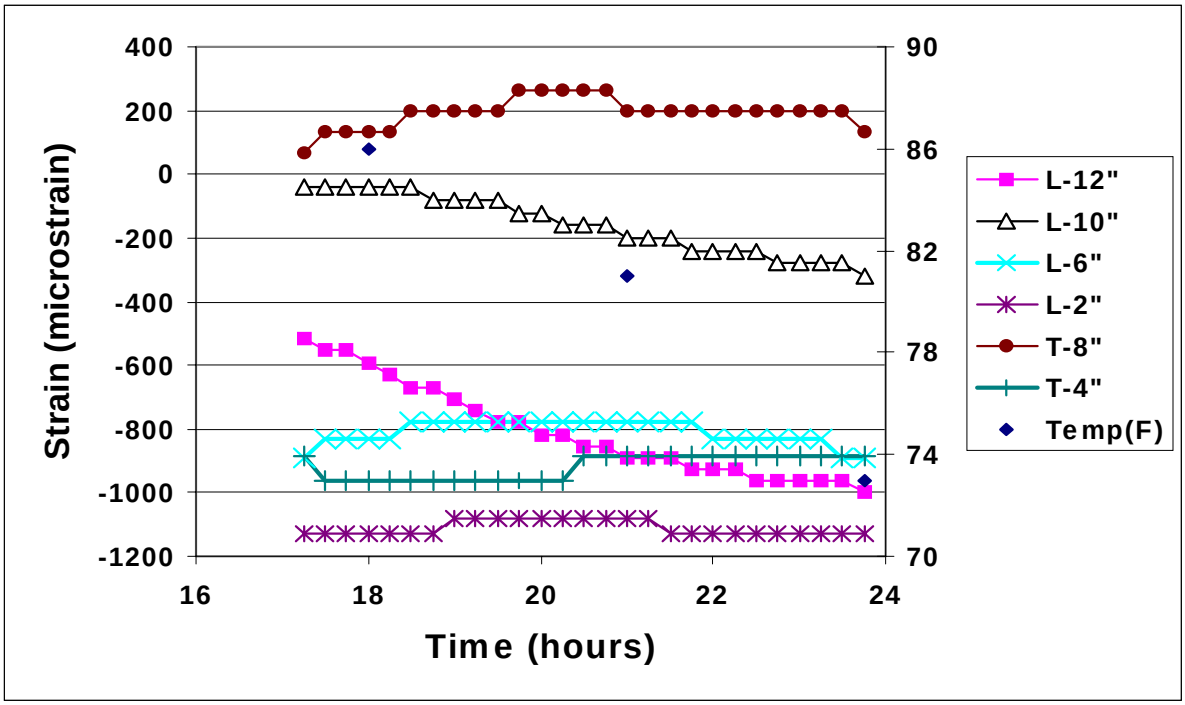

Figure B.142 Concrete Strain at Varying Depths versus Time (Day 29).

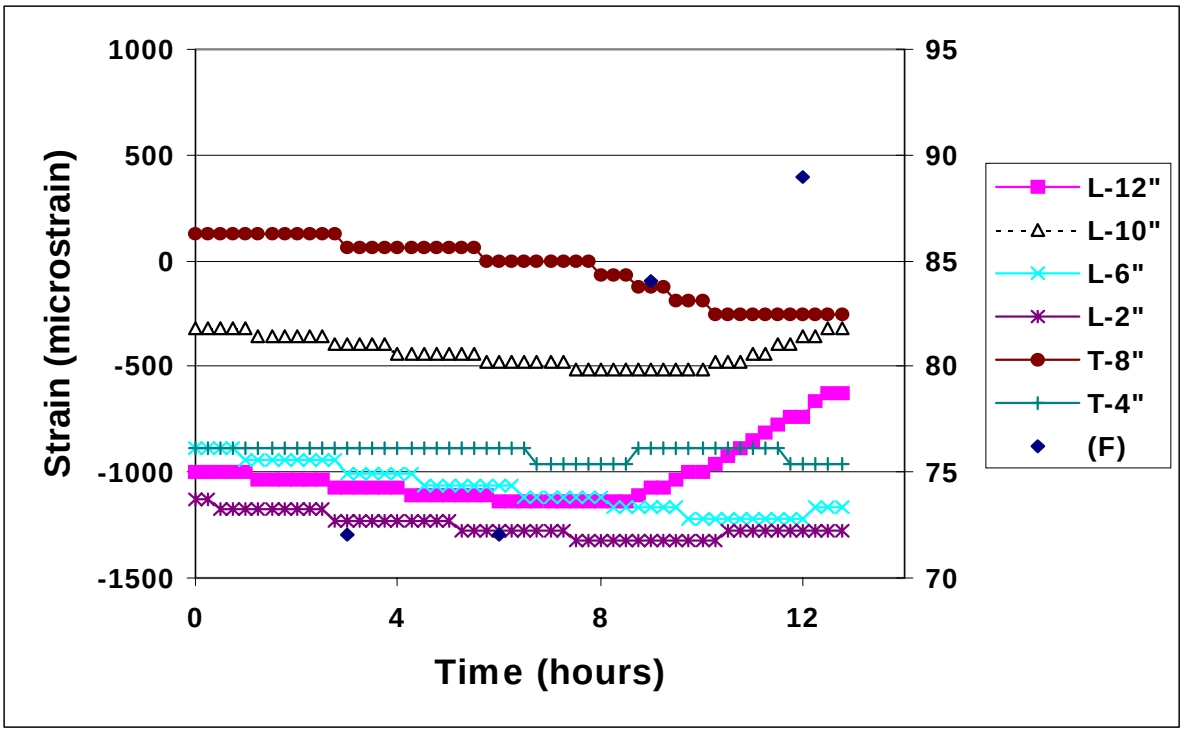

Figure B.143 Concrete Strain at Varying Depths versus Time (Day 30).

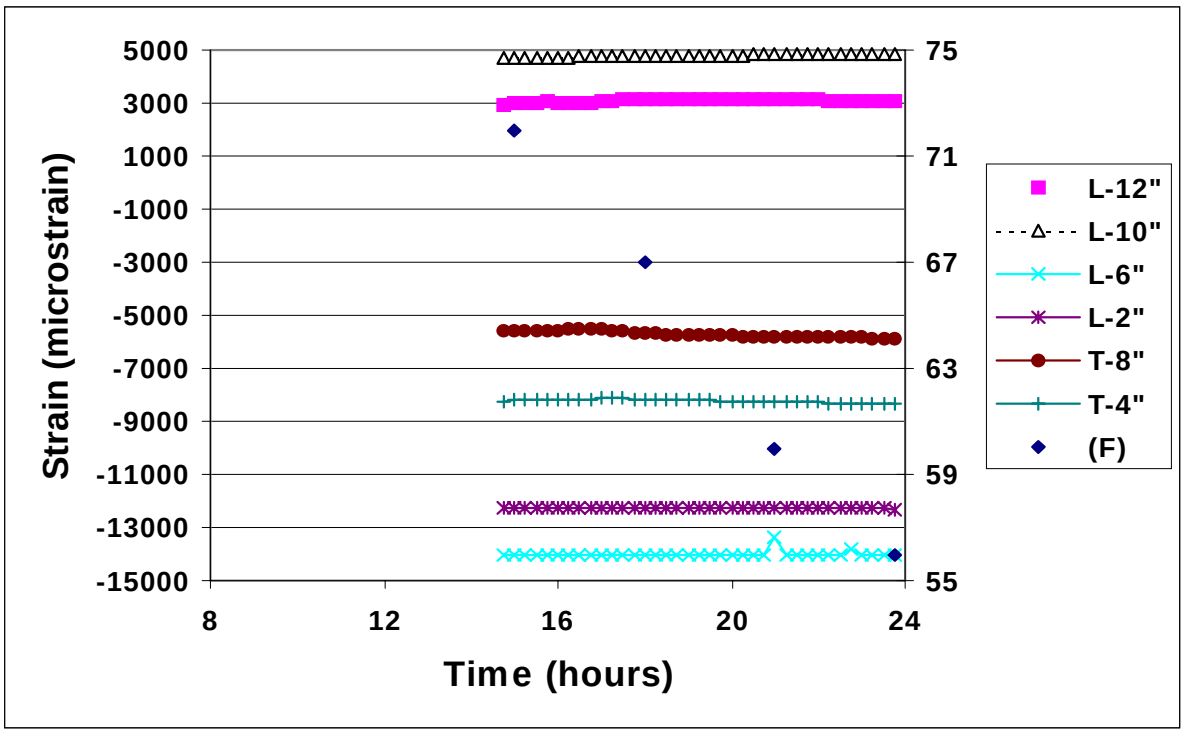

Figure B.144 Concrete Strain at Varying Depths versus Time (Day 161).

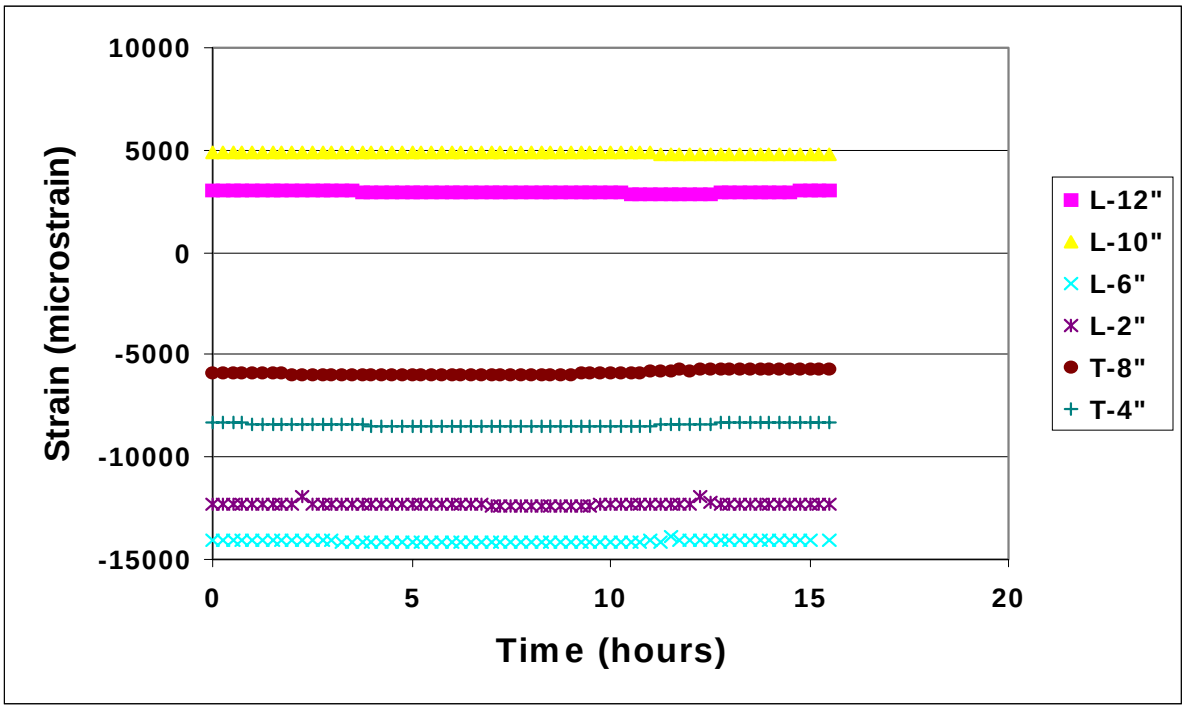

Figure B.145 Concrete Strain at Varying Depths versus Time (Day 162).

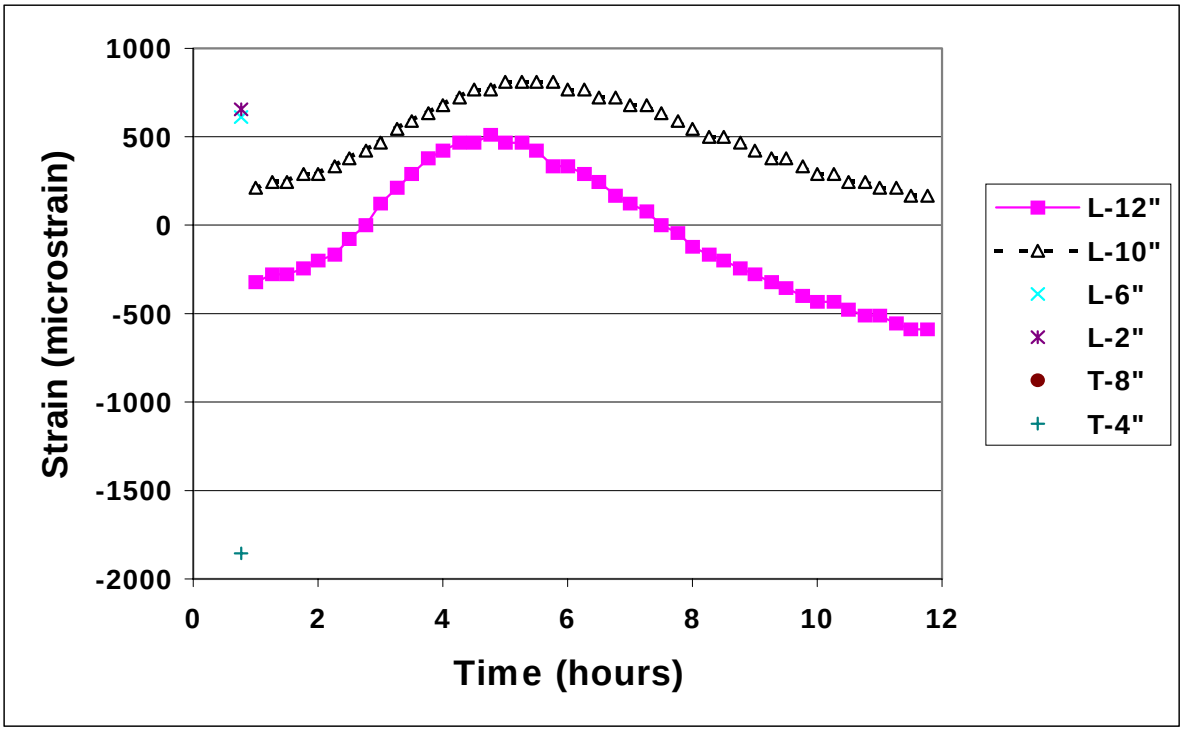

Figure B.146 Concrete Strain at Varying Depths versus Time (Day 269).

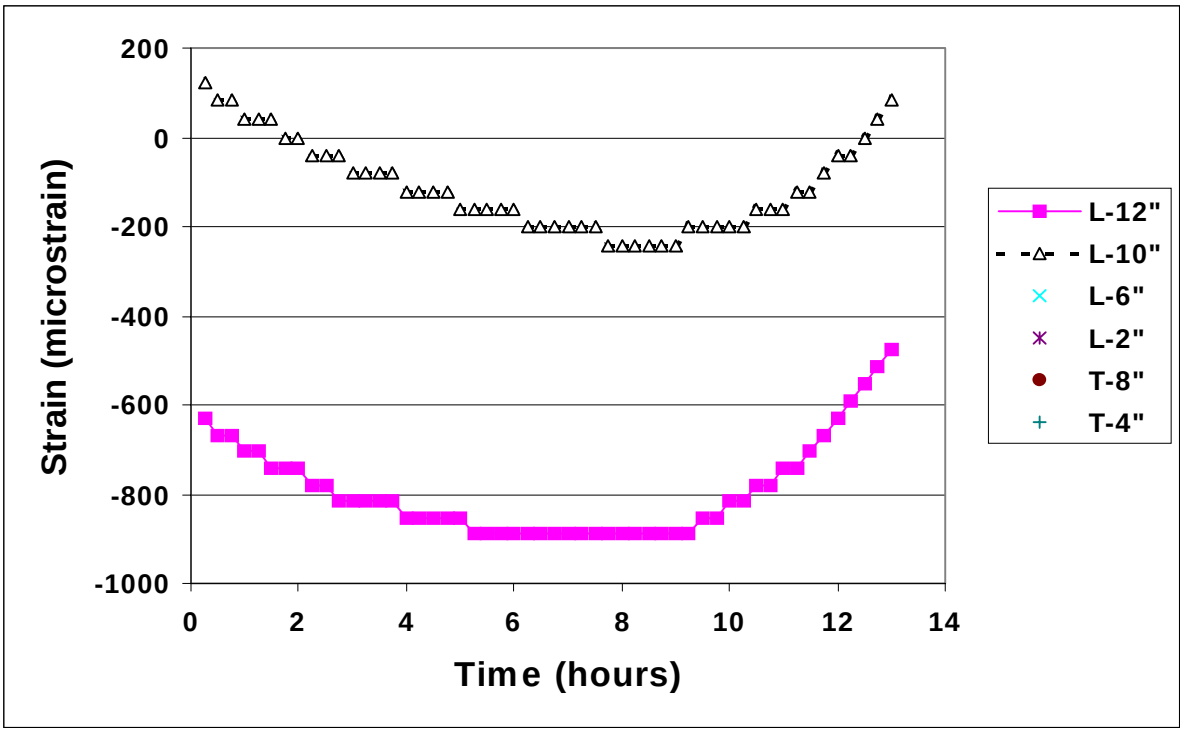

Figure B.147 Concrete Strain at Varying Depths versus Time (Day 270).

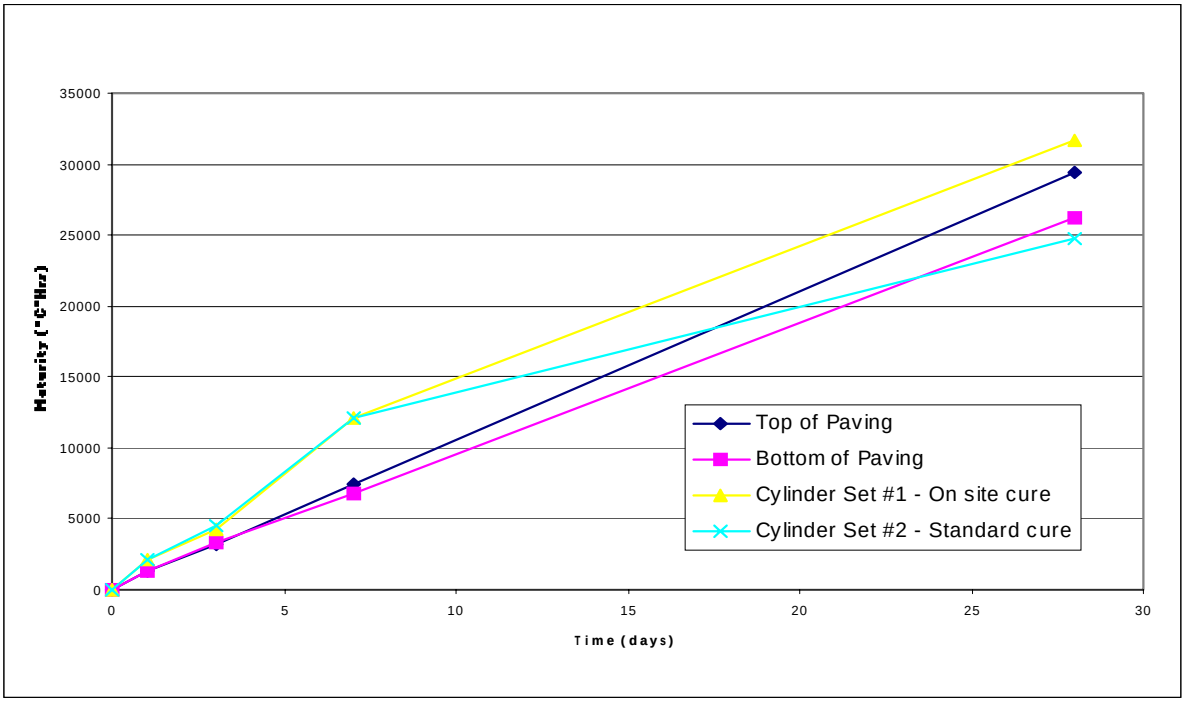

Figure B.148 Maturity versus Time.

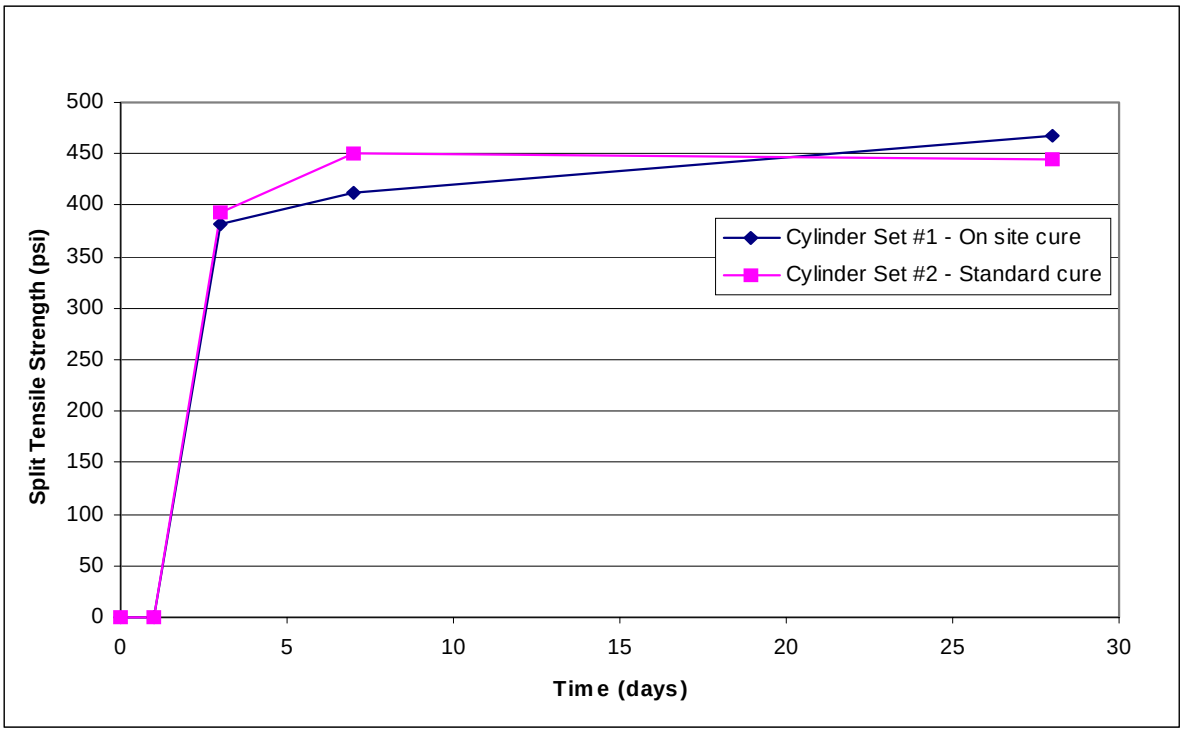

Figure B.149 Split Tensile Strength.

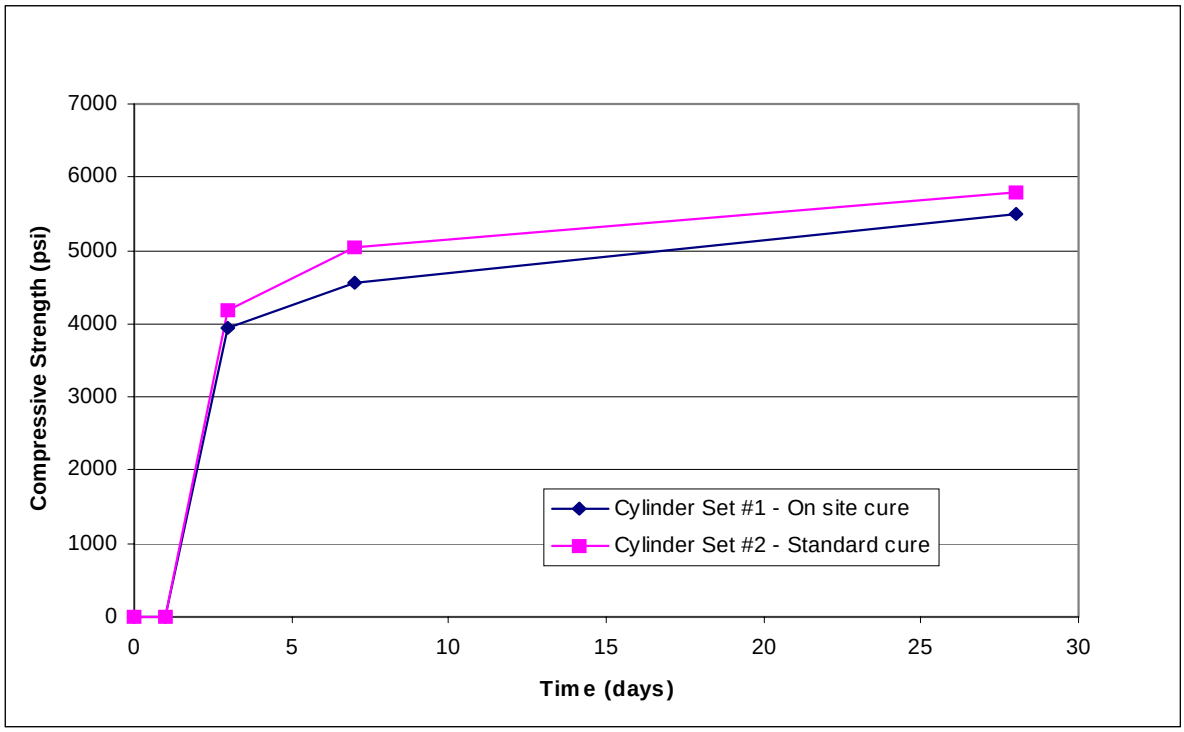

Figure B.150 Comprehensive Strength.

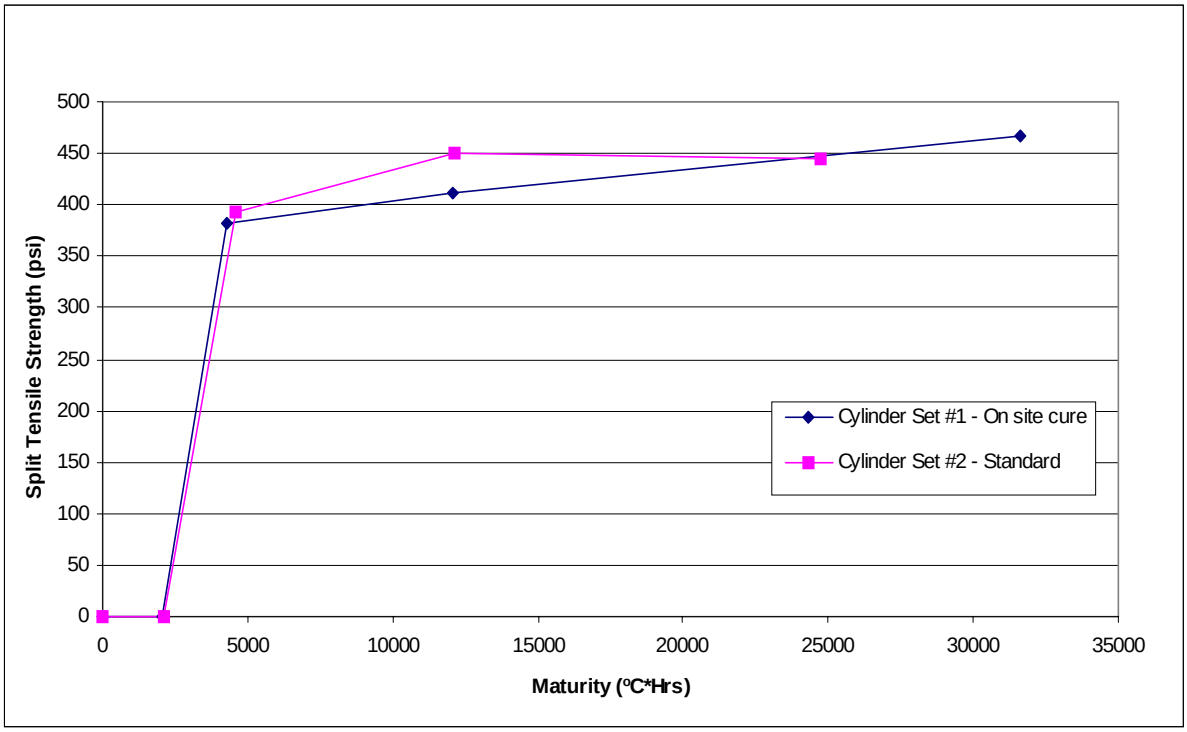

Figure B.151 Split Tensile Strength versus Maturity.

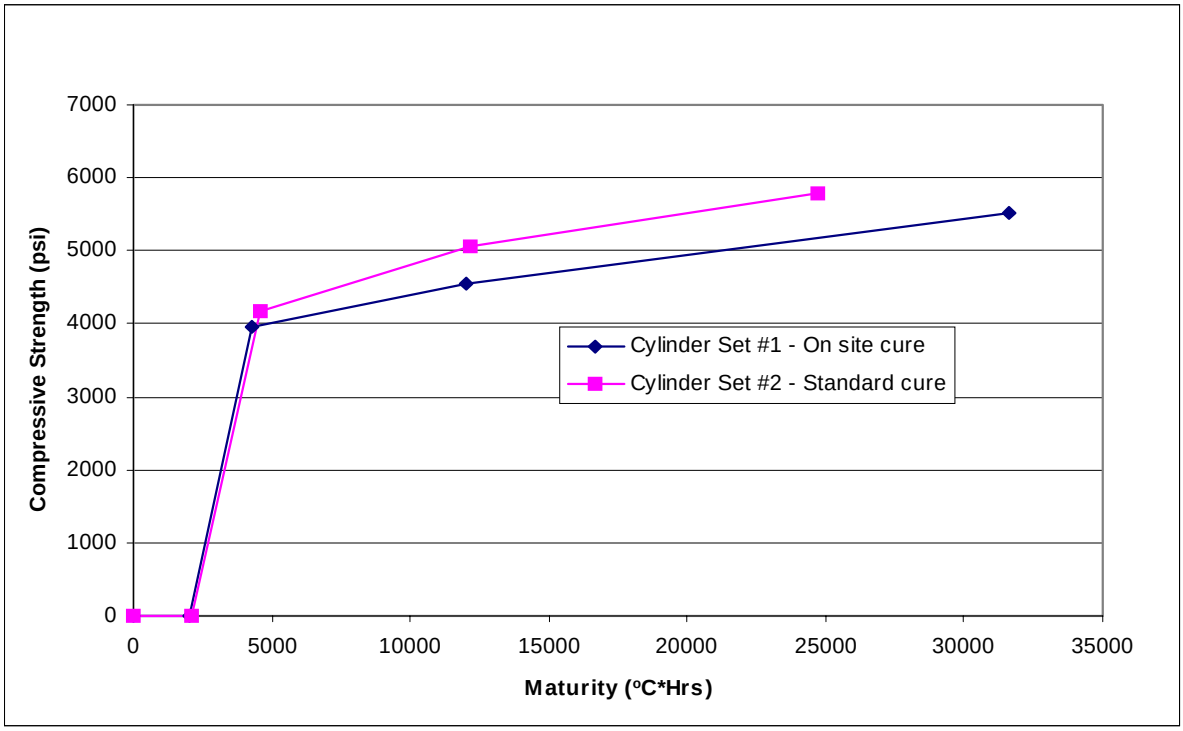

Figure B.152 Compressive Strength versus Maturity.

APPENDIX C

STEEL FORCE DATA

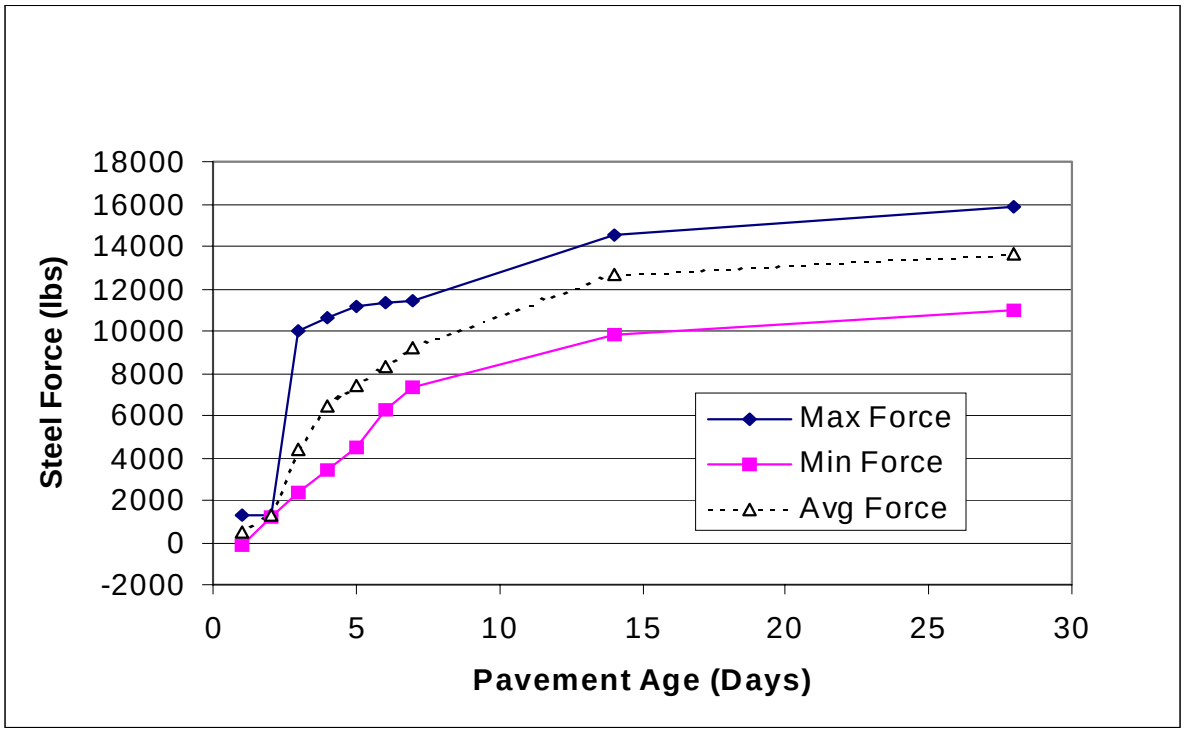

Figure C.1 Steel Force versus Age of Pavement Gage SG3.

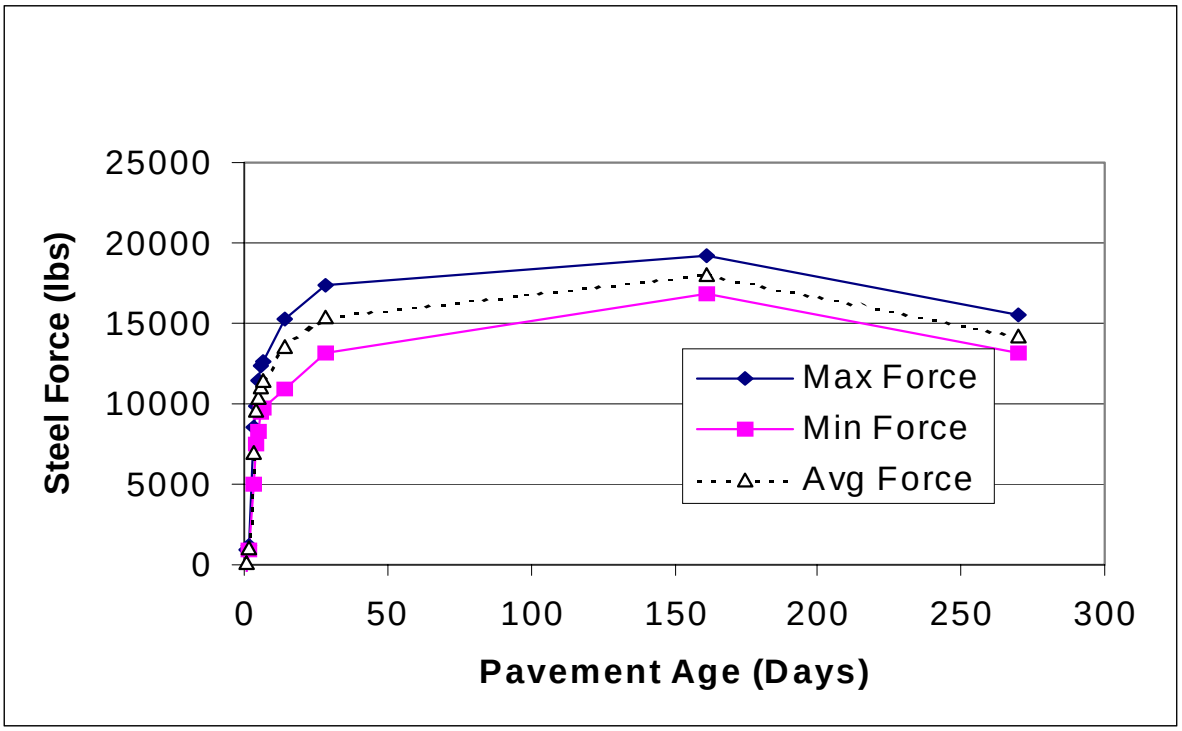

Figure C.2 Steel Force versus Age of Pavement Gage SG1.

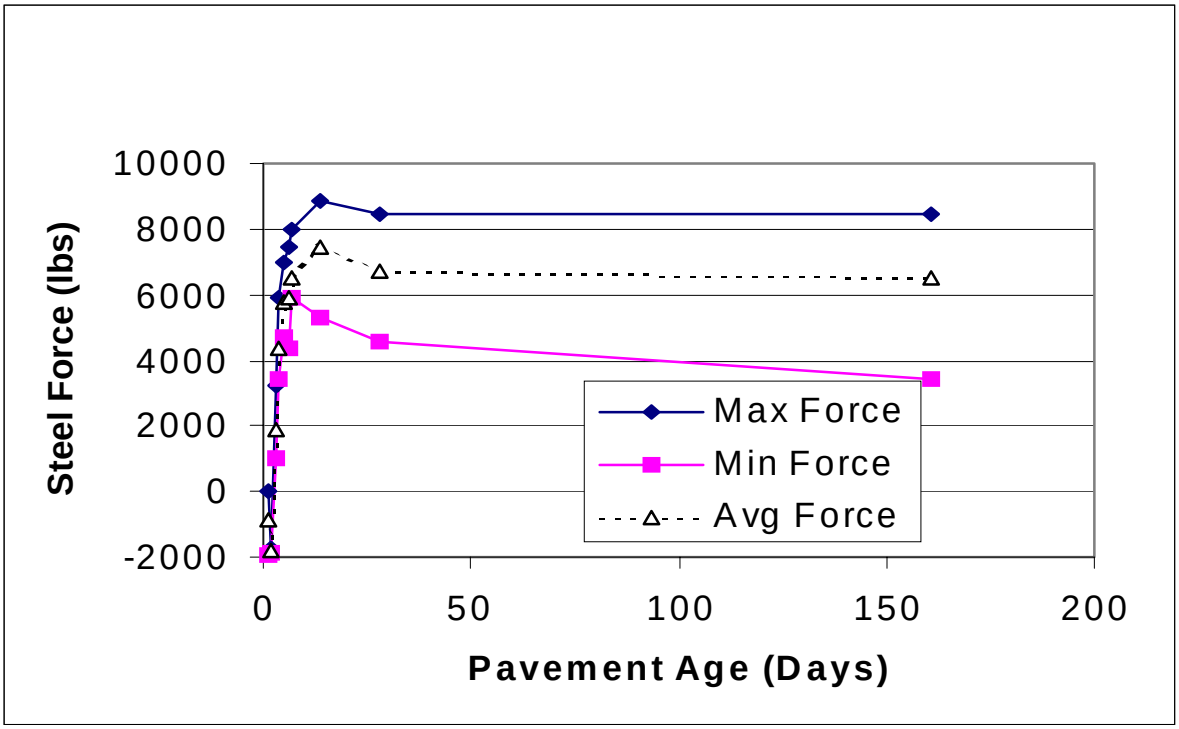

Figure C.3 Steel Force versus Age of Pavement Gage SG5.

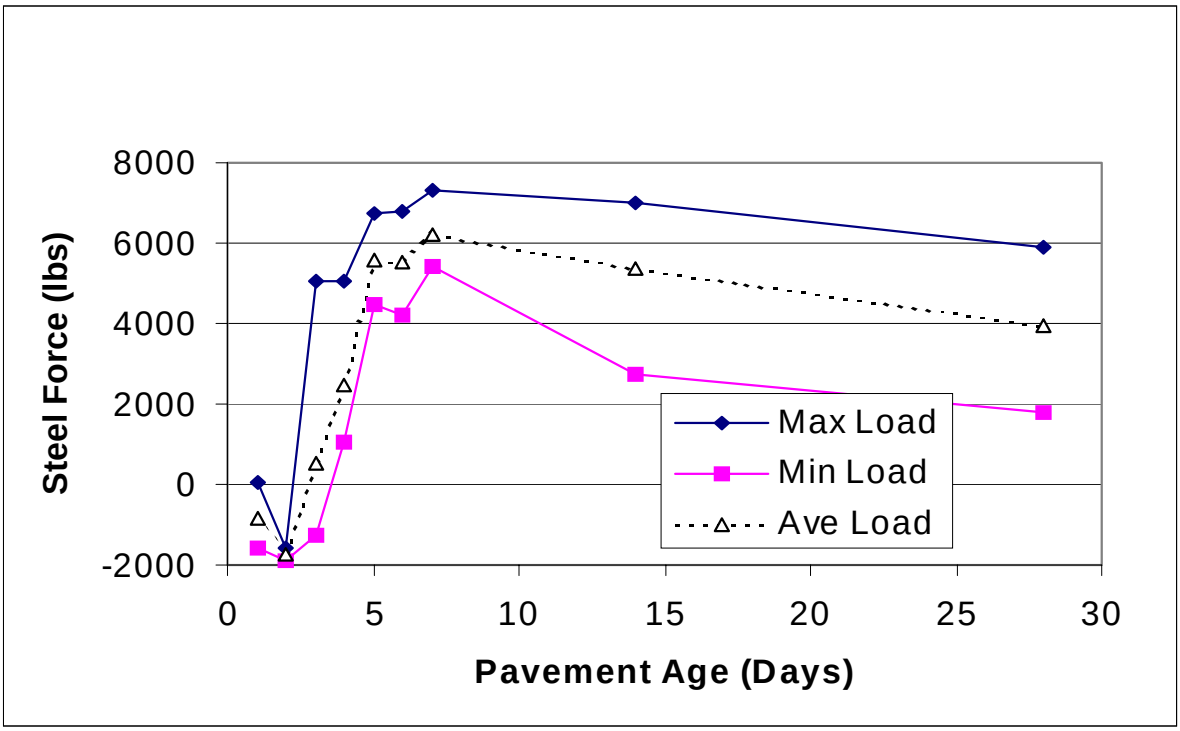

Figure C.4 Steel Force versus Age of Pavement Gage SG1.

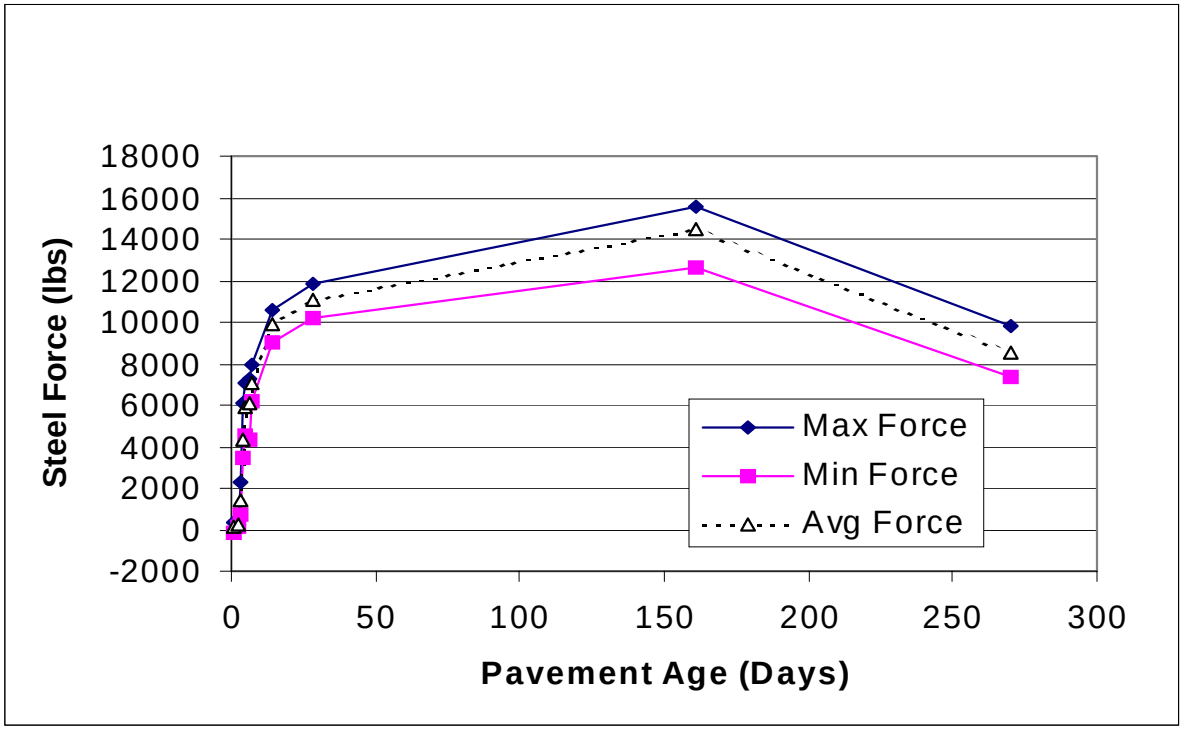

Figure C.5 Steel Force versus Age of Pavement Gage SG5.

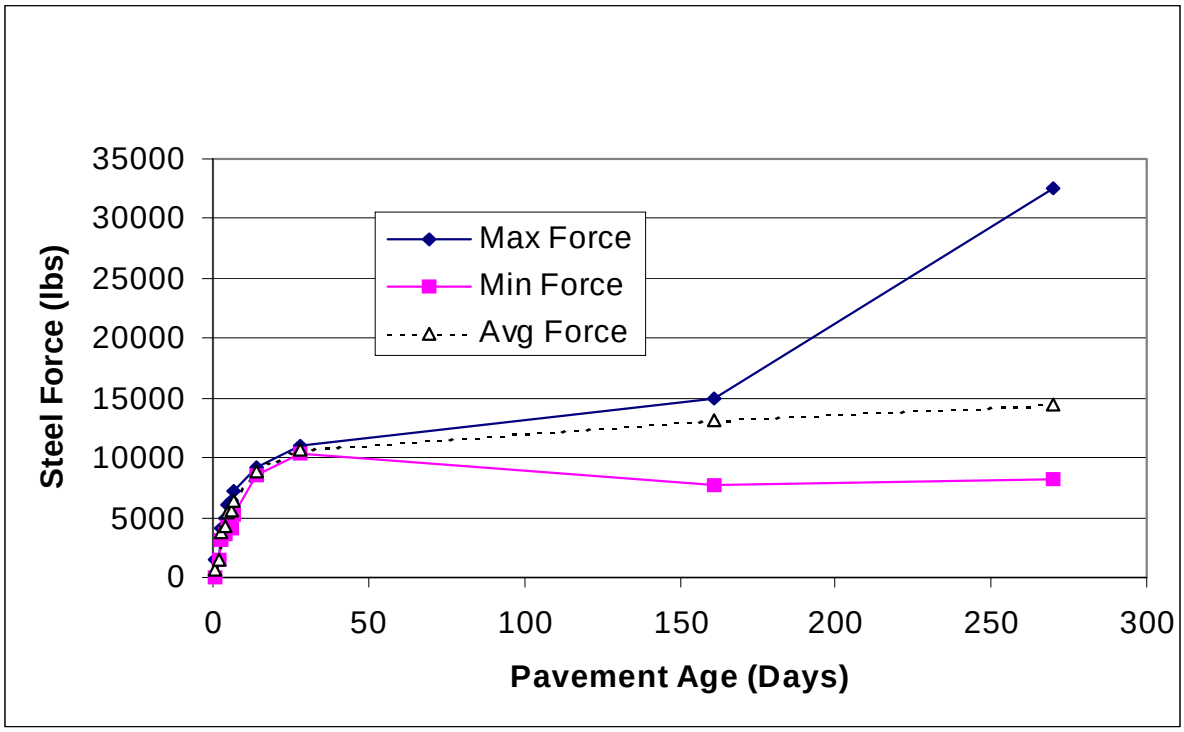

Figure C.6 Steel Force versus Age of Pavement Gage SG6.

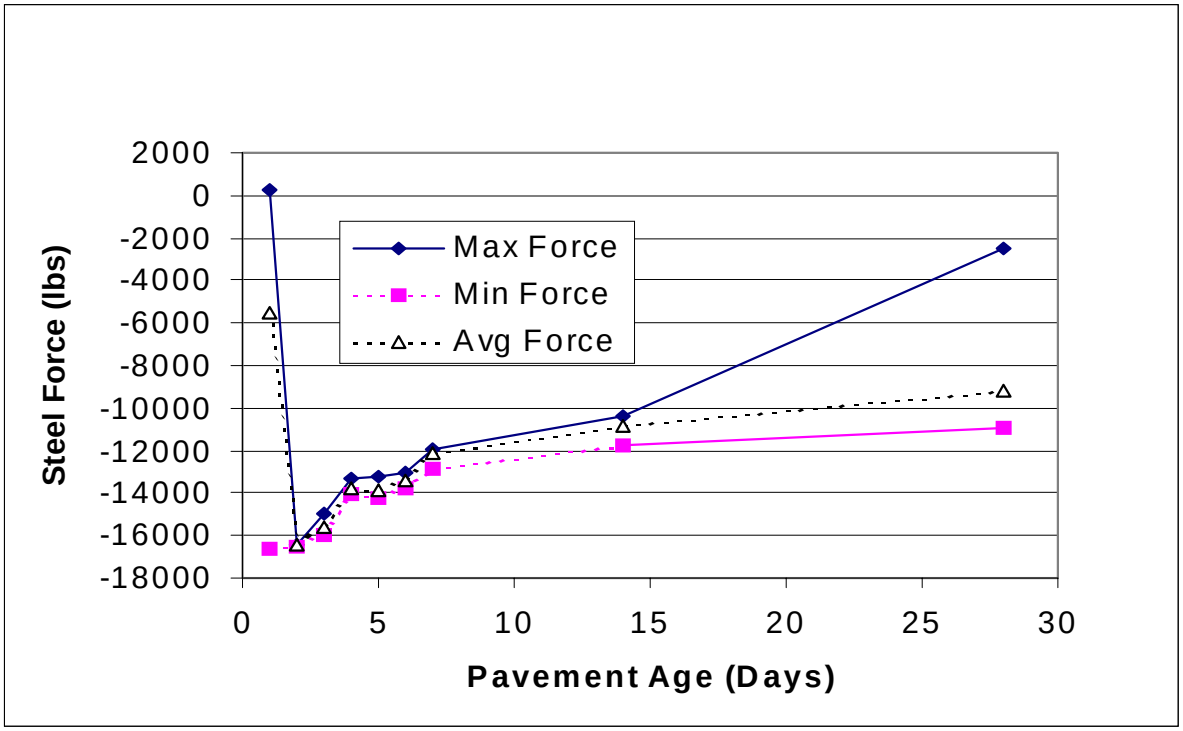

Figure C.7 Steel Force versus Age of Pavement Gage SG7.

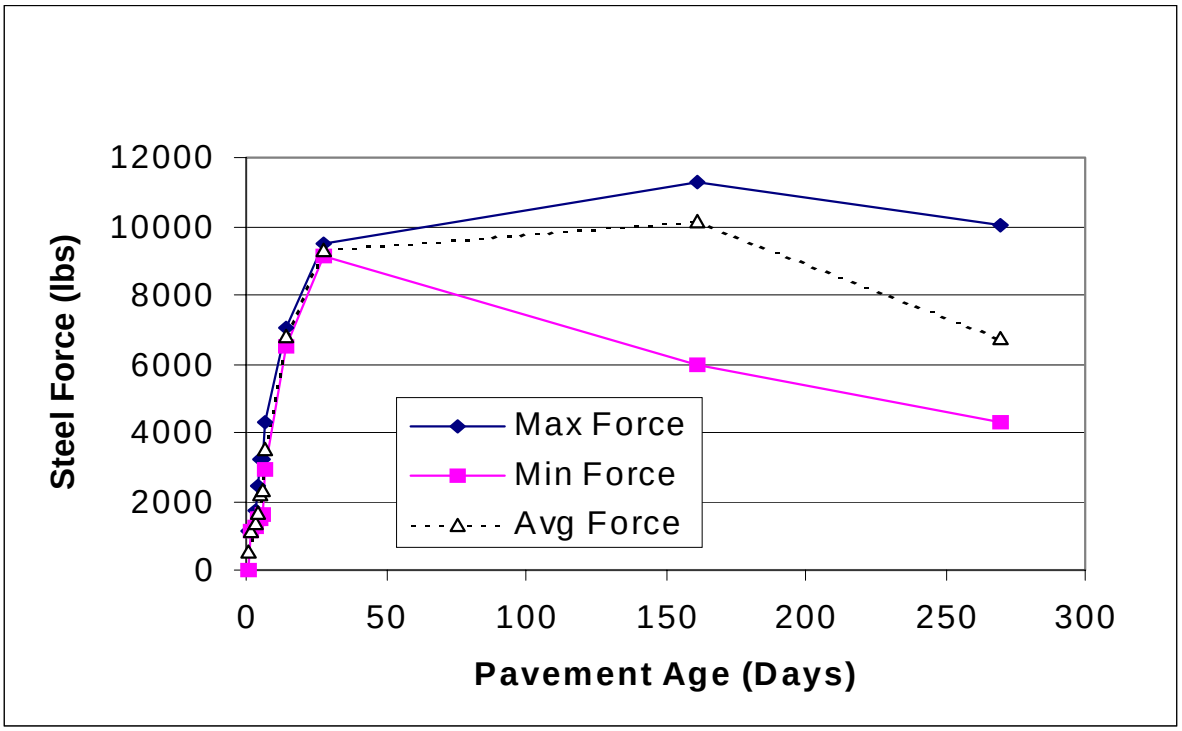

Figure C.8 Steel Force versus Age of Pavement Gage SG8.

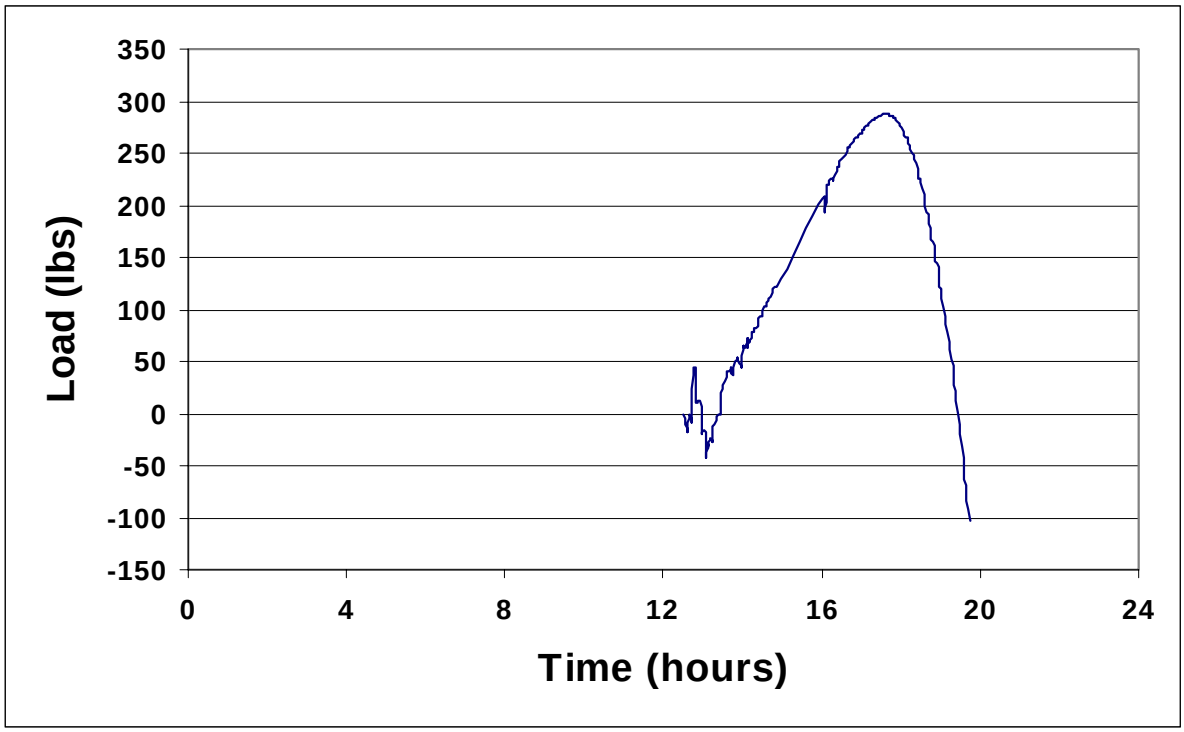

Figure C.9 Steel Force versus Time at Gage SG3 (Day 1).

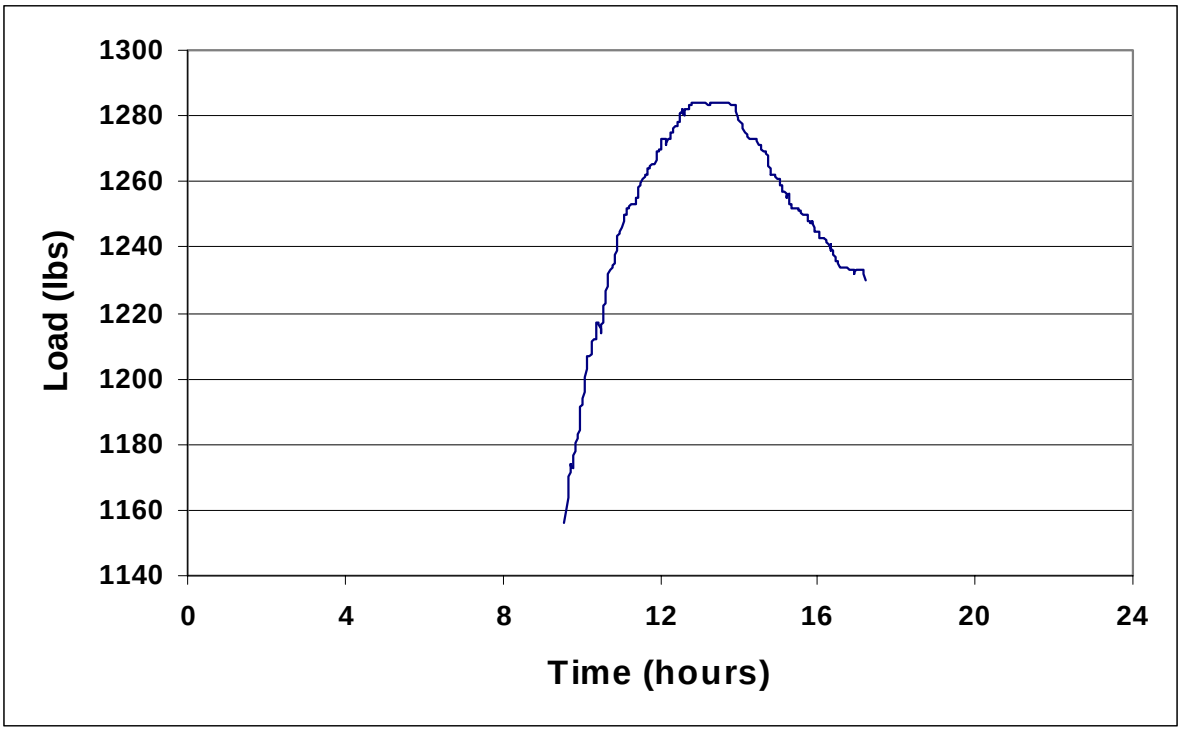

Figure C.10 Steel Force versus Time at Gage SG3 (Day 2).

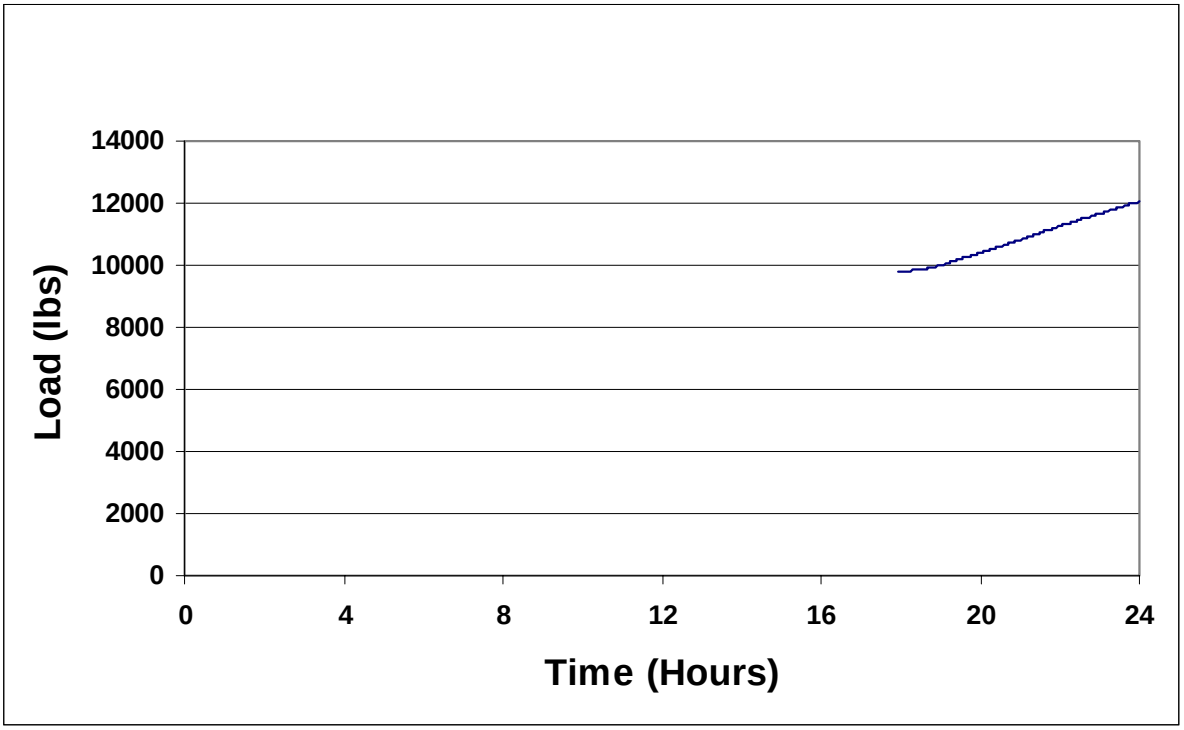

Figure C.11 Steel Force versus Time at Gage SG3 (Day 15).

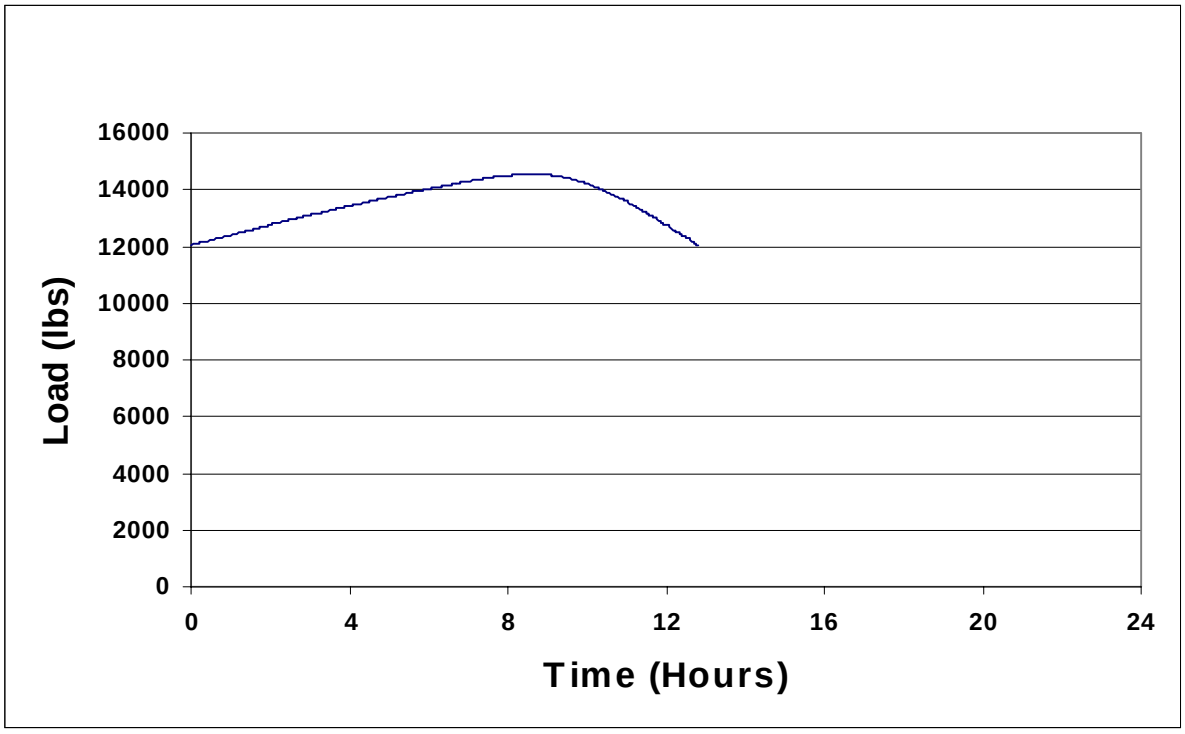

Figure C.12 Steel Force versus Time at Gage SG3 (Day 16).

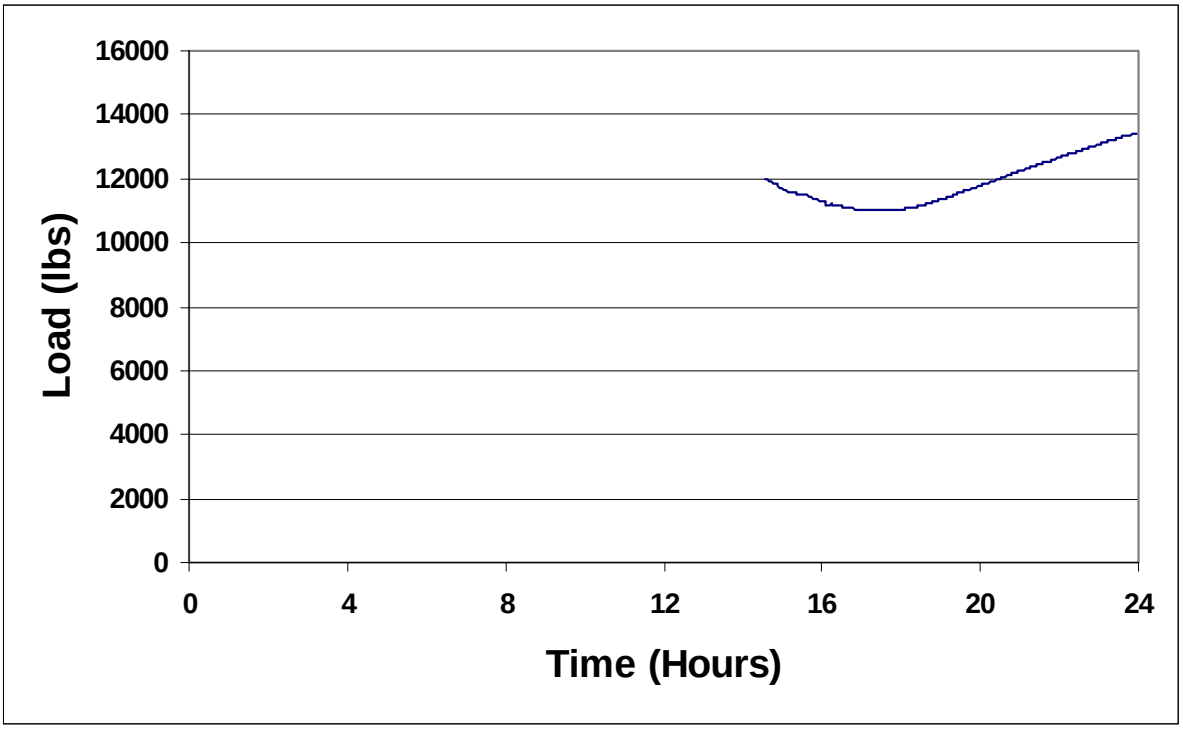

Figure C.13 Steel Force versus Time at Gage SG3 (Day 29).

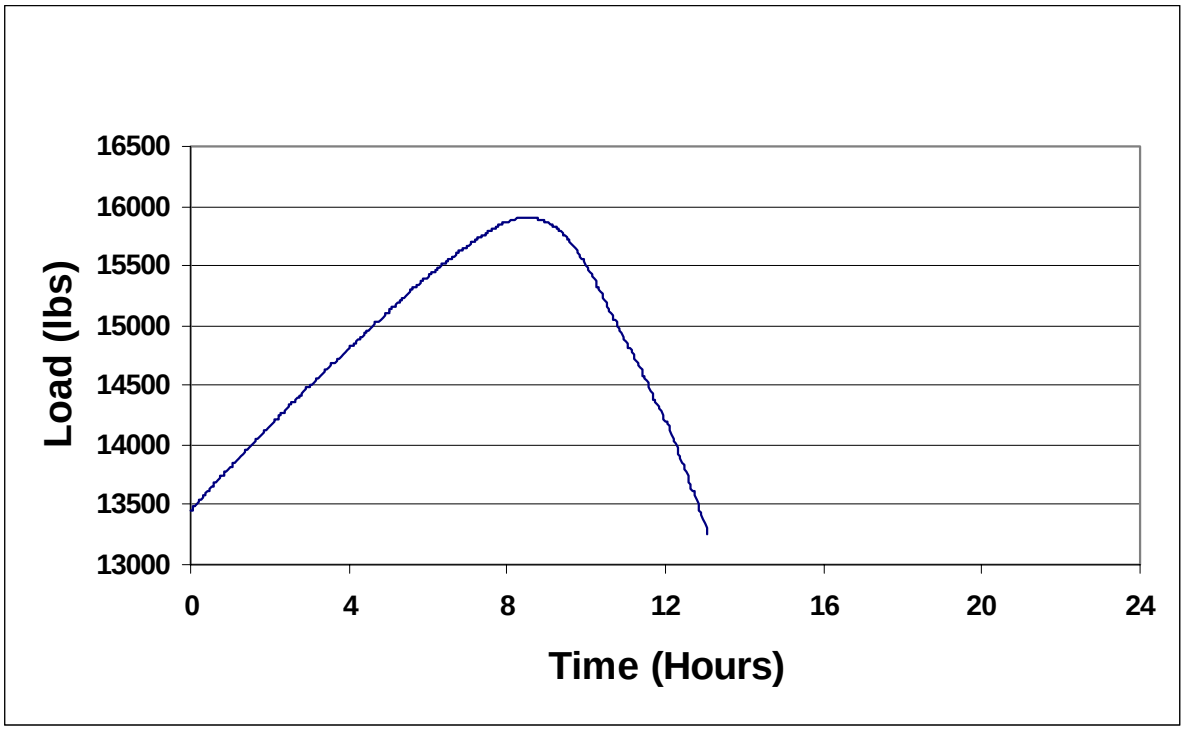

Figure C.14 Steel Force versus Time at Gage SG3 (Day 30).

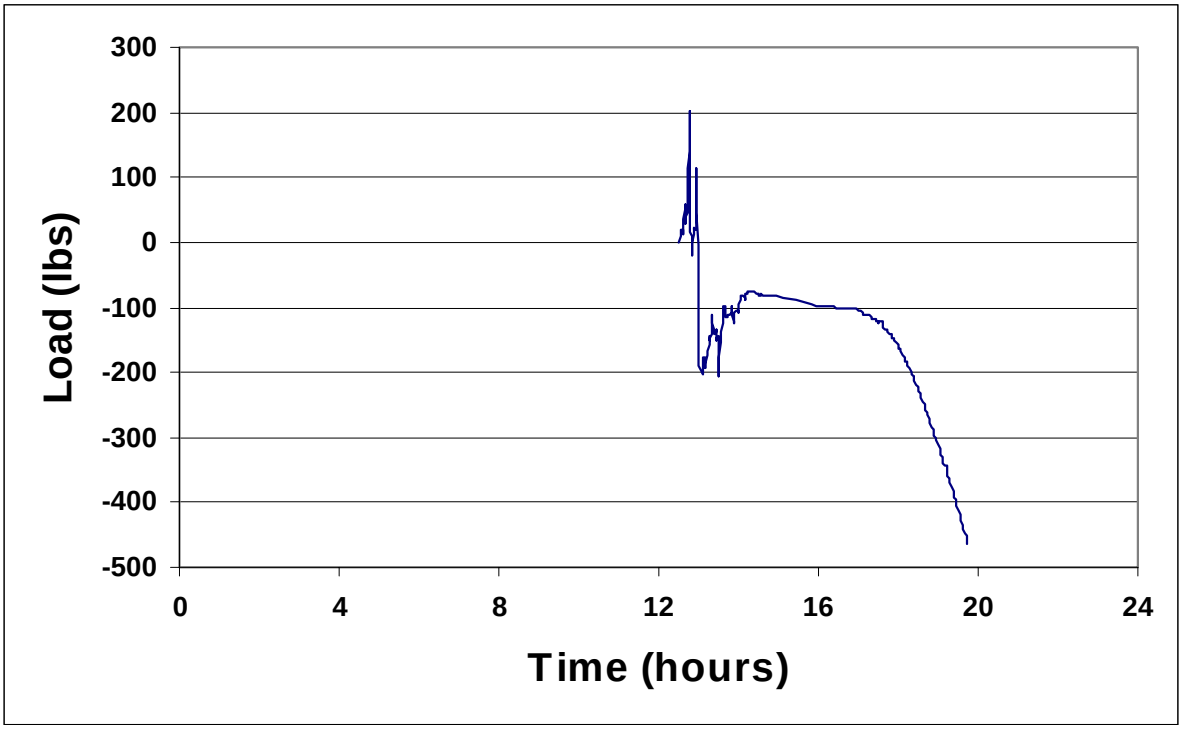

Figure C.15 Steel Force versus Time at Gage SG1 (Day 1).

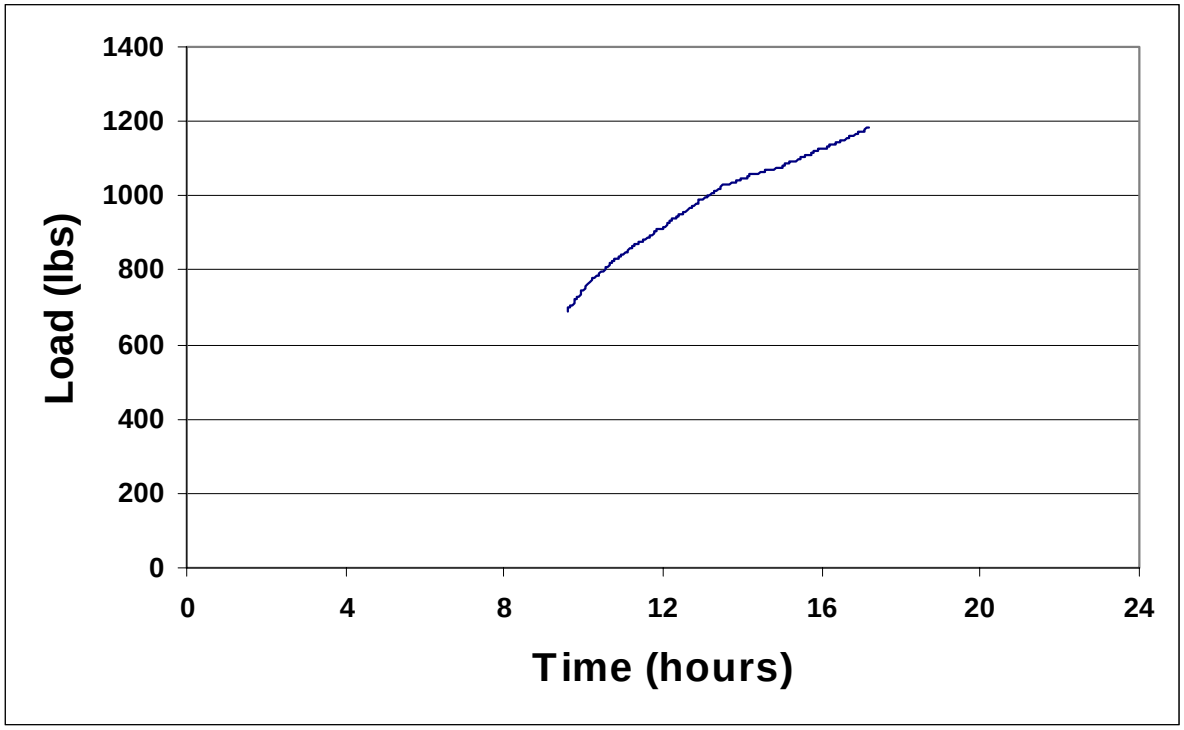

Figure C.16 Steel Force versus Time at Gage SG1 (Day 2).

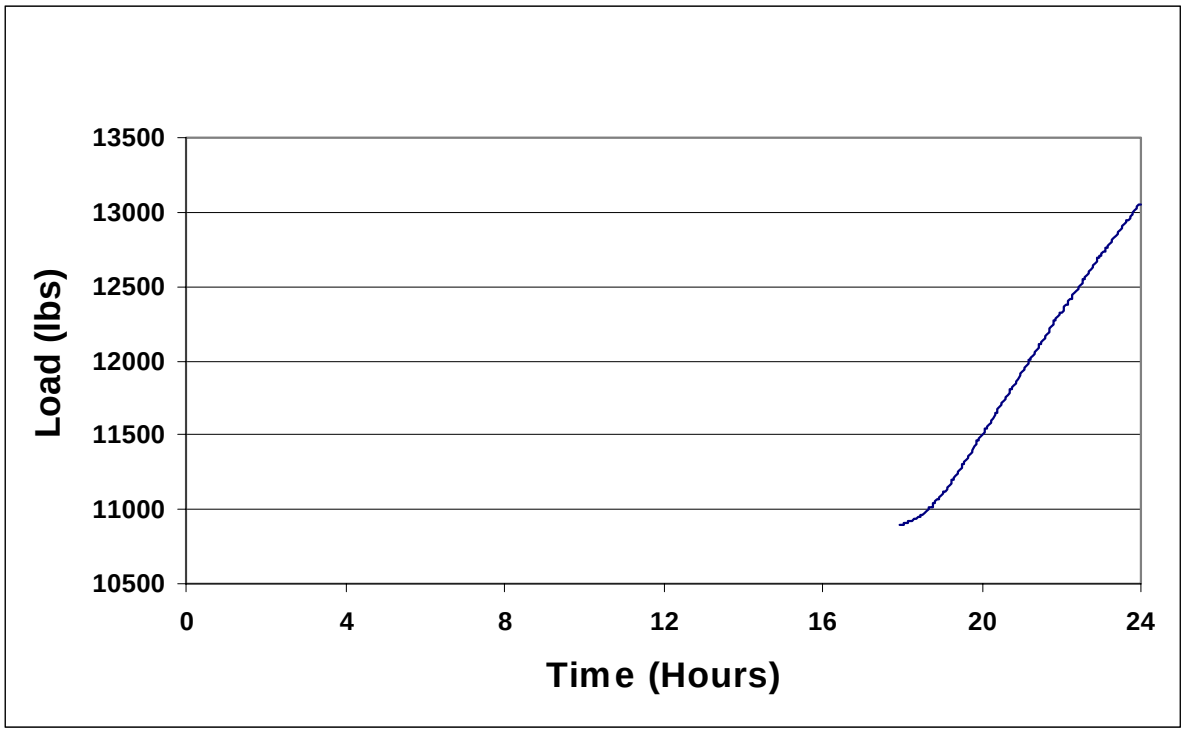

Figure C.17 Steel Force versus Time at Gage SG1 (Day 15).

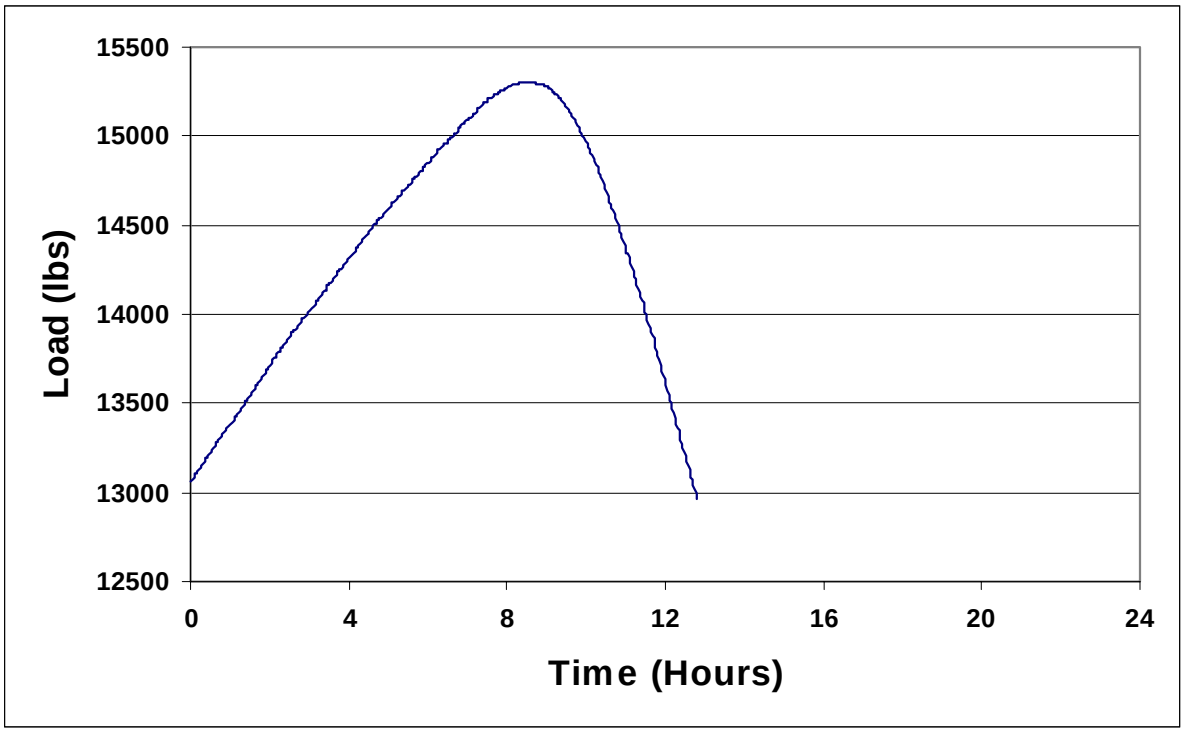

Figure C.18 Steel Force versus Time at Gage SG1 (Day 16).

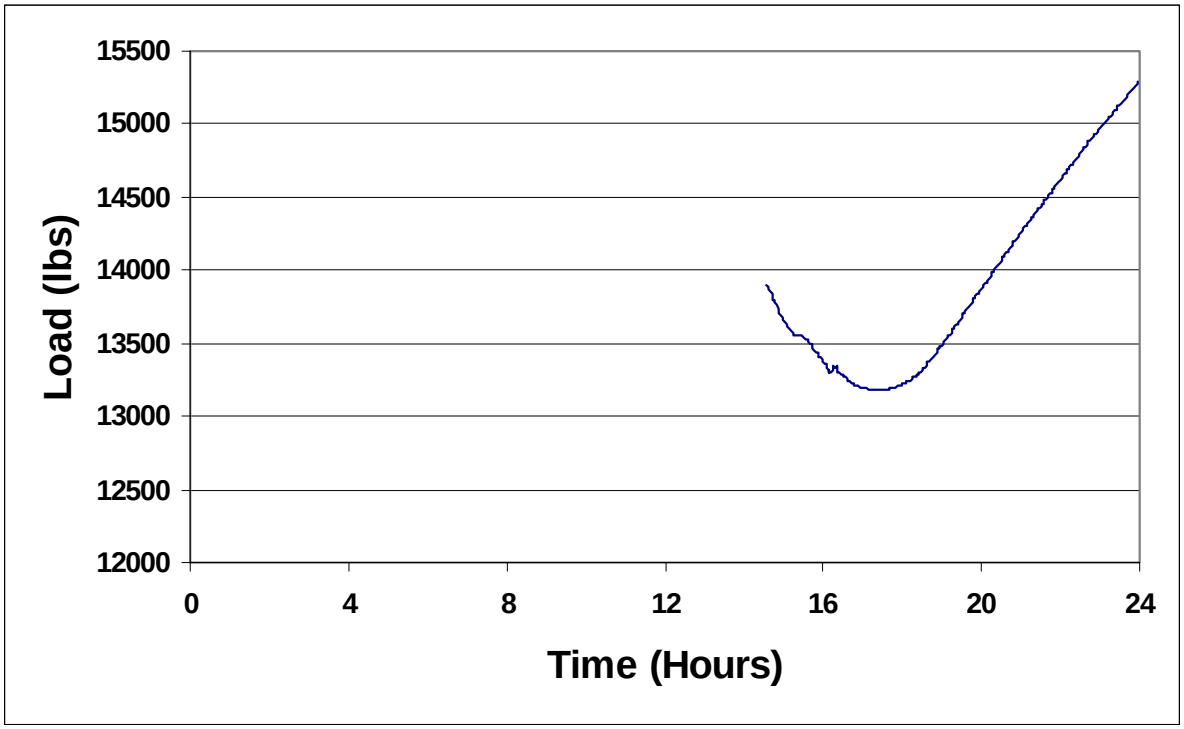

Figure C.19 Steel Force versus Time at Gage SG1 (Day 29).

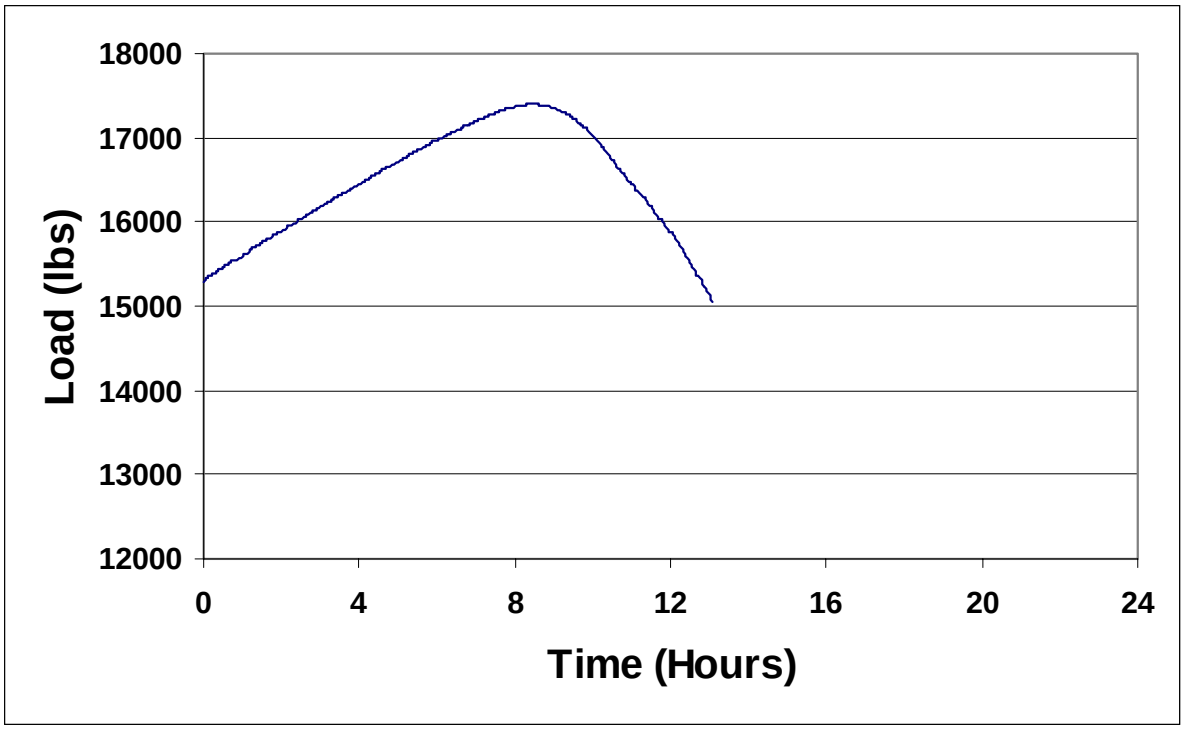

Figure C.20 Steel Force versus Time at Gage SG1 (Day 30).

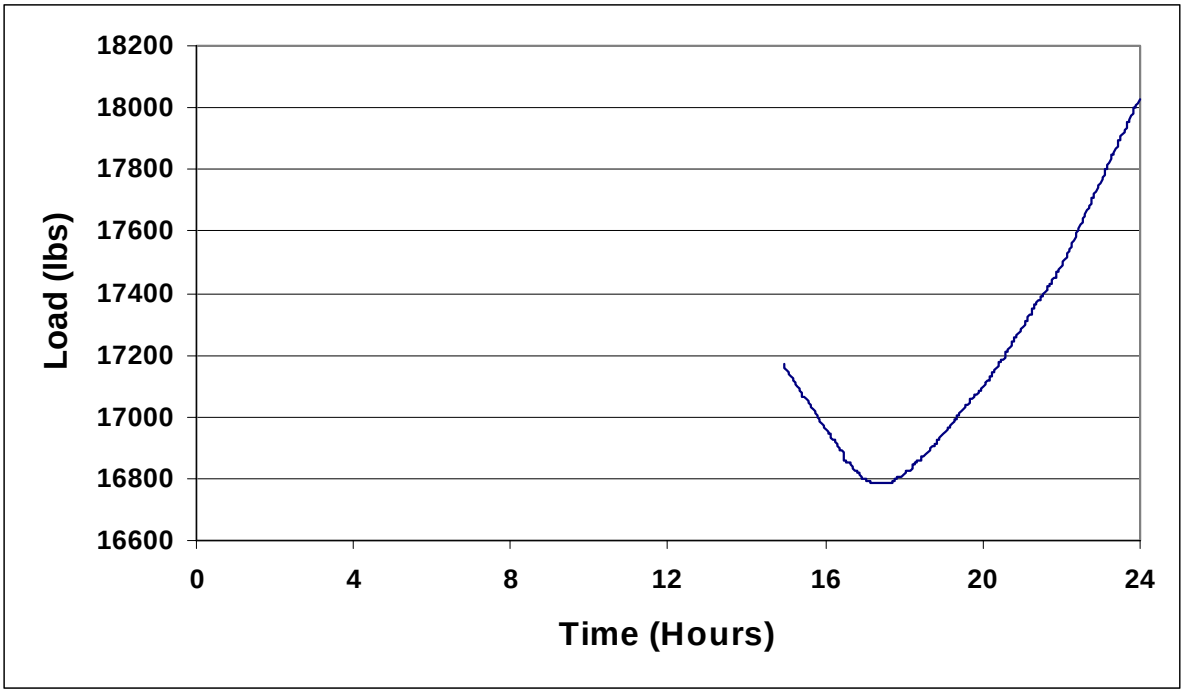

Figure C.21 Steel Force versus Time at Gage SG1 (Day 161).

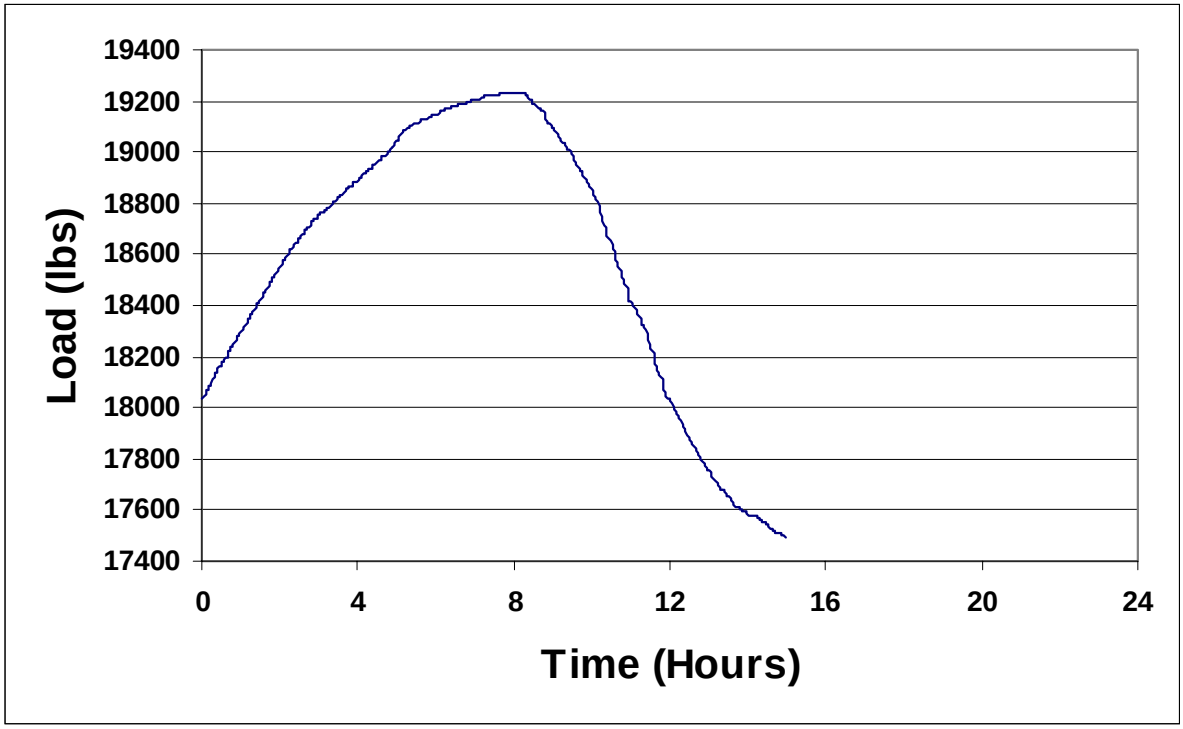

Figure C.22 Steel Force versus Time at Gage SG1 (Day 162).

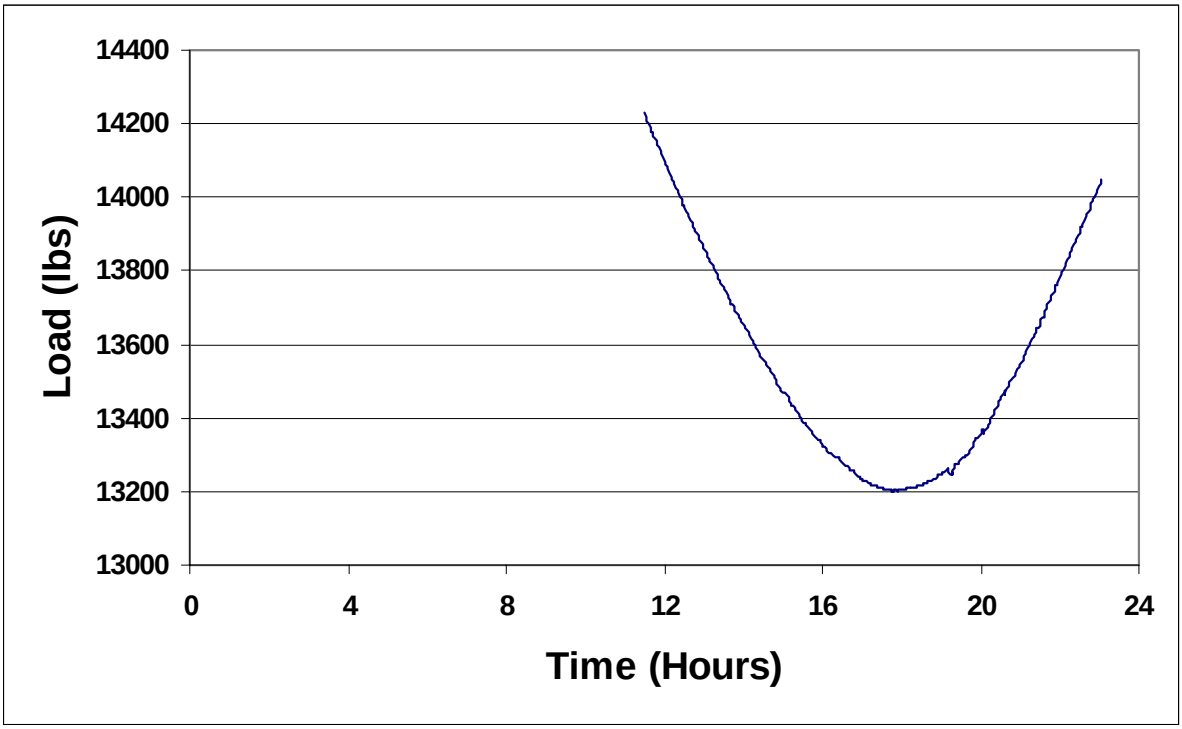

Figure C.23 Steel Force versus Time at Gage SG1 (Day 269).

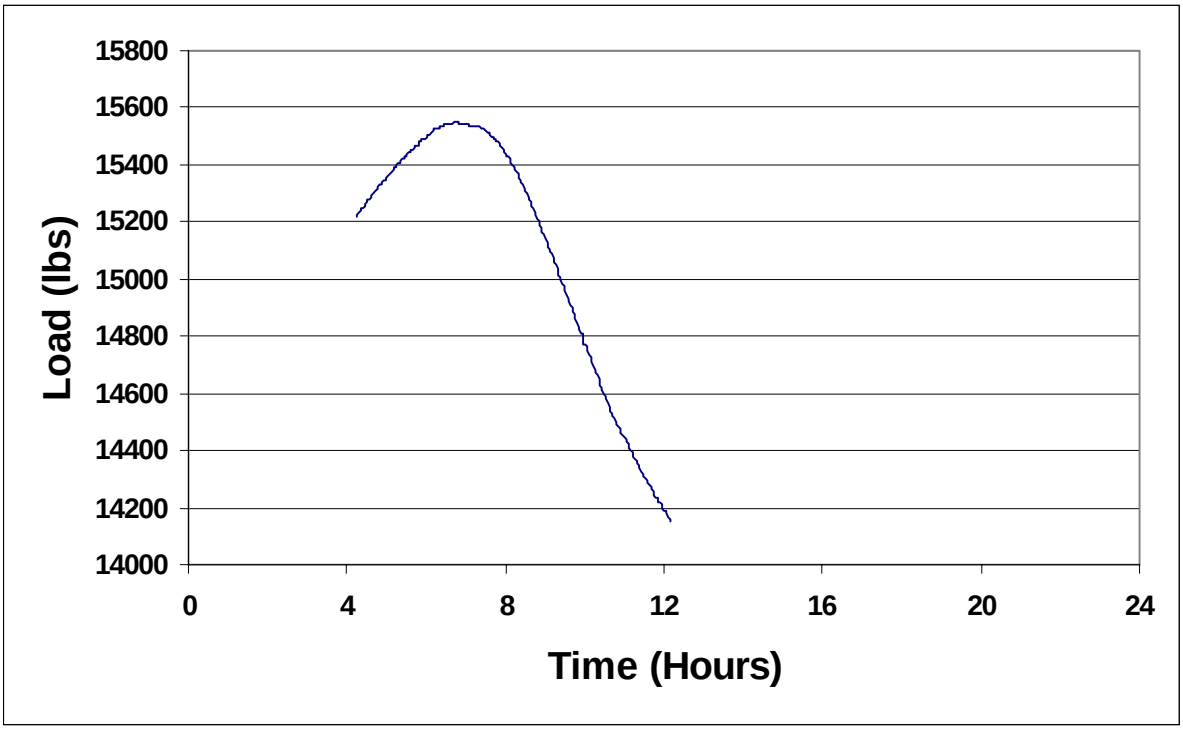

Figure C.24 Steel Force versus Time at Gage SG1 (Day 270).

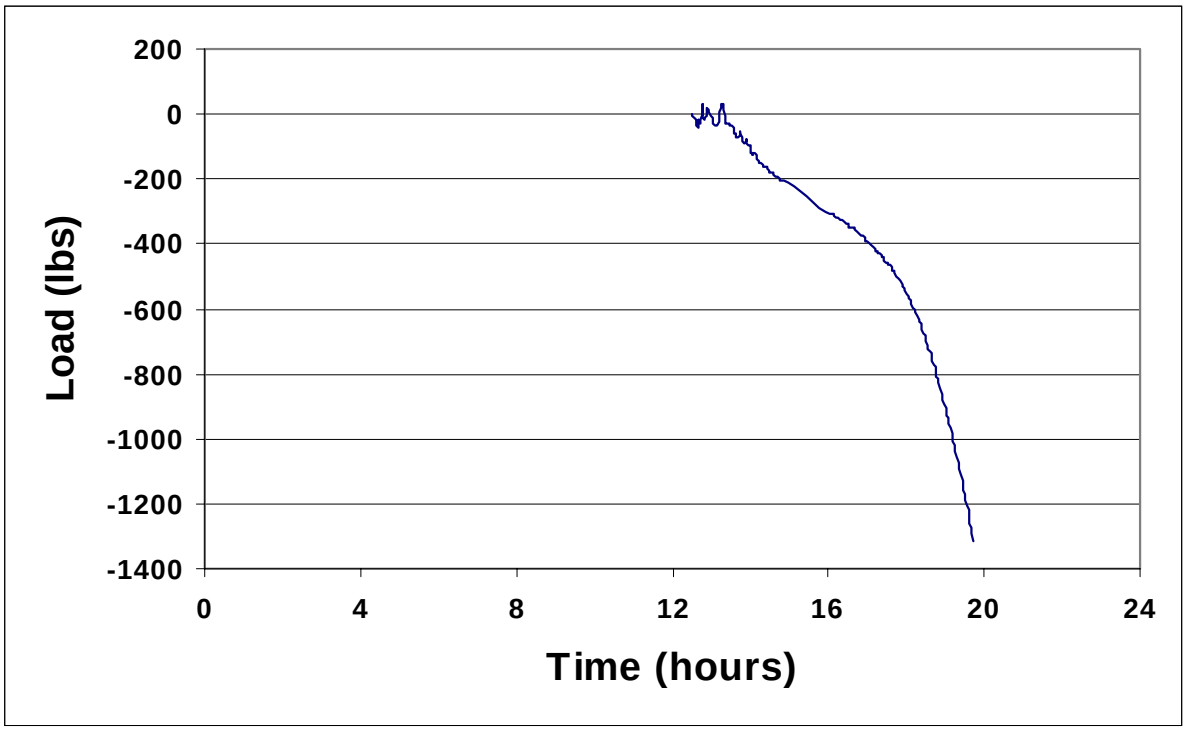

Figure C.25 Steel Force versus Time at Gage SG5 (Day 1).

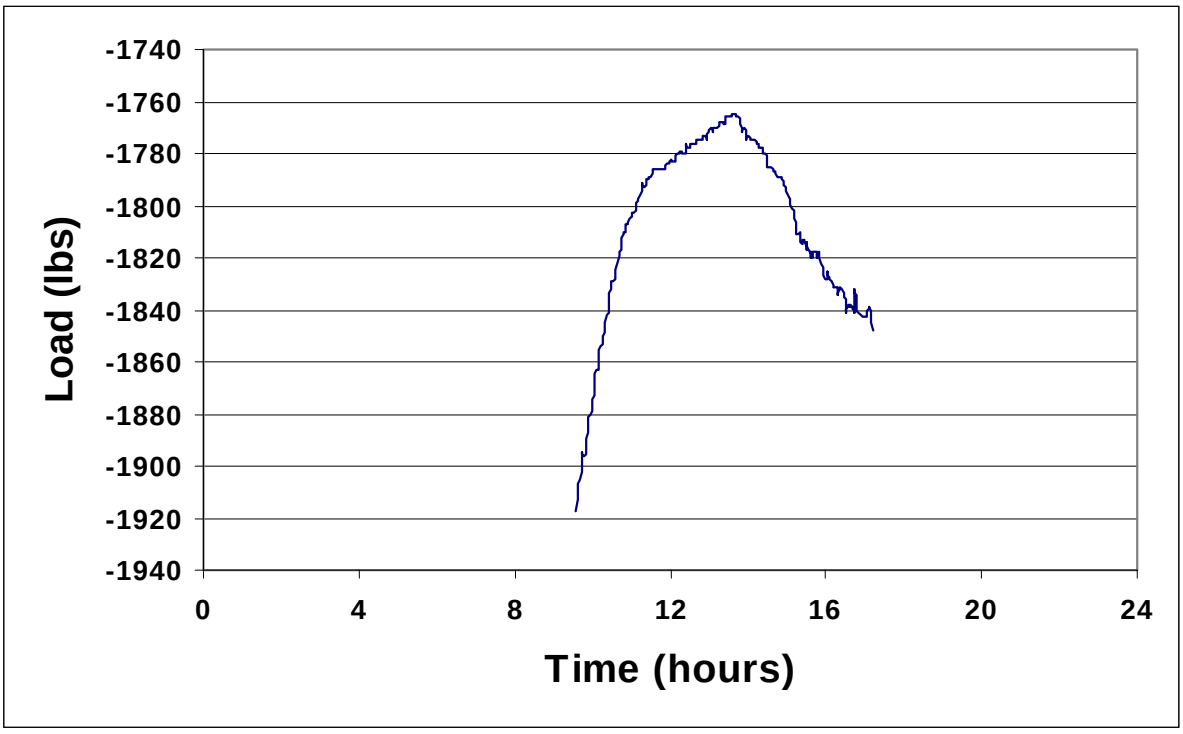

Figure C.26 Steel Force versus Time at Gage SG5 (Day 2).

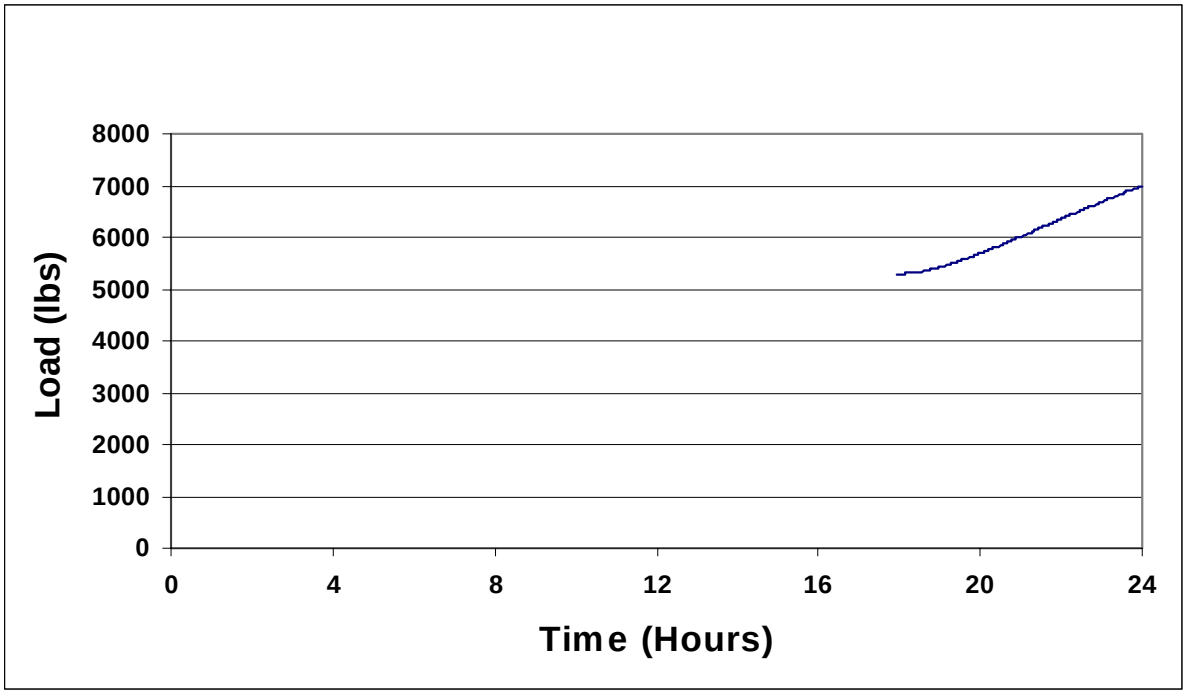

Figure C.27 Steel Force versus Time at Gage SG5 (Day 15).

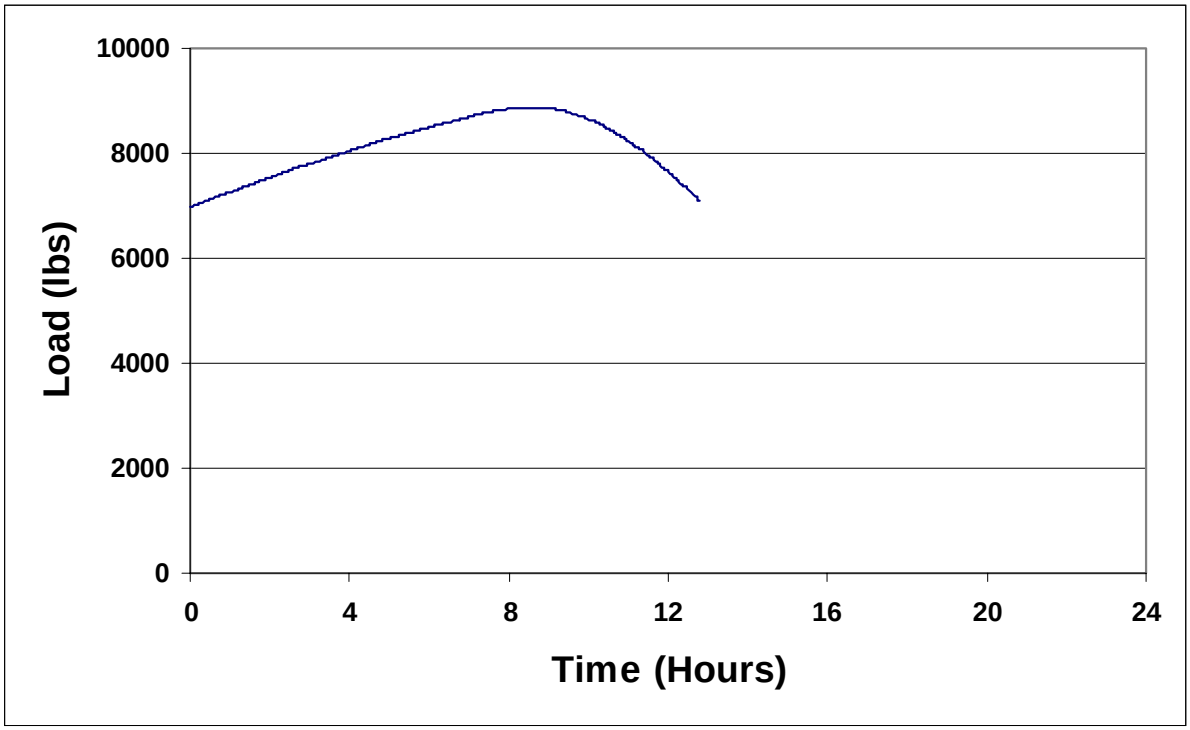

Figure C.28 Steel Force versus Time at Gage SG5 (Day 16).

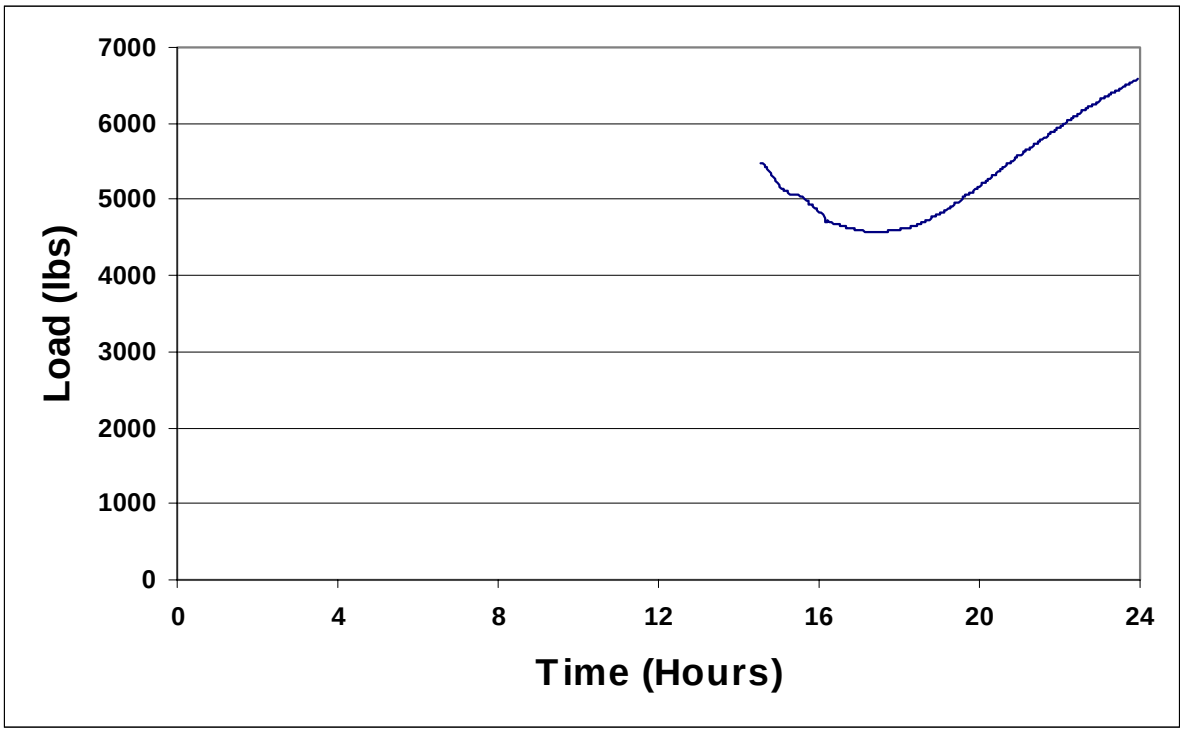

Figure C.29 Steel Force versus Time at Gage SG5 (Day 29).

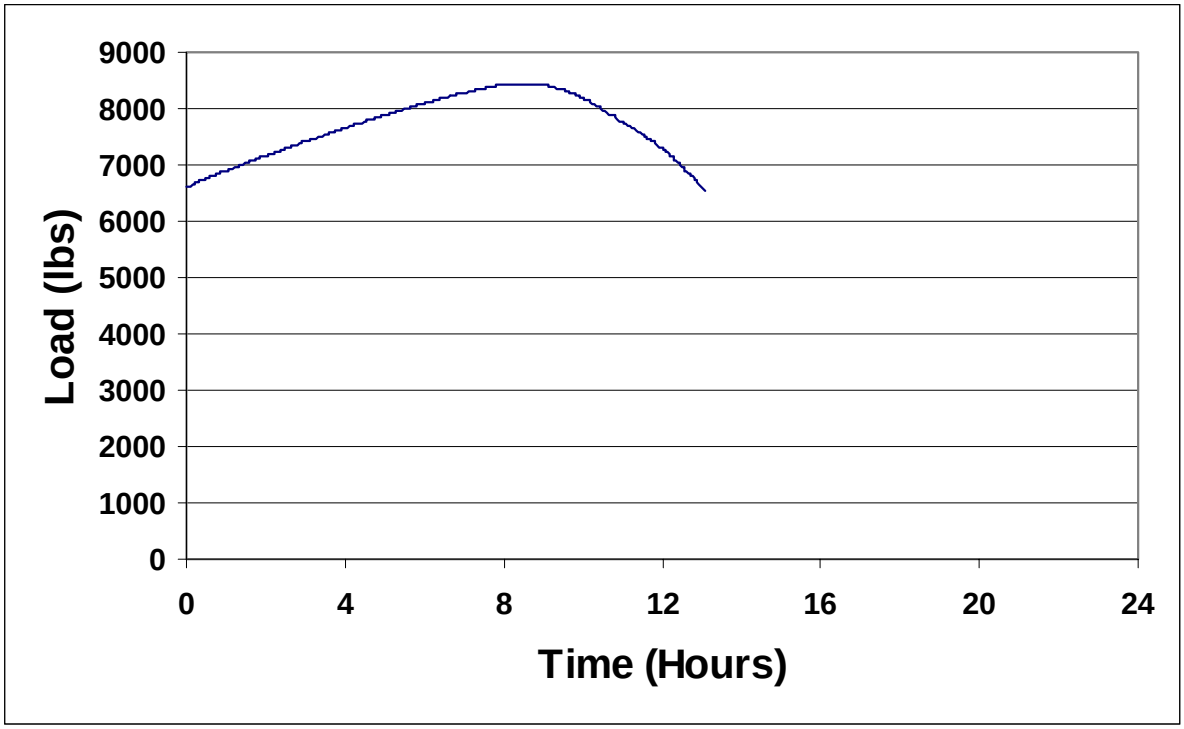

Figure C.30 Steel Force versus Time at Gage SG5 (Day 30).

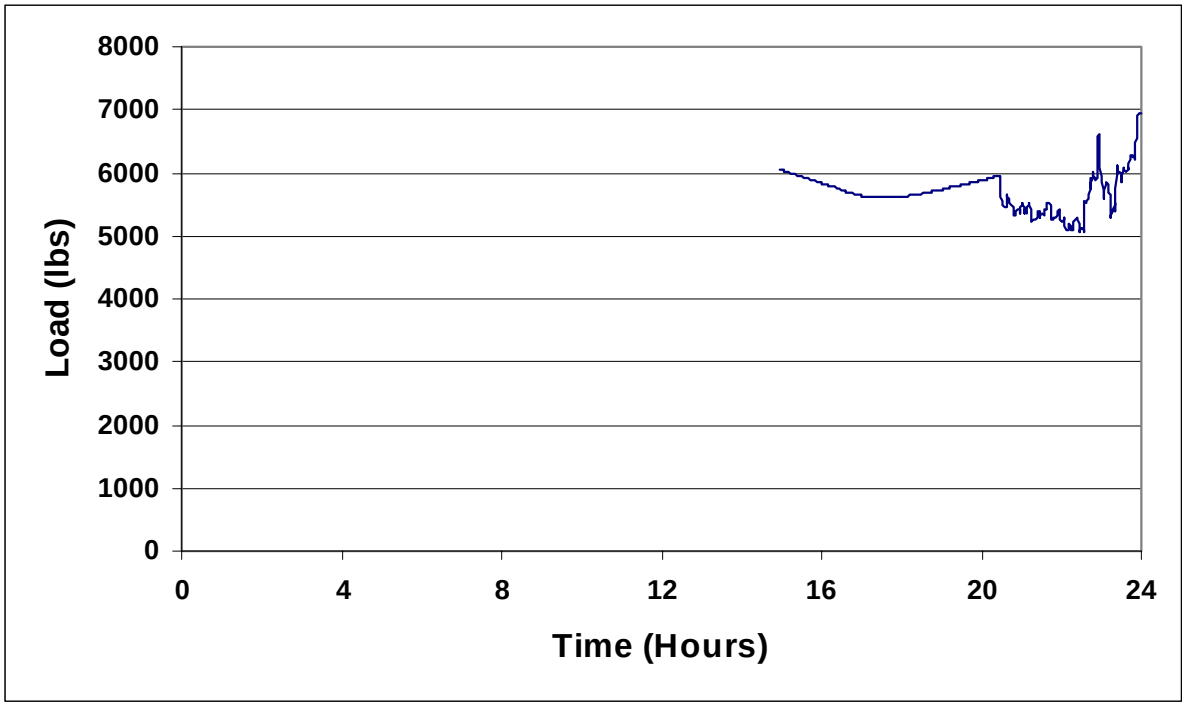

Figure C.31 Steel Force versus Time at Gage SG5 (Day 161).

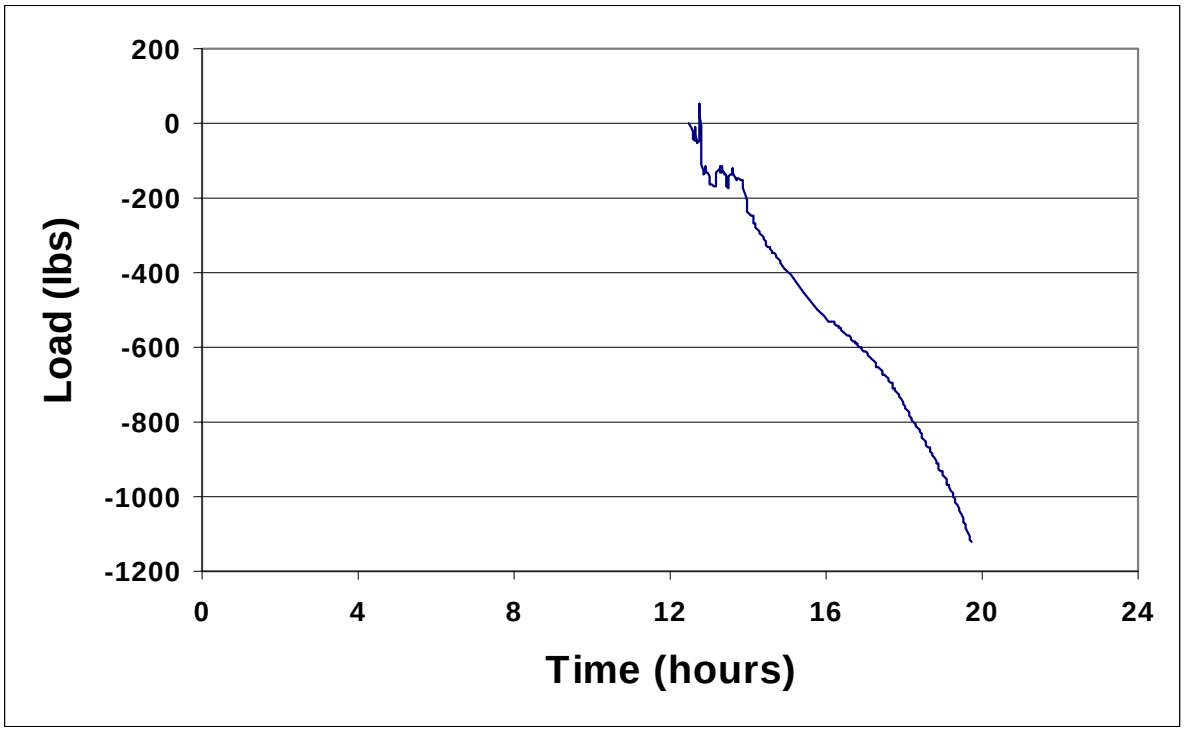

Figure C.32 Steel Force versus Time at Gage SG2 (Day 1).

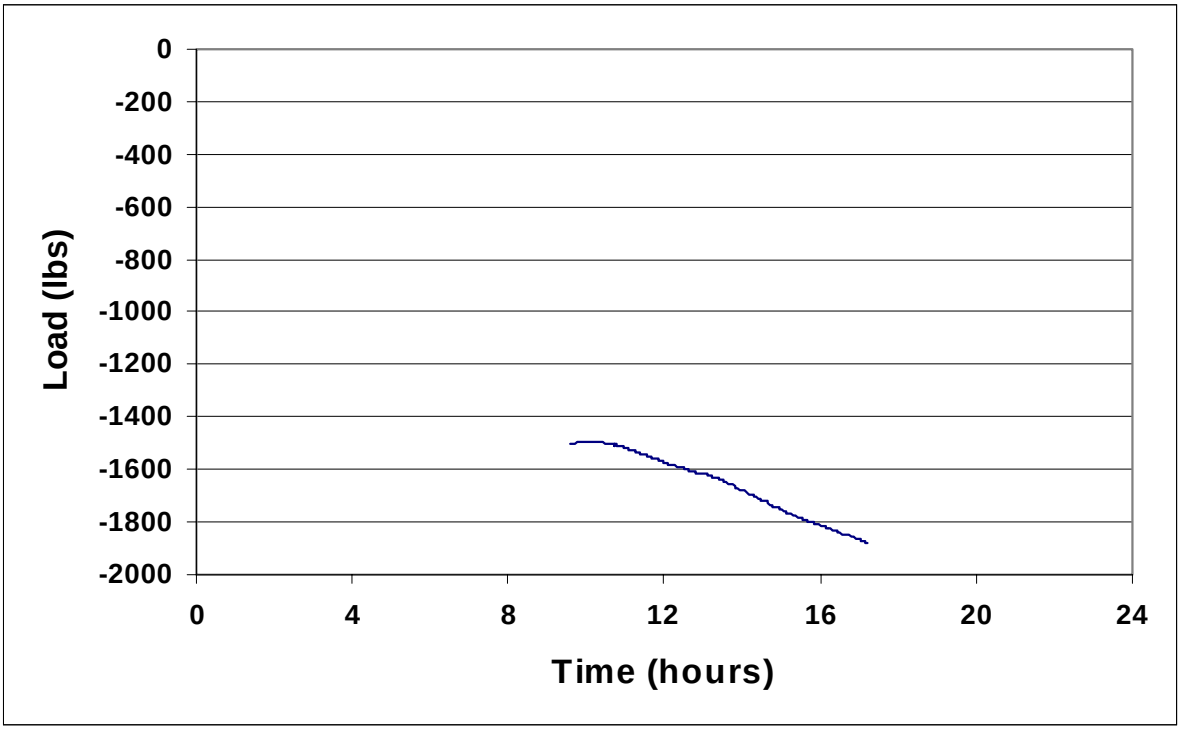

Figure C.33 Steel Force versus Time at Gage SG2 (Day 2).

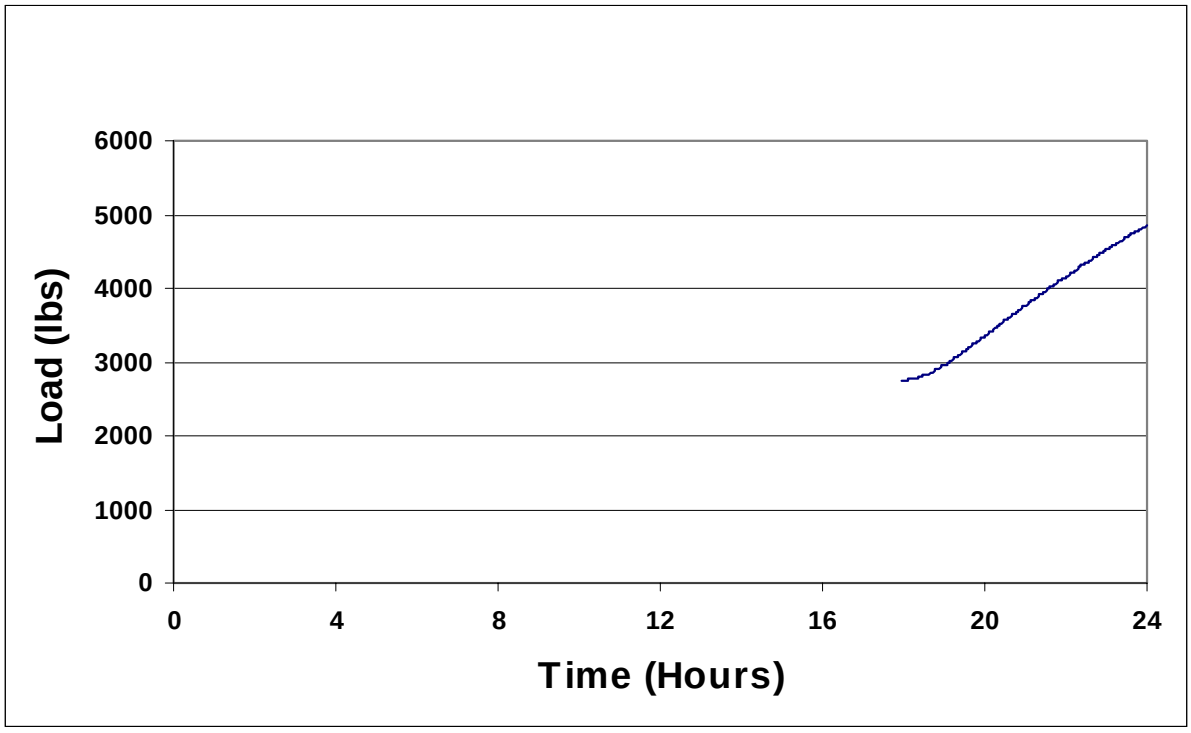

Figure C.34 Steel Force versus Time at Gage SG2 (Day 15).

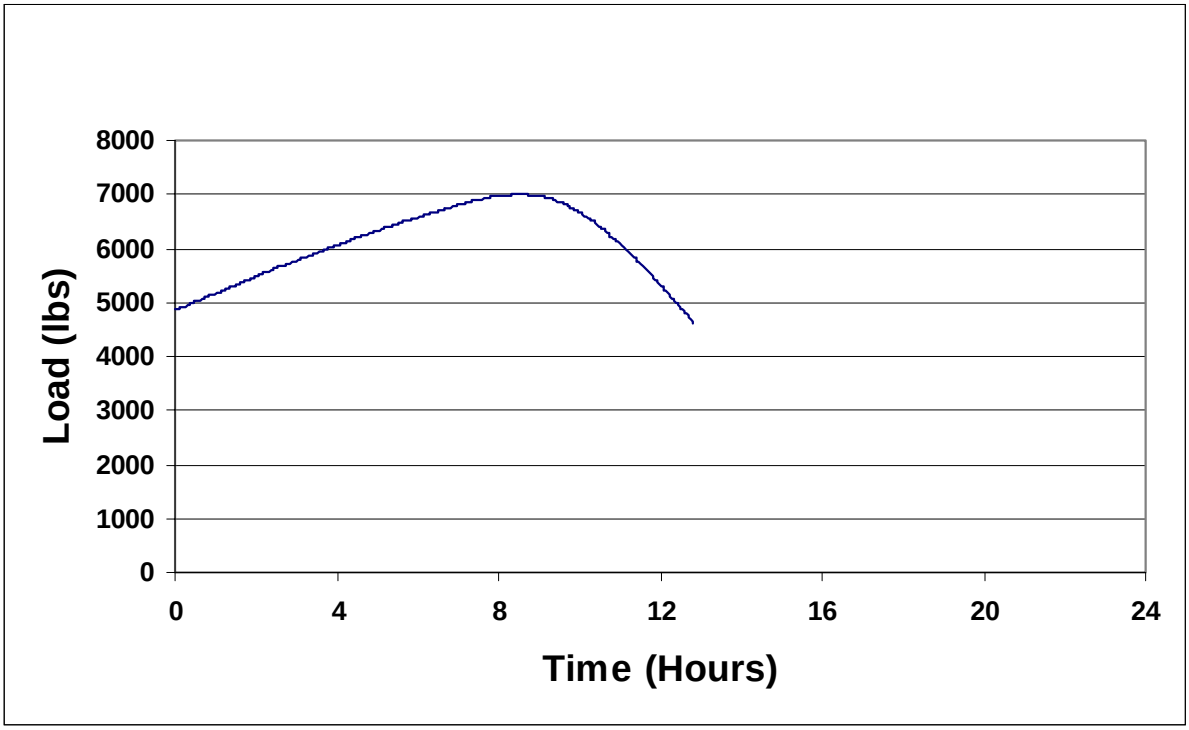

Figure C.35 Steel Force versus Time at Gage SG2 (Day 16).

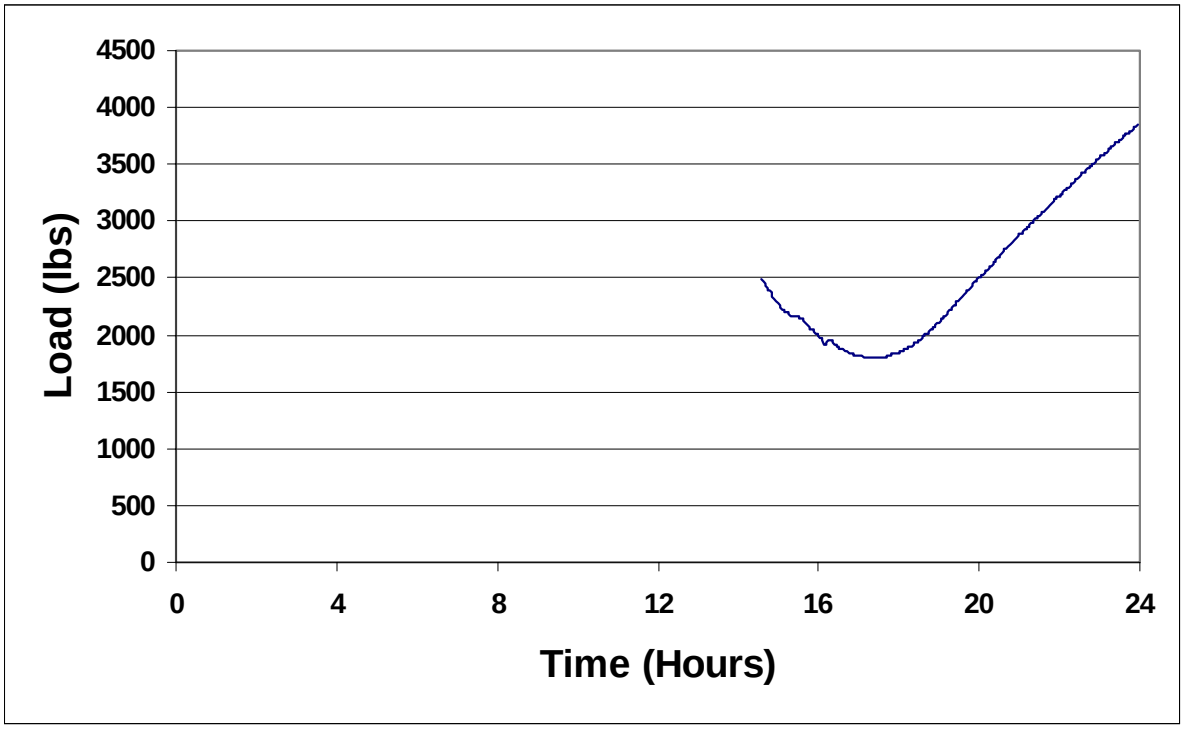

Figure C.36 Steel Force versus Time at Gage SG2 (Day 29).

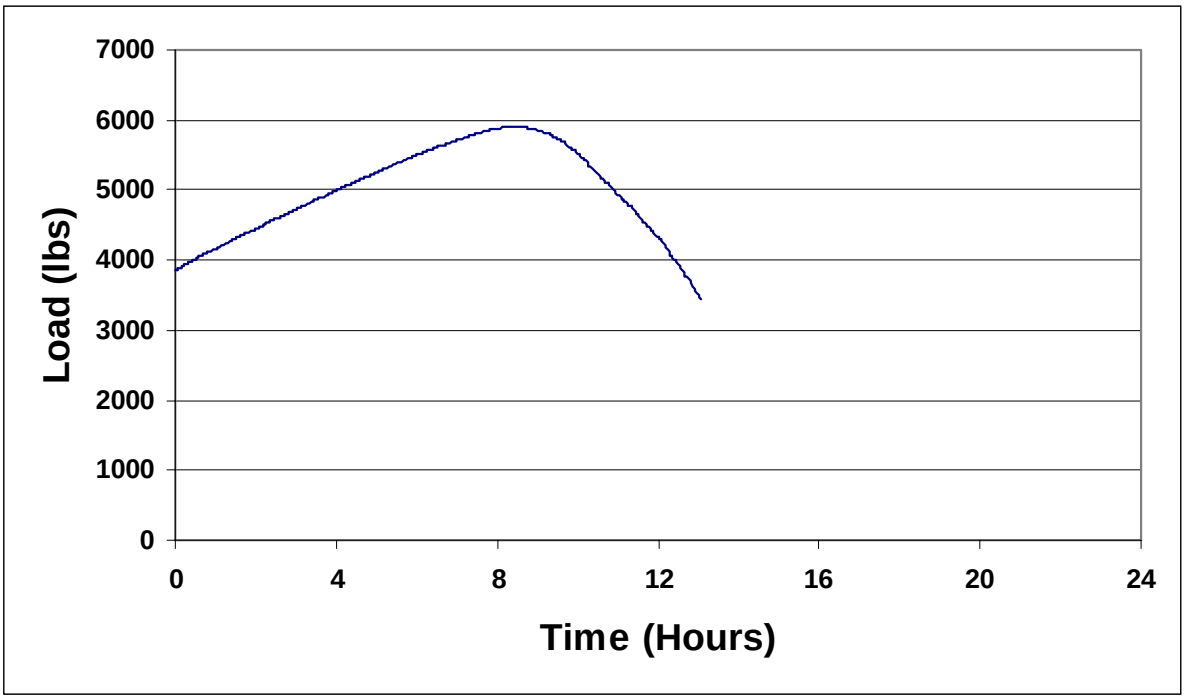

Figure C.37 Steel Force versus Time at Gage SG2 (Day 30).

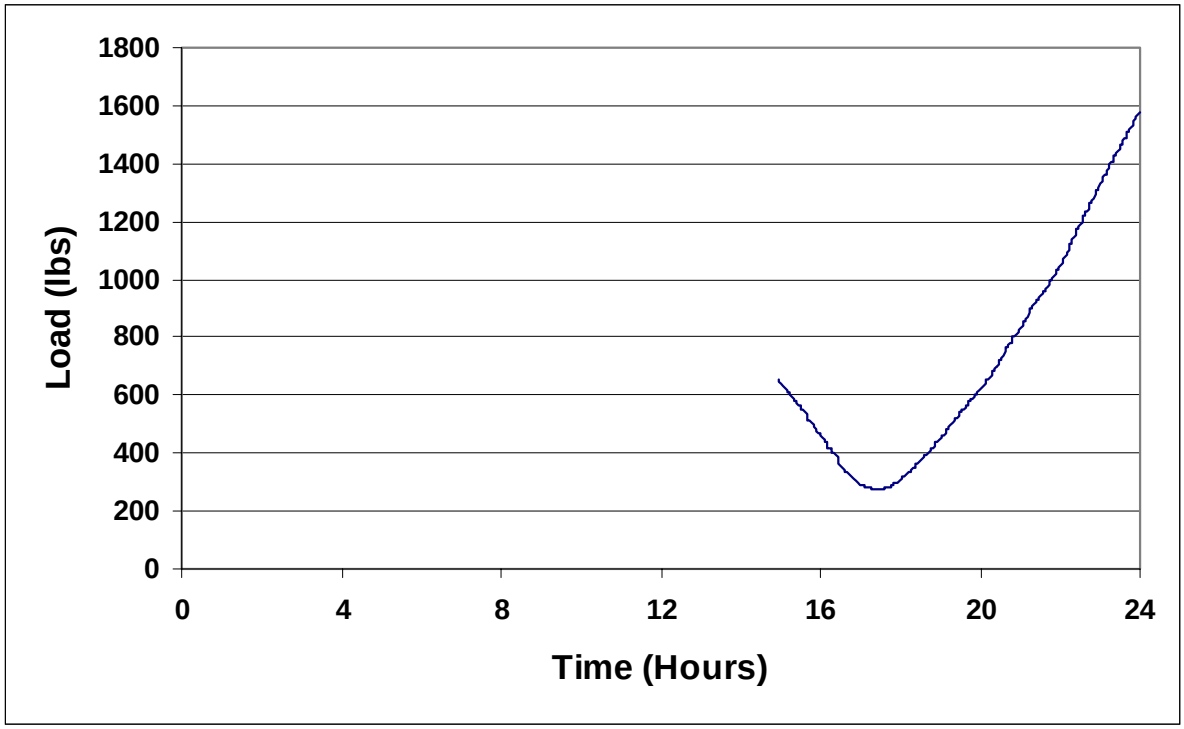

Figure C.38 Steel Force versus Time at Gage SG2 (Day 161).

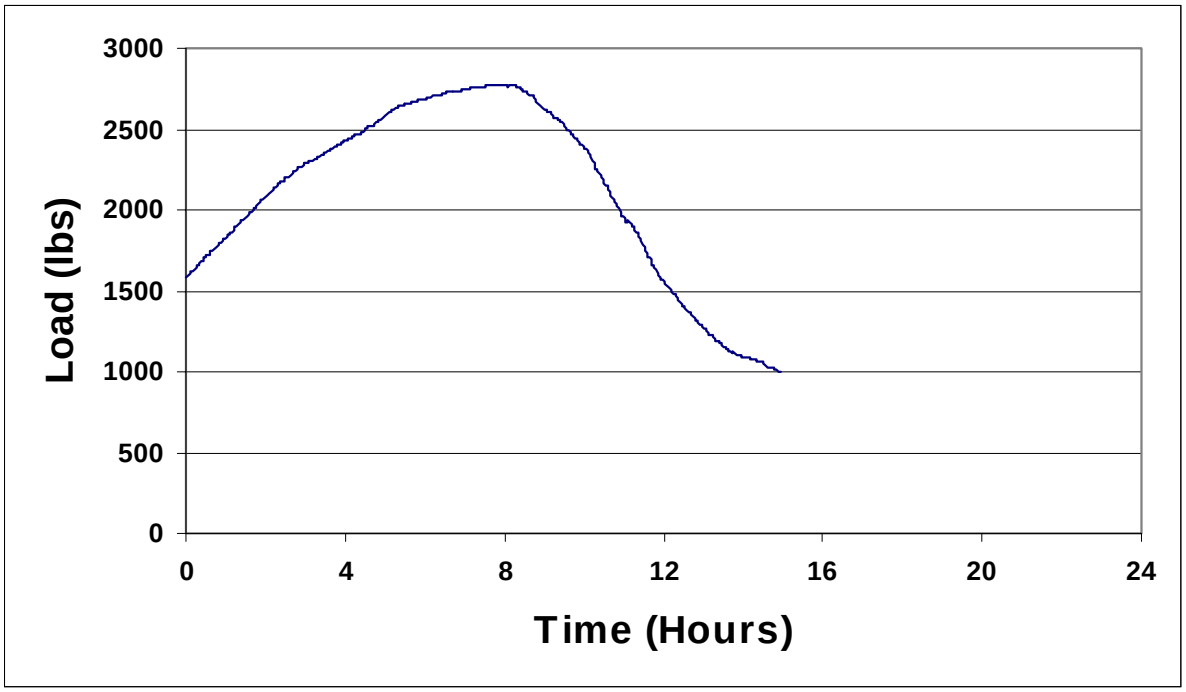

Figure C.39 Steel Force versus Time at Gage SG2 (Day 162).

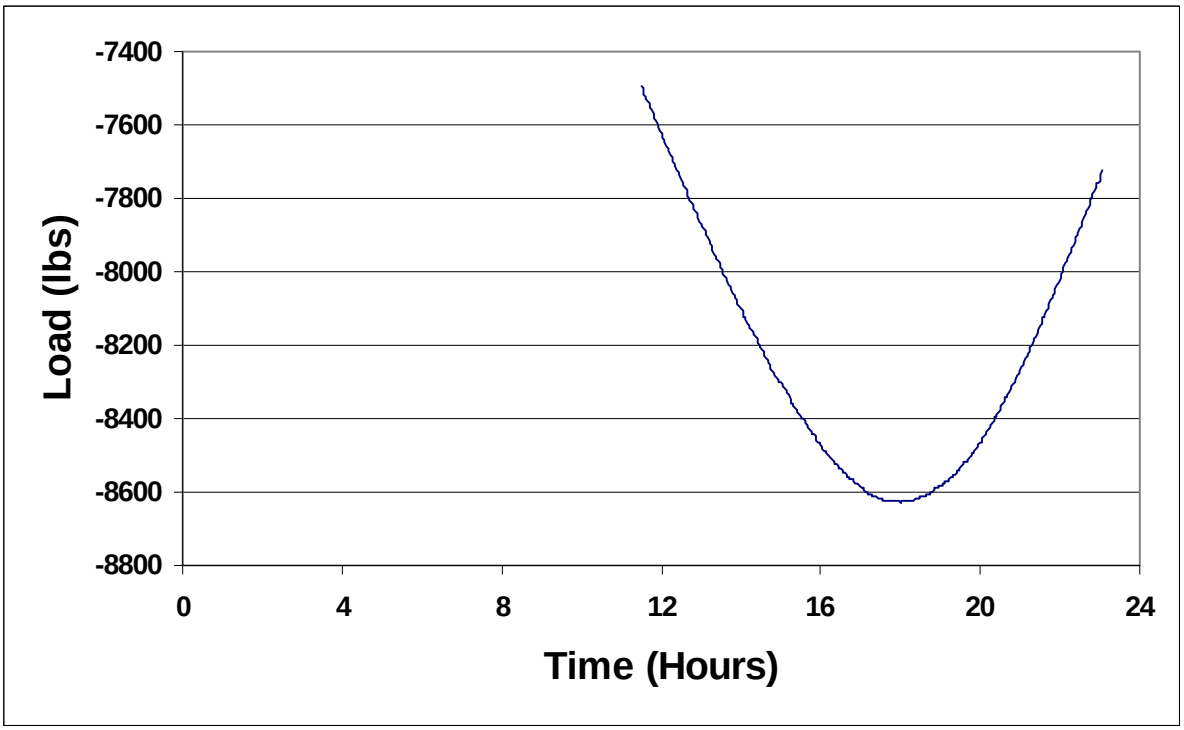

Figure C.40 Steel Force versus Time at Gage SG2 (Day 269).

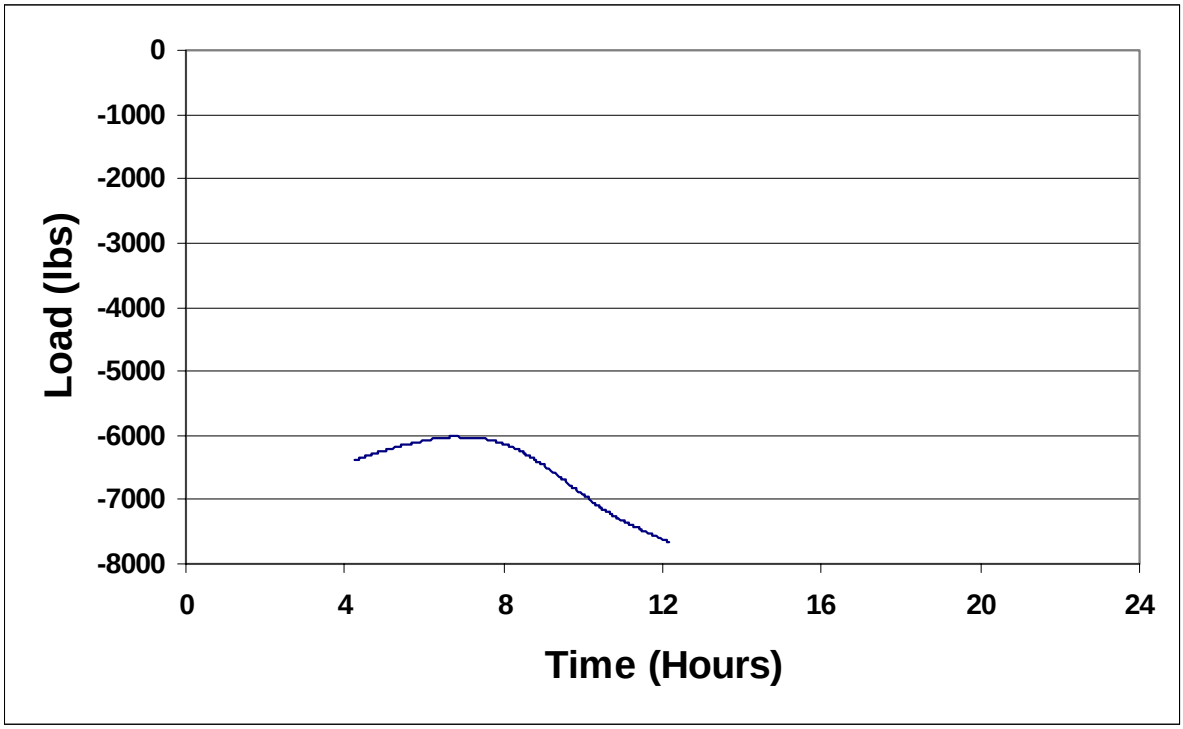

Figure C.41 Steel Force versus Time at Gage SG2 (Day 270).

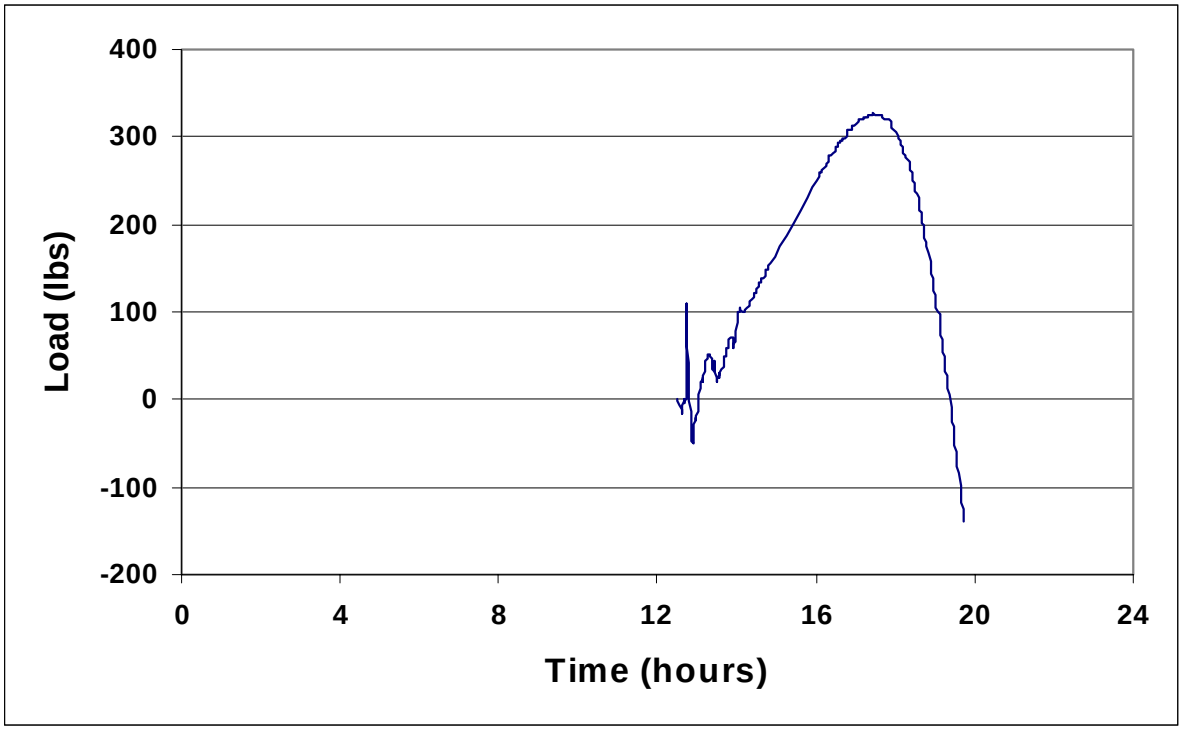

Figure C.42 Steel Force versus Time at Gage SG4 (Day 1).

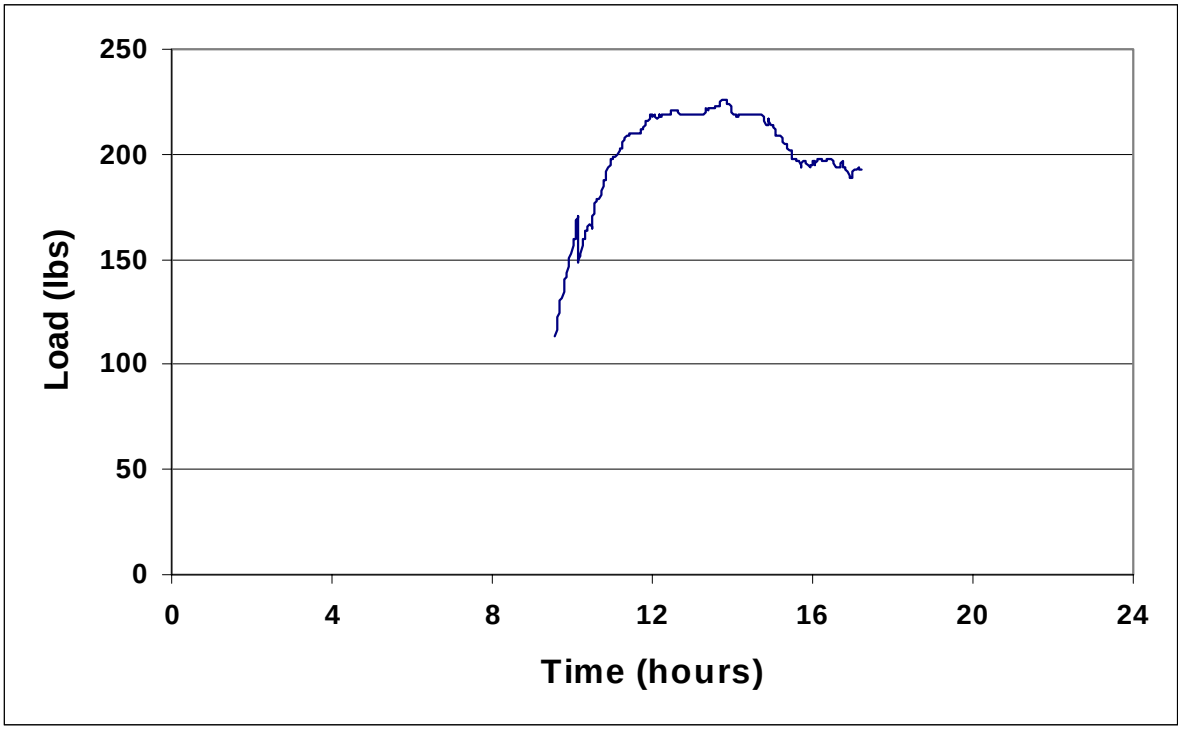

Figure C43 Steel Force versus Time at Gage SG4 (Day 2).

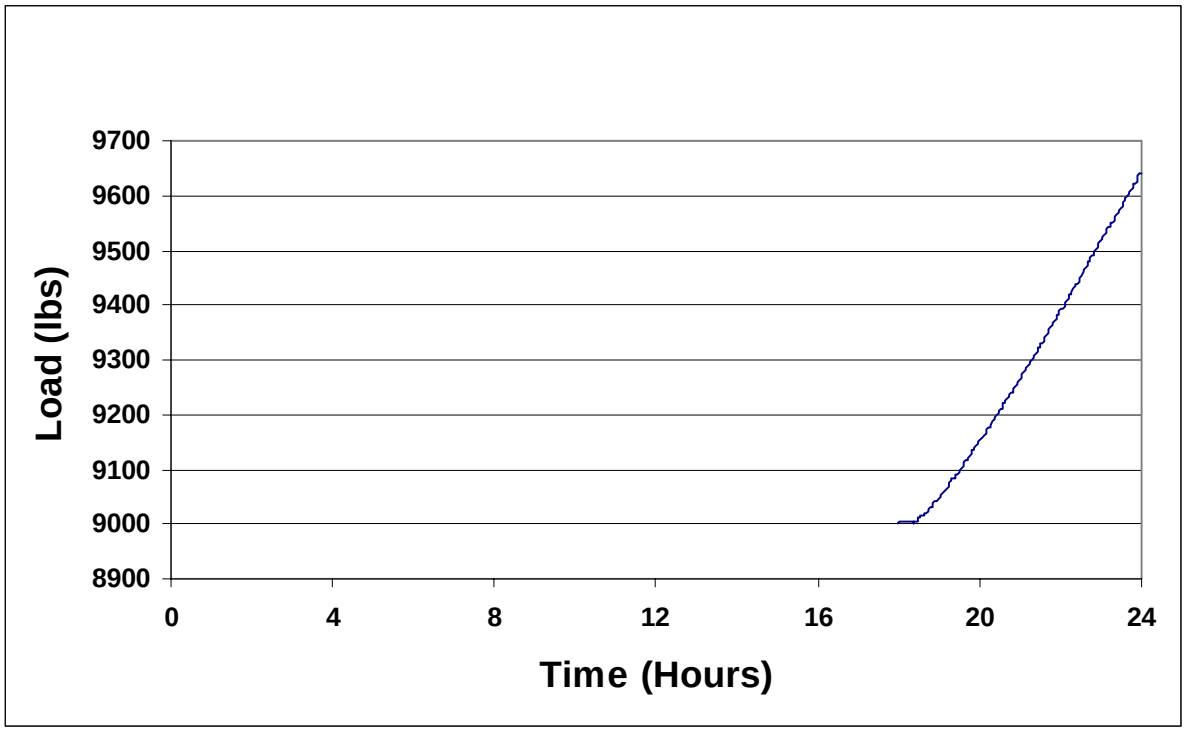

Figure C.44 Steel Force versus Time at Gage SG4 (Day 15).

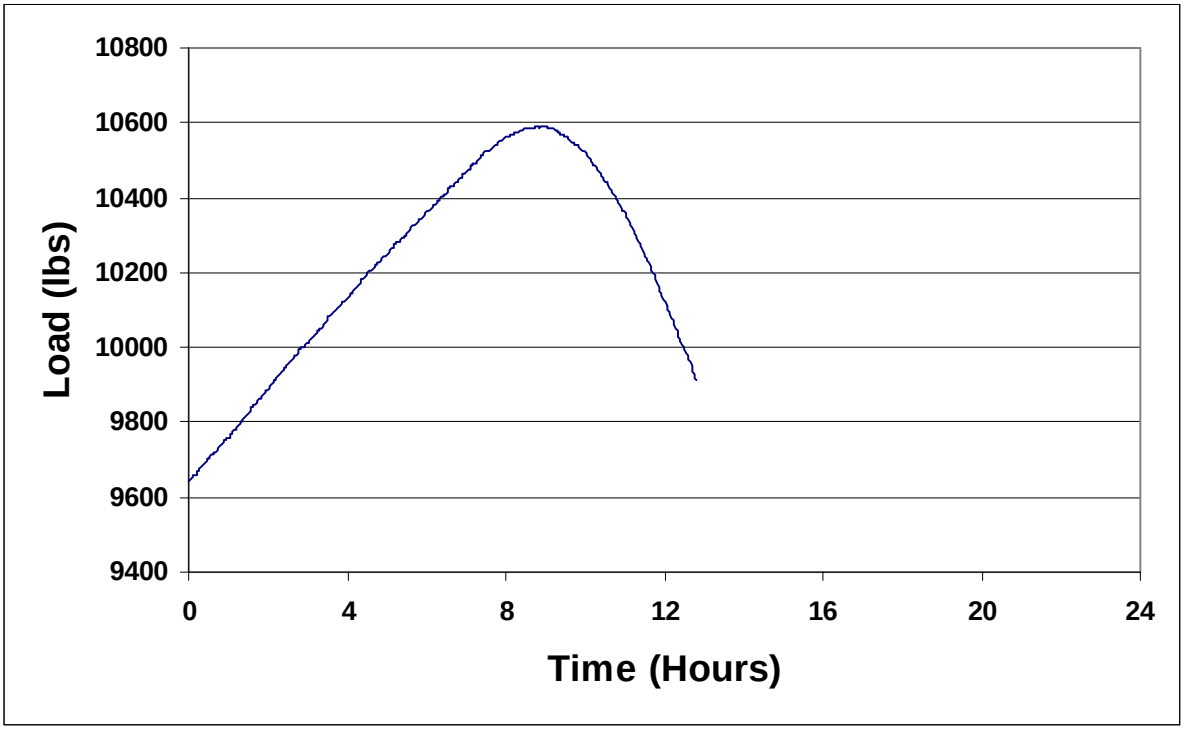

Figure C.45 Steel Force versus Time at Gage SG4 (Day 16).

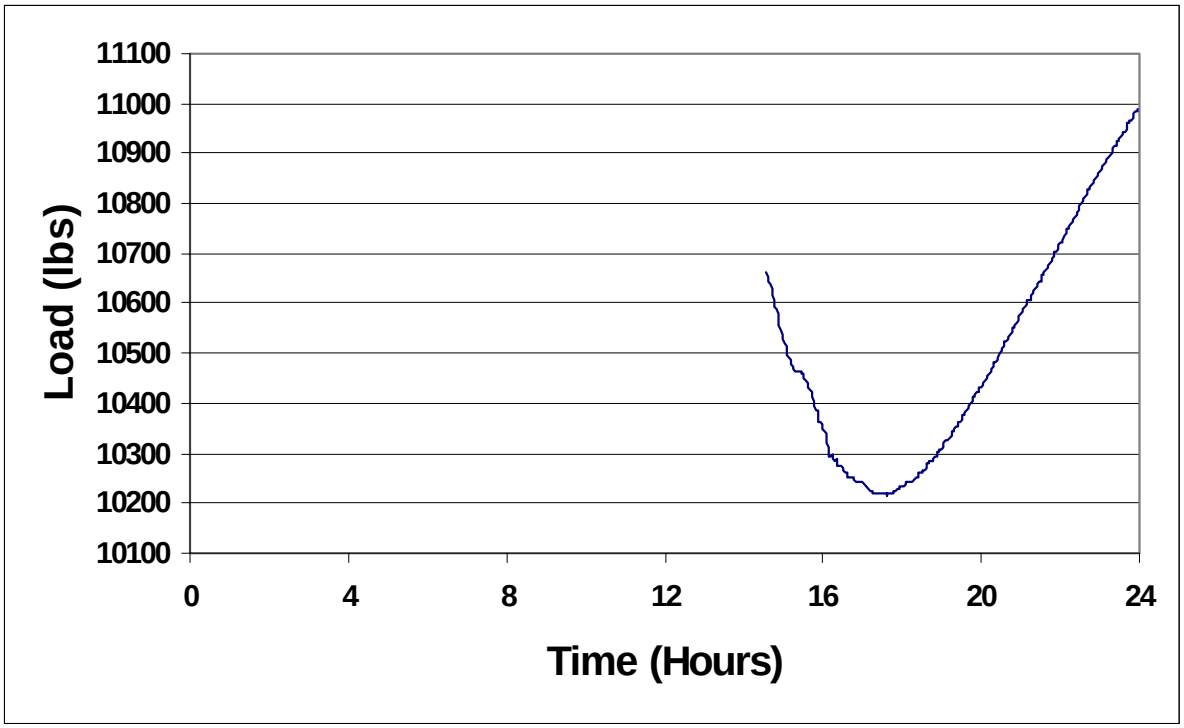

Figure C.46 Steel Force versus Time at Gage SG4 (Day 29).

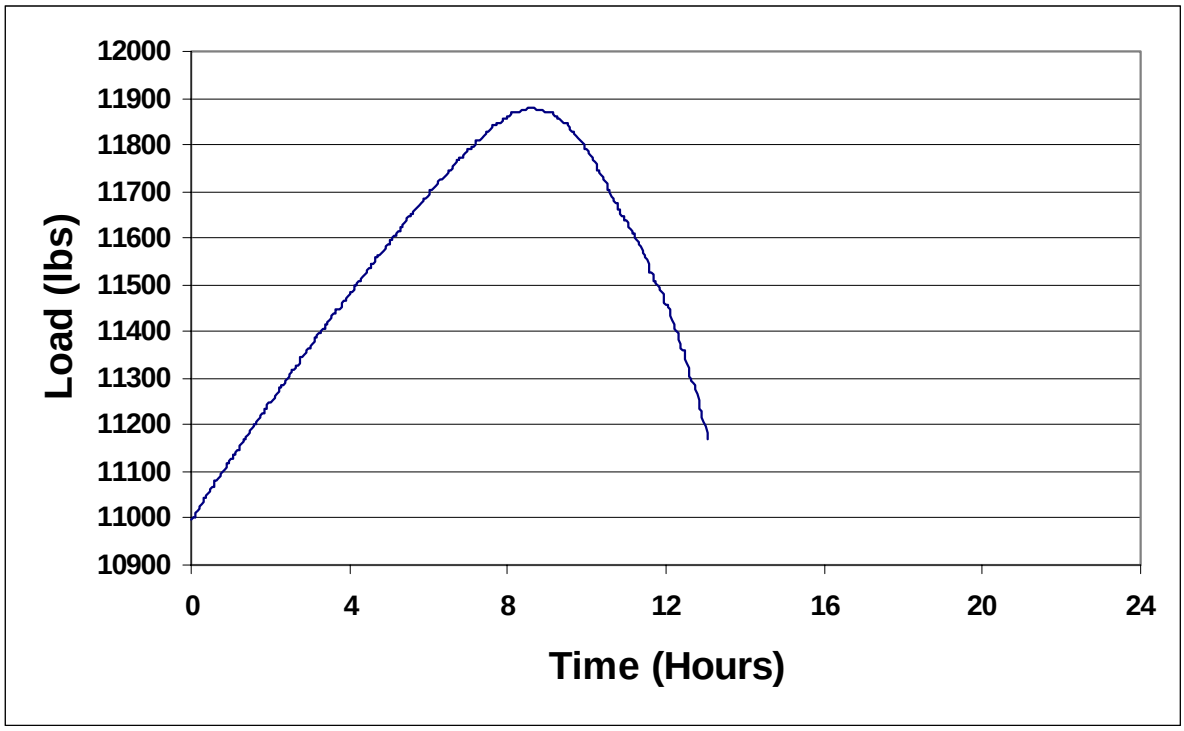

Figure C.47 Steel Force versus Time at Gage SG4 (Day 30).

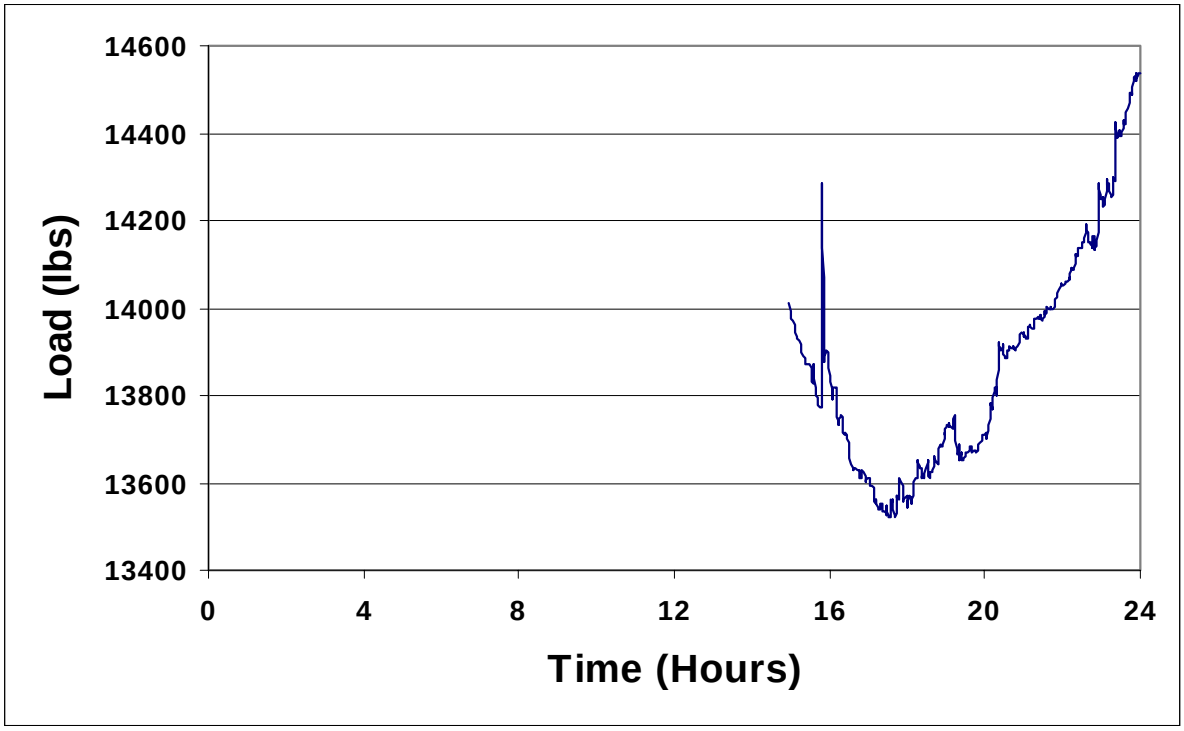

Figure C.48 Steel Force versus Time at Gage SG4 (Day 161).

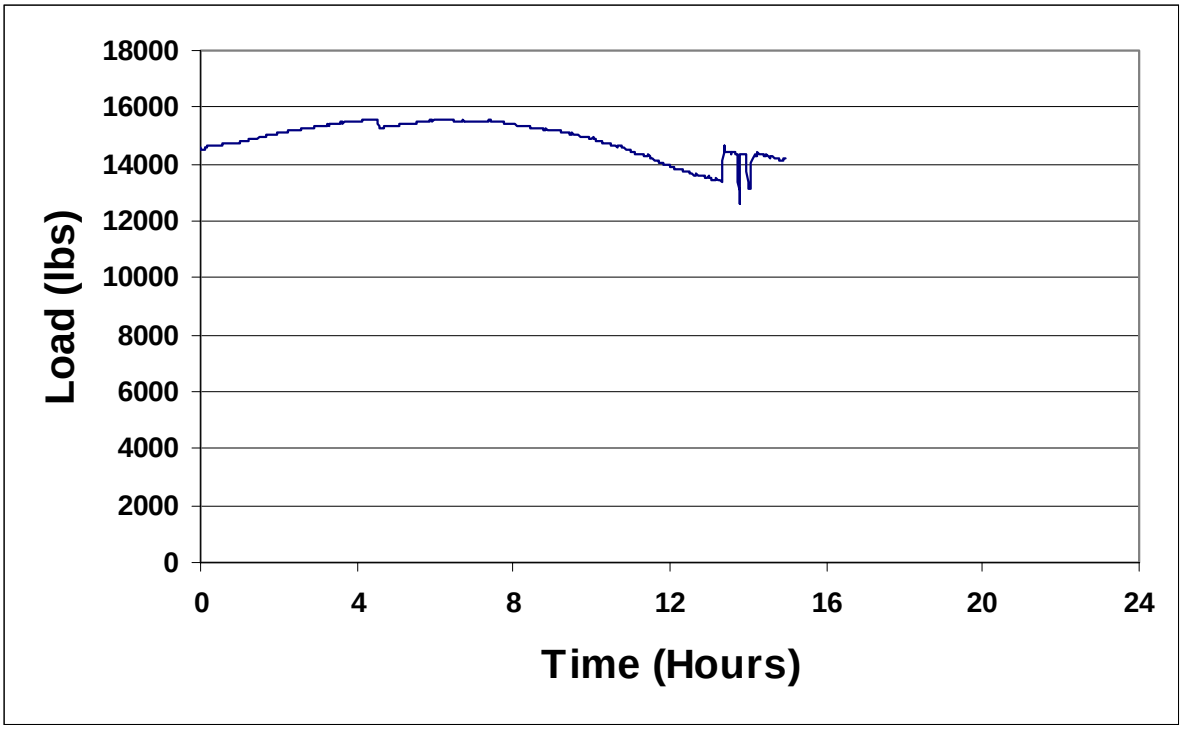

Figure C.49 Steel Force versus Time at Gage SG4 (Day 162).

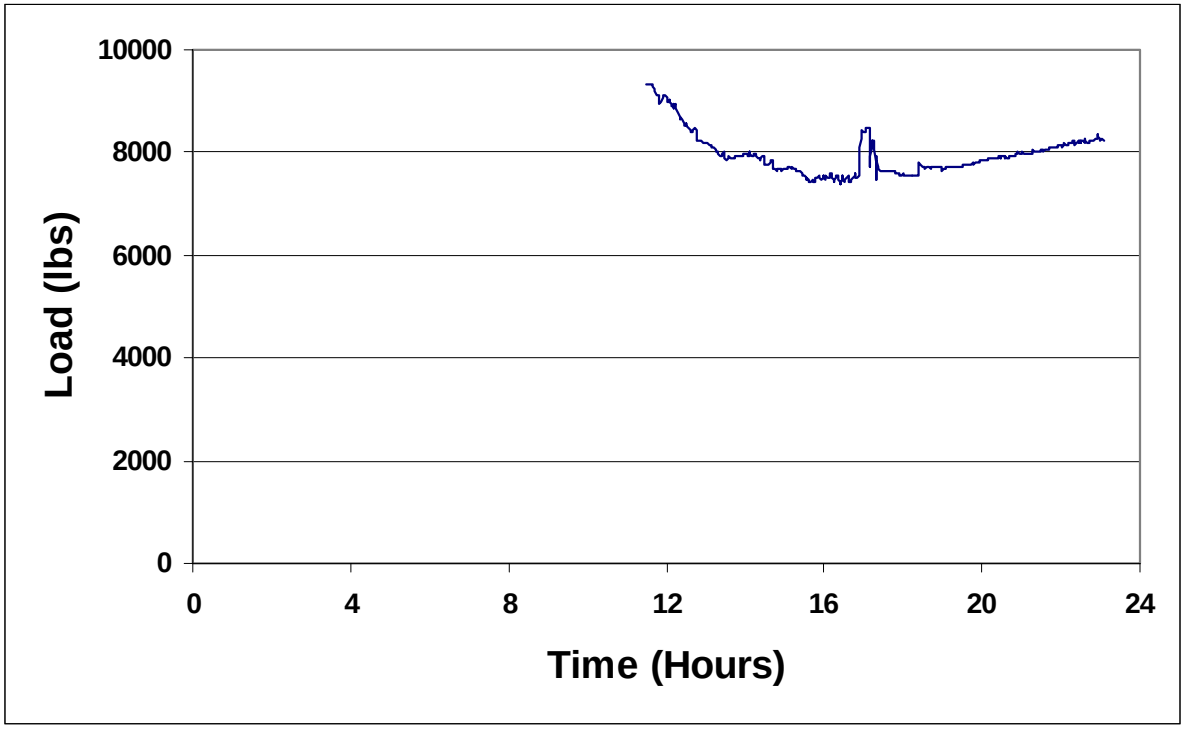

Figure C.50 Steel Force versus Time at Gage SG4 (Day 269).

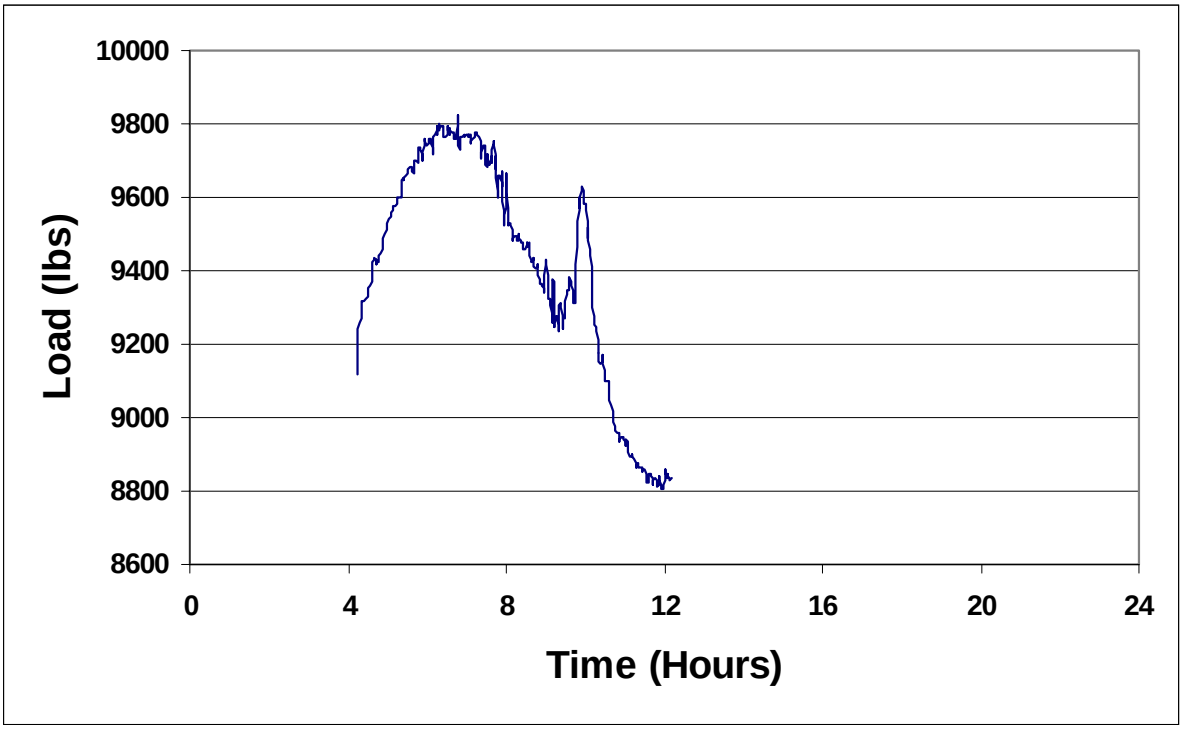

Figure C.51 Steel Force versus Time at Gage SG4 (Day 270).

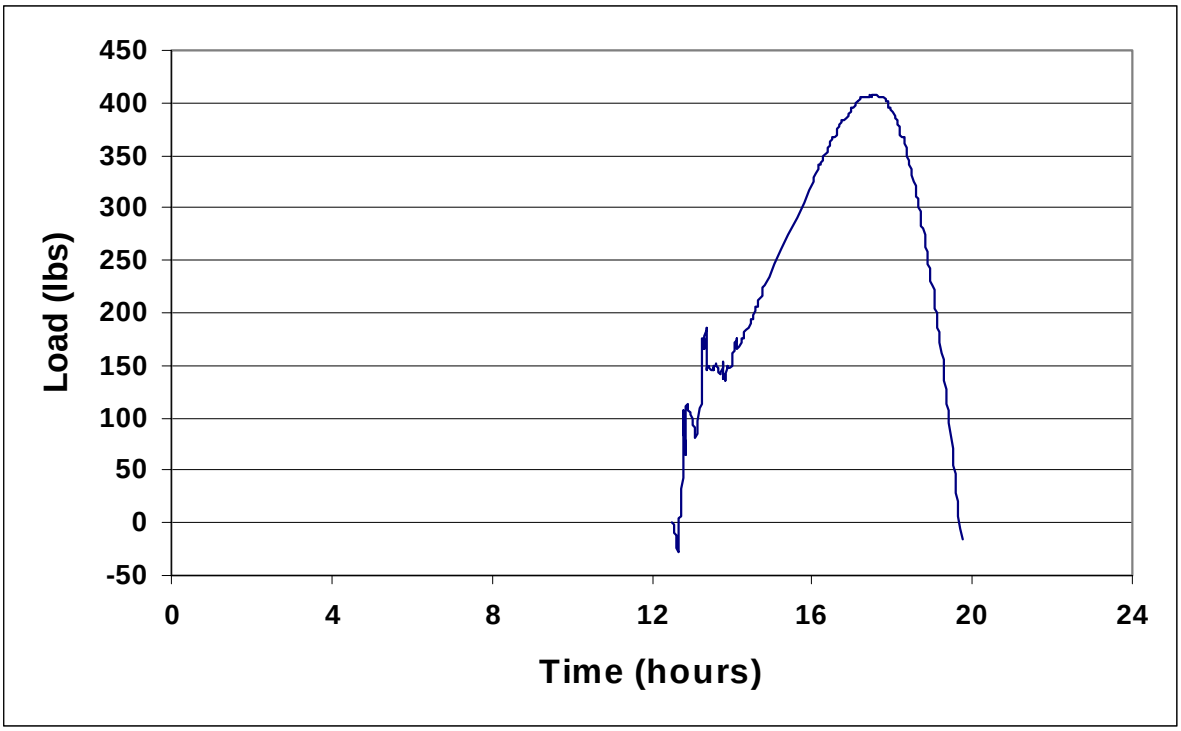

Figure C.52 Steel Force versus Time at Gage SG6 (Day 1).

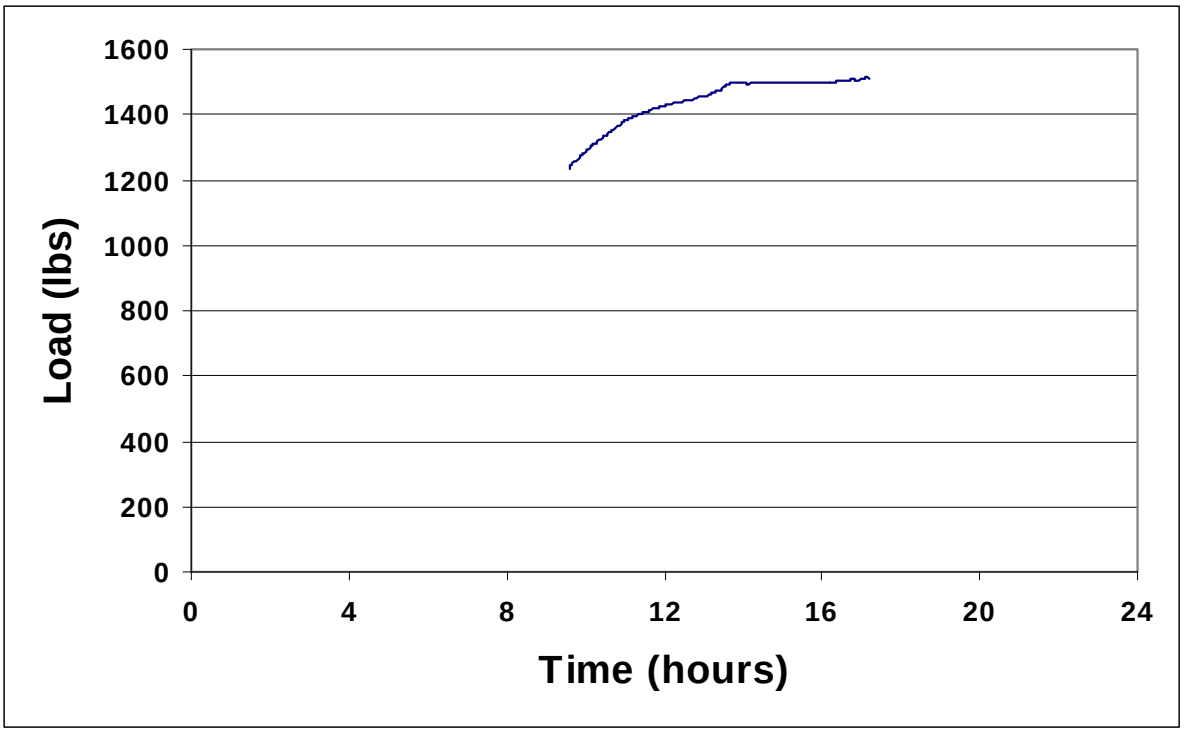

Figure C.53 Steel Force versus Time at Gage SG6 (Day 2).

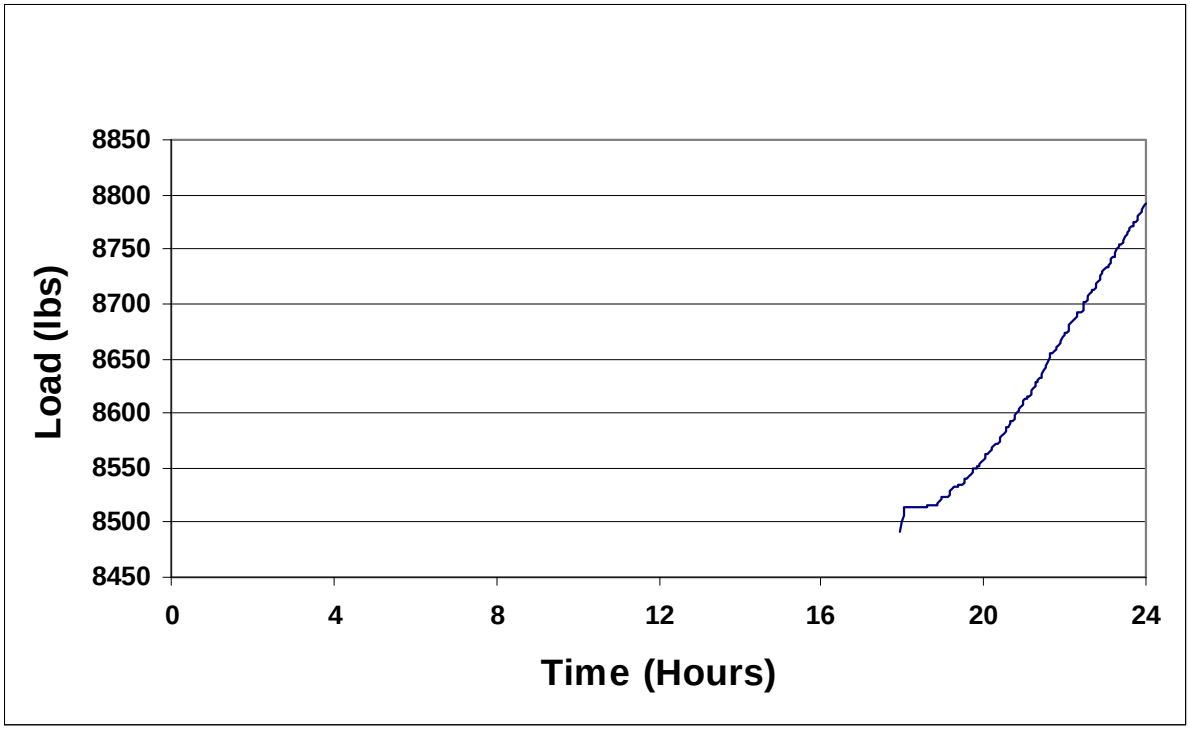

Figure C54 Steel Force versus Time at Gage SG6 (Day 15).

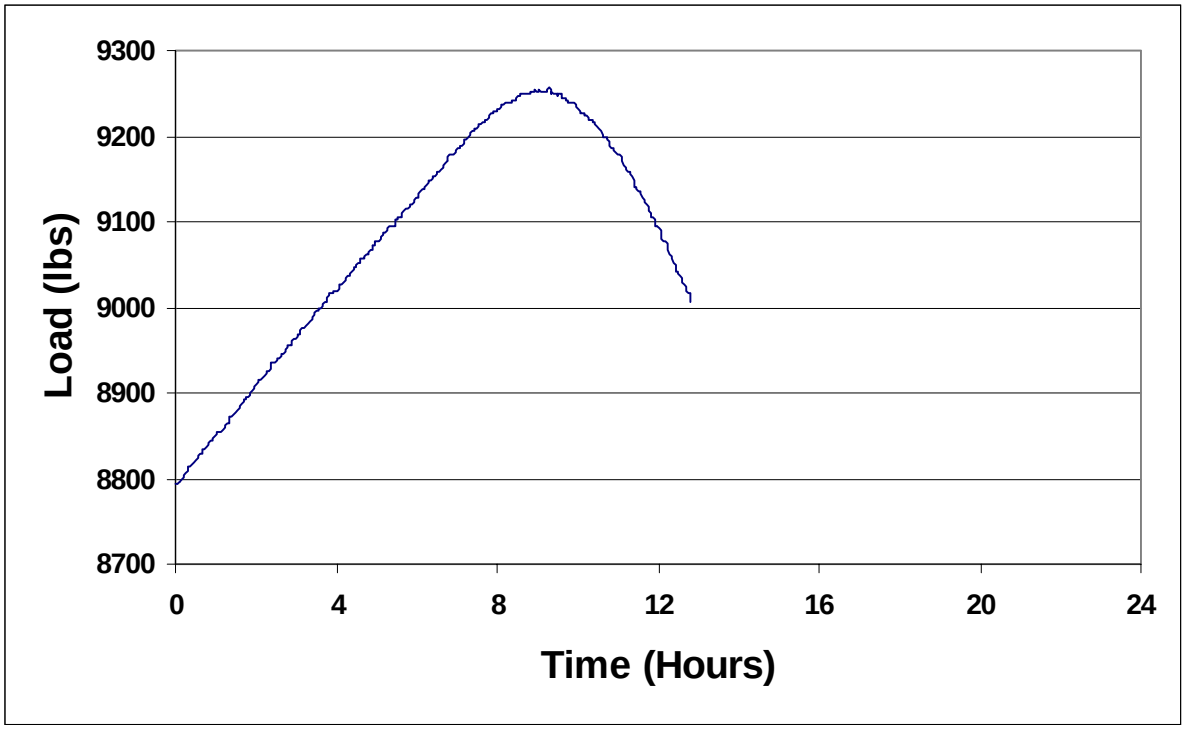

Figure C.55 Steel Force versus Time at Gage SG6 (Day 16).

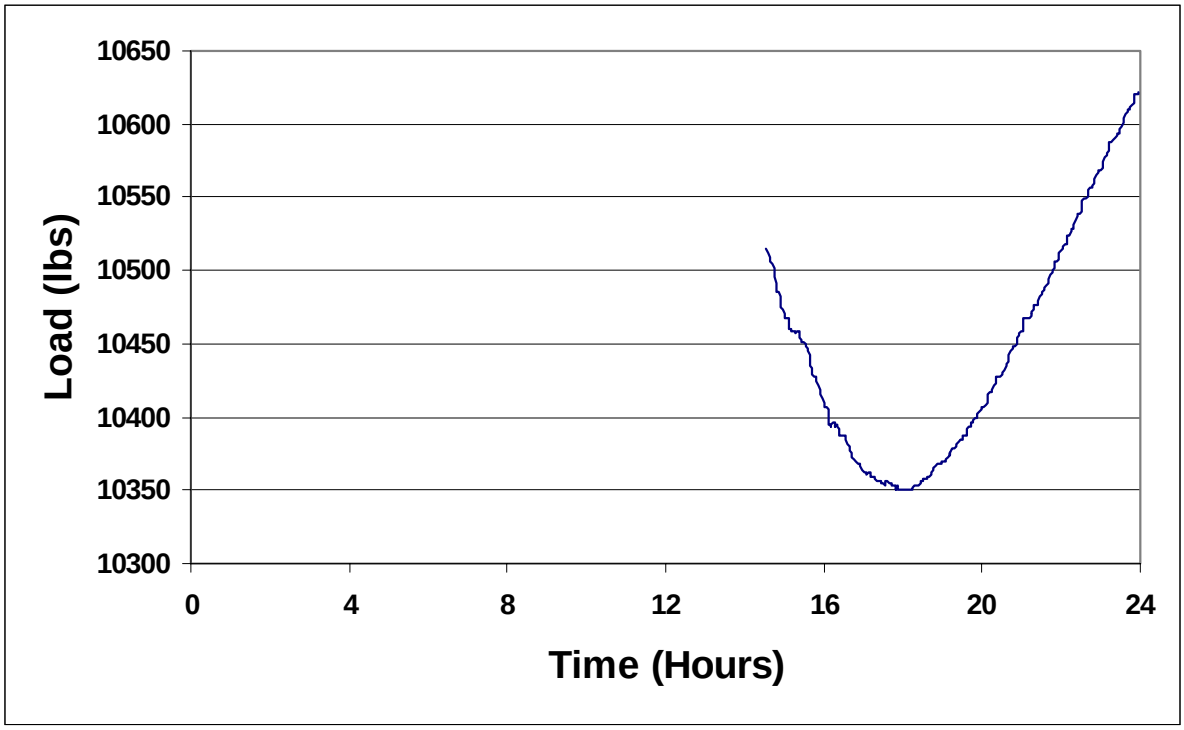

Figure C.56 Steel Force versus Time at Gage SG6 (Day 29).

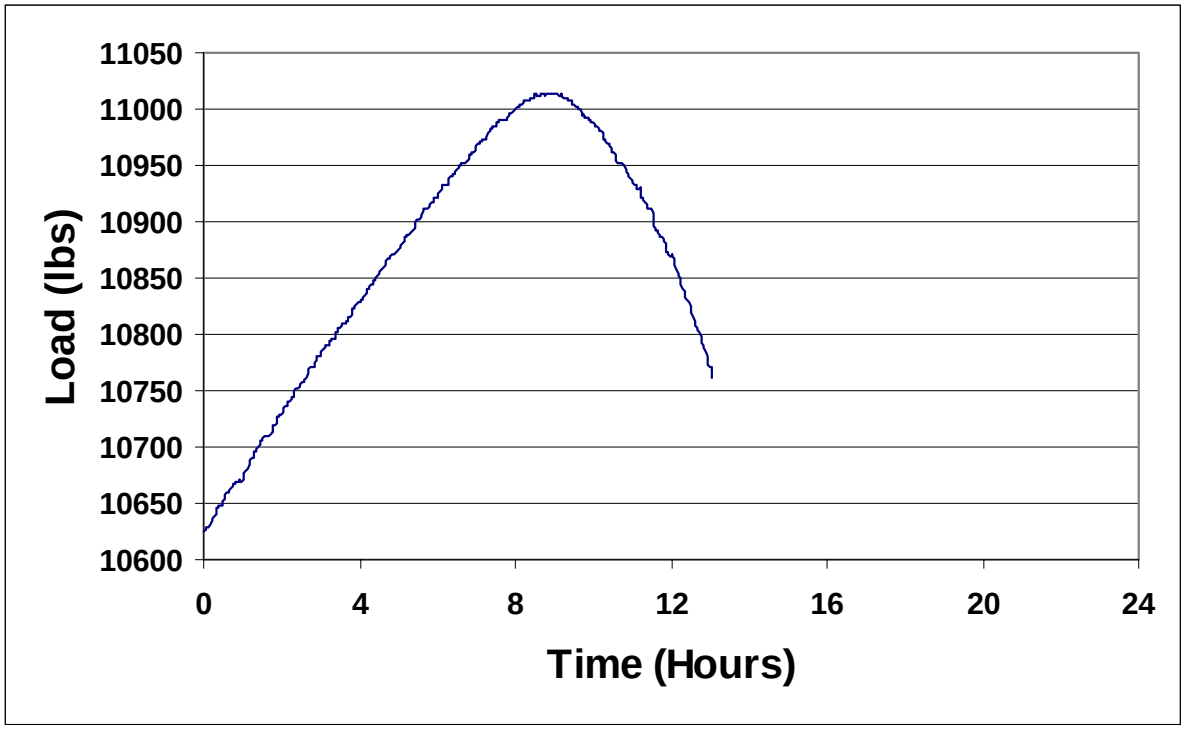

Figure C.57 Steel Force versus Time at Gage SG6 (Day 30).

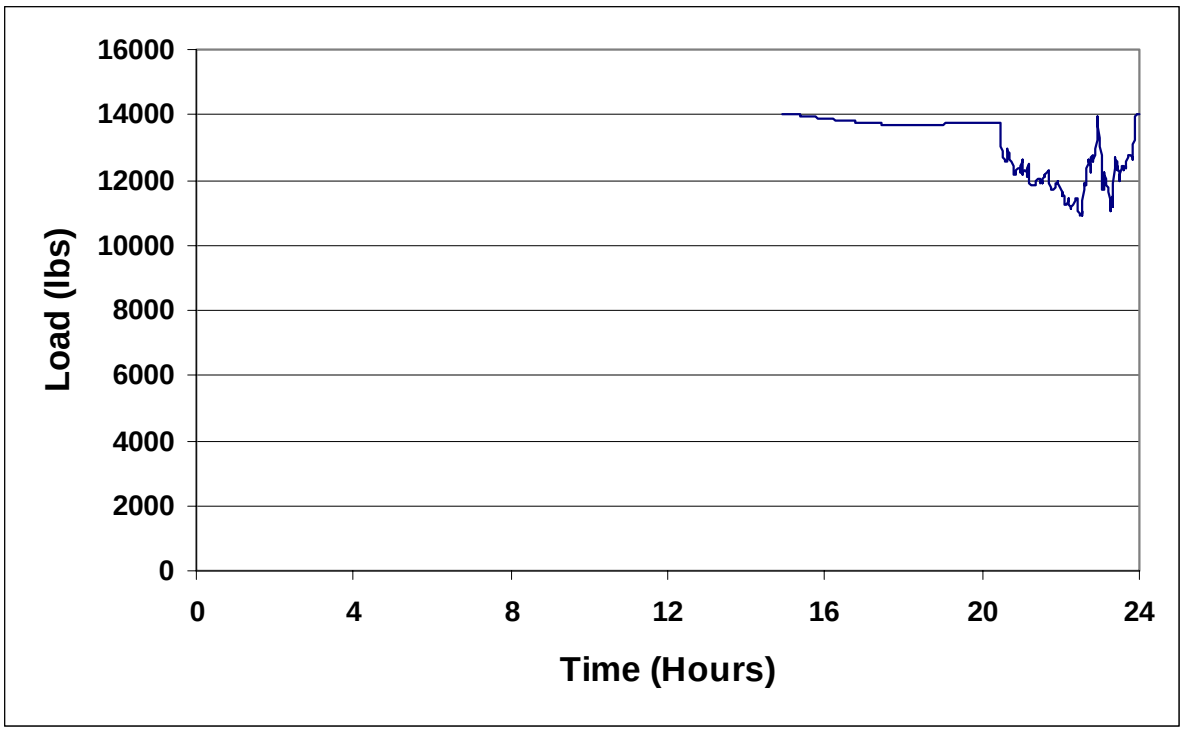

Figure C.58 Steel Force versus Time at Gage SG6 (Day 161).

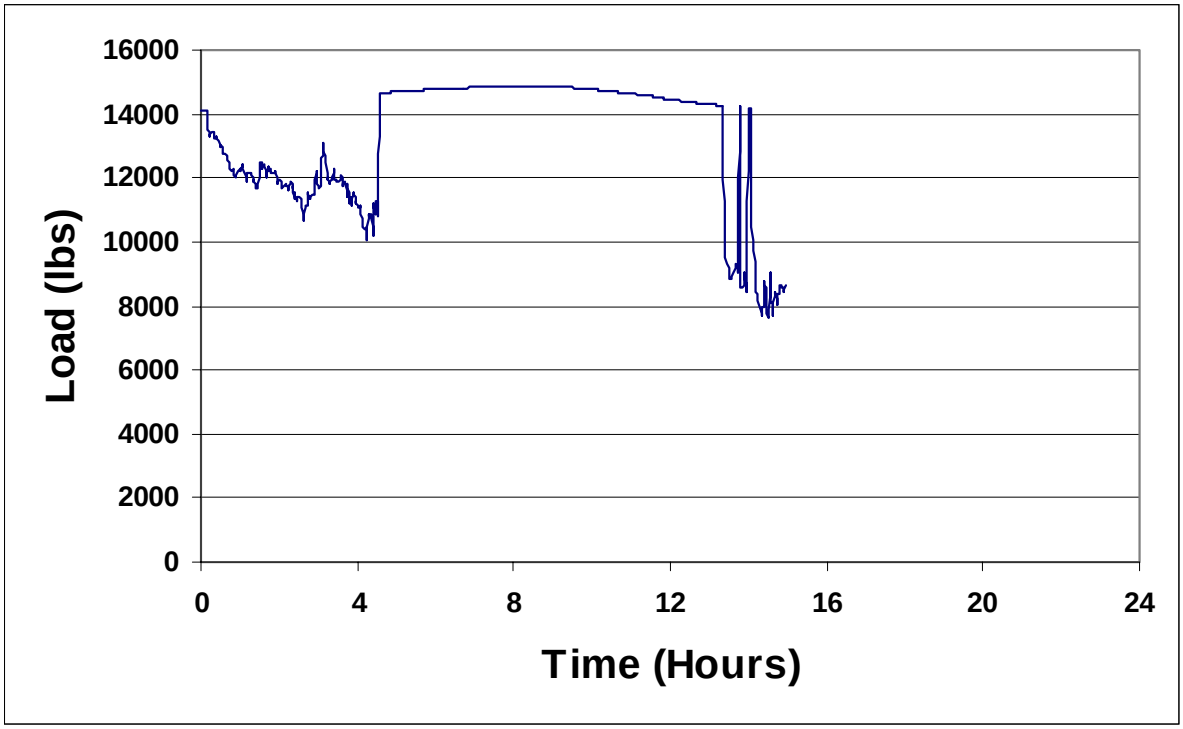

Figure C.59 Steel Force versus Time at Gage SG6 (Day 162).

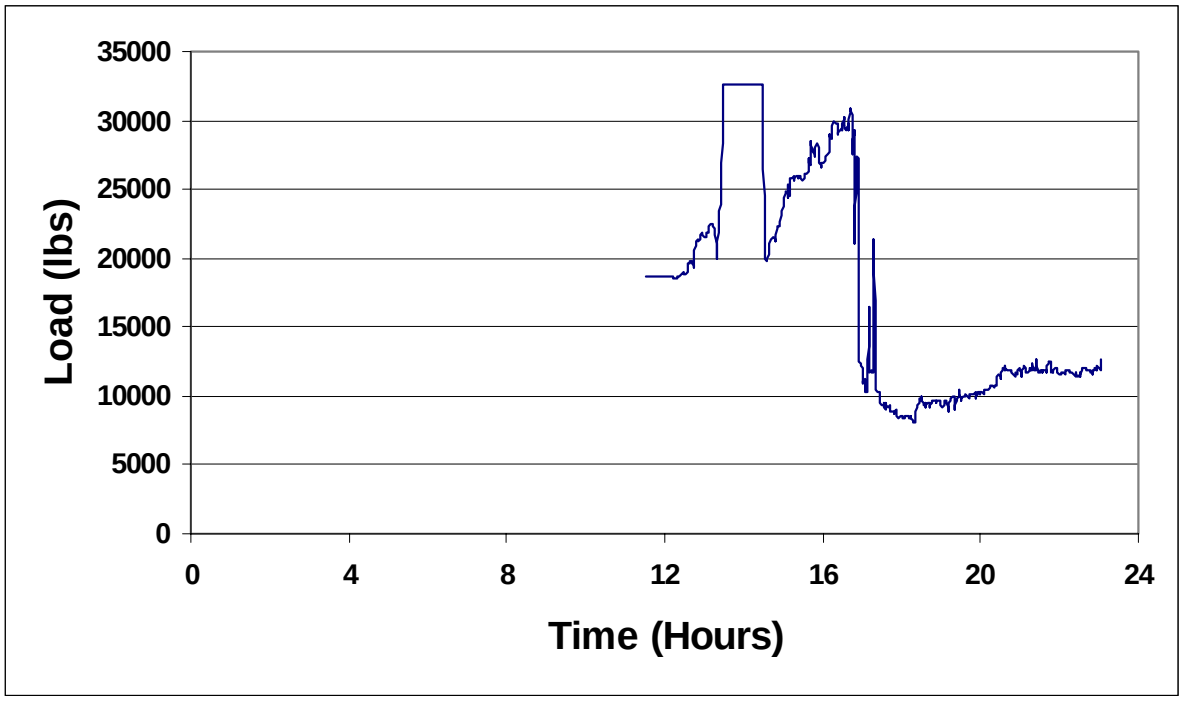

Figure C.60 Steel Force versus Time at Gage SG6 (Day 269).

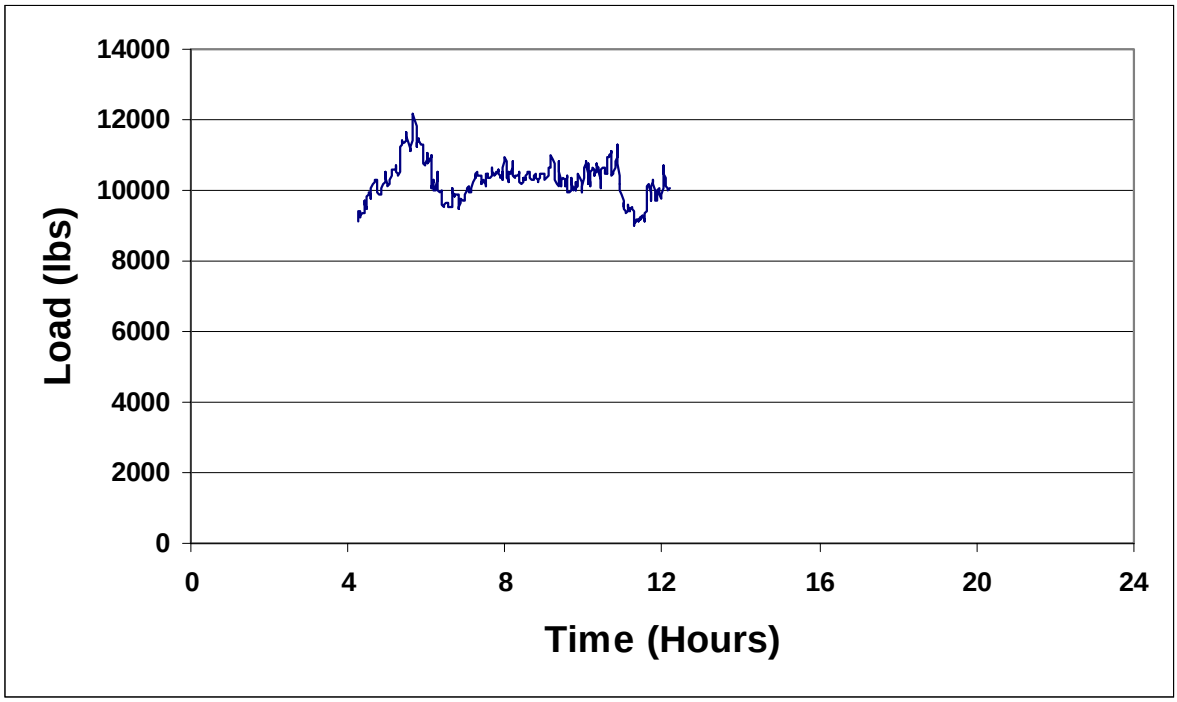

Figure C.61 Steel Force versus Time at Gage SG6 (Day 270).

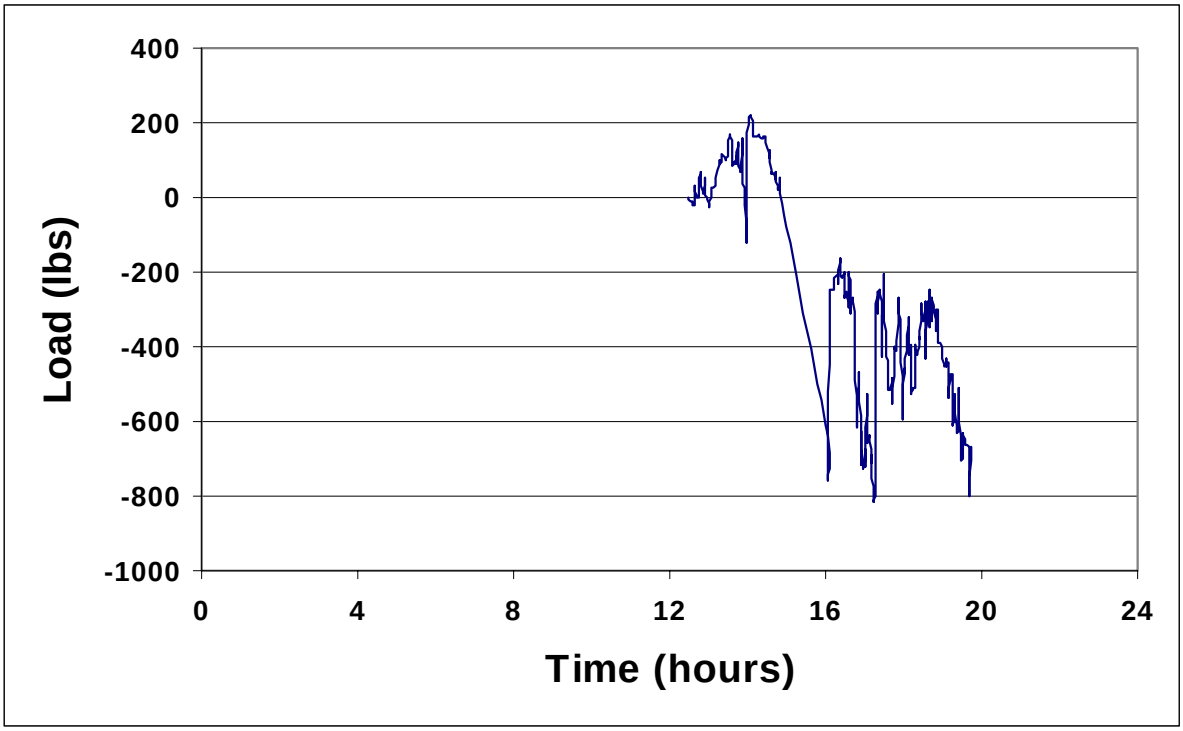

Figure C.62 Steel Force versus Time at Gage SG7 (Day 1).

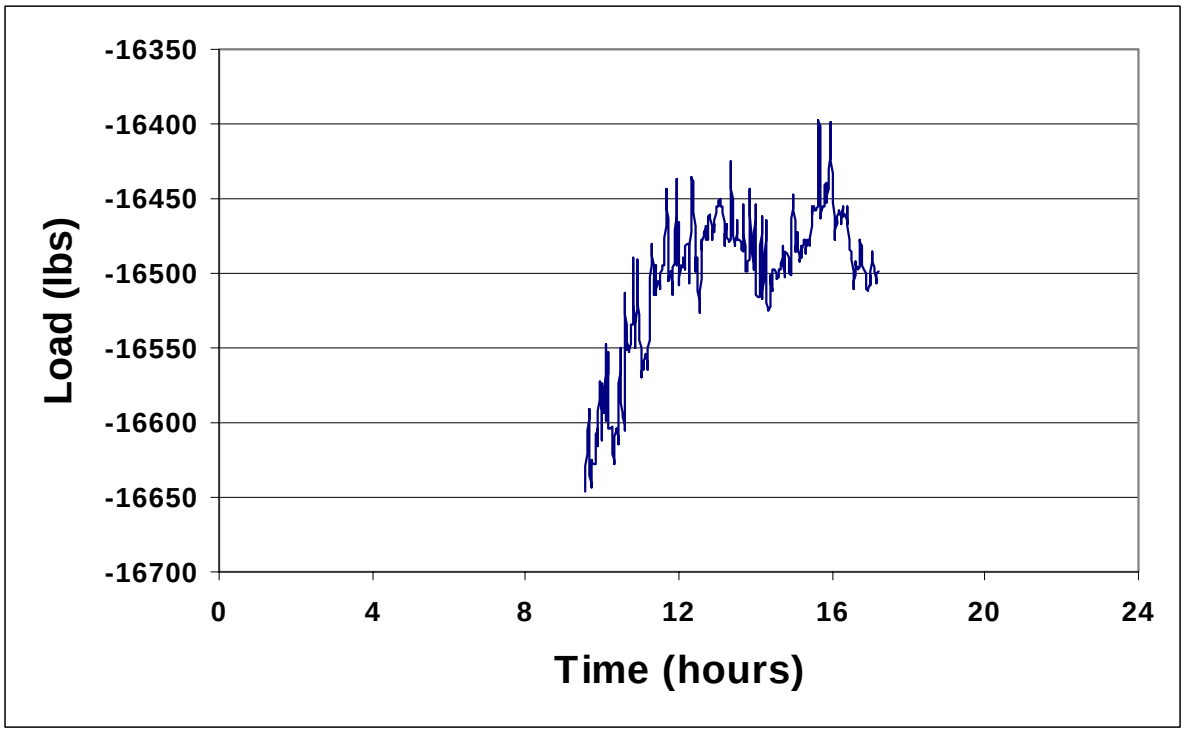

Figure C.63 Steel Force versus Time at Gage SG7 (Day 2).

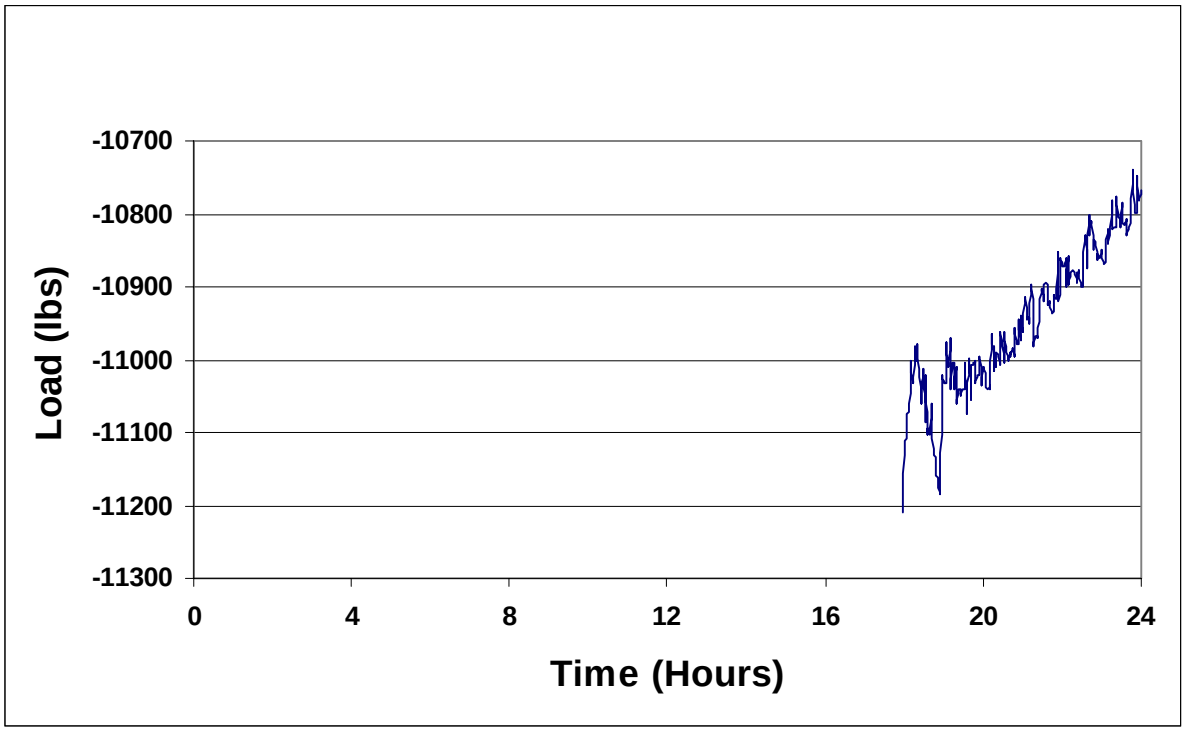

Figure C.64 Steel Force versus Time at Gage SG7 (Day 15).

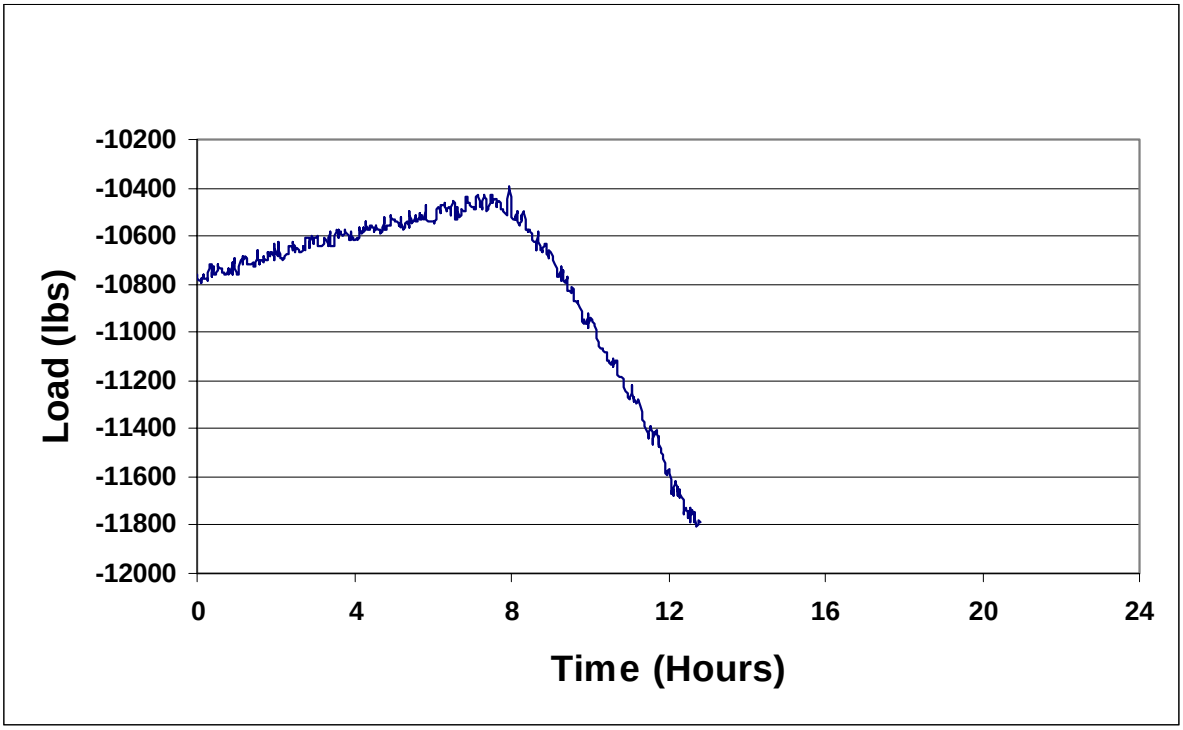

Figure C.65 Steel Force versus Time at Gage SG7 (Day 16).

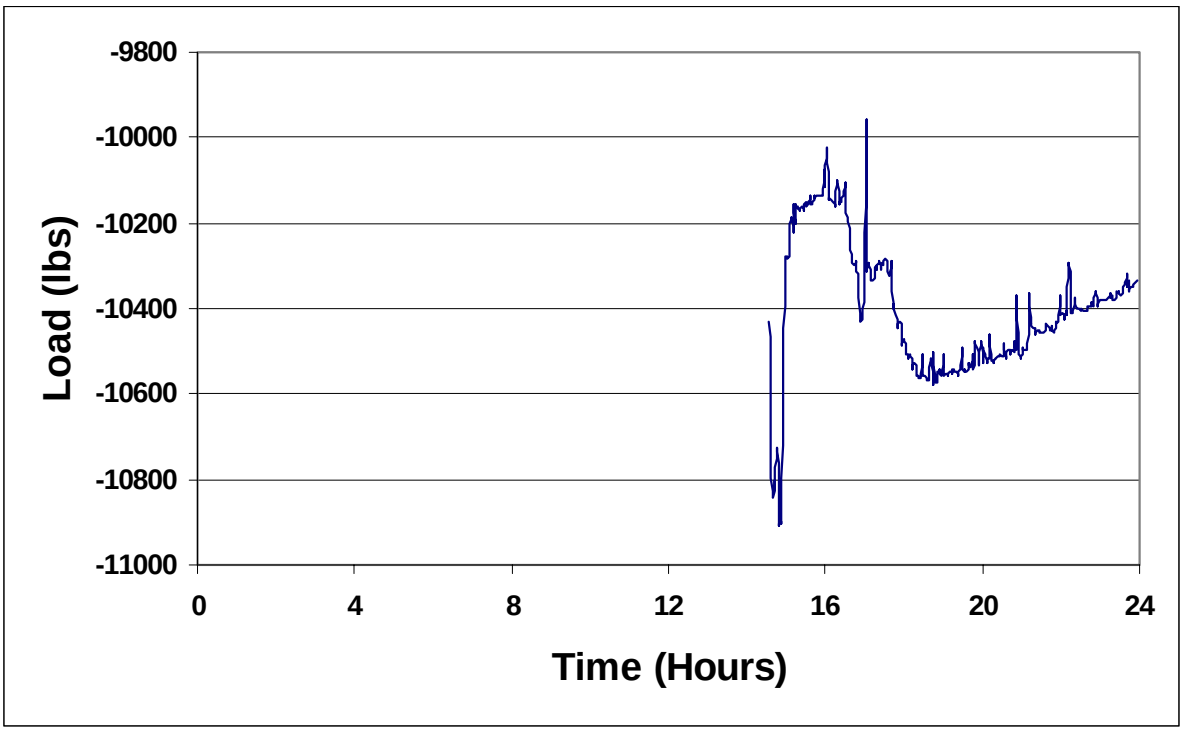

Figure C.66 Steel Force versus Time at Gage SG7 (Day 29).

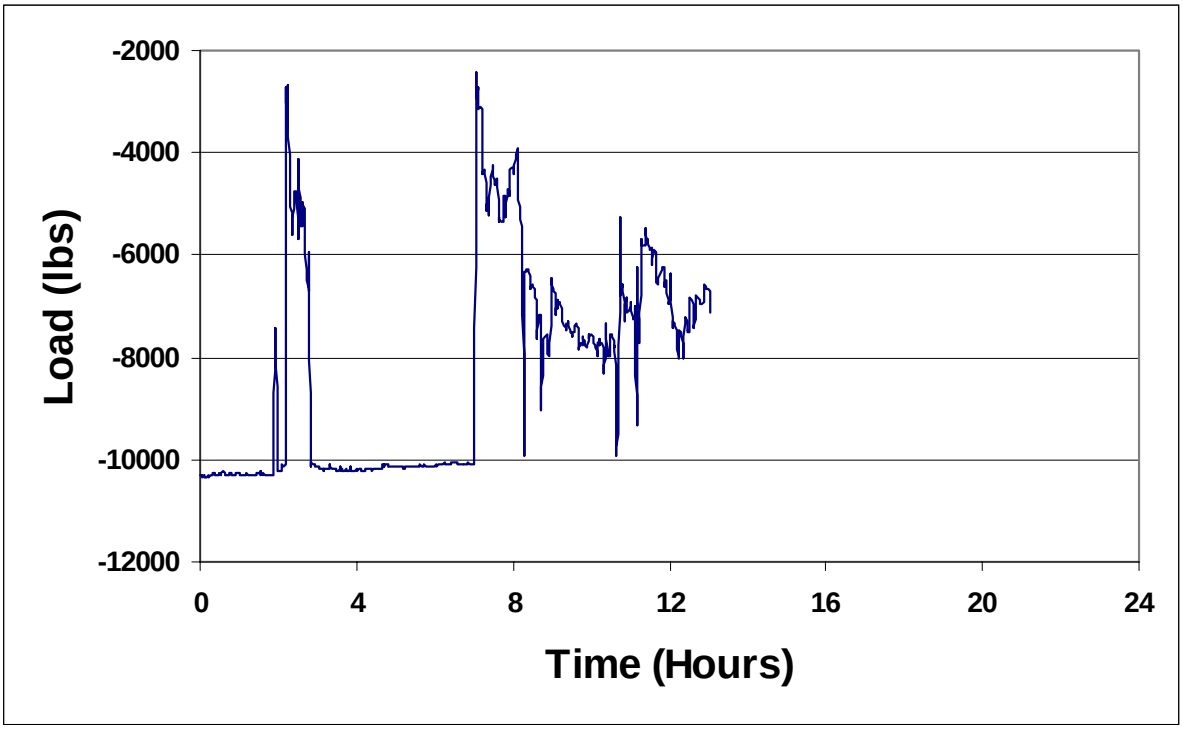

Figure C.67 Steel Force versus Time at Gage SG7 (Day 30).

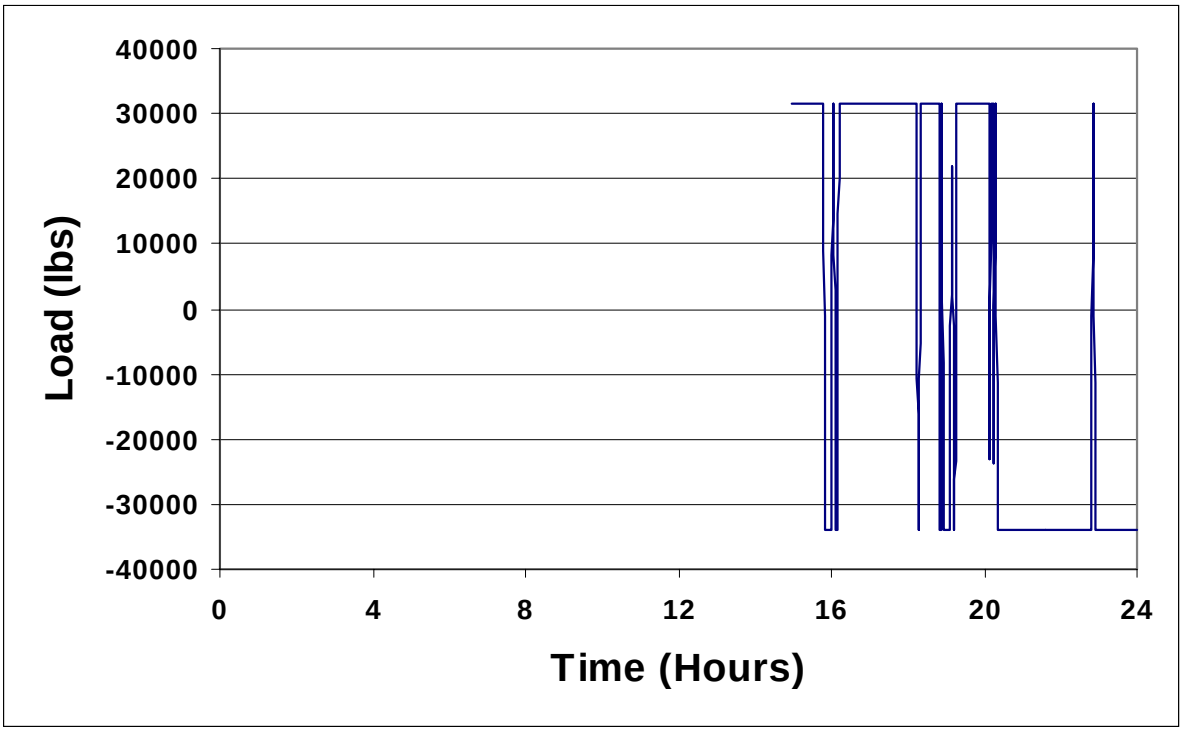

Figure C.68 Steel Force versus Time at Gage SG7 (Day 161).

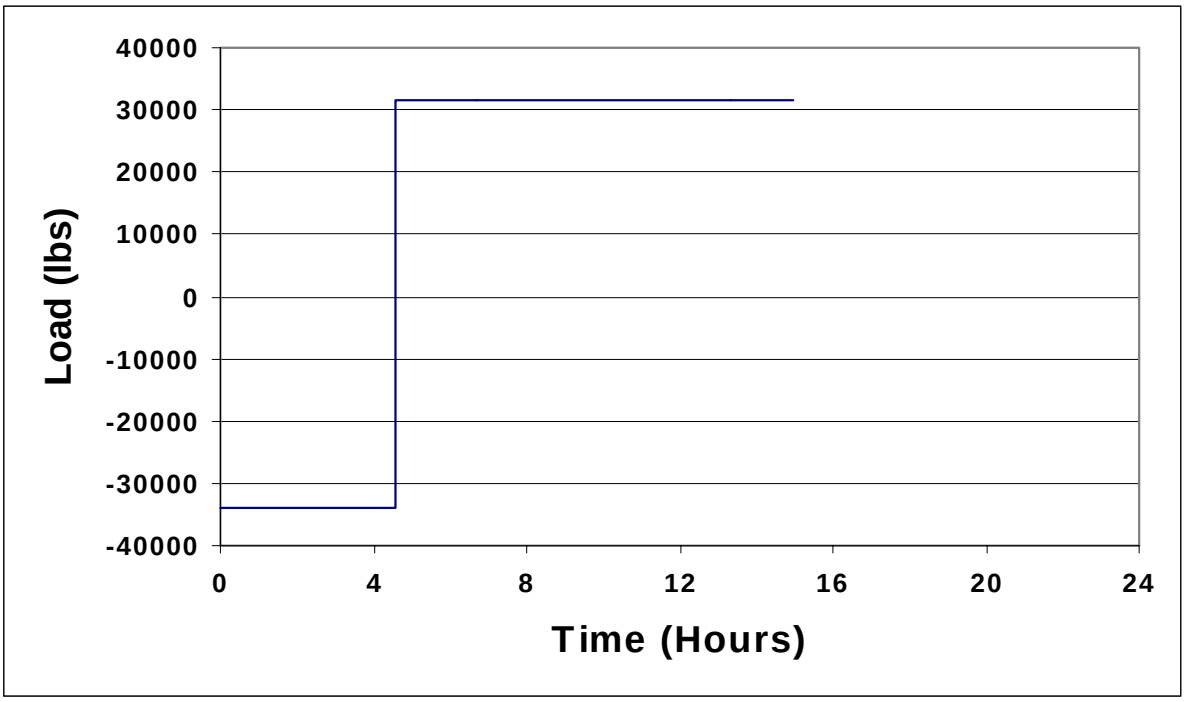

Figure C.69 Steel Force versus Time at Gage SG7 (Day 162).

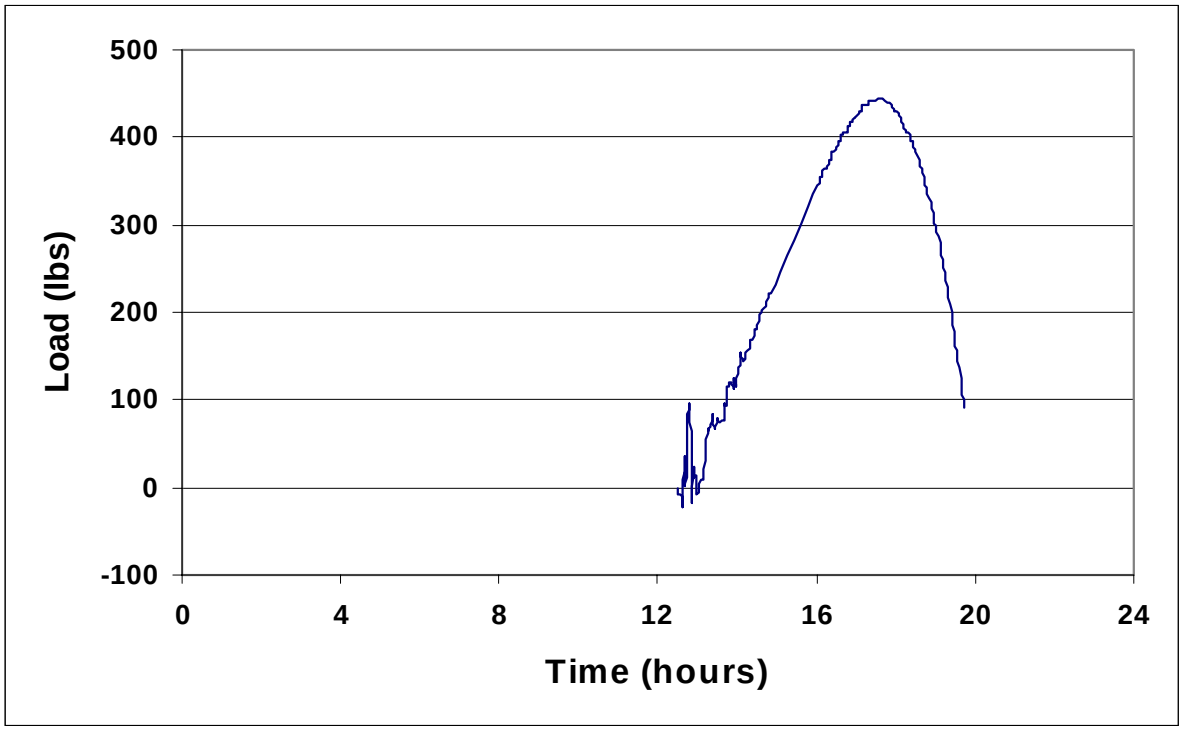

Figure C.70 Steel Force versus Time at Gage SG8 (Day 1) .

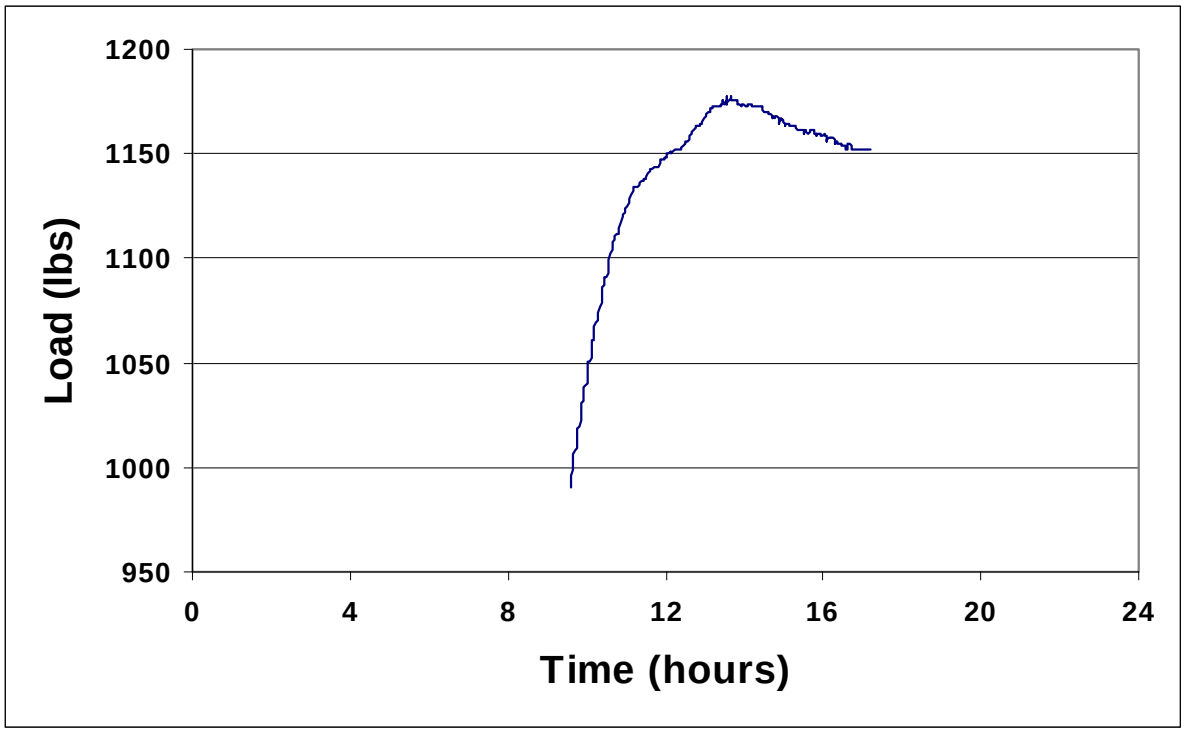

Figure C.71 Steel Force versus Time at Gage SG8 (Day 2).

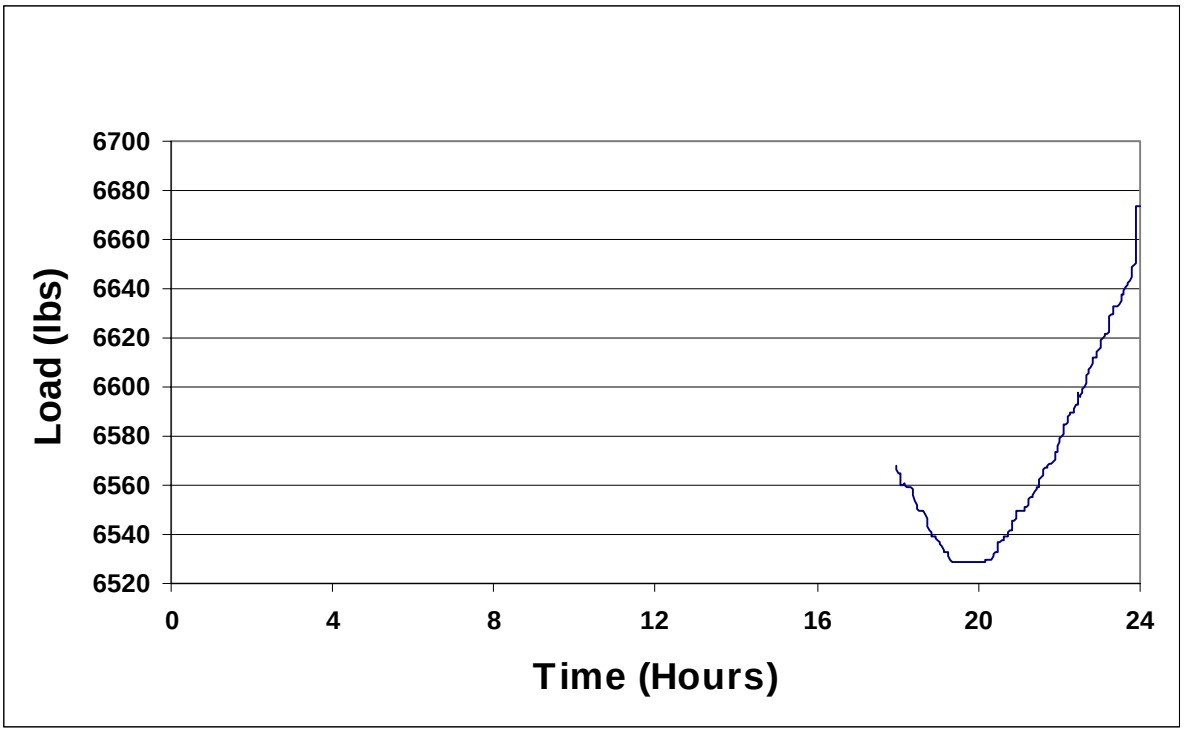

Figure C.72 Steel Force versus Time at Gage SG8 (Day 15) .

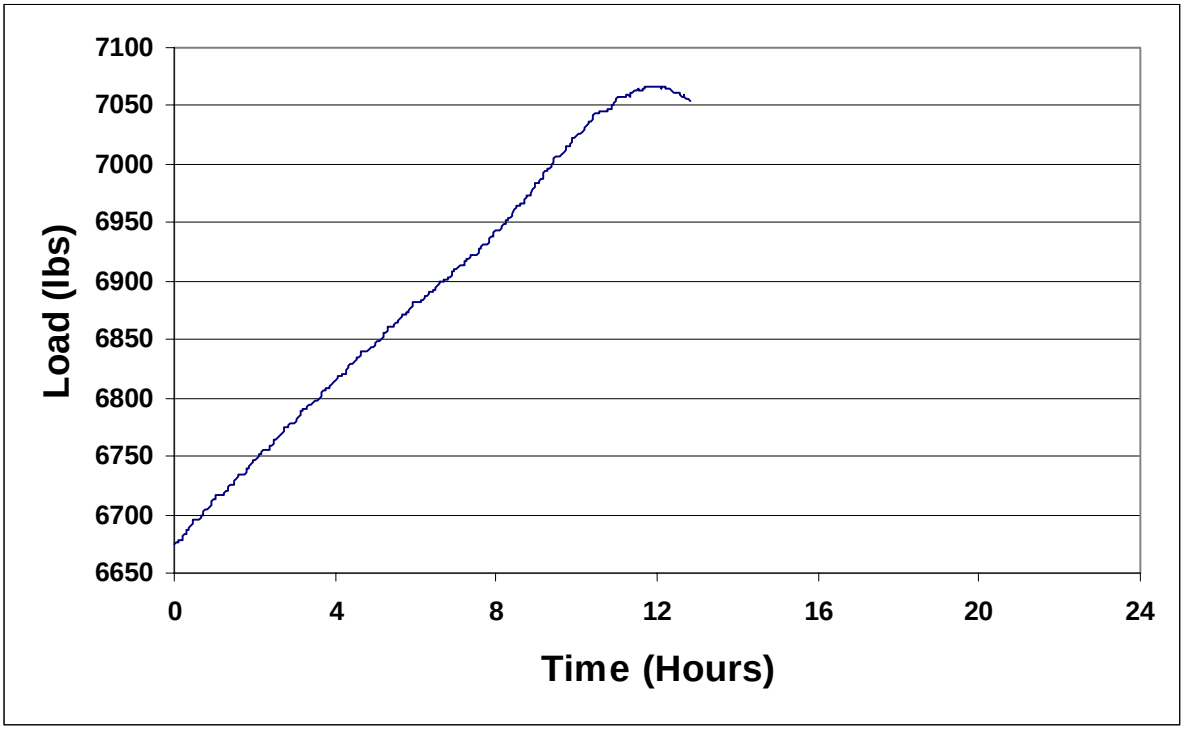

Figure C.73 Steel Force versus Time at Gage SG8 (Day 16).

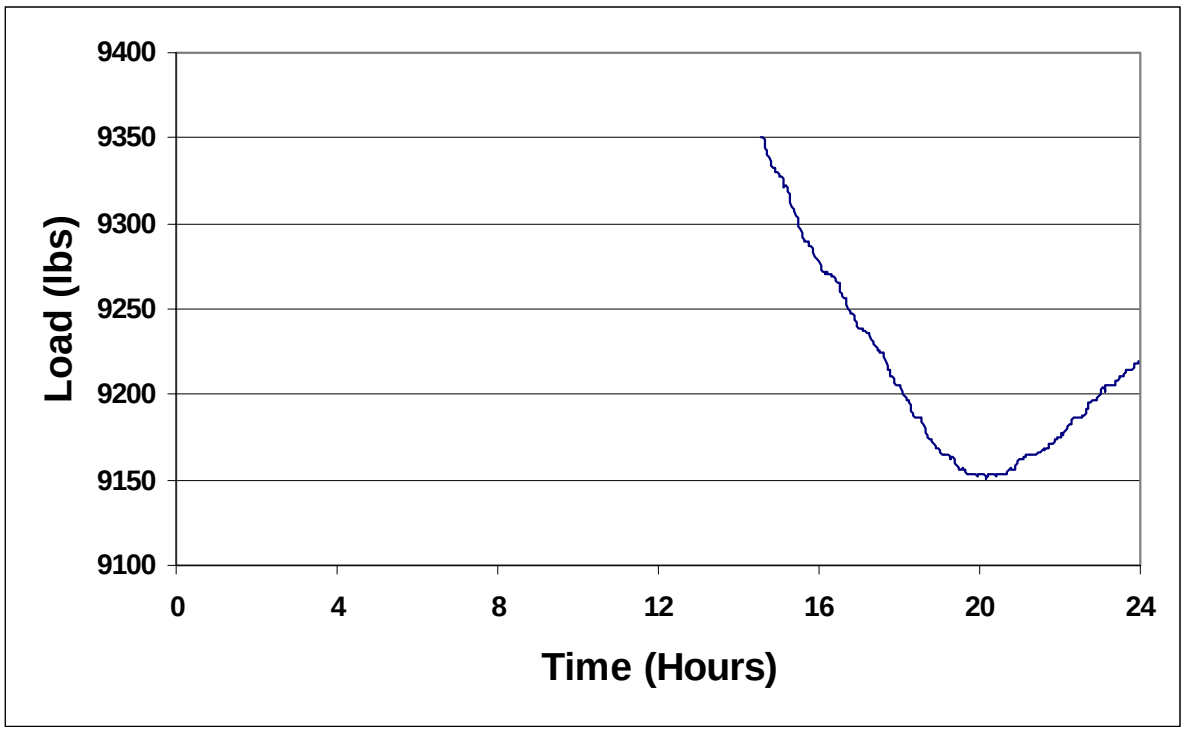

Figure C.74 Steel Force versus Time at Gage SG8 (Day 29).

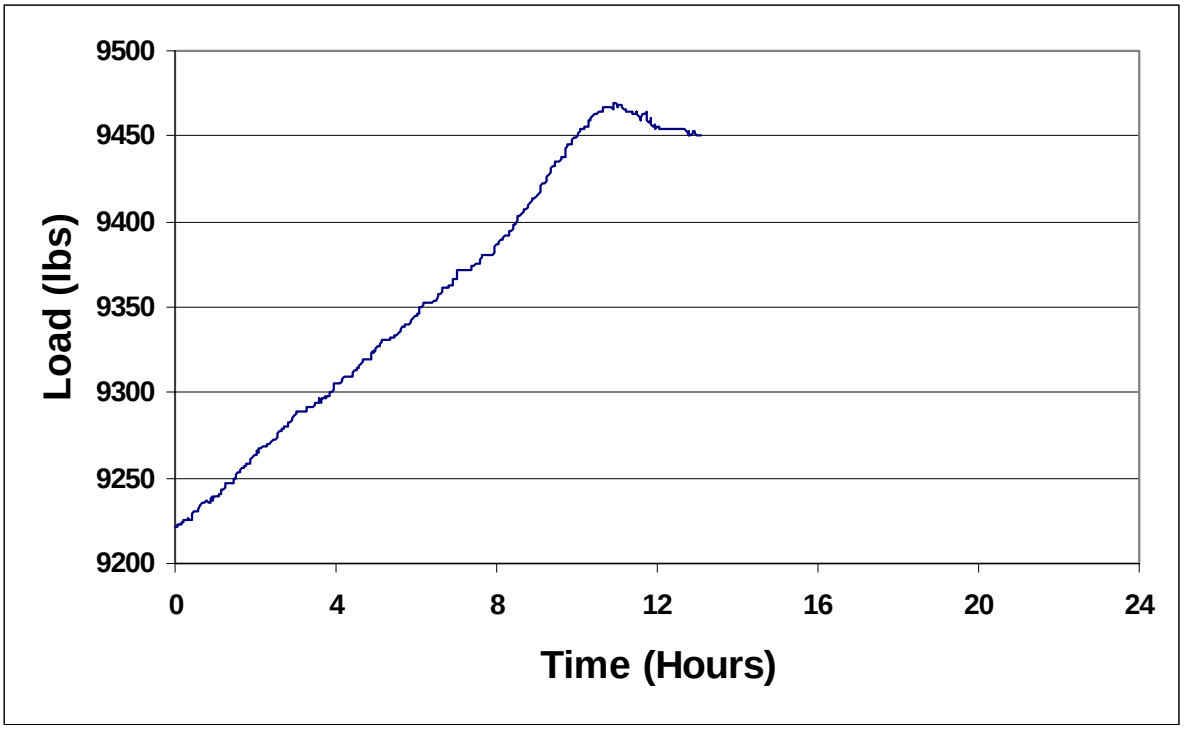

Figure C.75 Steel Force versus Time at Gage SG8 (Day 30).

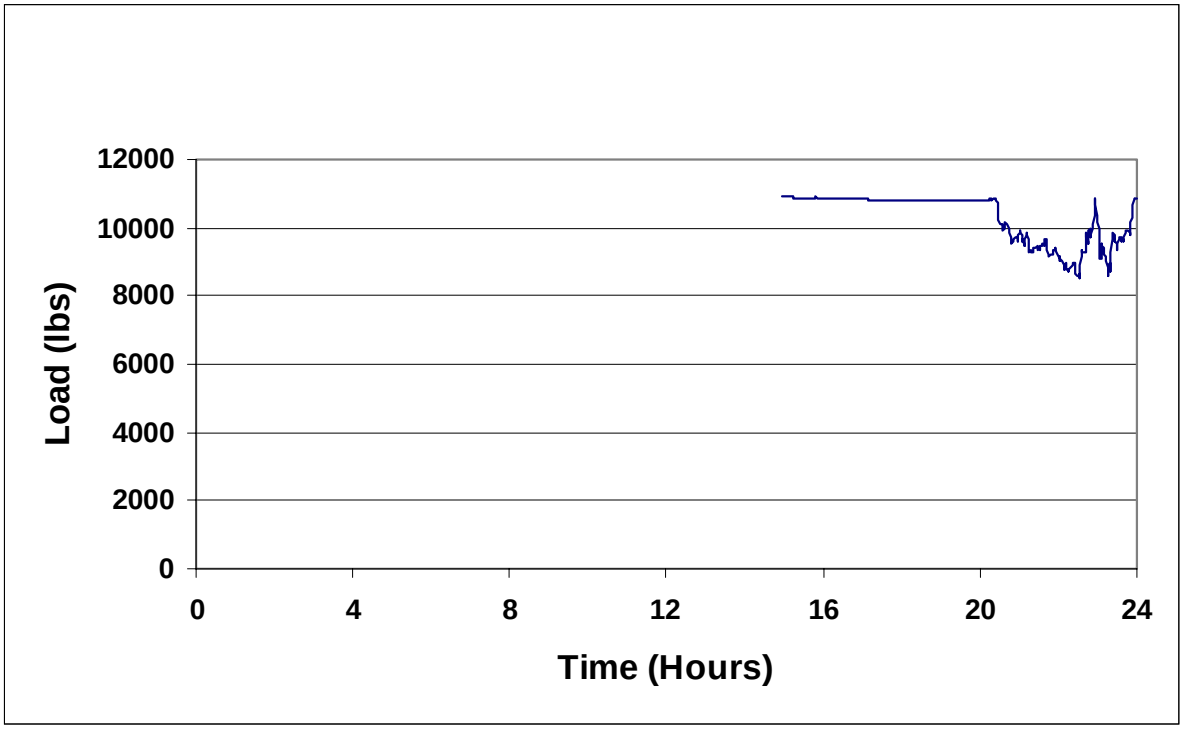

Figure C.76 Steel Force versus Time at Gage SG8 (Day 161).

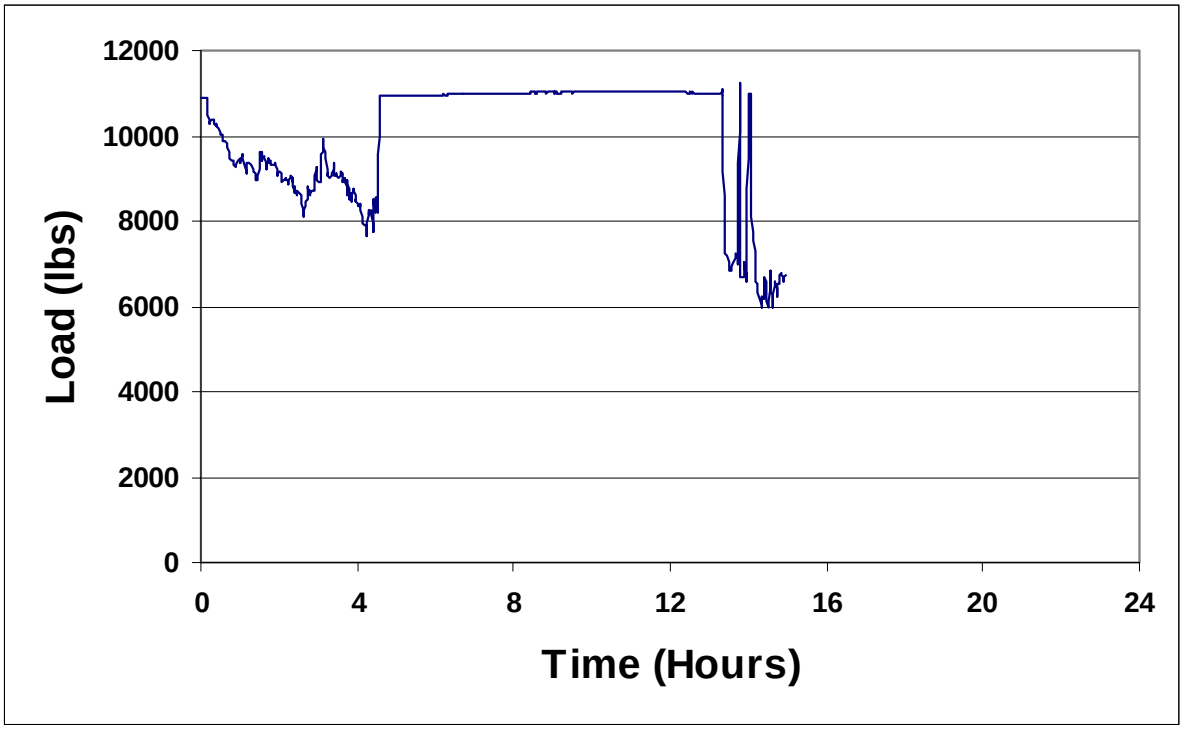

Figure C.77 Steel Force versus Time at Gage SG8 (Day 162).

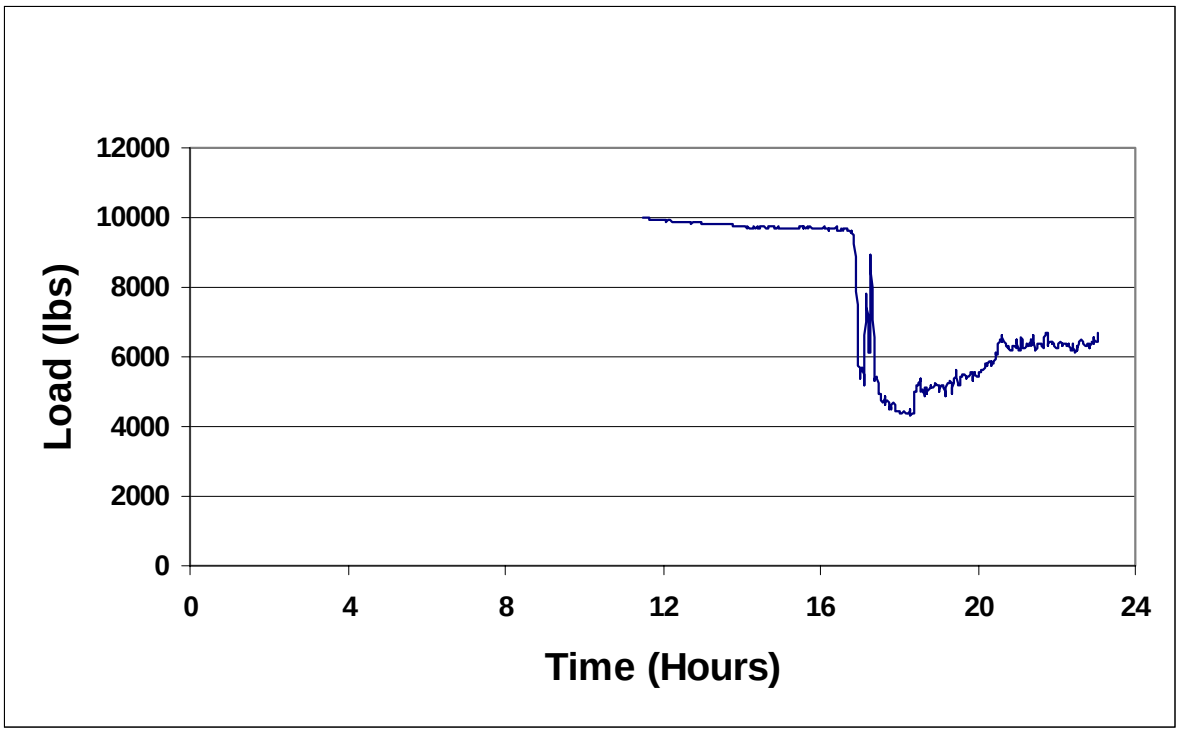

Figure C.78 Steel Force versus Time at Gage SG8 (Day 269).

APPENDIX D

WEATHER AND PAVEMENT TEMPERATURE

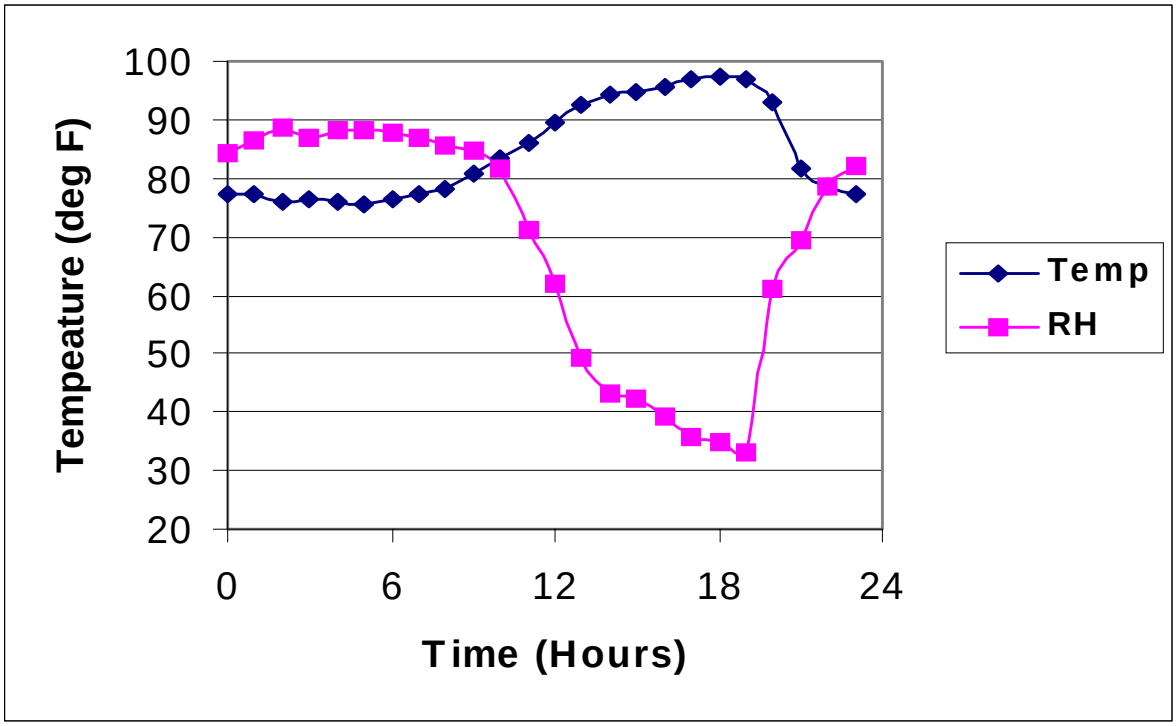

Figure D.1 Temperature and Relative Humidity versus Time (Day 1).

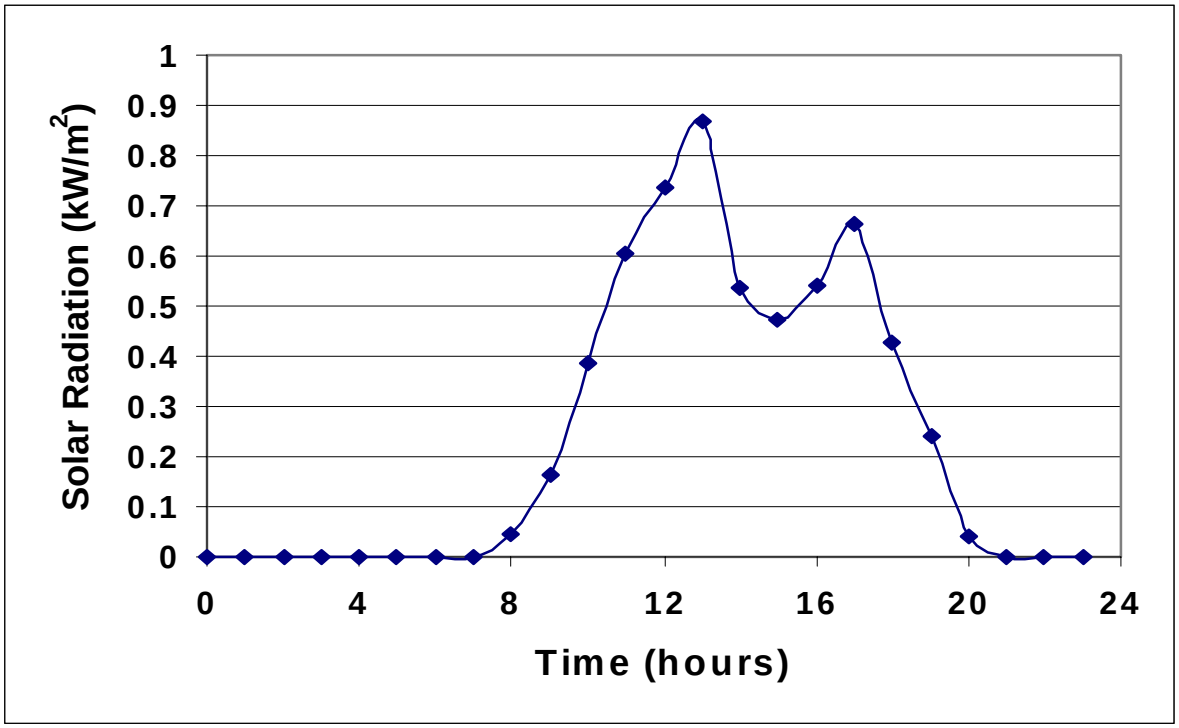

Figure D.2 Solar Radiation versus Time (Day 1).

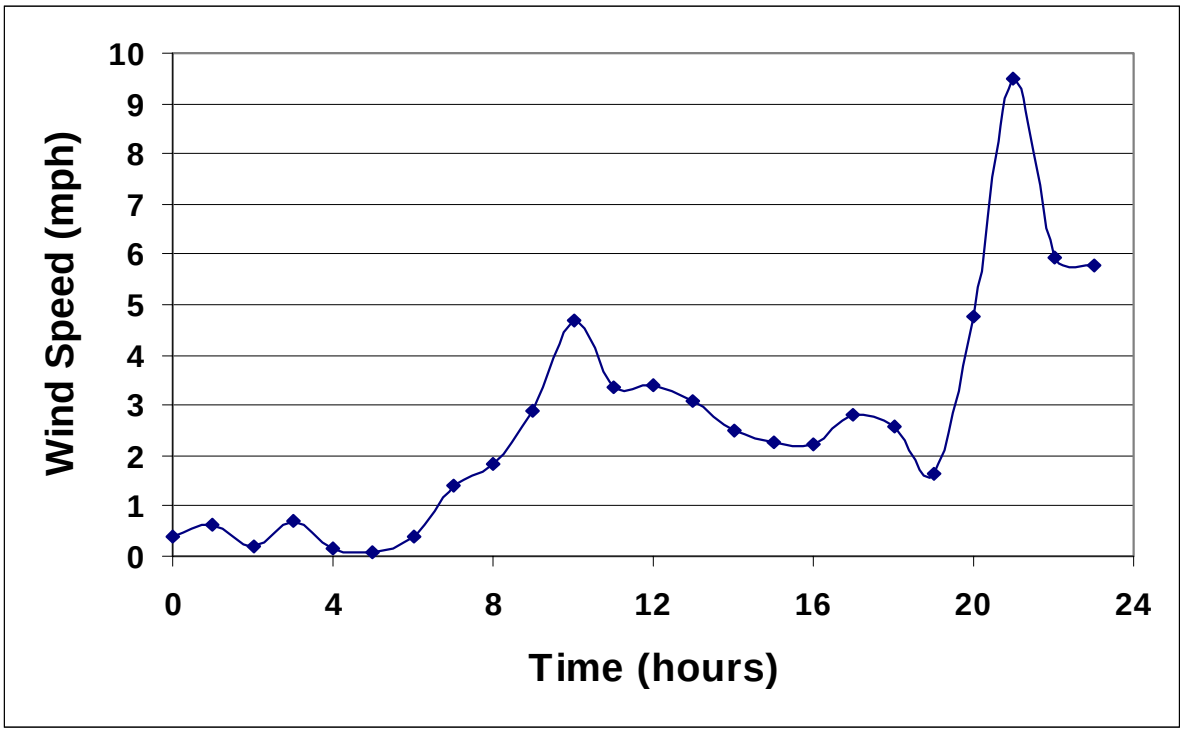

Figure D.3 Wind Speed versus Time (Day 1).

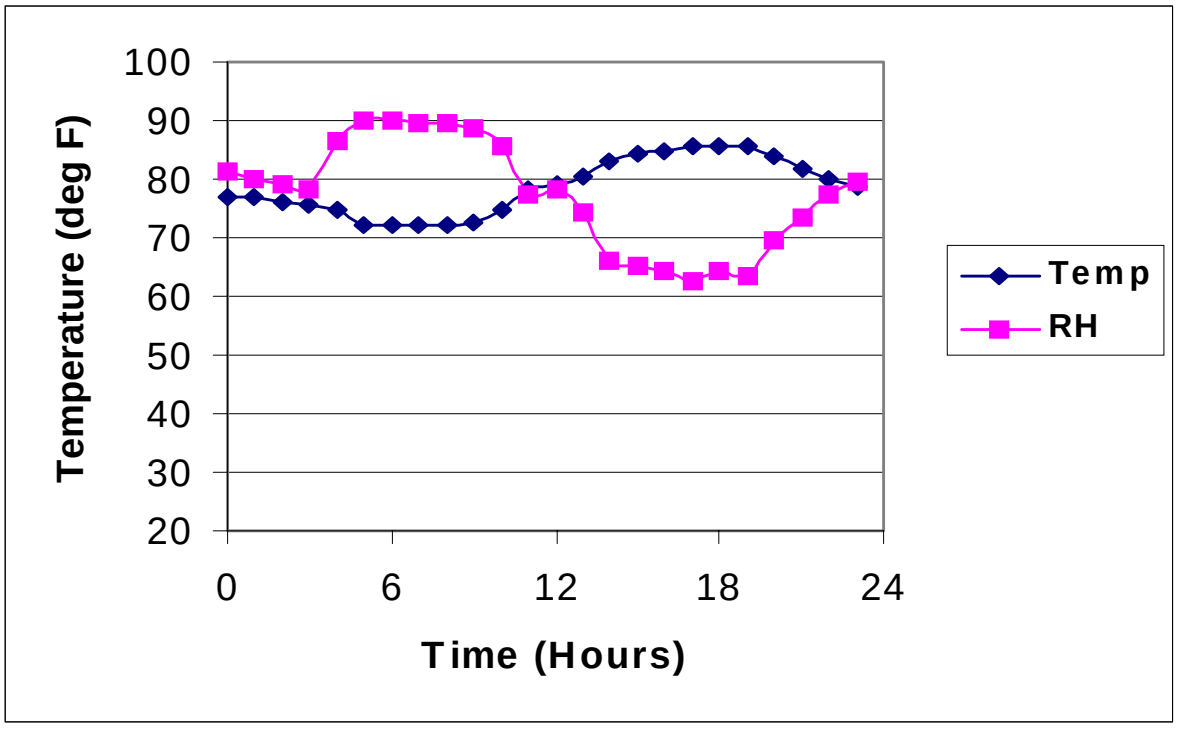

Figure D.4 Temperature and Relative Humidity versus Time (Day 2).

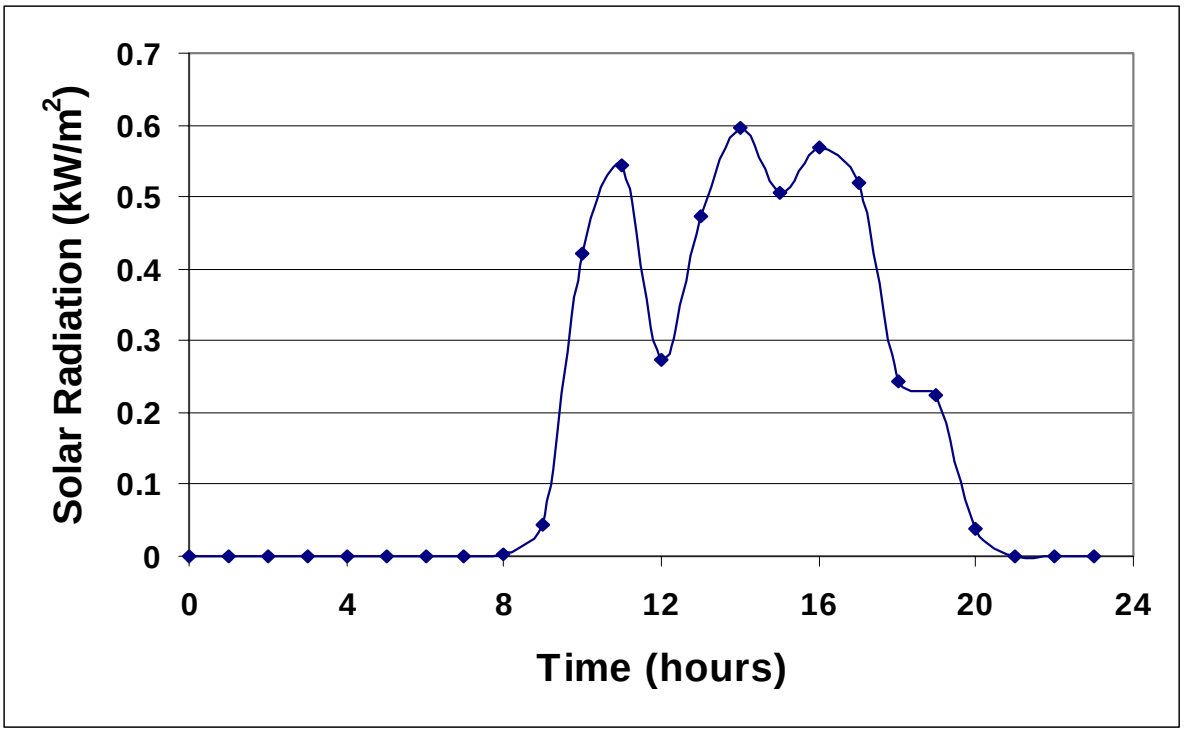

Figure D.5 Solar Radiation versus Time (Day 2).

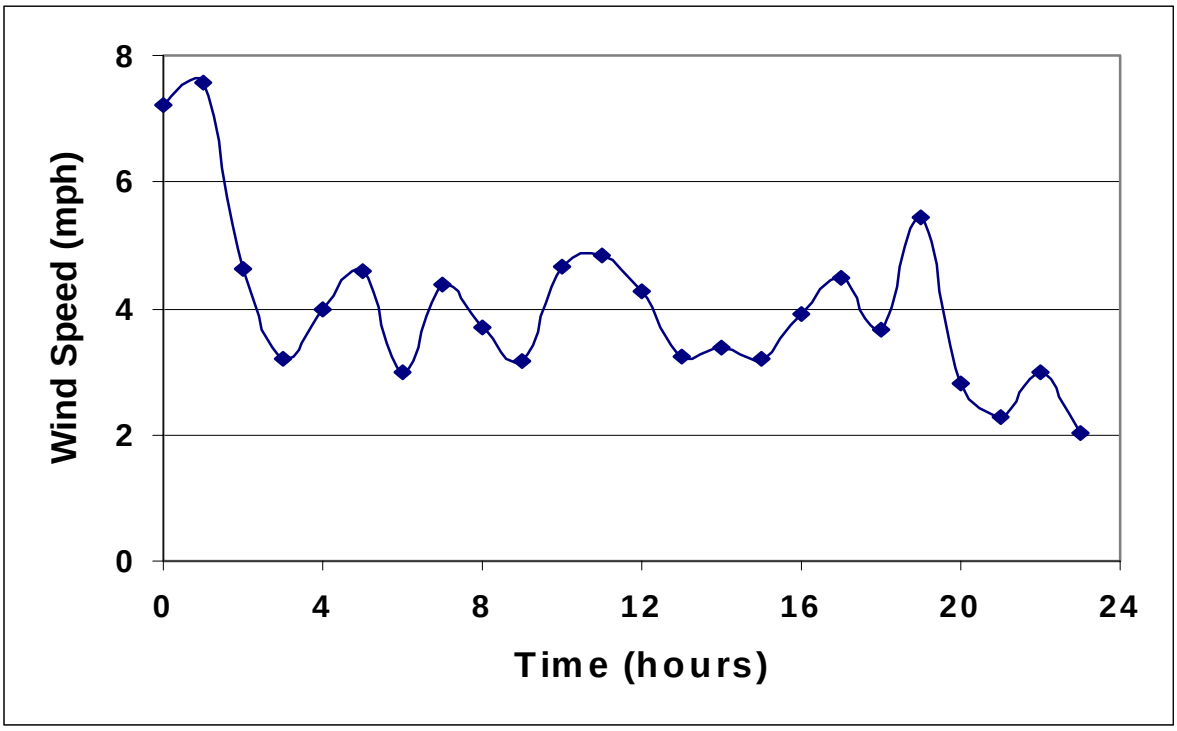

Figure D.6 Wind Speed versus Time (Day 2).

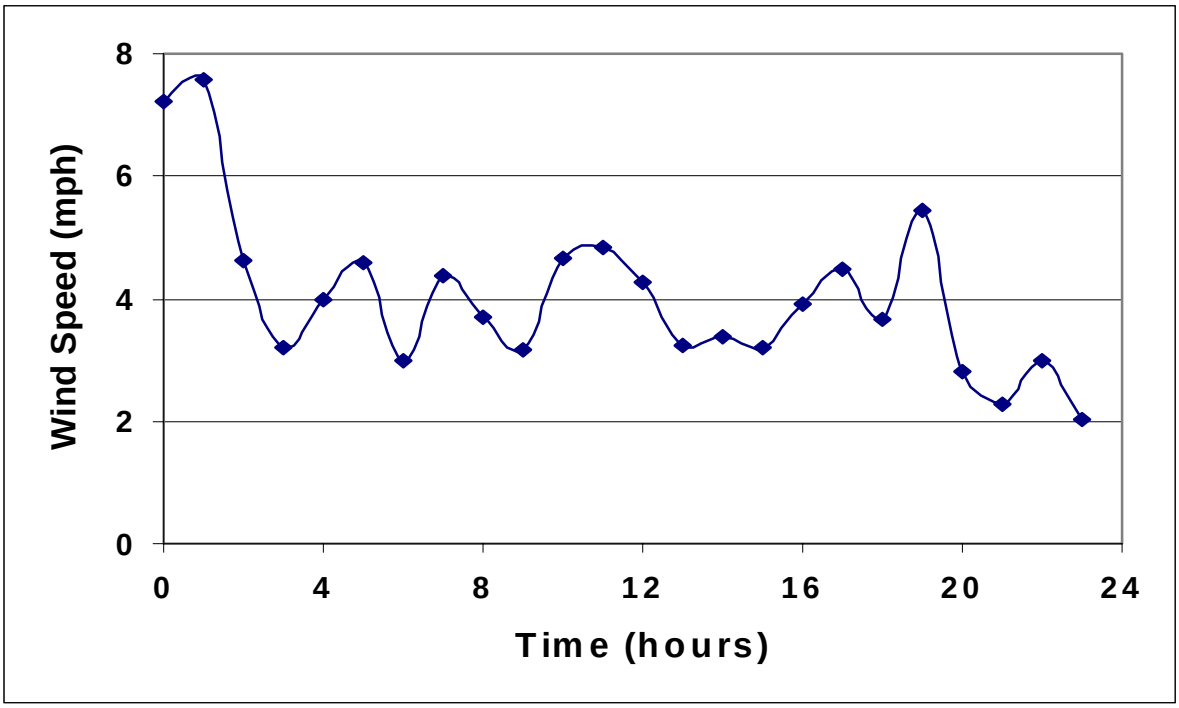

Figure D.7 Wind Speed versus Time (Day 3).

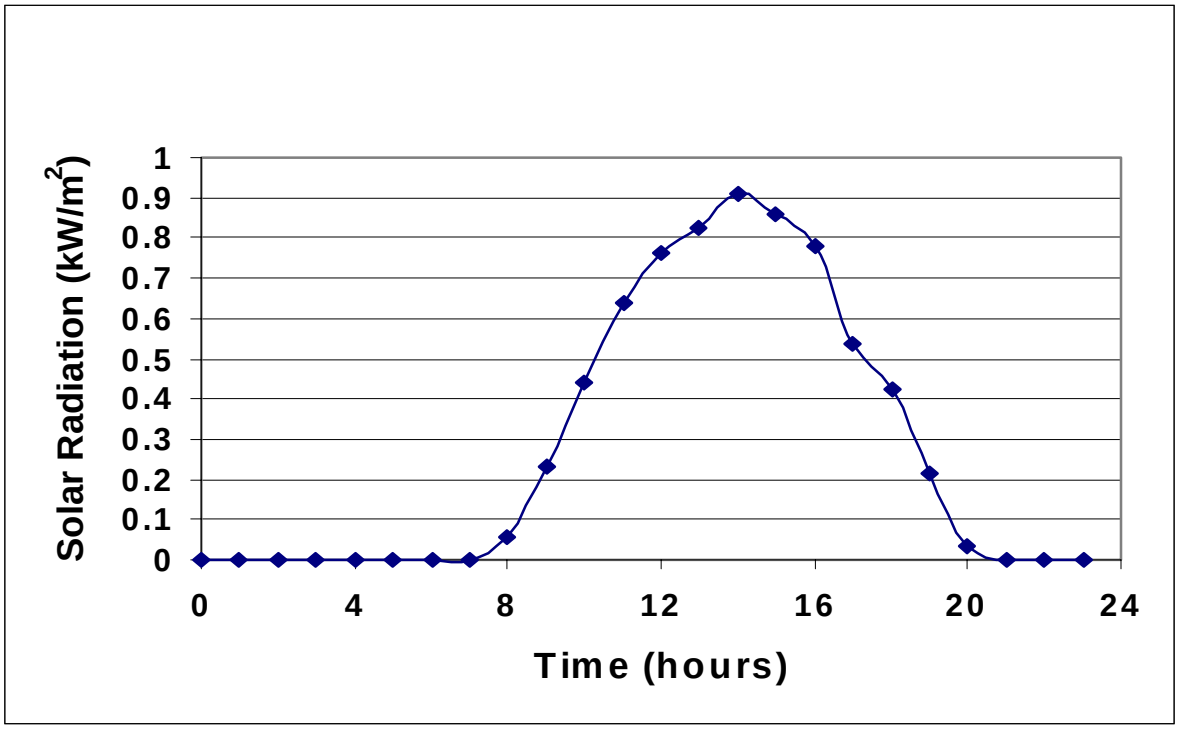

Figure D.8 Solar Radiation versus Time (Day 3).

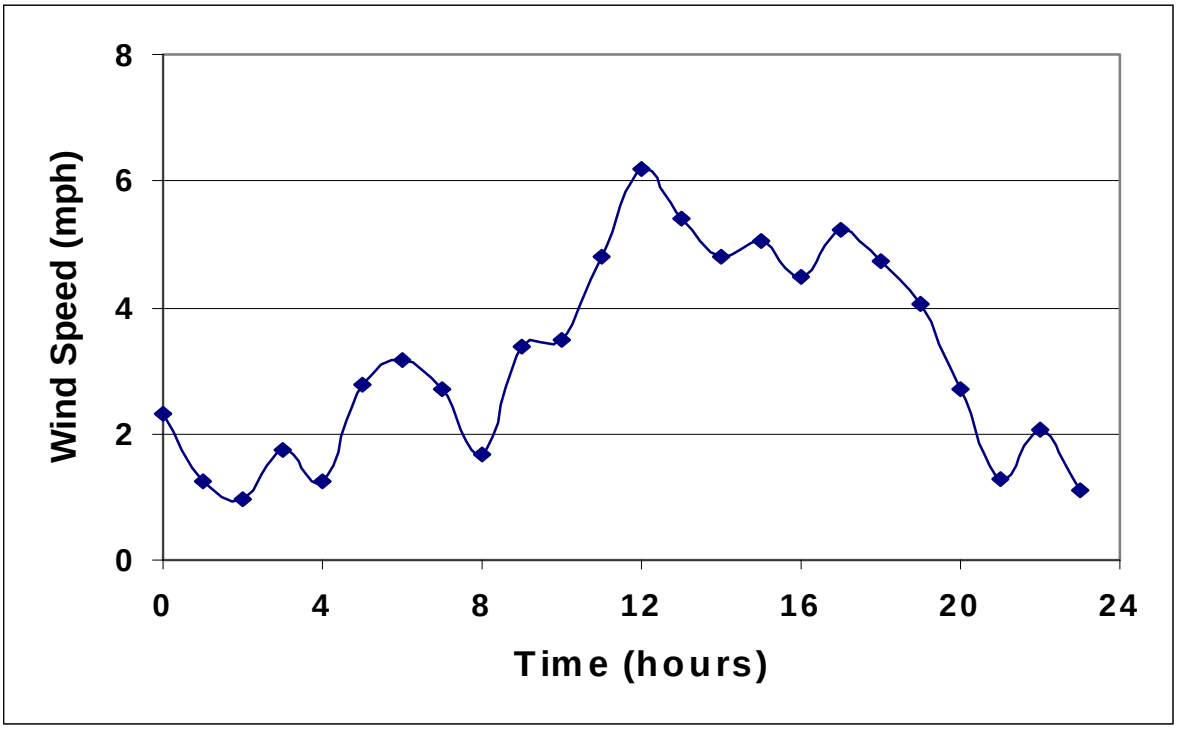

Figure D.9 Wind Speed versus Time (Day 3).

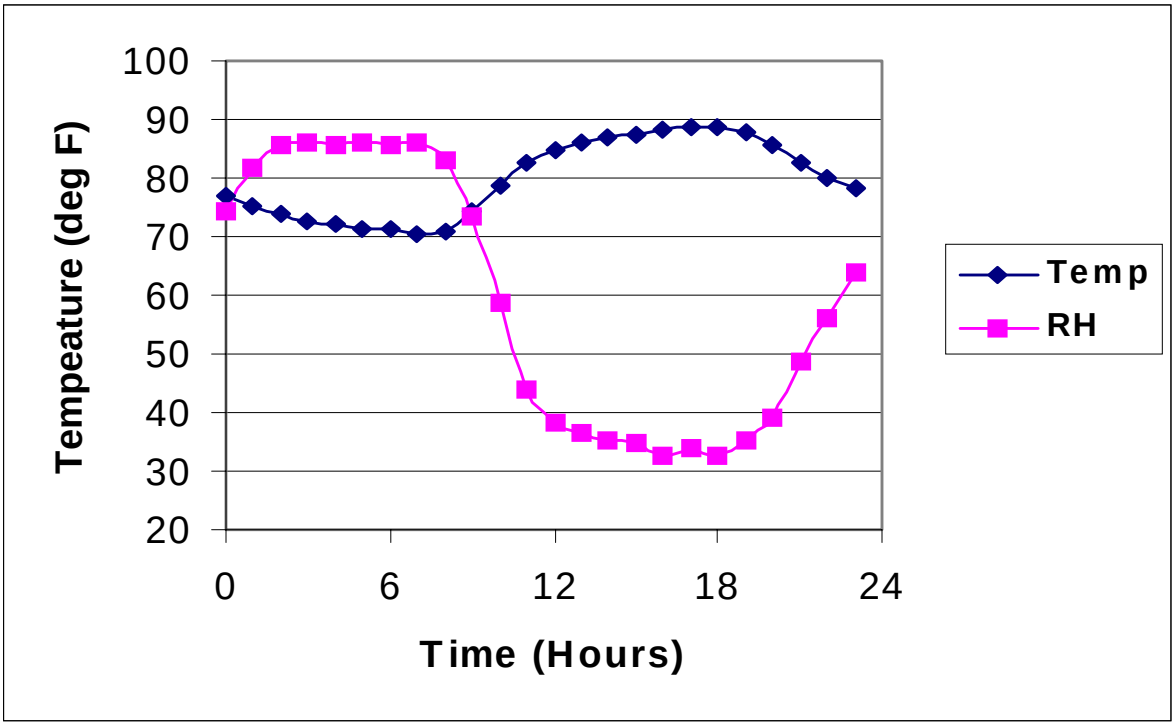

Figure D.10 Temperature and Relative Humidity versus Time (Day 4).

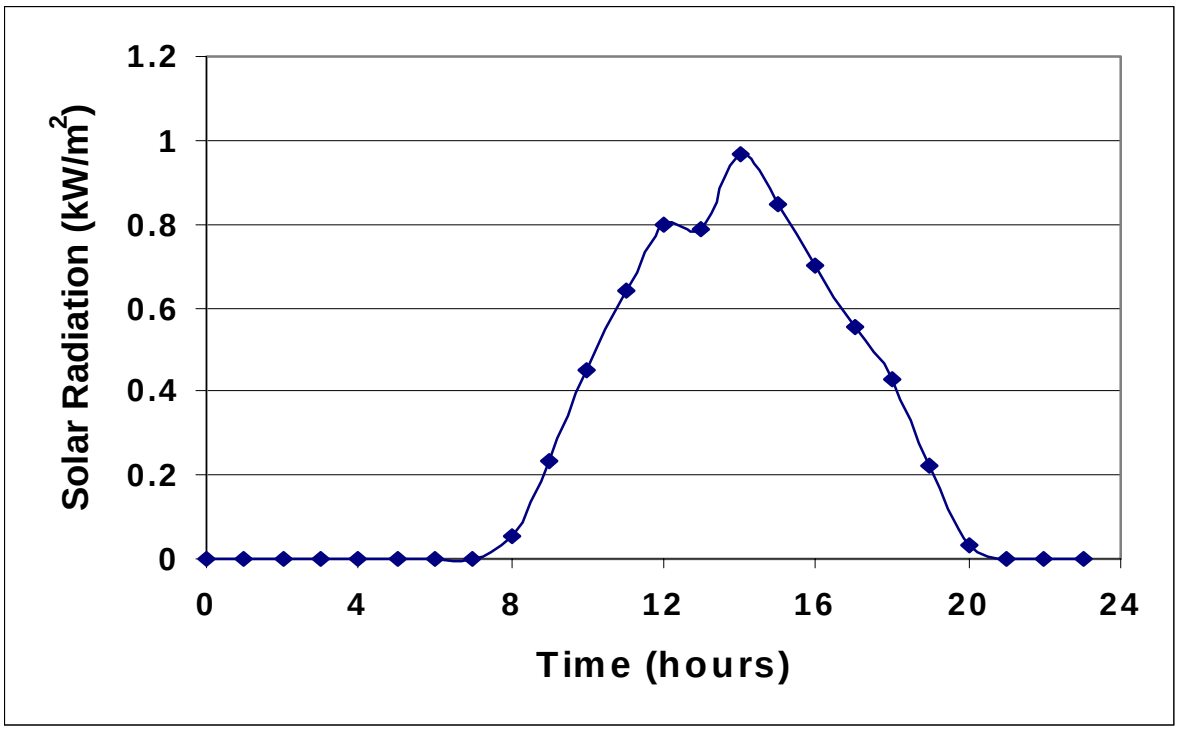

Figure D.11 Solar Radiation versus Time (Day 4).

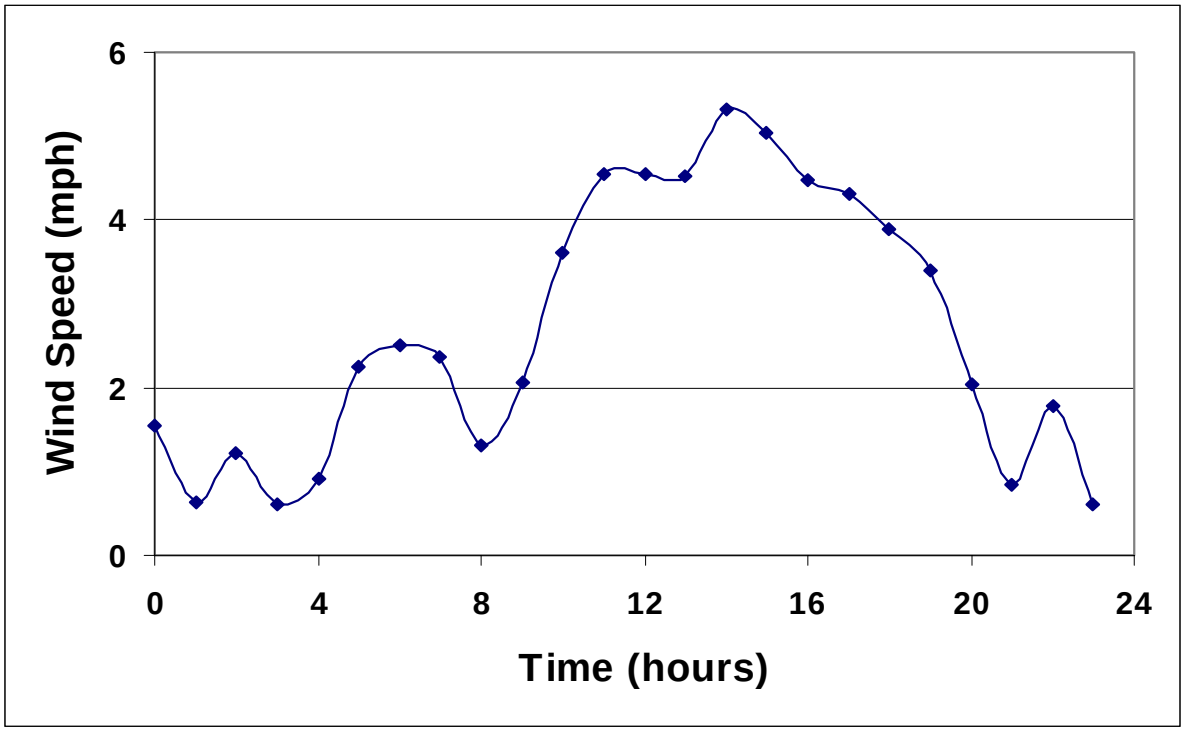

Figure D.12 Wind Speed versus Time (Day 4).

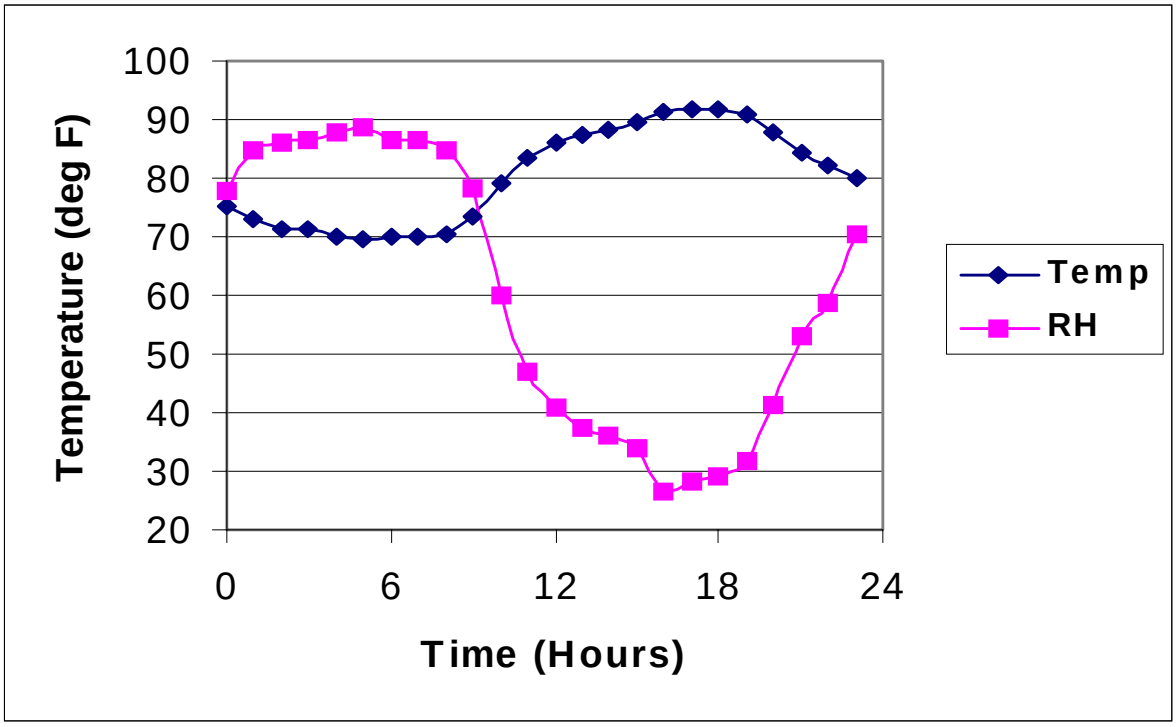

Figure D.13 Temperature and Relative Humidity versus Time (Day 5).

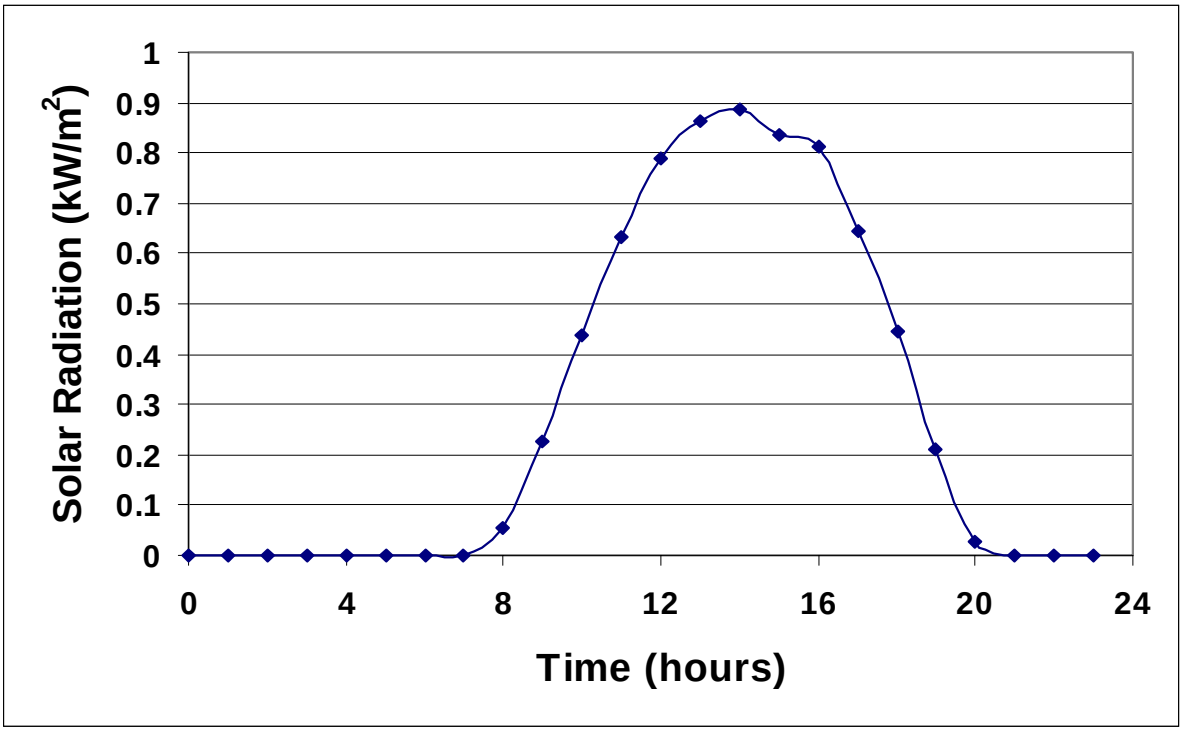

Figure D.14 Solar Radiation versus Time (Day 5).

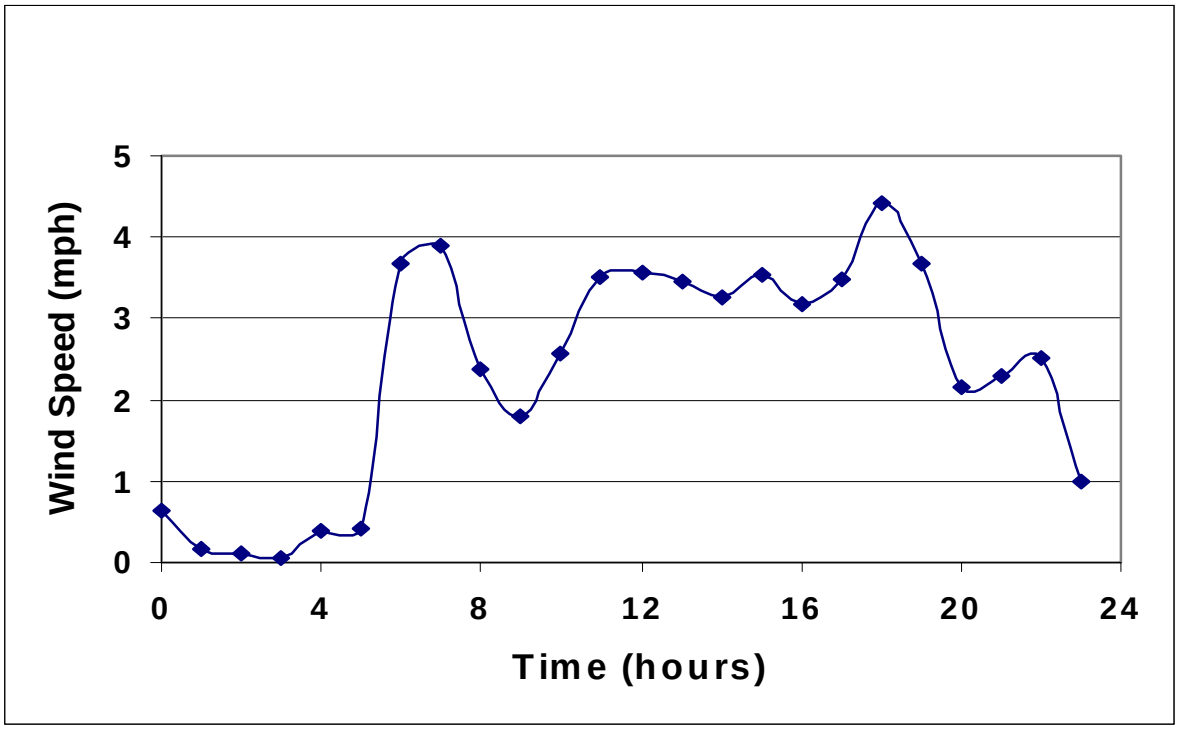

Figure D.15 Wind Speed versus Time (Day 5).

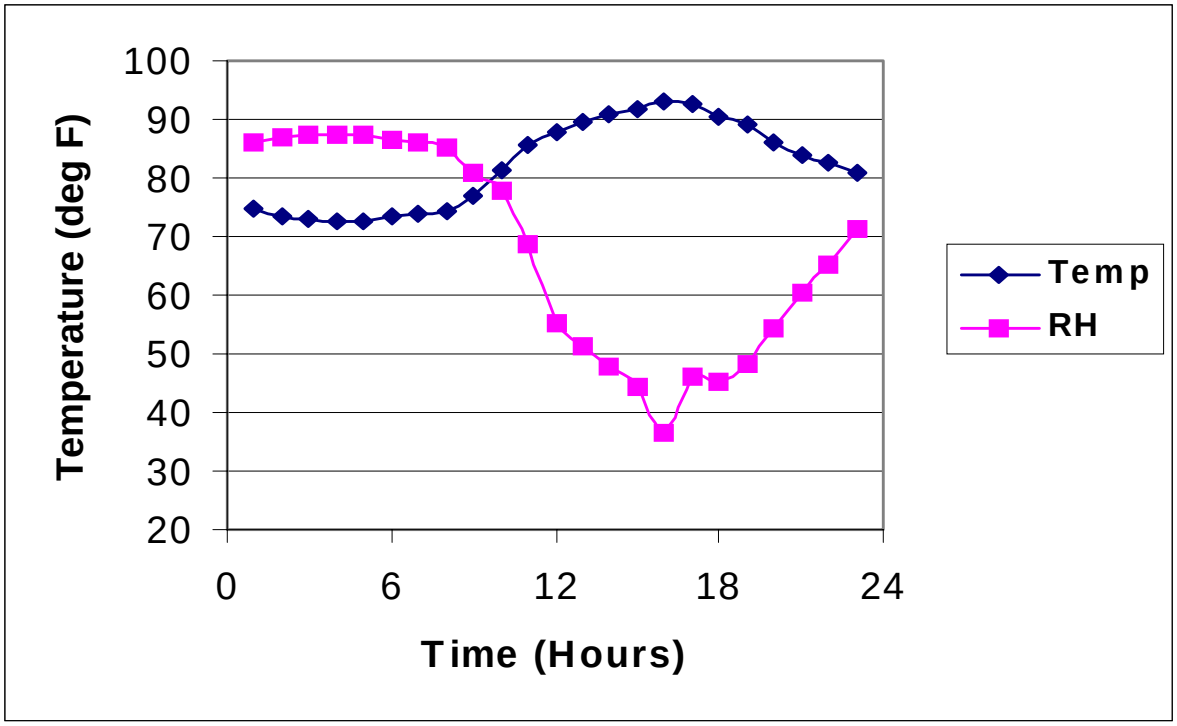

Figure D.16 Temperature and Relative Humidity versus Time (Day 6).

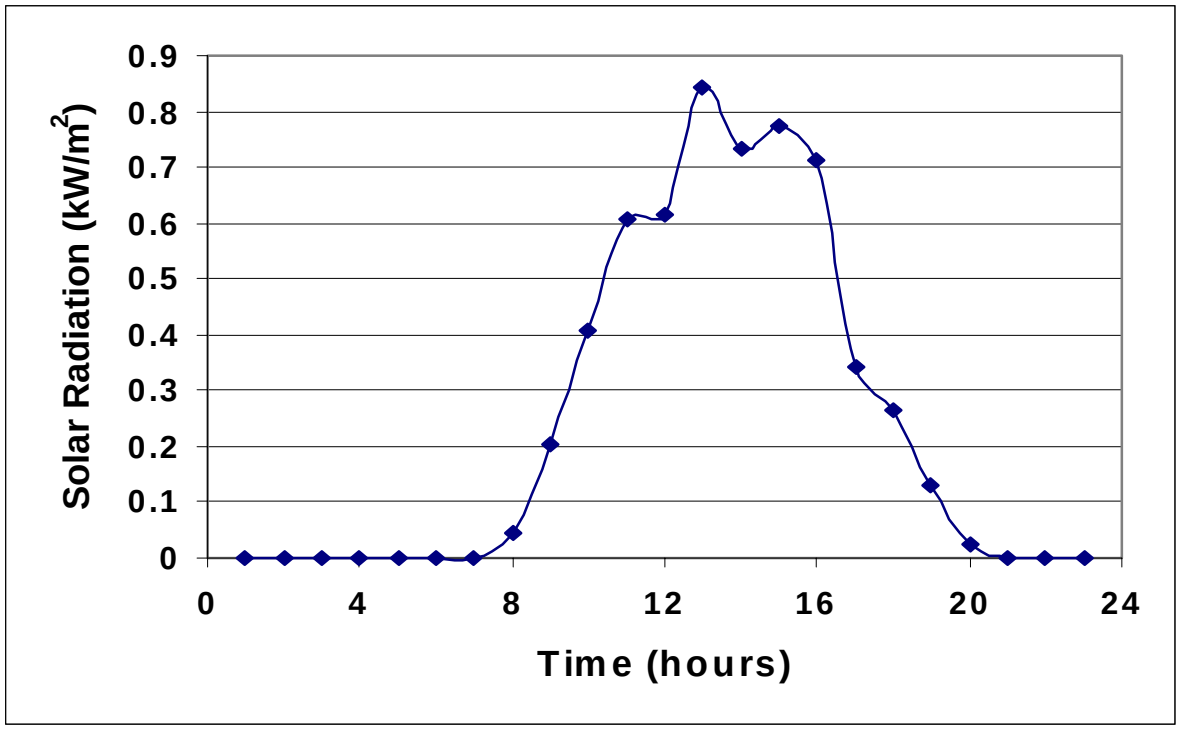

Figure D.17 Solar Radiation versus Time (Day 6).

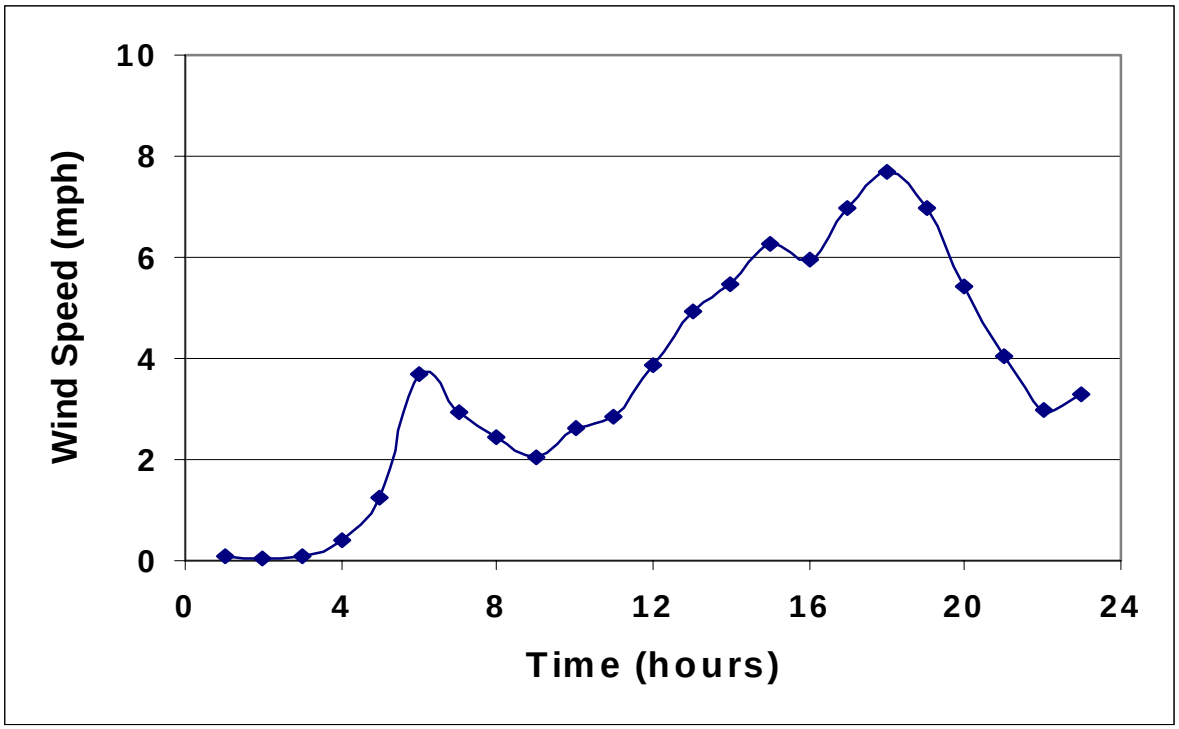

Figure D.18 Wind Speed versus Time (Day 6).

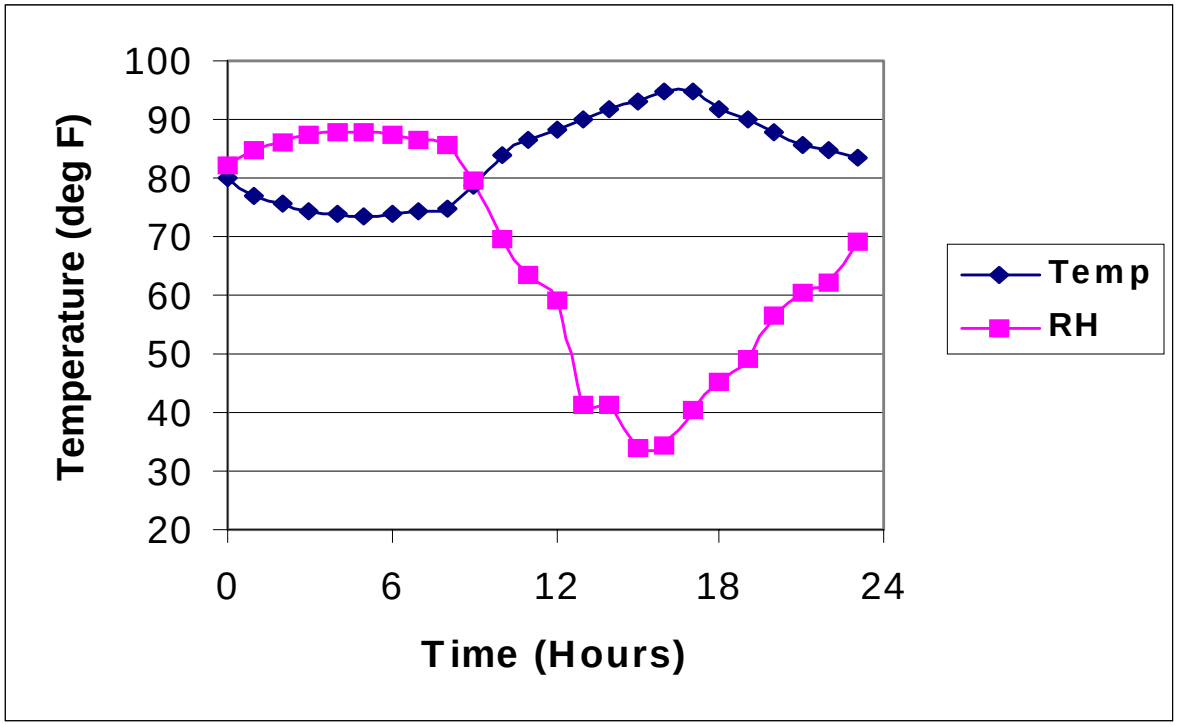

Figure D.19 Temperature and Relative Humidity versus Time (Day 7).

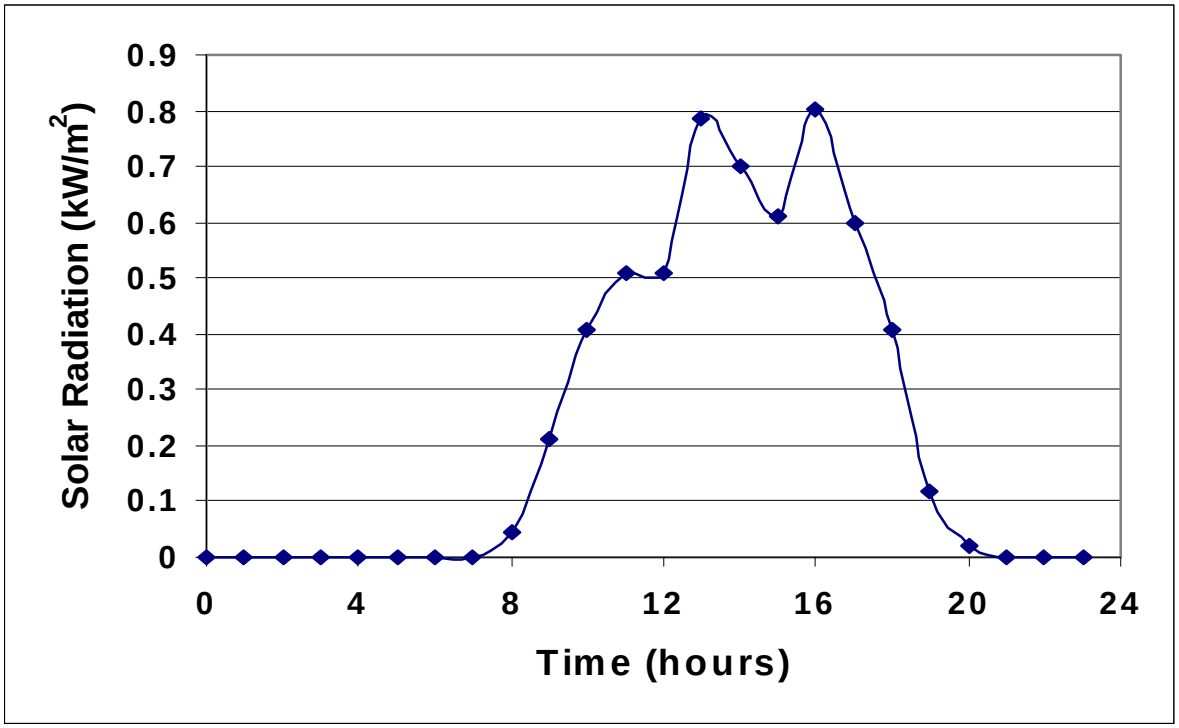

Figure D.20 Solar Radiation versus Time (Day 7).

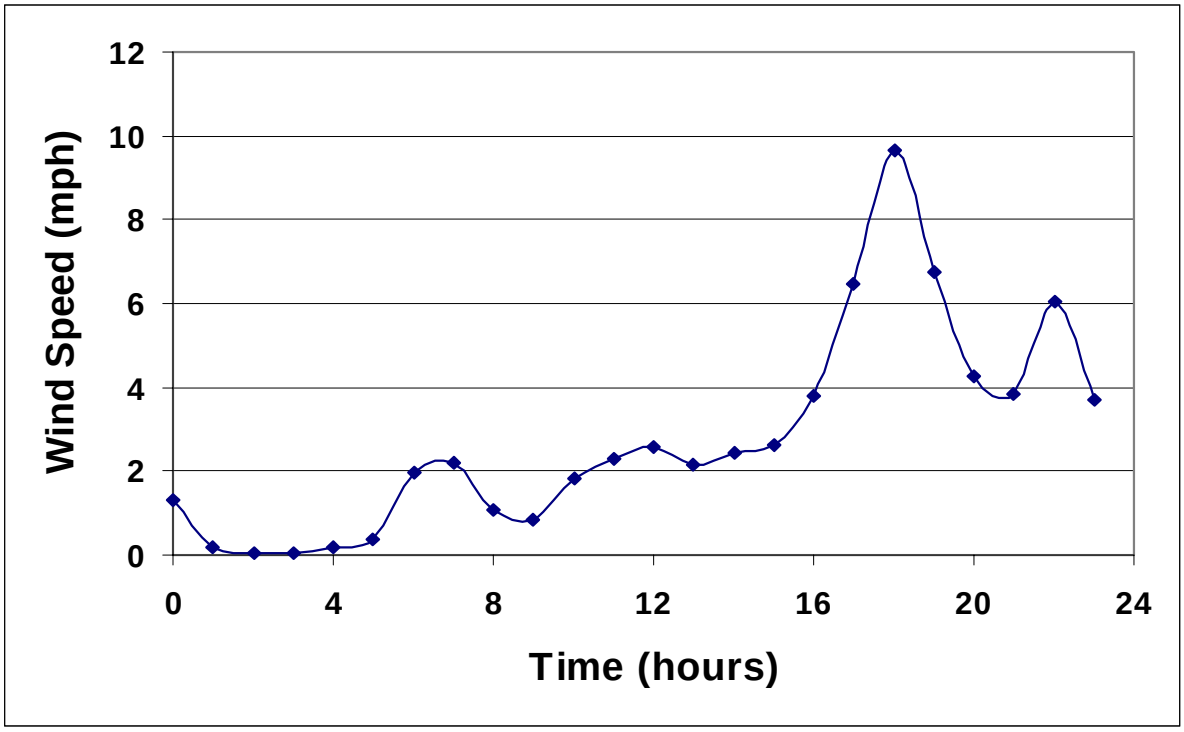

Figure D.21 Wind Speed versus Time (Day 7).

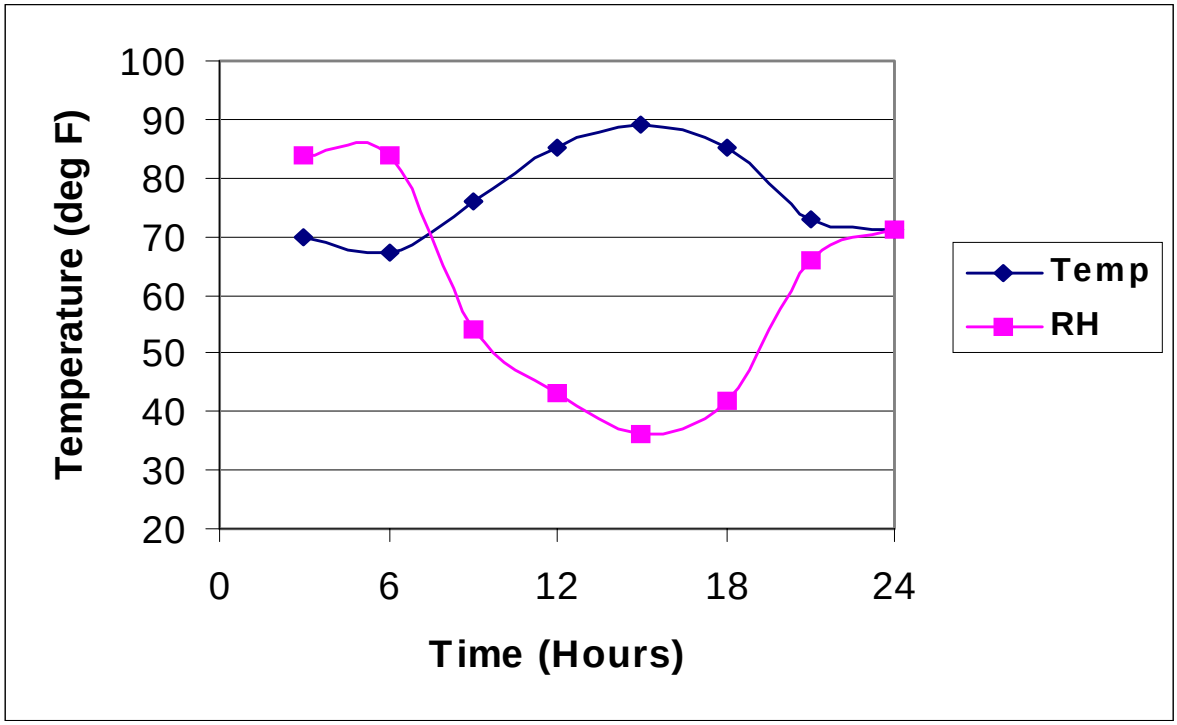

Figure D.22 Temperature and Relative Humidity versus Time (Day 15).

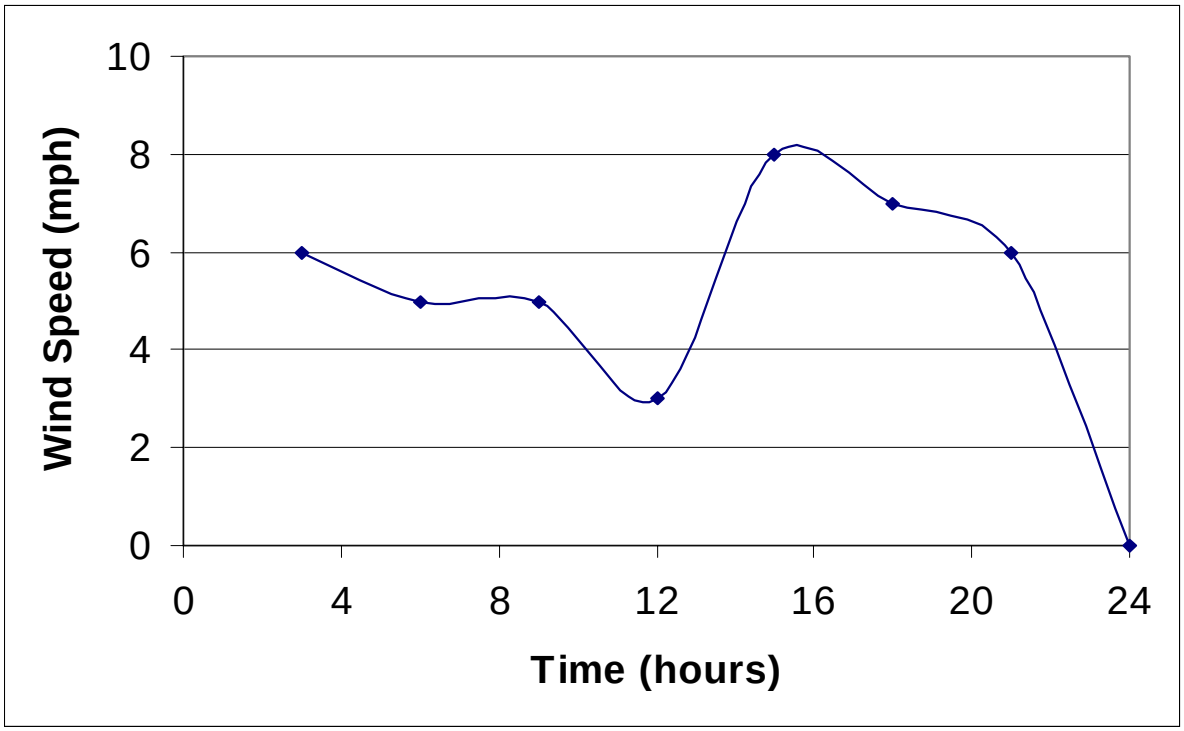

Figure D.23 Wind Speed versus Time (Day 15).

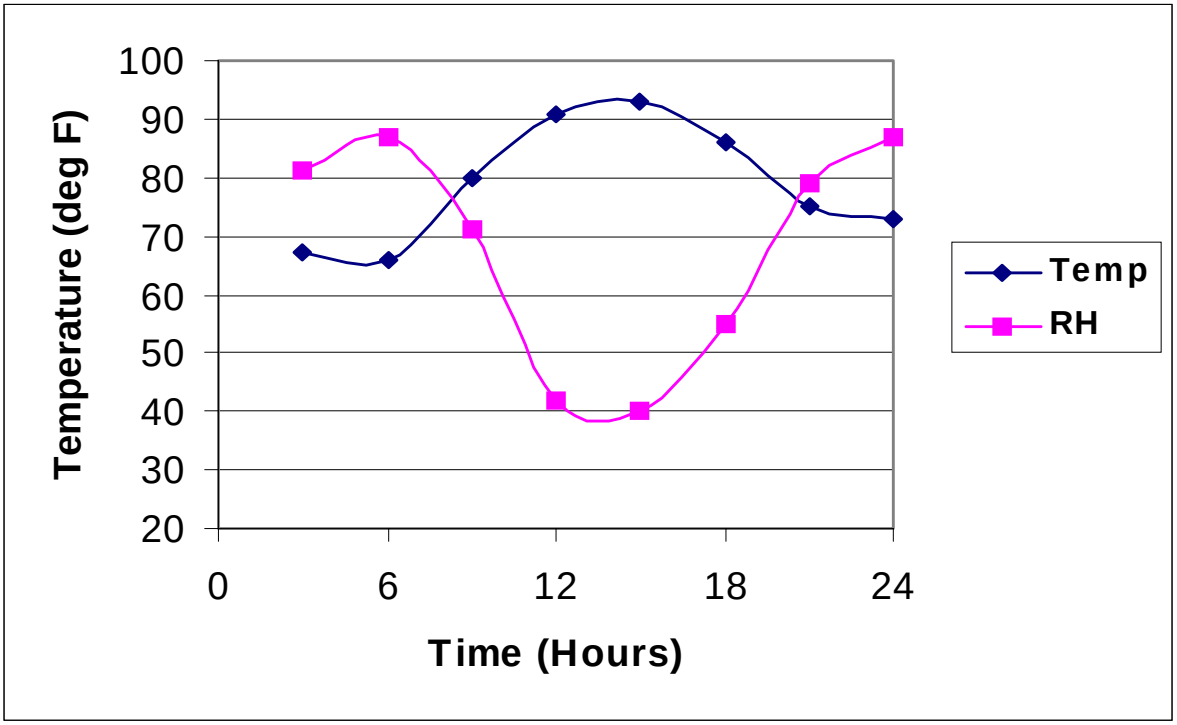

Figure D.24 Temperature and Relative Humidity versus Time (Day 16).

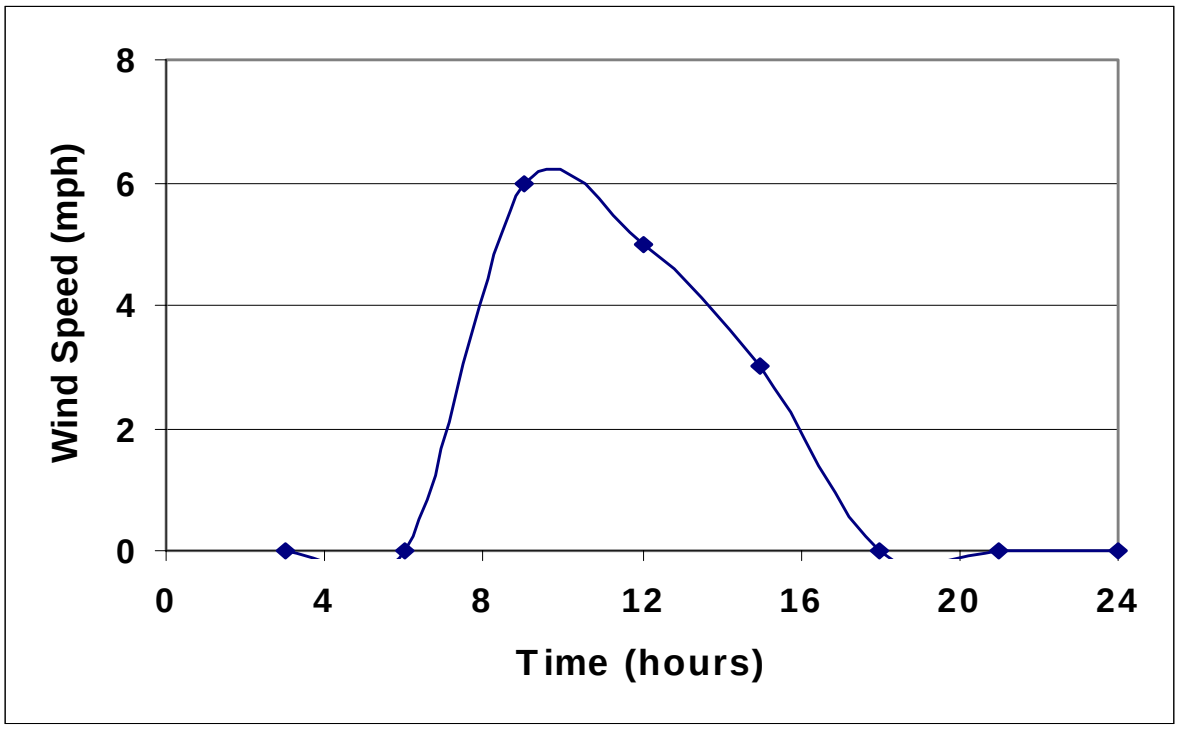

Figure D.25 Wind Speed versus Time (Day 16).

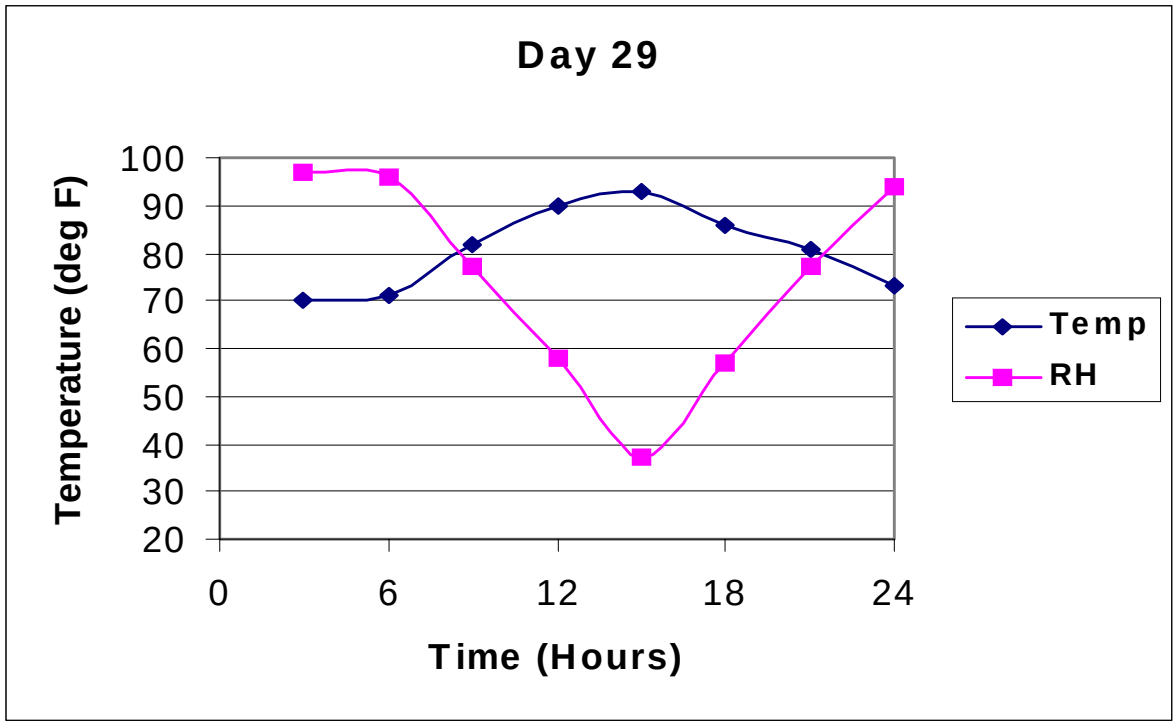

Figure D.26 Temperature and Relative Humidity versus Time (Day 29).

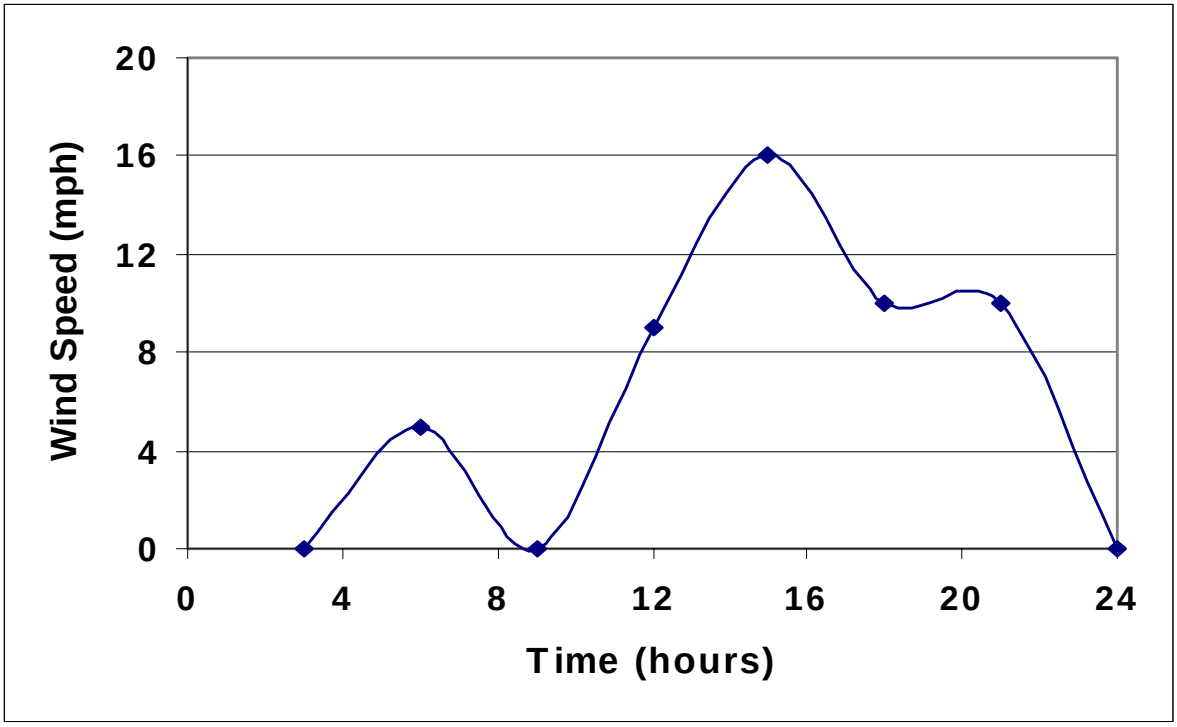

Figure D.27 Wind Speed versus Time (Day 29).

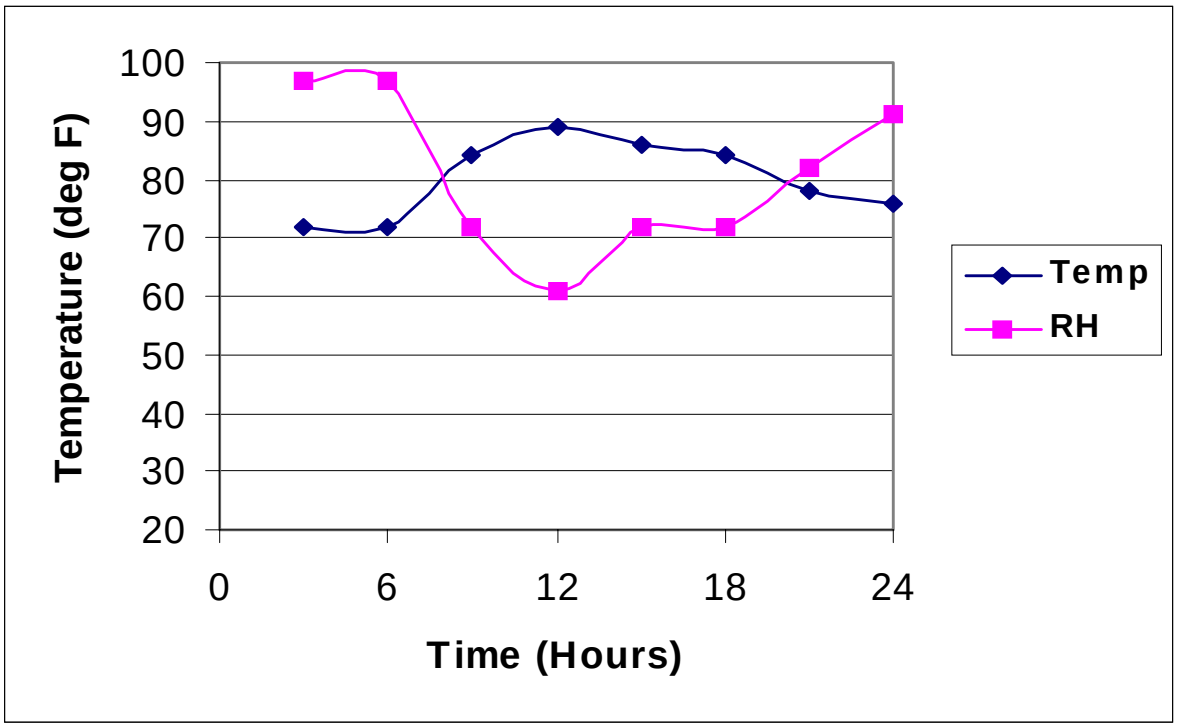

Figure D.28 Temperature and Relative Humidity versus Time (Day 30).

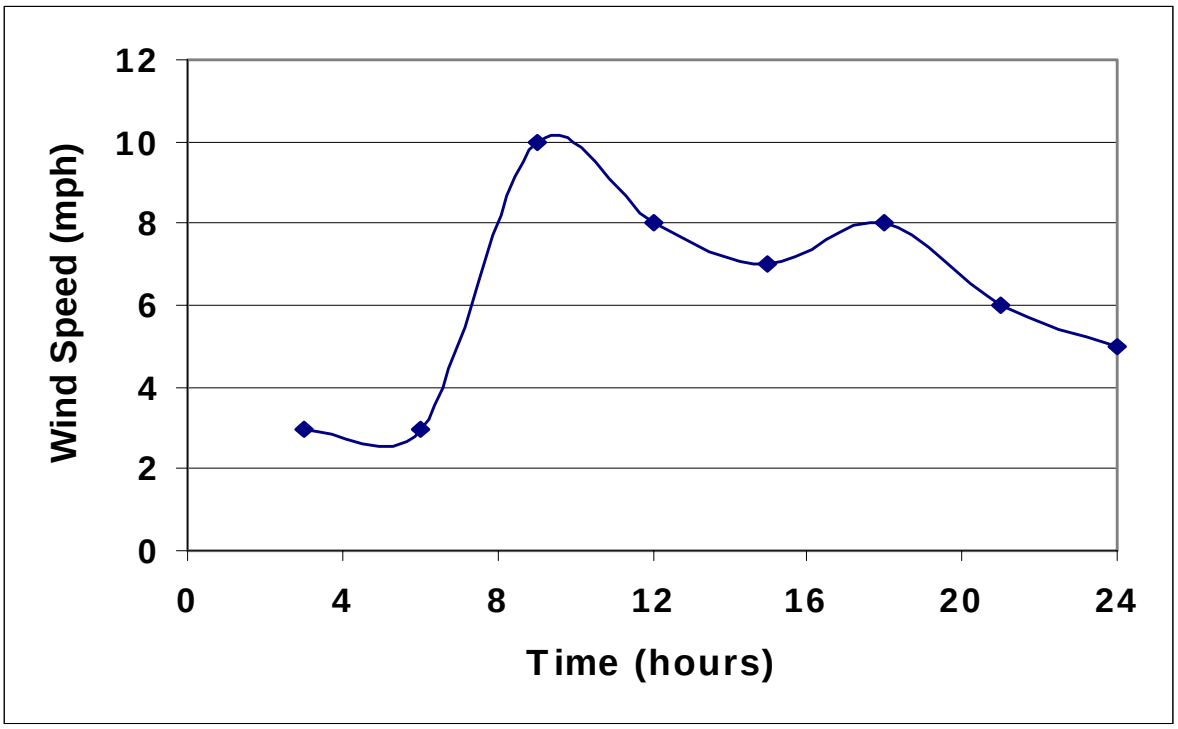

Figure D.29 Wind Speed versus Time (Day 30).

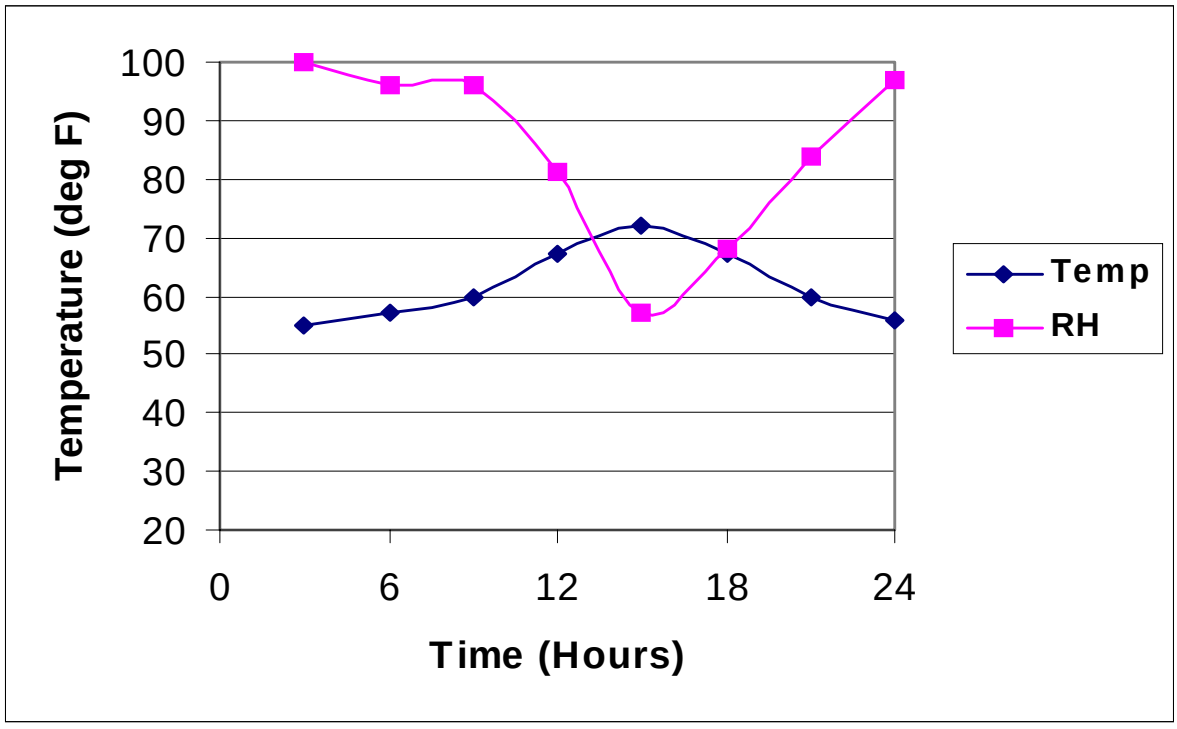

Figure D.30 Temperature and Relative Humidity versus Time (Day 161).

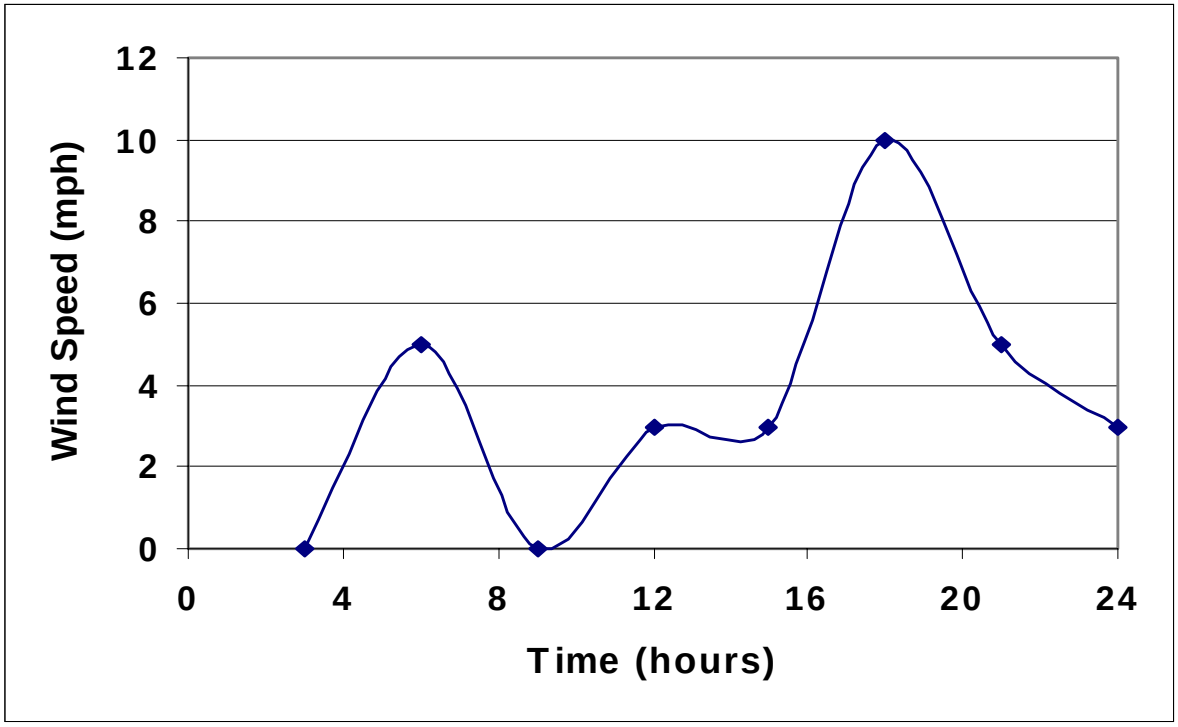

Figure D.31 Wind Speed versus Time (Day 161).

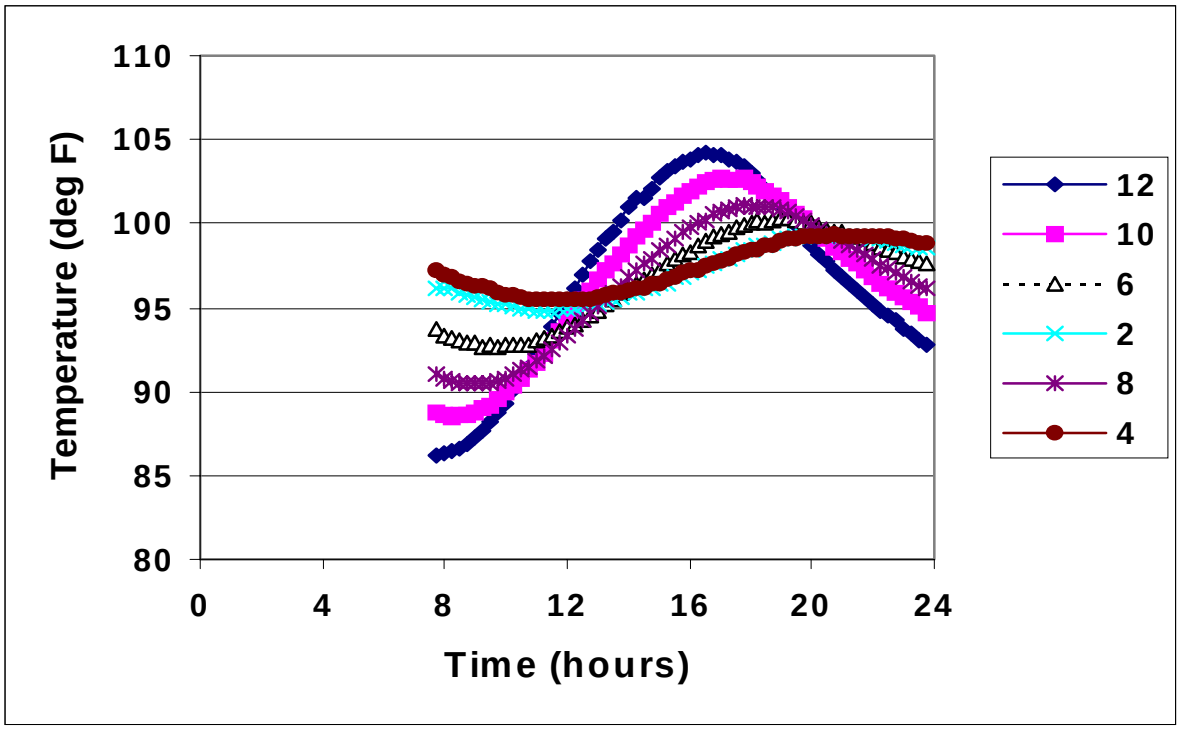

Figure D.32 Slab Temperatures (Day 4).

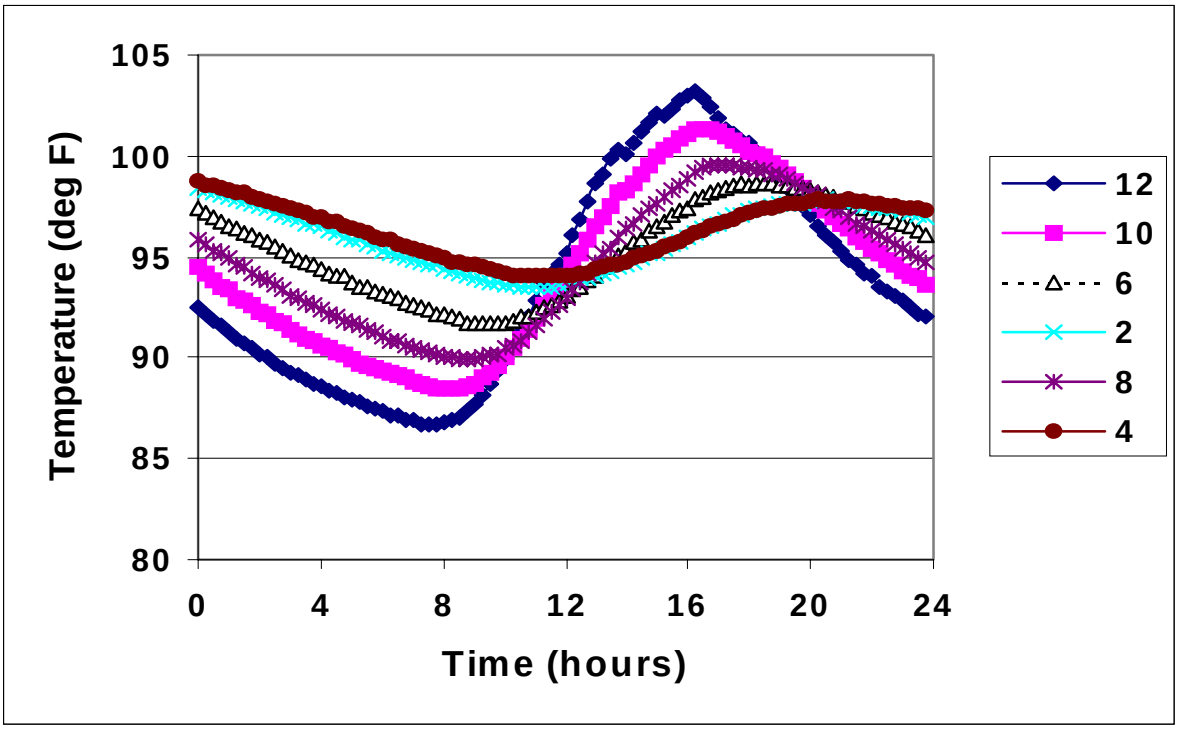

Figure D.33 Slab Temperatures (Day 5)**.**

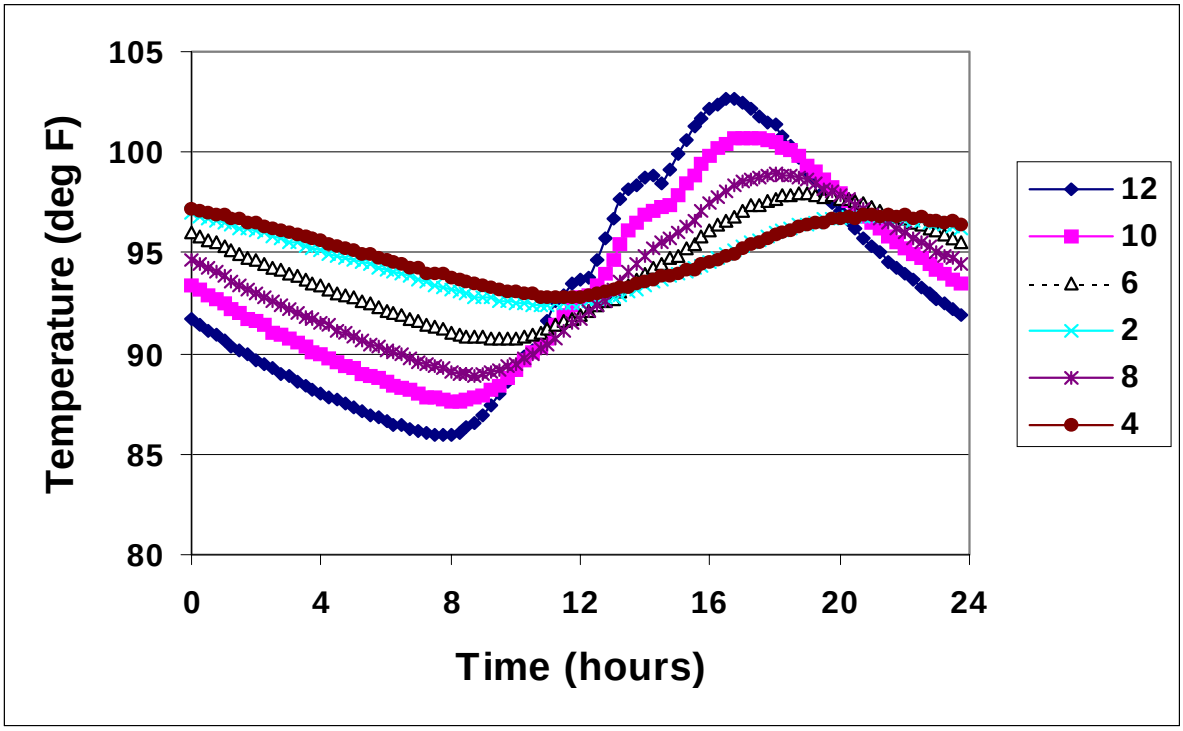

Figure D.34 Slab Temperatures (Day 6).

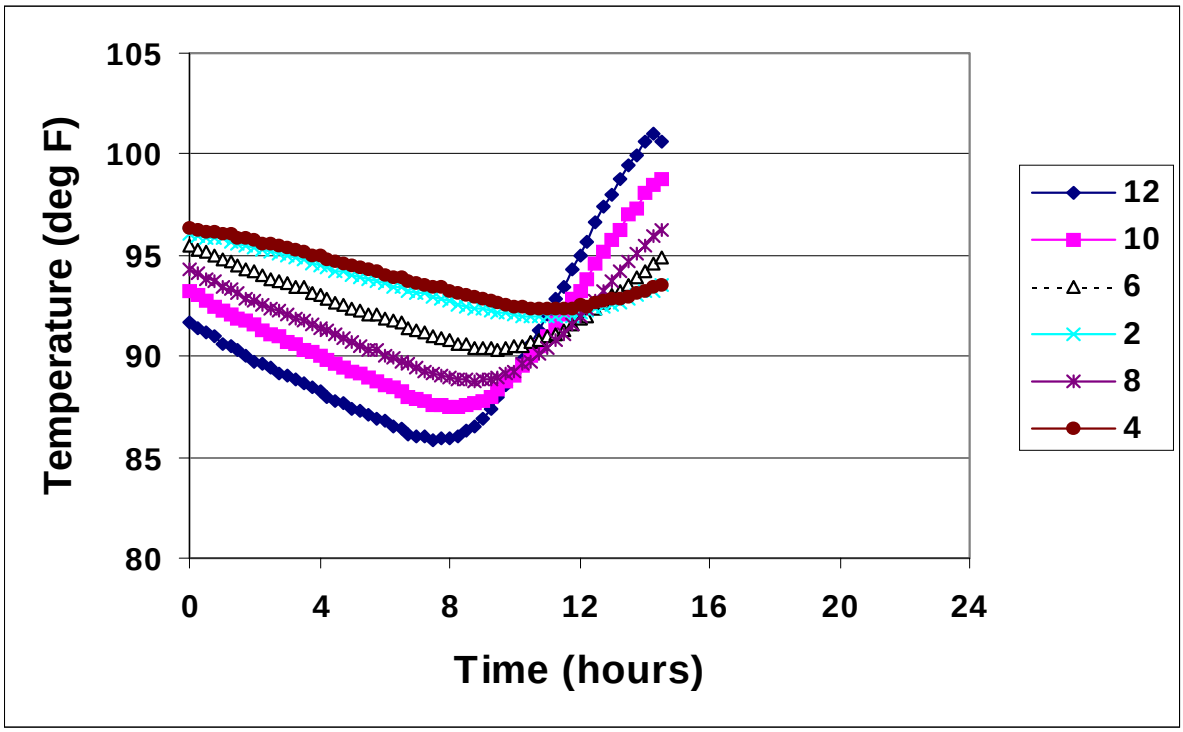

Figure D.35 Slab Temperatures (Day 7).

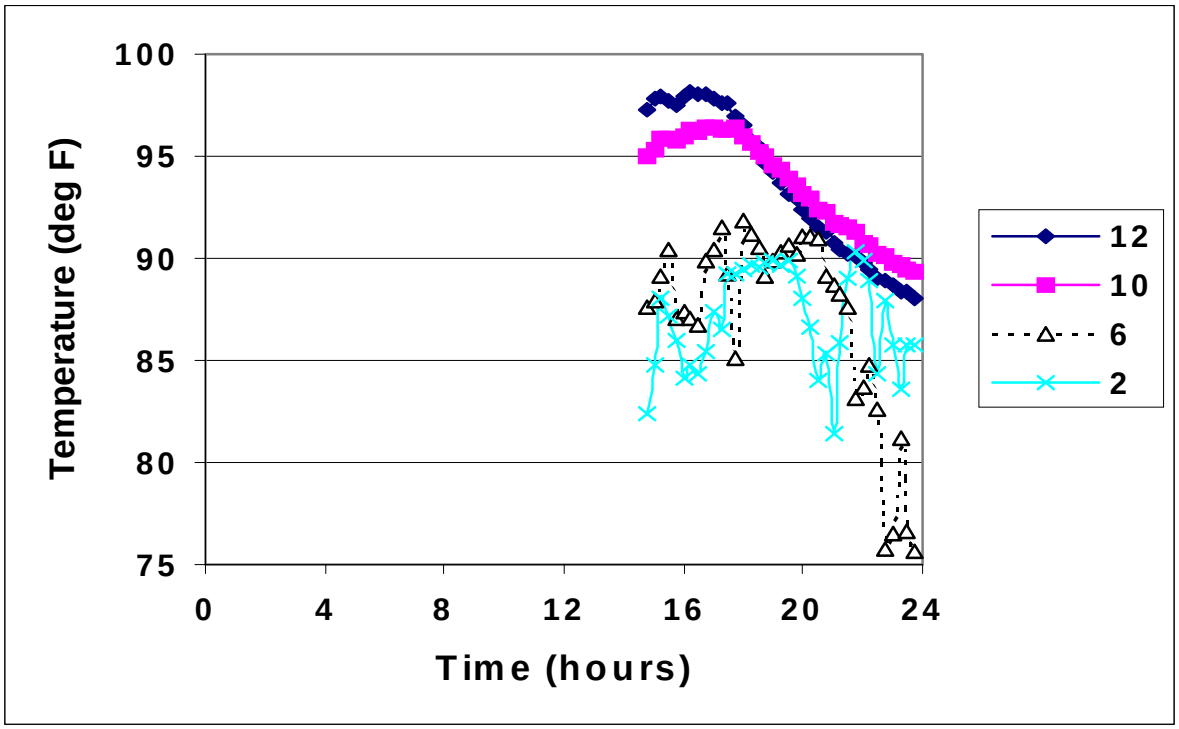

Figure D.36 Pavement Temperatures versus Time (Day 15).

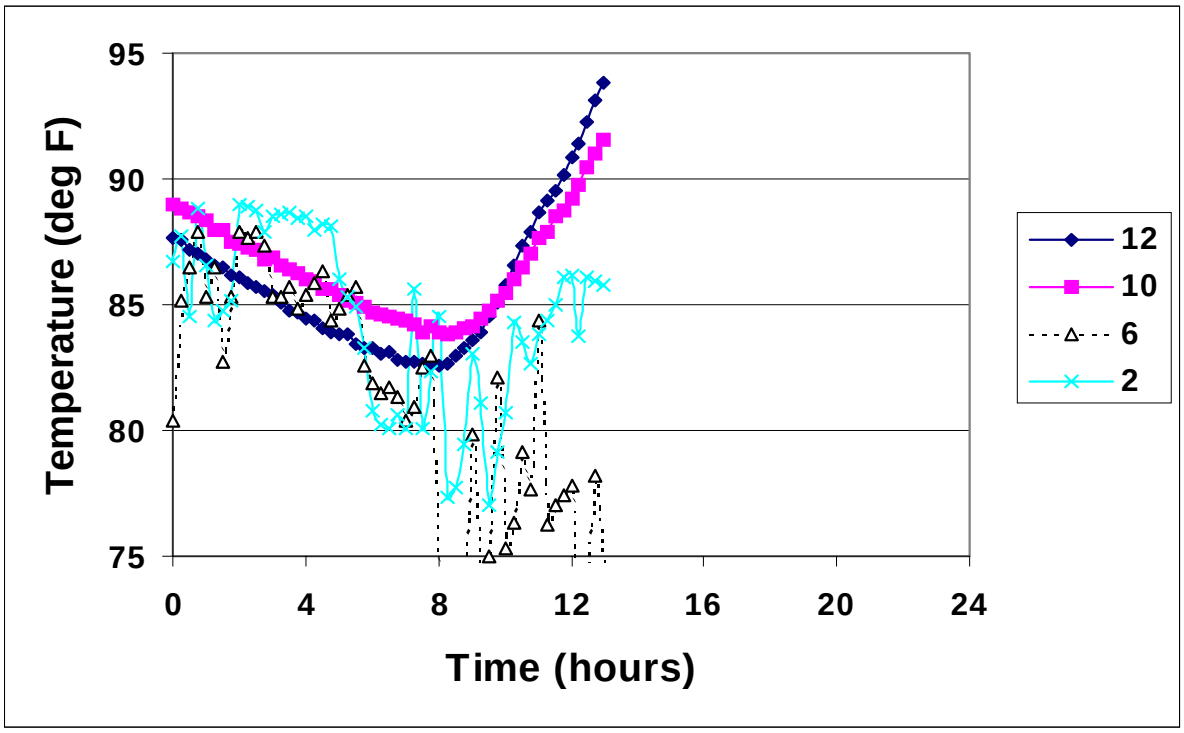

Figure D.37 Pavement Temperatures versus Time (Day 16).

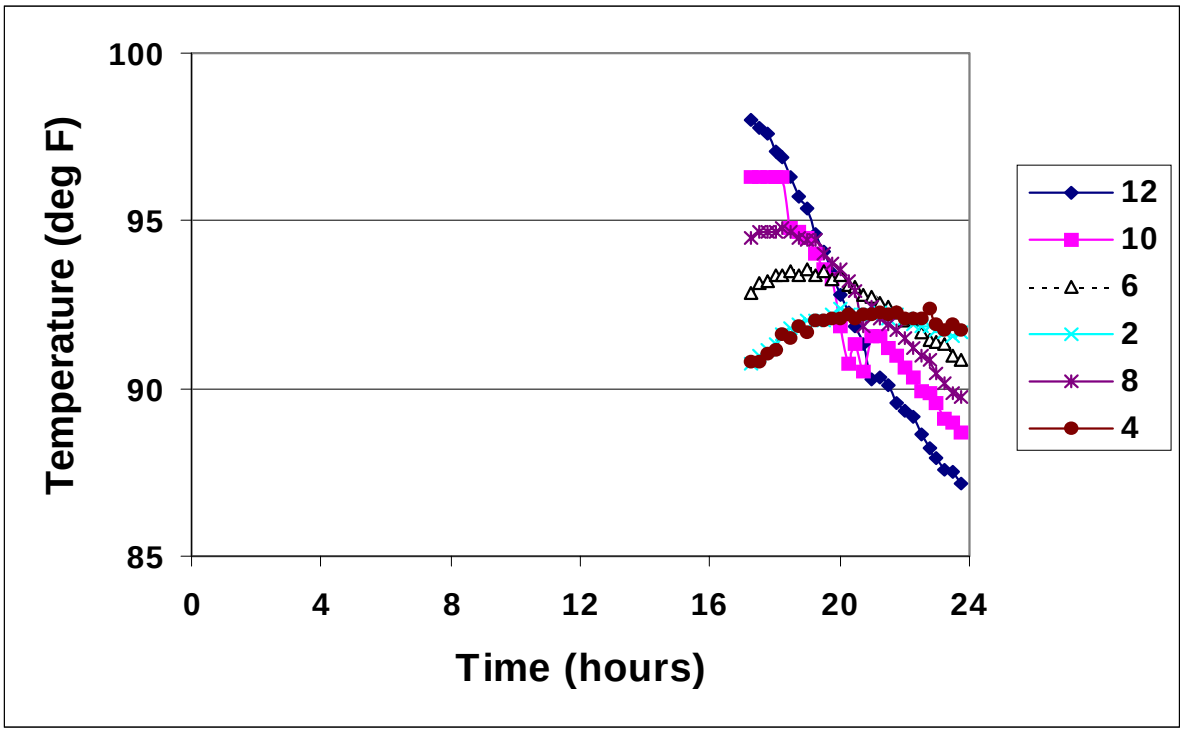

Figure D.38 Pavement Temperatures versus Time (Day 29).

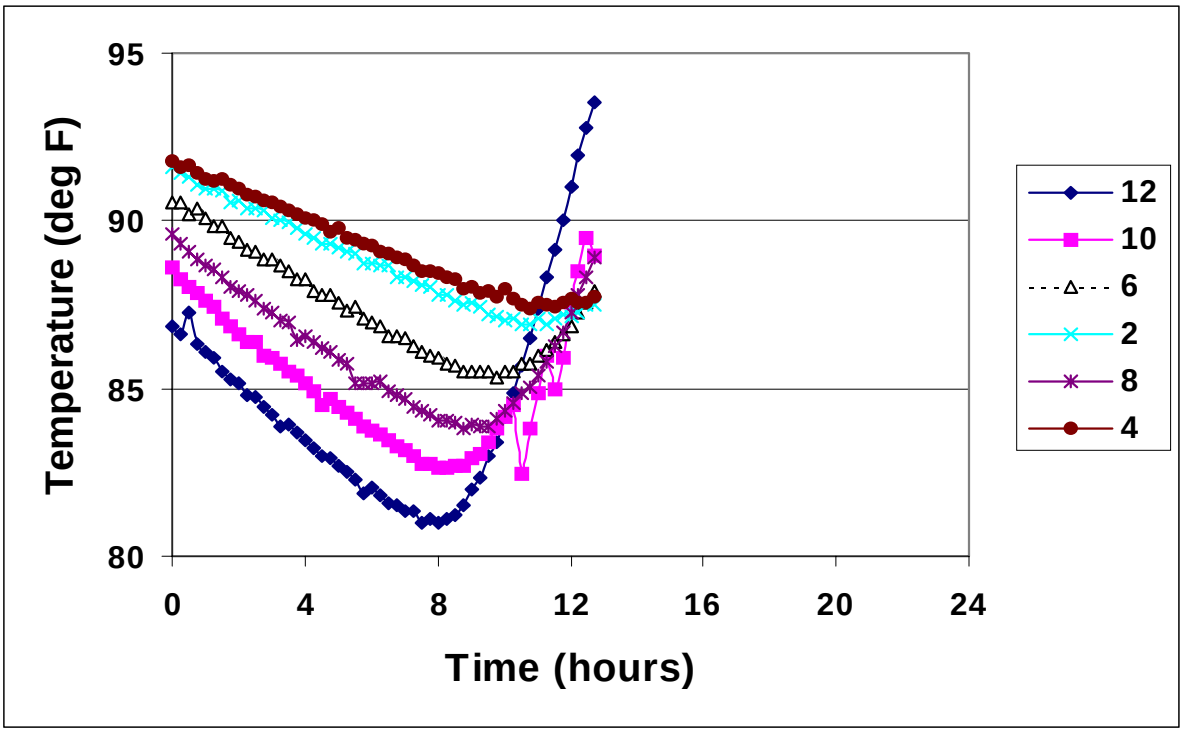

Figure D.39 Pavement Temperatures versus Time (Day 30).

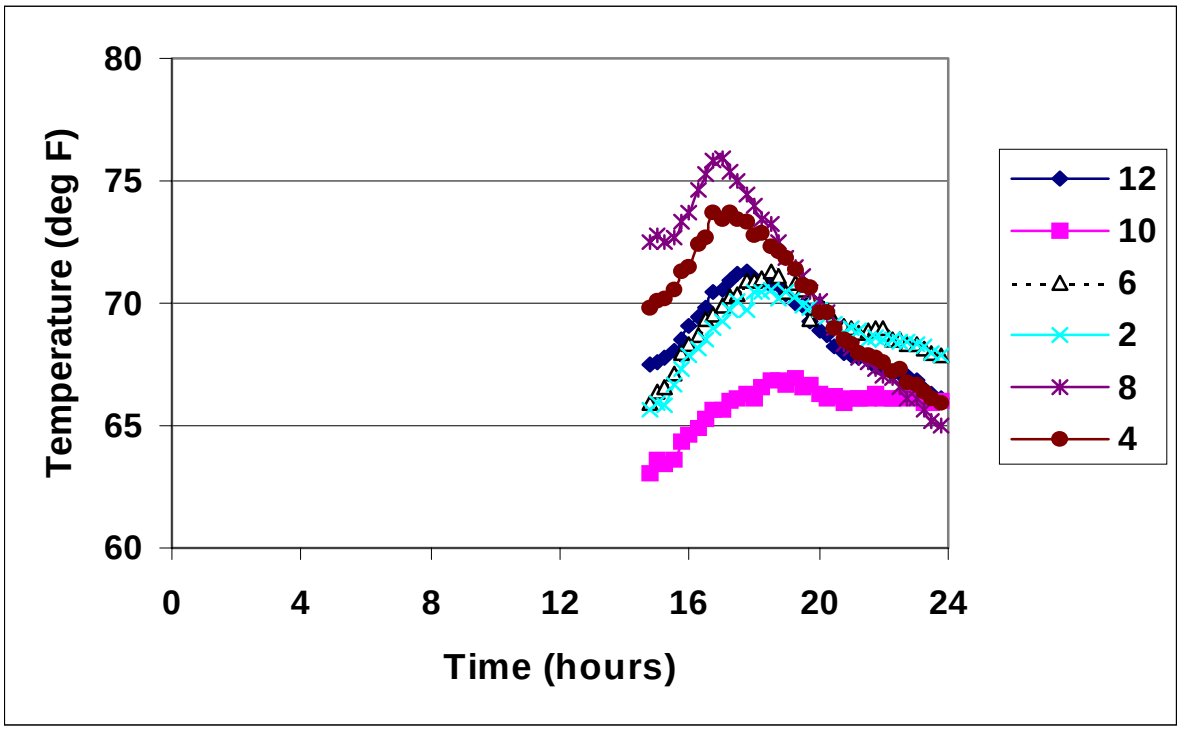

Figure D.40 Pavement Temperatures versus Time (Day 161).

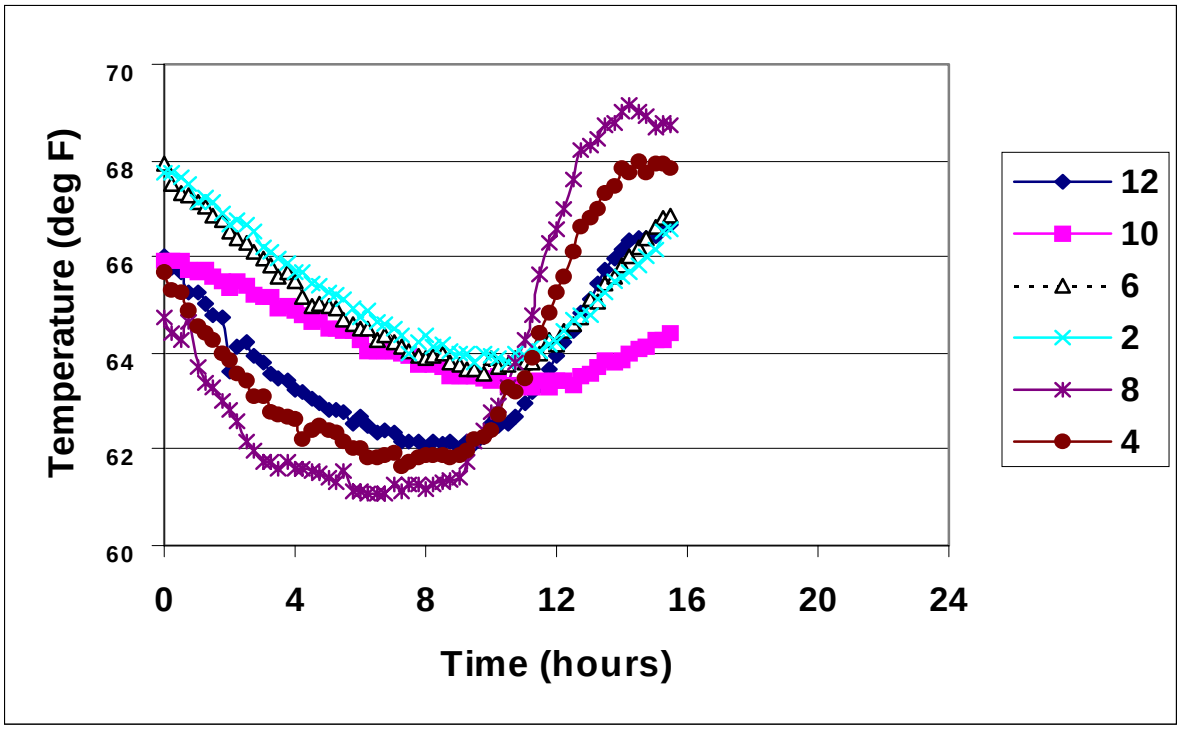

Figure D.41 Pavement Temperatures versus Time (Day 162).

APPENDIX E

CONCRETE MOISTURE DATA

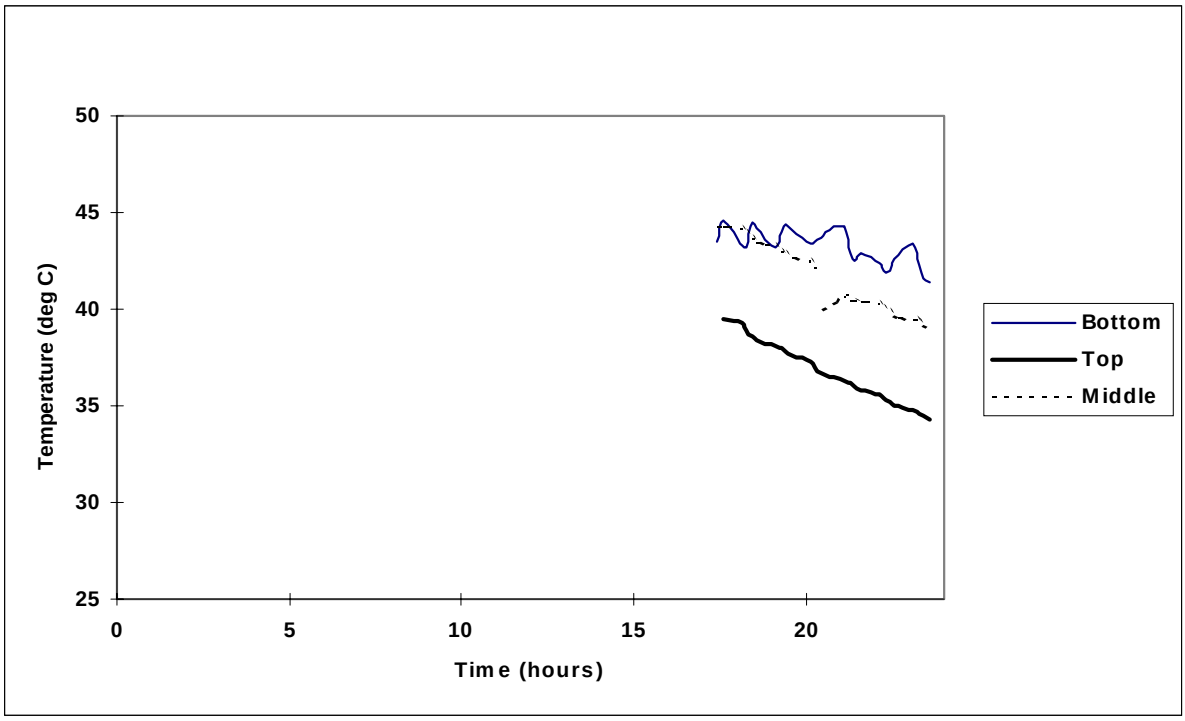

Figure E.1 Dry-Bulb Temperature versus Time for Day 1 of I-45 Pavement.

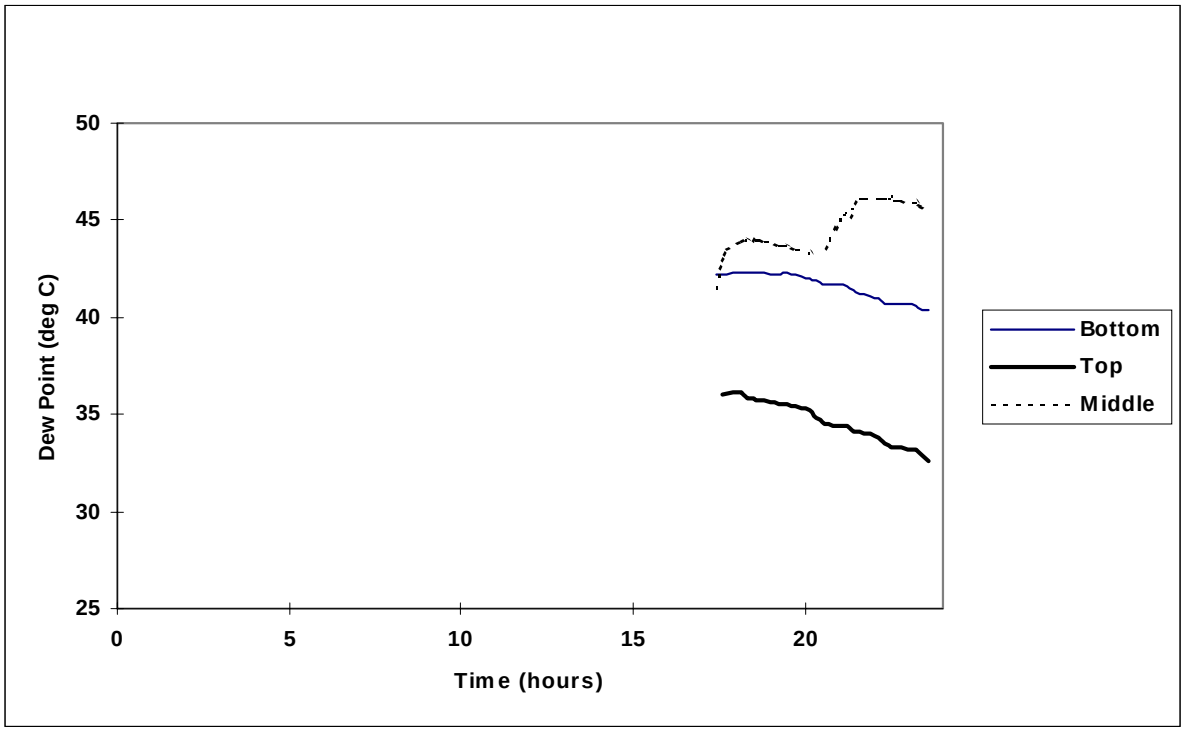

Figure E.2 Dew Point versus Time for Day 1 of I-45 Pavement.

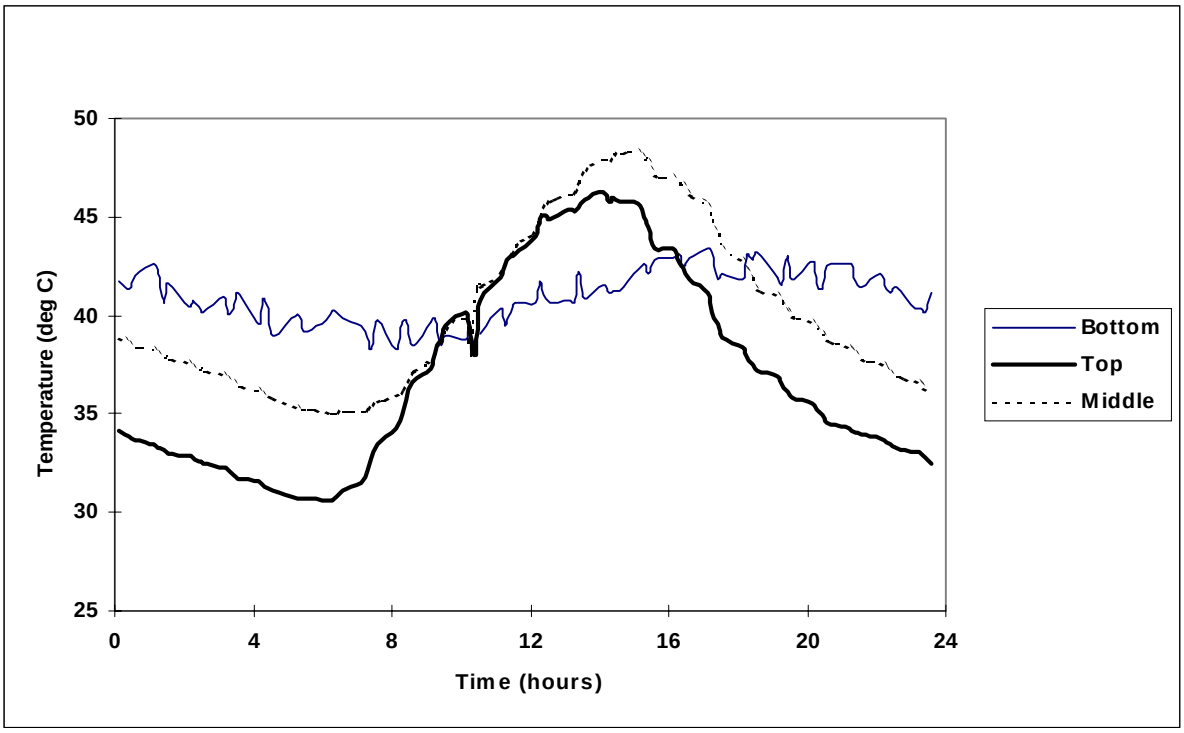

Figure E.3 Dry-Bulb Temperature versus Time for Day 2 of I-45 Pavement.

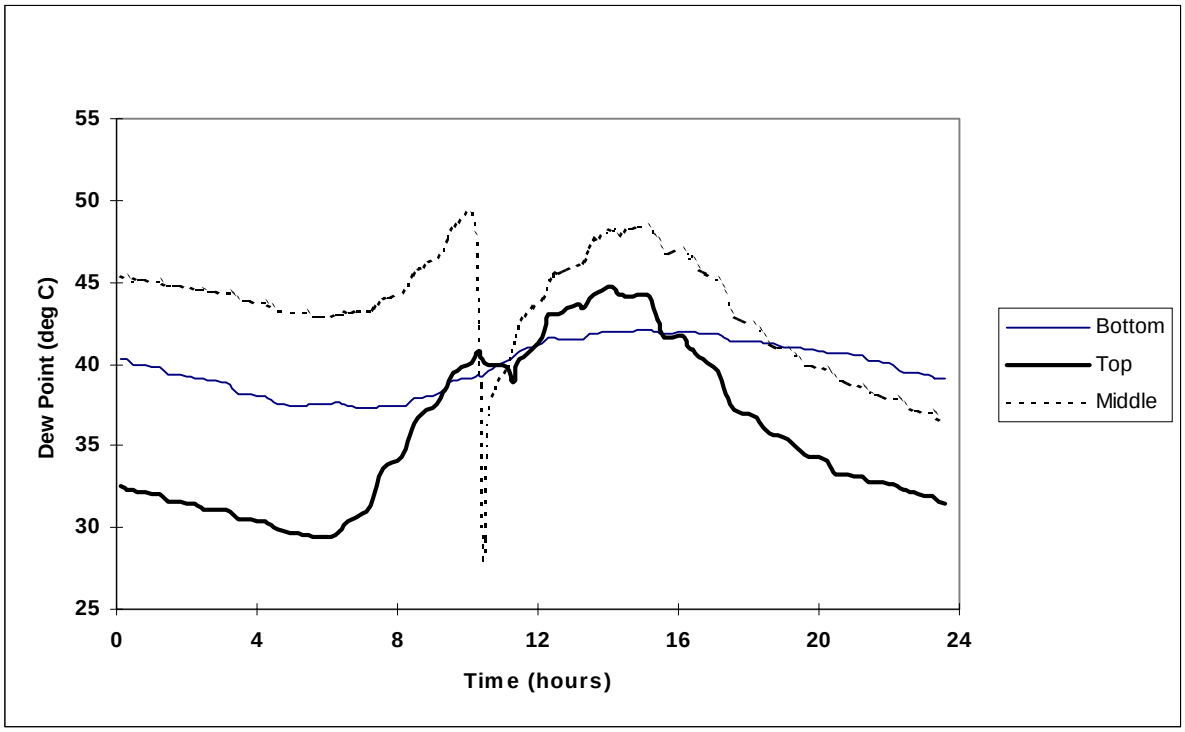

Figure E.4 Dew Point versus Time for Day 2 of I-45 Pavement.

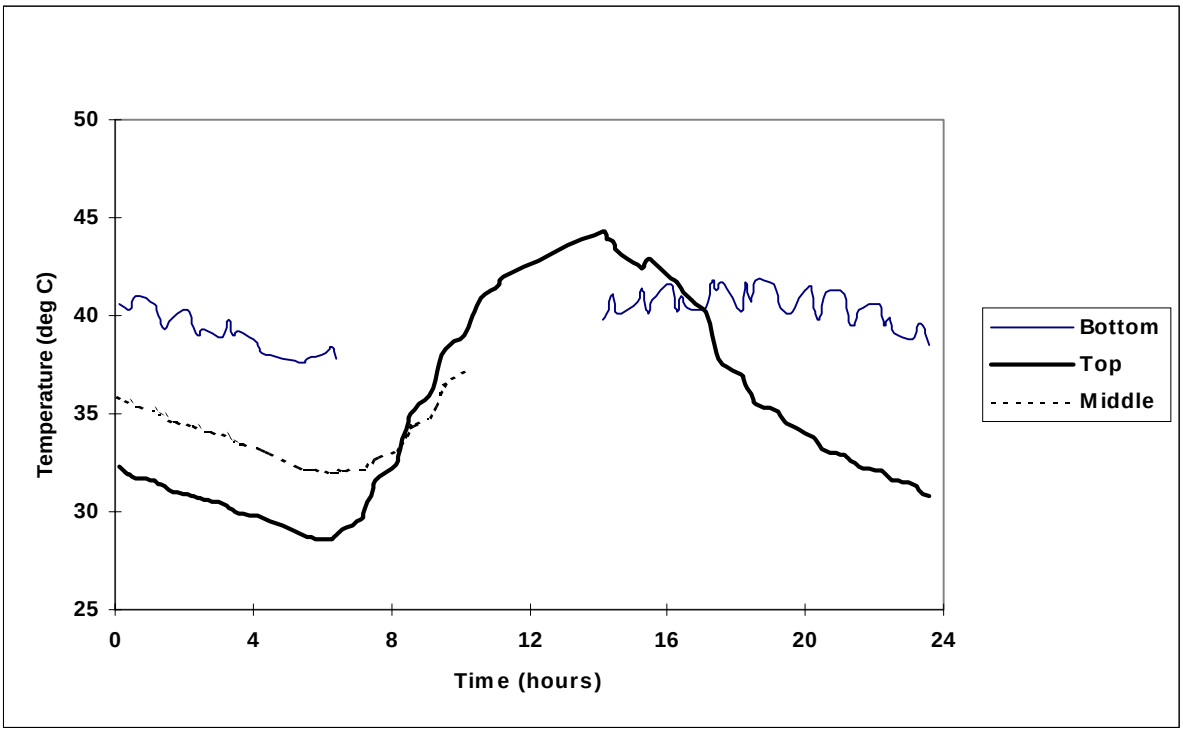

Figure E.5 Dry-Bulb Temperature versus Time for Day 3 of the I-45 Pavement.

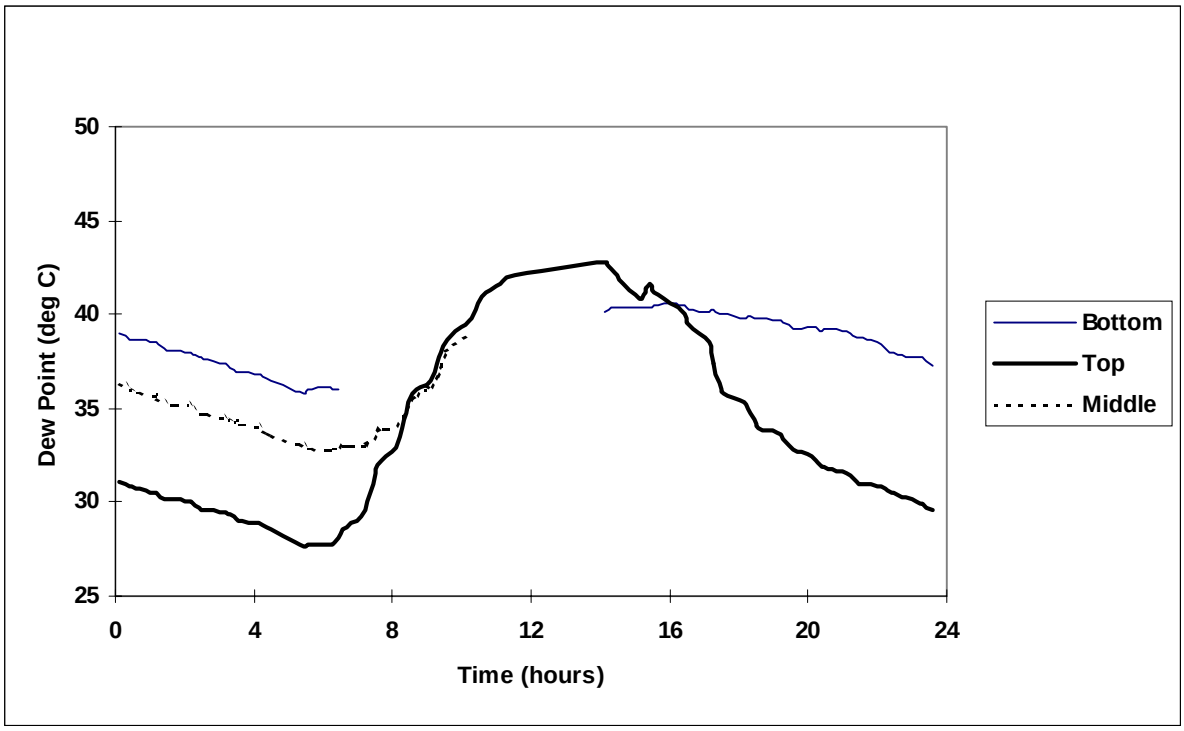

Figure E.6 Dew Point versus Time for Day 3 of the I-45 Pavement.

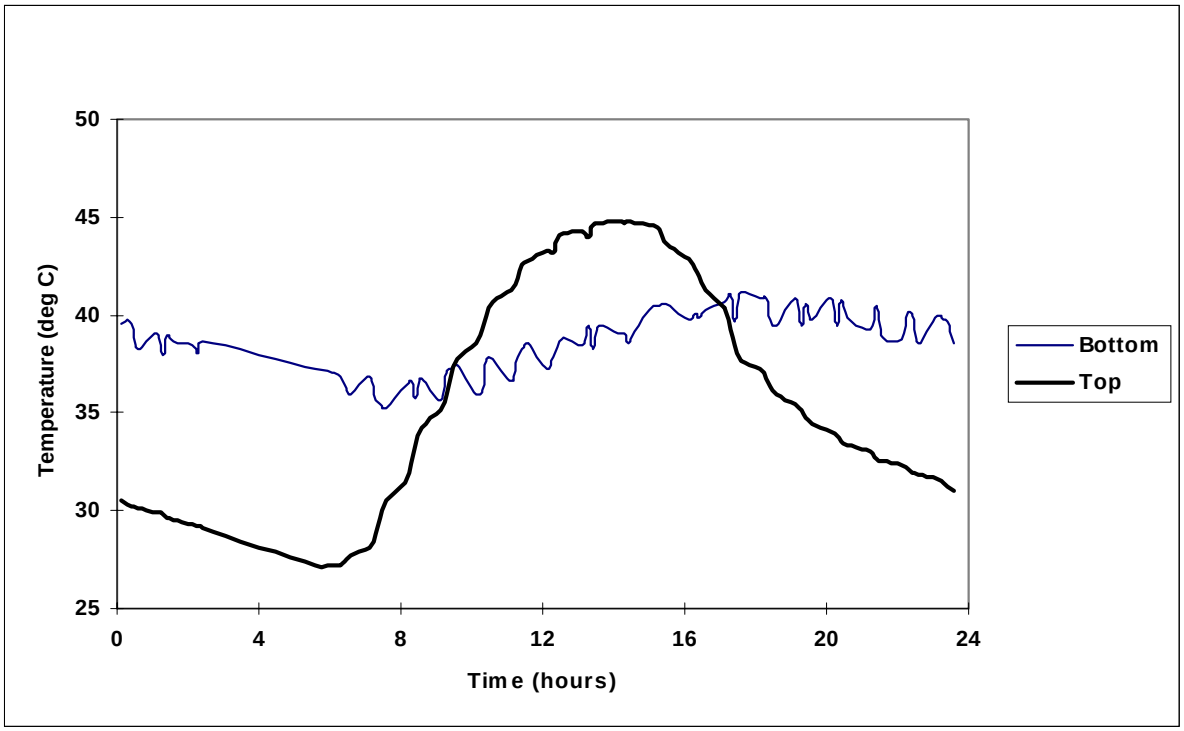

Figure E.7 Dry-Bulb Temperature versus Time for Day 4 of the I-45 Pavement.

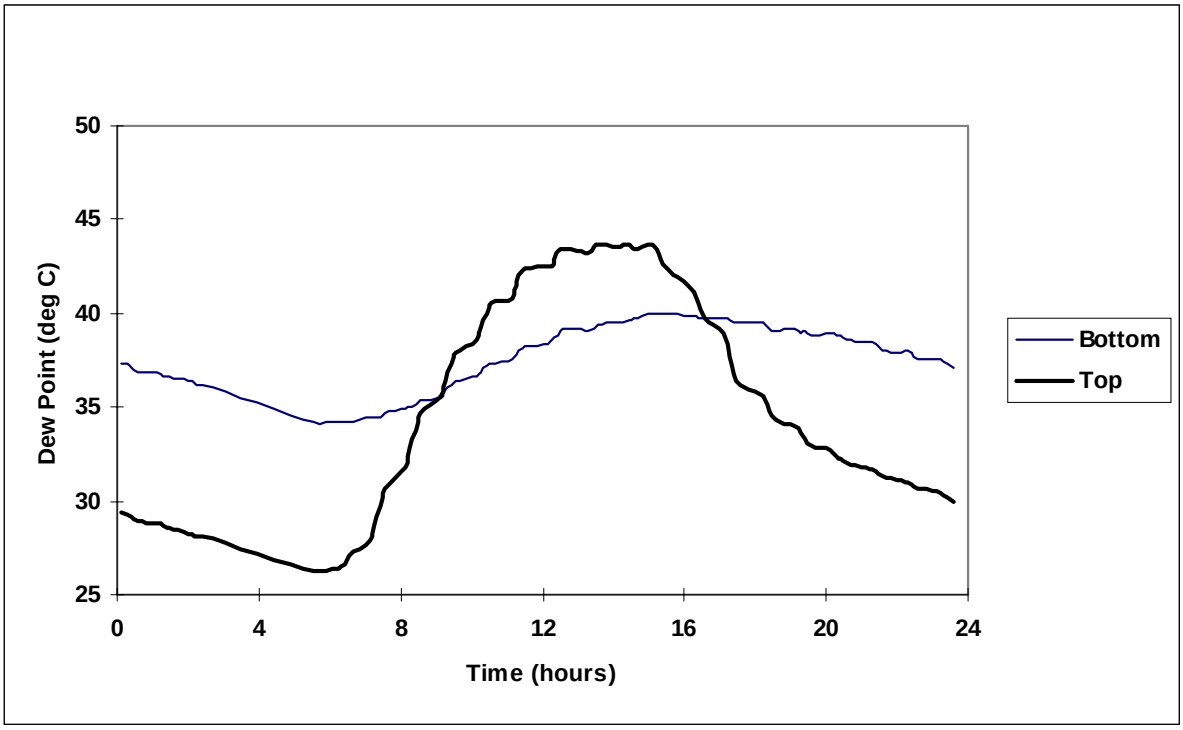

Figure E.8 Dew Point versus Time for Day 4 of the I-45 Pavement.

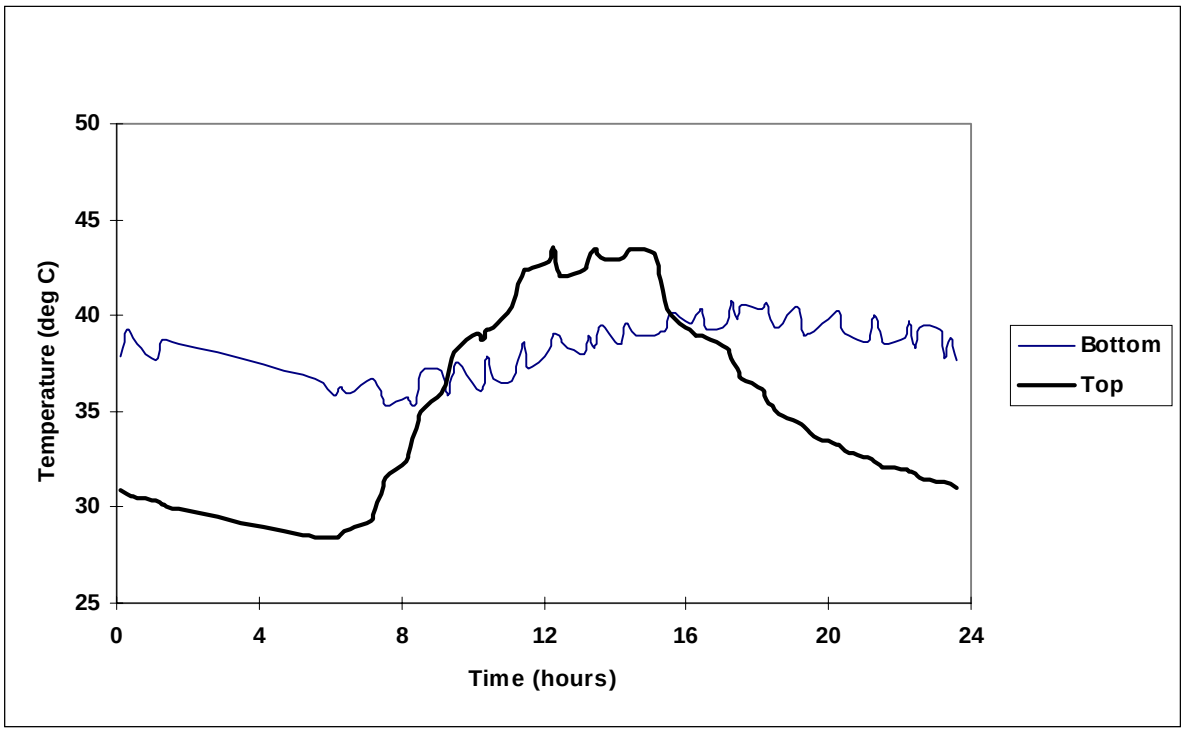

Figure E.9 Dry-Bulb Temperature versus Time for Day 5 of the I-45 Pavement.

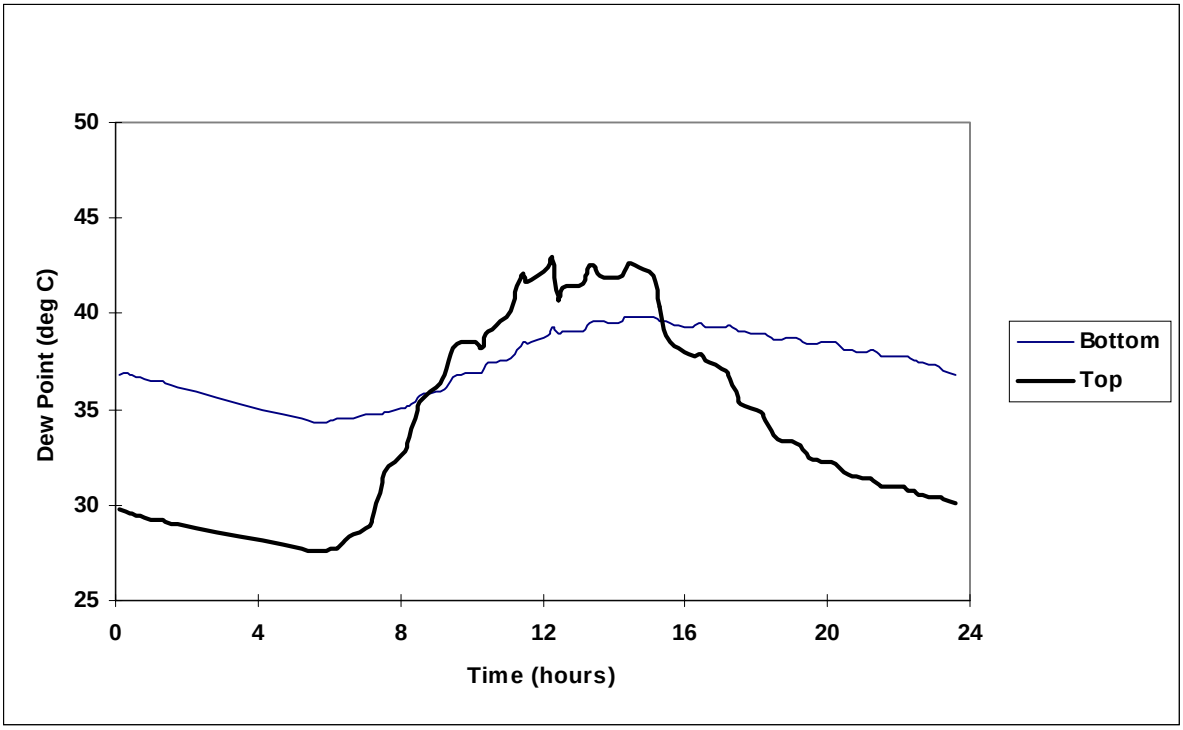

Figure E.10 Dew Point versus Time for Day 5 of the I-45 Pavement.

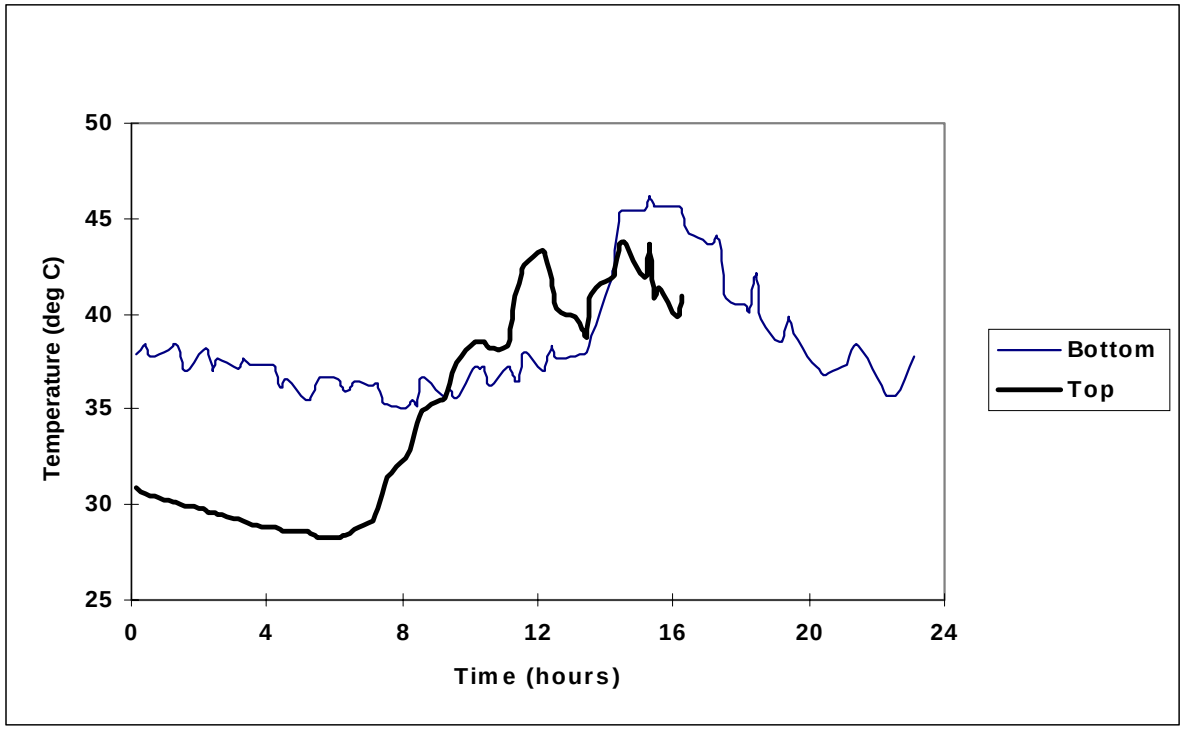

Figure E.11 Dry-Bulb Temperature versus Time for Day 6 of the I-45 Pavement.

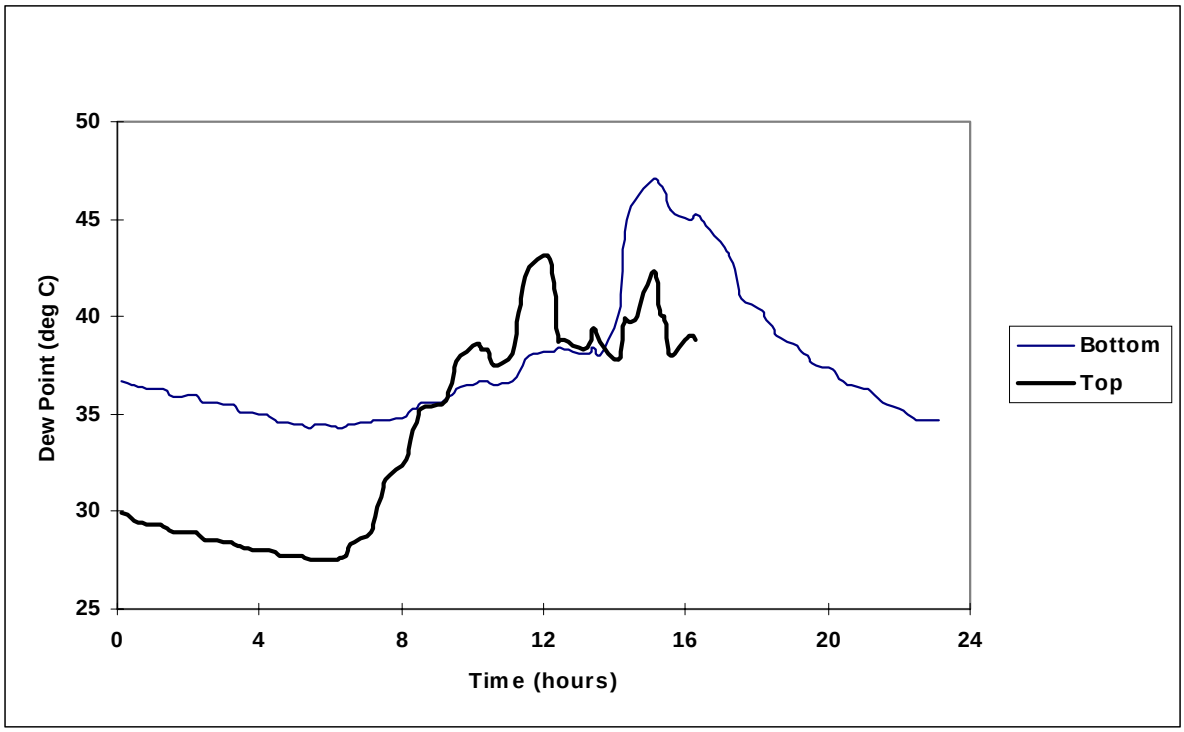

Figure E.12 Dew Point versus Time for Day 6 of the I-45 Pavement.

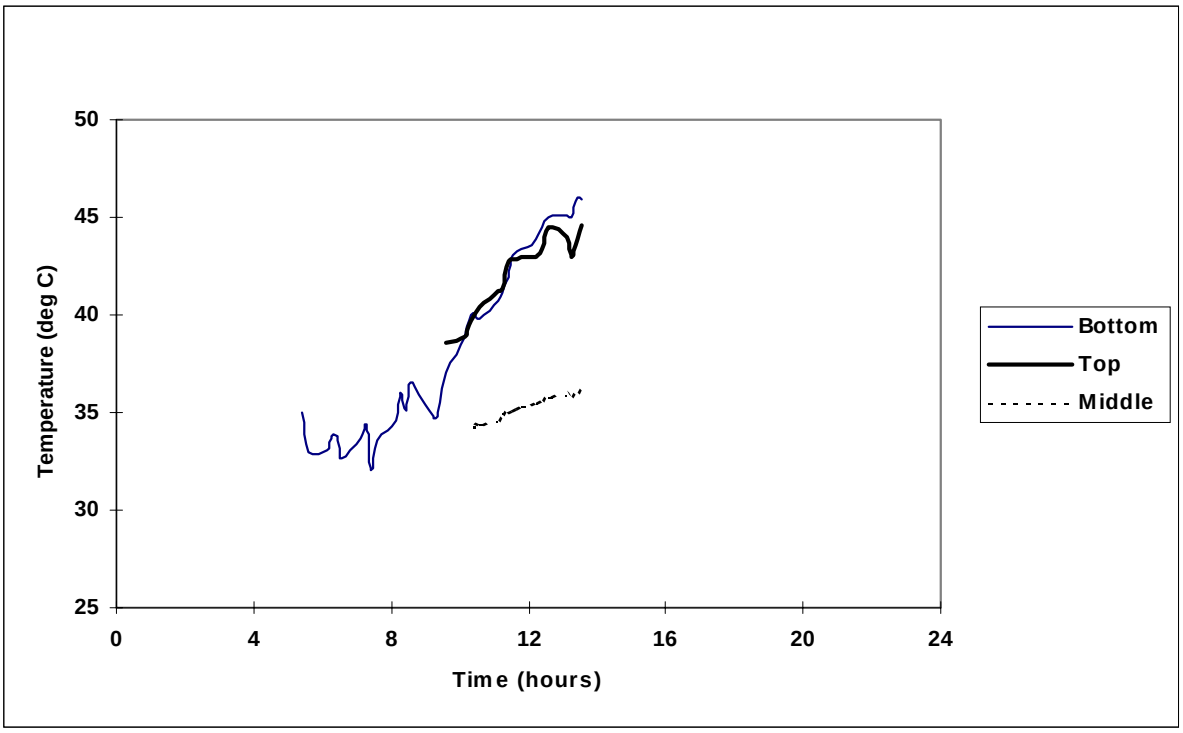

Figure E.13 Dry-Bulb Temperature versus Time for Day 7 of the I-45 Pavement.

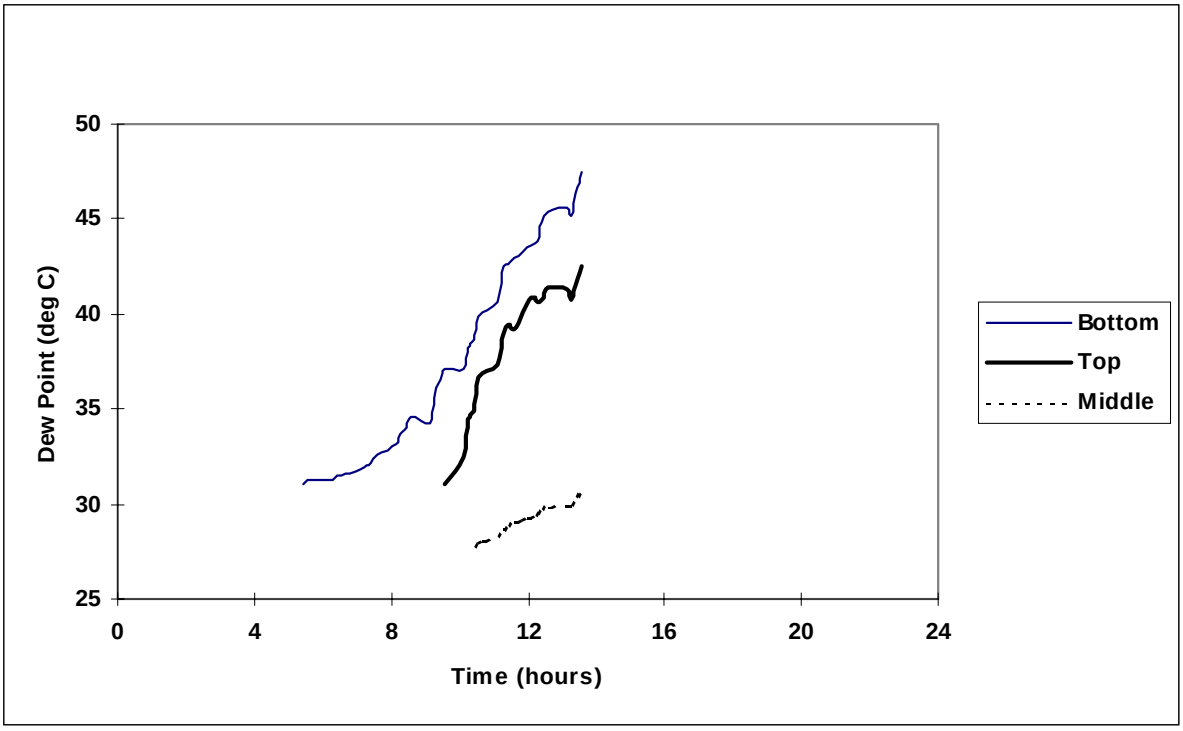

Figure E.14 Dew Point versus Time for Day 7 of the I-45 Pavement.

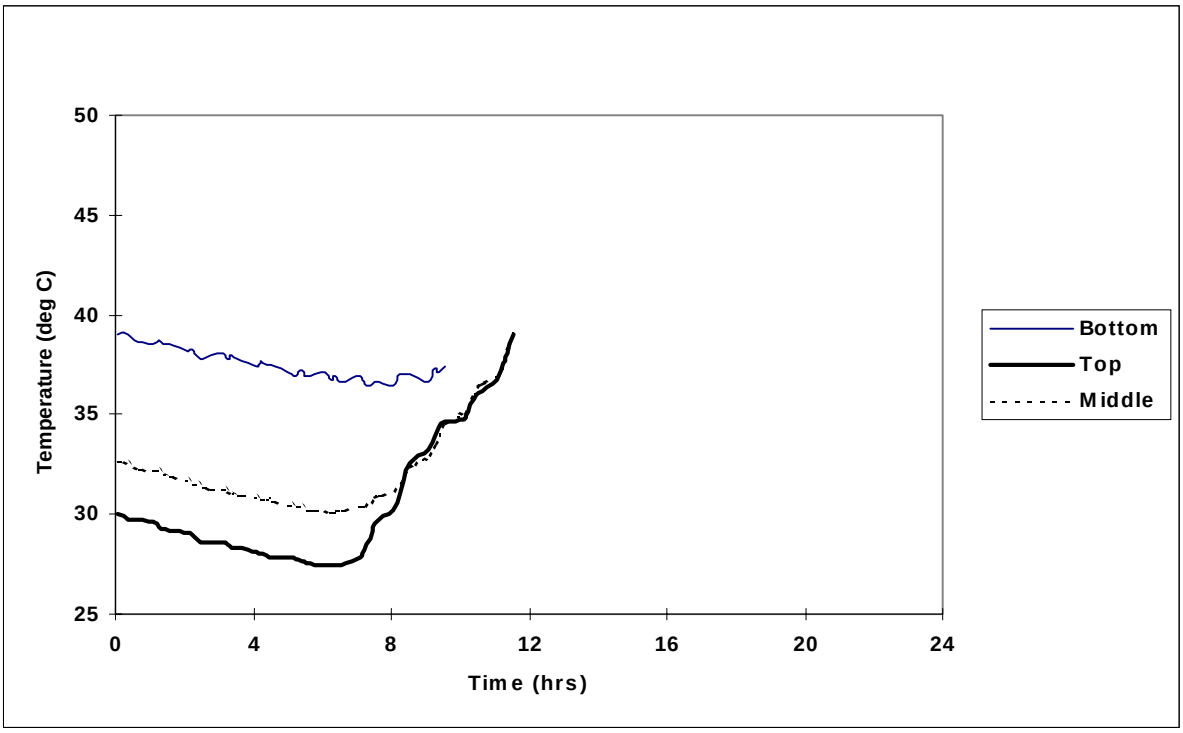

Figure E.15 Dry-Bulb Temperature versus Time for Day 30 of I-45 Pavement.

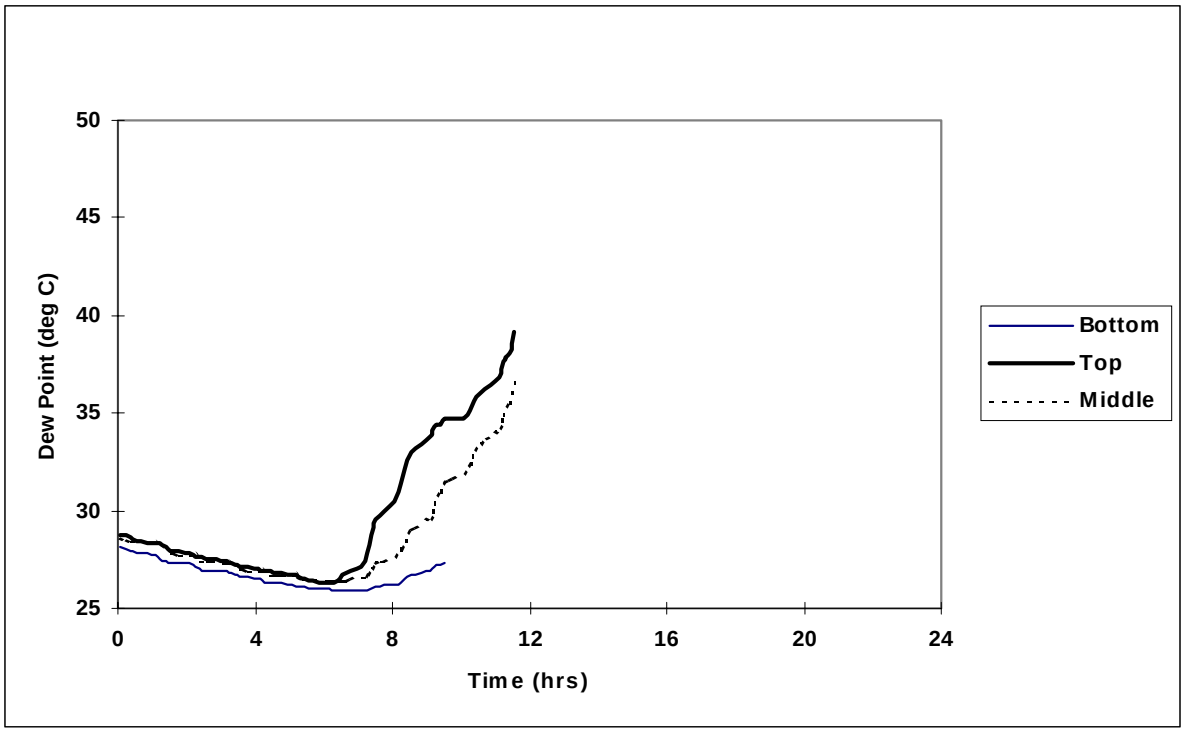

Figure E.16 Dew Point versus Time for Day 30 of I-45 Pavement.

APPENDIX F

CRACK WIDTH DATA

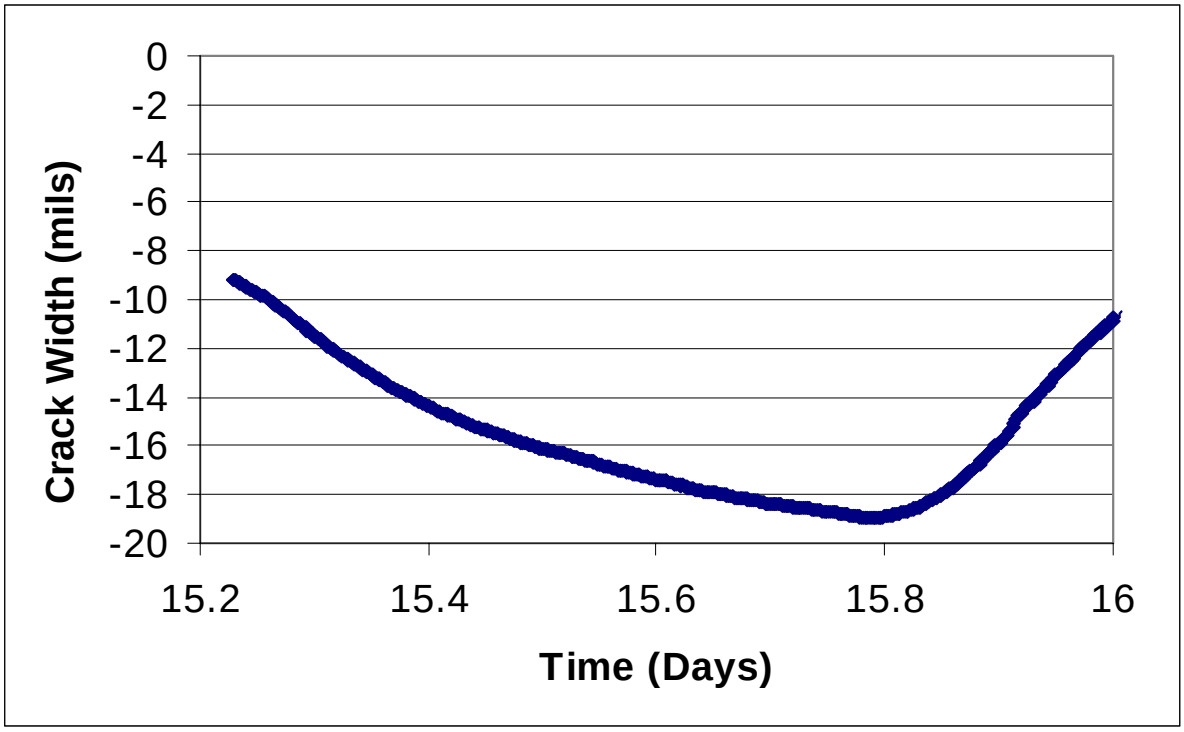

Figure F.1 Day 16 Crack Widths.

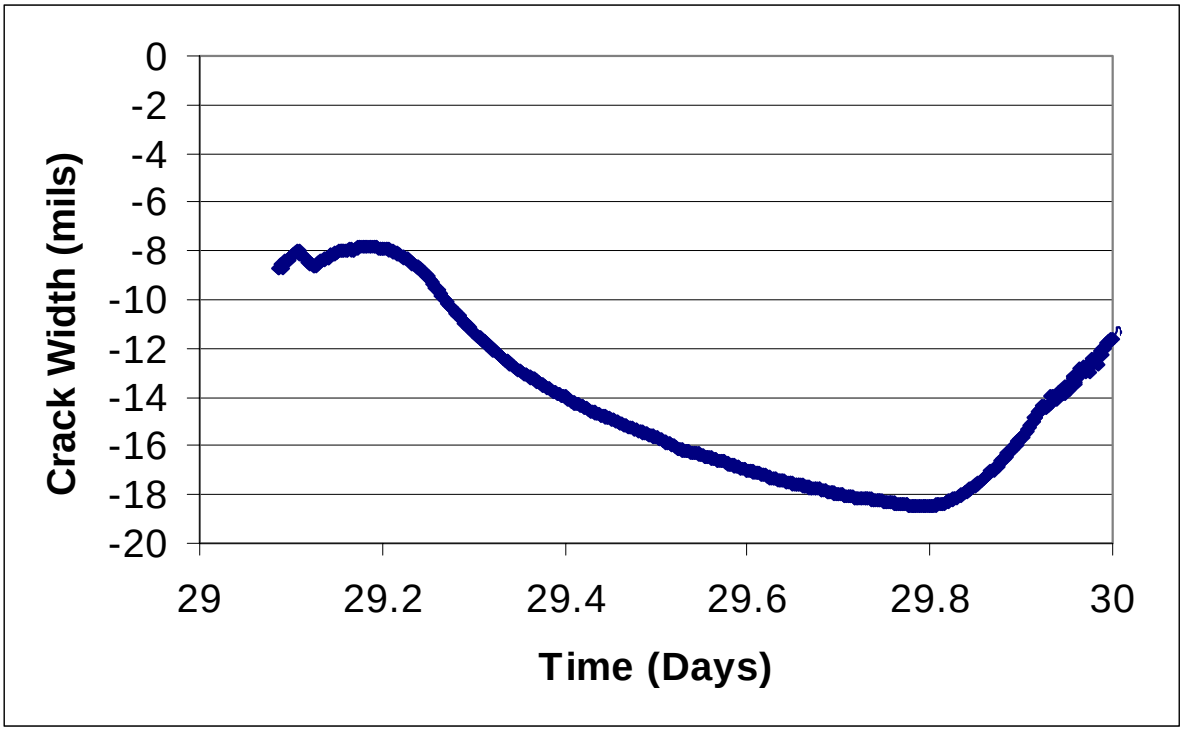

Figure F.2 Day 30 Crack Widths.